AUTONOMOUS UNIVERSITY OF SAN LUIS POTOSÍ

FACULTY OF CHEMICAL SCIENCES

CHEMICAL AND FOOD PROCESS SIMULATION LABORATORY

EXPERIMENTAL AND SIMULATION STUDY OF THE HYDROTHERMAL CARBONIZATION OF BIOMASSES FOR THE PRODUCTION OF SYNTHETIC FUELS

A thesis submitted in fulfillment of the requirements for the degree of doctor of philosophy in chemical engineering sciences

by

MSc. DIAKARIDIA SANGARÉ

THESIS DIRECTORS:

DR. MARIO MOSCOSA SANTILLÁN

DR. STÉPHANE BOSTYN

FACULTAD DE CIENCIAS QUÍMICAS

SAN LUIS POTOSI, JULY 2021

UNIVERSIDAD AUTÓNOMA DE SAN LUIS POTOSÍ

FACULTAD DE CIENCIAS QUÍMICAS

LABORATORIO DE SIMULACIÓN DE PROCESOS QUÍMICOS Y ALIMENTARIOS

ESTUDIO EXPERIMENTAL Y SIMULACIÓN DE LA CARBONIZACIÓN HIDROTÉRMICA DE BIOMASAS PARA LA PRODUCCIÓN DE COMBUSTIBLES SINTÉTICOS

TESIS PARA OBTENER EL GRADO DE DOCTORADO EN CIENCIAS EN INGENIERÍA QUÍMICA

PRESENTA:

M.C. DIAKARIDIA SANGARÉ

DIRECTORES DE TESIS

DR. MARIO MOSCOSA SANTILLÁN

DR. STÉPHANE BOSTYN

SAN LUIS POTOSI, S.L.P. JULIO 2021

FACULTAD DE CIENCIAS QUÍMICAS

El programa de doctorado en Ciencias en Ingeniería Química de la Universidad Autónoma de San Luis Potosí pertenece al Programa Nacional de Posgrados de Calidad (PNPC) del CONACyT, registro 00897, en el Nivel de Consolidado. Numero de registro de la beca otorgado por CONACyT: 659625/574996 y beca mixta No. 291276

Experimental and Simulation Study of the Hydrothermal Carbonization of Biomasses for the Production of Synthetic Fuels by Sangaré Diakaridia is licensed under a Creative Commons Reconocimiento-NoComercial-SinObraDerivada 4.0 Internacional License.

AUTONOMOUS UNIVERSITY OF SAN LUIS POTOSÍ

FACULTY OF CHEMICAL SCIENCES

CHEMICAL AND FOOD PROCESS SIMULATION LABORATORY

EXPERIMENTAL AND SIMULATION STUDY OF THE HYDROTHERMAL CARBONIZATION OF BIOMASSES FOR THE PRODUCTION OF SYNTHETIC FUELS

A thesis submitted in fulfilment of the requirements for the degree of Doctor of Philosophy in Chemical Engineering Sciences

by

MSc. Diakaridia Sangaré

Thesis Committee:

Dr. Mario Moscosa Santillán (FCQ-UASLP): _____

Dr. Pedro Antonio Alonso Davila (UASLP):| _____

Dr. Brent Edward Handy (FCQ-UASLP): _____

Dr. Raúl Ocampo Pérez (FCQ-UASLP): _____

Dr. Vicente Rodríguez González (IPICYT): _____

Dr. Pedro García-Alamilla (DACA-UJAT): _____

SAN LUIS POTOSI, JULY 2021

FACULTAD DE CIENCIAS QUÍMICAS

San Luis Potosí, S.L.P

12 de julio 2021

Comité Académico del Posgrado

En Ciencias en Ingenierías Químicas

Facultad de Ciencias Químicas/UASLP

Presente:

Por medio de la presente comunicamos que la tesis llevada a cabo por el alumno de doctorado de PCIQ. Diakaridia Sangaré, titulada "Experimental and Simulation Study of the Hydrothermal Carbonization of Biomasses for the Production of Synthetic Fuels", ha sido concluida y aprobada por el comité tutorial para dar inicio a los tramites correspondientes para su titulación, la cual tendrá lugar el próximo día 16 de julio a las 10:00 hrs. en CICBI (Centro de Información en Ciencias Biomédicas).

ATENTAMENTE

Dr. Mario Moscosa Santillán — Director de tesis

Dr. Raúl Ocampo Pérez — Asesor

Dr. Brent Edward Handy — Asesor

Dr. Vicente Rodríguez González — Asesor

Acknowledgement:

Praise be to ALLAH (ﷲ), the Gracious, the Merciful, the Cherisher, and Sustainer of the worlds, by whose grace this work has been done…

I have incurred many debts during the research and writing of this thesis, which I am pleased to acknowledge. This thesis would have not been possible without the support of my supervisors, colleagues, family, and friends who in different ways encouraged me and shared this long journey. To all of you, I express my sincere thanks and gratitude for helping this thesis to become a reality.

With the greatest appreciation, I acknowledge the friendship, support, insight, and guidance of my thesis supervisor, Dr. Mario Moscosa Santillán, for providing scientific consultation advice in all phases of my work and especially for his constant belief in my capabilities, being present at all times, giving me the needed strength to carry on when difficulties appeared, encouraging me to study earnestly, and for his fatherly role inside and outside of the work throughout my masters and doctoral years; Dr. Stéphane Bostyn for his advice, for being present and helping me in every way possible, for his support and valuable comments, for believing in me, and for his relentless efforts. I was blessed to work with such a researcher who has a spirit of innovation for new ideas and applications in scientific research. By their encouragement, the constant hard work inspired me to better myself and to aspire to greater heights.

In the course of my research, I called upon the resources of a few others. Dr. Iskender Gökalp is one of them. I am therefore grateful for his valuable comments, recommendations, and his kindness. Thanks also to Dr. Verónica Belandria for her patience, her dedication, for being there and helping me in many things. I also thank Dr. Raúl Ocampo, Dr. Brent Handy, Dr. Pedro Alonso, Dr. Vicente Rodríguez, Dr. Pedro García-Alamilla for his valuable observations and guidance during this time of doctoral studies.

Thanks to Dr. Agnes Chartier at the Institute of Organic and Analytical Chemistry—ICOA UMR 7311 for her collaboration. I am grateful to Dr. Marco Martín at FCQ-UASLP, and to Dr. Antonio Aragón Piña at the Institute of Metallurgy of the UASLP, for contributing their time to help me with this research. I am no less indebted to many of my professors who supported help me from the first day I set foot in Mexico-UASLP: Dr. Ma. Guadalupe Cadena, Dr. Roberto Leyva, Dr. J. Fernando Toro, Dr. Erika Padilla, Dr. Omar González and Dr. Alicia Román and my colleagues in UASLP: Alex, Anahi, Daniel, Byron, Adín, Fabbiola, Sonia, Liliana, Doris, Oscar, Chema, Eva, Leoncio, Jorge, Yadira, Paulina, Ham, César, Héctor, Liz, Ale, Brenda, Sustaita, Anahy, Mike, Karen, Virry. Thank you very much Angeles and Magda for your conversation and your help. Special thanks to Msc. Rosa Elena Delgado for her valuable comments, advice, and recommendations.

I thank my Orléans friends from different countries, who were the best of friends during my stay in Orléans: Ayoub, Yassine, Ahmad, Hajar, Xavier, Guillaume, Isabela, Jean-Noël, Ahlam, Yasser, Alaa, Fabian, Babacar, Leticia, Alka, Sharath, Sam, Lydia, Ayan, Laura, Edison, Yangang, and drs. Brahim Sarh, Benoît Grosselin, Saïd Abid, Andrea Commandini, Toufik Boushaki, Christian Chauveau,

Maxence Lailliau, Rodrigo Gastón, Abdallah Elorf, Philippe Dagaut. I doubt whether all the people of the workshop realize how much I owe them. I thank all the people of the workshop, especially Eric, Laurent, and Stéphane.

I would like to thank all the people who have been like a family during these last years, supporting and advising me, especially Dalina and her family, Heidys, Niurys, Manar, and friends who have been like brothers, especially Courtney and Kassim, thank you for your advice and support. Sincere thanks to my brothers, friends, and fellow travelers, especially Bouba and Idi, during these last 13 years. Thanks for everything. I recognize that I can be overbearing, hahaha! Also, thanks to my compatriots here in Mexico, especially Ismael, Zoumana, Marc, Abou, Aziz, Idrissa, and also those, like Raul and Therese, and their children, who have already returned to our native country.

Of course, despite the help and encouragement of others, I alone am responsible for this thesis, especially for any weaknesses that may remain.

As always, I have been buttressed by the love and solidarity of my family. Therefore, I dedicate this work to my father, my mother, my sisters, and my brothers. Without their unfailing care and support from childhood to the present, I would never have made it through this process or any of the tough times in my life. I also dedicate this work to the memory of my uncle Balla Diallo, who was a father to me; without him, this work would perhaps not have been possible. May Almighty *ALLAH (الله)* receive him in his paradise. Tremendous thanks also to my cousin-brother, especially Mama, Papi, Youssouf Otto, Bamoussa, Sahibou, and Alassane Fah for their help.

Special thanks to my friend and brother Djoukouba Doumbia, his wife Aminata Tembely, and all his family, for their advice and support, and especially their patience for putting up with me, and making my stay in Paris a journey of unforgettable experiences.

I am grateful to all the professors who contributed to my university education, especially to: Dr. Suyén Rodríguez, Dr. Benigno Labrada, Dr. Manuel Díaz Velázquez, Dr. Ana Sánchez, Dr. Rosa María, Dr. Harold Crespo, Dr. Jose Falcon, Msc. Antonio Pons, Msc. Jorge Infante, Msc. Héctor Rodríguez, and Msc. Nurian Serret. Also, thanks to all the teachers and professors who contributed to my formation in general, from primary school up to the present, starting with prof. Dissa, Lala, Mariam, S. Diallo, Gonsogo, A. Sangare, Agnes, Traore, Dao, Maiga, Tolo, and others.

This doctoral thesis has been achieved through financial support provided by CONACYT for granting scholarships No. 659624 and No. 291276 for this research. I am also grateful to ICARE-CNRS—France and the Région Centre-Val de Loire for financial support within the INFLUX project and FITe federation.

Finally, I thank everybody who was instrumental in the realization of my thesis. I even express my apology to anyone I, unfortunately, forgot to mention. Their contribution is no less appreciated. Merci, Aw ni tiɛ, اشكرك, Gracias, Thank you!

Abstract:

Renewable energies allow us to reduce our dependence on fossil fuels and greenhouse gas emissions. In this study, a suitable methodology for the conversion of wet biomass into fuels was established by using the hydrothermal carbonization process (HTC). The hydrocarbons obtained in the HTC process show better fuel properties compared to those of the raw biomasses during gasification. The use of modeling and process simulations allowed us to determine the optimum conditions for converting biomass moisture into energy. Furthermore, the simulation results show that the HTC process is economically feasible for producing hydrocarbons as pellets and could compete with bulk pine pellets.

Keyword: *Biomass, hydrothermal carbonization, synthetic fuels, gasification, hydrochar, modeling, simulation.*

Resumen:

Las energías renovables nos permiten reducir nuestra dependencia de los combustibles fósiles y las emisiones de gases de efecto invernadero. En este trabajo, se estableció una metodología adecuada para la conversión de biomasas húmedas en combustibles, utilizando el proceso de la carbonización hidrotermal (HTC). Los hidrocarbones obtenidos en el proceso de HTC mostraron mejores propiedades como combustibles en comparación con las biomasas brutas durante la gasificación. La utilización de modelado y simulaciones de proceso nos permitió encontrar las mejores condiciones de conversión de biomasa humedad en energía. Además, el resultado de la simulación mostro que el proceso de HTC es económicamente factible para producir hidrocarbones como pellet y podría competir con el pellet de pino a granel.

***Palabra clave**: Biomasa, carbonización hidrotermal, combustibles sintéticos, gasificación, hidrocarbon, modelado, simulación.*

Résumé :

Les énergies renouvelables nous permettent de réduire notre dépendance vis-à-vis des combustibles fossiles et les émissions de gaz à effet de serre. Dans ce travail, une méthodologie appropriée pour la conversion de biomasses humides en carburants a été établie en utilisant le procédé de carbonisation hydrothermale (HTC). Les hydrochar obtenus dans le procédé de l'HTC ont montré de meilleures propriétés en tant que combustibles par rapport aux biomasses brutes pendant la gazéification. L'utilisation de la modélisation et des simulations de procédés nous a permis de trouver les meilleures conditions pour la conversion de la biomasse humide en énergie. En outre, le résultat de la simulation a montré que le procédé HTC est économiquement réalisable pour produire des hydrochar sous forme de pellets et qu'il pourrait concurrencer les pellets de pin en vrac.

Mot clé : *Biomasse, carbonisation hydrothermale, carburants synthétiques, gazéification, hydrochar, modélisation, simulation.*

Table of Contents

INTRODUCTION **1**

THESIS CONTENT AND STRUCTURE **4**

Chapter1 BACKGROUND **8**

1.1. Current energy situation **8**

1.1.1. Fossil fuel 8

1.1.2. Renewable energies 10

1.1.2.1. Hydropower 10

1.1.2.2. Wind power 11

1.1.2.3. Solar power 12

1.1.2.4. Geothermal power 12

1.1.2.5. Bioenergy 13

1.2. Biomass, characteristics and their relationship with energy production **14**

1.2.1. Biomass structure and composition 15

1.2.1.1. Cellulose 17

1.2.1.2. Hemicellulose 18

1.2.1.3. Lignin 18

1.2.2. Sources of biomass 19

1.2.2.1. Agave bagasse 19

1.2.2.2. Cacao shell 21

1.2.2.3. Avocado stone 23

1.3. Biomass conversion technologies **24**

1.3.1. Biochemical conversion process 24

1.3.2. Thermochemical conversion process 25

1.3.2.1. Pyrolysis 26

1.3.2.2. Gasification 30

1.3.2.3. Combustion 31

1.3.2.4. Hydrothermal liquefaction 32

1.3.2.5. Hydrothermal carbonization 33

1.4. Fischer-Trospch process **40**

1.4.1. SFT reaction mechanism 41

1.4.1.1. Mechanism of carbides 41

1.4.1.2. Mechanism of hydroxy-carbenes 42

1.4.1.3. CO insertion mechanism 43
1.4.2. Product distribution and selectivity 44
1.5. Modeling and simulation studies of biomass conversion processes 46
1.5.1. Kinetic models 48
1.5.2. Statistical models 49
1.5.3. Computational fluid dynamics models 49
1.6. Conclusion 50
Chapter2 RESEARCH APPROACH 53
2.1. Justification 53
2.2. Hypothesis 54
2.3. Research Objectives 54
2.3.1. General objective 54
2.3.2. Specific objectives 54
2.4. Methodology of the project 55
Chapter3 CHARACTERIZATIONS OF BIOMASSES 56
3.1. Materials and methods 58
3.1.1. Feedstock 58
3.1.2. Experimental procedure 58
3.1.2.1. Determination of extractives, hemicellulose, cellulose and lignin 58
3.1.2.2. Thermogravimetric analysis (TGA/DTG) 60
3.1.2.3. Procedure of proximate analysis of biomass 61
3.1.2.4. Procedure of ultimate analysis of biomass 63
3.1.2.5. Procedure of heating value 63
3.1.2.6. Particle size distribution of biomass 64
3.1.3. Biomass microstructures and chemical composition 65
3.1.3.1. Fourier transform infrared (FTIR) 65
3.1.3.2. Scanning Electron microscopy (SEM) pending experiment 65
3.1.4. Thermophysical properties of biomass 65
3.1.4.1. Heat capacity measurement 65
3.1.4.2. Thermal conductivity 66
3.1.4.3. Density 68
3.2. Results and Discussion 69
3.2.1. Compositional analysis of biomasses: Extractible, hemicellulose, cellulose and lignin 69

3.2.2. Thermogravimetric analysis (TGA) 73
3.2.3. Proximate and ultimate analysis results 75
3.2.4. Heating value 77
3.2.4.1. Experimental HHV analysis 77
3.2.4.2. Correlation based on proximate analysis 78
3.2.4.3. Correlation based on ultimate analysis 81
3.2.4.4. Correlations based on chemical analysis 83
3.2.5. Fourier transform infrared (FTIR) analysis 84
3.2.6. Scanning electron microscopy (SEM) analysis 86
3.2.7. Thermophysical properties analysis of biomass 87
3.3. Conclusion 91
Chapter4 HYDROTHERMAL CARBONIZATION OF BIOMASSES 93
4.1. Experimental Procedure 94
4.1.1. HTC reactor description and types of reactors used 94
4.1.1.1. Reactor operating in a closed-loop system (non-stirred reactor) 94
4.1.1.2. Reactor operating in an open -loop system (stirred reactor) 96
4.1.2. The operational conditions of the different HTC studies 98
4.1.3. Hydrochar characterization procedure 99
4.1.4. Tar contents in hydrochar, extraction of tar and GC–MS analysis 100
4.1.4.1. Tar contents extraction by Soxhlet extractor 100
4.1.4.2. GC–MS analyzer for the main components of tar in hydrochar. 102
4.1.4.3. PAHs compounds analysis by GC–MS analyzer 103
4.1.5. Kinetic models and mechanisms of hydrochar formation 103
4.1.5.1. Model-free methods 106
4.1.5.2. Model-fitting methods 107
4.1.5.3. Kinetic reaction mechanism models 108
4.1.6. Methods of HTC liquid quantification 109
4.1.6.1. Total organic carbon content (TOC) 109
4.1.6.2. High-performance liquid chromatography 110
4.1.6.3. Ultraviolet–visible spectroscopy 113
4.1.6.4. Determination of total sugars using UV-VIS 114
4.1.7. Methods of HTC gases quantification 115
4.1.7.1. HTC gas recovery 115
4.1.7.2. Gas chromatography (GC) 116

4.1.7.3. Quantification of non-condensable gases produced during HTC 117
4.1.7.4. Heat of HTC reaction measurements 118
4.2. Results and Discussion 119
4.2.1. Reactor Control System 119
4.2.1.1. Open-loop Control System 120
4.2.1.2. Closed-loop control system 121
4.2.1.3. Calibration of reactor operating in an open-loop system 122
4.2.2. Effect of operating conditions on the HTC process 126
4.2.2.1. Effect of reaction temperature 127
4.2.2.2. Effect of holding time 128
4.2.2.3. Effect of biomass-to-water ratio 130
4.2.3. Characterization and analysis of the chemical composition of hydrochar 132
4.2.3.1. FTIR of hydrochars 132
4.2.3.2. SEM of hydrochars 134
4.2.4. Evolution of hydrochar mass yield with HTC temperature. 137
4.2.4.1. HTC reactor heat-up and reaction time 138
4.2.4.2. Hydrochar mass yield or total solid yield analysis 138
4.2.4.3. Hydrochar mass yield and derivative mass yield analysis using different heating rates 140
4.2.4.4. Tar content and analysis 143
4.2.4.5. Analysis of the kinetic studies of hydrochar formation 149
4.2.5. Higher heating value of biomasses and hydrochars 157
4.2.6. Analysis of the main products in the HTC liquid phase 159
4.2.6.1. Quantification of main compounds in biocrude produced 159
4.2.7. Effect of biomass-to-water ratio and heat of HTC reaction 166
4.2.7.1. Temperature profiles inside the HTC reactor 166
4.2.7.2. Heat of reaction 169
4.2.7.3. Pressure profiles inside the HTC reactor 170
4.2.8. Gas by-products 172
4.3. Conclusion 173
Chapter5 THERMOCHEMICAL CONVERSION OF DRY BIOMASS 175
5.1. Materials and methods 178
5.1.1. Experimental setup and procedure. 178
5.1.2. Analytical methods. 179

5.1.3. Pyrolysis and gasification reactions 179
5.1.4. Estimation of gasification performance 181
5.1.5. Kinetic analysis 182
5.1.5.1. Theoretical consideration 182
5.1.5.2. Kinetic models for non-isothermal decomposition 184
5.2. Results and discussion 187
5.2.1. Pyrolysis of biomasses: Overall product distribution 187
5.2.1.1. Influence of pyrolysis temperature on char product 188
5.2.1.2. Influence of pyrolysis temperature on bio-oil product 189
5.2.1.3. Influence of pyrolysis temperature on gas product 190
5.2.2. Main pathways of lignocellulosic biomass pyrolysis reactions and their products 190
5.2.2.1. Main pathways of cellulose pyrolysis reactions and their products 191
5.2.2.2. Main pathways of hemicellulose pyrolysis reactions and their products 194
5.2.2.3. Main pathways of lignin pyrolysis reactions and their products 197
5.2.3. Analysis of the gaseous products of biomass pyrolysis 200
5.2.3.1. Online analysis of the gaseous products of biomass pyrolysis 200
5.2.3.2. Pyrolysis gas yield analysis 205
5.2.4. Analysis of the gas products during pyro-gasification of ASB 207
5.2.4.1. Effect of air to biomass ratio on the gas product evolution 207
5.2.4.2. Effect of air to biomass ratio on pyro-gasification performance 211
5.2.4.3. Influence of heating rate on pyro-gasification performance 212
5.2.5. Influence of biomass type on the pyro-gasification products 215
5.2.5.1. Effect of biomass type on gas evolution 215
5.2.5.2. Effect of biomass type on pyro-gasification performance 217
5.2.6. Comparison between hydrochar and raw biomass gasification. 221
5.2.7. Kinetic analysis of pyrolysis 224
5.2.8. Kinetic analysis of AS pyrolysis 224
5.2.8.2. Kinetic analysis of ASB pyrolysis 227
5.2.8.3. Flynn-Wall-Ozawa (FWO) method 227
5.2.8.4. Friedman method 228
5.2.8.5. Kinetic analysis of CS pyrolysis 229
5.2.8.6. Kinetic analysis of CEL pyrolysis 231
5.2.8.7. Kissinger-Akahira-Sunose (KAS) method 232
5.3. Conclusion 237

Chapter6 MODELLING AND CFD SIMULATION.....240
6.1.1. Kinetics models.....240
6.1.2. Statistical models.....241
6.1.3. Numerical simulation model.....241
6.2. Computational modeling and simulation methodology.....242
6.2.1. Kinetics models of intermediate product formation by HTC.....242
6.2.1.1. Reaction pathways and kinetics of intermediate product formation.....242
6.2.1.2. Kinetic model for the formation of the main intermediate compounds.....244
6.2.1.3. Parameter determination by optimization techniques.....246
6.2.2. Modeling of the HTC conversion using Doehlert experimental design.....247
6.2.2.1. Design of experiments approach to model and optimize the HTC process.....247
6.2.2.2. Experimental matrix of the Dohlert design (DoE).....248
6.2.2.3. Optimization of the HTC conversion of ASB using a Doehlert experimental design 250
6.2.2.4. Characteristic combustion temperatures.....251
6.2.3. Criteria to determine HTC performances.....252
6.2.4. Computational Fluid Dynamics (CFD) approach and methodology.....252
6.2.4.1. Geometry.....252
6.2.4.2. Governing Equations: conservation of momentum, mass, and energy.....254
6.2.4.3. Spatial discretization (mesh).....260
6.2.4.4. Solver settings.....261
6.2.4.5. Stirred reactor hydrodynamic simulations.....261
6.3. Results and Discussion.....263
6.3.1. Kinetic model results of intermediate product formation by HTC.....263
6.3.1.1. Results of optimized kinetic parameters of HTC.....264
6.3.1.2. Model predictions.....267
6.3.2. Experimental design models results: Doehlert.....272
6.3.2.1. Raw biomass characterization.....272
6.3.2.2. Thermal behavior (TG/DTG) of raw ASB and hydrochars.....273
6.3.2.3. FTIR of raw ASB and hydrochars produced.....274
6.3.2.4. Ultimate analyses models.....276
6.3.2.5. Van-Krevelen diagram analysis.....277
6.3.2.6. Proximate analyses models.....279
6.3.2.7. Combustion characteristics.....286

6.3.3. Computational Fluid Dynamics (CFD) modelling results 290
6.3.3.1. Mesh independence study 292
6.3.3.2. Hydrodynamics 295
6.3.3.3. Heat transfer study results 301
6.4. Conclusion 308
Chapter7 PROCESS SIMULATION OF BIOMASS CONVERSION 310
7.1.1. Types of process simulators 311
7.1.1.1. Sequential modular simulators 312
7.1.1.2. Simultaneous simulators 313
7.1.1.3. Hybrid simulators 313
7.1.2. Aspen Plus® and Aspen HYSYS® 314
7.2. Process simulation strategy 315
7.2.1. Description of hydrothermal carbonization simulation process 316
7.2.2. General description of the biomass gasification process 316
7.2.3. Description of the Fischer Tropsch synthesis process 318
7.2.4. Calculation procedure 318
7.2.4.1. Main assumptions for the simulation 318
7.2.4.2. Simulation procedure in Aspen Plus® 319
7.2.4.3. Char gasification reaction 325
7.2.4.4. Simulation procedure in Aspen HYSYS® 332
7.3. Discussion of simulation results 338
7.3.1. Simulation results of HTC process 338
7.3.2. Simulation results of the gasification process 339
7.3.2.1. Validation of the simulation result 339
7.3.2.2. Effect of air/biomass ratio during the gasification process. 342
7.3.2.3. Effect of residence time in the gasifier 343
7.3.3. Simulation results of Fischer-Tropsch synthesis 344
7.3.3.1. Effect of H_2/CO ratio on product selectivity. 345
7.4. Conclusion 349
Chapter8 ENERGY BALANCE 350
8.1. Materials and methodology 351
8.1.1. Design of the current HTC process at laboratory scale. 351
8.1.1.1. Energy consumption of the HTC process in laboratory 352
8.1.1.2. Usable energy from hydrochar 354

8.1.1.3. Carry out of HTC experiments....354
8.1.2. Energy balance of the HTC process at laboratory scale....354
8.2. Results and discussion....354
8.2.1. Energy balance results of the HTC process at laboratory scale....354
8.3. Plant design of the HTC process at industrial scale....356
8.3.1. Process modelling and simulation....356
8.3.1.1. Agitator....359
8.3.1.2. Pumps....359
8.3.1.3. Heat exchanger (heater)....360
8.3.1.4. Reactor....360
8.3.1.5. Heat exchanger (condensers)....360
8.3.1.6. Filter....361
8.3.1.7. Dryer....361
8.3.1.8. Pelletizer....361
8.3.1.9. HTC liquid composition....361
8.3.1.10. Biogas production estimation....362
8.3.2. Criteria to determine HTC performances....362
8.3.2.1. HTC process energy efficiency....364
8.3.2.2. Thermal efficiency....364
8.3.3. Economic feasibility of HTC process....365
8.3.3.1. Investment costs....365
8.3.3.2. Estimated total capital or total investment....366
8.3.3.3. Estimation of revenue....370
8.3.3.4. Cash flow calculations....372
8.3.3.5. Economic indicators....375
8.4. Conclusion....381
GENERAL CONCLUSIONS AND PERSPECTIVES....382
Conclusion....382
Perspectives and recommendations....384
REFERENCES....386
Publication of scientific papers....421

List of Figures:

Figure 1-1: Global primary energy consumption by different sources (Looney, 2020) 8

Figure 1-2: CO_2 Emissions from fuel combustion 1970-2019 (Braun, 2020). 9

Figure 1-3: The main components and structure of lignocellulose (Isikgor and Becer, 2015; Rubin, 2008) 16

Figure 1-4: The primary structure of cellulose. 18

Figure 1-5: The structure of xylan (Hemicellulose). 18

Figure 1-6: Chemical structures used to construct the lignin polymer. 19

Figure 1-7: *Agave salmiana* plant, piñas and bagasse 20

Figure 1-8: Global cacao bean production in 2018/19 to 2020/21 (Shahbandeh, 2021). 22

Figure 1-9: Parts of cocoa beans (Okiyama et al., 2017)) 22

Figure 1-10: Thermochemical conversion processes and end products (Pandey et al., 2015). 25

Figure 1-11: TGA curves of rice husks, cellulose, hemicellulose and lignin (Cheng et al., 2018) 28

Figure 1-12: HTC reaction pathways for lignocellulosic biomass (Reza et al., 2014a)) 35

Figure 1-13: Mechanism of carbides (Fischer and Tropsch, 1926) 42

Figure 1-14: Mechanism of hydroxy-carbenes (Kummer et al., 1948). 42

Figure 1-15: CO insertion mechanism (Pichler and Schulz, 1970). 43

Figure 1-16: SFT reaction mechanism proposed by Dry (1996) 44

Figure 1-17: Diagram of the distribution and selectivity of the product proposed by Anderson et al. (1958) 44

Figure 1-18: Distribution of products as a function of parameter α (Rojas et al., 2011). 45

Figure 3-1: Diagram of the STA 449 F3 Jupiter® - NETZSCH analyzer used in ICARE-CNRS. 60

Figure 3-2: TG Analysis program 61

Figure 3-3: Simplified diagram of a calorimetric bomb 63

Figure 3-4*:* Measurement apparatus of thermal conductivity and diagram of in cross-section 68

Figure 3-5*:* Pycnometer 69

Figure 3-6. (a) TG and (b) DTG curves of biomasses 73

Figure 3-7. FTIR spectra of raw biomass of CS, ASB, AS, and CEL. 85

Figure 3-8. Scanning electron microscopy (SEM) images of raw AS 86

Figure 3-9. Scanning electron microscopy (SEM) images of raw AS 87

Figure 4-1: HTC experimental apparatus 95

Figure 4-2: Clamping and opening system for the 50 mL non-agitated autoclave reactor 96

Figure 4-3: Experimental apparatus of the stirred reactor 97

Figure 4-4: Conventional Soxhlet extractor 101

Figure 4-5: Trace Ultra-ISQ gas chromatograph - mass spectrometer Thermo Scientific (ICOA-UMR7311) 102

Figure 4-6: Trace Ultra-ISQ gas chromatograph - mass spectrometer Agilent technologies 70000C (ICARE-UPR3021-CNRS). 103

Figure 4-7: Calibration line for the determination of TOC 109

Figure 4-8: Schematic representation of an HPLC unit. 110

Figure 4-9: Calibration lines for furfural (retention time = ~17 min), and 5-HMF (retention time = 9.5 min), and acetic acid (retention time = ~6.8 min) 112

Figure 4-10: Calibration line for the determination of total phenolic compounds by the Folin-Cioacalteu method 114

Figure 4-11: Calibration line for the determination of total sugars compounds by Anthrone method 114

Figure 4-12: Gas bag to recover HTC gas 115

Figure 4-13: HTC gas analysis system in micro-GC 117

Figure 4-14: Schematic representation of the open-loop control system 120

Figure 4-15: Schematic representation of the closed-loop control system 121

Figure 4-16: The temperature profiles inside the reactor (a): Top, (b): Bottom at power supplied in the reactor from room temperature to equilibrium temperature. 123

Figure 4-17: Dynamic process response to an HTC step test 124

Figure 4-18: Calibration of power with temperature inside the reactor 126

Figure 4-19: Effect of reaction temperature on the distribution of HTC products (for biomass-to-water ratio=1/10 and holding time =0 min, stirred speed 550 rmp) 127

Figure 4-20: Effect of holding time on the distribution of HTC products (for biomass-to-water ratio B/W=1/10 and temperature = 230 ºC, stirred speed 550 rmp) 129

Figure 4-21: Effect of biomass-to-water ratio on the distribution of HTC products (for holding time =0 min and reaction temperature = 230 ºC, stirred speed 550 rmp) 131

Figure 4-22: FT-IR spectra of AS and hydrochars. 132

Figure 4-23: FT-IR spectra of CS and hydrochars. 134

Figure 4-24: SEM images of (**a)** raw AS, and (**b-f)** hydrochars 135

Figure 4-25: SEM images of (**a)** raw CS, and (**b-f)** hydrochars 137

Figure 4-26: Temperature trends vs. time of hydrothermal tests, **(a)** conducted at 200W to set-point temperature, (**b)** different powers (heating rate) from ambient temperature to 250 °C. 138

Figure 4-27: Mass yields of hydrochar or total solids as a function of temperature at B/W=1/10 and a power of 200 W 139

Figure 4-28: Hydrochar yield (Y_{HC}) curves of various powers (heating rates) of 160, 200 and 240W, (a) AS and (b) CS. 141

Figure 4-29: Derivative hydrochar yield (DY_{HC}) curves of various powers (heating rates) of 160, 200 and 240W, (**a**) AS and (**b**) CS. 142

Figure 4-30: The main aliphatic compounds detected in the tar solution removed in the hydrochar structure and raw AS. 145

Figure 4-31: The main aliphatic compounds detected in the tar solution removed in the hydrochar structure and raw CS 146

Figure 4-32: The main PAHs compounds detected in the tar solution removed in the hydrochar structure and raw AS. 148

Figure 4-33: The dependence of Eα on the degree of conversion (α) for HTC process of (a) AS and (b) CS according to FWO, KAS, and Friedman model-free kinetics methods 152

Figure 4-34: Eα values according to the degree of conversion (α) for HTC process of AS from 210 °C to 250 ºC according to the FWO and KAS methods. 153

Figure 4-35: Comparison of kinetic parameters from model-fitting methods for AS of temperature between 150 and 210ºC 156

Figure 4-36: Comparison of kinetic parameters from model-fitting methods for CS of temperature between 150 and 230ºC 156

Figure 4-37: Comparison of kinetic parameters from model-fitting methods for AS of temperature between 210 and 250ºC 157

Figure 4-38. Effect of temperature on HHV of hydrochars..... 158

Figure 4-39. Effect of temperature on the main components in the liquid phases during HTC of the 3 biomasses: (a) TOC; (b) Sugars; (c) Furfural; (d) 5-HMF. (means and standard deviations, n = 3). .160

Figure 4-40. Effect of temperature on the main components in biocrude during HTC of the 3 biomasses (means and standard deviations, n = 3): (a) Formic acid; (b) Lactic acid; (c) Acetic acid; (d) Polyphenols. 162

Figure 4-41: The influence of holding time on the stability of 5-HMF in HTC of AS..... 163

Figure 4-42: The influence of holding time on the stability of furfural in HTC of AS..... 163

Figure 4-43: The influence of holding time on the stability of formic acid in HTC of AS 164

Figure 4-44: The influence of holding time on the stability of lactic acid in HTC of AS 164

Figure 4-45: The influence of holding time on the stability of formic acid in HTC of AS 165

Figure 4-46: The influence of holding time on the stability of sugar in HTC of AS 165

Figure 4-47: The influence of holding time on the stability of polyphenols in HTC of AS 166

Figure 4-48: Temperature profile inside the reactor: a) T_{Top}, b) T_{Bottom} versus heating time of HTC process (pure water, B/W: 1/10, 1/8, 1/6, and 1/4)..... 167

Figure 4-49: Temperature profile inside the reactor: a) T_{Top}, b) T_{Bottom} versus heating time of HTC process (pure water, B/W: 1/10, 1/8, 1/6, and 1/4) after isolation..... **Error! Bookmark not defined.**

Figure 4-50: Pressure profile inside the reactor and heating time of HTC process (water, biomass-to-water ratio (B/W): 1/10, 1/8, 1/6, and 1/4). 171

Figure 5-1: Scheme of the TG/μ-GC setup used in this work..... 178

Figure 5-2: The main pathways of cellulose pyrolysis reactions and their products: 193

Figure 5-3: The main pathways of Hemicellulose(xylan) pyrolysis reactions and their products..... 196

Figure 5-4: The main pathways of lignin pyrolysis reactions and their products 199

Figure 5-5: TGA and release profile of the gas products during the AS pyrolysis with temperature for 10 ºC/min..... 202

Figure 5-6: TGA and release profile of the gas products during the ASB pyrolysis with temperature for 10 ºC/min..... 203

Figure 5-7: TGA and release profile of the gas products during the ASB pyrolysis with temperature for 10 ºC/min..... 203

Figure 5-8: TGA and release profile of the gas products during the CS pyrolysis with temperature for 10 ºC/min..... 204

Figure 5-9: The total gas yields produced during the pyrolysis of biomasses. 206

Figure 5-10: Online and offline comparison of gas yield products: a) CEL, b) ASB..... 207

Figure 5-11f: The effect of the air/biomass ratio (ABR) on the evolution of the online gaseous products during pyro-gasification (heating rate 40 ºC/min ABR=1.0) 210

Figure 5-12: Effect of heating rate on gas yield during the pyro-gasification of ASB for ABR=0.50. 214

Figure 5-13d: The effect of CEL evolution of the online gaseous products during pyro-gasification (heating rate 40 ºC/min and ABR=0.1875) 217

Figure 5-14c: characteristic of gas product of CEL gasification between hydrochar and raw biomass 222

Figure 5-15: FWO-model plots of AS pyrolysis at different values of conversion (**a**) and activation energy vs conversion **(b**) 225

Figure 5-16: KAS-model plots of AS pyrolysis at different values of conversion (**a**) and activation energy vs conversion **(b**) 226

Figure 5-17: Friedman-model plots of AS pyrolysis at different values of conversion (**a**) and activation energy vs conversion **(b**) 227

Figure 5-18: FWO-model plots of ASB pyrolysis at different values of conversion (a) and activation energy vs conversion (b).....227

Figure 5-19: KAS-model plots of ASB pyrolysis at different values of conversion (**a**) and activation energy vs conversion **(b**) 228

Figure 5-20: Friedman-model plots of ASB pyrolysis at different values of conversion (**a**) and activation energy vs conversion **(b**).....229

Figure 5-21: FWO-model plots of CS pyrolysis at different values of conversion (a) and activation energy vs conversion (b).....230

Figure 5-22: KAS-model plots of CS pyrolysis at different values of conversion (a) and activation energy vs conversion (b).....230

Figure 5-23: Friedman-model plots of CS pyrolysis at different values of conversion (a) and activation energy vs conversion (b).....231

Figure 5-24: FWO-model plots of CEL pyrolysis at different values of conversion (a) and activation energy vs conversion (b).....232

Figure 5-25: KAS-model plots of CEL pyrolysis at different values of conversion (a) and activation energy vs conversion (b).....233

Figure 5-26: Friedman-model plots of CEL pyrolysis at different values of conversion (a) and activation energy vs conversion (b).....233

Figure 6-1: Proposed reaction pathway of hydrothermal conversion of biomass 243

Figure 6-2: Spatial distribution of the experimental points in a Doehlert design (a) for 2 (points 1–7) and 3 (points 1–13) factors; (b) cross section projection of the initial sphere (Araujo and Janagap, 2012). 248

Figure 6-3: Graphical representation of Doehlert design for two-factor optimization.....249

Figure 6-4: Stirred reactor geometry details schematic 253

Figure 6-5 : The reactor geometry **a**) experimental **b**) CFD domain 253

Figure 6-6b. Calculated (continuous curves) and experimental (discrete points) concentration evolution of the HTC intermediates of ASB at 210 ºC.....268

Figure *6-7*. Calculated (continuous curves) and experimental (discrete points) concentration evolution of the HTC intermediates of AS at 210 ºC 270

Figure *6-8*. Calculated (continuous curves) and experimental (discrete points) concentration evolution of the HTC intermediates of AS at 210 ºC 271

Figure 6-9: a) TG and **b**) DTG curves for raw ASB and hydrochars obtained 273

Figure 6-10: FTIR spectra raw ASB and hydrochar obtained 274

Figure 6-11: The main effect and 2D contour plots of temperature (X_1) and holding time (X_2) on the oxygen (a,c) and carbon (b,d) 277

Figure 6-12: Van Krevelen diagram of raw ASB and hydrochars obtained 278

Figure 6-13: 2D contour plots showing the effects of temperature (X_1) and holding time (X_2) on: a) H/C, b) O/C 279

Figure 6-14: Main effects of temperature (X_1) and holding time (X_2) on **a)** HHV, **b)** fixed carbon, **c)** volatile matter, and **d)** mass yield of hydrochar produced 281

Figure 6-15: Pareto chart of standardized effects of Temperature (X_1) and holding time (X_2) on: a) HHV, b) fixed carbon, c) volatile matter and d) mass yield. 282

Figure *6-16*: 2D contour plots showing the effects of temperature (X_1) and holding time (X_2) on HHV 283

Figure 6-17: 2D contour plots showing the effects of temperature (X_1) and holding time (X_2) on FC 283

Figure 6-18: 2D contour plots showing the effects of temperature (X_1) and holding time (X_2) on FC 284

Figure 6-19: 2D contour plots showing the effects of temperature (X_1) and holding time (X_2) on VM 285

Figure 6-20: 2D contour plots showing the effects of temperature (X_1) and holding time (X_2) on energy yield 285

Figure 6-21: 2D contour plots showing the effects of temperature (X_1) and holding time (X_2) on ignition temperature (Ti) 288

Figure 6-22: 2D contour plots showing the effects of temperature (X_1) and holding time (X_2) on the temperature at the point of the maximum weight loss rate (Tm) 289

Figure 6-23: 2D contour plots showing the effects of temperature (X_1) and holding time (X_2) on the burnout temperature (Tb) 290

Figure 6-24: Meshed hydrodynamic domain for mesh independence study 293

Figure 6-25: Meshed hydrodynamic domain for mesh independence study 294

Figure 6-26: Effect of number of mesh elements on: a) average velocity of the dispersed phase, b) average temperature at 480 min of holding time and CPU time 295

Figure 6-27: The effect of the stirring rate on the volume fraction φb=0.1375: **a-d**) r-z plane defined by the angular coordinate θ = 0° and **e-h**) r-θ plane defined at the top of the impeller for z=21mm.. 296

Figure 6-28: Comparisons of a) Axial velocity for z=21mm and b) tangential velocity for θ=0° in this simulation with previous works 297

Figure 6-29: Distribution of turbulent flow velocity induced in a, b) r–z plane for θ = 0° and c, d) r–θ plane on the impeller top for z=21mm, and N=550 rpm 298

Figure 6-30: Two-phase CFD simulation of volume fraction φ_b=0.1375 on water: the rheological distribution: **a-d**) induced in the r-z plane defined by the angular coordinate θ = 0° and **e-h**) in the r-θ plane defined at the top of the impeller for z=21mm, and N=550 rpm 299

Figure 6-31: Biomass particles distributions inside the reactor: Experimental comparison and CFD simulation using particle tracing, for biomass-water-ratio ¼ and N=550 rpm 300

Figure 6-32: Determination of the heat-transfer coefficient between the insulator and the environment 301

Figure 6-33: Comparison of simulated and experimental data using the thermal properties of biomass 302

Figure 6-34d: Temperature profiles and relative mass yield on different HTC products, using the reaction heat of reaction for φ_b=0.1375 306

Figure 6-35: The temperature, velocity and volume fraction evolution contour 307

Figure *7-1*: Block diagram of synthetic fuels production process.....315

Figure 7-2: Simulation HTC model flowchart with Aspen Plus®.....323

Figure 7-3: Schematic diagram of moving bed biomass gasifier 324

Figure 7-4: Simulation model flowchart with Aspen Plus®.....330

Figure 7-5: The mole fraction of the chain growth probability as a function of the n carbon atoms. 334

Figure 7-6: The selectivity of the catalytic reaction products of the Fischer Tropsch synthesis. 335

Figure 7-7: Simulation model flowchart with Aspen HYSYS®. 337

Figure 8. Simulated (continuous curves) and experimental (discrete points) concentration evolutions of biomasses during HTC process of AS. 339

Figure 7-9: Comparison between simulation and experimental results for ASB. 340

Figure 7-10: Comparison between simulation and experimental results for CS. 340

Figure 7-11: Comparison between simulation and experimental results for AS.....341

Figure 7-12: Effect of air/biomass ratio during the ASB gasification for residence time 15s. 343

Figure 7-13: Effect of residence time during the ASB gasification for ABR=0.187. 344

Figure 7-14: Synthetic fuels obtained in the Fischer Tropsch reactor for H_2/CO =0.88: a) main products and b) CO, H_2 unreacted and H_2O product. 345

Figure 7-15: Effect of H_2/CO ratio on synthetic fuels product.....346

Figure 7-16: Synthetic fuels obtained in the Fischer Tropsch reactor for H_2/CO =2.5: a) main products and b) CO, H_2 unreacted and H_2O product. 346

Figure 8-1: Schematic flowsheet of the HTC process at laboratory scale.....352

Figure 8-2: Estimated hydrochar energy (QHC) and energy consumed (QU) as a function of biomass/water ratio.....356

Figure 8-3: Schematic flow sheet of the HTC process an industrial scale 358

List of Tables:

Table 1-1: Summary of the different pyrolysis modes with their process conditions and product distribution. 29

Table 1-2: Advantages and limitations of biomass conversion process models. 48

Table 3-1: Extractives, hemicellulose, lignin and cellulose content of the different biomasses used. 70

Table 3-2: Characteristics and chemical composition of biomasses. 76

Table 3-3: Equations that correlate HHV with proximate analysis. 79

Table 3-4: HHV estimation by proximate analysis correlation 80

Table 3-5: Equations that correlate HHV with ultimate analysis. 81

Table 3-6: HHV estimation by ultimate analysis correlation 82

Table 3-7: Equations that correlate HHV with chemical analysis 83

Table 3-8: HHV estimation based on chemical analysis 84

Table 3-9: Heat capacity and thermal conductivity of avocado stone and hydrochars 88

Table 4-1: Expressions for functions f(α) and g(α) of some reaction models to describe thermal decomposition solid state reactions (Jayaraman et al., 2017; Mishra et al., 2015; Papari and Hawboldt, 2015; Yao et al., 2020). 105

Table 4-2: The characteristics values of a regulated signal at different powers (Bottom temperature) 124

Table 4-3: The characteristics values of a regulated signal at different powers (Top temperature) 125

Table 4-4: The temperature of the equilibrium and the time required to reach it, from the power supplied. 125

Table 4-5: The tar removed in the structure of the hydrochars at different HTC temperatures. 144

Table 4-6: main aliphatic components detected in the tar solution. 147

Table 4-7: Kinetic parameters of AS and CS determined by the model-free kinetics methods. 151

Table 4-8: Kinetic parameters of AS determined by model-fitting method in HTC process for AS and CS 155

Table 4-9: Equilibrium temperature reached at the top and bottom 168

Table 4-10: Equilibrium temperature reached at the UP and down after insulation 168

Table 4-11: Experimental results for the heat of reaction of hydrothermal carbonization of Avocado Stone 170

Table 4-12: Pressure behavior at different equilibrium temperature reached 171

Table 4-13: HTC gas composition at 250 ºC, B/W=1/10 172

Table 5-1: Major gas-phase and gas-solid reactions during biomass pyro-gasification (Acar and Böke, 2019; Hai et al., 2019; Widyawati et al., 2011). 180

Table 5-2: Overall product distribution of biomasses pyrolysis 188

Table 5-3: Pyrolysis gas product of biomasses 204

Table 5-4: Product gas analysis and gasifier performance of ASB at 40 ºC/min. 211

Table 5-5: The ASB gasification performance at ABR=0.5 215

Table 5-6: Effect of biomass type on pyro-gasification performance for (40 ºC/min and ABR=0.1875) 220

Table 5-7: Kinetic parameters calculated for AS by three isoconversional methods. 234
Table 5-8: Kinetic parameters calculated for ASB by three isoconversional methods. 235
Table 5-9: Kinetic parameters calculated for CS by three isoconversional methods. 235
Table 5-10: Kinetic parameters calculated for CEL by three isoconversional methods. 236
Table 6-1 : Experimental matrix of the Doehlert design 249
Table 6-2: N_{Re} values at different rotation frequency and different biomass water ratio 262
Table 6-3: Optimized parameter results (SSE and R^2) at set temperatures for the three biomasses .. 265
Table 6-4: Reaction rate constants (ki) for the simplified reaction pathway proposed. 266
Table 6-5: Arrhenius model parameters for the reaction pathway at 210 ºC, 230 ºC and 250 ºC. 267
Table 6-6: Proximate, ultimate, chemical structure analysis, and HHV characteristics of ASB 272
Table 6-7: Fuel characteristics and chemical composition of hydrochars. 276
Table 6-8: Doehlert matrix design responses for Temperature (X_1) and holding time (X_2) effects. .. 280
Table 6-9: Characteristic temperatures and parameters on the combustion of raw ASB and hydrochars, at different HTC X_1 and X_2 287
Table 6-10: Autoignition temperatures of ASB and hydrochars, at different HTC $X_1$and X_2 289
Table 6-11: The values used for the kinetic study 304
Table 7-1: Ultimate and immediate analysis of biomasses 320
Table 7-2: Expressions of ϕ for different size of biomass particle 326
Table 7-3: Parameters for kinetics of reactions **Eq. (7-25)** and **(7-26)** (Wen and Chaung, 1979) ... 327
Table 7-4: Function of Each Block 329
Table 7-5: Values of the pre-exponential factor and energy of activation for the kinetic constants of the Fischer-Tropsch reaction 335
Table 7-6: Main simulation units and their operating conditions 336
Table 8-1 : Energy balance of the AS HTC process in the laboratory. 355
Table 8-2 : Electrical energy demand during the AS HTC process. 363
Table 8-3 : Capital cost estimate of bare-module equipment for the HTC plant 366
Table 8-4 : Estimated Fixed Capital Investment 367
Table 8-5: Estimated income for different scenarios 370
Table 8-6:Multiplication factors for estimating manufacturing cost 371
Table 8-7: Cash flow calculations in normal scenario 372
Table 8-8: Cash flow calculations in optimist scenario 373
Table 8-9: Cash flow calculations in pessimist scenario 374
Table 8-10: Parameters for NPV estimation 375
Table 8-11: Values of parameters for NPV estimation in normal scenario 376
Table 8-12: Values of parameters for NPV estimation in optimist scenario 377
Table 8-13: Values of parameters for NPV estimation in pessimist scenario 378
Table 8-14: Values of IRR of the three scenarios 379
Table 8-15: Values of CRP of the three scenarios 380

INTRODUCTION

The current socio-economic growth would not have occurred if fossil fuels had not been exploited. Coal, oil, natural gas, and other alternative energy sources have been the global economic engine. Energy consumption is one of the outstanding gauges of a society's progress and well-being as well as a fundamental factor for economic development. An economic model, such as the present one, whose functioning depends on continuous growth, also requires an equally increasing demand for energy. The productions of clean and sustainable fuels are the main challenge facing the impending energy crises and global warming. These clean and sustainable fuels are called renewable energy and represent the fourth largest energy source globally, behind oil, coal, and natural gas, accounting for about 19% of global primary energy production (Mujtaba et al., 2017). Renewable energy sources will constitute a major part of the future energy on the planet if sustainable development is promoted. In many countries, there are appropriate conditions to the use of some of these sources, which can contribute not only to partially solve part of the energy demand but also to the environment protection. Fossil fuels have been the primary source of energy so far. These fuel resources are not sustainable and cause Green House Gas emissions (GHGs) responsible for global warming (Deng et al., 2020). The immediate consequence is the increase in global temperature and extreme climatic events, which are increasingly frequent and harm health and agriculture. According to World Bank data (2019), there is a growing accumulation of emissions of polluting gases globally. Therefore, it is essential to utilize renewable energy resources that provide low GHGs emissions, which contributes to limiting the greenhouse effect. Many researchers in the world have been looking for alternative energy resources and fuels, including wind power, Hydropower, Solar energy, Geothermal energy, and Bioenergy (Dunn, 1986; Mohtasham, 2015).

Among these forms of renewable energy resources, bioenergy is expected to be one of the predominant forms of renewable energy sources in the future due to its abundance, manageability, and accessibility. Unlike other renewable energies, bioenergy is the only renewable energy utilized and stored in different forms, such as solid, liquid, or gas. For this versatility, bioenergy is gaining special attention among all renewable energy sources as a potential alternative for energy independence from fossil fuels. The use of bioenergy continues to grow, both in industrialized and developing countries. Today, bioenergy is set to play an increasingly important role in energy supply, both in the industrialized world and in developing

countries, as concern about the state of the global environment grows. Bioenergy is energy produced from biomass or biofuel. Biomass can be converted into liquid, solid, or gaseous fuels; through a series of conversion processes to enhance its energy content. The ability to convert biomass materials through physical, chemical, or biological processes allows transforming solid carbonaceous materials that can be difficult to handle due to their bulkiness and low energy density, fuel with enriched physicochemical characteristics, high energy density, and ease to store and transport (Welfle, 2015). The least expensive biomass resources are agricultural waste products, municipal waste residues, but their supply is limited. To overcome this limitation, many countries worldwide are considering biomass crops for energy purposes and have begun to develop technologies to use biomass more efficiently (Baum et al., 2013; Börjesson et al., 2017; Cosentino et al., 2008). To contribute to a larger extent to the world's energy supply, the cultivation of dedicated biomass crops for energy purposes will be required, using uncultivated land and marginal land (McKendry, 2002). Recently, many researchers have studied the economic and environmental impact of energy obtained from biomass (Basu, 2010; Damartzis and Zabaniotou, 2011; Goldemberg and Coelho, 2004; López González, 2013; McKendry, 2002). However, biomass conversion efficiency and production costs with current biomass conversion technologies remain the two biggest challenges (Mafakheri and Nasiri, 2014). One of the main obstacles to constructing large biomass plants is the transportation of large quantities of biomass fuels from forest sources to the point of use.

Compared to fossil fuels, biomass has a low energy density and a high moisture content (Acharjee et al., 2011; Medic et al., 2010). These properties make biomass relatively expensive to transport, and thus higher transport levels are a barrier to large-scale plants. In contrast, small-scale biomass electricity generation plants can be fuelled by local resources from small adjacent catchment areas, such as agricultural waste that can be turned into electricity. Even though biomass fuels are dried, they can rehydrate and rot during storage. In general, moisture plays a fundamental role in any biologically derived material (Vasquez and Coronella, 2009). Dry biomass is much more stable and exhibits reduced rates of biological deterioration. Furthermore, increasing the energy density is recommended because, in applications like combustion and gasification, a significant biomass volume is needed to substitute an equal amount of coal. To solve this moisture problem and increase the energy content, one of the alternatives can be hydrothermal carbonization or wet roasting, which results in high energy density and low moisture.

Thermochemical conversion, including pyrolysis, liquefaction, combustion, gasification, and other processes, is one of the most common biomass-to-energy conversion pathways (Liu et al., 2017; Nsaful et al., 2013). Pyrolysis, liquefaction, and gasification turn biomass into more practical, flexible fuels and high-value-added chemical products that can be used in various applications, while combustion is mainly limited to the generation of thermal energy from biomass. Furthermore, combustion, which entails the oxidation of carbonaceous materials into biomass to release steam, creates polluting and undesirable gaseous compounds with no energy, such as CO2, NOx, and SOx (Okoro et al., 2020). One of the most promising routes for generating green energy is biomass gasification due to its high energy efficiency, lower impact on the environment, and flexibility for the producer gas to be utilized considering its availability. Therefore, in this project, wet biomass is used to convert it into energy; for them, it is necessary to know its conversion's best process and technologies.

THESIS CONTENT AND STRUCTURE

This doctoral thesis deals with an Experimental and Simulation Study of the Hydrothermal Carbonization of Biomasses for the Production of Synthetic Fuels. The experimental and simulations results obtained and their discussion are presented in eight chapters.

Chapter 1 consists of a literature review of the essential elements of the importance of energy consumption on economic development. The main problem is linked to fossil fuels and the need to use alternative renewable energy sources. Among these renewable sources, the advantages of the use of biomass as an energy source are explained. Different technologies or ways of converting biomass into energy are presented. The thermochemical conversion process (hydrothermal carbonization, pyrolysis, gasification, and combustion) is explained. It was explained the thermochemical conversion process (hydrothermal carbonization, pyrolysis, gasification, and combustion). It is also discussed with converting the gasification products to synthetic fuels by Fischer-Tropsch synthesis. Finally, the importance of modeling and simulation to carry out these processes is explained.

Chapter 2 explains the problem statement, the justification, the hypotheses, the objectives, and a global approach of how the project will be carried out, both in the experimental part and in the simulations.

Chapter 3 is dedicated to the development and characterization of the raw biomasses used. This chapter presents the different analytical approaches to biomass characterization during the biomass pretreatment and conversion process. The main methods used to characterize these biomasses were: Analysis of the thermochemical properties such as compositional analysis of biomass (extractible, hemicellulose, cellulose, and lignin), thermogravimetric analysis (TGA/DTG), Heating value analysis (HHV and LHV), proximate and ultimate analysis. Analysis of the microstructure and chemical composition of the biomass was carried out as Fourier transform infrared (FTIR) and Scanning Electron microscopy (SEM). In addition, the thermophysical properties of biomasses such as heat capacity, thermal conductivity, and density are determined.

Chapter 4 presents the experimental setup and the principle of the hydrothermal carbonization (HTC) process to produce hydrochar. An in-depth study of the effect of operating conditions on the HTC process of biomasses is presented, with a particular interest

in the properties and yields of hydrochar. This chapter aims to understand better and qualitatively analyze the effect of operating conditions on the HTC process and properties of hydrochar yields.

Chapter 5 explains the experimental studies of pyrolysis and gasification of biomasses and the corresponding hydrochars produced using TGA. The TGA was coupled with an online Micro Gas Chromatograph (TG/μ-GC) to analyze the gas product. In addition, this chapter focuses on the effects of biomass types, operating conditions, emphasizing the air-to-biomass ratio (ABR), temperature, and heating rate during the pyrolysis and gasification process on product distribution. A parametric study of the effect of operation conditions on gas product properties such as cold gas efficiency or process efficiency, gas yield, and heating value was carried out. The quantification of gas evolution as a function of the temperature was performed. Also, the kinetics of the pyrolysis reaction and the gasification of these biomasses were studied.

Chapter 6 focuses on modeling and numerical simulation in CFD. The main objectives of this study were to use the CFD technique to produce a 3D simulation of the HTC stirred reactor for an open-loop control system using COMSOL Multiphysics software: (a) to study hydrodynamics and to determine the biomass distribution inside the reactor, the mixing intensity, and stagnation zones. (b) to determine the heat of the reaction and the type of chemical reaction. c) to combine the kinetics, temperature, mass, and velocity fields to predict the biomass conversion inside the reactor, considering the thermal properties of the AS and the heat of reaction, and the effect of the biomass/water ratio on the heat transfer. These results were compared with the experimental data of the AS HTC. In addition, the design of experiments was studied to present a mathematical model describing the effects of the HTC operation parameters on the final product.

Chapter 7 simulated the hydrothermal carbonization process and the pyrolysis and gasification process of the biomass in Aspen Plus®. The results obtained were validated with experimental data. These results propose a plant for the production of hydrochar combined with pyrolysis and gasification of a continuous system, which can be designed on an industrial scale. In addition, this chapter provided a theoretical study of the production of synthetic fuels from synthesis gas obtained experimentally in Aspen HYSYS® to show the potential of using biomass to produce liquid fuels.

Chapter 8 groups the steps and equations to estimate the energy balance of the HTC process in a global way to identify the most influential parameters in this process. The HTC process is broken down into unit operations with a detailed presentation of the equations used in the energy balance calculations. The results of the energy balance calculations at the laboratory level are presented. Based on these results, a simulation was performed in Aspen plus® a continuous industrial-scale process considering the integration of energy in the HTC process.

The result of the simulation allowed an economic study of the use of hydrochar as an energy source. In general, the HTC process is economically feasible and competitive price of pelletized hydrochar compared to palletized bulk pine wood. This study could encourage the development of HTC plants, therefore, the hydrochar pellet market.

At the end of this manuscript, we present the most salient conclusions of this work and some perspectives regarding future research on biomass conversion into an energy source.

Some of the results of the research work carried out during the development of this thesis are collected in the following papers:

1. **Sangare, D.,** Bostyn, S., Moscosa-Santillan, M., Gökalp, I. (2021). Hydrodynamics, heat transfer and kinetics reaction of CFD modeling of a batch stirred reactor under hydrothermal carbonization conditions. *Energy*, 219, 119635.

2. **Sangare, D**., Missaoui, A., Bostyn, S., Belandria, V., Moscosa-Santillan, M., Gökalp, I. (2020). Modeling of Agave Salmiana bagasse conversion by hydrothermal carbonization (HTC) for solid fuel combustion using surface response methodology. *aimspress energy*, 8(4), 538-562.

3. **Sangare, D.,** Bostyn, S., Moscosa-Santillan, M., Belandria, V., Gökalp, I. (2021). Quantification and Kinetic Study of the Main Compounds in Biocrude Produced by Hydrothermal Carbonization of Lignocellulosic Biomass. *Bioresource Technology Reports*, xxx

4. **Sangare, D.,** Chartier, A., Bostyn, S., Moscosa-Santillan, M., Gökalp, I. (2021). Kinetic Studies of Hydrothermal Carbonization of Avocado Stone and Analysis of the Polycyclic Aromatic Hydrocarbon Contents in the Hydrochars Produced. (Submitted for publication)

5. **Sangare, D.,** Bostyn, S., Moscosa-Santillan, M., Belandria, V., Gökalp, I. (xxx). Pyro-gasification of Biomass: Use of TGA Coupled to μ-GC for Analysis and Quantification of Gas Evolution (Ready to submit for publication).

6. **Sangare, D.,** Bostyn, S., Moscosa-Santillan, V., Gökalp, I., Belandria, V….., (xxx). Hydrothermal Carbonization of biomass: Laboratory Trials, Energy balance, Process Simulation, Design and Cost Analysis (Ready to submit for publication).

Chapter1 BACKGROUND

1.1. Current energy situation

Energy consumption has increased since the industrial revolution. Global energy demand is increasing rapidly because of population and economic growth, especially in emerging market economies. While accompanied by greater prosperity, rising demand creates new challenges. Global energy consumption has increased by more than 50% (Looney, 2020). **Figure 1-1** shows the increase in primary energy consumption in recent years, and it can be seen that most consumption comes from fossil fuels (oil, coal, and natural gas).

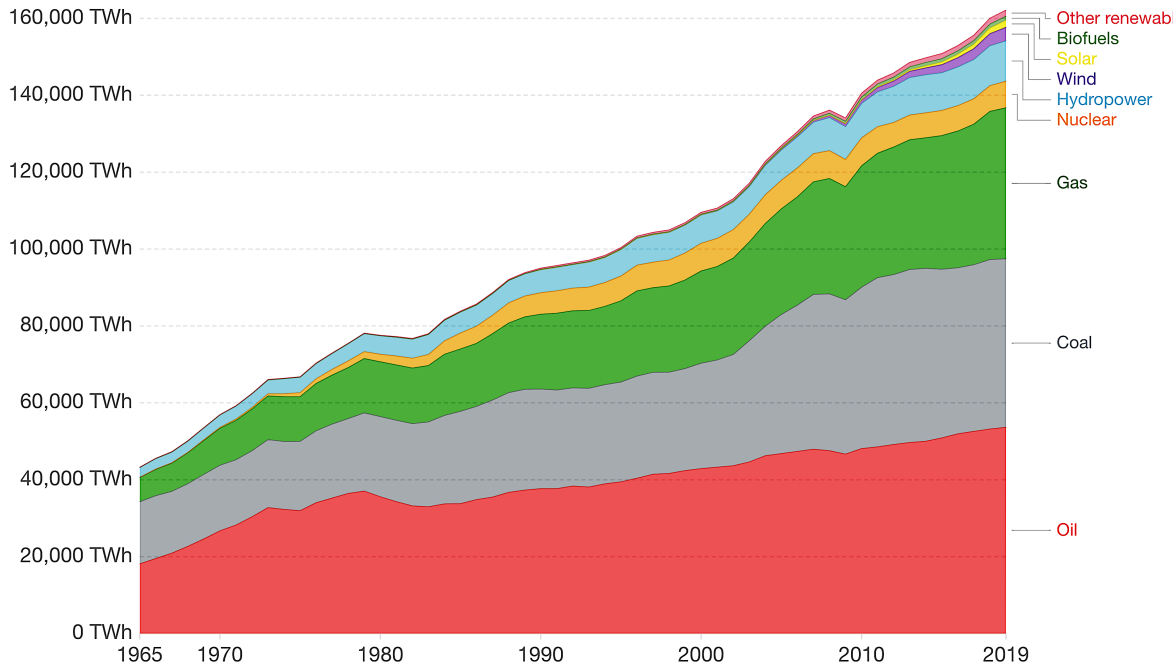

Figure 1-1: Global primary energy consumption by different sources (Looney, 2020)

The majority of consumption comes from fossil fuels (oil, coal, and natural gas). Today, fossil fuels satisfy more than 80% of the world's primary energy consumption (Looney, 2020). However, the percentage of renewable energy contribution to global demand has remained almost constant over the past 20 years.

1.1.1. Fossil fuel

Most of the world's energy comes from fossil fuels (oil, coal, and natural gas). In the nineteenth century, crude oil was chemically transformed into a financially viable fuel supply, resulting

in a massive economic boost. The oil industry's advancement paved the way for the growth of other sectors such as shipping, electricity, telephones, and even pharmaceuticals. This impulse also impacted the generation of jobs, helped in the industrialization of the world, raising the quality of life of millions of people. Although fossil fuels were the engine of the world economy, they have caused numerous environmental problems. Their use is directly linked to global warming. As fossil fuels are burned, they release large amounts of gases, known as Greenhouse Gases (GHGs), mainly carbon dioxide. Recent years have seen a significant increase in the levels of GHGs in the atmosphere, mainly carbon dioxide (CO_2), sulfur oxides (SOx), and nitrogen oxides (NOx). These compounds are largely the problem of environmental pollution (Akimoto and Narita, 1994). In fact, in 2019, the CO_2 concentration was about 75 % higher than it was in the mid-1980s (Braun, 2020). **Figure 1-2** shows the main countries that increase GHGs through CO_2 emissions.

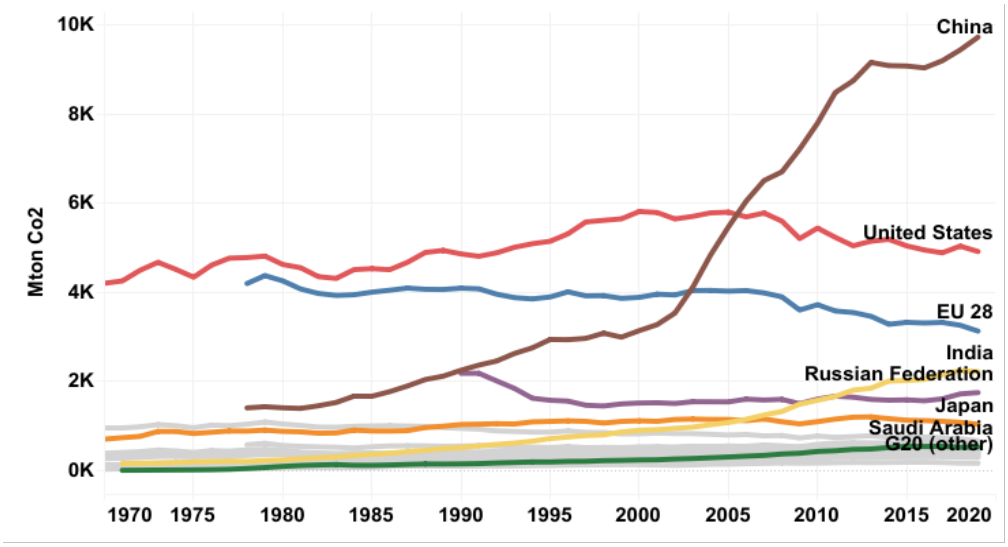

Figure 1-2: CO_2 Emissions from fuel combustion 1970-2019 (Braun, 2020).

The CO_2 emissions are strongly linked to the greenhouse effect. As a result, the United Nations proposed reducing GHGs by the Kyoto Protocol in 1992 and the COP21 in Paris in 2015, an international negotiation to reduce greenhouse gas emissions that affect global warming. The proposed emissions reduction for the period 2008-2012 was 5.2% compared to those reported in 1990. This agreement has been ratified by 166 nations, including Mexico. Human operations are responsible for various greenhouse gas emissions (land use, livestock, transportation, so forth). About 90% of GHGs emissions come from the electricity industry due to fossil fuel combustion (Agency, 2015). The need to reduce CO_2 emissions derived from the use of fossil fuels is imperative, not only because of the future extinction of oil reserves but also because of

the irreparable environmental damage that is increasing day by day on our planet. This situation has given rise to a growing interest in the study and development of new technologies for energy production that are sustainable from an environmental, economic, and social point of view. In this sense, renewable energy sources are expected to play a significant role in the future.

1.1.2. Renewable energies

Renewable energies are all those forms of energy obtained or generated from the use of natural and renewable resources. There are many forms of renewable energy. Most of these renewable energies depend in one way or another on sunlight. Wind and hydroelectric powers are the direct results of differential heating of the earth's surface, which leads to air moving about (wind) and precipitation forming as the air is lifted. Biomass energy is stored sunlight contained in plants. Other renewable energies that do not depend on sunlight are geothermal energy, which results from radioactive decay in the crust, combined with the original heat of accreting earth, and tidal energy, which is a conversion of gravitational energy. The energy obtained from these sources can be classified differently, such as solar energy, wind energy, hydropower, geothermal energy, biomass energy, and so forth (Goldemberg and Coelho, 2004). Based on REN21's 2017 report, renewables contributed 19.3% to human beings' global energy consumption. This energy consumption is divided up into 8.9% from traditional biomass, 4.2% as heat energy (modern biomass, geothermal and solar power), 3.9% hydropower and 2.3% is electricity from wind, solar, geothermal, and biomass (REN21, 2017).

The advantages and disadvantages of some common renewable energies are explained below: hydropower, wind power, solar power, geothermal power and biomass.

1.1.2.1. *Hydropower*

Hydropower or water power is based on a simple process, taking advantage of the kinetic energy freed by falling water. It is a process that transforms the kinetic energy of falling or flowing water into electrical or mechanical energy (Egré and Milewski, 2002). Hydropower is a sustainable and environmentally friendly energy source. Most countries favor hydropower production because of its fiscal, technological, and environmental benefits. China, for example, has the world's richest hydropower resources, with a gross theoretical hydropower output of 694GW(Huang and Yan, 2009). Hydropower development is critical for alleviating the energy shortage and emissions caused by China's and other countries' rapid economic growth in the

twenty-first century. Hydropower has many benefits over most other forms of renewable or sustainable energy. High reliability, proven technologies, high performance, relatively low operation, and maintenance costs, and the ability to easily respond to load changes are only a few of them. Many hydropower plants are built next to reservoirs, which provide the city with electricity, flood protection, and recreational opportunities. Furthermore, hydropower does not generate waste materials that contribute to acid rain and greenhouse gas emissions (Salame et al., 2015). However, the high initial facility costs; reliance on precipitation (no control over the volume of water available); changes in stream regimens can impact fish, vegetation, and biodiversity by altering stream flows, flow patterns, and temperature; inundation of land and wildlife habitat; and relocation of people living in the reservoir area are only a few of the disadvantages of hydropower (Liu et al., 2013a).

1.1.2.2. *Wind power*

Wind power, also known as wind energy, is a relatively simple technique. Wind power systems convert the kinetic energy of the wind into other forms of energy such as electricity (Bull, 2001). The electricity is pumped into a generator, converted to electrical energy a second time, and then fed into the grid to be transmitted to a power plant. One of the fastest-growing clean energy technology is wind power. Globally, use is increasing, partly due to lower prices (Salame et al., 2015). Wind energy, like all alternative energy sources, has several advantages. It reduces greenhouse gas emissions and lowers power prices by using wind turbines, which provide energy and electricity when moved by the wind (Jacobson and Delucchi, 2011). All required for the turbines to operate is wind, which is simply air in motion, and the air is found everywhere. Wind represents a cheap, abundant, and renewable energy source that would not depreciate if we use it. It can make the most of this opportunity, and it will only serve to make our planet a safer and healthier environment (Salame et al., 2015). Wind power has been used for thousands of years, but it has only recently been a major industrial electricity source. Many of the world's windiest regions, such as northern Canada and Russia, are situated far from urban centres, where transmission and repair costs will be extremely expensive. Wind power's erratic and unreliable existence would restrict its contribution to any area unless large-scale energy storage or intercontinental transmission were possible. Environmental limits, such as forests and conservation areas, and general approval, restrict the placement of wind turbines. Wind turbines are not desirable, and they've caused concerns about pollution, radio and TV signal

interference, and the killing or messing with migratory birds (Khatoniar, 2020; Salame et al., 2015).

1.1.2.3. *Solar power*

Solar power or solar energy is the most abundant renewable resource on our planet. Despite its abundance, only 0.04% of primary human energy comes directly from solar sources. The cost of using a photovoltaic (PV) panel is the main reason for the non-use of this energy source. Recently, organic materials have been intensively studied for photovoltaic applications to generate energy from organic photovoltaic (OPV) materials. The use of OPVs can considerably decrease the cost of photovoltaic technologies (Moulé, 2010). Solar energy is a true renewable resource. Most of planet earth has the ability to collect some amount of solar power. Solar energy is non-polluting, does not create greenhouse gases, such as oil-based energy does, nor does it create waste that must be stored, such as nuclear energy. It is also far quieter to create and harness, drastically reducing the noise pollution required converting energy to a useful form. Residential size solar energy systems also have very little impact on the surrounding environment, in contrast with other renewable energy sources such as wind power and hydropower (Pogson et al., 2013). Solar panels have no moving parts and need only routine cleaning for repair. Maintenance and replacement costs are very low after the initial costs of assembling the panels, so there are no moving components to crack and restore. It's also worth noting that photovoltaic solar panels are the only option that can meet current demand (Pogson et al., 2013; Salame et al., 2015). The main disadvantage of solar energy is its high cost. Despite technological advances, solar panels continue to be expensive. Even if the panels' expense is not taken into account, the device used to store and use the energy can be very expensive (Fitzgerald et al., 2015).

1.1.2.4. *Geothermal power*

Geothermal power is an energy used to produce electricity. Dry steam power plants, flash steam power plants and binary cycle power plants are operating technologies. Geothermal power generation is currently used in 26 countries (El Bassam et al., 2013). Geothermal energy is produced by storing heat underground and releasing energy as heat rises to the surface. This heat is harnessed and used to transform a steam engine to generate electricity as it spontaneously produces hot water or steam. Geothermal energy, or energy derived from heat from inside the Earth, has many different uses. These uses can be grouped into three categories: heating systems (and direct use), electricity generation, and use in geothermal heat pumps. In

addition to these practical uses of geothermal energy, many other things make geothermal energy a valuable energy resource. Since the Earth's core continuously produces heat with the radioactive decay of potassium and uranium, geothermal energy becomes a renewable, abundant, and reliable energy source. A geothermal power plant uses no fuel, making it sustainable and environmentally safe. Geothermal power operations produce few emissions. These operations do not pollute the air or contribute to global warming (Edenhofer et al., 2011). The disadvantages of geothermal energy power plants are their location since it is difficult to locate suitable sites for these power plants. The number of places where geothermal power plants can be built is extremely small. The site must have hot rocks that can be drilled quickly. There is also the question of sustainability and the scarcity of appropriate geothermal power plant locations. Geothermal energy is typically localized along plate margins, where volcanoes are concentrated, and earthquakes are most common (Salame et al., 2015). Geothermal power plants occasionally run out of steam for a few months, which prevents the plant from producing electricity. Compared to other energy sources, geothermal energy produces a smaller amount of electricity. It is difficult to transport geothermal energy. Therefore, geothermal power plants can only supply electricity to the regions in their immediate vicinity. Although the steam itself may be clean and pure, it may contain toxic materials such as hydrogen sulfide, mercury, ammonia, and arsenic that have been released from underground. Finally, geothermal energy can cause earthquakes (Gupta and Roy, 2006).

1.1.2.5. *Bioenergy*

Bioenergy is energy obtained from biomass. Any organic matter that has absorbed sunlight and retained it as chemical energy is known as biomass. Wood, agricultural, and poultry residues; short-rotation forest plantations; energy crops; the renewable components of urban solid waste; and other organic waste sources will all be used to produce bioenergy. This material may be used to generate electricity or heat directly via a variety of processes. They can also be used to make liquid, gaseous, or solid fuels. Bioenergy systems come in a wide variety of forms, with varying degrees of technological sophistication. In both centralized and decentralized environments, bioenergy technologies are being used. The most popular existing applications in developed countries are conventional biomass uses (primarily for cooking and heating). Bioenergy projects are typically dependent on the availability of local and regional fuel supplies, but recent trends indicate that solid biomass and liquid biofuels are rapidly traded globally (Edenhofer et al., 2011). Bioenergy can minimize greenhouse gas emissions, reduce reliance on oil, and benefit local agriculture and forest product sectors. Agro-industrial wastes,

urban wastes, and other biomass feedstocks are the most common biomass feedstocks for energy production. Corn grain (for ethanol) and soybeans are now the most widely used feedstocks for biomass fuels (biodiesel). The planting and use of specific energy crops, such as fast-growing trees and grasses, as well as algae, are among the long-term plans. These feedstocks can be grown sustainably on land that does not support intensive food crops. Another advantage of biomass is its ability to be converted into a range of valuable fuels in solid, liquid, and gaseous forms and chemical products (Demirbas, 2001a; Kumari and Singh, 2018; Salame et al., 2015).

- **Biofuel:** Converting biomass into liquid fuels for transportation.
- **Biopower**: Burning biomass directly (combustion), or converting it into gaseous or liquid fuels that burn more efficiently, to generate electricity.
- **Bioproducts**: Converting biomass into chemicals for making plastics and other products that typically are made from petroleum.

Despite its many advantages, biomass can be harmful to the environment if it is not used for biomass energy production from the following sources:

- Energy crops that do not compete for land with food crops.
- Agro-industrial waste, sustainably grown timber, and tree residues
- Dispose of urban and agricultural wastes in a safe and environmentally friendly manner.

Aside from all the advantages of bioenergy, there are several disadvantages. Biomass energy, for example, has lower energy content than fossil fuels. Growing and processing the biomass feedstock, transporting the feedstock to the power plant, and burning or gasifying the feedstock can contribute significantly to global warming emissions, even if less than fossil fuels. For all forms of biomass, emissions from transport and combustion are about equal. Therefore, it is important to distinguish between biomass resources that are beneficial in reducing net carbon emissions, those that have an ambiguous impact, and those that increase net emissions (Spath and Mann, 2004). Another environmental impact of bioenergy is associated with land erosion due to the removal of green vegetation (Pimentel et al., 1995).

1.2. Biomass, characteristics and their relationship with energy production

What is biomass? The answer depends on who is asking the question.

- From an ecological perspective, the amount of living matter in a given habitat is expressed either as the weight of organisms per unit area or the volume of organisms per unit volume of habitat (Dayton and Foust, 2019).
- From an energy perspective, biomass can be defined as "any organic substance of plant or animal can be converted into energy (McKendry, 2002)."

If we consider biomass as an energy source, it can be defined as organic matter that captures sunlight to convert CO_2 and water through photosynthesis into stored chemical energy (carbohydrates) for plant growth. The CO_2 converted to fixed carbon in biomass is indiscriminate of renewable or fossil-derived sources, but biomass is considered a renewable resource because it is grown, used, and regrown on a comparatively short time scale in large quantities. Biomass also includes plant or animal matter that can be converted into fibers or other industrial chemicals, including biofuels (McKendry, 2002). Energy in biomass is one of the energies very commonly used throughout the world. Unfortunately, the most popular is the burning of trees for cooking and warmth. This process releases significant amounts of carbon dioxide gases into the atmosphere and is a significant contributor to unhealthy air in many areas. The energy available in biomass by combustion is around 8-20 MJ/kg, a relatively low value compared to coal which is 23-30 MJ/kg(Demirbas, 1997). Biomass can be used directly (e.g. in the combustion of wood for heating and cooking); or indirectly, by converting it into a liquid or gaseous fuel (e.g. bioethanol from alcoholic fermentation, synthesis gas from thermochemical conversion) etc. (Gropelli and Giampaoli, 2001). According to the International Energy Agency (IEA), In 2017, biomass contributes to about 10% of global energy demand (IEA, 2018), especially in Africa. Solid biomass is the largest renewable energy source globally, owing to the existence of traditional biomass in developing countries. One of the reasons why biomass has become so important is its high availability; it is estimated at approximately 220 billion tons of dry biomass per year (López González, 2013).

1.2.1. Biomass structure and composition

Bioenergy or biofuels are usually classified as follows:

- First-generation: First-generation bioenergy include ethanol and biodiesel and are directly related to a biomass that is more than often edible.
- Second-generation: Second-generation bioenergy are defined as fuels produced from a wide array of different feedstocks, especially but not limited to non-edible lignocellulosic biomass.

- Third-generation: The most accepted definition for third-generation biofuels is fuels that would be produced from algal biomass, which has a very distinctive growth yield as compared with classical lignocellulosic biomass (Brennan and Owende, 2010).

The second-generation bioenergy is sourced from lignocellulosic biomass. Biomass used for the production of second-generation bioenergy is usually separated into three categories: homogeneous, such as white wood chips with a price value; quasi-homogeneous, such as agricultural and forest residues; and non-homogeneous, including low-value feedstock as municipal solid wastes as reported by Lavoie et al.(Lavoie et al., 2011). Lignocellulosic biomass is a significant component of biomass. Cellulose, hemicellulose, and lignin are the main constituents of lignocellulosic biomass, with small amounts of acetyl groups, minerals, and phenolic substituents. The proportions are as follows: 20-55% cellulose, 16-85% hemicellulose, 10-40% lignin, and 1-3% of others (Howard et al., 2004). Depending on the type of lignocellulosic biomass, these polymers are organized in complex non-uniform three-dimensional structures to different degrees and varying relative compositions. Unlike carbohydrates or starch, lignocellulose is not easily digestible by humans. For example, we can eat rice, which is a carbohydrate, but we cannot digest straw, which is lignocellulose. The structure of lignocellulosic material is shown in **Figure 1-3.**

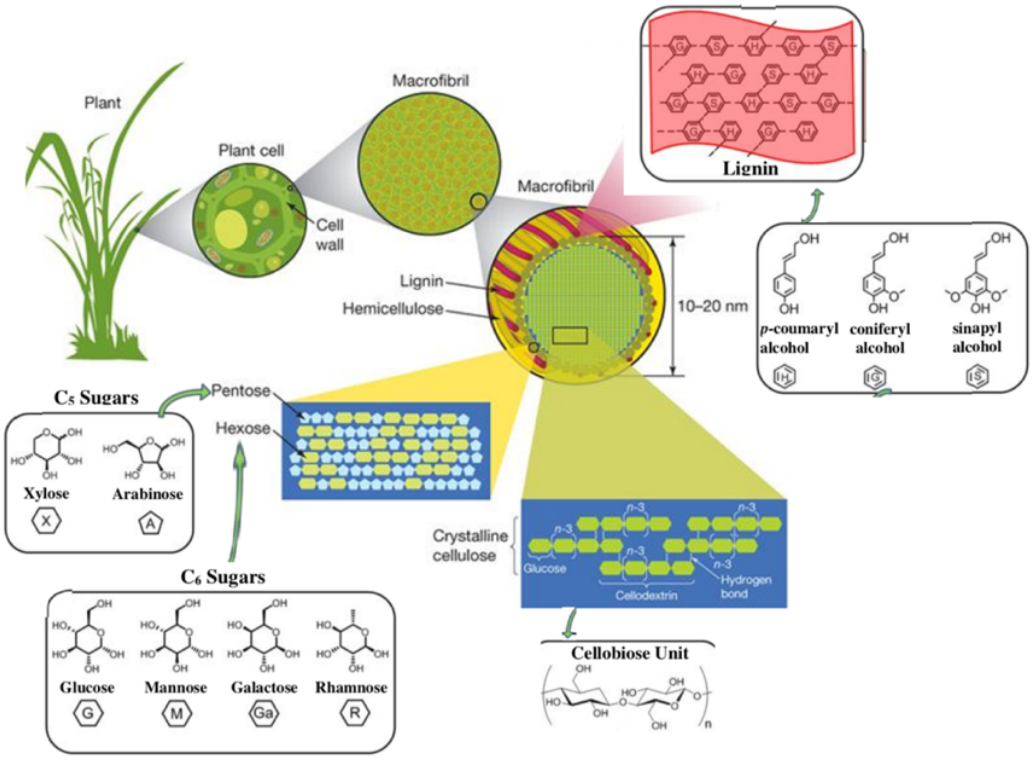

Figure 1-3: The main components and structure of lignocellulose (*Isikgor and Becer, 2015*; *Rubin, 2008*)

The main structural components of biomass are three polymers: cellulose, hemicellulose, and lignin. Cellulose and hemicellulose are linked to the lignin component through covalent bonds and hydrogen bridges, making the structure robust and resistant to any treatment. The major component of lignocellulosic biomass is cellulose. Unlike glucose in other glucan polymers, the repeating unit of the cellulose chain is the disaccharide cellobiose. Its structure consists of extensive intramolecular and intermolecular hydrogen bonding networks, which tightly bind the glucose units. The conversion of cellulose into fuels and high added value chemical products is of paramount importance (Somerville et al., 2010; Zhou et al., 2011). Hemicellulose is the second most abundant polymer.

The heteropolymers of hemicellulose are composed of sugar of 5- and 6-carbon monosaccharide units; pentoses (xylose, arabinose), hexoses (mannose, glucose, galactose), and acetylated sugars. Unlike cellulose, hemicellulose has a random and amorphous structure, which is composed of several heteropolymers, including xylan, galactomannan, glucuronoxylan, arabinoxylan, glucomannan, and xyloglucan (**Figure 1-3**) (Knauf and Moniruzzaman, 2004; Scheller and Ulvskov, 2010a). Lignin is an aromatic polymer with a rather complex, highly branched, and amorphous three-dimensional phenylpropanoid unit structure, a cross-linked polymer with molecular masses above 10,000 u. It is relatively hydrophobic and rich in aromatic subunits. The degree of polymerization is difficult to measure since the material is heterogeneous. It functions as the cellular glue, which provides compressive strength to the plant tissue and the individual fibers, stiffness to the cell wall, and resistance against insects and pathogens. The oxidative coupling of three different phenylpropane building blocks, that is, monolignols: p-coumarin alcohol, coniferyl alcohol, and sinapyl alcohol, forms the structure of lignin. The corresponding phenylpropanoid monomeric units in the lignin polymer are identified as p-hydroxyphenyl (H), guaiacyl (G), and syringyl (S) units, respectively (**Figure 1-3) (**Abdel-Hamid et al., 2013**;** López González, 2013**;** Rubin, 2008**).**

1.2.1.1. *Cellulose*

The cellulose is a polysaccharide composed exclusively of glucose molecules; it is therefore a homopolysaccharide (composed of a single type of monosaccharide β-glucose from hundreds to several thousand units). **Figure 1-4** shows the primary structure of cellulose.

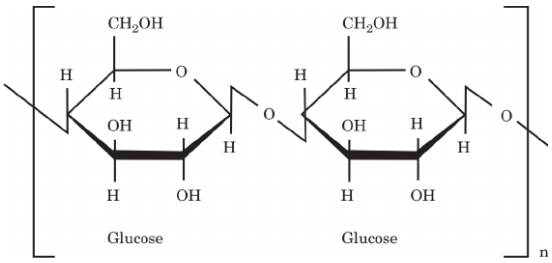

Figure 1-4: The primary structure of cellulose.

1.2.1.2. *Hemicellulose*

Hemicelluloses are heteropolysaccharides (polysaccharides composed of more than one type of monomer). Among these monosaccharides, the following stand out glucose, pentose, hexose. They form branched chains with a lower degree of polymerization than cellulose. Besides, hydrogen bonds are less effective, making hemicelluloses polysaccharides more accessible to attack by chemical reagents. Xylan is used as a representative compound for hemicellulose because it is one of the main components of hemicellulose and has been shown to have similar thermal behavior (Yang et al., 2006c).

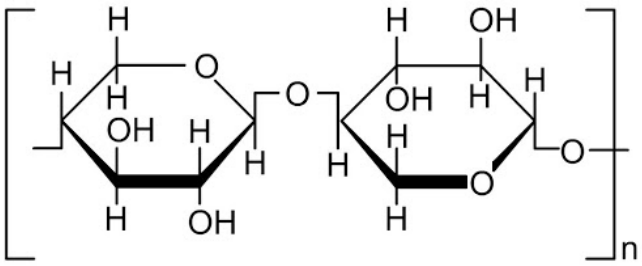

Figure 1-5: The structure of xylan (Hemicellulose).

1.2.1.3. *Lignin*

Lignin is an insoluble aromatic polymer of high molecular weight, which has complex and variable three-dimensional structures. For this reason, it is difficult to describe a definite structure of lignin. However, lignin is essentially composed of many methoxylated benzene derivatives (phenylpropanoid alcohols, also called monolignols), especially the coniferyl, sinapyl, and coumaryl alcohols (López González, 2013). **Figure 1-6** shows the structure of the three lignin constituents. The proportions of these three differ among different plants. The way in which lignin are synthesized in the plant is still unresolved, despite many decades of research

(David Moore et al., 2011). For several years, the theory that monolignols are randomly assembled to create a complex polymer that is strongly cross-linked in three dimensions reigned supreme, but it is now giving way to the idea that lignin has unique sequences of monolignols that fit the lignin to various roles in the plant cell wall, and that only a few native lignin primary structures exist. These three polymers make up the lignocellulosic materials. The main sources of lignocellulosic biomass are agro-industrial waste such as agave bagasse, avocado stone, cacao shell, and so forth.

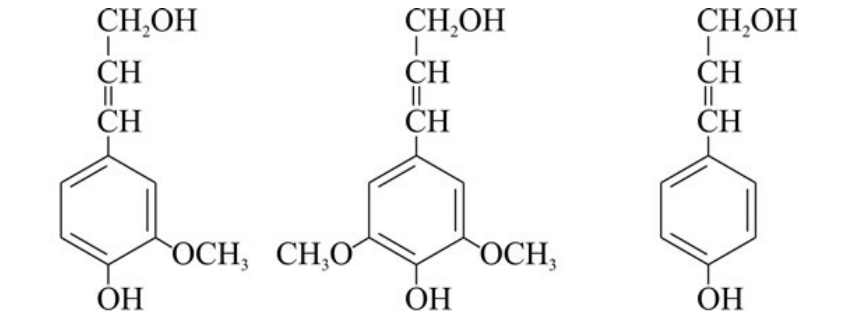

Figure 1-6: Chemical structures used to construct the lignin polymer.

1.2.2. Sources of biomass

Biomass is a key renewable energy resource that includes plant and animal material, such as wood from forests, material left over from agricultural and forestry processes, and organic industrial, human, and animal wastes. The major biomass sources currently used are sugarcane and corn to produce bioethanol and rapeseed for biodiesel production. Other sources are also used, such as sunflower seeds, jatropha curcas, soybean, peanuts, coconut, and palm oil for biodiesel production, wheat, sugar beet, sweet sorghum, and cassava for bioethanol. In Mexico, the major biomass source is agave bagasse, cacao shell, avocado stone, and so forth.

1.2.2.1. *Agave bagasse*

Agave bagasse is the main solid waste generated by the tequila and mezcal industries in Mexico. The production of distilled alcoholic beverages using agave has been a tradition since the XVII century (Marín et al., 2007). Depending on the production region, these beverages have different names, the most popular being tequila and mezcal. This last one is made from over 30 agave species, but the commonly used ones are *Agave angustifolia, karwinskii, Rodacantha, Potatorum, and Agave salmiana*. The production of mezcal begins with the

harvesting of agave plants that are more than six years old. After removing the leaves and roots, agave heads "piñas" are obtained. These piñas rich in fructans are cooked in traditional broilers or autoclaves to hydrolyze the fructans and release fermentable sugars, mainly fructose. Once the heat treatment is completed, a syrup consisting mainly of fructose, glucose, xylose, and maltose is obtained. This syrup is transformed into mezcal, a large amount of waste is generated. **Figure 3** shows the agave harvesting stage until bagasse is generated.

Figure 1-7: *Agave salmiana* plant, piñas and bagasse

San Luis Potosi's state produces about 720 000 liters/year of mezcal (Baena González, 2005) from *Agave salmiana* bagasse. To produce 1 liter of mezcal, 15 kg of wet bagasse (moisture content equal to 70%) are produced (Chávez-Guerrero and Hinojosa, 2010). It is estimated that this mezcal industry generates more than 141 tons of bagasse monthly (Martinez Gutierrez et al., 2013), which is an environmental concern due to its considerable production volume.

Agave salmiana bagasse is lignocellulosic biomass that has been considered a potential feedstock for different industrial uses in the lignocellulosic biorefinery concept framework.

The *Agave salmiana* bagasse is a lignocellulosic material composed of three main fractions, cellulose (40.7% w/w), hemicellulose (43.8% w/w), lignin insoluble (14.2% w/w), and extractible (1.4% w/w). In many of the mezcal-producing states, such as San Luis Potosi, this bagasse has no benefit for the mezcal producers. These wastes are given to the community for fodder. Sometimes the air dries it and burns it.

There are different studies on the valorization of bagasse. For example, Iñiguez-Covarrubias et al. (Iñiguez-Covarrubias et al., 2001) studied the use of bagasse as feed for ruminants, however this application was limited by the presence of lignin, the difficulty of animals to digest bagasse. The bagasse has been used to produce paper, the authors claim that this application is feasible, however a low mechanical resistance paper is found (Idarraga et al., 1999). *Agave salmiana* bagasse was also studied as biosorbents precursor by Velazquez-Jimenez et al.

(Velazquez-Jimenez et al., 2013)The authors show that this application is efficient to remove Cd (II), Pb (II) and Zn (II) from water. However, these studies were not carried out in the practice; this waste has no practical application today. There are also studies on the use of bagasse as a renewable energy source, through the combustion of bagasse (Chávez-Guerrero and Hinojosa, 2010), this application is limited by the high moisture content (70%) of bagasse. Due to a large amount of waste generated monthly and the lack of utilization, it can be used as an energy source.

1.2.2.2. *Cacao shell*

Cocoa or Cacao, a native to the Americas, was a valuable crop in the earliest South American cultures. The term cocoa originated from the Nahuatl word “cacahuatl”. Many believe that the plant first grew in the Amazon and upper Orinoco basins, but the Mayans and the Aztecs eventually developed techniques to cultivate cocoa successfully. For these cultures, the plant was regarded as a token of prosperity, and its beans were used as currency. Cacao beans are the primary component of chocolate production. Cacao beans are grown in tropical areas along the Equator, where the climate is ideal for growing cocoa trees. Côte d'Ivoire, Ghana, Indonesia, Nigeria, Ecuador, Cameroon, and Brazil are the world's top cocoa bean producers, accounting for nearly 90% of global production as shown in **Figure 1-8**.

The four West African countries of Cote d'Ivoire, Ghana, Nigeria, and Cameroon produce roughly 70% of the world's cocoa beans (Shahbandeh, 2021). The cacao shell is removed together with the germ before or after roasting and the broken fragments of cotyledon, called nibs, free of the shell, are used in chocolate production (Wood, 2008). Cacao shells are considered an agro-industrial waste during the production of chocolate. This waste is of low commercial value (González-Alejo et al., 2019). The fruit of the cocoa tree is known as cocoa (Theobroma cacao L.). Its seeds, also known as cacao beans, are made up of an outer layer called a testa surrounding two cotyledons and a small germ (**Figure 1-9**) (Okiyama et al., 2017). It is estimated that cocoa shell production is very significant, since it represents 12–20% (w/w) of the cocoa seed (Okiyama et al., 2017). Considering the world production of cocoa beans, the world generation of this waste can be calculated at approximately 1000 thousand tons, which is a substantial amount. However, as we consider the shelling waste, this amount may be much higher if we consider that the germ and perhaps a portion of the nibs that are attached to the shell are extracted along with the shell (Okiyama et al., 2017). Owing to the lack of

natural resources and significant environmental issues, the importance of agricultural by-products such as cocoa shells has recently gained increased interest.

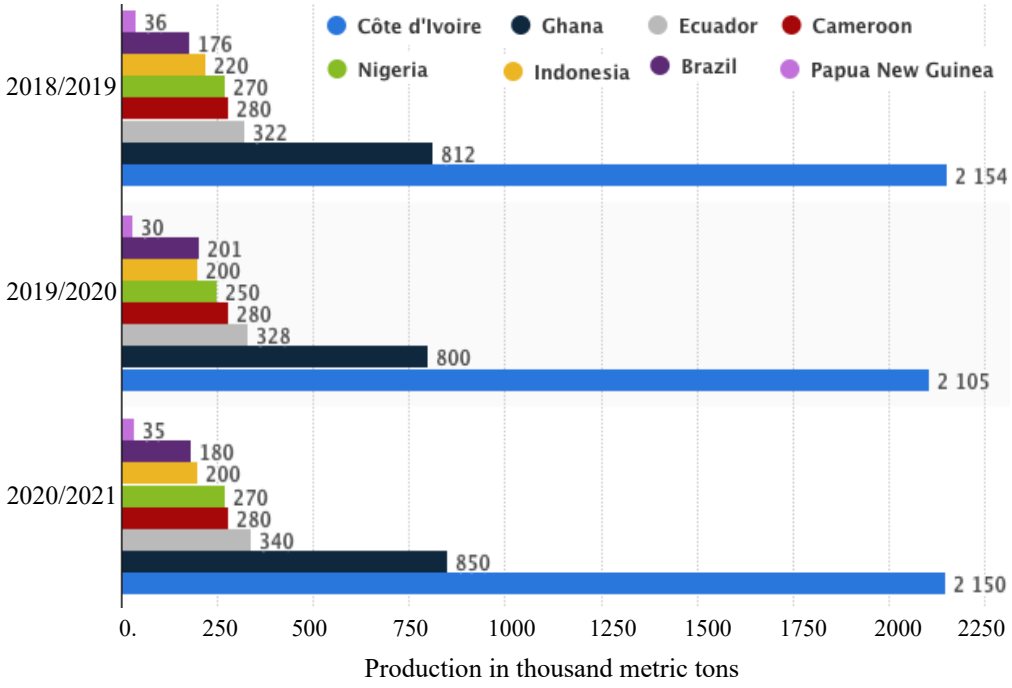

Figure 1-8: Global cacao bean production in 2018/19 to 2020/21 (Shahbandeh, 2021).

Many researchers recommend that these by-products be used in applications such as agricultural additives or other high-value-added products (Jahurul et al., 2013; Yusof et al., 2016). As a result, further research into using these ingredients as additives in high-nutrient foods or supplements is gaining traction, owing to their nutritional properties and, secondarily, that their recovery can be cost-effective (Murthy and Naidu, 2012).

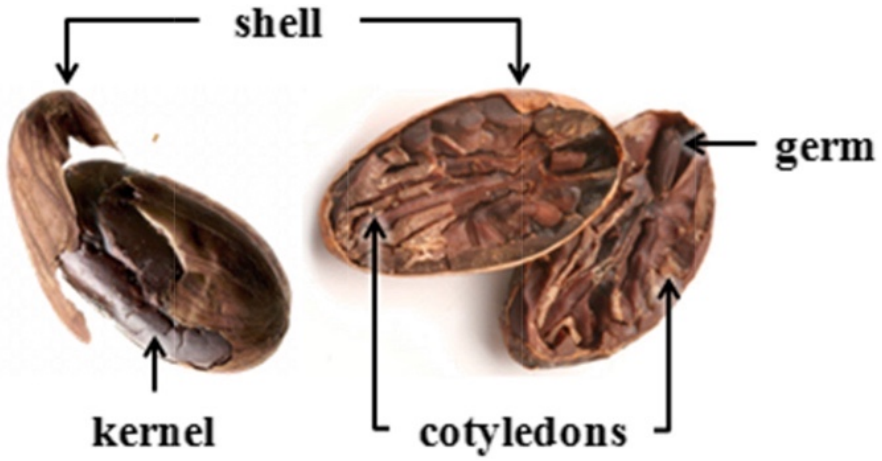

Figure 1-9: Parts of cocoa beans (*Okiyama et al., 2017*)) .

Since it is a green substance that contains fascinating compounds from a nutritional standpoint, such as phenolic compounds, fibers, and an actual fat content with a very attractive lipid profile, very close to that of cocoa butter, several studies and patents have recently been established that suggest alternative uses for this material. However, certain substances, such as mycotoxins and theobromine, should be closely analyzed since they are potentially harmful (Adamafio, 2013; Copetti et al., 2010; Okiyama et al., 2017).

1.2.2.3. *Avocado stone*

Mexico is the top avocado-producing country globally, producing 45% (1.89 million tons) of the total production in 2016 (FAO, 2017). Avocado in Mexico is not just a relationship between a fruit and its original place, but it is connected to its history and culture; it is connected to how Mexicans understand the lifestyle. Michoacán is Mexico's leader in avocado production and accounts for 80% of total Mexican avocado production (SAGARPA, 2018). There are different varieties of avocado in Mexico (*Hass, Criollo, Bacon, Fuerte, Pinkerton, Gwen*, so forth). The Hass variety is the most popular and most produced in Michoacán, with more than 85% of the total production annually (Oviedo and López). Avocados are often consumed fresh, but the processing industry for this product is increasing because of the increase in the product's production and seasonality. Products derived from avocados include ice cream, drinks, and, guacamole being the most marketed product (Perea-Moreno et al., 2016; Ramtahal et al., 2007). There are also examples of the production of avocado oil, which is of similar quality to olive oil (Salgado et al., 2008). Avocado processing generates a large amount of waste, particularly the skin and seed or stone. The stone represents 15.0–16.0% of the fruit weight (García-Fajardo et al., 1999; Rodríguez-Sánchez et al., 2013). In Mexico, the top producing country, 5% of fruit produced in 2008 was destined for processing (mostly for guacamole), producing 20,000 tons of waste (Perea-Moreno et al., 2016). Some pharmacological properties are attributed to avocado stone because of the presence of fatty acids (Werman and Neeman, 1987), steroids (Lozano et al., 1993), and polyphenols, which showed that it has high polyphenol content (Segovia Gómez et al., 2013). Although these subproducts may draw commercial interest in the cosmetic industry, they are discarded because they bring pollution issues in landfills (Schaffer et al., 2013) and, to date, have been valued for use as compost (González-Fernández et al., 2015).

It can be observed that there are several studies on these biomasses in the literature. However, many of these studies are limited. Also, there is no scientific study available to evaluate the

technical feasibility of using these biomasses as a bioenergy source. The present research consists of studying the conversion of these biomasses into fuels and chemical products with high added value.

1.3. Biomass conversion technologies

Bioenergy development requires multidisciplinary competencies, from chemistry and biology to process development, agriculture, policymaking, and more. Due to the pervasiveness of energy issues in the world today, policymakers must be actively involved in the decision-making process to select strategies for the development of the next generation of bioenergy (Pandey et al., 2015). The conversion technologies for bioenergy production are divided into physicochemical, thermochemical, and biochemical treatment. The physicochemical approach serves mainly as pretreatment and does not involve any chemical transformation of the matter. The thermochemical and biochemical conversion of biomass changes its chemical structure by treating heat, chemicals, catalysts, or combinations (Basu, 2010; Zinoviev et al., 2010). The most appropriate technology for converting biomass depends fundamentally on its compositions, moisture content, and of course, on the desired final product (Martínez, 2014). The bioenergy obtained from the biochemical process can be liquid fuels or gases, while the bioenergy obtained from the thermochemical process can be solids, liquids, or gases. The fuel liquid obtained can be used directly or mixed with existing liquid fuels. Solid and gaseous fuels can be used to produce electrical power from purpose-designed direct or indirect power plants.

1.3.1. Biochemical conversion process

The biochemical conversion process includes biological and chemical conversion. The biological conversion of biomass involves bacteria, microorganisms, and enzymes to break down biomass into gaseous or liquid fuels, such as biogas or bioethanol. The most popular biological technologies are anaerobic digestion and fermentation (Ortega, 2014). Anaerobic digestion is a series of chemical reactions during which organic material is decomposed through the metabolic pathways of naturally occurring microorganisms in an oxygen-depleted environment to produce biogas. Biomass wastes can also yield liquid fuels, such as cellulosic ethanol for alcoholic fermentation, which can be used to replace petroleum-based fuels.

Chemical conversion involves the use of chemical agents to convert biomass into liquid fuels. Transesterification is the most common form of chemical-based conversion (Boz et al., 2009). Transesterification is a chemical reaction through which fatty acids from oils (triglycerides)

are bonded to alcohol. This process reduces the viscosity of the fatty acids and makes them combustible. Biodiesel is a typical product of transesterification, as are glycerin and soaps. Almost any bio-oil (such as soybean oil), animal fat or tallow, or tree oil can be converted into biodiesel.

1.3.2. Thermochemical conversion process

Thermochemical conversion involves the use of heat as the primary mechanism for converting biomass into another form. This method encompasses everything from biomass combustion, one of the most basic forms of human energy production, to experimental methods for producing liquid transportation fuels and chemicals. Pyrolysis, torrefaction, combustion, gasification, and hydrothermal carbonization are examples of thermochemical conversion technologies (Panwar et al., 2012). The different thermochemical routes of conversion of biomass and their products are shown in **Figure 1-10**.

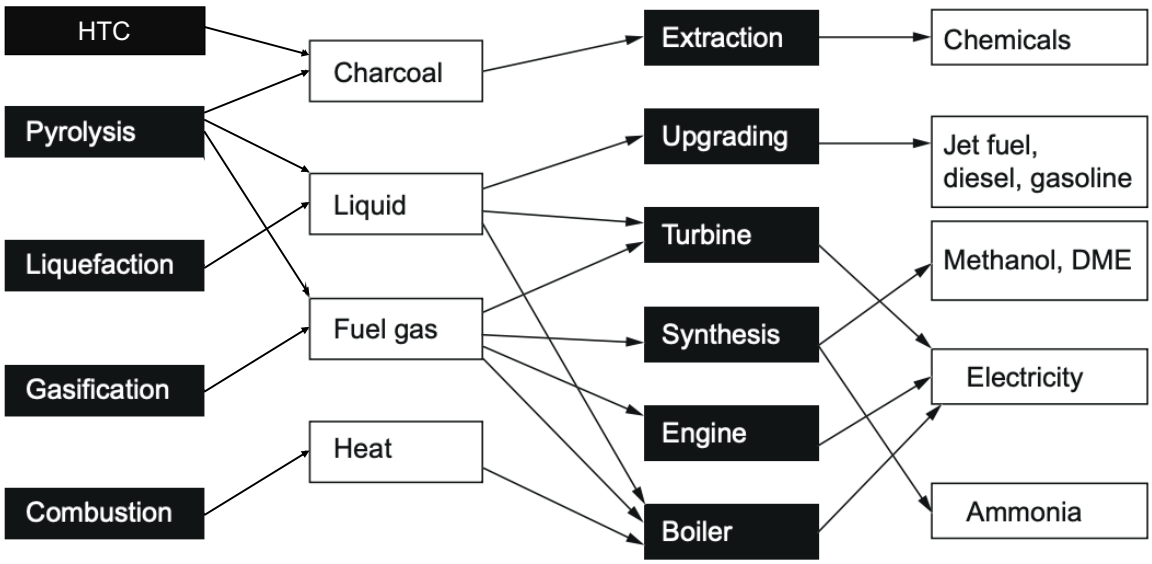

Figure 1-10: Thermochemical conversion processes and end products (Pandey et al., 2015).

Direct combustion of biomass produces heat for steam generation, and thus electricity can be produced, as seen in **Figure 1-10**. Gasification also provides a fuel gas that can be combusted to generate heat or used in an engine or turbine for electricity generation. The pyrolysis and liquefaction produce a liquid fuel used to replace fuel oil in any static heating or electricity generation application. Pyrolysis and hydrothermal carbonization (HTC) produce charcoal, which can be used as a feedstock for combustion or all of the above processes. Charcoal also has other uses.

1.3.2.1. *Pyrolysis*

Pyrolysis is the thermochemical process that converts biomass by the action of heat and in the absence of oxygen (Balat et al., 2009). The pyrolysis of biomass is produced through complex chemical reactions as well as mass and heat transfer processes, which make it difficult to predict the course of pyrolysis, because many variables, such as operating conditions or the type of biomass, are influenced (Melgar et al., 2008; Titirici and Antonietti, 2010). Pyrolysis of the three components of lignocellulosic biomass (cellulose, hemicellulose, and lignin) occurs as follows: Up to 200°C, moisture loss, and some volatile compounds occur. The hemicellulose pyrolysis starts at 220°C, and its maximum temperature value is 260 °C. In this range, the less stable biomass constituents decompose with the release of water and carbon oxides, forming alcohols and acids. Cellulose pyrolysis focuses on a temperature range of 315 to 390 °C and forms high molecular weight carbonaceous products (tars and coke). Pyrolysis itself begins at 275°C and is almost complete at 450°C, although some molecules of the formed products may rupture (cracking) at higher temperatures. From the ambient temperature to 700 °C, only ~40 %(w/w) of lignin is lost at a considerably slow rate (<0.15 %/°C). It might be attributed to the slow carbonization of lignin, and carbon could be the main product; lignin is mainly responsible for char production (Demirbas, 2010; Yang et al., 2006c). The main products of pyrolysis are liquid, solid, and gases, depending on the operating condition. The liquid product (bio-oil) is a heterogeneous mixture characterized by high oxygen content and alkalinity, which can be upgraded to fuels or chemicals. The solid product (biochar) can be used as a fuel or soil repairer. The pyrolysis mechanism is essential in all thermochemical biomass conversion processes because it determines the kinetics of the chemical reaction and, as a result, the reactor configuration and product structure, and properties (Balat et al., 2009; Sensöz and Can, 2002).

Pyrolysis is differentiated between fast and slow pyrolyzes. Fast pyrolysis, with residence times on the order of seconds to minutes, is optimized for pyrolysis bio-oil production, whereas slow pyrolysis, with residence times ranging from minutes to days, is optimized for the production of biochar (Babu, 2008; Tanger et al., 2013). The challenge of current research in engineering is to optimize process variables (temperature, heating rate, particle size, organic and inorganic matter, oxidation environment, residence time, son on) and product upgrading via catalytic and thermal processes to produce infrastructure-compatible liquid transportation fuels (Balat et al., 2009; Demirbas, 2007; Sensöz and Can, 2002).

1.3.2.1.1. *Pyrolysis mechanism*

Biomass pyrolysis starts with drying; once this stage is completed, the biomass undergoes devolatilization by breaking organic chemical bonds and vaporizing light gases and tars and char formation. During primary pyrolysis, weaker linkages are broken, producing molecular fragments during depolymerization (Solomon et al., 1993). These fragments abstract hydrogen from the hydrocarbon aromatic and aliphatic components and are subsequently released tar to the gas phase if they are small enough to vaporize and be transported out of the char particle (Solomon et al., 1992). In addition, permanent gases (CO_2, H_2, CO, CH_4, among others) are released during char condensation due to the decomposition of the functional groups. Tar species may be converted to char, light gas, and soot through secondary actions (Migliavacca et al., 2005). The depolymerization reactions compete with condensation and cross-linking reactions, responsible for tar formation with more significant aromatic sites. Condensation is assumed to act on species that are still connected to the fuel matrix, whereas cross-linking disconnects the bonds with the biomass matrix. During condensation and cross-linking reactions, aliphatic chains form light gases and aliphatic compounds. Char is formed from the unreleased or recondensed fragments (Trubetskaya, 2016).

1.3.2.1.2. *Effect of operating conditions on biomass pyrolysis*

Biomass pyrolysis operating conditions, such as temperature, heating rate, and residence time, affect yield and product composition. High heating rates, up to 10 °C/s, at temperatures of 650 °C and rapid cooling, favor the formation of liquid products and minimize char and gas formation; these process conditions are often referred to as "flash pyrolysis." High heating rates at temperatures of 650 °C tend to favor the formation of gaseous products at the expense of liquids. Slow heating rates coupled with low maximum temperatures maximize char yield (Horne and Williams, 1996; Onay and Kockar, 2003). Slow heating over long periods leads to maximum char yields with moderate amounts of tar (liquid), whereas high yields of liquids can be obtained with high heating rates and short reaction times (Onay and Kockar, 2003).

Heat treatment temperature

Figure 1-11 shows the mass loss of the main components in lignocellulosic biomass as a function of pyrolysis temperature. The decomposition temperature of all biomasses is in the range of the decomposition temperature of these three constituents. As can be seen in **Figure**

1-11, the TGA curve of rice husks lies in the TGA curves of the three biomass constituents. In this case, rice husk was mainly composed of hemicellulose, cellulose, and lignin. Lignin is challenging to break down compared to cellulose and hemicellulose. Therefore, its decomposition occurs slowly over the entire temperature range, as shown in **Figure 1-11**..

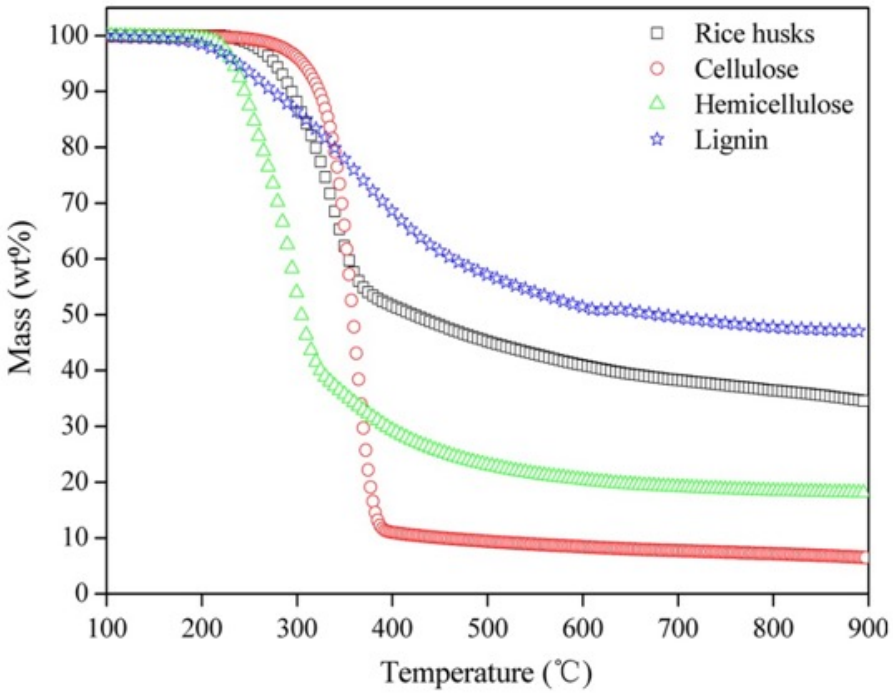

Figure 1-11: TGA curves of rice husks, cellulose, hemicellulose and lignin (Cheng et al., 2018)

For pyrolysis temperatures below 260 °C, the weight loss of rice husk is low, as shown in **Figure 1-11**. This phenomenon is mainly caused by dehydration and the low degree of decomposition of hemicellulose. For the temperature range of 260-300 ºC, the cellulose shows a minimal mass loss and hardly decomposes at all. At this temperature, the pyrolysis reactions of cellulose are mostly intramolecular dehydration. Therefore, the changes in the cellulose structure are relatively slight, and its crystalline form is maintained (Cheng et al., 2018; Xin et al., 2015). The significant changes in rice husk mass loss are observed at the temperature between 280 and 300 °C, resulting mainly from the decomposition of hemicellulose. A large amount of hemicellulose decomposes in this temperature range, as shown in the hemicellulose mass loss in **Figure 1-11**. Shafizadeh (1984) has shown for cellulose that at lower temperatures, below 300 ºC, the dominant reaction mechanism produces water, CO, CO_2, and char. At higher temperatures, cellulose is decomposed by an alternative pathway, and the primary evolved product is tar, which contains levoglucosan as the significant component with aldehydes, ketones and organics acids, and CO, CO_2, H_2, and char. The hemicellulose (xylan

main component in hemicellulose) at 500 ºC produced mostly tar together with CO_2, water, char, and other hydrocarbons. The lignin decomposition involves lower-temperature releases of CO, CO_2, water, methanol, and tar and temperature above 500 ºC, the H_2 and CO are released.

Heating rate

The heating rate during pyrolysis has a significant effect on the distribution of the products. Pyrolysis is classified depending on the heating rate. There are three types of pyrolysis: 1) conventional/slow pyrolysis, 2) fast pyrolysis, and 3) flash pyrolysis (Onay and Kockar, 2003). The slow pyrolysis is typically used to modify the solid material, minimizing the liquid produced. Fast pyrolysis and flash pyrolysis maximize the gases and liquid produced.

In slow pyrolysis, the reactions that occur are always in equilibrium. The heating period is slow enough to permit equilibrium during the pyrolysis process. In this case, the final yield and the distribution of the products are limited by the heating rate. The residence time of the products in the reactor is also necessary because their presence can influence the primary and secondary reactions. **Table 1-1** summarize how each method differs in temperature, residence time, heating rate, and products distribution.

Table 1-1: Summary of the different pyrolysis modes with their process conditions and product distribution.

Process conditions	Slow pyrolysis	Fast pyrolysis	Flash pyrolysis
Temperature (°C)	400–900	450–850	600–1200
Heating rate (°C/s)	0.1–10	10–200	> 1000
Process time (min)	> 5	10–25	< 1
Vapor residence time (s)	≤550	0.5–10	< 0.5
Char yield (wt.%	25–50	15–25	5–15
Bio-oil yield (wt.%)	20–40	60–75	25–40
Gas yield (wt.%)	10–25	10–20	50–60

In fast pyrolysis, there are a negligible number of reactions during the heat-up period. Whatever pyrolysis reactions occur take place isothermally at the final temperature. Volatile residence time is a significant factor affecting the yields of gaseous and liquid products in a biomass

sample. Fast pyrolysis is the most common of the methods, both in research and in practical use. Flash pyrolysis is a highly rapid thermal decomposition pyrolysis with a high heating rate. The main products are gases and bio-oil.

1.3.2.2. *Gasification*

Gasification is the exothermic partial oxidation of biomass with process conditions optimized for high yields of gaseous products (syngas) (Ciferno and Marano, 2002) rich in CO, H_2, CH_4, and CO_2 and some hydrocarbons (CH_4, C_2H_4, C_2H_6). Very small amounts of H_2S, NH_3, and liquid may also be produced (Pandey et al., 2019; Zhang et al., 2015c). Based on the gasification agents used, biomass gasification processes can be divided into air gasification using air (Wang et al., 2008a; Zhang et al., 2015c; Zhang et al., 2017), steam gasification using steam (Elorf et al., 2019; Jayaraman and Gökalp, 2015; Moghadam et al., 2014), oxygen gasification using oxygen (Niu et al., 2014), carbon dioxide gasification using carbon dioxide (Gao et al., 2016c), supercritical water gasification using supercritical water (Guo et al., 2015a).

The heat content of the syngas is dependent upon the type of the gasifying agent. The calorific values of the product gas from air, steam, and oxygen gasification are around 4–7, 10–18, and 12–28 MJ/Nm^3, respectively (Basu, 2010). Biomass gasification decreases the carbon-to-hydrogen mass ratio. Consequently, H_2 fraction is increased, which in turn enhances the calorific value of the output gaseous product. Feedstock parameters, such as particle size and shape, moisture content, heating value, carbon, and ash content, may significantly affect the performance of the gasifier. Therefore, information on the feedstock's volatility, its elemental analysis, heat content, and potential for slagging/fouling is very important in evaluating a gasification process (Ptasinski, 2008). In general, feeds with low volatile content are better for partial oxidation gasification, while biomass products with higher volatile content may be used as indirect gasification feedstocks. Biomass feedstocks come in a variety of forms, each with its own set of issues. Predicting specific biomass forms for a specific gasifier type under a range of conditions is critical. Although the chemical composition of biomass organisms or types is identical, the size and form of biomass feedstock particles are critical in deciding the difficulties in transporting and shipping the feedstock, as well as the behavior of the feedstock until delivered (Reed and Das, 1988). The gaseous products, or syngas can be cleaned and used directly as an engine fuel or upgraded to liquid fuels or chemical feedstocks to produce methanol or it can be used in the Fischer-Tropsch process to produce synthetic fuel (Huber et al., 2006; Wang et al., 2008b). One of the challenges of gasification is the management of

higher molecular weight volatiles that condense into tars; these tars are both a fouling challenge and a potential source of persistent environmental pollutants, such as polycyclic aromatic hydrocarbons (Milne et al., 1998; Tanger et al., 2013).

1.3.2.3. *Combustion*

Combustion has been the most commonly used biomass conversion process since the dawn of humanity. Still today, a large majority of the human population relies on the burning of wood and agricultural residues in three-pot fires and stoves to supply heat and light energy for cooking and space heating (Kataki et al., 2015). This process is still the dominant bioenergy pathway worldwide. Furnaces and boilers are used typically to produce steam for use in district heating/cooling systems or to drive turbines to produce electricity (López González, 2013). During combustion, biomass fuel is burnt in excess air to produce heat. This process involves the production of heat due to the oxidation of carbon- and hydrogen-rich biomass to CO_2 and H_2O. However, the detailed chemical kinetics of the reactions during biomass combustion are complex (Babu, 2008; Jenkins et al., 1998; Tanger et al., 2013) and poor combustion results in the release of intermediates, including environmental air pollutants CH_4, CO, and particulate matter. Additionally, fuel impurities, such as sulfur and nitrogen, are associated with SOx and NOx emission (Tanger et al., 2013). In the combustion process, the main activities that occur are initial fuel drying, ignition and combustion of volatile constituents, and finally, the char's burning. The combustion is frequently proposed for the conversion of lignin-rich feedstocks. This process can be used to convert biomass in two ways: for direct conversion of the whole biomass or for parts of the biomass that exist after biochemical conversion (Kataki et al., 2015).

All the process described above uses dry biomass to transform it into energy. Therefore, it needs a previous drying. The reduction of water content in biomass, i.e., drying, results in the simultaneous increase in thermal value, preservation potential, ease in storage and transportation, less negative impact on the environment, and more uniform combustion. However, other thermochemical conversion processes do not require drying. These processes are known as wet biomass conversion processes or hydrothermal processes, including hydrothermal liquefaction (HTL) and hydrothermal carbonization (HTC).

1.3.2.4. *Hydrothermal liquefaction*

Hydrothermal liquefaction of biomass is the thermochemical conversion of biomass into liquid fuels by processing in a hot, pressurized water environment for sufficient time to break down the solid biopolymeric structure to mainly liquid components. Typical hydrothermal processing conditions are 250–374 ºC of temperature and operating pressures from 4 to 22 MPa of pressure (Elliott et al., 2015). The main products are liquid, as well as by-products in a gaseous, aqueous, and solid phase (Toor et al., 2011). HTL transforms 5% to 61% of the wet biomass into a liquid product called bio-oil, consisting of water-soluble components such as acids, alcohols, cyclic ketones, phenols, and naphthols, this bio-oil produced, with an energy value close to fossil petroleum (Jena and Das, 2011), is not directly suited as transportation fuel, but it is expected to be a suitable renewable feedstock for co-refining in existing fossil-based refineries. The recovery of the bio-oil is made by liquid-liquid extraction with hexane. A solid residue (20-49%) and a gaseous phase (15-30%), composed mainly of CO2 and CO, are also the by-products of HTL of the biomass (Beauchet et al., 2011; Xiu et al., 2010). The quality of the bio-oil in terms of oxygen content is increased with the use of catalysts; these decrease the production of solid residues. The catalysts such as Raney Ni and m-ZrO2 can be used (Beauchet et al., 2011). The literature has thoroughly identified and outlined the precise classification, reaction conditions, and reaction pathways for HTL processes of biomass (Behrendt et al., 2008; Toor et al., 2011; Zhang, 2010). Compared with pyrolysis, an HTL process can produce higher quality bio-oils with beneficial chemical and physical properties (e.g., lower oxygen content and smaller molecular weights, and increased heating values). Many literature studies have reported HTL technologies' ability to produce a variety of chemicals, such as vanillin, phenols, aldehydes, and acetic acids, among others (Behrendt et al., 2008; Toor et al., 2011; Zhang, 2010). For biomass liquefaction, Behrendt et al. (Behrendt et al., 2008) objectively analyzed different historical and existing HTL processes' theoretical implementations. HTL processes involving sub- and supercritical water were stated by Peterson et al. (Peterson et al., 2008) and Toor et al.(Toor et al., 2011). Furthermore, Zhang (Zhang, 2010) has published an overview of biomass HTL processes for various feedstocks. As reviewed by Akhtar et al.(Akhtar and Amin, 2011), the yield of bio-oil is highly dependent on different operating parameters such as feedstock form, solvent type, temperature, substrate concentration, reaction time, catalyst, and so on.

1.3.2.5. *Hydrothermal carbonization*

The HTC is a thermochemical process that occurs in subcritical water between 180 °C and 250 °C and can last from a few minutes to several hours. The pressure is autogenous with the saturated vapor pressure of the subcritical water and the gas produced during the HTC process (10-40 bars) (Arellanoa et al., 2016; Hitzl et al., 2015; Hoekman et al., 2011; Missaoui et al., 2017). During HTC, the feedstock undergoes a complex network of simultaneous reactions. The final products are a carbon-enriched residue (hydrochar), characterized by high carbon content (55–74 % (w/w) carbon) and high calorific value (21.1-30.6 MJ/kg) (Hoekman et al., 2011; Vassilev et al., 2010; Xiao et al., 2012), a liquid phase contains important chemicals, such as furfurals and small organic acids and a relatively small amount of gas, low in carbon and consequently harmless for greenhouse effects (Libra et al., 2011). Like HTL, the HTC process allows the treatment of substrates with a high moisture content >50 % (w/w) without requiring a drying pretreatment step (Libra et al., 2011; Missaoui et al., 2017). In recent years, the HTC process has been considered an alternative method of processing biomass for value-added products. The solid product created during HTC is called hydrochar in order to distinguish it from biochar or pyro-char. HTC process has several advantages over another thermochemical process, such as lower energy consumption and less emission over pyrolysis; it can be used for biomass with high moisture content. Therefore, a greater variety of feedstocks could be considered for processing into hydrochar since drying the feedstock is unnecessary for HTC. Compared to biochar produced at typical temperature ranges, hydrochar generally has a lower C content due to lower dehydration during the HTC process (Bargmann et al., 2013; Libra et al., 2011). Hydrochar has a much lower ash content than biochar; the ash in biomass enters the liquid phase during HTC, while biochar retains all of the ash in the biomass (Fang et al., 2015a; Fang et al., 2017). Consequently, hydrochar is slightly more acidic than biochar (Parshetti et al., 2014), has higher H/C ratios and less aromaticity than biochar, and little or no molten aromatic ring structure (Bejarano et al., 2017). Depending on the applications, the characteristics of hydrochar may be more desirable than those of biochar. The relatively low ash content of most hydrochars is desirable when they are to be used as a fuel (Demirbas, 2007; Yang et al., 2016b). Also, the surface area of biochar or pyrochar is much larger than hydrochar, since during HTC, reactions such as condensation and polymerization make pore formations much smaller than during pyrolysis. The physical, chemical, and mechanical properties of hydrochar make it susceptible to different uses. Hydrochar thus is used directly as a solid fuel that can be burned for energy or used to synthesize fuel cells,

electrode supercapacitors, and batteries as a medium for converting and storing energy (Ding et al., 2012; Lin et al., 2015; Sik et al., 2015; Yang and Wang, 2016). Most hydrochars, particularly the ones derived from plant biomass, are considered an excellent potential solid fuel is owing to their low ash content; the inorganic minerals in the biomass enter the processing liquid during the HTC process (Fang et al., 2015a).

1.3.2.5.1. *Mechanism and steps of hydrothermal carbonization of biomass*

Many chemical reactions that can occur during the hydrothermal carbonization process are mentioned in the literature. Although there is a divergence of opinion between studies on the type of reactions that occur during hydrothermal carbonization, but it is known that the decomposition of biomass in the HTC process is governed in sum by hydrolysis (endothermic reaction), dehydration and decarboxylation (exothermic reactions). These reactions occur simultaneously, thus the functional groups of the biomass are removed to some extent (Funke and Ziegler, 2010; Yan et al., 2010; Zhang et al., 2018). However, the complex network of reactions and the combined mechanism for all these reactions is not yet known in detail. So, for the time being, only a separate discussion of the general reaction mechanisms that have been identified can provide useful information on the possibilities for manipulating the reaction. These mechanisms include hydrolysis, dehydration, decarboxylation, condensation, aromatization and polymerization (Kambo and Dutta, 2015; Kruse et al., 2013; Lu et al., 2012; Lucian et al., 2019; Volpe et al., 2018). The pathways of the main HTC reactions for lignocellulosic biomass are shown in **Figure 1-12**. The Liquid biocrude in the **Figure 1-12** is a complex liquid solution of condensation, aromatization and polymerization products. The reactions in the **Figure 1-12** are not necessarily consecutive or in series, but can form a parallel network of different reaction pathways. The nature and mechanisms of these reactions depend mainly on the feedstock. The main components of the biomass are hydrolyzed in large quantities from oligomers and monomers of sugars (pentose and hexoses) (Kumar, 2013). The extractives compounds of biomass are being eluted; most of these compounds have a good solubility in water in the HTC condition. The fragments of the extractives dissolved in water undergo further degradation mechanisms, such as dehydration and decarboxylation, while condensation reactions occur. These reactions form highly reactive intermediates such as furfurans, 5-HMF and its derivatives. They can also represent high value-added chemicals. During the polymerization reaction, they form humic acids, bitumen and insoluble solids that partially precipitate to form the main product of HTC (hydrochar).

In addition, there may be components of the biomass or oligomer fragments of the biomass that do not hydrolyze under the given reaction conditions, like crystalline cellulose (Funke and Ziegler, 2010).

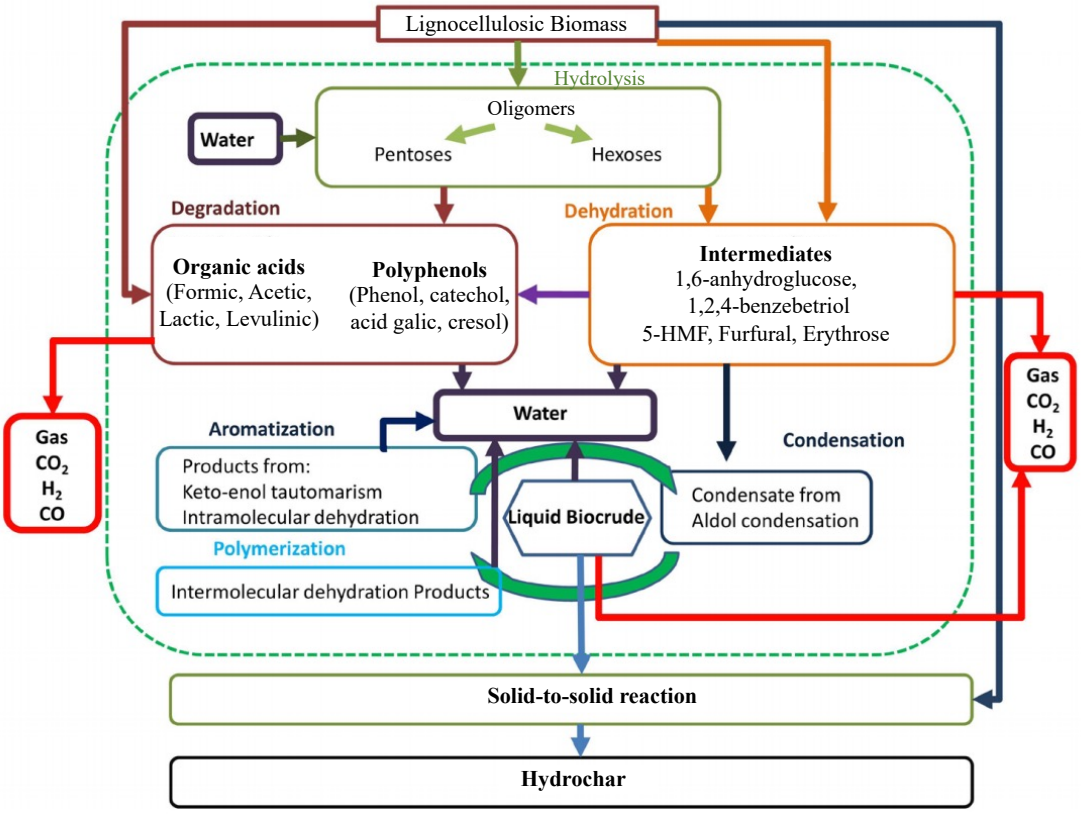

Figure 1-12: HTC reaction pathways for lignocellulosic biomass (Reza et al., 2014a))

Hydrolysis reaction

The hydrolysis reaction is endothermic; this reaction leads to the cleavage of mainly ester and ether bonds of the biomacromolecules by adding water. The hydrolysis has the lowest activation energy being the first step to be initiated in the HTC process (Fang et al., 2018; Gao et al., 2016a). The extensive product range in this reaction includes (oligo)-saccharides of cellulose and phenolic fragments of lignin (Fakkaew et al., 2015; Fang et al., 2018; Gao et al., 2016a). The complexity of the hydrolysis reaction can be summarized by the detailed mechanism of the D-fructose reaction explained by Antal Jr et al. (1990), since D-fructose is a specific substance in contrast to biomass. Next to other degradation mechanisms mentioned below, the resulting fragments are being further hydrolyzed, such as 5-HMF, erythrose, and

aldehydes (Krylova and Zaitchenko, 2018), to yield levulinic and formic acid. Hemicellulose is readily hydrolyzed above 150 °C, but the detailed reaction pathways are less well known due to the complexity of its structure. Cellulose is being hydrolyzed significantly under hydrothermal conditions above approximately 180°C; details of the reaction mechanisms were summarized by Peterson et al. (2008). Hydrolysis of lignin is very complex; however, it is most likely at about 200 °C due to its large amount of ether bonds. Nucleophilic reactions form highly reactive products with a low molecular weight. One of them of potential interest is acetic acid, which is most likely formed by hydrolysis of the side chains (Funke and Ziegler, 2010). The number of different fragments formed is high, including the hydrolysis of selected components (D-fructose) (Concin et al., 1983). Most of these fragments are very reactive, and condensation reactions rapidly form precipitates. The different biomass components interact with each other. The effect of these interactions on hydrolysis is mainly unknown. In general, lignin is bonded to hemicelluloses by covalent bonds. Therefore, hemicellulose fragments interact with lignin and thus increase the solubility of their aromatic structures, which is consistent with the observation that lignin and hemicellulose from an oligomer that is usually stable under hydrothermal conditions (Funke and Ziegler, 2010). In the case of forced convection (e.g., stirring), the hydrolysis reaction is swift, and its rate is mainly determined by the adjusted flow rate and not by the reaction temperature. It can be concluded that the rate of biomass hydrolysis is mainly determined by diffusion and thus limited by transport phenomena in the biomass matrix; this may lead to the condensation of fragments in the biomass matrix at high temperatures (Hashaikeh et al., 2007; Mochidzuki et al., 2005; Shoji et al., 2005).

Dehydration reaction

The dehydration reaction is the removal of water from the biomass structure. Hydrothermal carbonization dehydration refers to all chemical reactions and physical processes, which remove water from the biomass matrix without changing its chemical constitution. Biomass dehydration reaction during the HTC process means reducing the H/C and O/C ratios. According to many studies, cellulose in biomass starts to decompose by pure dehydration according to the following reaction:

$$4(C_6H_{10}O_5)_n \leftrightarrow 2(C_{12}H_{10}O_5)_n + 10H_2O \quad (1\text{-}1)$$

The meaningful decarboxylation is only observed after that specific amount of water is formed. Several experimental studies under hydrothermal conditions show that, at low HTC reaction

conditions, dehydration can also be achieved without significant decarboxylation (Funke and Ziegler, 2010). Several experimental studies under hydrothermal conditions show that, at low HTC reaction conditions, dehydration can also be achieved without significant decarboxylation. However, the extent to which biomass can be carbonized without significant decarboxylation is mainly unknown (Titirici et al., 2007). The molar ratio between decarboxylation and dehydration (CO_2/H_2O) ranges from 0.2 for cellulose to 1 for lignite and is largely independent of temperature under HTC conditions. The rate of dehydration is higher or equal to decarboxylation. The removal of hydroxyl groups generally explains dehydration (Funke and Ziegler, 2010). There is practically no more detailed study of biomass dehydration reactions; however, it is reported that glucose dehydrates to form 5-HMF or 1,6-anhydroglucose (Funke and Ziegler, 2010; Kabyemela et al., 1999). For the case of lignin, the dehydroxylation of catechol is mentioned, and the possible formation of water during the cleavage of phenolic and alcoholic groups above 150°C and 200°C, respectively (Funke and Ziegler, 2010; Murray and Evans, 1972).

Decarboxylation reaction

Decarboxylation is a chemical reaction that removes a carboxyl group and releases carbon dioxide (CO_2). Detailed reaction mechanisms are largely unknown, including the effect of the presence of water (Peterson et al., 2008). Carboxyl and carbonyl groups rapidly degrade above 150°C, forming CO_2 and CO, respectively (Sevilla and Fuertes, 2009a). The gas formation (CO_2 and CO) increases with increasing temperature and reaction time (Missaoui et al., 2017). One likely source for CO_2 is formic acid, which is formed in significant amounts during the degradation of cellulose and decomposes under hydrothermal conditions to yield CO_2 and H_2O (Nelson et al., 1984). A significant decarboxylation reaction increases the formation of gas, thus increasing the saturation pressure of the system. The decarboxylation pathway involves the degradation of extractives, hemicellulose, and cellulose. Under hydrothermal conditions, these materials can degrade into monomers such as formic acid, acetic acid, and furfurans, which further degrade into CO_2 and H_2O (Hoekman et al., 2013). With the increase in temperature of HTC, most monosaccharides decrease substantially, degrading into carboxylic acids, such as acetic and formic acids (Hoekman et al., 2011; Hoekman et al., 2013). The presence of acids can be confirmed from the low pH of the liquid solution after HTC. Other possible decarboxylation pathways involve condensation reactions, resulting in the formation of CO_2 (Funke and Ziegler, 2010).

Condensation- polymerization reactions

The intermediates (5-HMF, furfural) formed from hydrolysis reactions in hydrothermal carbonization are highly reactive. Also, it depends on the type of biomass, as well as the degree of conversion. They are unsaturated compounds that readily polymerize by aldol condensation or intermolecular dehydration involving the removal of the carboxyl and hydroxyl groups. These reactions (dehydration and decarboxylation), explained above, create H_2O and CO_2, respectively (Reza et al., 2014b). Condensation reactions (e.g., of aromatic nuclei) may account for part of the CO_2 formation. A theoretical observation of possible condensation reactions can explain the experimental observations (formation and composition of gases, influence of temperature and pressure). Also, the carbonization rate is increasingly determined by steric influences with a higher degree of condensation of aromatics. Therefore, it can be argued that the formation of hydrochar during hydrothermal carbonization is mainly characterized by polymerization and condensation, specifically aldol condensation (Kabyemela et al., 1999; McCollom et al., 1999). Condensation proceeds mainly with the formation of H_2O. Free radical mechanisms can occur under hydrothermal conditions but are more likely to be dominant under supercritical conditions and at low density. Under subcritical conditions, the free radicals are effectively saturated by the water present and the hydrogen donated by aromatization (Sevilla and Fuertes, 2009b). Thus, condensation polymerization is most likely based on step-growth polymerization supported by the low polymerization rate observed during the experiments. In the case of lignin fragments (highly reactive), it has been reported that polymerization is completed in several minutes above 300 °C, whereas at low temperatures, it can take hours, even days (Funke and Ziegler, 2010; Masselter et al., 1995). Condensation reactions of monosaccharides are still slower, mainly since cross-linked polymerization competes with the recondensation to oligosaccharides. However, some degradation products of monosaccharides, such as 5-HMF, show higher reactivity, which may accelerate polymerization (Bobleter, 1994; Reza et al., 2014b). It has also been observed that hemicellulose fragments appear to stabilize lignin fragments, slowing down condensation reactions significantly. Therefore, the results from model compounds have clear limits for extrapolation to "real" biomass. Not everything is known about detailed polymerization sequences during HTC of biomass (Reza et al., 2014b). Polymerization that forms solid precipitation is usually considered an undesirable secondary reaction. It cannot be known whether the soluble hydrochar fraction is a precursor to the incompletely condensed non-soluble fraction (precipitate) or whether the two are components of distinct reaction pathways. However, it is known that it is not easy to distinguish analytically

between the characteristics of the two hydrochars; because both appear as a single solid mass of char (Paksung et al., 2020).

On the other hand, the observation that the remaining insoluble fraction exhibits a specific surface area two orders of magnitude higher unfractionated hydrochar provides some evidence that the reaction pathways might be different. Other experiments reported that condensation fragments within the biomass matrix are able to "block" the remaining transport of biomacromolecules, thus trapping hydrolysis products inside the pore, impeding access of water to the pore. This phenomenon could also contribute to the increased hydrophobicity of HTC hydrochar (Garrote et al., 2001; Reza et al., 2014b).

Aromatization reaction

Although hemicellulose and cellulose are linear polymeric carbohydrate chains, they can form aromatic structures under hydrothermal conditions. Aromatic structures exhibit high stability under hydrothermal conditions and can therefore be considered as a fundamental building block of the resulting hydrochar (Funke and Ziegler, 2010). The cross-linked condensation of aromatic rings also constitutes the main components of natural carbon, which could explain the excellent agreement between natural carbonization and hydrochar (Peterson et al., 2008). Similar chemical structure characteristics of hydrochar and natural carbon have been mentioned in several publications. Based on these considerations, it is evident that the effect of hydrothermal treatment on oxygen content decreases with an increasing number of aromatic bonds. Aromatization appears to be significantly temperature dependent. Hydrothermal dehydration experiments of lignite and peat reported aromatization above 270°C (Funke and Ziegler, 2010); however, this depends on the type of biomass and the treatment time. Aromatization reactions increase the formation of polycyclic aromatic hydrocarbons (PAHs). The intermediate unsaturated compounds produced from dehydration and decarboxylation readily polymerize by aldol condensation, forming initially into long-chain aliphatic compounds. These hydrocarbons promote the formation of PAHs by aromatization reactions. As the temperature is increased, the ring number increases (Peng et al., 2017; Shen et al., 2017).

During HTC, there are some stable compounds with a crystalline structure and oligomer fragments that do not hydrolyze, and it is carried out from the solid-to-solid pathway reaction. Although their quantitative contribution is estimated to be considerably low at temperatures above 200°C (Funke and Ziegler, 2010), these reactions could become significant. However,

Falco et al. (2011) reported that the solid-to-solid pathway dominates during the HTC of cellulose due to the large aromatic groups in the hydrochar.

The demethylation reaction has been used to explain the mechanism that results in a phenol becoming part of a catechol-like carbon structure. Several experimental setups measured the development of lower amounts of CH_4, which seems to confirm this mechanism (Bevan et al., 2020; Hatcher, 1995).

Also, it has been reported that pyrolytic reactions also compete with hydrothermal conditions; and could become significant above 200°C, although typical pyrolysis products (e.g., CO and tars) have not been reported to form in significant amounts during hydrothermal carbonization. Carbonization of biomacromolecules, which have no contact with H_2O because they have been blocked by precipitation of condensation fragments, has also been explained by pyrolytic reactions (Hashaikeh et al., 2007). Other reactions observed are the Fischer-Tropsch type; given the large amount of CO2 formed during HTC, they could play a role that has not been investigated in detail so far (Funke and Ziegler, 2010; McCollom et al., 1999).

The main product of HTC is hydrochar, a solid material 55-74% rich in carbon, is the stable, a lignite-like material which is characterized by a high calorific value (21.1–30.6 MJ/kg) (Danso-Boateng et al., 2013) and its physical, chemical, and mechanical properties make it susceptible to different uses. Hydrochar can thus be used directly as a solid fuel that can be burned for energy or produce syngas (Peng et al., 2017). Syngas produced from hydrochar can be used in Fioscher-Tropsch synthesis to produce synthetic fuels.

1.4. Fischer-Trospch process

The Fischer-Tropsch process (SFT) consists of the transformation of syngas (H_2 and CO) in a catalytic reactor to obtain liquid hydrocarbons (Hoek et al., 1985). Among the liquid products derived from this synthesis, gasoline, naphtha, diesel, methanol, among others, have a high added value.

The primary reaction of the SFT process is the synthesis of alkanes **Eq.(1-2)** and linear olefins or alkene **Eq. (1-3)**. However, several secondary reactions also occur, including the synthesis of oxygenated products **Eq. (1-4)** the water-gas shift reaction **Eq.(1-5)** and the Boudouard reaction **Eq.(1-6)** (Rojas et al., 2011). These reactions can be represented as follows:

Alkanes

$$nCO + (n+2)H_2 \rightarrow C_nH_{2n+2} + nH_2O \quad (1\text{-}2)$$

Alkene or linear olefins

$$nCO + 2nH_2 \rightarrow C_nH_{2n} + nH_2O \quad (1\text{-}3)$$

Alcohols

$$CO + 2nH_2 \rightarrow C_nH_{2n+2}O + (n-1)H_2O \quad (1\text{-}4)$$

Water-gas shift:

$$CO + H_2O \rightarrow CO_2 + H_2 \quad (1\text{-}5)$$

Boudouard reaction

$$2CO \rightarrow CO_2 + C \quad (1\text{-}6)$$

Although the details of the mechanism of SFT are not fully understood, most researchers accept that hydrocarbon formation occurs through a polymerization reaction of CHx* units formed in situ on the catalyst surface from CO and H_2 and act as initiator and monomeric species in the chain growth process.

1.4.1. SFT reaction mechanism

The Fischer-Tropsch synthesis resembles an oligomerization reaction or polymerization with the following steps: (a) adsorption of reagents; (b) chain initiation; (c) chain growth; (d) chain termination; (e) desorption of products; and (f) re-adsorption and subsequent reaction of those products. The product distribution described in the previous section demonstrates the polymeric nature of the Fischer-Tropsch synthesis, but at present, a great deal of controversy persists about the nature of the monomer and, more specifically, the path followed by the hydrocarbon chain growth. Today there are many mechanisms of SFT (Adesina, 1996; Dry, 1996; Hindermann et al., 1993).The three main proposed reaction mechanisms are explained below:

1.4.1.1. *Mechanism of carbides*

It was proposed by Fischer and Tropsch (1926). The first step of the reaction is the dissociative adsorption of carbon monoxide on the catalyst surface, which gives rise to a metal carbide that subsequently transforms into the M-CHx species. The carbide mechanism is presented in **Figure 1-13.** Insertion into the metal-carbon bond of another similar neighboring species

results in the formation of a hydrocarbon with more carbon atoms. Chain growth can be interrupted by adding or eliminating hydrogen, giving rise to the corresponding alkane or olefin, respectively. This mechanism does not explain the formation of oxygenated compounds (alcohols and aldehydes).

This scheme presupposes the formation of a metal carbide; this would be possible with Fe catalysts; however, other Fischer-Tropsch active metals such as Co or Ru cannot form carbides under the reaction conditions; this model would fail.

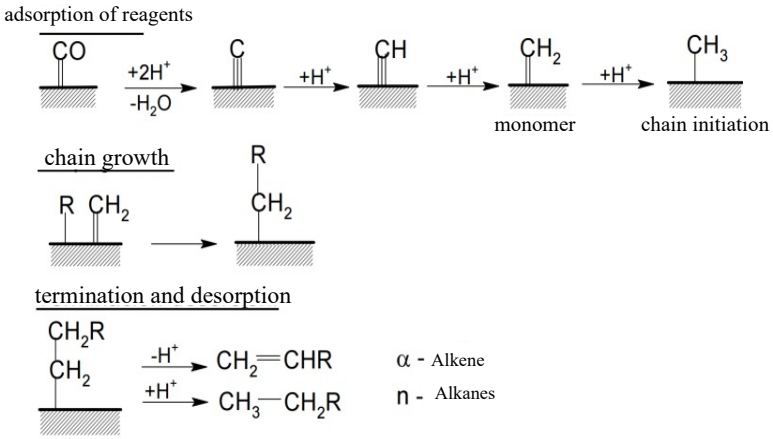

Figure 1-13: Mechanism of carbides (*Fischer and Tropsch, 1926*)

1.4.1.2. *Mechanism of hydroxy-carbenes*

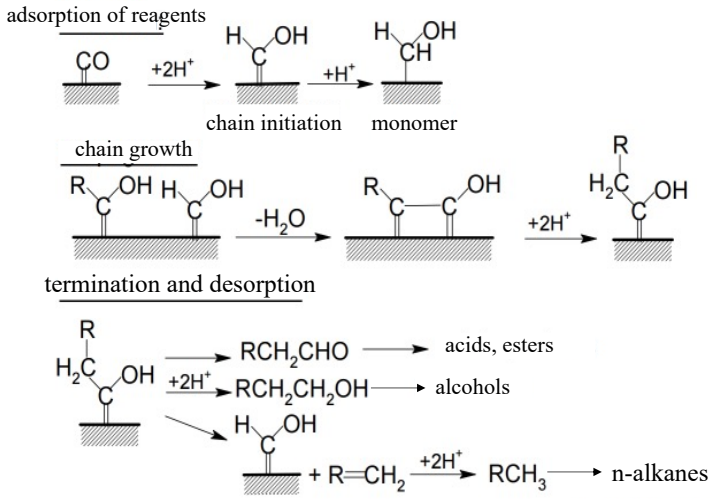

Figure 1-14: Mechanism of hydroxy-carbenes (Kummer et al., 1948).

This mechanism was proposed by Kummer et al. (1948). This mechanism consists of chain growth by condensation of two hydroxy-carbene species (M-CHOH) to eliminate water. First, a non-dissociative adsorbed CO molecule is partially hydrogenated to create the surface M-CHOH species. This model explains the formation of hydrocarbons and oxygenated compounds. In **Figure 1-14**, the mechanism of hydroxy-carbenes is presented.

1.4.1.3. *CO insertion mechanism*

In this mechanism, chain growth occurs by inserting a carbonyl intermediate (M-CO) into an alkyl chain metal bond. It was proposed by Pichler and Schulz (1970). In this case, the CO will act as a monomer, while the chain initiator will be the alkyl group. Chain growth occurs when CO is inserted into the M-CH3 bond, giving surface acetyl radical. The mechanism of CO insertion is presented in **Figure 1-13**.

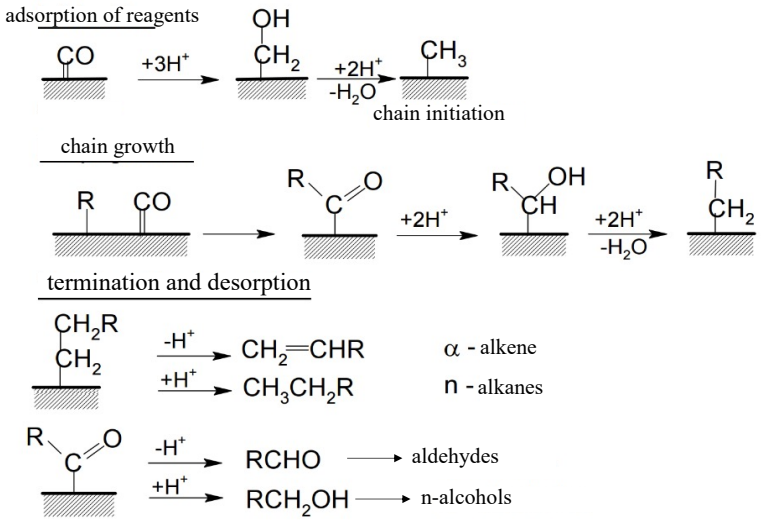

Figure 1-15: CO insertion mechanism (Pichler and Schulz, 1970).

These three mechanisms share an essential common feature: the presence of a single species responsible for chain growth (CH_2, CHOH, and CO). However, none of these mechanisms alone can explain the great diversity of products formed in SFT, so some researchers have proposed other mechanisms where more than one reaction intermediate is involved and presented in **Figure 1-16**. Thus, according to the mechanism proposed by Dry (1996), hydrocarbons are produced by the insertion of -CH_2- units into alkyl chains, while the insertion of CO produces the oxygenated compounds. This mechanism has been accepted by several researchers (Biloen and Sachtler, 1981).

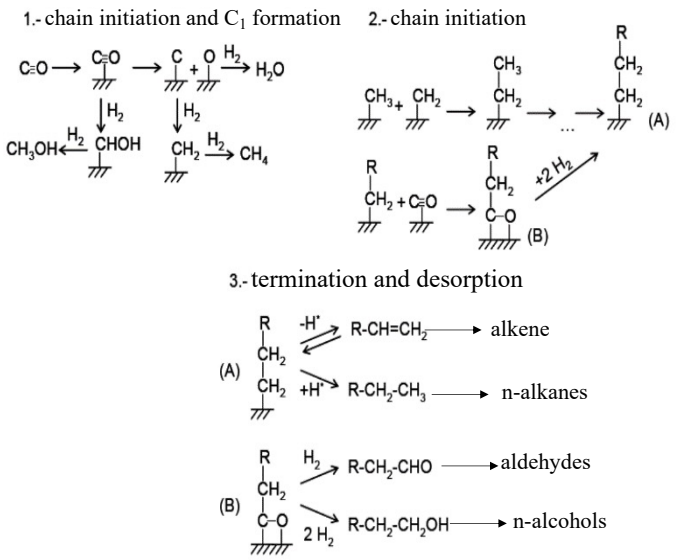

Figure 1-16: SFT reaction mechanism proposed by Dry (1996)

1.4.2. Product distribution and selectivity

The Fischer-Tropsch synthesis has been characterized as a reductive CO oligomerization or polymerization. Then, the distribution of the products obtained can be determined from an analogy with oligomerization and polymerization, as performed by Anderson et al. (1958). Schematically it is proposed:

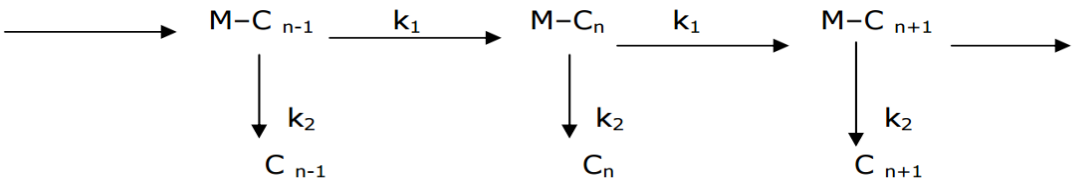

Figure 1-17: Diagram of the distribution and selectivity of the product proposed by Anderson et al. (1958).

This scheme shows that after each incorporation of a CO-derived "monomer" C1 into the growing chain, propagation of the chain with a rate constant k1 can occur, or the chain ends with a constant rate k2 by forming a product. In this simple method, it is assumed that under steady-state conditions, k1 and k2 are independent of chain length and that C2 or larger "monomers" are not inserted into the chain. As a result, the mass fraction Wn of each hydrocarbon produced decreases with the number of carbon atoms according to a geometric progression:

$$\frac{W_n}{n} = \alpha^{n-1}(1-\alpha)^2 \qquad (1\text{-}7)$$

where Wn is the mass fraction of the hydrocarbon of n carbon atoms, n is the number of carbon atoms, α is Schulz-Flory coefficient, α = k1 / (k1+k2) (the probability of chain growth or degree of polymerization).

If k1 << k2, essentially low molecular weight products such as methane or C2-C4 are formed if k1 ≈ k2 the reaction could produce hydrocarbons in a wide range C1-C20 and k1 >> k2, the reaction will allow obtaining high molecular weight products such as waxes or poly-methylene.

Figure 1-18 depicts the selectivity towards various product groups as a function of α-chain growth probability. In any case, it should be noted that in Fischer-Tropsch synthesis, a broad spectrum of C1 - C50+ hydrocarbons are produced, being one of the significant challenges of this process to find catalysts that manage to produce the desired product or product fraction selectively. Generally, this fraction is the one between C13 -C18 (diesel fraction) since it has excellent properties, such as a high cetane number (>70) (Rojas et al., 2011).

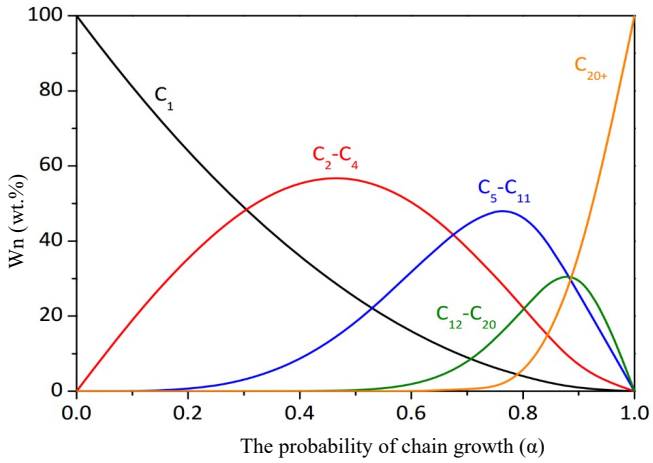

Figure 1-18: Distribution of products as a function of parameter α (Rojas et al., 2011).

Typically, SFT is carried out in a range of pressures between 2 and 6 MPa and temperatures: low temperature (200-250 ºC) and high temperature (300-350 ºC). In the first case, iron (Fe) or cobalt (Co) catalysts are usually used, obtaining mainly long-chain hydrocarbons, while in the second process, mainly Fe catalysts are used, forming lighter hydrocarbon fractions (*Rojas et al., 2011*).

In general, the conversion of biomass into synthetic fuels or energy is complex, involving complex chemical reactions, different transport phenomena, and different reactor structures. The study of this process in a laboratory and pilot plant is very tedious and expensive. For this reason, other researchers have looked for alternatives such as modeling and simulation studies, which are undoubtedly necessary and complementary to experimental studies. Besides, this contributes to the design, operation, optimization, and control of the process.

1.5. Modeling and simulation studies of biomass conversion processes

As we have seen before, biomass conversion strategies include thermochemical conversions, such as pyrolysis, gasification, hydrothermal carbonization, combustion, and biochemical conversions. The performance of each of these processes is highly dependent on transport phenomena, i.e., the mechanisms by which heat, mass, and momentum are transferred throughout a system and, of course, the kinetics of chemical reactions and reactor hydrodynamics.

In the case of thermochemical biomass conversion, transport phenomena are very important. For example, in fast pyrolysis, effective heat transfer combined with the rapid escape of volatile products is essential to reducing char formation and optimizing the yield of desirable products (bio-oil). The rapid heating rates combined with reactor residence times on the order of a few seconds will shift pyrolysis products' yields toward condensable gases while minimizing char formation. (Bridgwater, 1999; Wiley, 2017). In processes that involve heat transfer between solid and fluid phases, the rate at which heat can move across the solid/fluid interface is of critical importance. Jacque Lede explains the difficulties related to the experimental determination of the biomass particle's temperature in their recent critical review on the "Scientific Challenges and Related Recommended Research Topics" regarding biomass fast pyrolysis reactors and heat transfer rates (Lede, 2013). He points out that using a thermocouple to measure the temperatures of very fine biomass particles passing through the reactor quickly during fast conversion reactions is virtually impossible. The mathematical simulation of biomass conversion processes can be very useful, since it allows to predict the products yields and their characteristics. Modeling and simulation of biomass thermochemical is very complex, because it requires to take into account chemical, fluid dynamic, and thermodynamic phenomena (Gagliano et al., 2018).

Accurate representation of heat transfer, mass, momentum, and chemical reaction kinetics inside a reactor is critical when modeling processes that combine heat conduction through solids (biomass particles) and convective heat from fluids (inert gas or water). In this context, modeling and simulation-based on generalized biomass particle geometry, heat and mass transfer; physical constants; reaction kinetics, and reactor hydrodynamics can facilitate the understanding of biomass-to-energy conversion. Understanding these phenomena can help optimize and provide more reliable process models to reduce commercialization's economic uncertainty.

In general, there are several investigations on modeling and simulation of the biomass-to-energy process. However, there is little research on the modeling and simulation of the hydrothermal carbonization process to date. The great variety of phenomena that take place during the HTC process of biomass make the analysis of the process and its simulation difficult; only a few studies have been carried out in this aspect, focusing mainly on pure materials instead of heterogeneous biomasses, for example, (Álvarez-Murillo et al., 2016), who studied the kinetics of cellulose HTC. Besides, (Reza et al., 2013) proposed the kinetics of hemicellulose decomposition as a first-order reaction. However, most studies on HTC kinetics have been limited to the solid phase, while research on the liquid phase's evolution and gases during the process is relatively scarce. Besides, progress in the development of models capable of describing the kinetics and governing mechanisms of the process is very important for designing the equipment and operating conditions required to produce hydrochar with the desired characteristics. Most of the mathematical models describing the biomass HTC process's kinetics have been developed in recent years, but there is room for improvement of the proposed models. Most of the kinetic models reported for biomass HTC processes are (0D) models that analyze the process's kinetics by a simple analytical expression. Mathematical models describing the thermochemical conversion process of biomass can be divided into three categories: kinetic models, statistical models, and computational models. The advantages and limitations of these are summarized in **Table 1-2**. There is some overlap between these categories of models since each variable's mass balance is the basis for all mathematical models. Statistical models are empirical models, i.e., they are based on direct observation, measurement, and experimental data that allow us to predict the system's behavior without understanding the mechanisms that are occurring. In contrast, computational models based on the laws of physics are mechanistic because they try to explain the process, analyzing how experimental conditions affect chemical reactions, such as the transfer of mass, heat, and

momentum. In the computational model, the entire process domain is discretized. The most commonly used discretization methods are the finite difference method, the finite element method, and the finite volume method, the latter being the most widely used in Computational Fluid Dynamics (CFD). With these methods, the continuous domain is exchanged for a discrete domain, where a set of control volumes is used to represent the original domain (Mattiussi, 1997).

Table 1-2: Advantages and limitations of biomass conversion process models.

Models	Advantages	Limitations
Kinetic	Easy to implement	- It does not provide sufficient information for large-scale installations.
Statistical	Qualitative and quantitative analysis of the effect of process parameters.	- Empirical models - Its application is limited to raw materials and experimental conditions.
Computational	-Complete descriptions of space and time variations -Combines reaction kinetics and physical laws to produce accurate simulation of full-scale applications. -Effective and intuitive visual analysis of results	- Numerical simulation is very complex

1.5.1. Kinetic models

Kinetic models provide essential information on kinetic mechanisms to describe the chemical reactions involved in biomass conversion, which is crucial for designing, evaluating, and improving reactors. These models are based on chemical reaction rates and can predict both overall performance and profiles of gas and liquid compositions with time and inside the reactor. Kinetic models are based on the evaluation of the kinetic constants k(T) of the chemical reactions used to simulate the thermochemical conversion processes (Gagliano et al., 2018) . The kinetic models are known as 0D model i.e., no influence of spatial variables; the system behaves in the same way at any point of the reactor. These constants can be calculated by an analytic technique known as thermogravimetric analysis (TG) (White et al., 2011). Indeed, TG allows the evaluation of the Arrhenius kinetic parameters, that is, activation energy (Ea) and

preexponential factor (A), necessary for the determination of the constant rate of a chemical reaction through the Arrhenius mathematical expression (Doherty et al., 2009).

1.5.2. Statistical models

The Design of Experiments - Response Surface Methodology (DoE/RSM) approach has proven to be a handy tool to investigate several variables' influence on a given magnitude .The implementation of a DoE/RSM approach allows to identify the importance of each variable, as well as their interactions, by developing a model with input parameters (processing variables) and output functions (parameters of interest); therefore, it can provide information on the effect of experimental conditions on the direction and magnitude of the measured response. In this way, it has enormous potential to study and optimize a wide range of engineering systems and has often been used in energy production processes such as pyrolysis, gasification, hydrothermal carbonization, so forth. Furthermore, this methodology allows the design of experiments under particular conditions to maximize the information that can be extracted from the results and, provided that the model works and the fit of the experimental data is good, it can be used to predict the behavior of the system under different conditions (Álvarez-Murillo et al., 2015b).

1.5.3. Computational fluid dynamics models

Computational fluid dynamics modeling is based on the principles of fluid mechanics, utilizing numerical methods and algorithms to solve problems that involve fluid flows. CFD models attempt to simulate the interaction of liquids and gases where the surfaces are defined by boundary conditions. They also track the flow of solids through a system. These models employ the principles of the Navier-Stokes equations. Simulations are then conducted by solving the equations iteratively as either a steady-state or transient condition (Tillman et al., 2012). Three-dimensional (3D) computational models offer a versatile approach to study the complete descriptions of space and time variations inside the reactor, combines kinetics reactions with mass, temperature, and velocity fields to produce an accurate simulation of full-scale applications. Practical and intuitive visual analysis of results can help us determine, for example, transport of dissolved components, rates of energy dissipation, biomass particle trajectories inside the de reactor, and determine volumes of high mixing intensity and stagnant zones, based on reactor geometry and operating conditions. These models provide an accurate picture of the processes taking place in the HTC reactor and verify the validity of the 0D kinetic model and constant temperature assumption. However, the versatility of three-dimensional

models has disadvantages because errors may occur for simple models or simplified boundary conditions; also, computation time may extend for large models and complex geometries. Every CFD problem has the same workflow, which can be divided into three basic steps: (1) Pre-processing, which includes preparing geometry and meshing the geometry. (2) Processing: specifying the numerical parameters, i.e., setting up solver parameters, discretization schemes, setting boundary conditions, initial conditions, defining the properties of different phases (gas, liquid, and solids), and selected numerical method on the calculation mesh. (3) Post-processing: The results of calculations are visualized, and the major part of any numerical simulation is interpreting the results; this is done in post-processing (Blocken and Gualtieri, 2012; Gyurik et al., 2019; Román et al., 2018). The CFD solution's accuracy is strongly dependent on the mesh quality while the computational time increases with the number of mesh elements. When the accuracy is not changing significantly with the increasing number of mesh elements, the calculation can be considered mesh independent (Egedy et al., 2013; Gyurik et al., 2019). Once the results are validated as mesh independent, and the results are validated with experimental data, the CFD model can be used to design, scale up, test, and optimize the process.

1.6. Conclusion

- In the last twenty years, global energy consumption has increased by more than 50%. Most energy consumption comes from fossil fuels (oil, coal, and natural gas). Today, fossil fuels account for more than 80% of the world's primary energy consumption. These fuel resources are not sustainable and cause Green House Gas emissions responsible for global warming. Clean and sustainable fuels productions are the main challenges facing the next energy crisis and global warming. In recent years, it has become clear that climate change is no longer strictly an environmental problem, but an economic and safety problem related to the energy sector, the leading emitter of greenhouse gases.
- Renewable energy can solve the great challenge of the energy future and reduce the environmental problem. There are different renewable energy sources, such as solar energy, wind energy, hydro energy, geothermal energy, and biomass energy. Based on the recent REN21 report, renewables contributed 19.3% to human beings' global energy consumption. This consumption is divided into 8.9% from traditional biomass, 4.2% as heat energy (modern biomass, geothermal and solar power), 3.9% hydropower, and 2.3% is electricity from wind and other renewable energy. The exploitation of these

renewable energy has its advantages and some disadvantages due to the current technology available.

- Hydropower has many benefits over most other forms of renewable or sustainable energy. High reliability, proven technologies, high performance, relatively low operation, and maintenance costs, and the ability to easily respond to load changes are only a few of them. Many hydropower plants are built next to reservoirs, which provide the city with electricity, flood protection, and recreational opportunities. However, the high initial facility costs; reliance on precipitation (no control over the volume of water available); changes in stream regimens can impact fish, vegetation, and biodiversity by altering stream flows, flow patterns, and temperature; inundation of land and wildlife habitat; and relocation of people living in the reservoir area are only a few of the disadvantages of hydropower.
- Solar energy is non-polluting and does not create greenhouse gases, such as oil-based energy, nor does it create waste that must be stored, such as nuclear energy. It is also far quieter to create and harness, drastically reducing the noise pollution required to convert energy to an application form. The main disadvantage of solar energy is its high cost. Despite technological advances, solar panels continue to be expensive. Even if the panels' expense is not taken into account, the device used to store and use the energy can be very expensive. Geothermal power operations produce few emissions. The disadvantages of geothermal energy power plants are their location since it is difficult to locate suitable sites for these power plants. The number of places where geothermal power plants can be built is minimal.
- Bioenergy can minimize greenhouse gas emissions, reduce reliance on oil, and benefit local agriculture and forest product sectors. Agro-industrial wastes, urban wastes, and other biomass feedstocks are the most common biomass feedstocks for energy production. Corn grain (for ethanol) and soybeans are now the most widely used feedstocks for biomass fuels (biodiesel). The planting and use of specific energy crops, such as fast-growing trees and grasses, as well as algae, are among the long-term plans. Additionally, bioenergy can also be used, stored, and transported in different forms such as solids, liquids, and gases, depending on the transformation technology. Nevertheless, bioenergy production is very complex, involving complex chemical reactions, different transport phenomena, and different reactor structures. The study of this process in a laboratory and pilot plant is very tedious and expensive. For this reason,

including tools such as modeling and simulation can be necessary and complementary to experimental studies. Besides, this contributes to the design, operation, optimization, and control of the process. Several mathematical models have been described to simulate the biomass-to-energy process, and these models include kinetic models, experimental design models, and CFD models. Each type of these models has its advantages and disadvantages, as the models have different approaches to handle the complicated process involving hydrodynamics, heat and mass transfer, and various chemical reactions.

Chapter2 RESEARCH APPROACH

2.1. Justification

The clean and sustainable fuels productions are the main challenges facing the next energy crisis and global warming. In recent years, it has become clear that climate change is no longer strictly an environmental problem, but an economic and safety problem related to the energy sector, which is the main emitter of greenhouse gases.

In the last twenty years, the global energy consumption has increased by more than 50% (BP, 2017). The majority of consumption comes from the fossil fuels (oil, coal and natural gas). In fact, today, fossil fuels satisfy more than 80% of the world's primary energy consumption (BP, 2017). However, the percentage contribution of renewable energy to global demand has remained almost constant over the last 20 years.

Additionally, the continued growth of agro-industrial waste such as *Agave Salmiana* bagasse, avocado stone and cacao shell can represent a serious environmental problem. In Mexico, it is estimated that millions of tons per year are generated in these biomasses (Chávez-Guerrero and Hinojosa, 2010; García-Fajardo et al., 1999; González-Alejo et al., 2019). Besides, their nature represents a major problem. Therefore, most of the waste generated is incinerated to reduce its volume to ashes and facilitate its management.

Consequently, the main objective of this project is to determine the appropriate technology and conditions for converting these biomasses (*Agave salmiana* bagasse, avocado stone and cacao shell) into fuels and high added value chemical products. To realize this project, studies of HTC of these biomasses will be carried out. The development of thermochemical processes for biomass conversion and proper equipment design requires knowledge and proper understanding of the several chemical and physical mechanisms which interact in the thermal degradation process. Mathematical modeling and simulation of the HTC reactor and simulation of the pyrolysis and gasification processes represent a very useful tool for understanding the operating condition of these processes. The performance of this process is highly dependent on transport phenomena and chemical reactions. Understanding these transport phenomena and kinetics of chemical reactions in the context of real biomass will facilitate their optimization and control of the products, the results of which can be used in the design and control of large-scale converters. This study comprises an experimental part and a simulation of the different

processes. Four typical biomass species have been selected for the processes. These are *Agave salmiana* bagasse, avocado stone, cacao shell, and cellulose.

2.2. Hypothesis

Through the process of thermochemical conversion, agro-industrial waste such as *Agave salmiana* bagasse, avocado stone, cacao shell and cellulose can be transformed into products of interest, such as synthesis gas and synthetic fuels, with energy values similar to fossil fuels.

2.3. Research Objectives

2.3.1. General objective

To propose a sustainable alternative for the use of biomass as a renewable energy resource through the thermochemical conversion process, with the help of modeling and simulation of the process and the analysis of the factors that contribute to its viability.

2.3.2. Specific objectives

The specific objectives and approaches of this research are:

- To characterize biomass used in thermal processes
- To study the hydrothermal carbonization process of the biomasses
- To characterize the HTC process liquid in terms of identification and quantification of the intermediate components produced at different reaction temperatures
- The modeling and simulation of HTC reactor during HTC using COMSOL Multiphysics ® (hydrodynamics, heat transfer and kinetics reaction).
- To investigate the effect of reaction time, temperature, and biomass/water ratio on the mass yield, energy density, and combustion characteristics of the hydrochar samples.
- To determine the kinetic and reaction mechanism of HTC process.
- To study the gasification process of biomasses and hydrochars
- To determine and quantify the composition of the pyrolysis and gasification products.
- To determine the kinetic parameters of the pyrolysis process.
- To simulate the pyrolysis and gasification process in Aspen Plus ®
- To simulate the synthesis of the production of synthetic fuels in Aspen HYSYS ®
- To make an energy balance of the hydrothermal carbonization process.

2.4. Methodology of the project

This project consists of two main parts: The first part is the experimental studies of hydrothermal carbonization, pyrolysis, and gasification of the selected lignocellulosic biomasses. The second part consists of modeling and simulation of the experimental parts (hydrothermal carbonization, pyrolysis, and gasification) and a theoretical simulation based on the experimental data of the gasification (simulation of the production of synthetic fuels).

The experimental part of the project was carried out at the Institute of Aerothermal Combustion Reactivity and Environment "Institut de Combustion Aérothermique Réactivité et Environnement- Centre National de la Recherche Scientifique" ICARE-CNRS, Orléans-France. The modeling and simulation of this project were carried out in the Chemical and Food Process Simulation Laboratory (LSPQA) in the Faculty of Chemical Sciences at the Autonomous University of San Luis Potosí (FCQ-UASLP).

The different raw materials of biomass feedstocks, *Agave salmiana* bagasse (ASB), avocado stone (AS), cocoa shell (CS), and cellulose (CEL) was studied to investigate the effect of HTC on lignocellulosic biomass. The liquid by-product from the HTC process at different reaction temperatures was also characterized for the chemical composition. The study results were used for further modeling and simulation to optimize the design of an HTC reactor.

The hydrochars obtained, and the raw biomasses were used in the pyrolysis and gasification process. The products were analyzed and quantified using different analytical equipment. These results were used for the simulation of the chemical process. Subsequently, the syngas obtained were used to simulate a process for the production of synthetic fuels.

This part is only the global approach to address the problem; the specific methodology of each part will be described in detail in each chapter for a better understanding.

Chapter3 CHARACTERIZATIONS OF BIOMASSES

Biomass is a term used to describe an organic material found primarily in plant and agricultural wastes that contains carbon, hydrogen, and oxygen as a result of photosynthesis (Odetoye et al., 2020). The sources of bioenergy are biomass resources. The material has to be characterized in order to optimize its potential output and uses before conversion and conversion of biomass to useful bioenergy. Characterizing the physical, chemical, and thermochemical characteristics of biomass is a crucial stage in the effective generation of biofuel (Cai et al., 2017). It is important for the proper design and operation of the process of biomass conversion. Biomass is a complex biopolymer, and its compositional and structural characteristics broadly vary depending on its species and growth environments. Because of the complexity and variety of biomass, understanding its physicochemical characteristics is vital for effective biomass utilization. The characterization of biomass does provide critical information on biomass during pretreatment and conversion and gives valuable insights on how to utilize the biomass (Dayton and Foust, 2019). Biomass can come from plants and animals, such as wood from forests, agricultural wastes, agro-industrial wastes, human and animal organic waste.

Forest-derived biomass is mainly wood or wood by-products such as sawdust., wood scraps, and wood logs (Akhator et al., 2017). They are primarily used for combustion (heat energy), electrical energy generation, and biofuels production. Food crops, food by-products, agricultural waste, and residues are agricultural products that are sources of bioenergy. Energy crops are mostly grassy, aquatic plants that are grown and harvested seasonally for bioenergy. Miscanthus, algae, and sugarcane are examples of biomasses. Biomass can also be found in the waste and by-products of food processing. Corn cobs, straw, cocoa shells, and oat husks are only a few examples. Biomass is composed of a variety of agricultural wastes, including sewage sludge, animal waste, and crop production waste (Kominko et al., 2018). These wastes are subjected to different forms of thermal processing, such as combustion and pyrolysis, to generate bioenergy.

Due to the removal and processing of pollutants to create energy, household solid waste produced daily is also a viable source of biomass. Biomass is also considered suitable for energy generation in heat or electric power from landfills. The biogas is primarily methane and carbon dioxide produced from the biological activity of biodegradable waste through anaerobic

digestion (Odetoye et al., 2020). As can be seen, there are different types of biomasses, and their physical and chemical composition depends on the source and the type of biomass.

Biomass characterization is the basis for understanding conversion chemistry and developing new biofuel processes. It provides the basis for determining process performance in terms of carbon conversion efficiency and energy efficiency and facilitates process optimization to maximize product yield. Basic physical property measurements of biomass resources, such as bulk density and moisture content, help define preparation and treatment needs. Elemental analysis is essential to determining element balances in conversion processes. The chemical structure of biomass is a complex, integrated network of three structural biopolymers such as cellulose, hemicellulose, and lignin with other organic constituents called extractives (Dayton and Foust, 2019). To better understand biomass characteristics, a good grasp and proper selection of analytical methods are necessary. This chapter presents the different analytical approaches to biomass characterization during the biomass pretreatment and conversion process. The main methods used to characterize these biomasses were:

Analysis of the thermochemical properties.

- Compositional analysis of biomass (extractible, hemicellulose, cellulose and lignin)
- Thermogravimetric analysis (TGA/DTG)
- Heating value analysis (HHV and LHV)
- Proximate and ultimate analysis.

Analysis of the microstructure and chemical composition of biomass.

- Fourier transform infrared (FTIR)
- Scanning Electron microscopy (SEM)

Analysis of thermophysical properties of biomass

- Heat capacity measurement
- Thermal conductivity
- Density
- Particle size distribution

3.1. Materials and methods

3.1.1. Feedstock

Bioenergy can be produced from different biomass feedstocks, from trees and crops to garden and animal waste. In this study, the biomass used comes from agro-industrial waste, such as *Agave salmiana* bagasse, avocado stone, and cacao shell. These biomasses are some of the agro-industrial wastes that are generated in large quantities in Mexico. Furthermore, cellulose was used as a representative material of the lignocellulosic biomass, because it is a primary structural component of the plant cell wall, which makes up 40−60 wt.% besides hemicellulose and lignin(Paksung et al., 2020).

***Agave salmiana* bagasse:** The *Agave salmiana* bagasse (ASB) used in this study was collected from the distillery "Santa Teresa," located in San Luis Potosi, Mexico. The ASB derives from *Agave salmiana* plants commonly known as 'Maguey', an agro-waste material generated from the production of mezcal. The residue remaining after the juices have been extracted (bagasse pulp). Initially, ASB was air-dried, to reduce the moisture content, for storage and later transport from Mexico to France. It was subjected to natural open-air sun-drying, to a residual moisture content equal to 5% (dry bagasse), and used in experiments.

Avocado Stone: There are different varieties of avocado, but in this study, the *Hass* variety (*Persea americana*) from Michoacán (Mexico). In general, the avocado stone has a moisture content between 65-75% (Ceballos and Montoya, 2013). Initially, it was cut and dried in a stove at 80 °C to reduce its moisture content between 3-5 % for storage.

Cacao shell: Cacao shells were collected from a batch of approximately 80 kg of toasted Mexican Trinitario cacao. The cacao was shelled after the roasting; this process was done manually. The sample was dried in the sun and ground to obtain a particle size between 0.5 and 1mm.

3.1.2. Experimental procedure

3.1.2.1. *Determination of extractives, hemicellulose, cellulose and lignin*

Extractives, hemicellulose, cellulose, and lignin were analyzed according to the protocol described by Li et al. (2004), and Selvaraju and Bakar (2017). The analysis was performed at least twice with a maximum standard deviation of 2.8 %. Below are the different steps of the adopted protocol. The sample was previously dried at 105°C for 12-24 hours.

3.1.2.1.1. *Analysis of extractives*

The dried biomass sample (W0) is leached with mixture of benzene/ethanol (2:1 in volume) at a constant temperature for 3 h. After air-drying, the residue is dried in an oven at 105 ºC to a constant weight for 24 hours. Then the residue is cooled to room temperature in a desiccator and then weighted (W1). The extractive wt.% is calculated as:

$$\mathrm{Ex(wt.\,\%)} = \frac{\mathrm{W0} - \mathrm{W1}}{\mathrm{W0}} \cdot 100 \qquad (3\text{-}1)$$

The residue obtained is used for the determination of hemicellulose and lignin contents.

3.1.2.1.2. *Analysis of hemicellulose*

Fill a flask with 150 ml NaOH solution (20 g/l) and the residual W2 from the extractive analysis above. The mixture is placed in a flask and topped in a reflux system. It is boiled for 3.5 h. The solid obtained by Büchner filtration is washed four times with 150 mL of distilled water to remove Na+ ions. It is then dried at 105°C for 24 h and weighed (W3). The hemicellulose wt.% is calculated as:

$$\mathrm{He(wt.\,\%)} = \frac{\mathrm{W2} - \mathrm{W3}}{\mathrm{W2}} \cdot (100 - \mathrm{Ex}) \qquad (3\text{-}2)$$

3.1.2.1.3. *Analysis of lignin*

Put about 1 g of residue after extractives analysis as above into a weighed flask and dry it to a constant weight. The sample is then cooled in a desiccator and weighed (W4). Slowly pour 30 ml of sulphuric acid (72%) into the sample. Keep the mixture at 8 – 15 ºC for 24 h. Then transfer it into a flask and dilute it with 300 ml of distilled water. Boil the sample for 1 hour with recycled distilled water. After cooling and filtration, the residue is washed until there is no more sulfate ion in the filtrate. The residue is then dried to a constant weight, cooled to room temperature in a desiccator, and weighted (W5). The hemicellulose wt.% is calculated as:

$$Li\mathrm{(wt.\,\%)} = \frac{\mathrm{W5}}{\mathrm{W4}} \cdot (100 - \mathrm{Ex}) \qquad (3\text{-}3)$$

3.1.2.1.4. *Analysis of cellulose*

The cellulose content Ce (wt.%) is determined by difference:

$$Ce(\text{wt.}\%) = 100 - \text{Ex} - \text{He} - \text{Li} \qquad (3\text{-}4)$$

3.1.2.2. *Thermogravimetric analysis (TGA/DTG)*

Thermogravimetric analysis is the easiest way to assess the thermal properties of biomass. Furthermore, the obtained thermal data can be used to validate the comparative analysis process. Thermogravimetric analysis (TGA) is a technique for determining a sample's weight loss in a controlled environment. The collected data is used to map a weight loss graph against temperature or time. TGA helps to understand biomass in terms of its structural, kinetic, and physical characteristics. TGA analysis can anticipate the behavior of these materials during pyrolysis, as biomass samples thermally decompose under circumstances similar to those, they undergo during pyrolysis tests. The focus is on the decomposition behavior of the lignin, hemicellulose, and cellulose content of biomass samples. The TGA is carried out with the STA 449 F3 apparatus of the NETZSCH brand (**Figure 3-1**). The analyzer is equipped with an electronic microbalance whose range can reach a maximum mass of 500 mg. The silicon carbide furnace temperature is raised at a maximum rate of 50°C/min, up to a maximum temperature of 1600°C, by the heating machine.

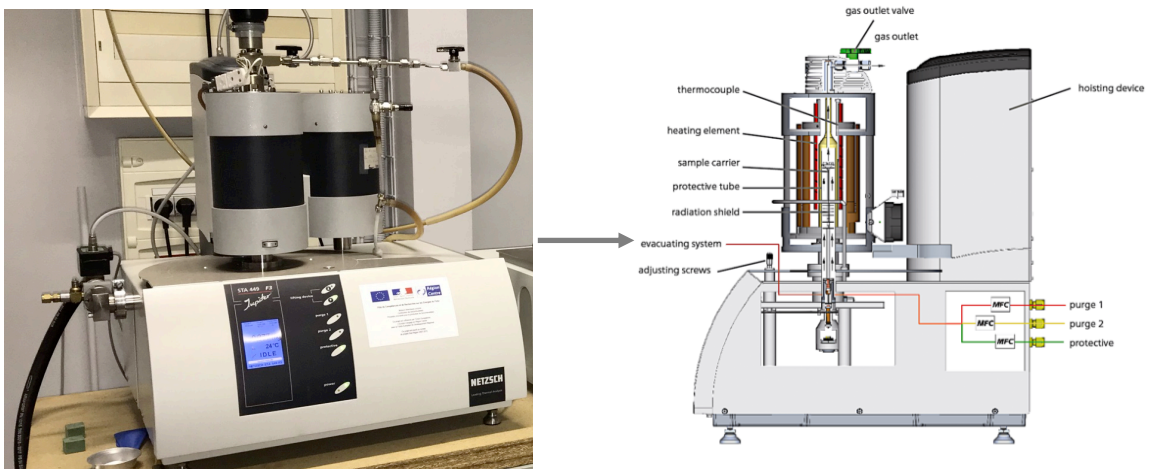

Figure 3-1: Diagram of the STA 449 F3 Jupiter® - NETZSCH analyzer used in ICARE-CNRS.

We have chosen the TGA to follow the decomposition of biomass and hydrochar at selected temperatures in an inert or oxidizing atmosphere to study their thermal behavior of pyrolysis, gasification, and combustion. Thus, to determine the immediate analysis (volatile matter, fixed carbon, ash) and the samples' maximum degradation rates.

TG analysis procedure: To avoid sample exhaustion and clogging of the furnace with pyrolysis residues (inert atmosphere), we set sample size of about 50 mg to perform the GTA. According to European standards for determining the parameters of immediate analysis of materials, the temperature is programmed in five stages, as shown in **Figure 3-2**:

- Heating ramp of 10°C/min from 25°C to 900°C under an inert atmosphere (N2=79 ml/min).
- 7 minutes in isotherm ramp at 900°C under an inert atmosphere
- Cooling ramp of 40°C/min from 900°C to the combustion temperature (biomass: 550°C, hydro-char: 815°C);
- 2 hours at the temperature chosen to ensure the total combustion (N2/O2 =79/21 ml/min) of the sample.

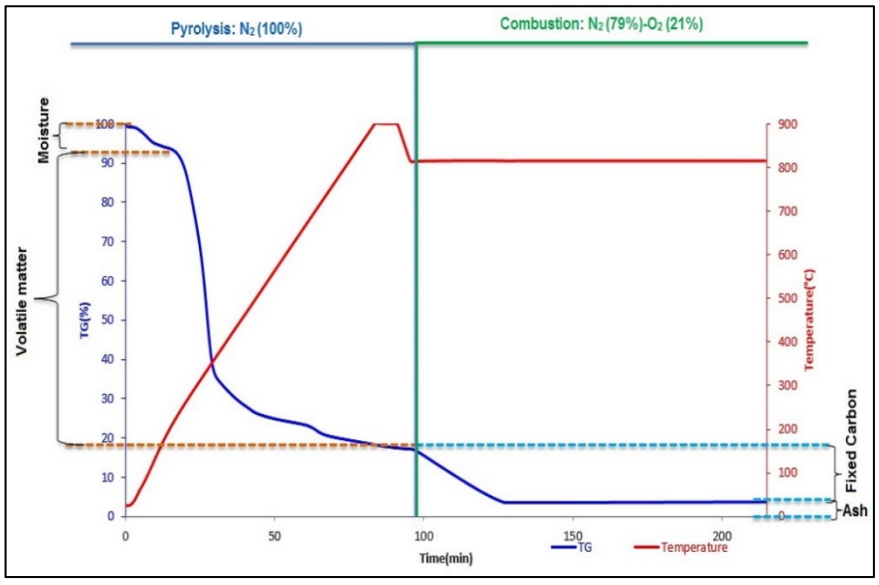

Figure 3-2: TG Analysis program

3.1.2.3. *Procedure of proximate analysis of biomass*

The proximate analysis consists of determining the following parameters: moisture content, a fraction of volatile matter, percentage of fixed carbon, and ash content. In this case, the

proximate analysis procedure for both biomass and hydrochar will be explained below. These parameters are determined from the TGA data in **Figure 3-2**.

3.1.2.3.1. *Moisture content*

The moisture content (MC) is measured by the gravimetric method according to the European standard EN 14774-3: 2009: E (CEN, 2009a). About 7 g of sample is placed in a stove at 105°C. We considered that the mass is stabilized after 24 h of drying. The mass loss corresponds to the mass moisture content of the sample. It can also be determined from TGA; however, this determination is not reliable.

3.1.2.3.2. *Volatile matter content*

The determination of the volatile matter (VM) content consists of holding the raw biomass and hydro-chars at 900°C for 7 min under inert atmosphere (nitrogen) according to the European standard EN 15148: 2009: E (CEN, 2009b). The volatile matter content corresponds to the sample mass loss after deducting the mass loss due to moisture water evaporation.

3.1.2.3.3. *Ash content*

The ash content represents the amount of inorganic material contained in a sample. The ash content is obtained by burning the sample at 550°C for biomass and 815°C for hydrochar (EN 14775: 2009: E) for 2 hours (CEN, 2009c). It corresponds to the amount of residue after combustion of the substrate formed during the pyrolysis step. The determination of ash rates allows the calculation of ash removal rates from biomass during the HTC process as follows:

$$\mathrm{Ash_{removal}(wt.\,\%)} = 100 - \frac{\mathrm{Ash_{hydrochar}}}{\mathrm{Ash_{raw\ biomass}}} \cdot (\mathrm{Mass\ yield_{Hydrochar}}) \quad (3\text{-}5)$$

3.1.2.3.4. *Fixed carbon content*

Fixed carbon (FC) is the difference in mass between the solid residue after the pyrolysis step (fixed carbon + ash) and the ash obtained from the sample combustion. The fixed carbon results from a calculation and not from analysis. It is given by the following relation:

$$\mathrm{FC(wt.\,\%)} = 100 - [\mathrm{MC} - \mathrm{MV} - \mathrm{Ash}] \cdot 100 \quad (3\text{-}6)$$

3.1.2.4. *Procedure of ultimate analysis of biomass*

Ultimate analysis or elemental analysis of a biomass sample defines the elemental composition of the biomass. It contains the determination of the carbon, hydrogen, nitrogen, oxygen, and sulphur in the biomass sample. The analyzer used is the FLASH 2000 CHNS/O (Thermo Scientific). Approximately 0.5-1.0 mg of sample is placed in a tin (CHNS assay) or silver (O assay) boat. For the CHNS assay, rapid combustion of the samples at 1000°C is performed in oxygen. This combustion transforms carbon, hydrogen, nitrogen, and sulfur respectively into CO_2, H_2O, NO_2, SO_2. The gas mixture passes through a chromatographic column. The different constituents are eluted successively and detected at the exit by a thermal conductivity detector. C, H, N, and S contents are calculated from a calibration performed with reference substances (sulfanilamide and BBOT). For the determination of oxygen, the sample is pyrolyzed at 950°C under helium. The different gaseous elements are separated in a chromatographic column and then analyzed by a thermal conductivity detector. The sample oxygen content is determined using the same reference substances to determine CHNS (sulfanilamide and BBOT).

3.1.2.5. *Procedure of heating value*

The heating value is the enthalpy of the combustion reaction per unit mass. To determine its value experimentally, a calorimeter bomb consisting of a steel cylinder is placed in a calorimeter equipped with a stirrer and a thermocouple (**Figure 3-3**). To ensure complete combustion of the sample, the cylinder is filled with excess oxygen.

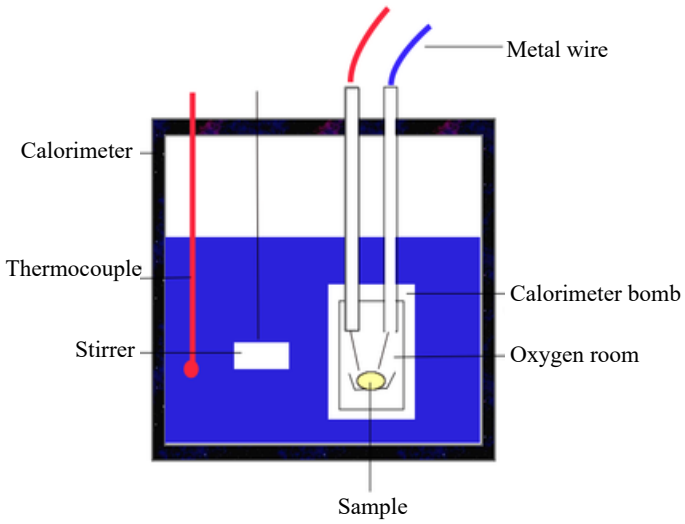

Figure 3-3: Simplified diagram of a calorimetric bomb

The sample is ignited by placing a metal wire in contact with it, which causes the sample to burn due to the electric current. The bomb is submerged in bottled water in a bucket. During the ignition, the device records the initial temperature and the thermal equilibrium temperature at the end of the combustion. The energy consumed to cool the surrounding water corresponds to the heat released during the sample's combustion. In this study, the higher heating value (HHV) of samples dried at 105°C for 24 h was determined using a Parr 1261 calorimeter bomb. The measurement was repeated in triplicate with a maximum standard deviation of 0.5 MJ/kg. The bomb is previously calibrated with benzoic acid.

3.1.2.6. *Particle size distribution of biomass*

The different sizes of biomass particles have distinctive properties that affect the drying rate, the mechanism of transport phenomena, and the consistency of the final product. Particle size analysis is a method of determining particle size distribution. This process consists of classifying a powder sample into discrete size ranges by sieving it through a series of metal mesh sieves. The particle size distribution of biomasses was determined according to ASTM B214-07.

A sieve shaker is used to vibrate the sieve stack for a specific period. The vibration allows irregularly shaped particles to reorient themselves as they fall through the sieves. Additionally, the shaking of the sieves serves to break up weak agglomerates, allowing a more reliable measurement of the particle size distribution.

The ASTM standard provides a recommendation on the size of the sample used is sieve analysis. If the apparent density of the sample (powder) is more extensive than 1.50 g/cm^3, a sample size between 90-110g should be used. Otherwise, a smaller sample between 40-60g may be used.

Procedure

- Record the mass of the sample to be used.
- Stack sieves in order from most minor to largest, starting at the bottom, with the pan below the smallest sieve.
- Add the biomass sample to the top sieve.
- Tighten the equipment to ensure that the sieve stack is held firmly in the shaker assembly.

- Set the sieve shaker to vibrate for 15 minutes. A shorter time may be required for brittle materials.

3.1.3. Biomass microstructures and chemical composition

3.1.3.1. *Fourier transform infrared (FTIR)*

The spectrophotometer is an instrument that measures a compound's absorption spectrum. As opposed to a conventional spectrophotometer, the Fourier transform spectrophotometer provides the IR spectrum much faster.

Basically, the IR spectrum obtained from FTIR spectrometer lies in the mid-IR region 2.5-15 µm between 4000 and 666 cm^{-1}. Transition energies corresponding to changes in vibrational energy state for many functional groups are located in the mid-IR region (4000-400 cm^{-1}) and hence the appearance of an absorption band in this region can be used to determine whether specific functional groups exist within the molecule (Mohamed et al., 2017). The functional groups of raw biomasses were analyzed by FTIR using a NICOLET 6700 FT-IR spectrometer (Thermo Scientific). Each spectrum was recorded over 64 scans, in a wavenumber range from 4000 cm^{-1} to 800 cm^{-1} with a resolution of 16 cm^{-1}.

3.1.3.2. Scanning Electron microscopy (SEM) pending experiment

Scanning electron microscope (SEM) analysis was used to observe the structure of the raw biomasses (AS and CS). Images were acquired using an ultra-high resolution scanning electron microscope (Phillips XL30 tungsten filament). The sample was placed in an aluminum SEM holder with a conductive carbon tape attached, and then the sample surface was coated with a conductive gold film to eliminate any possible static charge that could affect the quality of the images. The processed samples were separately mounted on SEM disks, coated with gold, and examined with the SEM running at 10 kV at a WD working distance of 10 mm using different zooms from 500x to 5000x.

3.1.4. Thermophysical properties of biomass

3.1.4.1. *Heat capacity measurement*

In In this experiment, the heat capacity of biomass and hydrochar is determined following the protocol described by Blackman and Black (1977). In each case, the sample is weighed (m_s),

it was heated on the stove to the temperature (T_S). The hot sample is mixed with water at known temperature (T_{H2O}) and mass (m_{H2O}). After some time, the mixtures between the water and the sample reach an equilibrium temperature (T_M). The heat absorbed by the sample is presented in the following equation:

$$\Delta Q_1 = Cp_S m_S (T_M - T_S) \quad (3\text{-}7)$$

The heat variation in the water is the following equation:

$$\Delta Q_2 = Cp_{H2O} m_{H2O} (T_{H2O} - T_M) \quad (3\text{-}8)$$

The heat exchanges for the set (Dewar + Water + Samples) lead to thermal equilibrium at temperature T_M. The energy balance relative to this set is written:

$$\Delta Q_1 = \Delta Q_2 => Cp_{H2O} m_{H2O} (T_{H2O} - T_M) = Cp_s m_s (T_M - T_s) \quad (3\text{-}9)$$

The heat capacity of water Cp_{H2O} is assumed to be known. The temperature (T_s) is equal to the temperature of the stove. The unknown quantity Cp_s can, therefore, be calculated from the measured quantities T_2, T_M, m_1, and m_2:

$$Cp_s = Cp_{H2O} \frac{m_{H2O}(T_M - T_{H2O})}{m_s(T_s - T_M)} \quad (3\text{-}10)$$

The heat absorbed by calorimeter vessel (Dewar) can be considered negligible, because the system is adiabatic.

3.1.4.2. *Thermal conductivity*

Thermal conductivity can be measured in a variety of ways, each of which is suitable for a certain set of materials based on their thermal properties and medium temperature. In this analysis, the thermal conductivity of biomass and hydrochar is determined using the same method as Mason et al. (2016). Since the experiment was aimed at small test pieces with relatively low thermal conductivities, it was necessary to design and build a bespoke test apparatus. The design was based on the "split-bar" method, which has been used for measuring the thermal conductivity of polymers. The solid sample (pellets of biomass or hydrochar) is put into the small piece made, then placed between two plates (brass) of known thermals' conductivities. One plate reference temperature is determined at both ends after a heat source is applied to one of the plate's extremities. The axial temperature gradient across the two

reference parts is monitored until it remains constant. The steady-state temperatures, the thickness of the sample, and the heat input to the hot plate are used to calculate thermal conductivity. The description of the system is presented in **Figure 3-4**. The axial heat flow in the upper rod is calculated from the ideal heat flow and a correction for the radial heat loss. The calculation is approximated in the expression.

$$Q_1 = \frac{\lambda_{brass} A_{cs} (T_1 - T_3)}{X} - \left\{ \left(\frac{(T_1 - T_3)}{2} - T_{amb} \right) \left(\frac{A_{ins} \lambda_{ins}}{d_{ins}} \right) \right\} \quad (3\text{-}11)$$

where T_1 and T_3 are the temperatures measured by thermocouples T_1 and T_3, respectively. T_{amb} is the ambient temperature λ_{brass} is the thermal conductivity of brass (123W/m·K); A_{CS} is the cross-sectional area of brass rod (490.78 mm^2); X is the axial distance between the two thermocouples T_1 and T_3 (30mm); A_{ins} is the effective surface area of the insulation layer (1.18 $\times 10^{-3}$ m^2); di_{ns} is the thickness of the insulation layer (55 mm); and λ_{ins} is the thermal conductivity of insulation (0.065 W/m·K). The axial heat flow in the lower rod, Q_2, is calculated with a similar expression substituting T_1 and T_3 with T_4 and T_6, respectively.

$$Q_2 = \frac{\lambda_{brass} A_{cs} (T_4 - T_6)}{X} - \left\{ \left(\frac{(T_4 - T_6)}{2} - T_{amb} \right) \left(\frac{A_{ins} \lambda_{ins}}{d_{ins}} \right) \right\} \quad (3\text{-}12)$$

The axial heat flow in the sample, Q_S, is calculated in the same way, substituting T_1 and T_3 with T_3 and T_4, respectively.

$$Q_s = \frac{\lambda_s A_s (\Delta T_S)}{X_S} - \left\{ \left(\frac{(\Delta T_S)}{2} - T_{amb} \right) \left(\frac{A_{insS} \lambda_{insS}}{d_{insS}} \right) \right\} \quad (3\text{-}13)$$

Where λ_S, A_S and $X_{S\ are}$ the thermal conductivity, the effective surface area, the axial distance of sample respectively, and λ_{insS}, $A_{insS,}$ and di_{nsS} are the thermal conductivity, the effective surface area and the thickness of the insulation layer of sample respectively. Furthermore, the axial heat flow through the sample approximated as the average of the heat flows in the upper and lower brass rods:

$$Q_S = \frac{Q_1 + Q_2}{2} \quad (3\text{-}14)$$

Combining equation (3-13) and (3-14).

$$\frac{Q_1 + Q_2}{2} = \frac{\lambda_s A_s (\Delta T_S)}{X_S} - \left\{ \left(\frac{(\Delta T_S)}{2} - T_{amb} \right) \left(\frac{A_{insS} \lambda_{insS}}{d_{insS}} \right) \right\} \quad (3\text{-}15)$$

Considering the system is perfectly isolated: $\lambda_{insS} = 0$

$$\lambda_s = \left(\frac{X_S}{A_s(\Delta T_S)}\right)\left[\frac{Q_1 + Q_2}{2}\right] \quad (3\text{-}16)$$

The temperature differential across the sample, ΔT_S is derived from the difference of T_3 and T_4 with a correction for the 10 mm of brass rod between the thermocouples and interface surface as:

$$\Delta T_S = \left(T_3 - \frac{0.01Q_1}{\lambda_{brass}A_{cs}}\right) - \left(T_4 - \frac{0.01Q_2}{\lambda_{brass}A_{cs}}\right) \quad (3\text{-}17)$$

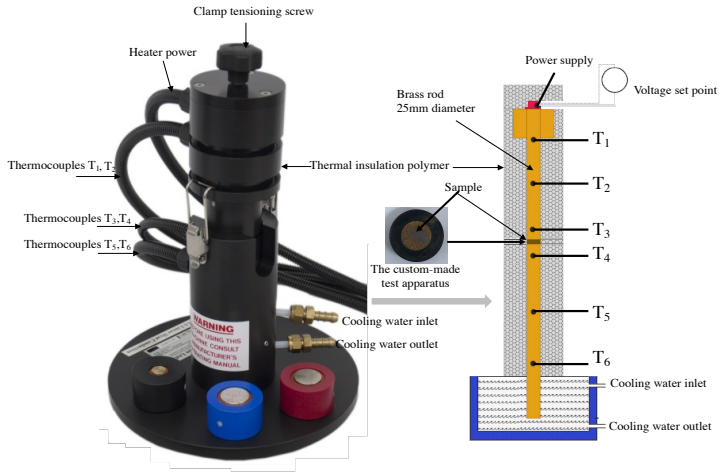

Figure 3-4*:* Measurement apparatus of thermal conductivity and diagram of in cross-section

3.1.4.3. *Density*

The density of a substance is a fundamental physical property. For a homogeneous object, it is defined as the ratio of its mass to its volume. The density of biomasses and hydrochars were determined with a pycnometer. The use of a pycnometer to determine density is a precise tool. It works with a known density operating liquid, such as water. The pycnometer is a glass flask with a capillary hole in it and a close-fitting ground glass stopper. After closing a top-filled pycnometer, this fine hole releases excess liquid, allowing for the precise measurement of a given volume of measured or operating liquid. The density of a homogeneous solid material that does not melt in a working liquid can also be determined with a pycnometer.

The following are the different steps of the protocol adopted per the procedure established by ASTM D4892 (Eser and Andrésen, 2004).

Figure 3-5*:* Pycnometer

First, it is necessary to measure the weight of the pycnometer together with the inserted object. Then, the liquid is added, and the solid weight from the total measured weight is determined. The volume of added water can then be obtained. The volume of the measured solid object is the difference between the volume of water that fills the empty pycnometer and the total volume. Once the volume of the object and the known weight have been determined, the object's density is determined.

3.2. Results and Discussion

3.2.1. Compositional analysis of biomasses: Extractible, hemicellulose, cellulose and lignin

The biomasses used are lignocellulosic, i.e., second-generation biomass. Compositional analysis of lignocellulose before and after pretreatment is used in almost all second-generation bioenergy production studies. Lignocellulose is derived from the cell walls of plants and is composed of cellulose, hemicellulose, and lignin(Giger-Reverdin, 1995). The composition of the three lignocellulosic materials and the extractives are shown in **Table 3-1**. Each experiment was replicated twice; reported results indicate the average values of the replicated experiments.

Extractives in biomass refer to the nonstructural components that can be extracted by solvents (e.g. water, ethanol, acetone, benzene, hexane, dichloromethane, and toluene) (Kallioinen et al., 2003; Roy et al., 1990). Extractives are mainly a group of cell wall chemicals that contain fats, waxes, proteins, terpenes, gums, resins, simple sugars, starches, phenolics, essential oils, pectins, mucilages, glycosides and saponins, fatty acids, sterols, flavonoid, and many other minor organic compounds. From the result in this study, the cacao shell (25.25 wt%) have

higher extractives compare to the avocado stone (3.6 wt%) and *Agave salmiana* bagasse (1.4 wt%). The extractives are responsible for the color, smell, and durability of the biomass itself (Rowell, 2012).

Hemicellulose of avocado stone (76.4 wt%) shows the highest content, followed by the cacao shell (45.4 wt%) and *Agave salmiana* bagasse (43.8 wt%). Hemicellulose consists of several types of sugar units and is sometimes referred to by the sugars they contain. Hemicellulose is associated with cellulose and contributes to the structural component of the plant (Rowell, 2012).

A hemicellulose is a group of structurally diverse polysaccharides with amorphous structures and a lower degree of polymerization. The building blocks in hemicelluloses are pentoses (arabinose and xylose), hexoses (galactose, glucose, and mannose), and hexuronic acids (glucuronic acid).

Table 3-1: Extractives, hemicellulose, lignin and cellulose content of the different biomasses used

	Avocado stone	***Agave salmiana* bagasse**	**Cacao shell**	**Cellulose**
Extractible (%)	3.6±0.4	1.4±0.0	25.3±0.9	-
Hemicellulose (%)	76.4±0.3	43.8±0.4	45.4±0.3	-
Cellulose [a] (%)	3.0±0.3	40.7±0.5	7.8±0.5	100
Lignin (%)	17.0±0.3	14.2±0.1	21.5±0.3	-

[a]:by difference

The hemicellulose nomenclature is principally determined by the most occurring sugar present in their structure or the most occurring sugar unit in the backbone (Scheller and Ulvskov, 2010b). In softwood trees, glucomannans (the backbone of both β-D-mannose and β-D-glucose units) and mannans (the backbone of (1→4)-linked β-D-mannose units) are the predominating hemicelluloses (Aspinall, 1959; Heinze, 2005; Scheller and Ulvskov, 2010b). Glucomannan, together with galactoglucomannan, may occur close to cellulose and represent the major (10–30%) hemicellulose component in softwood, but only a minor fraction of hardwood (Scheller and Ulvskov, 2010b; Werner et al., 2014). In the hardwood tree, xylan-based hemicelluloses

are predominating. Xylans are composed of chains of (1 → 4)-linked β-D-xylose, with single 4-O-methyl-D-glucuronic acid (Werner et al., 2014). The hemicellulosic fraction of herbaceous plants differs significantly from that of woody biomass, both in relative abundance and composition. Glucuronoarabinoxylan and β-glucan are two forms of hemicelluloses found in herbaceous plants. Glucuronoarabinoxylan has both 4-O-methyl-D-glucuronic acid and arabinose side chain residues bound to the xylan backbone chain, while β-glucan is an unbranched homopolymer of glucose with both (1 → 3) and (1 → 4) linkages, resulting in a non-linear configuration. β-glucan is present in grasses' primary cell walls in amounts of 2–12%, but it is absent from other biomasses (Scheller and Ulvskov, 2010b; Werner et al., 2014). Arabinogalactan is hemicellulose used in all forms of biomass. Since the distinction between pectin and hemicellulose components of the cell wall is not well-defined, arabinogalactan is sometimes classified as a pectin polysaccharide because of its β-(1 → 4) linkages with the non-equatorial configuration of C1 and C4 (Scheller and Ulvskov, 2010b).

Moreover, xyloglucan is a form of hemicellulose found in all higher plants, and it is the most abundant (20–25%) in primary cell walls (Heinze, 2005; Werner et al., 2014). It has a cellulose-like backbone branched by principally xylose units and is tightly bound to the cellulosic microfibrils by hydrogen bonds (Heinze, 2005). As can be seen, the different compositions and structures of hemicellulose make it difficult to explain in a generalized form for lignocellulosic biomass. In addition, the close relationship between hemicelluloses and other cell wall components, principally cellulose and lignin, makes it very difficult to extract hemicelluloses without changing the chemical structure.

Cellulose is a primary structural component in a plant cell. From the result, ASB (40.7 wt%) claim the highest content of cellulose, followed by the CS (7.8 wt%) and AS (3.0 wt%). There are several types of cellulose in the plant: crystalline and non-crystalline or amorphous, also accessible and non-accessible, which is referred to as the capability to interact with water, and so on (Rowell, 2012). Both crystalline and amorphous types of cellulose can be found in biomass. The primary cellulose is found in crystalline cellulose, while amorphous cellulose is composed of a small proportion of unorganized cellulose chains. The amorphous type of cellulose is more susceptible to degradation. The cellulose microfibrils are generally independent but, the cellulose ultrastructure are largely caused by covalent connection, hydrogen bonds, and the force of Van der Waals. The 'straightness' of the chain depends on hydrogen bonding inside the cellulose-microfibril but, interchain-hydrogen bonds can introduce the structure of the cellulose (crystalline) or disorder (amorphous) (Laureano-Perez

et al., 2005). The major component present in all cell walls is cellulose. Cellulose is an important part. It is a linear homopolymer formed by a D-glucose monomer connected by β-(1 to 4)-glycosides that may include more than ten thousand glucose units (Cheng and Timilsina, 2011). Cellulose is found in various macromolecular conformations that can be generally classified as crystalline or amorphous. Strong hydrogen bonds cross-link the cellulose chains to form cellulose microfibrils. These microfibrils have a highly crystalline area that reverberates to deterioration and a tiny section that is simpler to degrade to amorphous cellulose (Van Dyk and Pletschke, 2012). The structural properties of different plant types are strongly influenced by the orientation of cellulose microfibrils in the secondary cell wall (Khalil et al., 2012). The secondary cell wall contains cellulose microfibrils, which are usually trapped in an amorphous hemicellulose matrix and lignin (Huber et al., 2012; Michelin et al., 2015). Bundles or macro fibrils are often paired with these microfibrils in the matrix (Menon and Rao, 2012). In primary and secondary cell membranes, as well as the middle lamellae, lignin and hemicellulose occupy the gaps between cellulose microfibrils (Michelin et al., 2015). The high molecular weight and ordered tertiary structure make natural cellulose insoluble in water. Natural cellulose is water-insoluble due to its large molecular weight and its orderly tertiary structure. Although starchy materials at 60–70°C can be converted from crystalline form to amorphous, 320°C and a pressure of 25 MPa are needed to turn the cellulose from a hard crystalline structure in water to an atmospheric structure (Deguchi et al., 2006; Limayem and Ricke, 2012). The chemical pulp and cotton are the purest sources of cellulose (containing up to 90% cellulose), while wood contains at most 50% cellulose (Limayem and Ricke, 2012; Michelin et al., 2015). When looking at the cellulose content of the biomasses used, it can be said that *Agave salmiana* bagasse has cellulose content similar to softwoods cellulose content (40–45%) (Rowell, 2012). However, the cellulose content of avocado stone and cacao shell is very low.

Lignin is another highly polymerized yet somewhat amorphous compound compared to cellulose and hemicellulose (Werner et al., 2014). It is a complex hydrophobic cross-linked aromatic biopolymer with a molecular weight of 10.000 Da (Limayem and Ricke, 2012), It consists of three main phenolic components - p-coumaryl, coniferyl, and synapyl - alcohol (Menon and Rao, 2012). Lignin differs naturally in content and composition between biomass materials at various levels, e.g., between species, within species and between components (such as wood and bark), and is influenced by plant growth stage and environmental stress. To provide rigidity and strength to cell walls, older and more woody plants have higher amounts

of lignin embedded in cell walls, conferring impermeability to cell walls and creating an important physic–chemical shield against microbial attack and oxidative stress (Van Dyk and Pletschke, 2012). Lignin binds to hemicellulose covalently and accounts for much of the mechanical strength of wood (Werner et al., 2014). Forest woody biomass mostly consists of lignin monomers and cellulose polymers. The greatest amount of lignin is softwood barks (30-60%) followed by hardwood barks (30-55%); while the lowest level of lignin is found in grass and agricultural wastes (10%-30% and 3%-15%) (Demirbas, 2005). From the data, CS (21.5 wt%) showed the highest content of lignin, followed by the AS (17.0 wt%) and ASB (14.2 wt%). High lignin content in CS can increase the hardness of the compacted biomass product and the most recalcitrant component of the lignocellulosic material to degradation.

3.2.2. Thermogravimetric analysis (TGA)

To better understand the thermal behavior, thermal decomposition was monitored by thermal gravimetric analysis (TGA). Lignocellulosic biomass consists mainly of cellulose, hemicellulose, and lignin. Decomposition temperatures of these fractions depend on the lignocellulosic material type. **Figure 3-6**. shows the typical curves of the thermogravimetric (TG) and derivative thermogravimetric (DTG) behavior of raw biomasses, demonstrating the relative mass loss of the compound during a temperature variation.

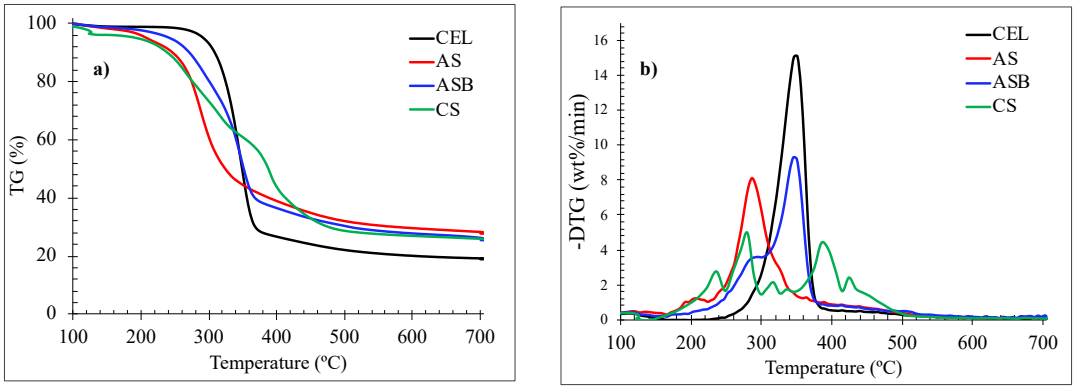

Figure 3-6. (a) TG and (b) DTG curves of biomasses

The nature of the TGA curve combined with the corresponding derivative (DTG) curves/peaks indicates the number of stages of thermal degradation, which is related to the chemical composition. **Figure 3-6** shows the weight loss curves obtained in TGA curves and the DTG curves from the different biomasses such as *Agave salmiana* bagasse (AS), cacao shell (CS), avocado stone (AS), and cellulose (CEL). According to various studies (Garcia-Maraver et al., 2013; Liu et al., 2002; Marcilla et al., 2009), these curves reflect different decomposition steps

directly related to the decomposition of the main components. The first stage corresponds to a biomass drying phase during which moisture and certain volatile compounds are eliminated at temperatures ranging from room temperature to 180 ºC. The TG curves below 180 °C, which are related to moisture and volatiles releases, are almost similar for all samples. A significant weight loss was observed at a temperature of 180–380 °C. In this range, the cellulose and hemicellulose decomposed, leading to the formation of volatiles, primary char, and gases (Demirbas, 2004). The initial degradation temperature was higher for CEL and ASB since both contain more cellulose compared to AS and CS (**Table 3-1**). Also, it should be noted that biomass with a higher content of ash and impurities in its composition has lower initial degradation temperatures (Garcia-Maraver et al., 2013; Huang and Li, 1998). This impact was visible in the case of CS, which produced a high amount of ash (**Figure 3-6a**). Consequently, the decomposition of the biopolymer was manifested by a significant weight loss starting at 180 ºC, at which time the hemicellulosic component began to decompose. The rate of weight change increased rapidly at temperatures above 200 ºC, as the hemicellulose was essentially converted to gases and acetic acid (Grioui et al., 2006; Liu et al., 2002). In the case of AS, the maximum decomposition rate peak was observed at 285 ºC. A first CS peak was observed at 270 ºC (**Figure 3-6b**); these peaks are in the range of hemicellulose decomposition. The behavior of the AS and CS samples differed from that of the other two samples (ASB and CEL) due to their lower cellulose content (**Table 3-1**). Moreover, a small peak of ASB was observed at this temperature range. The maximum mass loss occurred in the region between 305-370 °C for CEL and ASB. This corresponds in the temperature range of the cellulose composition. As shown in **Figure 3-6b**, AS and CS do not contain much cellulose; therefore, no cellulose decomposition peaks were observed for AS. Specifically, for the TG/DTG curves of CS, four events involving mass loss can be distinguished during the pyrolysis of the CS, where this complex devolatilization is composed of overlapping events of extractives (high content), hemicellulose, cellulose, and lignin in a parallel decomposition reaction. Between 180 and 220 ºC, the first event is possibly the devolatilization of extractives with an average mass loss of 15-20 wt%. At this temperature range, the devolatilization of extractive species is expected since they are less thermally stable than hemicellulose, cellulose, and lignin. The second event can be attributed to the devolatilization of hemicellulose between 220 and 300 ºC, with an average mass loss of 30-40 wt%. Hemicellulose is composed of various polysaccharides such as xylose, mannose, glucose, and galactose, and it is decomposed to volatile at low temperatures as compared with cellulose (Yuan et al., 2015). The third event is characterized by a small peak in the DTG profile in a temperature range of 300-325 °C and is related to the

devolatilization of cellulose (Biagini et al., 2008; Mumbach et al., 2020). The fourth event is associated with lignin decomposition, which often occurs at an extensive temperature range and slows the decomposition rate. According to Wang et al. (2016), this behavior for lignin is observed at a temperature range from 177 to 900 ºC. In the pyrolysis profiles, the active zone of the CS pyrolysis occurred inside the temperature range of 120–500 ºC with a characteristic high release of volatile matter (about 70 wt% caused by parallel devolatilization of the pseudo-components (extractives, hemicelluloses, cellulose, and lignin). The DTG curves show that CS pyrolysis is kinetically complex, with multiple overleaped reactions occurring simultaneously. According to Gani and Naruse (2007), biomass is burned in flow stages. First, the hemicellulose and cellulose components of the biomass are volatilized so that the porosity of the biomass char particles increases and the volatile compounds diffuse quickly into the char particles. Next, the lignin components of the biomass can also react with the diffused volatile compounds, although the reactivity of the lignin itself is low.

The lignin decomposition continued at a low rate above 500 ºC, which corresponded to the slow decomposition of the solid residue resulting from the previous step. At that temperature, a solid residue is only composed of ashes and fixed carbon contents. At higher temperatures, the fixed carbon passes the combustion stage. Once the fixed carbon combustion stage is completed, only the ash, composed of inorganic compounds, remains. The mass loss was high in CEL because it does not contain ash, whereas their higher ash content was directly related to their high lignin content (Liu et al., 2002).

3.2.3. Proximate and ultimate analysis results

The results of the proximate and ultimate analysis of all biomasses are shown in **Table 3-2.** The moisture content (MC) represents the quantity of water present in the biomass, expressed as a percentage of the raw biomass weight. The MC of the raw biomasses was less than 4 % before the start of each experiment. The volatile matter (MV) of biomass is composed of condensable vapor and permanent gases (exclusive of water vapor) released during the devolatilization of biomass (Cavalaglio et al., 2020). The MV is usually a mixture of aromatic hydrocarbons, short and long-chain hydrocarbons, and many oxygenated compounds. High volatile matter in the fuel is undesirable as it produces more tar, causing problems to the internal combustion engine (Kumar and Anand, 2019). The high MV content of CEL (79.1%) makes it less attractive compared to AS (72.5%), ASB (77.9%) and CS (71.6%). A high MV implies a high reactivity in comparison with coals (Mumbach et al., 2020). The ash content of the fuel is essential for

choosing the appropriate combustion and gas cleaning technologies. Furthermore, fly ash formation, ash deposit formation, and logistics concerning ash storage and ash utilization/disposal depend on the fuel's ash content. These biomasses' ash content is shallow (< 7%); this is important for fuel utilization.

The high ash content of CS (6.5%) is in accordance with the typical composition of commercial biomass fuels (with a range from 0.6 to 9.8 wt%) (García et al., 2012), and is considerably lower than that of typical Brazilian coals (from 27.4 to 83.1 wt%)(Kalkreuth et al., 2006), which is an advantage for use in the thermochemical route. Low ash content implies a low possibility of occurrence of operational problems that can limit mass and heat transfer, mainly in large-scale production, such as fouling and slagging (Mumbach et al., 2020).

Table 3-2: Characteristics and chemical composition of biomasses.

	Avocado stone (AS)	***Agave salmiana* bagasse (ASB)**	**Cacao shell (CS)**	**Cellulose (CEL)**
Proximate analysis (%)				
MC	3.2±0.4	3.4±0.1	3.8±0.4	2.2±0.3
VM	72.5±1.7	77.9±1.7	71.6±2.1	79.1±2.01
FC [a]	22.4±1.0	14.8±1.6	18.0±0.9	18.6±1.4
Ash	1.9±0.6	3.9±0.4	6.5±0.2	-
Ultimate analysis (%)				
Carbon	46.1±0.2	38.0±0.1	51.4±0.9	41.4 ± 0.5
Hydrogen	6.4±0.1	4.1±0.1	6.8±0.2	6.5 ± 0.1
Nitrogen	0.4±0.0	0.6±0.1	3.2±0.2	nd
Sulphur	nd	nd	nd	nd
Oxygen [a]	47.1±0.9	57.3±0.2	34.9 ±0.6	52.1 ± 0.6
HHV(MJ/kg)	**18.6±0.2**	**16.8±0.2**	**23.0±0.2**	**16.5±0.3**

MC: moisture content; VM: volatile matter; FC: fixed carbon; nd: not detected (<0.1%); [a]:by difference

The fixed carbon (FC) is the portion of biomass that remains residue after VM distills off, after MC and ash content in the biomass is subtracted. In general, a high level of FC in biomass is

always preferable and desirable. It should be noted that FC and total carbon are usually not the same. Total carbon represents the carbon present in the biomass under normal conditions. The FC in biomass includes elemental carbon in the original fuel plus any carbonaceous residue formed during biomass devolatilization. In the pyrolysis process, the cellulose in biomass mainly produces volatiles, while the lignin mainly forms fixed carbon (Sharma et al., 2004; Sun et al., 2017). FC is an important information of biomass quality since it is the most resistant portion that remains in biochar after pyrolysis. It is organized in aromatic chains (Amonette and Joseph, 2009)and is inversely related to volatile materials and ash content, which explains its higher content in AS (22.4%) . FC and lignin content are the most important components for thermal stability(Veiga et al., 2017).

The ultimate analysis gives the weight percent of the elements C, H, O, N, and S. The C, H, and O are the main elemental components of solid biofuels. From the energy point of view, the C and H are oxidized during combustion by exothermic reactions (formation of CO_2 and H_2O). So, the content of C and H contributes positively to the gross heating value. The C content is the highest for CS (51.4%), which means that CS is more energetic than AS, ASB and Cell. The H content is similar for all biomasses. Furthermore, the low content of N (< 3.5 wt%) and the absence of S of these biomasses are favorable for the thermochemical conversion of these biomasses into bioenergy products in an environmentally friendly way, i.e., without significant release of toxic emissions, such as (NOx) and (SOx). The elemental composition of various biomasses suggested as feedstocks for thermochemical conversion ranges from 41.2 to 49.0 wt% of C, from 5.3 to 6.2 wt% of H from 41.7 to 46.3 wt% of O, and from 0.4 to 8.2 wt% of N (Vickers, 2017). The elemental composition of these biomasses was shown to be within these ranges of values, which is a favorable indication of their suitability for thermochemical conversion.

3.2.4. Heating value

3.2.4.1. *Experimental HHV analysis*

The heating value of a fuel indicates the energy available in the fuel per unit mass. The net heating value is the actual energy available for heat transfer. The difference in available energy is explained by the fuel's chemical composition, moisture and ash content. For comparison, the energy content of fuels is reported on a dry basis. For example, most agricultural residues have heating values that fall in the range of 14–19 MJ/kg; coal ranges from 17–30 MJ/kg (Clarke

and Preto, 2011). The variations of the HHV registered between the biomass species and components were related to the differences in the chemical composition of the biomass (Ríos Saucedo et al., 2018). Only cellulose has a standardized chemical composition in theory, so its HHV is almost constant (nearly 18.6 MJ/kg). Hemicellulose is assumed to have a molecular structure comparable to cellulose, but its chemical composition varies depending on the biomass species and research method (Graboski and Bain, 1981). It is well known that lignin has a wide range of chemical structures, resulting in HHV values ranging from 23.3 to 25.6 MJ/kg. The biomass species also influence the chemical composition of extractives and the extractive solvents used. The chemical components of biomass, except cellulose, have different structures and chemical compositions; consequently, the heating values of these components can vary greatly between biomass species.

Additionally, the chemical composition of biomass varies depending on the biomass materials and the analysis procedure (Sheng and Azevedo, 2005).

According to the results obtained for the biomasses studied, CS has the highest HHV (23.0 **MJ/kg)** due to its high lignin and elemental carbon content, as shown in **Table 3-2.** The second biomass with the highest HHV is AS (18.6 **MJ/kg**) due to its higher lignin and C content than ASB.

The heating value is divided into two categories; the higher heating value (HHV) and the lower heating value (LHV). The HHV is the total energy produced in the combustion phase divided by the mass of the fuel, while the LHV is subtracting the heat of vaporization of water formed in combustion from the HHV (Domalski et al., 1986). The adiabatic calorimetric bomb was used to determine the HHV of these biomasses. However, another method to estimate the calorific value is to perform proximate and final analyses and then use the resulting results to calculate the calorific value using analytical correlations (Yin, 2011).

3.2.4.2. *Correlation based on proximate analysis*

The moisture (MC), volatile matter (VM), fixed carbon (FC), and ash in a biomass content are presented in the proximate study. It is the simplest and most commonly used approach for determining the characteristics of biomass fuel. As a result, fuel researchers and engineers are still interested in correlating the heating value with the proximate analysis results (Sheng and Azevedo, 2005). A review of state of the art about equations that correlate the proximate

analysis with HHV was carried out. The different equations with the lowest absolute error that appear in the literature were selected and are shown in **Table 3-3** (Montero et al., 2016).

For estimating the HHV, a good correlation between the HHV and the biomass ash content may be used. Jiménez and González (1991) proposed an equation to correlate the HHV against the sum of VM and FC contents. Considering Ash =100 –(FC+VM), it can be converted to the HHV and ash content correlation. According to the results, the equation calculated the calorific value with an error of < 5wt.% compared to those obtained experimentally.

Sheng and Azevedo (2005) have given a unified correlation for estimating HHV of biomass fuel from basic analysis data. It was based on MV and ash (in wt.% on dry basis) and HHV is determined in MJ/kg. In this equation HHV was assumed to be a lineal function of VM and ash of biomass. A similar model was proposed by Parikh et al. (2005) from proximate analysis of solid fuels.

Table 3-3: Equations that correlate HHV with proximate analysis.

Model		A.E.[a]	Ref.
M1	HHV= -10.81408+0.3133·(VM+FC)	4.43	Jiménez and González (1991)
M2	HHV= -0.0368+0.2218·MV+0.2601·Ash	3.65	Sheng and Azevedo (2005)
M3	HHV=0.3536·FC+0.1559·MV-0.0078·Ash	3.74	Parikh et al. (2005)
M4	HHV=0.3543·FC+0.1708·VM	5.68	Cordero et al. (2001)
M5	HHV=0.196·FC+14.119	6.1	Demirbas (1997)
M6	HHV=0.312·FC+0.1534·VM	7.69	Demirbas (1997)

[a] A.E. is the average value of the absolute error associated with each equation.

A simple equation based on proximate analysis is presented by Cordero et al. (2001), which allows the HHV of lignocellulosic and charcoals to be calculated. This equation was obtained from a multiple linear regression analysis using the least-squares fitting program. It is evident from the equation that the weighting of FC is more than twice the weighting of VM on the HHV, which probably limits the application of this equation only for coal with high FC content.

Demirbas (1997) proposed two correlations for determining the HHV of biomass fuels. One correlation is based only on a single independent variable, i.e., FC (on a dry basis). The FC of

different biomass is assumed to be of fixed composition and fixed HHV. The composition and HHV of FC differ from one matter to another and are assumed to depend on matter. These assumptions limit the utility of this correlation. The author also proposed another model based on MV and FC content. Other correlations also exist but they also have similar limitations to those mentioned above. Patel et al. (2007) suggested several nonlinear models for estimating HHV of Indian coals using artificial neural networks (ANN) methodology. The complexity of these models limits their applicability.

Table 3-4 presents the results obtained by the application of the different equations that correlate the HHV with the proximal analysis performed in the experimentation of the present study.

The estimation of the HHV value using the correlations proposed by Demirbas (1997)was the closest to the experimentally determined HHV for all biomasses except CS. For CS, no correction could estimate the experimental HHV values; this may be due to the high content of extractives. The extractives in biomass can contain fats, waxes, proteins, fatty acids, and so on. These compounds can increase the energy content, as they are more energy-dense than the biomass itself.

Table 3-4: HHV estimation by proximate analysis correlation

Model	AS			ASB			CS			CEL		
	HHVc (MJ/kg)	HHVe (MJ/kg)	Error (%)	HHVc (MJ/kg)	HHVe (MJ/kg)	Error (%)	HHVc (MJ/kg)	HHVe (MJ/kg)	Error (%)	HHVc (MJ/kg)	HHVe (MJ/kg)	Error (%)
M1	18.9	18.6	1.71	18.22	16.8	8.5	17.3	23.0	25.0	19.79	16.5	20.0
M2	17.0	18.6	8.7	18.7	16.8	11.54	18.0	23.0	21.8	18.0	16.5	9.1
M3	19.2	18.6	3.3	17.3	16.8	3.2	17.5	23.0	24.0	18.9	16.5	14.6
M4	20.3	18.6	9.2	18.5	16.8	10.4	18.6	23.0	19.1	20.1	16.5	21.8
M5	18.5	18.6	0.5	17.0	16.8	1.3	17.6	23.0	23.3	17.7	16.5	7.7
M6	18.11	18.6	2.6	16.6	16.8	1.4	16.6	23.0	27.8	17.9	16.5	8.7

HHVc: HHV estimated by correlation (MJ/kg)

HHVe: HHV experimental (MJ/kg)

3.2.4.3. *Correlation based on ultimate analysis*

Biomass is composed of elements C, H, O, N, and S, where the former three are the major (cellulose, hemicellulose, and lignin), representing up to 97–99% of the organic biomass mass. The ultimate analysis gives the content of these elements in biomass. In general, HHV increases with increasing C and H content, consistent with common sense that higher C and H content means higher energy content of biomass. On the other hand, there is no positive trend between HHV and oxygen content, although it is generally considered that oxygen is not a reactive element and that increasing O content leads to a decrease in HHV (Sheng and Azevedo, 2005). Due to the high correlation between HHV and C. For estimating the HHV, Tillman (2012) proposed a simple equation to calculate the HHV from the carbon content of the biomass. The author indicates that the evaluation of this simple equation (**Table 3-5**) gives a reasonably good correlation for estimating the HHV of biomass.

Table 3-5: Equations that correlate HHV with ultimate analysis.

Model		A.E.[a]	Ref.
M7	HHV= 0.4373·C	3.73	Tillman (2012)
M8	HHV= 0.349·C+1.1783·H+0.1005·S-0.10334·O-0.0151·N-0.0211·Ash	3.65	(Channiwala and Parikh, 2002)
M9	HHV=0.335·C+1.423·H-0.154·O-0.145·N	3.47	Demirbas (1997)
M10	HHV=0.3516·C+1.1625·H-0.1109·O+0.0628·N+0.10465·S	3.51	Annamalai et al. (1987)
M11	HHV=-1.3675+0.3137·C+0.7009·H+0.0318·O[b]	2.59	Sheng and Azevedo (2005)

[a] A.E. is the average value of the absolute error associated with each equation.

[b]Here O=100-C-H-Ash.

Many empirical correlations have been developed in the literature to estimate the HHV from the elemental composition, particularly for coals and other hydrocarbon fuels such as biomass, char, oil. The majority of these formulae are modifications to Dulong's equation. The Dulong equation is one of the earliest and most popular correlations, first introduced in the late 19th century and based on the final coal analysis data (Channiwala and Parikh, 2002). Additionally,

several correlations have been proposed especially for biomass. The evaluation parameters calculated from these correlations, presented in Table 1, indicate that, except for the equation proposed by Demirbas (1997), all these correlations are more accurate than those based on proximate analysis data because the ultimate analysis quantifies the elemental contents providing more detailed information on the chemical composition of the biomass. Among the equations based on the contents of all elements, the correlation proposed by Graboski and Bain (1981) is the poorest as it was empirically derived from the formation energy, while the equations proposed by Annamalai et al. (1987) and Channiwala and Parikh (2002) have very similar accuracy. On the other hand, Sheng and Azevedo (2005) proposed a similar model, based on C, H and O content. **Table 3-5**, the results of HHV estimation by ultimate analysis are presented. For this case, the HHV value estimation using the equation by Tillman (2012) was the nearest to the HHV determined experimentally. Moreover, in all correlations, HHV obtained for CS are closer to the experimental values, except for the model of Sheng and Azevedo (2005), which was not the case with the proximate analysis.

Table 3-6: HHV estimation by ultimate analysis correlation

Model	AS			ASB			CS			CEL		
	HHVc (MJ/kg)	HHVe (MJ/kg)	Error (%)	HHVc (MJ/kg)	HHVe (MJ/kg)	Error (%)	HHVc (MJ/kg)	HHVe (MJ/kg)	Error (%)	HHVc (MJ/kg)	HHVe (MJ/kg)	Error (%)
M7	20.2	18.6	6.7	16.6	16.8	1.1	22.5	23.0	2.3	18.1	16.5	9.7
M8	18.7	18.6	0.6	12.1	16.8	27.2	22.2	23.0	3.7	16.7	16.5	1.4
M9	17.2	18.6	7.3	9.7	16.8	42.5	21.1	23.0	8.4	15.0	16.5	9.0
M10	18.8	18.6	0.8	11.5	16.8	29.7	22.3	23.0	3.0	16.3	16.5	1.0
M11	19.0	18.6	2.2	15.1	16.8	10.0	20.4	23.0	11.2	17.8	16.5	8.1

HHVc: HHV estimated by correlation (MJ/kg)

HHVe: HHV experimental (MJ/kg)

It is a great advantage to calculate the HHV of any fuel and biomass simply from its proximal analysis and ultimate analysis. It can provide a helpful tool for modeling biomass thermochemical conversion processes and examining all data for likely errors when the results are far outside the predicted results.

3.2.4.4. *Correlations based on chemical analysis*

Biomass contains similar chemical elements, such as cellulose, hemicellulose, lignin, and extractives. Chemical analysis is sometimes conducted to characterize biomass materials. As a result, a few equations were proposed to correlate the HHV with the chemical composition. **Table 3-7** lists the equations suggested in the literature tested on a database of 49 biomass materials collected (Demirbas, 2001b; Jiménez and González, 1991; Tillman, 2012).

As explained above, only cellulose has a uniform chemical formula; therefore, it has a nearly constant HHV

Table 3-7: Equations that correlate HHV with chemical analysis

Model		A.E.[a]	Ref.
M12	HHV= 0.1739·Ce+0.2663·(1-Ce')	9.24	Tillman (2012)
M13	HHV= [1-Ash/(100-Ash)] · (0.1739·Ce+0.2663·L+0.3219·E)	7.41	Jiménez and González (1991)
M14	HHV=0.0889·L+16.8218	10.96	Demirbas (1997)
M15	HHV=0.1739·Ce+0.2663·L+0.33219·E	7.62	Sheng and Azevedo (2005)

Ce, L, E are weight percent of cellulose (including cellulose and hemicellulose), lignin and extractives on dry biomass basis, respectively.

Ce' is holocellulose (cellulose and hemicellulose) on dry extractable-free basis.

Although the hemicellulose structure is made up of pentoses and hexoses, its chemical composition depends on the biomass species and the analysis procedure. Lignin also has several three-dimensional chemical structures constituted by high carbon content; this makes it has high HHV value than hemicellulose and cellulose. Extractives can have a higher HHV than other chemical compounds because they are made up of compounds such as oil and waxes, which have higher energy density. Moreover, the chemical composition of biomass varies with biomass materials and the analysis procedure. Therefore, it is not surprising that the accuracy of the correlations based on the biomass chemical composition is not good. Even only on a dry, ash, and extractive-free basis, there is still a lack of correlation between the HHV and the chemical composition. Since the chemical analysis is not conventional to characterize biomass

as a fuel in engineering practice and the analysis data, including both the HHV and the chemical analysis data, are not widely available, no attempt was made for a more accurate correlation. **Table 3-8** shows the HHV data obtained using chemical correlations.

For this case, the HHV value estimation using the equation by Demirbas (1997) was the nearest to the HHV determined experimentally. Moreover, in all correlations, HHV obtained for CEL are closer to the experimental values, this is because cellulose is a model biomass and its HHV value is constant.

In general, the quality of correlations based on chemical analysis proved to be very poor due to the variation in the properties of the biomass components studied (except for the model biomass as cellulose) and their chemical composition.

Table 3-8: HHV estimation based on chemical analysis

Model	AS			ASB			CS			CEL		
	HHVc (MJ/kg)	HHVe (MJ/kg)	Error (%)	HHVc (MJ/kg)	HHVe (MJ/kg)	Error (%)	HHVc (MJ/kg)	HHVe (MJ/kg)	Error (%)	HHVc (MJ/kg)	HHVe (MJ/kg)	Error (%)
M12	6.0	18.6	67.7	11.7	16.8	30.1	13.8	23.0	39.9	17.4	16.5	5.4
M13	6.1	18.6	67.3	10.8	16.8	35.4	14.2	23.0	38.4	17.4	16.5	5.4
M14	18.33	18.6	1.4	18.1	16.8	7.6	18.7	23.0	18.5	16.8	16.5	1.9
M15	6.2	18.6	66.4	11.3	16.8	32.6	15.5	23.0	32.7	17.4	16.5	5.4

HHVc: HHV estimated by correlation (MJ/kg)

HHVe: HHV experimental (MJ/kg)

3.2.5. Fourier transform infrared (FTIR) analysis

Figure 3-7 shows the FTIR spectra of the biomasses. Strong hydrogen bond (O-H) stretching absorption around 3400 cm^{-1} **(1)** and prominent C-H stretching absorption around 2995 cm^{-1} **(2)** are observed this peak shows the presence of alkanes (Pandey and Pitman, 2003).

Asymmetric and symmetric H-C-H stretching, the C-H branch of C=O, were detected around 2850 cm^{-1} **(3)** (Reza et al., 2019), the existence of aldehyde groups. For unconjugated C = O in xylans (hemicellulose), it is observed around 1736 cm^{-1} **(4)** (Ahmed et al., 2018). The appearance of a peak at 1690 cm^{-1} **(5)** suggested the presence of compounds with C=O

stretching, which could be furans and other anhydrosugars. The stretching 1650/1660 cm^{-1} **(6)** for adsorbed O-H for the aromatic skeleton in lignin (Pandey and Pitman, 2003). Around 1620 cm^{-1} **(7)** C=C stretching for the α, β-unsaturated ketone (Cibulková et al., 2006). Strong stretching 1550 cm^{-1} **(8)** for N-O of the nitro compound. Around 1462 cm^{-1} **(9)** and 1425 cm−1 (10) for C-H deformation in lignin and carbohydrates (Charis et al., 2020). Around at 1375 cm^{-1} **(11)** for C–H deformation in cellulose and hemicellulose (Poletto et al., 2012). The stretching 1330/1320 cm^{-1} **(12)** for C–H vibration in cellulose and C–O vibration in syringyl derivatives. At 1260 cm^{-1} **(13)** for guaiacyl ring breathing, C–O stretch in lignin and C–O linkage in guiacyl aromatic methoxyl groups (Pandey and Pitman, 2003; Poletto et al., 2012). At 1240 cm^{-1} **(14)** for syringyl ring and C–O stretch in lignin and xylan,1158 cm^{-1} **(15)** for C–O–C vibration in cellulose and hemicellulose, 1122 cm^{-1} **(16)** for aromatic skeletal and C–O stretch, 1048 cm^{-1} **(17)** for C–O stretch in cellulose and hemicellulose and 898 cm^{-1} **(18)** for C–H deformation in cellulose (Braovac and Kutzke, 2012; Popescu et al., 2009).

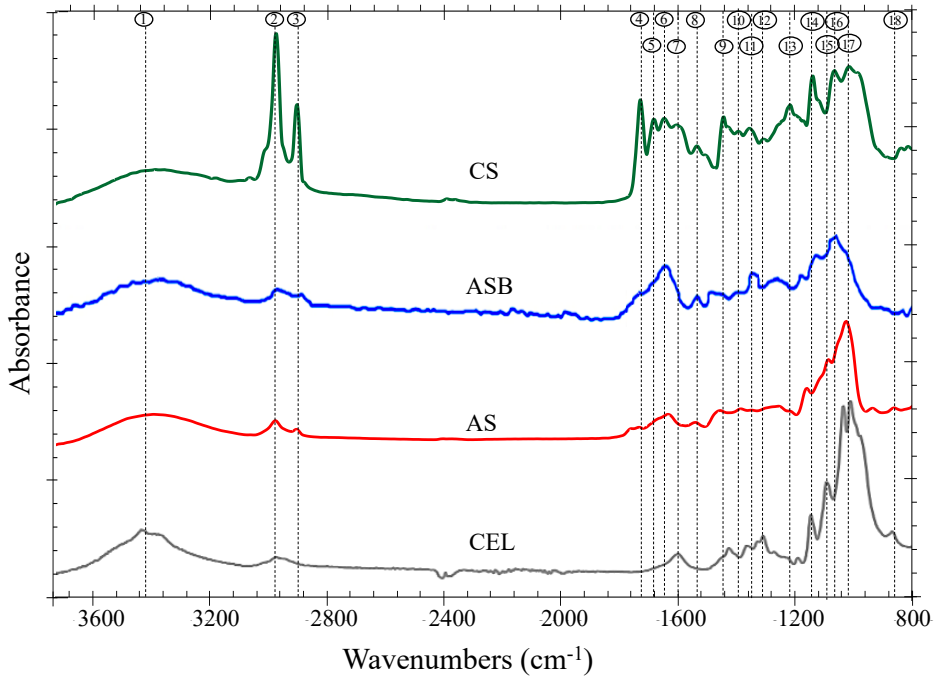

Figure 3-7. FTIR spectra of raw biomass of CS, ASB, AS, and CEL.

As shown in **Figure 3-7**, several functional groups (18) were detected in all biomass samples by FTIR analysis, indicating that the biomasses are heterogeneous. The functional groups in those peaks were defined by comparing the functional groups with criteria obtained from the literature. FTIR analyses indicated a wide range of compounds within cellulose, hemicellulose, and lignin structures (Liu et al., 2014). Reza et al. (2019) explicitly related the C-H bond stretch in the 2960-2850 cm^{-1} region to the presence of lignin, hemicellulose, and cellulose in the

biomasses. Bands at 2995 and 1736 cm^{-1} have higher relative intensities in the CS, while bands at 1048 cm-1 and 1158 cm^{-1} are heavier in ASB, CEL, and AS. The ASB and CEL have higher cellulose content than CS and AS, resulting in a stronger carbonyl band at 1738 cm^{-1}, while CS and AS have higher lignin content than ASB and CEL, resulting in a stronger aromatic band at 1260 cm^{-1}. The peak at the frequency of 2850 cm^{-1} seems to suggest a more substantial presence of aldehydes or alkanes in the CS, and 1425 cm^{-1} suggests a higher presence of lignin in this CS, as expected and in comparison, with ASB and CEL. The presence of aromatic rings, meta-substituted compounds was indicated by the other peaks at 898 cm^{-1} for the CEL and AS.

3.2.6. Scanning electron microscopy (SEM) analysis

The raw AS and CS were analyzed by SEM. **Figure 3-8** and **Figure 3-9** show SEM images of typical particles of crude biomasses (AS and CS). The micrographs show a large difference between the two samples.

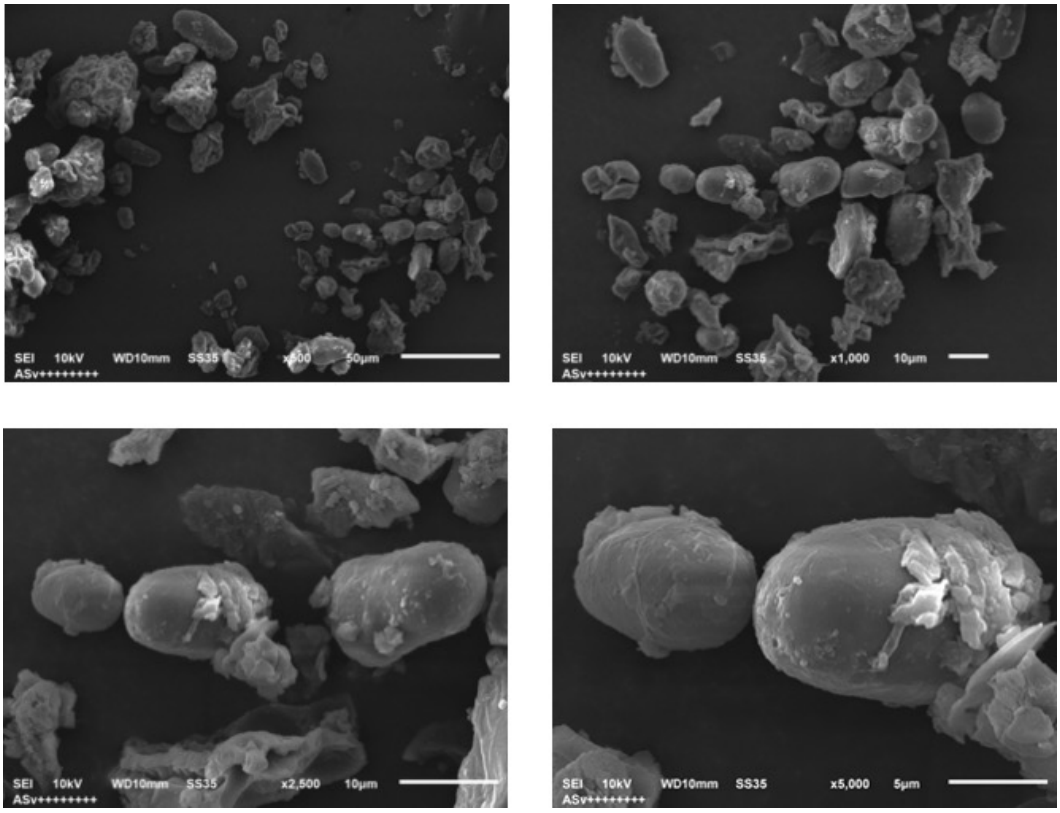

Figure 3-8. Scanning electron microscopy (SEM) images of raw AS

Figure 3-8 reveals that the crude AS particles have a fairly solid structure, with practically no pores. This solid structure explains their high density. The CS structure, on the other hand,

presents a very agglomerated structure. In addition, higher magnification images indicate that the CS sample shows many clumps. These agglomerations are because CS is a by-product of cocoa roasting, which occurs at 140 ºC. The effect of roasting temperature may be the main cause of CS agglomerations. Many small particles visible in **Figure 3-9** may probably be associated with the temperature of the heat treatment and thus the increased degradation of the sample.

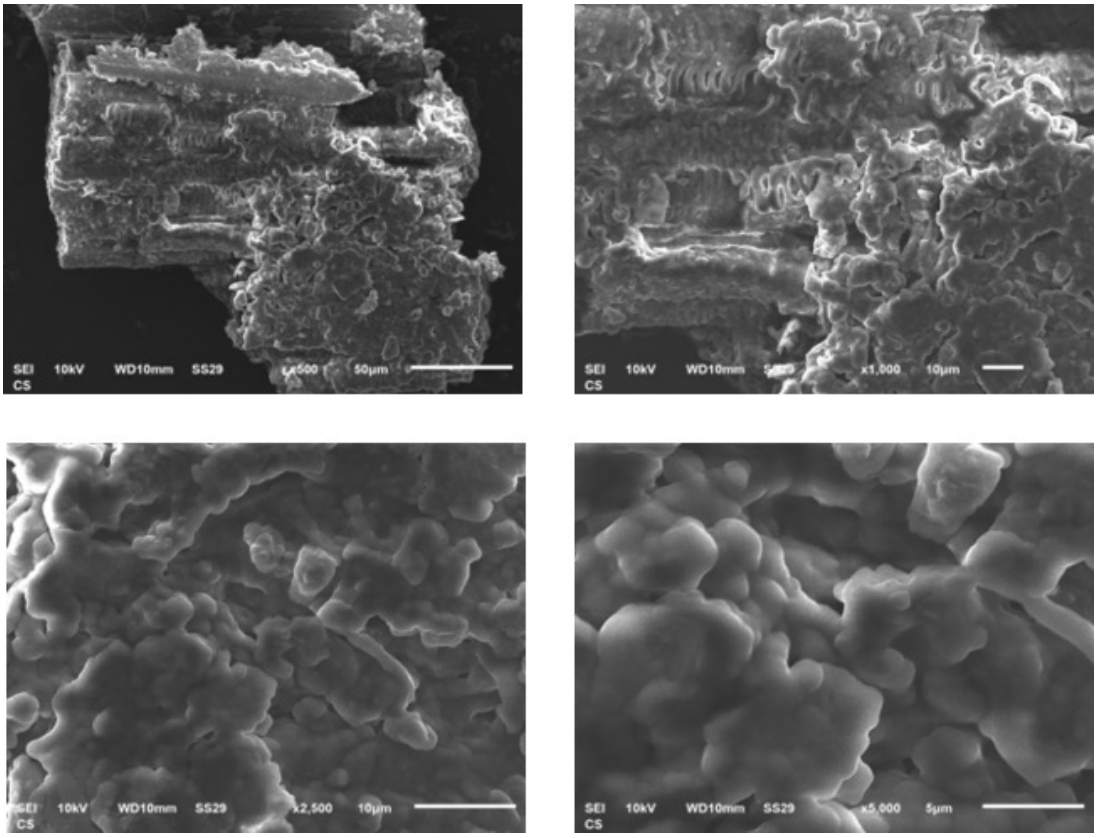

Figure 3-9. Scanning electron microscopy (SEM) images of raw AS

3.2.7. Thermophysical properties analysis of biomass

The transport phenomena (mass, energy, and momentum) are one of the most critical factors of biomass-to-energy conversion, especially in thermochemical conversion. Hence the thermal properties of biomass (heat capacity, thermal conductivity, and density).

The most critical factor during thermochemical biomass conversion is heat transfers within the biomass particles. These phenomena can limit the transformation under typical reactors conditions. This description requires knowledge of the thermal properties of biomass as well as their evolution with a conversion. Heat capacity and thermal conductivity are the most crucial heat transfer properties. The values obtained of the heat capacity and the thermal

conductivity of the biomass studies are presented in **Table 3-9**. Another important factor is density, which is vital during the carbonization or liquefaction hydrothermal of biomass. The density of the biomass particles could influence the heat transfer inside the HTC reactor. For example, if the biomass is denser than water, the particles will settle at the bottom of the reactor, if it is less dense than water, it floats on the water, this can cause non-homogeneity inside the reactor and, consequently, the heat transfer within the reactor will not be carried out correctly.

Table 3-9: Heat capacity and thermal conductivity of avocado stone and hydrochars

Samples	Heat capacity (J/kg·K)	Thermal conductivity (W/ m·K)	Density (kg/m^3)
AS	1518.17±3.7	0.1038 ±0.0039	1547.64±27.3
ASB	1402.82±12.5	0.1220±0.0014	810.48±19.7
CEL	1308.75±52.2	0.0812±0.0085	1525.23±32.8
CS	1213.54±25.8	0.1211±0.0027	435.32±8.8

AS and CEL is the densest for all biomasses studied, having a bulk density of 1548 $kg/m^3$and 1525 kg/m^3, respectively, and they are both denser than water. These biomasses, for example, will settle to the bottom of the reactor during hydrothermal carbonization, preventing proper heat and mass transfer. An agitation device would be needed to avoid this problem, which would raise the process's operational costs. On the other hand, ASB and CS have smaller densities, at 810 and 435, respectively, less dense than water.

There are several studies to determine the thermal properties of different biomasses; for example, for the heat capacity, values between 670 to 2500 J/kg·K have been obtained depending on the biomass (Dupont et al., 2014; Gupta et al., 2003; Raznjevic, 1976), while for thermal conductivity, values between 0.050 to 0.205W/m·K were found according to the biomass type and determination method (Gupta et al., 2003; Mason et al., 2016; Milosavljevic et al., 1996; Ragland et al., 1991). These properties depend on temperature; however, these values were determined at temperatures below 150°C, because many of the authors claim that the biomass begins to decompose when the temperature is higher than 150°C (Dupont et al., 2014; Gupta et al., 2003). On the other hand, Raznjevic (1976) determined the thermal properties of char between 140°C to 440°C, getting values similar to the biomass.

The heat capacity is the amount of heat that must be added (or removed) from a unit mass of a substance to change its temperature by one degree Celsius (Halliday et al., 2013). The heat capacities of the biomasses were 1518.17, 1402.82, 1308.75, and 1213.54 J/kg·K for AS, ASB,

CEL, and CS, respectively, as shown in **Table 3-9**, similar values commonly found on biomass and char in literature (Dupont et al., 2014; Gupta et al., 2003). Experimental studies on heat capacity can be found in the literature on biomass species of interest for current industrial applications. Many of these studies claim that the heat capacity of biomass is influenced by temperature (Dupont et al., 2014; Raznjevic, 1976). According to studies, there is a general consensus that the heat capacity of biomass increases linearly with temperature, ranging from 25 to 150 ºC, according to studies. In this regard, Dupont et al. (2014) studied the heat capacity of different biomasses, obtaining values between 1302 and 1822 J/kg·K in a temperature range of 40 and 80°C. However, this value range is due to the type of biomass and not the temperature range; Dupont et al. (2014) found that the heat capacity of softwood bar follows a linear increase from 40 °C to 140°C, obtaining values between 1364 and 1777 J/kg·K. This author and other studies claim that the heat capacity of biomass cannot be measured from 150°C, as biomass begins to decompose when the temperature is higher than 150°C (Dupont et al., 2014; Gupta et al., 2003; Raznjevic, 1976). The heat capacity values in this study were determined at temperatures ranging from 40 to 60 ° C. The results are comparable to those obtained by Dupont et al. (2014) and Gupta et al. (2003) for many forms of biomass.

Regarding char, Gupta et al. (2003) found that the heat capacity of char followed a linear increase from 40 °C to 140°C and then a smoother increase characterized by a second-order polynomial between 140 °C and 440 °C, finding values from 768 J/kg·K at 40 °C to 1518 J /kg·K at 440 °C This is in agreement with the findings of Raznjevic (1976) on charcoal. These values can help us understand how the heat capacity of biomass can vary during the thermochemical conversion process, especially pyrolysis and hydrothermal carbonization, since one of the main products of these processes is char, charcoal, or hydrochar. For example, comparing these values with the saturated water, where the HTC occurs, the heat capacity of saturated water at 180ºC is 4405.0J/kg·K, at 200ºC is 4495.8 J/kg·K and at 250ºC is 4878.8 J/kg·K (ToolBox, 2004). In the condition of hydrothermal carbonization (saturated water between 180°C and 250°C), the heat capacity of water is greater than the heat capacity of hydrochar and biomass. In this sense, according to the definition of heat capacity, in the same mass, the amount of heat needed to increase the water temperature by one degree is greater than the heat needed to increase the temperature of the biomass by one degree. Knowing this value for biomass before its conversion into energy is important for studying heat transfer since, depending on the biomass, there will be different heat transfer mechanisms. Knowing this value for biomass before its conversion into energy is important for studying heat transfer since,

depending on the biomass, there will be different heat transfer mechanisms. However, heat transfer depends not only on the heat capacity; another physical property that can significantly affect heat transfer is thermal conductivity.

The thermal conductivity can be defined as the rate at which heat is transferred by conduction through a unit cross-section area of a material when a temperature gradient exists perpendicular to the area (Ratna, 2012), which refers to the intrinsic ability of a material to transfer or conduct heat. Heat moves along a temperature gradient, from an area of high temperature and high molecular energy to an area with a lower temperature and lower molecular energy. Therefore, the conductivity of many materials is temperature-dependent, and biomass is no exception. Ragland et al. (1991), report that the thermal conductivity of wood increases with temperature, finding values between 0.087 W/ m·K at 25°C and 0.099 W/ m·K at 100°C, additionally, the values almost follow a linear pattern. The authors report that the thermal conductivity of wood increases by10% for every 50°C increase in temperature.

For an increase in temperature from 147 to 302 °C, Milosavljevic et al. (1996) have reported thermal conductivity values for virgin cellulose pellets to increase from 0.050 to 0.070 W/ m·K. Similar values were found by Gupta et al. (2003) for softwood, softwood bark, and softwood char of 0.099, 0.095, and 0.205W/m·K, respectively. The thermal conductivity of the biomasses is presented in **Table 3-9.** The values obtained are in the range of values reported by Gupta et al. (2003) for softwood, softwood bark, and softwood char. The thermal conductivity of biomass indeed varies with temperature. However, this variation can be considered non-significant, especially for the hydrothermal carbonization process. Since water is much more conductive than biomass, biomass can behave as an insulator during reactor heating. For example, compared to the thermal conductivity of saturated water in the range of hydrothermal carbonization. The thermal conductivity of saturated water at 180ºC is 0.6611 W/m·K, at 200ºC is 0.6650 W/m.K and at 250 ºC is 0.6160W/m·K (Crabtree and Siman-Tov, 1993). The thermal conductivity of the AS, ASB, CEL, and CS are 0.1038, 0.1220, 0.0812 and 0.1211W/m·K, respectively. According to this data, water is more heat-conductive these biomasses.

3.3. Conclusion

- Lignocellulosic biomass is a highly heterogeneous, complex multi-scale substance that significantly differs in structure and composition depending on the source and a range of genotypic, phenotypic, and environmental growth factors. The characterization of biomass to determine physical, chemical, and thermochemical properties is an important step in converting biomass to energy. It provides critical information about the biomass during pretreatment and conversion and offers valuable insights into using it. It also gives the basis for determining process performance in terms of carbon conversion efficiency and energy efficiency and facilitates process optimization to maximize product yield. To better understand biomass characteristics, a good grasp and proper selection of analytical methods are necessary. The compositional, thermogravimetric, microstructure, chemical composition, and thermophysical properties analysis of biomass is important for thermochemical conversion.
- The compositional analysis showed different chemical structural composition of the studied biomasses. The results obtained showed a high content of extractives (25.3 wt%) and lignin in CS (21.5 wt%), which gives it a higher energy content (25.3 MJ/kg). The high content of HHV in CS may be necessary for use as an energy source. However, its high content of extractive compounds may be an impediment to its use during the thermochemical conversion process. Perhaps the best process to convert CS into energy may be the chemical process (biodiesel conversion) due to its high oil content, in addition to its high ash content (6.5 wt%). The chemical characteristics of AS, ASB and CEL make interesting their comparative studies during the thermochemical conversion process. The AS contains 76.4 wt% hemicelluloses and 3.6 wt% cellulose; this is interesting because it can be used as a hemicellulose biomass model. The α-cellulose (100 wt%) is the cellulose model. The last biomass used was ASB; it contains 43.8 wt% of hemicellulose and 40.7 wt% of cellulose; this biomass can be used as an almost perfect mixture of hemicellulose and cellulose, which can be found naturally. This biomass (ASB) study can be enjoyable during thermochemical conversion, especially in the hydrothermal carbonization process, where the compounds that are degraded are hemicellulose and cellulose.
- Many empirical formulas which estimate the HHV of biomasses from basic analysis data, such as proximal, ultimate, and compositional analysis, were used to estimate the HHV of biomasses and compared with experimental data obtained. The quality of

correlations based on elemental analysis was found to be fitting for all biomasses. However, for the proximal analysis, the HHV estimation for CS was very poor for all the models used. The correlations based on chemical analysis proved to be very poor due to the variation in the properties of the biomass components studied (except for the model biomass as cellulose) and their chemical composition.

- A measurement method has been presented to determine the relative thermal conductivity of the studied biomasses. The method has been shown to be effective by comparison with data published in the literature. The experiment has provided data on the thermal properties of tiny particles of this biomass in the form of pellets. In reality, many published data about the thermal properties of various biomasses are available; there is little data about these biomasses. The heat capacity of the biomasses was determined between 40 to 60 ºC. The limitation of the experimental set-up prevented us from determining the heat capacity at higher temperatures since the heat capacity of the raw biomass can be determined up to 150 ºC. However, above 150 ºC, the biomass starts to decompose. No significant variation was observed in the heat capacity obtained for the different biomasses. These values are also similar to those reported in the literature for other types of biomasses. There were also some constraints in the study, particularly in the FTIR analysis. It is ideal to have a library of standards connected to the FTIR spectrometer to identify the functional groups directly; however, the equipment used did not have such a library. Therefore, the literature was used to make inferences, using findings done before by other authors.

Chapter4 HYDROTHERMAL CARBONIZATION OF BIOMASSES

Hydrothermal carbonization (HTC) is a thermochemical conversion process by which wet biomass is heated to a temperature typically between 180 and 250 °C under autogenous saturated vapor pressure between 10 and 40 bars residence time ranging from a few minutes up to several hours (Liu and Balasubramanian, 2012; Missaoui et al., 2017). Three main products are formed during the HTC process: solid (hydrochar), liquid (biocrude mixed with water), and small gas fractions (Becker et al., 2014; Missaoui et al., 2017).

The quality of HTC products depends on the biomass type and the operating process conditions. Recently, the behavior of several types of biomasses during the HTC process has been studied, e.g., olive pomace (Missaoui et al., 2017) , tomato waste (Sabio et al., 2016), olive stone (Álvarez-Murillo et al., 2015b), sugarcane bagasse (Chen et al., 2012), corn cob (Zhang et al., 2015a), and cellulose (Paksung et al., 2020). However, the results obtained depend mainly on the type of biomass and operating condition of the process. Numerous process parameters have been shown to influence HTC products. These include temperature, residence time or holding time, biomass-to-water ratio, and particle size. The influence of temperature has been studied by numerous authors, where it has been demonstrated that the ideal temperature range is between 180 and 250 °C. These actual limits are directly related to the consistency of the organic materials in use. Typical residence times ranging from a few minutes up to several hours (Batidzirai et al., 2016; Thrän, 2015; Zhang et al., 2019), although durations of a few seconds have been reported as well (Missaoui et al., 2017). Naturally, longer residence times ensure complete hemicellulose and cellulose decomposition and provide a higher carbonization degree (Kladisios and Sagia, 2018).

Recently Wüst et al. (2019) studied the influence of raw material particle size on hydrochar formation, and its result shows that smaller particle size 0-250 µm shows the worst results in terms of its percentage of carbon in hydrochar Yan et al. (2014b). showed similar results, where particle sizes between 1.68 and 2.38mm show higher mass yield than smaller particle sizes.

An additional process parameter that affects the final products of HTC is the biomass-to-water ratio. The process water mass is typically 3-10 times greater than that of the dry feedstock (Hoekman et al., 2013; Kambo and Dutta, 2015; Liu et al., 2013b). Although many studies have reported the effect of the biomass-to-water ratio, most are focused on its effect on the mass yield of hydrochar. The biomass-to-water ratio significantly affects the hydrochar yield;

a lower ratio of biomass in water causes a decrease in the solid yield. This is attributed to the greater impact of hydrolysis reactions caused by water quantity increase (Guo et al., 2016; Román et al., 2012; Sermyagina et al., 2015).

The main product of HTC is hydrochar, a solid material rich in carbon (55–74% carbon), stable, a lignite-like material that is characterized by a high calorific value (21.1–30.6 MJ/kg) (Heidari et al., 2018; Hitzl et al., 2015; Xiao et al., 2012). Its physical, chemical and mechanical properties make it susceptible to different uses, such as solid fuel that can be burned for energy or it can be used to synthesize fuel cells, additive agent for soil amendment, soil fertility, electrode supercapacitors, water retention, Heavy metal removal, batteries as a medium for converting and storing energy, and so on (Fang et al., 2015b; Fang et al., 2018; Kambo and Dutta, 2015; Libra et al., 2011). The most common uses of this liquid phase of HTC include the use in anaerobic reactors for methane production (Wirth et al., 2012), disposal via wastewater treatment plants (Becker et al., 2014), or reusing the water to treat a fresh load of biomass in consecutive HTC runs (Uddin et al., 2014).

The objective of this part of the study is to study the hydrothermal carbonization process using different types of biomasses (avocado stone, *Agave salmiana* bagasse, cacao shell and cellulose). The focus in this chapter is to study of the HTC process for the formation of hydrochar. To characterize the hydrochar formed. To investigate the effects of the biomass-to-water ratio on the hydrochar, liquid and gas. Determine the leading products in the liquid and gas phase. To analyze the different mechanisms of the HTC reactions and the kinetics of forming the main products in the liquid and gas phase.

4.1. Experimental Procedure

4.1.1. HTC reactor description and types of reactors used

Hydrothermal carbonization experiments were performed in two different reactor systems. A 50 mL reactor operating in a closed-loop system and a 300 mL stirred reactor working in an open-loop system.

4.1.1.1. *Reactor operating in a closed-loop system (non-stirred reactor)*

In this reactor, the HTC experiments were conducted in a 50 mL batch reactor (Top Industrie, France) made of a nickel-base alloy (Inconel 718) allowing to reach a Tmax of 550°C and a Pmax of 300 bars. The autoclave reactor consists of two parts screwed together: a reaction

vessel with an internal volume of 50 mL and a cap. This last one is hollowed out to measure the pressure, follow the temperature, and release the gases produced at the opening of the reactor. The tightness is maintained with a metallic seal. The reactor is mainly equipped with the following instruments

- a control box (panel) to adjust and display the temperature during the experiment
- a thermocouple K-type immersed inside the reactor
- an indicator to measure the pressure during the experiment

The HTC batch reactor is shown in **Figure 4-1**. The apparatus of HTC consists of a furnace (1) for heating the autoclave batch reactor (3). The pressure is controlled by a pressure sensor (4), and the temperature by a thermocouple (2) connected to a temperature regulator (6). The reactor also has a gas collector (5) to analyze the gases produced and a vacuum pump (7) to remove all reactors' gases before starting the experiments.

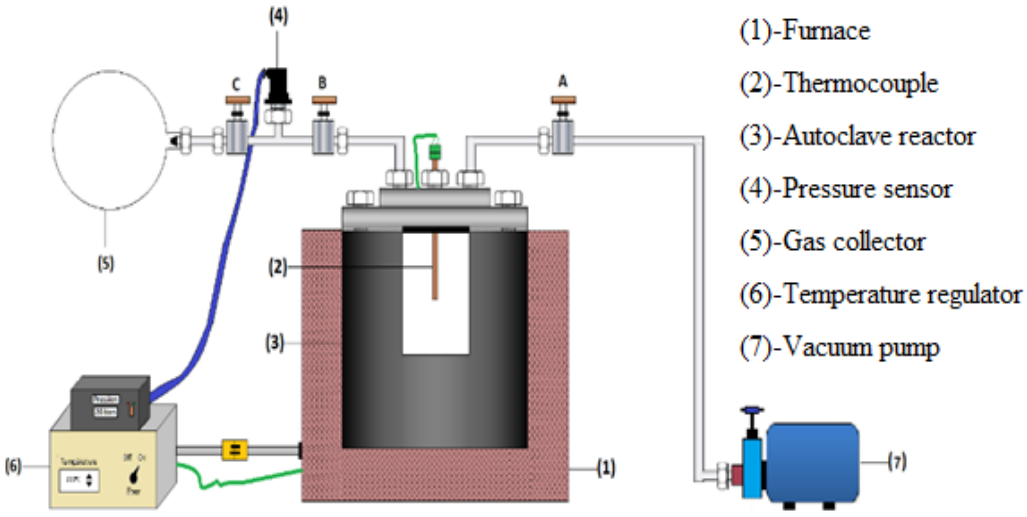

Figure 4-1*:* HTC experimental apparatus

In this reactor, ASB was used as biomass for each experiment. The ASB and distilled water were introduced into the batch reactor at room temperature. For each HTC run, 9± 0.05 g of dry sample were loaded into the reactor together with 27 ± 0.1 g of deionized water, with a biomass-to-water ratio (ASB/W) equal to 1/9 (w/w). The mixture was manually stirred to ensure thorough wetting of the feedstock. After manual mixing, the reactor was closed. The tightening is done by applying a torque of about 40 Nm to guarantee the pressure resistance. Then, the hermetic autoclave is placed in a Top industrie® furnace for heating (external electric

heating). The maximum power delivered by the heating device is 3000 W. **Figure 4-2** shows the procedure for closing and opening the flanged autoclave reactor.

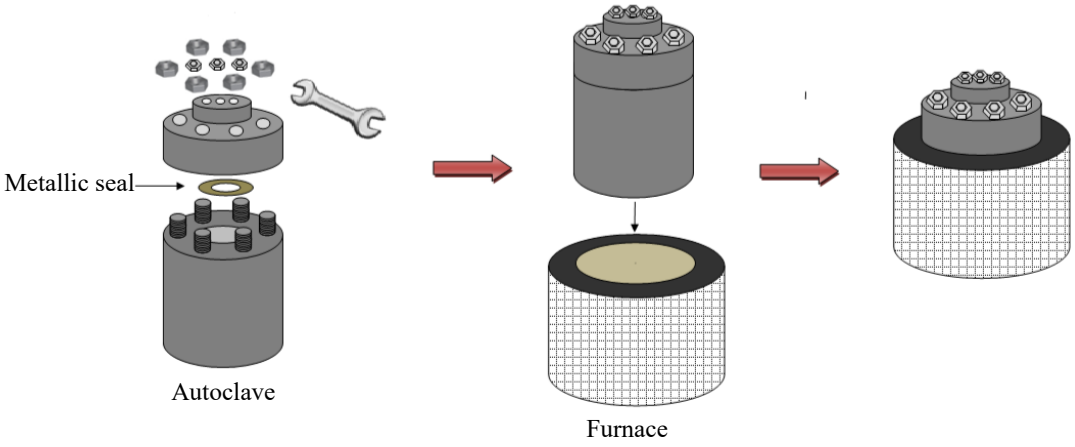

Figure 4-2: Clamping and opening system for the 50 mL non-agitated autoclave reactor

To eliminate the residual air, vacuum conditions were applied to the reactor with a pump. After reaching a less than 20−50 mbar, the heating program was started to reach the set temperature. Once the temperature reached the set value, the experiment was carried out for a fixed holding time. At the end of this time, the reactor was cooled to room temperature using air circulation. Pressure (Pexp) and temperature (Text) were measured, allowing calculation of the gas volume produced at room temperature. For this purpose, the total volume, including the reactor, pipes, and valve volumes, has been measured, giving a total volume of 66 mL. Gaseous products were purged. The solid and liquid products were separated via Büchner filtration. The liquid phase was weighed, stored, and protected from light in a refrigerator (~5 °C). The pH of the liquid phase was measured, and the collected hydrochar was weighed and dried at 105 °C for 24 h. The analytical techniques used to characterize the biomasses and the hydrochars are described in **chapter 2**. The holding time, temperature, and biomass-to-water ratio were chosen to study the effect of operating parameters on the performance of HTC conversion.

4.1.1.2. *Reactor operating in an open -loop system (stirred reactor)*

The HTC experiments were carried out in the stirred autoclave reactor (Top Industrie, France) with an internal volume of 300 mL suitable for a pressure of 100 bars and temperature of 300°C.

The stirred autoclave reactor (**Figure 4-3**) consists of two parts: a reactor vessel and a cylindrical capping vessel. The capping vessel included a central connection for a magnetic

stirrer (1500 rpm max, 50 W) and six connections for measuring pressure, monitoring temperature, and releasing the gases produced. The reactor is sealed with an O-ring between the vessel and the cap.

The reactor is mainly equipped with the following instruments:

- Furnace control panel for online temperature adjustment and display,

- K-type thermocouples immersed inside the reactor,

- Manometer to measure the pressure during the experiment,

- Stirrer control box to regulate, measure, and display the stirring speed.

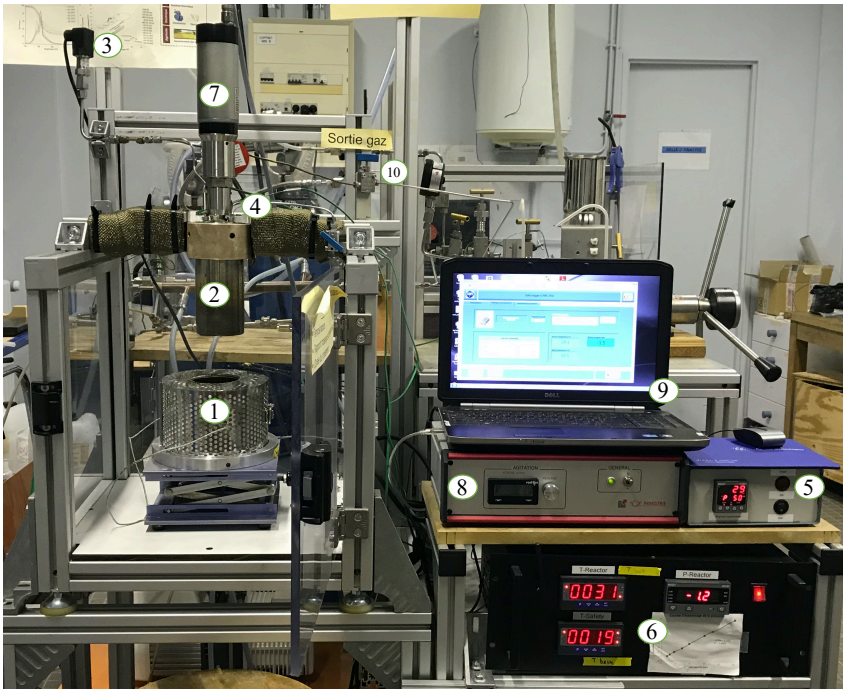

(1)-Furnace
(2)-Autoclave reactor
(3)-Pressure sensor
(4)-Thermocouples
(5)-Power regulator
(6)-T and P logger
(7)-Stirrer motor
(8)-Stirrer regulator
(9)- Computer
(10)-Gas outlet line

Figure 4-3: Experimental apparatus of the stirred reactor

The reactor is clamped with the cap by opening and closing it manually. Then, the autoclave is placed in a Top industrie® oven for heating. The maximum power delivered by the heating device is 400 W. The characteristics of the raw material, the experimental principle, and the experimental devices used to perform the HTC experiments were presented. The HTC experiments were performed under different operating conditions. The complete stirred reactor system is shown in **Figure 4-3**. The apparatus of HTC consists of a furnace (1) for heating the autoclave reactor (2). The pressure is controlled by a pressure sensor (3), and the temperature by a thermocouple (4) connected to a power regulator (5). The temperature and pressure are

recorded in the P y T logger (6). The stirrer motor (7) is connected to the stirrer regulator (8). All of the above is connected to a computer (9) to record the data. The reactor also has a gas outlet (10). Before starting the heating program, the residual air inside the reactor was removed using a vacuum pump to a pressure of less than 40 mbar. After reaching less than 40 mbar, power is applied to the reactor according to the desired setpoint temperature. Since this reactor worked in an open-loop system, a previous calibration was performed. The calibration was done using water inside the reactor before starting the experiments with biomass. The biomass to water ratio, the power used, the setpoint temperature, and the type of biomass (AS, ASB, CS, and CEL) used depending on the study's objectives. However, an equivalent volume of 200 mL of the reactor was used for each experiment, regardless of the biomass-to-water ratio and the operating condition.

4.1.2. The operational conditions of the different HTC studies

HTC transforms wet biomass into hydrochar, liquid phase (biocrude), and gas phase. The mass yield of these products depends on the operating conditions. In this part, the details of the different operating conditions for the experiments carried out are explained. The effects of holding times, temperature, and biomass-to-water ratios were studied. The operational conditions for the different objectives proposed in this chapter are presented below:

To perform the kinetic studies of hydrochar production, the mechanism of the HTC process and the separation of char and tar, the experimental conditions were as follows: The biomasses used were AS and CS. For each HTC run,18.65 ± 0.05 g of dry sample were loaded into the reactor together with 186.5 ± 1.5 g of deionized water, with a biomass-to-water ratio (B/W) equal to 1/10 (w/w). The reactor was heated from room temperature to setpoint temperature at different powers supplied in the reactor 160, 200, and 240 W; these represent an average heating rate of 1.5, 2.0, and 2.8 °C/min, respectively. The setpoint temperatures were 150, 160, 170, 180, 190, 200, 210, 220, 230 and 250 ºC. The setpoint temperatures of 150, 190, and 250 ºC were carried out in triplicate. The uncertainty of the error was less than 1.5% in all cases. During the experiment, the reactor was stirred at 550 rpm.

To analyze the main components of HTC liquid phase, the biomasses used were AS, ASB, and CEL. For each HTC run, about 18.65 g of dry sample was loaded into the reactor together with 186.5g of deionized water, with a biomass-to-water ratio (B/W) equal to 1/10 (w/w), and it was stirred at 550 rpm. The reactor was heated from room temperature to setpoint temperature at

200 W. The setpoint temperatures were 150, 160, 170, 180, 190, 200, 210, 220, 230, and 250 ºC, and the holding time was 1-120 minutes.

To study the effect of the biomass-to-water ratio, heat of HTC reaction, and the type of HTC reaction (exothermic or endothermic), avocado stone (AS) was used as biomass; HTC experiments were carried out with four ratios, AS-to-water (W), under the same operating conditions: residence time (8h), power supply in the reactor (120 W), particle diameters between 2.5 and 4 mm, and agitator speed (550 rpm). The biomass-to-water ratio (AS/W) was: AS-1/10 (18.74g/187.45g:AS/W), AS-1/8 (23.08g/184.68g:AS/W), AS-1/6 (30.04g/180.24g: AS/W), AS-1/4 (42.99g/171.98g: AS/W).

For each experiment, after the reactor reaches the setpoint temperature, it was immediately cooled down, and this took 5 to 10 minutes to cool it down by immersing it in a 5 °C water bath. After cooling the reactor, the system pressure was noted, the reactor was opened, the liquid and solids were separated with a Whatman filter paper with a pore size of 11 microns. The liquid was immediately used for the corresponding analysis, and the solid was weighed after drying at 105 °C for 24 hours on the stove. The hydrochar yield or total solid yield (Y_{HC}) was determined through the **Eq.(4-1)**:

$$Y_{HC} = \frac{m_{HC}}{m_{bio}}.100 \qquad (4\text{-}1)$$

Where m_{HC} is the mass of total solid (on a dry base), and m_{bio} is the raw biomass mass (on a dry base). The derivative hydrochar yield (DY_{HC}) is the first-order derivative of Y_{HC} with respect to time. From this approach, it is possible to determine the maximum temperature decomposition of biomass. The DY_{HC} was determined through the **Eq.(4-2)**:

$$DY_{HC} = \frac{\Delta Y_{HC}}{\Delta t} \qquad (4\text{-}2)$$

Where DY_{HC} is derivative hydrochar yield (%/min), and Δt is the time variation (min).

4.1.3. Hydrochar characterization procedure

The hydrochar characterization (Fourier-transform infrared spectroscopy (FTIR) and scanning electron microscope (SEM)) procedure was described in **Chapter 2**.

4.1.4. Tar contents in hydrochar, extraction of tar and GC–MS analysis

In this part AS and CS were used as biomass and hydrochars produced from these feedstocks.

4.1.4.1. *Tar contents extraction by Soxhlet extractor*

Soxhlet extractor has been a standard analytical practice for over a century and is certainly the most widely used and accepted method for the extraction of semi-volatile organic compounds (SVOCs) from solid samples. Although considered a more traditional technique, Soxhlet extraction is the accepted standard for comparison with other extraction approaches and therefore of central importance to the US EPA methods, as discussed in EPA Method 3540 (Weggler et al., 2020). The experimental Soxhlet extraction apparatus consists of a distillation flask, sample holder (thimble), siphon and condenser. A Soxhlet extraction procedure usually involves the following steps.

First, the sample material is packed in filter paper and placed in the thimble. Next, vapors of a fresh solvent, produced in a distillation flask, pass through the thimble containing the material to be extracted and are liquefied in the condenser. When the liquid reaches the overflow level in the thimble, a siphon aspirates the solution, and the liquid falls back into the distillation flask, carrying the extracted solutes into the bulk liquid. The separation of solute from solvent takes place in the distillation flask. Then solute is left in the flask and fresh solvent vapors pass back into the solid bed of sample material. The operation is repeated until complete extraction is achieved. The extraction time is long (up to 48 hours) (Slominska et al., 2012). A simplified schematic of a Soxhlet extractor is shown in **Figure 4-4**. Soxhlet extraction employing organic solvents is one of the most widely used techniques for extracting organic compounds from natural sources because they usually give good extraction results and are easy to perform. However, this technique requires high solvent consumption, long extraction times.

The extraction time is a disadvantage because it is related to increased energy consumption and can severely decrease the sample yield; therefore, it is a drawback in commercial applicability (Mussatto, 2015). Soxhlet extraction consists of extracting the desired component from a solid material using a liquid (an organic solvent such as ethanol, methanol, acetone, toluene, hexane, dichloromethane, pure or mixed) capable of dissolving the solute from the other components of the solid matrix. Soxhlet extraction has been used for the extraction of PAHs or tars within biochar from numerous sources. However, the conditions that promote high extraction efficiency, including the type of solvent, vary for each feedstock. Soxhlet extraction has been used for the extraction of PAHs or tars within biochar from numerous sources. For example,

Toluene 100% was used as a starting solvent (Jonker and Koelmans, 2002) and compared with several mixtures, i.e., toluene/ methanol (1:6, v/v; best suited for wood soot, according to Jonker and Koelmans (2002), dichloromethane/acetone (1:1, v/v; recommended solvent in the Dionex application note toluene/ethanol (2:1, v/v), toluene/propanol (2:1, v/v), toluene/hexane (2:1, v/v), toluene/ heptane (2:1, v/v), and toluene/dichloromethane (2:1, v/v). Hexane (100%) used by Fernandes and Brooks (2003) and heptane (100%) were also tested as alternative extraction solvents. Extractions were run for 15 or 36 h, and the sample size was 1 or 0.1 g (Hilber et al., 2012)

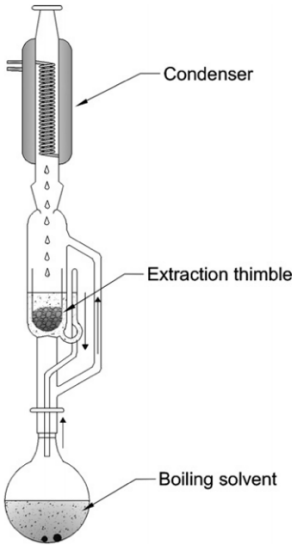

Figure 4-4: Conventional Soxhlet extractor

Hilber et al. (2012) reports that better extraction efficiency of PAHs is obtained using 100% toluene as solvent for 36 h of extraction. For this reason, the extraction of tar was performed with toluene (100%) as the extraction solvent in a Soxhlet extractor.

All hydrochars were first dried at 105 °C. Subsequently, it was finely ground using a laboratory batch mill Ika M20 (IKA-Werke, Staufen, Germany) and sieved to obtain a particle size between 0.1 and 0.25 mm in diameter. All hydrochars were stored in amber glass at a dry place and room temperature. A portion of the samples was placed in the furnace at 105 °C for four hours to determine the dry weight of the hydrochars. For the method development with Soxhlet extraction, about 2 g of the hydrochar samples (AS and CS) and 250 mL toluene were placed in the Soxhlet extractor for 36 h. After this time, the solution was concentrated by a rotary evaporator to obtain 25 mL volume.

4.1.4.2. *GC–MS analyzer for the main components of tar in hydrochar.*

The tar composition was detected using a GC–MS analyzer. The analysis was carried out by two different methods and columns to detect aliphatic and PAHs compounds.

4.1.4.2.1. *Chemicals and materials.*

Polynuclear Aromatic Hydrocarbons Mix, certified reference material, 2000 µg/mL each component in methylene chloride: benzene (1:1) was purchased from SIGMA-ALDRICH.

This solution is a mixture containing 18 PAHs [i.e., a-methylnaphthalene (MNAP), anthracene (ANT), fluoranthene (FLT), naphthalene (NAP), acenaphthene (ANA), benzo[a]anthracene (BaA), benzo[a]pyrene (BaP), benzo[b]fluoranthene (BbF), benzo[k]fluoranthene (BkF), chrysene (CHR), acenaphthylene (ANY), pyrene (PYR), benzo[ghi]- perylene (BPE), fluorene (FLU), phenanthrene (PHE), dibenz[a,h]anthracene (DBA), indeno[1,2,3- cd]pyrene (IPY), 2-methylnaphthalene (2MNAP)]. It was used as the standard solution to identify and calibrate the GC-MS because the tar solution contains several components.

4.1.4.2.2. *Aliphatic compounds analysis by GC–MS analyzer*

Aliphatic compounds were detected on a Trace Ultra-ISQ gas chromatograph single quadrupole mass spectrometer (Thermo Scientific, Villebon Sur Yvette, France) **(Figure 3-5**) equipped with a programmed temperature vaporizing injector (PTV) and a 2 mm diameter.

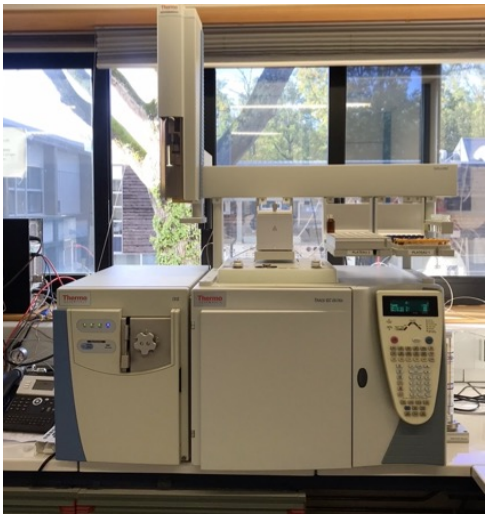

Figure 4-5: Trace Ultra-ISQ gas chromatograph - mass spectrometer Thermo Scientific (ICOA-UMR7311)

4.1.4.3. *PAHs compounds analysis by GC–MS analyzer*

In order to detect PAHs, the extracted liquid was diluted 50 times in dichloromethane. The PAHs were detected on a Trace Ultra gas chromatography coupled with a quadrupole mass spectrometer (**Figure 4-6**). A DB17ms Agilent column (30 m length, 0.32 mm internal diameter, and 0.25 μm film thickness) was installed in the GC oven. Initially, the temperature of the GC oven was set at 40 °C for 7 min followed by a 20 °C/min ramp to 75 °C, and it was held on for 15 minutes and then a 20 °C/min ramp to 200 °C for 8 minutes, and finally a 10 °C/min ramp to 220 °C, and it was held on for 55 minutes. For the data acquisition using the Electron Impact (EI) mode, both the temperature of the transfer line and the ion source was held at 200 °C. The temperature for the inlet injector was fixed at 300 °C for attaining a well-vaporization of the sample, and a spitless liner was installed. A mass range (m/z) of 50–300 amu was scanned, that is, in full scan acquisition.

Figure 4-6: Trace Ultra-ISQ gas chromatograph - mass spectrometer Agilent technologies 70000C (ICARE-UPR3021-CNRS).

4.1.5. Kinetic models and mechanisms of hydrochar formation

A model is a theoretical and mathematical description of what occurs experimentally. This study will analyze the kinetic models that can describe the kinetic reaction of the HTC process

of the biomass. The overall reaction of the biomass in the HTC process is presented in the following reaction:

$$\text{Biomass} + H_2O \rightarrow \text{Hydrochar} + \text{Liquid} + \text{Gas} \quad (4\text{-}3)$$

The mass yield of the solid or hydrochar produced during HTC for time (dα/dt), depends on the rate of reaction constants, which are influenced by temperature [k(T)] and conversion [f(α)], expressed as:

$$\frac{d\alpha}{dt} = k\,(T).\,f(\alpha) \quad (4\text{-}4)$$

where k(T) is the reaction rate constant depending on the temperature, f(α) is the function of α, and α is the conversion or weight loss rate that can be calculated with the following equation:

$$\alpha = \frac{m_{bio} - m_{HC_T}}{m_{bio} - m_{HC_\infty}} \quad (4\text{-}5)$$

where m_{bio} (g), is the initial weight of the sample, m_{HC_T} (g) is the weight of the sample at a given temperature and time, and m_{HC_∞} (g) is the final sample weight. The solid conversion rate (dα/dt) can be expressed as:

$$\frac{d\alpha}{dt} = \beta\frac{d\alpha}{dT} = k\,(T).\,f(\alpha) \quad (4\text{-}6)$$

where β is the heating rate or the rate of temperature change (dT/dt, K/min). The k(T) can be described according to the Arrhenius equation:

$$k\,(T) = A.\,e^{\frac{-E\alpha}{RT}} \quad (4\text{-}7)$$

where A (min^{-1}) refers to the pre-exponential factor, and Eα (J/mol) is the apparent activation energy, T (K) represent the absolute temperature, and R universal gas constant (8.314 J/ (mol·K)), respectively. Substituting Eq. (4-7) into (4-6) gives the following equation:

$$\frac{d\alpha}{dt} = \beta\frac{d\alpha}{dT} = A.\,e^{\frac{-E\alpha}{RT}}.\,f(\alpha) \quad (4\text{-}8)$$

The integral form of f (α) can be obtained after integrating Eq. (4-8) with respect to temperature.

$$g(\alpha) = \int_0^{\alpha} \frac{d\alpha}{f(\alpha)} = \frac{A}{\beta}\int_{T_0}^{T} e^{\frac{-E\alpha}{RT}}\,dT \quad (4\text{-}9)$$

where g(α) is the integrated reaction model, and some common forms of f (α) and g (α) for solid-state reactions are described in **Table 4-1**.

Table 4-1: Expressions for functions f(α) and g(α) of some reaction models to describe thermal decomposition solid state reactions (*Jayaraman et al., 2017*; *Mishra et al., 2015*; *Papari and Hawboldt, 2015*; *Yao et al., 2020*).

Symbols	Reaction models	Differential form f(α)	Integral form g(α)
		Reaction order models	
R1	First order	$1-\alpha$	$-\ln(1-\alpha)$
R2	Second order	$(1-\alpha)^2$	$(1-\alpha)^{-1}-1$
R3	Third order	$(1-\alpha)^3$	$[(1-\alpha)^{-2}-1]/2$
R4	One and half order	$(1-\alpha)^{3/2}$	$\left[(1-\alpha)^{-1/2}-1\right]$
		Diffusion models	
D1	1D diffusion	$1/2\alpha$	α^2
D2	2D diffusion-Valensi	$[-\ln(1-\alpha)]^{-1}$	$(1-\alpha)\ln(1-\alpha)+\alpha$
D3	3D diffusion-Jander	$(1-\alpha)^{3/2}/\left[1-(1-\alpha)^{1/3}\right]$	$\left[1-(1-\alpha)^{1/3}\right]^2$
D4	3D diffusion-Ginstling	$(3/2)/\left[(1-\alpha)^{-1/3}-1\right]$	$1-2\alpha/3-(1-\alpha)^{2/3}$
		Power law nucleation Models	
P1	Power law (1)	$(2/3)\alpha^{-1/2}$	$\alpha^{3/2}$
P2	Power law (2)	$2\alpha^{1/2}$	$\alpha^{1/2}$
P3	Power law (3)	$3\alpha^{2/3}$	$\alpha^{1/3}$
P4	Power law (4)	$4\alpha^{3/4}$	$\alpha^{1/4}$
		Random nucleation and subsequent growth Models	
A1	Avrami-Erofeev (1)	$(3/2)(1-\alpha)[-\ln(1-\alpha)]^{1/3}$	$[-\ln(1-\alpha)]^{2/3}$
A2	Avrami-Erofeev (2)	$2(1-\alpha)[-\ln(1-\alpha)]^{1/2}$	$[-\ln(1-\alpha)]^{1/2}$
A3	Avrami-Erofeev (3)	$3(1-\alpha)[-\ln(1-\alpha)]^{2/3}$	$[-\ln(1-\alpha)]^{1/3}$
A4	Avrami-Erofeev (4)	$4(1-\alpha)[-\ln(1-\alpha)]^{3/4}$	$[-\ln(1-\alpha)]^{1/4}$
A5	Random nucleation (1)	$(1-\alpha)^2$	$1/(1-\alpha)$
A6	Random nucleation (2)	$(1-\alpha)^3/2$	$1/(1-\alpha)^2$
		Geometrical contraction models	
F1	Contracting area	$2(1-\alpha)^{1/3}$	$1-(1-\alpha)^{1/2}$
F2	Contracting volume	$3(1-\alpha)^{2/3}$	$1-(1-\alpha)^{1/3}$

The kinetics of thermal reactions in solids has been widely studied in the literature (Jayaraman et al., 2017; Mishra et al., 2015; Papari and Hawboldt, 2015; Yao et al., 2020). There are two main methods to determine the kinetic parameters, the model-free methods, and the model-fitting method.

4.1.5.1. *Model-free methods*

The model-free method has been used in the pyrolysis, gasification, and combustion kinetic model and allows the kinetic parameters to be calculated as a function of the degree of conversion. Different methods have been used, such as the differential method proposed by Friedman and the integral methods, such as the FWO method and KAS method (Coats and Redfern, 1964b; Flynn and Wall, 1966; Friedman, 1964).

Friedman method: The Friedman method is the most common differential isoconversion method for determining activation energy as a function of conversion α, and it is given in the following equation:

$$\ln\left(\frac{d\alpha}{dt}\right) = \ln\left(\beta\frac{d\alpha}{dt}\right) = \ln[A_\alpha\, f(\alpha)] - \frac{E\alpha}{RT} \qquad (4\text{-}10)$$

Ea can be obtained from the slope of the fit line drawn between $\ln\left(\beta\frac{d\alpha}{dt}\right)$ versus $\frac{1}{T}$.

FWO method: This method is derived from the integral isoconversional method. The method uses the linear Doyle's approximation for the estimation of temperature integral (Doyle, 1961). All the integral isoconversional methods are based on different mathematical assumptions of p(x). Considering the approximation ln p(x)= -5.331-1.052x, the **Eq.(4-15)** can be converted into:

$$\ln\beta = \ln\frac{AE\alpha}{Rg(\alpha)} - 5.331 - 1.052\frac{E\alpha}{RT} \qquad (4\text{-}11)$$

Plots of ln β vs. 1/T, at fixed value of conversion help in evaluating the activation energy from the slope of straight-line plot.

KAS method: The KAS method is based on the Coats–Redfern approximation $p(x) = x^{-2}e^{-x}$ ($20 \leqslant x \leqslant 50$) and **Eq (4-18)** can be converted into

$$\ln\frac{\beta}{T^2} = \ln\frac{AR}{E\alpha\, g(\alpha)} - \frac{E\alpha}{RT} \qquad (4\text{-}12)$$

For a constant value of α, the activation energy Eα can be obtained from the plot of $\ln\frac{\beta}{T^2}$ against $\frac{1}{T}$ with − Eα/R as the slope.

Several solid-state kinetic models have been discussed in the literature, and many different reaction mechanisms have been proposed to describe solid-state reactions, some of which are listed in **Table 4-1**. The models can be expressed in a differential form f(α) and an integral form g(α). The most used reaction mechanisms are described below.

4.1.5.2. *Model-fitting methods*

Model-fitting methods are commonly applied because the kinetic parameters can be determined and provide information about possible reaction mechanism models. The Coats-Redfern method, the most popular form of model-fitting, proposed in 1964 (Coats and Redfern, 1964b), uses Taylor's series approach by limiting the number of terms in the series. The Taylor series expansion form can be given as:

$$g(\alpha) = \int_0^{\alpha} \frac{d\alpha}{f(\alpha)} = \frac{A}{\beta}\int_{T_0}^{T} e^{\frac{-E\alpha}{RT}} dT = \frac{AE\alpha}{\beta R}\int_x^{\infty} \frac{e^{-x}}{x^2} dx \quad (4\text{-}13)$$

$$g(\alpha) = \frac{AE\alpha}{\beta R}\int_x^{\infty} \frac{e^{-x}}{x^2} dx \cong \frac{AE\alpha}{\beta R}\left[\frac{e^{-x}}{x^2}\left(1 - \frac{2!}{x} + \frac{3!}{x^2} - \frac{4!}{x^3} + \cdots\right)\right] \quad (4\text{-}14)$$

$$\frac{AE\alpha}{\beta R}\left[\frac{e^{-x}}{x^2}\left(1 - \frac{2!}{x} + \frac{3!}{x^2} - \frac{4!}{x^3} + \cdots\right)\right] = \frac{AE\alpha}{\beta R}p(x) \quad (4\text{-}15)$$

where x is equal to $\frac{E\alpha}{RT}$, the p(x) is the temperature integral and it has no analytical solution. Therefore, **Eq.(4-15)** can only be solved using either numerical integration or approximation to deal with the complex integral. By introducing an approximation $p(x)=x^{-2}e^{-x}$ $(20 \leqslant x \leqslant 50)$ into **Eq. (4-14)**, the relationship between heating rate and inverse temperature becomes:

$$g(\alpha) = \frac{ART^2}{\beta E\alpha}\left(1 - \frac{2RT}{E\alpha}\right)e^{\frac{-E\alpha}{RT}} \quad (4\text{-}16)$$

Taking the natural logarithm of both sides of **Eq.(4-16)**.

$$\ln\frac{g(\alpha)}{T^2} = \ln\frac{AR}{\beta E\alpha}\left(1 - \frac{2RT}{E\alpha}\right) - \frac{E\alpha}{RT} \quad (4\text{-}17)$$

Since 2RT/Ea << 1, the equation can be converted into

$$\ln\frac{g(\alpha)}{T^2} = \ln\frac{AR}{\beta E\alpha} - \frac{E\alpha}{RT} \quad (4\text{-}18)$$

For a fixed β and proposed reaction mechanism g(α), plotting $\ln\frac{g(\alpha)}{T^2}$ versus $\frac{1}{T}$ gives a straight line. The equations corresponding to g(α) are presented in **Table 4-1**. The slope −Eα/R and intercept $\ln\frac{AR}{\beta E_\alpha}$ can be used to determine Eα and A, respectively (Yao et al., 2020).

4.1.5.3. *Kinetic reaction mechanism models*

All kinetic reaction mechanism models used in this study are presented in **Table 4-1**. Most solids contain different defects, weak points that can initiate physical and chemical changes during their reaction. These defects play an essential role when nucleation is the limiting step in a reaction (Qiu et al., 2016). If the reaction involves random nucleation followed by the growth of nuclei of a defined dimensionality, the Avrami-Erofeev equation can be derived and applied; in some cases, the nucleation rate follows the power law (Avrami, 1939; Avrami, 1940; Khawam and Flanagan, 2006; Yao et al., 2020). In other cases, the solid-state reactions, are controlled by diffusion of the reagents or products. This situation is not common because the mass transfer in the solid-state is slower (Brown et al., 1980; Khawam and Flanagan, 2006); however, in HTC processes, where one of the most important reactions is hydrolysis(Kambo and Dutta, 2015; Volpe et al., 2018), which modifies the biomass structure, the diffusion of water into the pores of the biomass particles can control the reaction mechanisms. This phenomenon was explained by Reza et al. (2014b). Some solid-state reactions involve two or more substances, where phase boundaries are formed between the reagents and the products. In this case, the advance in the phase boundary thus formed determines that reaction rate (Qiu et al., 2016). When the advancement of the phase boundary is one-dimensional, a reaction of zero-order is obtained; the two-dimensional equation of the phase boundary (contracting area) and the three-dimensional equation of the phase (contracting volume) (Galwey and Brown, 1999) these models are based on the assumption of spherical solid particles. Finally, the kinetics of the solid-state reaction can be controlled by the order of the reaction. These models are the simplest as they are similar to those used in homogenous kinetics (Khawam, 2007). Often, first and second-order reactions are used. Higher-order reactions are rarely used and difficult to interpret in solid-state reactions (Qiu et al., 2016).

4.1.6. Methods of HTC liquid quantification

4.1.6.1. *Total organic carbon content (TOC)*

The liquid products were filtered through using Whatman filter paper a with a pore size of 11 microns with Whatman filter paper and then diluted 30 times with ultrapure water. TOC was measured by using a Vario TOC cube analyzer, (model TOC ANALYZER Elementar, Germany). The amount of CO2 produced by the total oxidation of organic carbon atoms by an infrared detector is measured with a signal proportional to the amount of carbon. The protocol used to determine TOC is described below:

-The furnace temperature should be set at 850 °C and the O2 flow rate at ~1 bar.

-The HTC liquid sample is first diluted 40-50 times.

-A quantity of diluted sample (>10 ml) is transferred to a beaker. A mini-stirrer is placed in the cup to homogenize the solution.

-Two transparent tubes are separately inserted into the beaker to (i) take the sample and (ii) bubble the solution to remove volatile carbons and carbonates.

-Perform the analyses with an injection volume of 0.2 mL to evaluate repeatability.

Calibration was done using a solution of glucose as a standard. The calibration curve is shown in **Figure 4-7**.

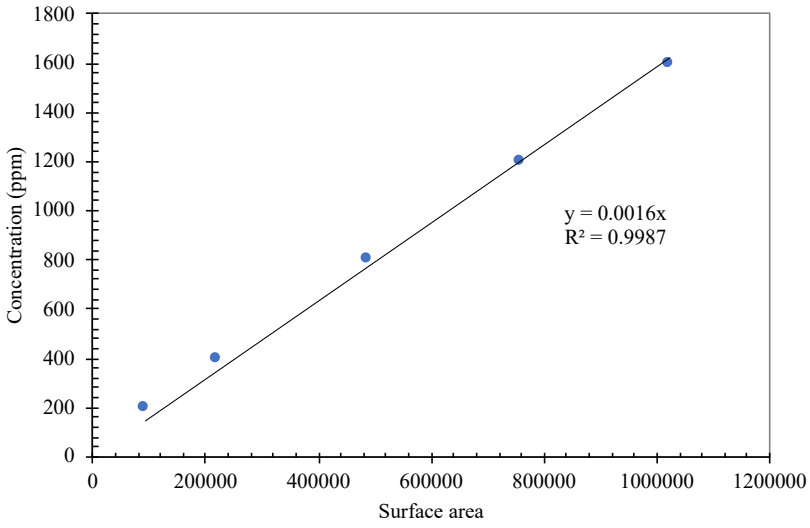

Figure 4-7: Calibration line for the determination of TOC

4.1.6.2. *High-performance liquid chromatography*

High-performance liquid chromatography (HPLC) is an advanced form of liquid chromatography used in separating complex mixtures of molecules encountered in chemical and biological systems. The specificity of the HPLC method is excellent, and sufficient precision is also simultaneously attainable. The HPLC method is excellent, and adequate accuracy is also simultaneously achievable. In liquid chromatography, the choice of detection approach is critical to guarantee that all the components are detected. The most widely applied detectors are: UV detector, which is capable of monitoring several wavelengths concurrently; photodiode array (PDA) detector; variable wavelength detector (VWD) is used when a sample must be injected numerous times, with changing wavelength, to be sure that all the peaks are detected (Yaneva and Georgieva, 2018). The HPLC is a form of column chromatography that pumps a sample mixture or analyte in a solvent (known as the mobile phase) at high pressure through a column with chromatographic packing material (stationary phase). A mobile phase pushes the liquid sample into the stationary phase. A high-pressure pump ensures the flow of eluent. At the exit of the column, the (UV) detector allows the detection of the compounds. UV detectors are based on the measurement of the wavelength of the compounds (Bélanger et al., 1997). **Figure 4-8** shows the general principle of HPLC.

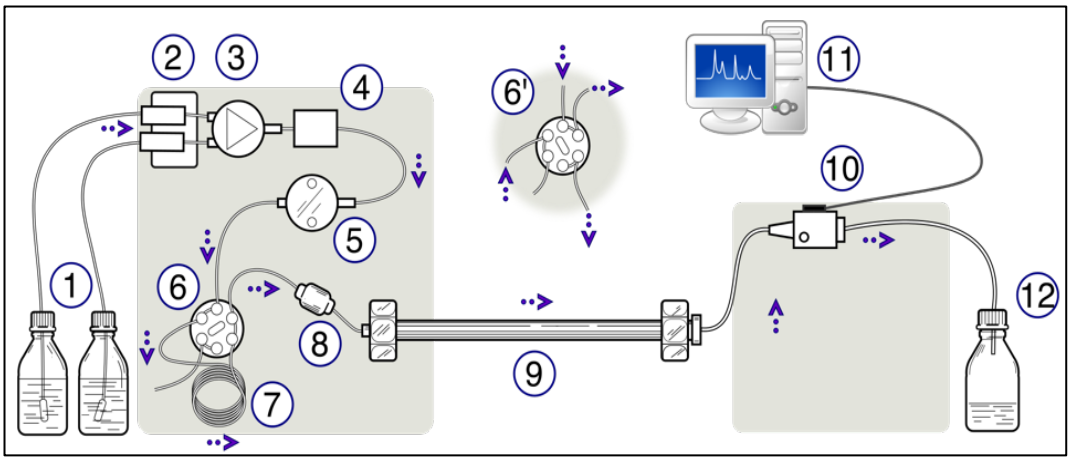

Figure 4-8: Schematic representation of an HPLC unit.

(1) Solvent reservoirs, (2) Solvent degasser, (3) Gradient valve, (4) Mixing vessel for delivery of the mobile phase, (5) High-pressure pump, (6) Switching valve in "inject position", (6') Switching valve in "load position", (7) Sample injection loop, (8) Pre-column (guard column), (9) Analytical column, (10) Detector (i.e., IR, UV), (11) Data acquisition, (12) Waste or fraction collector.

4.1.6.2.1. *Determination of organic acids (formic, lactic, acetic) using HPLC*

The HPLC system includes the following elements for the analysis of organic acids

-Pump: Prostar (VARIAN);

-Injector: SpectraSYSTEM AS3000;

-Column: LiChrospher® RP-18 (5µm);

-Integrator: Star 800 (VARIAN);

-Detector: UV SPD-6A Shimadzu.

The HTC liquid samples were diluted (20-40 times) and filtered with a PTFE membrane syringe - 0.2 µm before each analysis. Lactic acid, acetic acid, and formic acid were detected and analyzed on a Varian HPLC system equipped with a column LiChrospher® RP-18 (5µm) and a UV detector UV SPD-6A Shimadzu (λ= 210 nm) at 35 °C. The aqueous buffer solution of H_3PO_4/NaH_2PO_4 (0.1 M NaH_2PO_4 acidified by H_3PO_4 to pH = 2.6) was employed as the eluent and the flow rate was 0.6 mL/min. To calibrate the HPLC, standard solutions were prepared from formic acid (SIGMA-ALDRICH, 95%), lactic acid (VWR Chemicals, 90%), and acetic acid (ELVETEC SERVICE, 95-100%). Solutions were prepared by diluting the standard solution with distilled water. **Figure** shows the calibration curves of the organic acids analyzed.

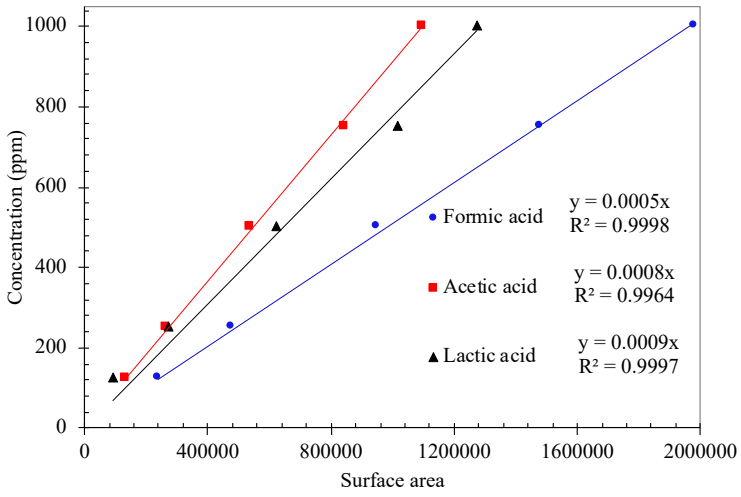

Figure: Calibration lines for formic acid (retention time = ~4.3 min), lactic acid (retention time = 6.2 min), and acetic acid (retention time = ~6.8 min)

4.1.6.2.2. *Determination of furfural and 5-hydroxymethylfurfuralusing HPLC*

The HPLC system includes the following components to analyze furfural and 5-HMF:

-Pump: SpectraSYSTEM P4000;

-Injector: Autosampler MODEL 400 (VARIAN);

-Column: LiChrospher® RP-18 (5µm);

-Integrator: C-R5A (SHIMADZU);

-Detector: UV SpectraSYSTEM UV2000.

The HTC liquid samples were diluted (50-100 times) and filtered with a PTFE membrane syringe - 0.2 µm before each analysis. For furfural and 5-HMF, the analysis is carried out in a Varian HPLC system equipped with a column LiChrospher® RP-18 (5µm) and a UV detector (λ= 275nm) at 30 ºC. The eluent used is a mixture of ultrapure water acidified (1% formic acid) and methanol in two steps: (1) acidified water: methanol = 90:10 (v/v) for 8 minutes, (2) acidified water: methanol = 70:30 (v/v) for 22 minutes. For all the compounds, external calibration was performed in the HPLC system for quantification.

The standard solutions were prepared from furfural (SIGMA-ALDRICH, 99%) and 5-(hydroxy-methyl)-furfural (SIGMA-ALDRICH, 99%). The solutions were prepared by diluting the standard solution with distilled water. **Figure 4-9** shows the calibration curves for furfural and 5-HMF.

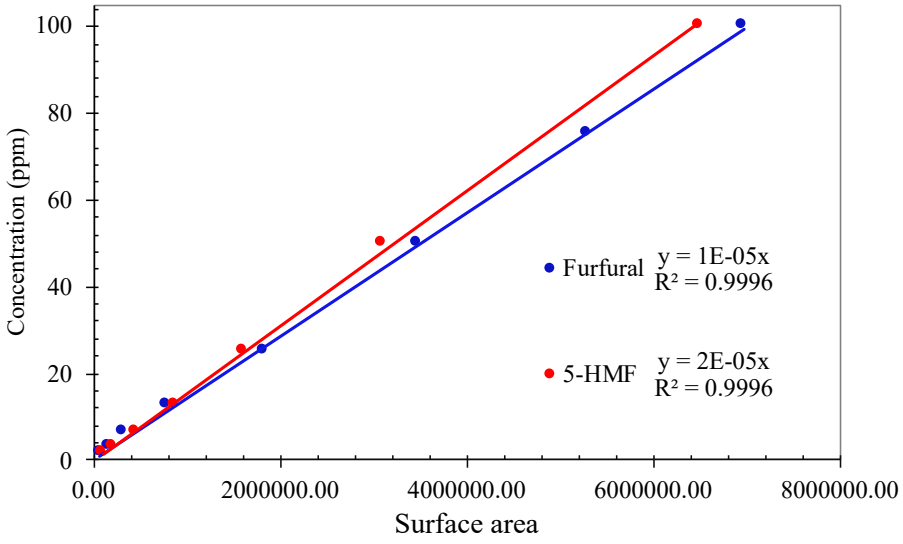

Figure 4-9: Calibration lines for furfural (retention time = ~17 min), and 5-HMF (retention time = 9.5 min), and acetic acid (retention time = ~6.8 min)

4.1.6.3. *Ultraviolet–visible spectroscopy*

UV-VIS spectrophotometry has been widely used for the identification and quantification of organic compounds. UV VIS spectroscopy is a type of absorption spectroscopy in which the molecule absorbs UV-visible light. Absorption of the UV-visible radiations results in the excitation of the electrons from lower to higher energy levels. Only some functional groups (chromophores) can absorb UV and visible radiation in the organic molecules, which have low energy valence electrons (Pentassuglia et al., 2018).

Generally, UV–vis spectroscopy is used to determine elemental concentrations quantitatively in a solution according to Beer-Lambert law:

$$A = \log_{10}\left(\frac{I_0}{I}\right) = \varepsilon \cdot c \cdot L \qquad (4\text{-}19)$$

where A is the measured absorbance, I_0 is the intensity of the incident light at a given wavelength, I is the transmitted intensity, L is the path length through the sample, c is the concentration of the absorbing species, and ε is a constant known as the molar absorptivity or extinction coefficient for each species and wavelength. Commonly, ε at the wavelength of maximum absorption (λmax) is employed in quantitative analysis as errors resulting from instrumental wavelength uncertainty are minimized at the peak of the absorbance curve. According to this relationship, the concentration of the analyte can be calculated when ε is known, L is fixed, and I_0 and I are measured. When a calibration curve of the analyte is available, the concentration of the analyte can be determined more accurately (Wang and Chu, 2013).

4.1.6.3.1. *Determination of total polyphenolics*

The phenolics of test and standard solutions were measured spectrophotometrically according to the the Folin-Ciocalteu (F-C) method, following the protocol explained by Bastola et al. (2017). In brief, 0.1 mL of sample/standard solution was mixed well with 5 mL of reagent A (1:10 v/v of F-C reagent and deionized water) and 3.5 mL of reagent B (11.5 %, w/v aqueous sodium carbonate) in a test tube, and incubated for 1 hour at 40˚C in a water bath. The absorption spectra of the blue-colored solution generated in the process were measured from 760 nm using Carry 60 UV-VIS. Calibration was done using a solution of gallic acid as a standard. The calibration curve is shown in **Figure 4-10**.

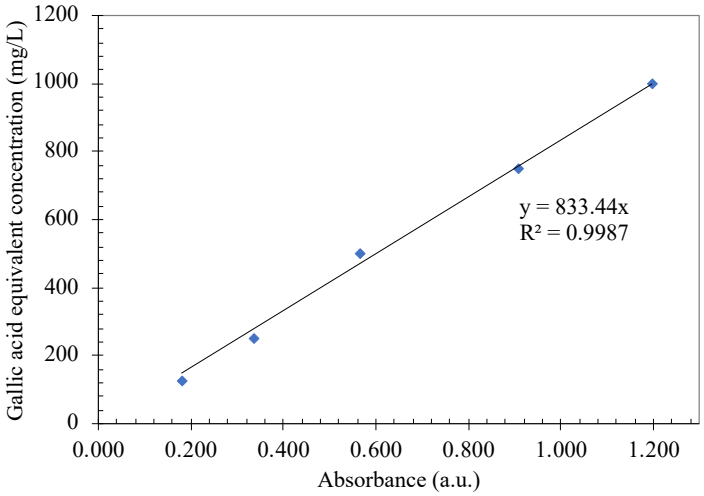

Figure 4-10: Calibration line for the determination of total phenolic compounds by the Folin-Cioacalteu method

4.1.6.4. *Determination of total sugars using UV-VIS*

Determination of the concentration of total sugars in the HTC liquid was performed with the Anthrone method, following the protocol explained by Le and Stuckey (2016), and Laurentin and Edwards (2003). The analysis is based on measuring the absorbance of a complex of sugars (pentose and hexoses) formed by hydrolysis of the biomass. A sample of 0.2 mL (0.2 g/L prepared in 96% sulfuric acid) is applied to a micropipette to 1 mL of Anthrone solution (HTC liquid). The mixture is heated to 80 °C for 30 min. The color developed during heating is measured by absorption with a spectrophotometer (Cary 60 UV-VIS) in single reading at 625 nm. Calibration was done using a solution of glucose as a standard. The calibration curve is shown in **Figure 4-11**.

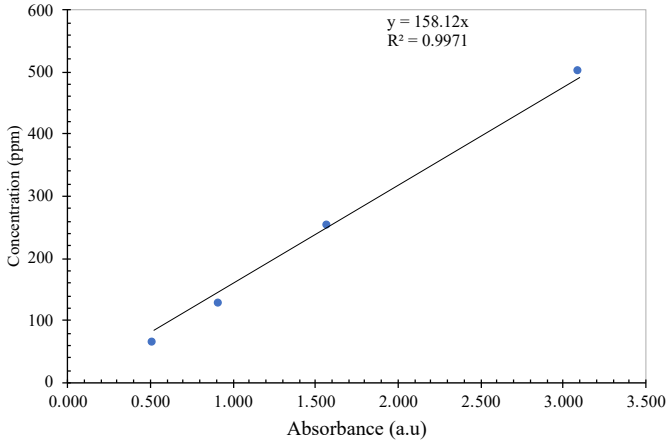

Figure 4-11: Calibration line for the determination of total sugars compounds by Anthrone method

4.1.7. Methods of HTC gases quantification

4.1.7.1. *HTC gas recovery*

For each experiment, after the reactor reaches the setpoint temperature and holding time, it was immediately cooled down. Once the reactor cooled down, a gas bag was used to recover the incondensable gas produced during the HTC process. The protocol for gas recovery is explained below.

-The gas pressure is noted after the reactor is cooled down.

- A small amount of gas is allowed to pass through to avoid clogging the gas outlet with solid particles.

-Connect the gas bag to the gas outlet.

-Gently open the gas outlet valve to fill the gas bag (**Figure 4-12**)

-The gas bag will be used to analyze the HTC gases recovered by the micro-GC.

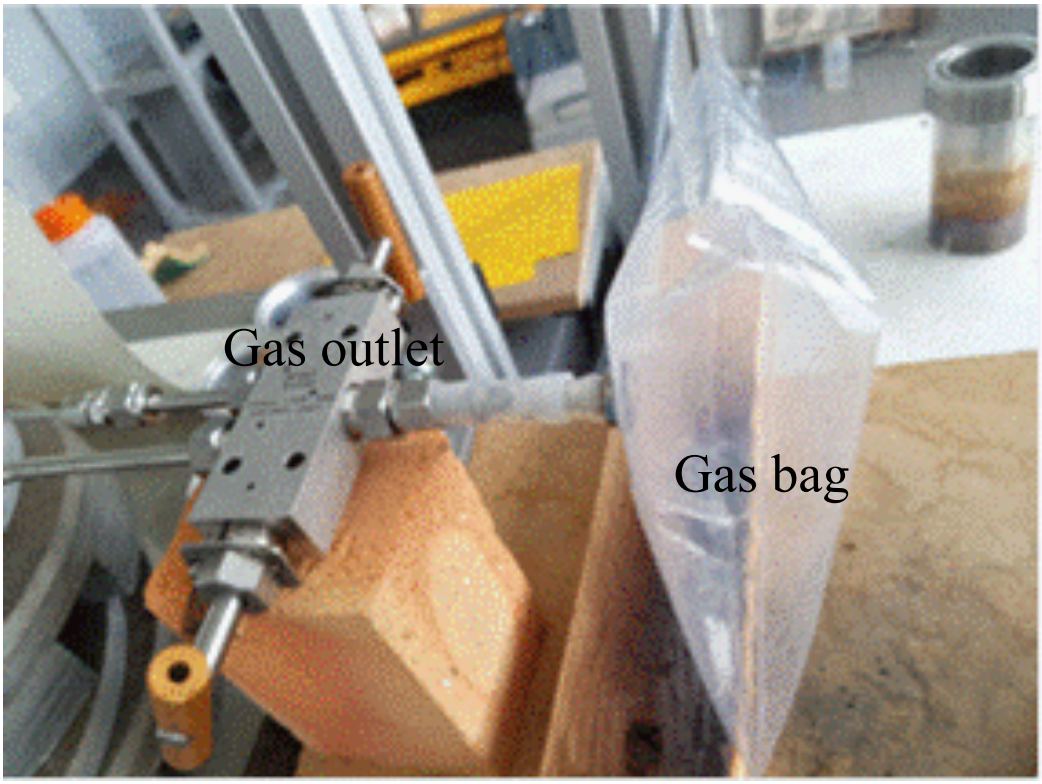

Figure 4-12: Gas bag to recover HTC gas

4.1.7.2. *Gas chromatography (GC)*

The gas composition of the HTC of the different biomasses is determined by gas chromatography (GC). The chromatography technique makes it possible to separate, identify and quantify the species present in the analyzed gas. It allows the analysis of gas mixtures or compounds that can volatilize without decomposition (boiling temperature < 250°C) according to their volatility and affinity with the carrier gas and the stationary phase. The gas sample is injected into a column that allows species to be separated according to their diffusion rate based on their molecular weight. At the column outlet, the gases successively reach a thermal conductivity detector (TCD) which measures the difference in thermal conductivity between the carrier gas and the gas under analysis and emits an electrical signal that allows a chromatogram be plotted.

For this part, micro gas chromatography (μ-GC) has been used to analyze qualitatively and quantitatively the gas components from HTC process. In this study, the gas product from different biomasses were analyzed using a triple channel micro-GC (SOLIA SRA instrument) with thermal conductivity detectors (TCD). Channel A with molecular sieve 5A column (MS-5A) was set at 100°C for determination of H_2, O_2, N_2, CO, and CH_4. Channel B with VAR PPU (PPU) was set at 75 °C for the determination of CO_2, H_2S and light hydrocarbons. Channel C with VAR Stabilwax was set at 90 °C for checking of Benzene, Toluene, Xylene, Acetone, and Methanol. The column pressure was 28 psi, carrier gas inlets were Argon and Helium. To calibrate the μ-GC, a cylinder of standard gas mixture (containing CO_2: 30 % (v/v), CH_4: 20 % (v/v), CO: 10 % (v/v), H_2: 25 % (v/v), and N2: 10 % (v/v)) was used, and the calibration was checked regularly. For O_2, the calibration was conducted using a cylinder of O_2 with 99.99% purity, mixing with argon to obtain different concentrations. Each gas sample was repeated in triplicate giving a maximum standard deviation of 2.3%. For the analysis, the gasbags were cleaned by argon purge and vacuumed before each gas sampling trial.

The protocol for analyzing gases by μ-GC stored in the gas bag is as follows:

-Connect the valve (**Figure 4-13**) followed by a flow meter (ProFLOW 6000, RESTEK®)

-Connect the HTC gas bag to the inlet of the μ-GC.

-Open valve at the outlet of the μ-GC and turn on the flowmeter.

-Open the bag.

-Gently squeeze the bag allowing a flow rate between 20 and 30 ml/min to pass through for 30s. --Close the valve.

-Perform the analyses with the Soprane software.

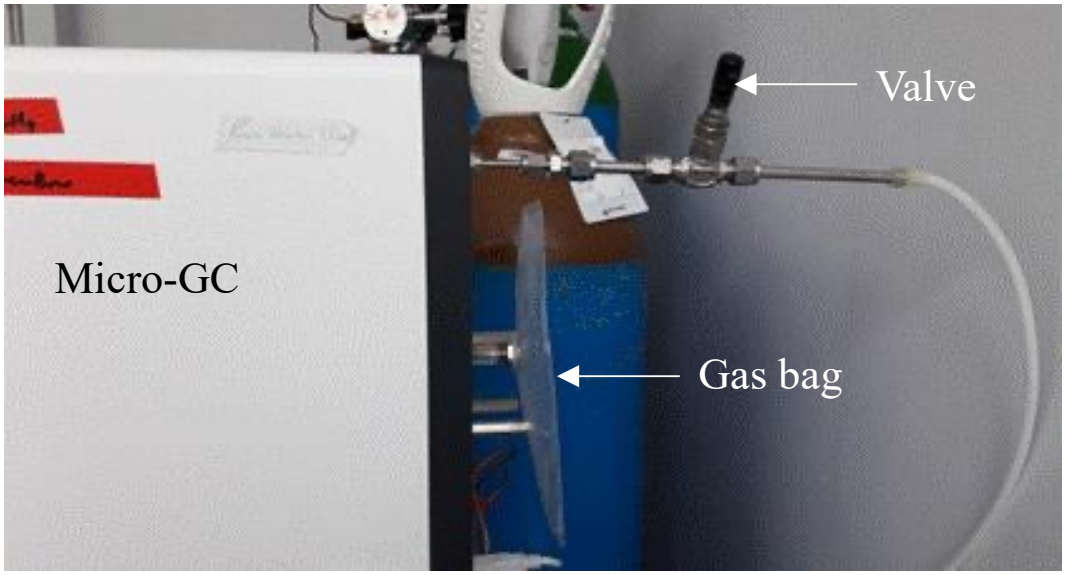

Figure 4-13: HTC gas analysis system in micro-GC
the outlet of the µ-GC.

4.1.7.3. *Quantification of non-condensable gases produced during HTC*

The mole number of the HTC gases produced (n_g) can be calculated with the perfect gas law:

$$n_g = \frac{P_{exp} \cdot V_{expHTC}}{R \cdot T_{exp}} \quad (4\text{-}20)$$

where Pexp is the experimental pressure of the reactor at room temperature (Pa), V_{expHTC} is the Volume of gas occupied inside the HTC reactor (m3), R is the constant of perfect gases (8.31 J/K·mol), and T_{exp} is the temperature of the cooled reactor (K), at which the pressure was noted. The mass of each HTC gas produced (m_{gi}) can be calculated with the following equations:

$$m_{gi} = n_{gi} \cdot M_{gi} \quad (4\text{-}21)$$

where M_{gi} is the molar mass of each gas produced (g/mol)

The total mass of gases produced (m_{Tg}) is calculated from the following equation:

$$m_{Tg} = \sum_{n=1}^{n} m_{gi} \quad (4\text{-}22)$$

4.1.7.4. *Heat of HTC reaction measurements*

The energy supplied to the external wall of the reactor during the distilled water heating is the sum of the energy used to heat the reactor, the room-temperature water to a final temperature and the energy lost in this heating over time (mostly at the reactor head), and is presented in the following equation:

$$\mathrm{E_{s1}} = \mathrm{E_{R1}} + \mathrm{E_{W1}} - \mathrm{E_{L1}} \quad (4\text{-}23)$$

Where E_{S1} (kJ) is the power or energy supplied to the reactor, E_{R1} (kJ) energy used to heat the reactor, E_{W1} (kJ) energy used to heat the distilled water, and E_{L1} (kJ) the energy lost. The same procedure is used for heating different biomass-to-water ratios.

$$\mathrm{E_{S2}} = \mathrm{E_{R2}} + \mathrm{E_{w2}} + \mathrm{E_{bi}} - \mathrm{E_{L2}} \quad (4\text{-}24)$$

Where E_{S2} (kJ) is the power or energy supplied to the reactor, E_{bi} (kJ) is the energy used heating biomass. If the decomposition of biomass produces or consumes energy, **Eq. (4-24)** is expressed as follows:

$$\mathrm{E_{S2}} = \mathrm{E_{R2}} + \mathrm{E_{w2}} + \mathrm{E_{bi}} - \mathrm{E_{L2}} \pm \mathrm{E_P} \quad (4\text{-}25)$$

Where E_P (kJ) is the energy produced or consumed during chemical reactions. As we are using an open-loop Controller System, the power consumption during HTC testing is already known. In this case, the power applied in each of the experiments is equal (120W), also, in all experiments, the same type of insulation was used, therefore, the same heat loss was assumed.

$$\mathrm{E_{S1}} = \mathrm{E_{S2}} \text{ and } \mathrm{E_{L1}} = \mathrm{E_{L2}} \quad (4\text{-}26)$$

If equating **Eq. (4-25)** in **Eq. (4-23),** the following equation is obtained:

$$\pm \mathrm{E_P} = \mathrm{E_{W1}} - (\mathrm{E_{W2}} + \mathrm{E_{bi}}) + (\mathrm{E_{R1}} - \mathrm{E_{R2}}) \quad (4\text{-}27)$$

The theoretical energy used for heating water and different biomass-to-water ratios can be determined in the following equation:

$$E_i = m_i C_{pi} \Delta T \quad (4\text{-}28)$$

Where Cp_i (kJ/kg.K) is the specific heat capacity, m_i (kg) is the total mass used, ΔT (K) is the temperature difference, Ei (kJ) is the energy used for heating.

In particular, when applying **Eq. (4-28),** the Cp_i and m_i values are specific to the considered mixture. Dividing the energy produced by the reaction into the initial amount of dry feedstock (M_{feed}), it is possible to calculate the heat of reaction.

$$\Delta H_r = \frac{E_P}{M_{feed}} \quad (4\text{-}29)$$

Where ΔH_r is the heat of reaction (kJ/kg)

4.2. Results and Discussion

4.2.1. Reactor Control System

A control system is defined as a system of devices that manages, commands direct, or regulates the behavior of other devices or systems to achieve the desired result. A control device does this by means of control loops, a mechanism configured to sustain a variable process at the desired set point. There are several types of control systems, but all of them are created to control outputs. The system used to control velocity, acceleration, temperature, pressure, voltage, and so on are examples of control systems. To clarify the concept, an example of the simple room temperature controller. Suppose a simple heating element is heated up as long as the electric power supply is switched on. While the heating switch is on, the room temperature rises and, once the desired room temperature is reached, the power is switched off. After that, the room temperature drops through the effect of the ambient temperature, and then the heating element is manually switched on to reach the desired room temperature again. In this way, the room temperature can be manually controlled to the desired level. This is an example of a manual control system. The system can be further enhanced by a timer, in which the supply of the heating element is switched on and off to reach the desired temperature level in the rooms at a predetermined interval. The room temperature can be regulated by another improved method. In this case, the actual and desired temperature is determined by a sensor. When

differences are observed, the heating system works to reduce the disparity, and the heating elements avoid working when the difference is less than a predetermined amount.

Both forms of the system are automatic control systems. In the first, the system input is independent of the system output. As long as the control switch is on, room temperature (output) increases. In other words, the heating element produces heat while the power supply remains on and the final room temperature has no control over the system's input power supply. This system is called an **open-loop control system**.

In the above case, the system's heating elements depend upon the difference between the actual and desired temperature. The difference between these two temperatures is called the system error.

4.2.1.1. *Open-loop Control System*

An open-loop control system is a control system in which the system's output does not influence the control actions **Figure 4-14**. A sequence of control actions is precalculated and stored in a feedforward controller in an open-loop control system and then executed when a trigger is activated. After the control action is initiated, it cannot be adjusted based on the system's response or external loads acting on it (Mehrabi and McPhee, 2019). The manual control system is also an open-loop control system.

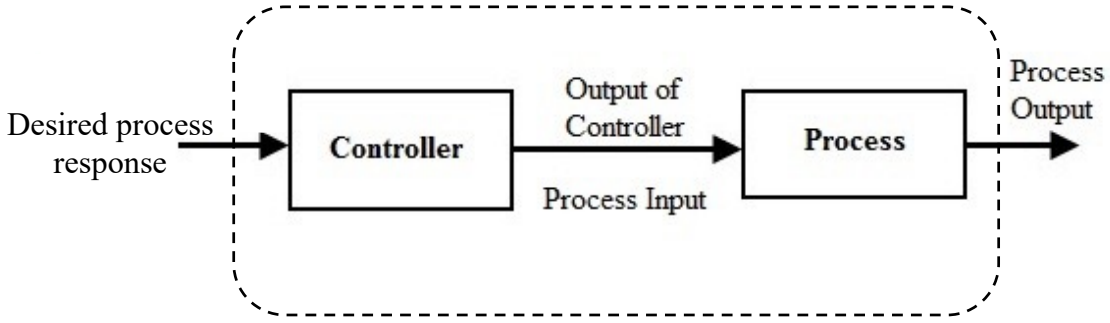

Figure 4-14: Schematic representation of the open-loop control system

Some of the advantages and disadvantages are as follows:

Advantages of open-loop control systems include:

- Simple in construction and design.
- Economical.
- Easy to maintain.

- Generally stable.
- Convenient to use as output is difficult to measure.

Disadvantages of open-loop control systems include:

- They are inaccurate.
- They are unreliable.
- Any change in output cannot be corrected automatically.
- These systems need a good calibration before use.

4.2.1.2. *Closed-loop control system*

The closed-loop control system can be defined as the output of the system depending on the input of the system. This control system has one or more feedback loops between its input and output. This system provides the required output by evaluating its input. This type of system produces the error signal and is the main disparity between the output and input of the system.

An open-loop control system can be converted into a closed-loop control system by giving feedback. This feedback automatically makes suitable changes in the output due to external interference. In this way, a closed-loop control system is called an automatic control system. **Figure 4-15** shows the block diagram of the closed-loop control system in which feedback is taken from the output and fed into the input.

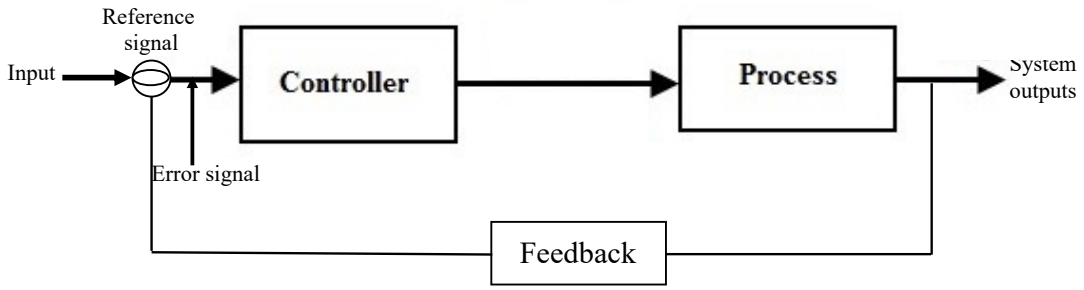

Figure 4-15: Schematic representation of the closed-loop control system

The main advantages of the closed-loop control system are:

- More accurate even in the presence of non-linearity.
- Highly accurate as any error arising is corrected due to the presence of a feedback signal.
- Facilitates automation.

- The sensitivity of the system may be made small to make the system more stable.
- This system is less affected by noise.

Disadvantages of closed-loop control systems include

- They are costlier.
- They are complicated to design.
- Required more maintenance.
- Feedback leads to an oscillatory response.
- Stability is the major problem and more care is needed to design a stable closed loop system.

This part of the overview of the difference between the open-loop control system and the closed-loop control system is explained. These are two types of control systems more using. The open-loop system depends mainly on the input, and its construction is simple, while the closed-loop system is challenging to design, and the output of this system depends mainly on the input. The accuracy of this open-loop system depends mainly on calibration, and its calibration is difficult. In contrast, the closed-loop system is accurate due to feedback; it does not require many calibrations.

4.2.1.3. *Calibration of reactor operating in an open-loop system*

One of the disadvantages of a reactor working in an open-loop system is its calibration. In this case, for a hydrothermal carbonization reactor, the input signal is the energy provided to the reactor. It is necessary to know what power must be supplied to the reactor to reach a setpoint temperature. The hydrothermal carbonization process usually works between 180 and 250 °C; therefore, it is necessary to know the range of power supplied to the reactor to reach these temperatures.

The calibration was done using 200 mL of distilled water inside the reactor; this volume corresponds to the volume used in each experiment. In addition, two thermocouples were used to measure the temperature at the bottom of the reactor (liquid phase) and the temperature at the top of the reactor (gas phase). **Figure 4-16** shows the evolution of the temperature inside the reactor at different powers. The LabVIEW SignalExpress software was used to record the two temperatures. The reactor was heated using different power ratings from 120 to 200 W.

For an open-loop system, the constant temperature during HTC is far from reality in batch autoclave reactors, where there is heating up time, a constant temperature period (holding time), and finally, cooling downtime. The heating-up time can be neglected if the heating is speedy (closed-loop control system), which could be when HTC is performed in batch microreactors. An open-loop system is used in this work, where the power supplied to the furnace is controlled. For them, it is important to know the different heating times and the power to reach these times. On the other hand, it is required to determine the characteristic parameters of a controlled signal.

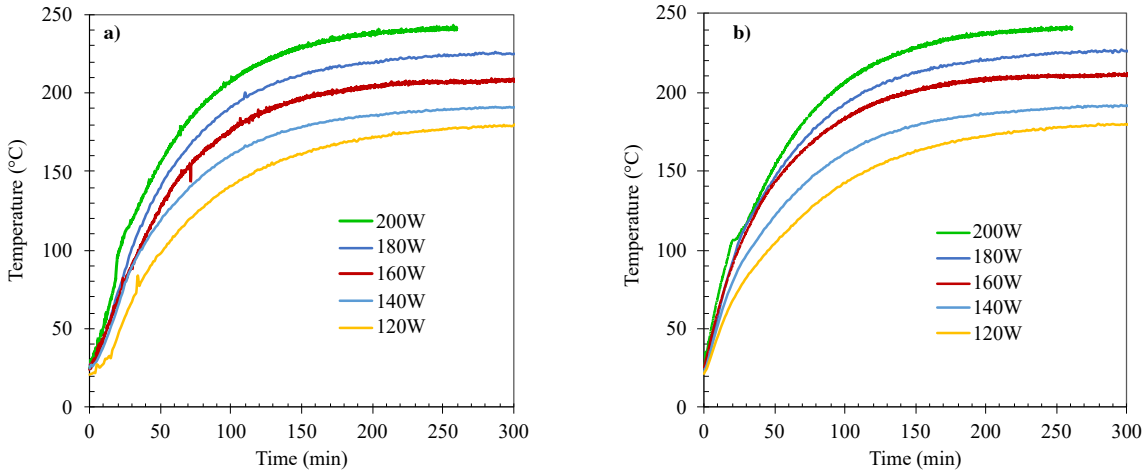

Figure 4-16: The temperature profiles inside the reactor (a): Top, (b): Bottom at power supplied in the reactor from room temperature to equilibrium temperature.

Typical parameters of a controlled signal are the process dead time (τ): which is the delay from when an output signal is issued from the controller until the measured process variable starts to respond. In this case, a variation of 5°C has been considered to calculate the dead time. The time constant (θ): is the time taken to reach 63% of the total variation. The response time (te): is the time required for the process output to reach and remain within a band whose width is equal to ±5% of the total variation. In this case, it is the time required for the temperature variation to reach 95% of the total variation. These values are determined as shown in the **Figure 4-17**.

Figure 4-17 shows the typical response of an automated process after a step change in controller output. The dead time, constant time, and response time of the process follow the controller output change (percentage of maximum power). These values and their corresponding temperatures are shown in **Table 4-2** for bottom temperature and ***Table 4-3*** for top temperature.

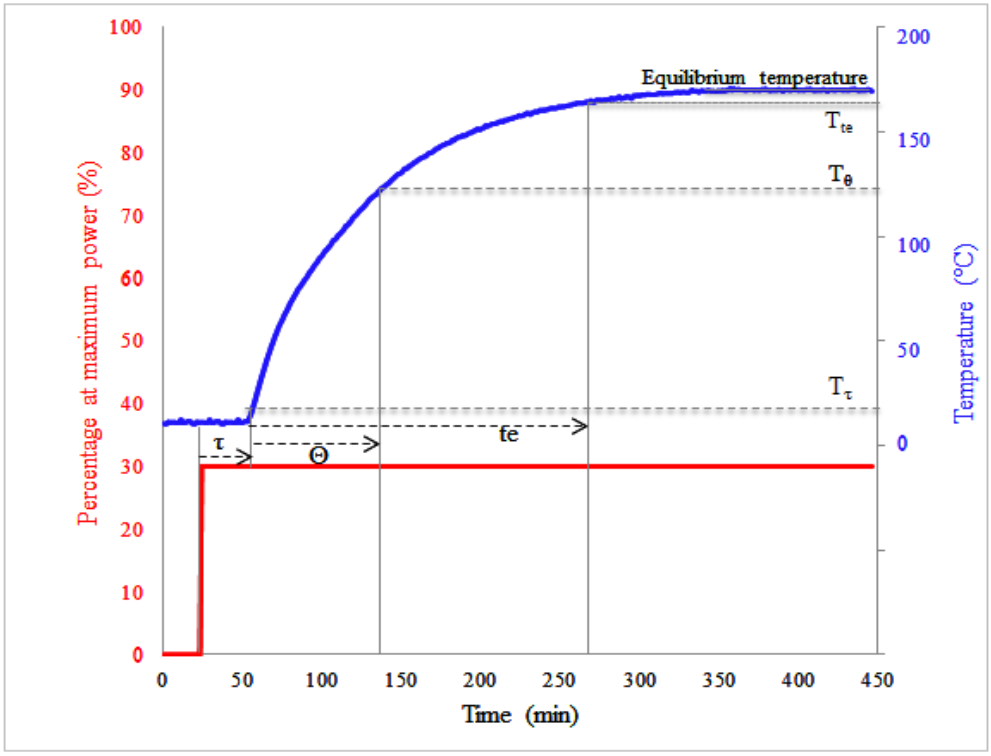

Figure 4-17: Dynamic process response to an HTC step test

Table 4-2: The characteristics values of a regulated signal at different powers (Bottom temperature)

Power		Bottom-temperature					
%Pmax	(W)	Dead time		Constant time		Response time	
		τ (min)	T_τ(°C)	Θ (min)	T_θ (°C)	te (min)	T_{te} (°C)
30	120	3.7	26.5	46.1	100.3	120.1	151.3
35	140	3.2	27.8	44.0	106.7	114.1	160.9
40	160	2.4	30.0	43.5	117.0	107.0	176.5
45	180	1.9	30.2	41.2	127.2	104.2	191.9
50	200	1.2	29.9	40.5	136.8	100.5	206.3

Table 4-3: The characteristics values of a regulated signal at different powers (Top temperature)

Power		Top-temperature					
%Pmax	(W)	Dead time		Constant time		Response time	
		τ (min)	T_τ(°C)	Θ (min)	T_θ (°C)	te (min)	T_{te} (°C)
30	120	5.7	25.8	54.1	100.6	118.1	151.8
35	140	5.1	29.8	48.2	115.8	113.8	165.7
40	160	3.8	29.3	45.8	120.1	109.5	182.5
45	180	3.0	31.9	42.1	127.8	106.2	192.2
50	200	2.2	29.6	38.5	137.7	102.5	207.6

The values obtained in **Table 4-2** for bottom temperature and in **Table *4-3*** for top temperature are used to determine the time required to reach the equilibrium temperature inside the reactor. These values are presented in the **Table 4-4**.

Table 4-4: The temperature of the equilibrium and the time required to reach it, from the power supplied.

Power		Equilibrium temperature			
%Pmax	(W)	Bottom- temperature		To-temperature	
		T(°C)	Time (min)	T(°C)	Time (min)
30	120	180±1	258	178±2	257
35	140	191±1	250	190±2	251
40	160	210±2	239	207±4	242
45	180	223±3	230	222±3	231
50	200	239±4	220	240±2	220

The information in **Table 4-4** extrapolates the temperature required with the HTC test with biomass from a given power. The calibration of the power with the temperature inside the reactor is shown in **Figure 4-18**. These results indicate that the power of 120W is needed to reach the carbonization temperature (180°C) in the reactor.

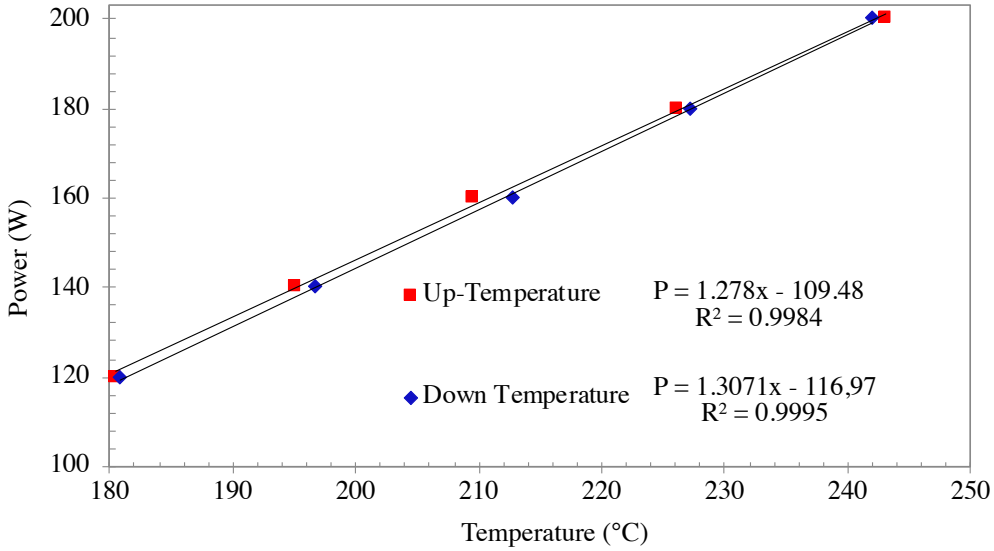

Figure 4-18: Calibration of power with temperature inside the reactor

4.2.2. Effect of operating conditions on the HTC process

The HTC process treatment induces some major transformations inside the biomass particles, following the severity of the performed process. The three main parameters that can be varied in an HTC process from an operational perspective are temperature, holding time, and biomass-to-water ratio. Each of these process variables has a differing impact on the yield and composition of different products such as hydrochar, HTC liquid, and gas (Sabio et al., 2016; Volpe and Fiori, 2017). Many studies have modeled the evolution of the main biomass components (lignin, cellulose, and hemicellulose) in relation to the reaction severity condition (Borrero-López et al., 2018; Heidari et al., 2019b). Heidari et al. (2019b) reported almost negligible interactions between lignin, cellulose, and hemicellulose on the hydrochar yield and hydrochar properties.

Another parameter that can significantly affect the composition of the final product is the origin of the biomass. It is well known that lignocellulosic biomass is mainly composed of hemicellulose, cellulose, and lignin, but its proportion in the overall biomass composition is strictly related to the nature of the considered material. At the same time, each of these components undergoes degradation processes to different extents according to the process conditions (Volpe et al., 2018; Volpe et al., 2020) In this study, the use of different biomass, with different proportions of the content of the main biomass components, will give us an

overview of the effects of the operating conditions. The results of the effects of operating conditions and biomass type are shown below.

4.2.2.1. *Effect of reaction temperature*

Figure 4-19 shows the effect of temperature variation on the distribution of the different HTC products of the biomasses. The results show that an increase in temperature from 150 °C to 250 °C decreases hydrochar yield. However, AS hydrochar does not follow the same rule since an increase in hydrochar yield was observed between 210 to 250 °C. The hydrochar yield of ASB decreased from 96.7 to 45.4 % (w/w), CS decreases from 97.9 to 50.8 % (w/w), and CEL was from 100 % to 35.4 % (w/w). On the other hand, the hydrochar from AS decreased from 92.5 to 37.6 % (w/w) between 150 to 210 °C, then increased from 37.6 to 45.7 % (w/w) between 210 to 250 °C.

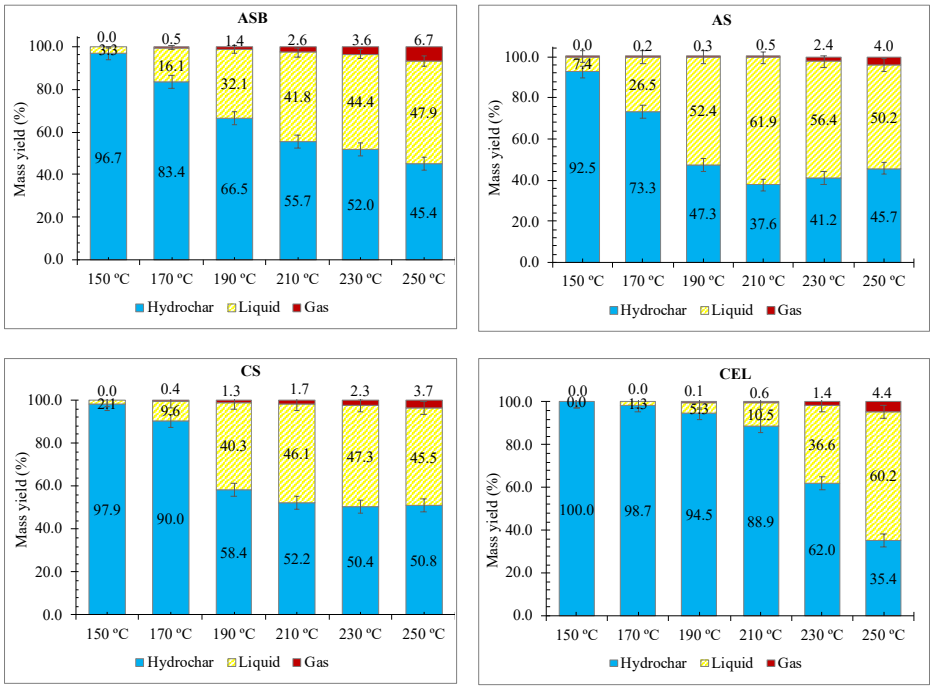

Figure 4-19: Effect of reaction temperature on the distribution of HTC products (for biomass-to-water ratio=1/10 and holding time =0 min, stirred speed 550 rmp)

In the HTC condition, saturated (compressed) water allows for better insertion within the porous biomass structure, resulting in lower activation energy(Khan et al., 2020; Libra et al., 2011). Hemicellulose degrades first at the lowest temperature (which represents the mass loss within the temperature range of 150–200 ºC), confirmed that biomass with high hemicellulose content would have lower hydrochar yield and a higher amount of liquid. As shown in **Figure**

4-19, AS has a lower hydrochar yield and higher liquid content due to its high hemicellulose concentration (as explained in **Chapter 2**).

As the temperature increases from 200 to 220 °C, the subsequent hydrolysis of cellulose results in a lower mass yield of hydrochar (Khan et al., 2020); therefore, it is reasonable to postulate that higher HTC process temperature causes decomposition of different biomass components, causing lower solid yield and higher liquid yield. This liquid undergoes further polymerization and aromatization to form secondary hydrochar, which decreases the liquid yield, thus increasing the hydrochar and gas content. Thus, biomass with high hemicellulose content (AS) undergoes rapid polymerization and aromatization reactions at high temperatures; since hemicellulose has a low hydrolysis temperature.

Temperature directly influences the HTC process by affecting the properties of pure water in the HTC range (150-250°C). Low temperatures favor ionic reactions that decompose biomass into solid residues. On the other hand, the decomposition of biomass into liquid and gaseous fractions is favored at high temperatures (Funke and Ziegler, 2010; Jain et al., 2016). Indeed, decreasing the dielectric constant of pure water from 51 F/m (150°C and 4.8 bar) to 28 F/m (250°C and 40 bar) increases the solubility of biomass organic components in water (Pavlovic et al., 2013). In addition, the ionic product of water varying from 10-11Kw (150-250°C) favoring acid-base catalyzed reactions of lignocellulosic biomass decomposition ((Kambo and Dutta, 2015).

4.2.2.2. *Effect of holding time*

Figure 4-20 shows the effect of holding time on the distribution of HTC products from the different biomasses (ASB, AS, CS, and CEL) for biomass-to-water ratio B/W=1/10, reaction temperature 230 ºC, and stirred speed 550 rmp. As the holding time increased from 0 min to 120 min, the mass yields of hydrochar decreased from 52.0 to 39.4% (w/w) for ASB, from 50.4 to 49.8% (w/w) for CS; and from 62.0 to 44.8% (w/w) for CEL.

However, an increase in the mass yield of AS hydrochar from 41.2 to 44.2% (w/w) was observed; this increase is due to the polymerization reactions of the intermediates (furfural and 5-HMF), similar increases of the hydrochar mass yield were observed by Yang et al. (2014) during the cellulose carbonization at a temperature above 275 °C. The same phenomenon of

decreasing hydrochar mass yield with increasing retention time was observed by Hoekman et al. (2011) for HTC of different lignocellulosic biomass.

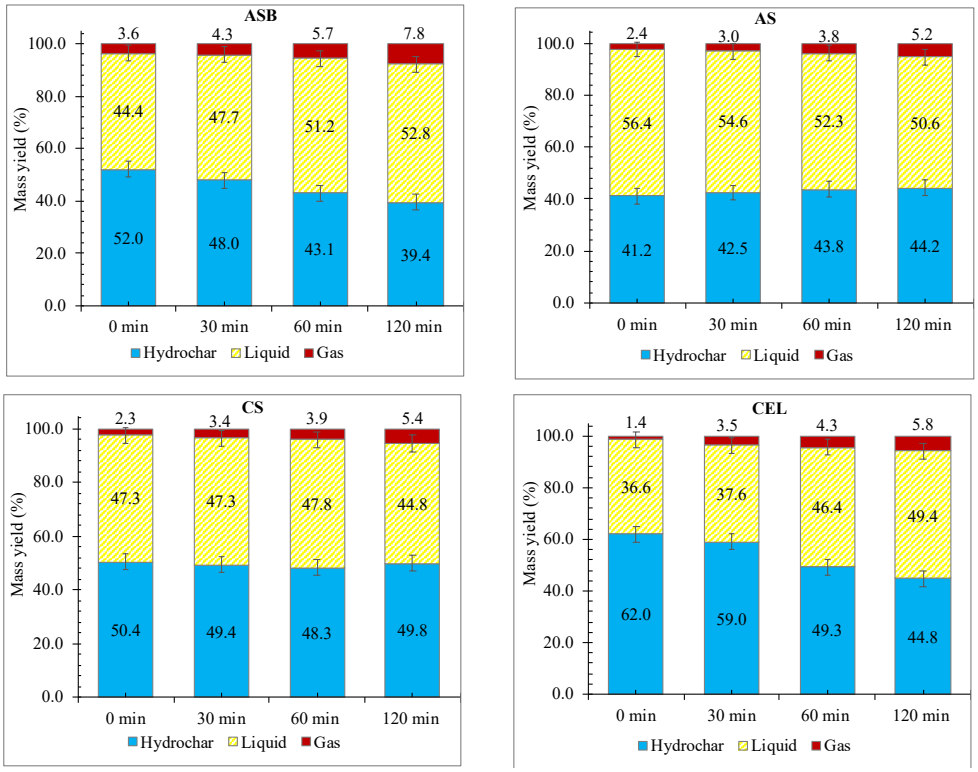

Figure 4-20: Effect of holding time on the distribution of HTC products (for biomass-to-water ratio B/W=1/10 and temperature = 230 ºC, stirred speed 550 rmp)

HTC also generates a small amount of a gas phase (mainly CO_2 and CO) and a large amount of liquid that contains simple sugars, furfural derivatives, phenolic compounds, organic acids (Basso et al., 2016; Hoekman et al., 2011; Missaoui et al., 2017; Reza et al., 2015). The production of gas is low (1.4-7.8%) for all biomass increases with increasing retention time between 0 min and 120 min. The decrease in AS and CS liquid may be due to the polymerization of the intermediates to form secondary hydrochar and decarboxylation of the organic acids to form the gases; since both for the hydrochar and gases increases with retention time for these two biomasses.

The high content of hemicellulose and the extractives of these two biomasses facilitate the rapid formation of intermediate products that are subsequently transformed into secondary hydrochar and gases in time. The increase of produced liquid with extended holding time indicates a continuation of liquid-phase reactions, while the relatively constant solid mass suggests an end of solid phase reactions. This result shows that a long holding time promotes

the formation of liquid up to a certain reaction time, then this liquid transforms to secondary hydrochar and gases during the HTC process, especially at high reaction temperature.

4.2.2.3. *Effect of biomass-to-water ratio*

The mass of the process water is typically 3-10 times greater than that of the dry feedstock (Hoekman et al., 2013; Kambo and Dutta, 2015; Liu et al., 2013b). Although many studies have reported the effect of the biomass-to-water ratio, most are focused on its effect on the mass yield of hydrochar. The biomass-to-water ratio has a significant effect on the hydrochar yield, a lower ratio amount of biomass in water causes a decrease in the solid yield. This is attributed to the greater impact of hydrolysis reactions caused by the increase in water quantity (Guo et al., 2016; Román et al., 2012; Sermyagina et al., 2015). Also, it plays a fundamental role in the different chemical reactions during the HTC, including hydrolysis, and polymerization, which are the most important chemical reactions (Kambo and Dutta, 2015; Kruse et al., 2013; Lu et al., 2012; Lucian et al., 2019; Volpe et al., 2018). But it was found that the biomass-to-water ratio are not affected on HHV and carbon content. (Guo et al., 2016; Kladisios and Sagia, 2018). **Figure 4-21** shows the effect of the biomass-to-water ratio on the HTC product distribution of the different biomass. The mass yield varies from one ratio to another. For example, the mass yield of hydrochar remains almost constant for B/W=1/8 and B/W=1/10 for one side, and B/W=1/6 and B/W=1/4 for the other hand. The liquid and gas yields follow the same trend.

The lower biomass water ratio (B/W=1/8 and B/W=1/10) maximizes the HTC liquid yield but produces less hydrochar than the other experiments (B/W=1/6 and B/W=1/4). Gas production remains low. These results agree with many works conducted in the literature on different biomass, e.g., miscanthus (Sermyagina et al., 2015) and a mixture of olive pulp and peel (Volpe and Fiori, 2017). Indeed, the high solvent ratio (B/W=1/8 and B/W=1/10) favors the solubilization of biomasses and the formation of liquid and gases. In addition, according to (Román et al., 2012) and (Sermyagina et al., 2015), a high proportion of water intensifies the decomposition of biomass by hydrolysis reactions. Funke and Ziegler (2010) and Jain et al. (2016) reported that low concentration reduces polymerization reactions, i.e., secondary hydrochar formed by polymerization reactions of organic components present in the liquid is affected by low substrate (biomass) concentration. Thus, the unpolymerized organic compounds are present in the liquid phase at the end of the experiment.

An increase in the biomass water ratio (B/W=1/10 to B/W=1/4) has a positive effect on the hydrochar yield. The hydrochar yield increased from 52.0 to 63.1% (w/w) for ASB, 41.2 to 51.6% (w/w) for AS, 50.4 to 55.2% (w/w) for CS, and 62.0 to 68.6% (w/w) for CEL, while the mass yield of liquid decreased. Möller et al. (2011) and Jain et al. (2016) reported that above a certain level of biomass concentration (high biomass to water mass ratio), biomass hydrolysis is incomplete. Thus, the formation of intermediate compounds is impaired, thus decreasing the liquid yield.

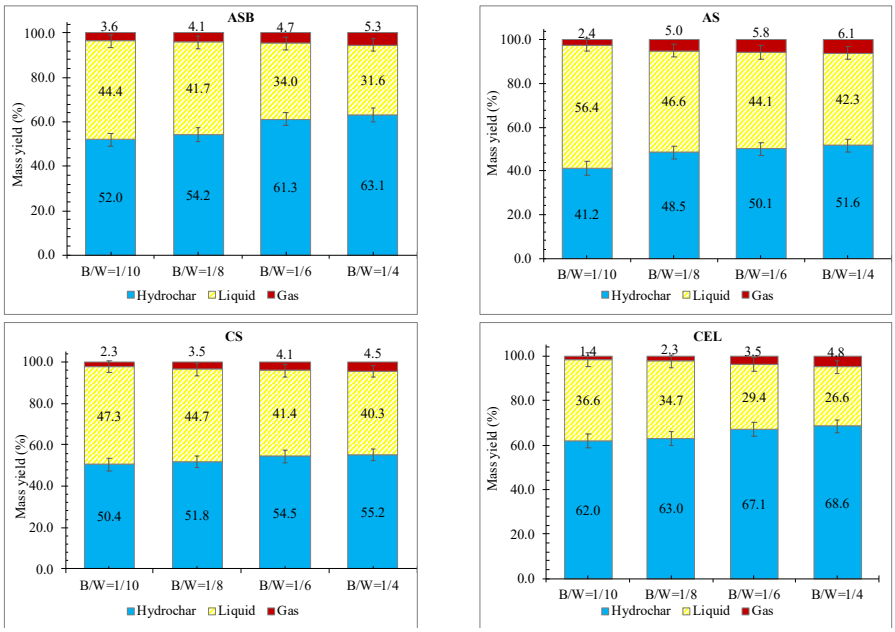

Figure 4-21: Effect of biomass-to-water ratio on the distribution of HTC products (for holding time =0 min and reaction temperature = 230 ºC, stirred speed 550 rmp)

The increase in temperature and retention time intensifies the decomposition reactions of the biomass during the HTC process. The biomass or solid-phase gradually decomposes into liquids and gases. The decrease in the mass yield of hydrochar can be explained by the release of volatile material from the biomass during the HTC process Hoekman et al. (2011). At the extreme conditions of temperature (250°C) and retention time (120 min), a high yield of liquid and gases was observed for ASB, CS, and CEL; in the same condition, an increase in hydrochar yield was observed for AS biomass, due to the polymerization of intermediates. The effect of biomass water ratio is small compared to the effect of temperature and retention time. For a retention time set at 0 min and a biomass water ratio B/W= 1/10 (Figure II-9), a more significant effect of temperature on the distribution of products than retention time and biomass water ratio was observed. This result is consistent with those reported in the literature on HTC conversion

of lignocellulosic biomassHoekman et al. (2011); (Sermyagina et al., 2015; Volpe and Fiori, 2017). The variation of operating conditions affects the decomposition reactions of biomass into solid, liquid, and gaseous products. The distribution of products shows that hydrochar is the majority product of the HTC process, although it was observed that liquid production is the most important in some cases.

4.2.3. Characterization and analysis of the chemical composition of hydrochar

4.2.3.1. *FTIR of hydrochars*

In this part, FTIR results of hydrochars produced from two biomass (AS and CS) are presented.

The FT-IR spectra of analyzed AS and CS; and their hydrochar with different HTC temperature presented in relevant spectral regions (4000–800 cm^{-1}) are given in **Figure 4-23** and **Figure 4-22**.

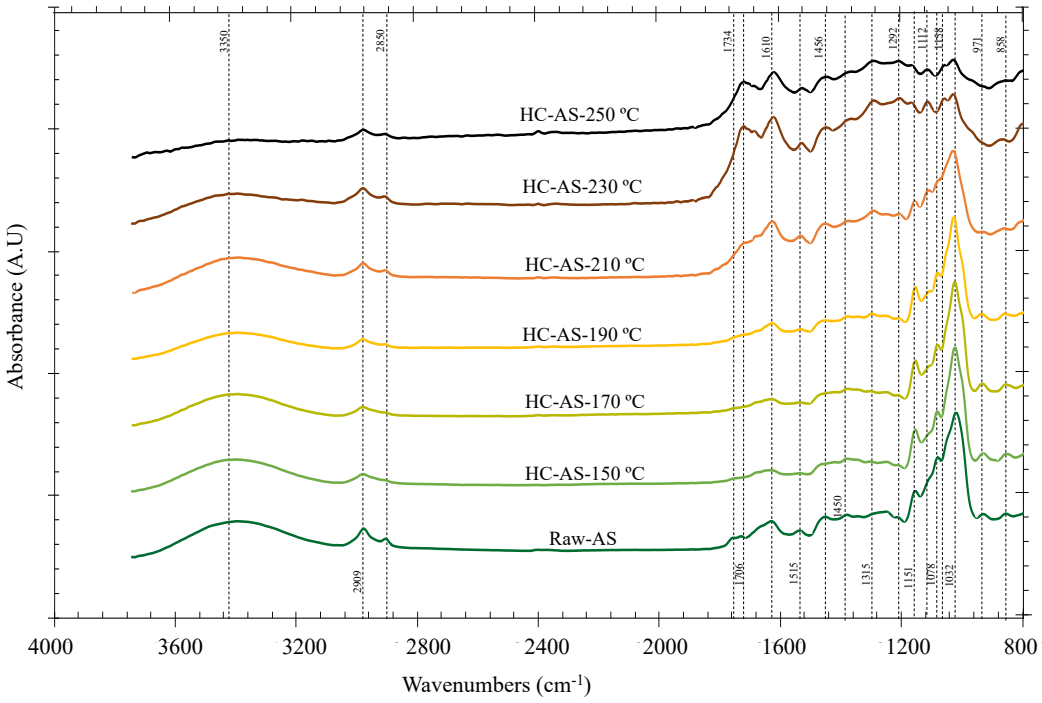

Figure 4-22: FT-IR spectra of AS and hydrochars.

A noticeable difference was observed after HTC showing that the surface functional groups changed during the HTC process. As it can be seen, the most prominent bands of AS and CS are basically in a similar location as those previously observed in FT-IR spectra of other lignocellulosic biomass (Arellanoa et al., 2016; Elmay et al., 2015; PetroviL et al., 2016).

In the first peculiar region, tree bands at 3350, 2909, and 2850 cm^{-1} correspond to OH^- vibration in the hydroxyl group, C-H, and -CHx stretching vibrations, respectively, are present in all samples. According to the results, the intensity of the peak around 3350 cm^{-1} for hydrochar was less than that of the raw biomass, revealing that dehydration occurred during HTC (Peng et al., 2016). The second band around 2909 cm^{-1}, related to asymmetric and symmetric methyl and methylene stretching groups of microcrystalline cellulose (Ciolacu et al., 2011), is also associated with the higher content of linear chain extractives in fibers (Poletto et al., 2014).

The intensity of this band shows an increase in all CS samples, both raw biomass and hydrochar (CS-HC), suggesting a higher content of extractive compounds than AS; this is in agreement with the analysis of the extractives of both biomass (discussed in **Chapter 3**) and previous literature findings (Arellanoa et al., 2016; Kambo and Dutta, 2015).

The band at 2850 cm^{-1} was attributed to aliphatic carbon -CHx stretching vibration corresponding to the alkyl aromatic structure. There was no apparent change at peak 2909 and 2850 cm^{-1}, attributing to the asymmetric and symmetric -C-H stretching of the methylene groups, respectively (J de Oliveira Silva et al., 2012). Also, the peak intensities for CS samples are much higher than AS samples, perhaps showing higher contents of compounds such as alkenes. The second region of the spectrum, between 1800 and 800 cm^{-1}, shows that HTC causes changes in the chemical characteristics of the samples. The band at 1734 cm^{-1}, attributed to acetyl and uronic ester groups of hemicellulose, shifts toward 1700 cm^{-1} attributed to unconjugated C=O and C=C of phenolic esters characteristic for lignin spectrum. The intensity of the peak at 1702 cm^{-1} increases in the hydrochars samples for both biomasses with increasing HTC temperature, thus confirming the carbonaceous structure of the hydrochars; this increase in carbon content in the hydrochars is the products of decarboxylation and dehydration.

Additionally, the "amorphous" absorption band at 889 cm^{-1} associated with C-O-C stretching of β-glucosidic linkages, and aliphatic C-H deformation vibrational band (at 1368 cm^{-1}) of cellulose and hemicellulose (Ciolacu et al., 2011; Gamgoum et al., 2016; Mihajlovic et al., 2018), decreases with carbonization; this is particularly noticeable for CS hydrochar samples produced between 210 to 250 °C, thus confirming the decrease of hemicellulose content in hydrochars obtained above 210 °C. Moreover, the visible peak at 1649 cm^{-1} in the CS spectrum, attributed to adsorbed water (Sun et al., 2000), increase in the hydrochar samples with increasing carbonization temperature. The band around 1550cm^{-1} was attributed to C=O

asymmetric stretching in the carboxylic group (Lin et al., 2012). This peak appears only in CS samples, and its intensity decreases with increasing HTC temperature.

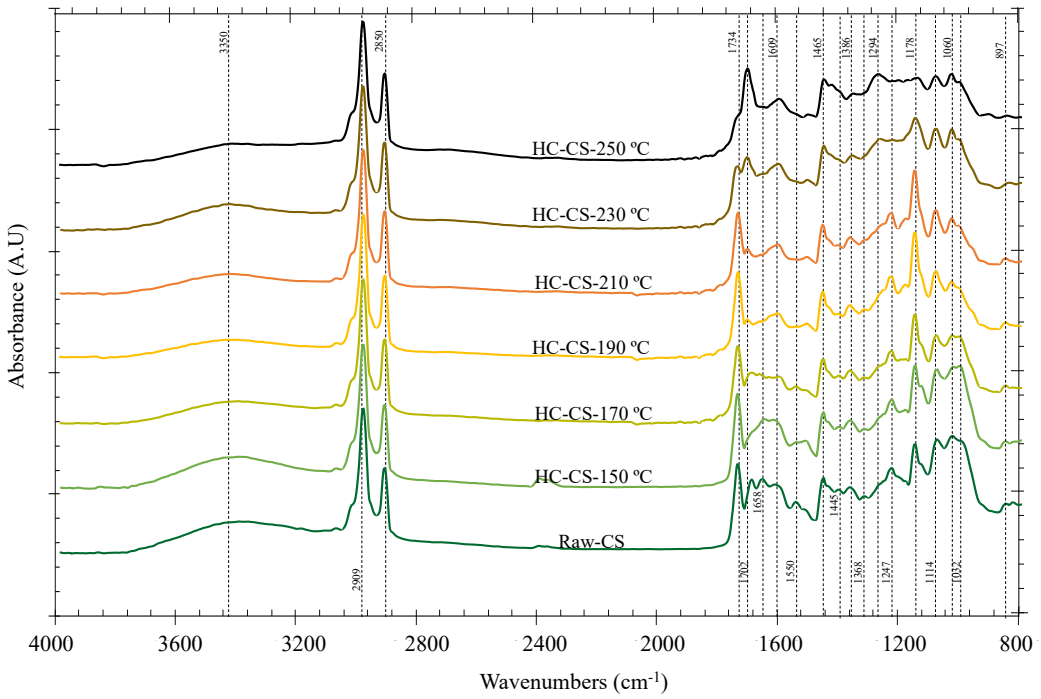

Figure 4-23: FT-IR spectra of CS and hydrochars.

This peak appears only in CS samples, and its intensity decreases in hydrochars, thus confirming a decarbonylation reaction with increasing temperature. An evident decrease in peak intensity was observed at 1658 cm^{-1}, implying that decarboxylation occurred during the HTC process. With an increase of HTC temperatures, intensities of bands characteristic for lignin spectrum around 1610 cm^{-1} (aromatic C=C), around 1515 cm^{-1} (aromatic skeletal vibration), around 1463 cm^{-1} (aromatic skeletal vibration with C-H plane deformation), and 1315 cm^{-1} (syringyl) are increasing in samples following HTC (Elmay et al., 2015). Concurrently, the typical cellulose bands of C-O stretching (at 1112, 1058, and 1032 cm^{-1}), asymmetrical C-O-C stretching (at 1161 cm^{-1}) become sharper; this suggests that HTC leads to the significant removal of hemicellulose, an increase in the proportion of lignin in the resulted hydrochars at given temperatures.

4.2.3.2. *SEM of hydrochars*

Figure 4-24 shows the physical structure of AS crude biomasses and their hydrochars produced at 150°C (b), 190°C(c), 210°C (d),230°C (e), and 250°C (f). The surface morphology

and physical structure of hydrochars and raw biomass are different in different HTC conditions. The raw biomass showed a smooth surface structure (**Figure 4-24a**) of different small particles.

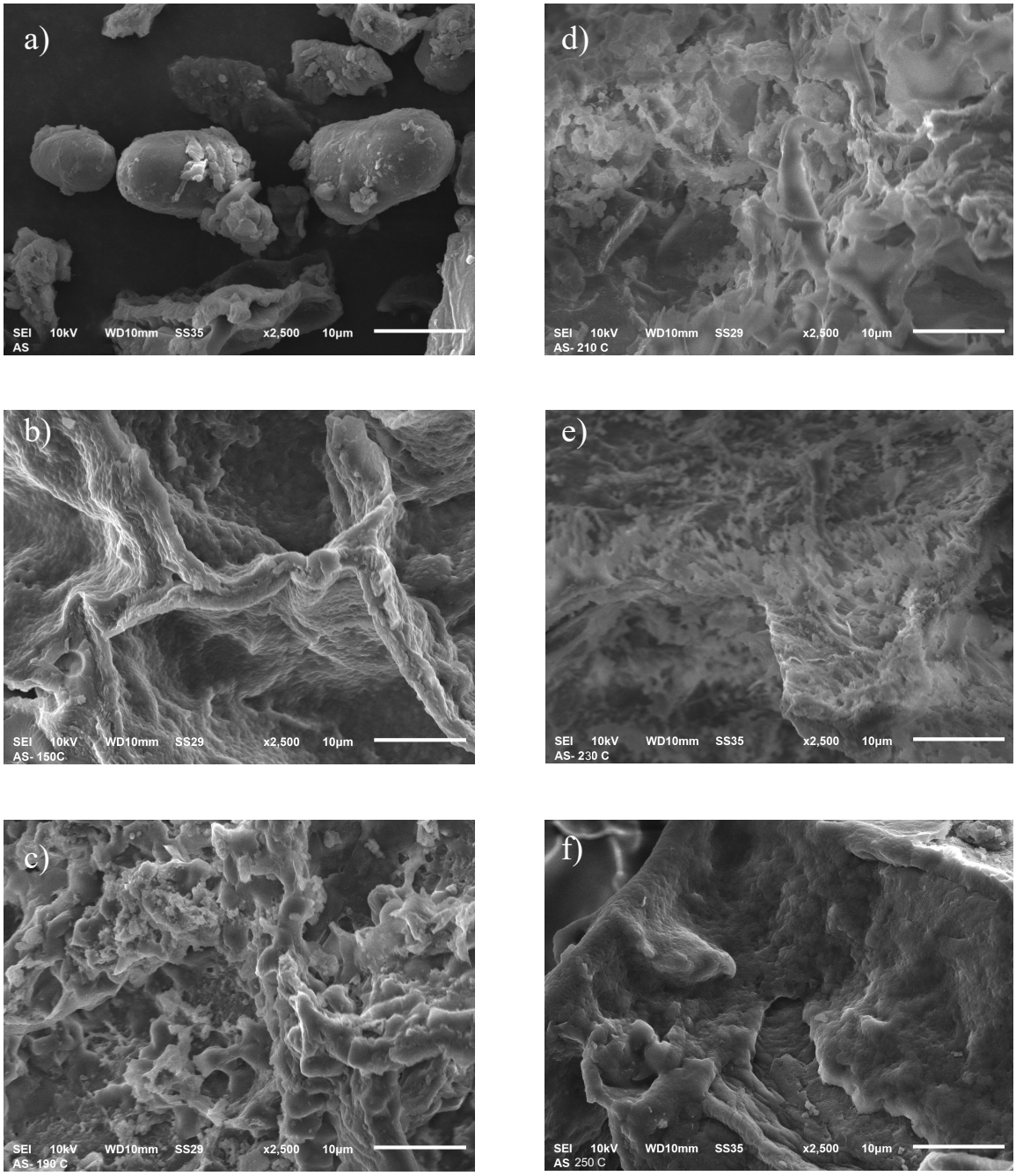

Figure 4-24: SEM images of (**a)** raw AS, and (**b-f)** hydrochars

After HTC treatment, the surface morphology and physical structure of hydrochar become rougher with increasing HTC temperature and reaction time. The hydrochar produced at 150 °C (**Figure 4-24b**) shows a smooth but irregular agglomerated structure with unevenness, which is due to hydrolysis. During hydrolysis, water enters the biomass structure, with agitation, a uniform and pasty structure are formed. Subsequently, this structure undergoes dehydration

and decarboxylation reactions leading to pore formations, as shown in **Figure 4-24c** and **Figure 4-24d**. The effects of temperature on morphology are evident in the HTC conditions at 190 and 210 °C (**Figure 4-24c-d**)). However, the small pores that were formed by dehydration and decarboxylation reactions start to agglomerate (**Figure 4-24e**) creating a block or layers covering the hydrochar surface, these are due to the condensation and polymerization reactions of the intermediate products, especially the furfurals, 5-HMF, and their derivatives. Similar observations were reported by Guo et al. (2015b). The hydrochar produced at 250 °C (**Figure 4-24f**) shows a surface similar to that of hydrochar produced at 150 °C (**Figure 4-24b**), this is due to the polymerization since all the surface and small pores of hydrochar have been covered by the formation of secondary hydrochar.

Figure 4-25 shows the morphologies of the CS crude biomasses and their produced hydrochars. In this case, no major differences are observed between crude CS (**Figure 4-25a**) and the hydrochars produced at 150 °C (**Figure 4-25b**); this is because raw CS is a by-product of cocoa roasting that has undergone heat treatment (140 ºC). Raw CS presents considerable agglomerations equal to hydrochar; this agglomeration can be attributed to the roasting temperature and its high-fat content. With the increase of HTC temperature to 190 °C (**Figure 4-25c**), small spherical particles gradually formed on the surface of hydrochars due to the process of volatile matter release by hemicellulose degradation. However, these small spherical particles are agglomerated due to the agitation effect and the high-fat content in the hydrochars produced. By HTC temperature above 210 °C (**Figure 4-25d**), the small spherical particles start to break up to form a layer on the primary hydrochar structures. The layer formed is due to polymerization by the formation of secondary hydrochar.

The structure of the hydrochar produced at 230 °C (**Figure 4-25e**) implies that its formation pathway can be attributed to condensation and polymerization since the temperatures of both stages are higher than 210 °C. In addition, coarser spherical particles and partial destruction of the agglomerate structure are formed. The surface morphology of hydrochar at 250 ºC (**Figure 4-25f**) differs from that at 150 ºC in this case, the structure is partially destroyed. All microspheres are practically destroyed at 250 ºC than at 150 ºC, the formation pathway of hydrochar 250 ºC may be predominantly by the polymerization reaction. The formation of secondary hydrochar, which occurs in the form of a layer, to cover the surface of primary hydrochar. It has been found that most of the lignin is difficult to dissolve in the aqueous phase below 265 °C (Kang et al., 2012). Therefore, this rough fragment is probably undissolved

lignin. This shows that the solid-solid reaction between the components of the mixture, such as undissolved lignin affects the hydrochar behavior.

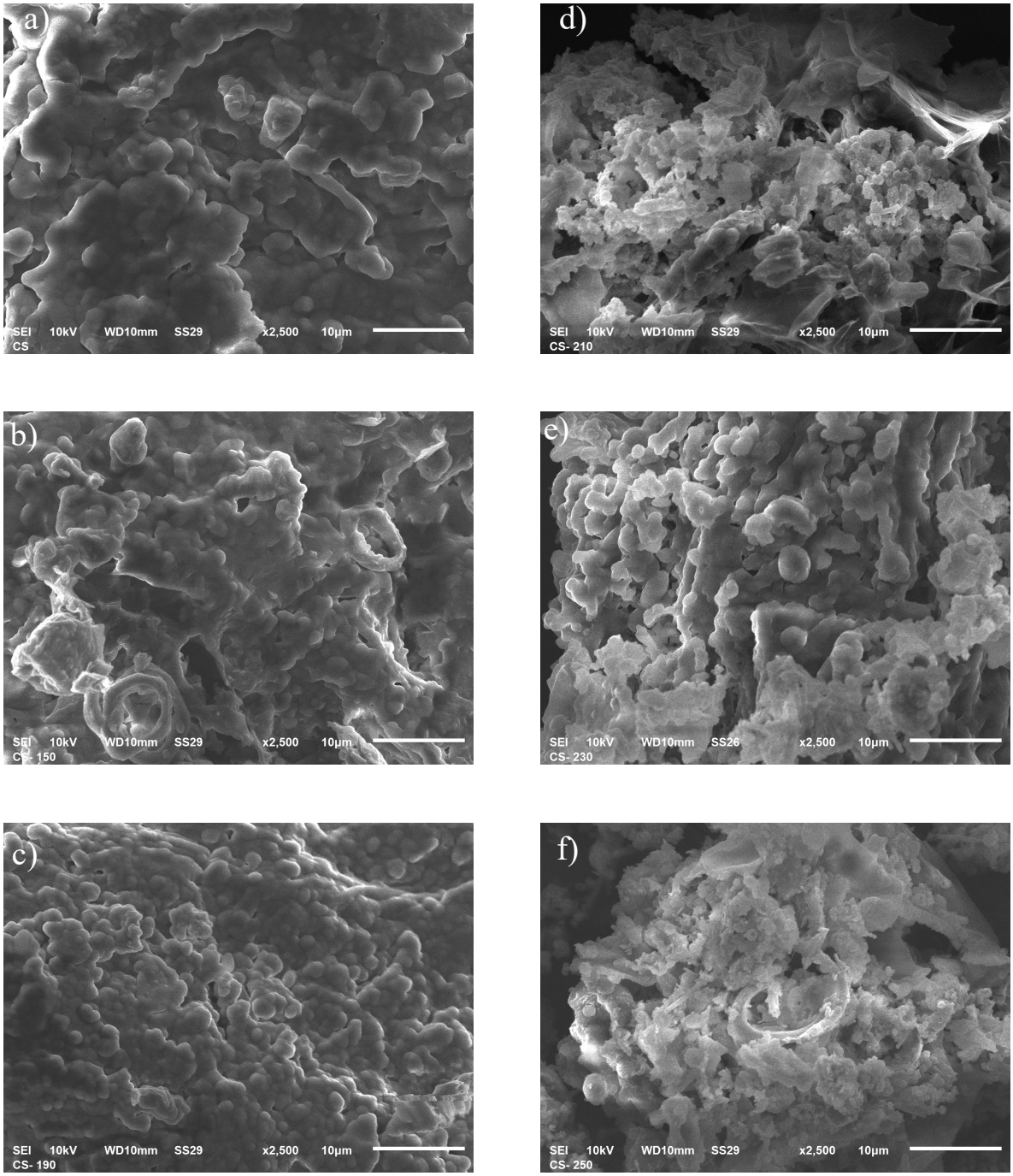

Figure 4-25: SEM images of (**a)** raw CS, and (**b-f)** hydrochars

4.2.4. Evolution of hydrochar mass yield with HTC temperature.

In this part, AS and CS were used as biomass. The main objective is this part is to analyze the evolution of hydrochar mass yield or total solid yield with increasing HTC temperature.

4.2.4.1. *HTC reactor heat-up and reaction time*

In reality, the constant temperature during HTC is not correct in batch autoclave reactors because there is a heating time, holding time temperature, and finally, a cooling time. In many publications in the literature, the definition of reaction time is not standardized. Often, HTC reaction time starts to be counted when the set HTC temperature is reached (Lucian et al., 2019; Missaoui et al., 2017) while in some other cases (Lu et al., 2012; Román et al., 2018) includes heat-up time. **Figure 4-26** shows the different heating time profiles established for different setpoint temperatures at 200 W electrical power (**Figure 4-26 a**) and for the different electrical powers used (**Figure 4-26 b**).

The heat-up time may be neglected only if it is very rapid as it could be the case when the HTC is performed in batch micro-reactors. In this study, an open-loop system was used, where the power supplied to the furnace of the reactor is controlled (i.e., constant in each experiment), and we consider the reaction time of the HTC is the heat-up time until the setpoint temperature is reached.

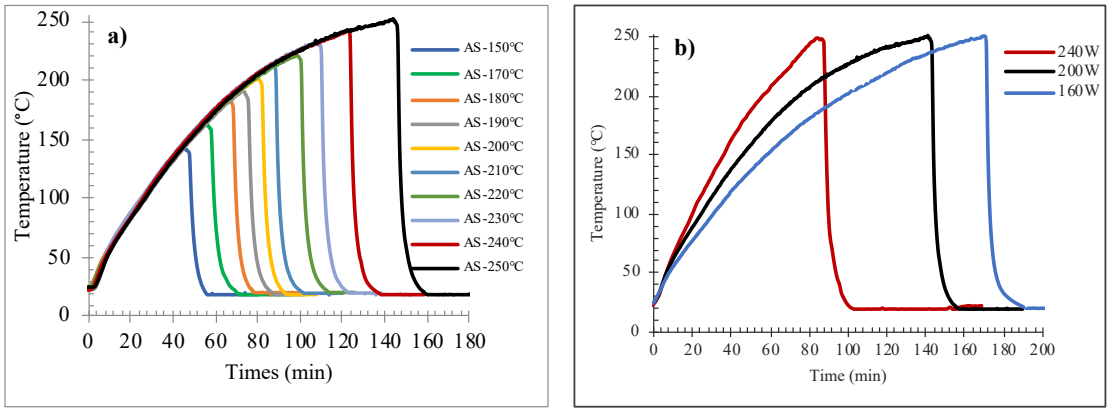

Figure 4-26: Temperature trends vs. time of hydrothermal tests, **(a)** conducted at 200W to set-point temperature, **(b)** different powers (heating rate) from ambient temperature to 250 °C.

In this case, holding time temperature and cooling time was not considered because when the setpoint temperature was reached, the reactor was cold down from setpoint temperature to room temperature; it took 5 to10 minutes to cool it down by immersing it in a 5°C water bath.

4.2.4.2. *Hydrochar mass yield or total solid yield analysis*

The degradation behavior of these biomasses was evaluated in the HTC temperature range between 150 and 250 °C, using biomass-to-water ratio of 1/10 (w/w), with a stirred speed of

550 rpm using a batch reactor (working in an open-loop control system) with a heating power of 200 W. **Figure 4-27** shows the evolution of hydrochar mass yield as a function of temperature. In general, the increase of temperature of HTC condition decreases the hydrochar yield. Two distinct zones can be observed in **Figure 4-27**. The first zone, from 150 to 210 ºC, can be related to the hemicellulose degradation zone. The hemicellulose begins to hydrolyze at HTC temperatures around 150 °C (Fregolente et al., 2020; Reza et al., 2014a). Most AS ASB and CS are degraded in this zone. In this zone, 62.36, 47.79, 45.95, and 13.82 wt.% of AS, CS, ASB, and CEL are degraded, respectively. The highest AS decomposition is due to its high hemicellulose content (>76%).

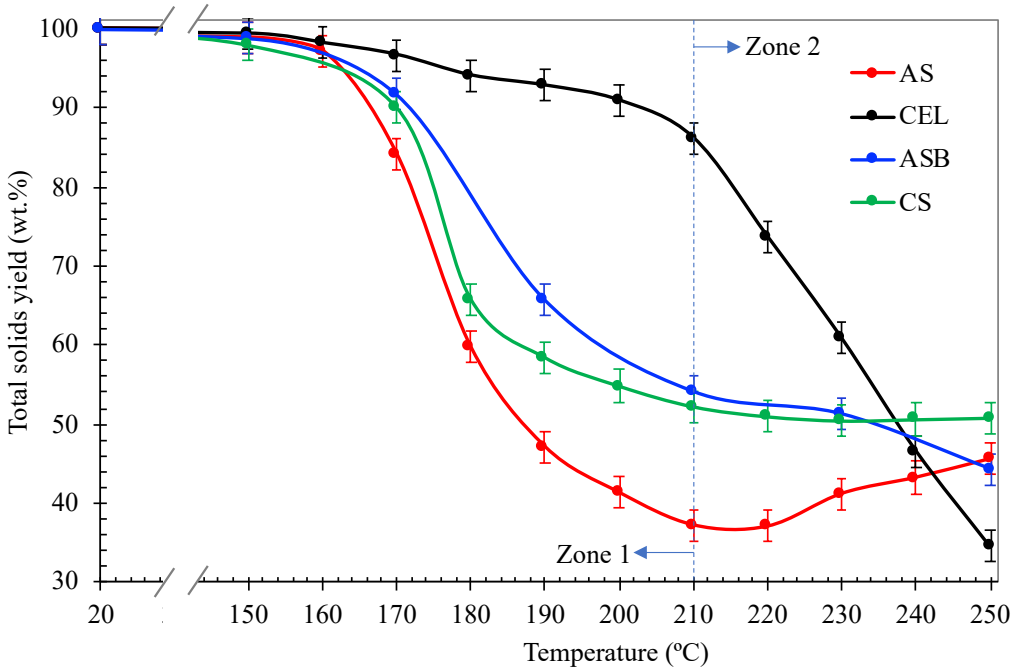

Figure 4-27: Mass yields of hydrochar or total solids as a function of temperature at B/W=1/10 and a power of 200 W

The second zone, between 210 and 250 ºC, corresponds to the cellulose degradation zone (Reza et al., 2014a; Reza et al., 2013). In this zone, CEL degrades from 86.18 to 34.5 wt.%; also, ASB degrades from 54.04 to 44.25 wt.%. The degradation of AS and CS are very low in this zone, confirming their low cellulose content. The mass yields of hydrochars produced from these biomasses increase in this zone. The AS yield gradually increases from 210 °C and reached 8.09 wt.% at 250. The increase of the AS mass yield could be due to a further decomposition of hemicellulose, which is then polymerized to form the secondary hydrochar.

The mass yields obtained for the biomasses were considered satisfactory compared to previous findings. For example, the hydrochar yield obtained for lignocellulosic agro-forest based biomass residues did not exceed 46.5 wt.% (conditions of 180–240 ºC) (Martinez et al., 2021), while hydrochar mass yield values of approximately 50–71% wt.% have been reported for wood samples (Hoekman et al., 2013), values supported by pinewood studies (Sermyagina et al., 2015). For agricultural residues, e.g., sugarcane bagasse, corn stover, and rice hulls, hydrochar mass yield values of 36–72% wt.% at HTC temperatures of 200–300 ◦C have been reported (Hoekman et al., 2013). Similar trends of hydrochar mass yield decrease with increasing temperature were observed in this research. The mass yield reduction is connected to the deoxygenating reactions and volatile matter conversion, as the hydrogen and oxygen contents become lower at higher temperatures (Martinez et al., 2021). The lowest values of hydrochar mass yield were observed for CEL at 250 ºC and AS at 210 ºC, whereas the highest mass yields were observed for CS at 250 ºC and AS at 250 ºC.

4.2.4.3. *Hydrochar mass yield and derivative mass yield analysis using different heating rates*

The hydrochar yield (Y_{HC}), or total solid yield and derivative hydrochar yield (DY_{HC}) curves of the samples (AS and CS) at different powers applied in the reactor (different heating rates) are shown in **Figure 4-28**, and **Figure 4-29**. At different heating rates, the evolution with a temperature of hydrochar yield is calculated based on **Eq.(4-1)** at different temperatures. For the Y_{HC} of the samples, four distinct zones can be identified in **Figure 4-28**. There is an initial induction period in the first zone in which the reaction rate is relatively slow (130-160°C). In this period, the temperature is not high enough to reach an energy level that allows energy activation. The reaction starts in the second zone, from ~160°C; the maximum rate of biomass decomposition is observed, and it is finished approximately for AS at 200°C and CS at 210°C.

This decrease in mass yield is due to decomposition reactions of biomasses, such as hydrolysis, dehydration, decarboxylation, so forth (Biller and Ross, 2016; Partridge et al., 2020; Volpe et al., 2018). The hydrolysis breaks down the biomass chemical structure through cleavage of ester and ether bonds of bio-macromolecules with water molecules. This process creates (oligo-) saccharides and fragments of lignin that enter the liquid phase (Fakkaew et al., 2015; Fang et al., 2018; Gao et al., 2016a), thus reducing the total solid yield, as shown in **Figure 4-28**.

The hydrolyzed products can degrade into furfurals, particularly 5-hydroxymethylfurfural (5-HMF), aldehyde, erythrose, and dehydration and decarboxylation (Krylova and Zaitchenko, 2018). Dehydration removes water from the biomass matrix without changing its chemical constitution, evidenced by the high carbon contents and decreased oxygen contents.

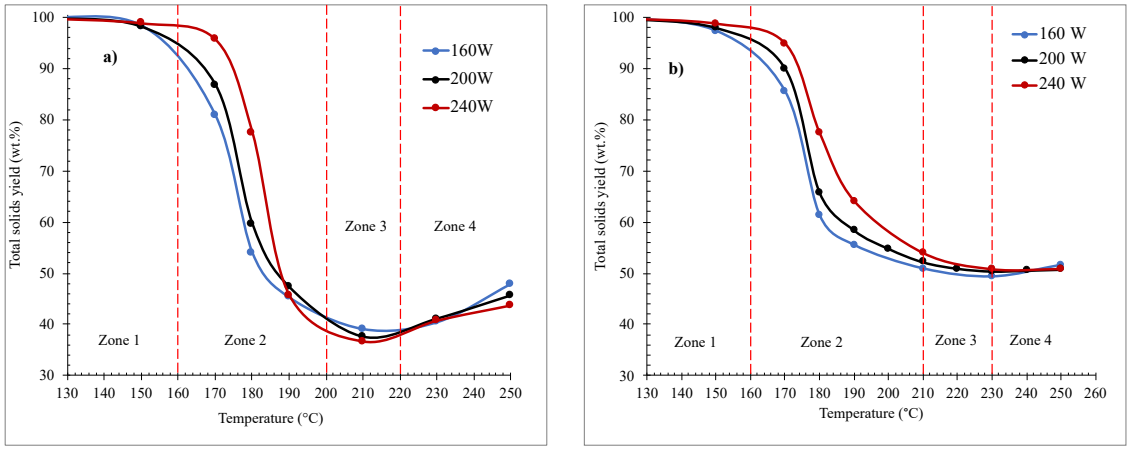

Figure 4-28: Hydrochar yield (Y_{HC}) curves of various powers (heating rates) of 160, 200 and 240W, (a) AS and (b) CS.

Decarboxylation involves the degradation of extractives, hemicellulose, and cellulose; these materials can degrade into monomers such as acetic acid, formic acid, lactic acid, and furfurals, which further degrade into CO_2 and H_2O (Reza et al., 2014b). The decarboxylation reaction removes carboxyl and carbonyl groups. Carboxyl and carbonyl groups rapidly degrade above 150-180°C, yielding CO_2 and CO, respectively (Peterson et al., 2008). All these reactions mentioned above are decomposition reactions, causing a decrease in the total solid yield and increasing the liquid and gas production. Other reaction mechanisms of HTC are aromatization and polymerization. HTC increases aromatics production from intermediates products formed during hydrolysis (Reza et al., 2014b). Moreover, lignin is composed of many aromatic compounds polymerized by various linkages. Hydrochar produced during HTC is a cross-linked polymer and has similar properties to lignin, so hydrochar is almost impossible to distinguish from the unreacted lignin fraction. Also, a linear polymer such as cellulose and hemicellulose can be converted into a cross-linked polymer similar to lignin (Reza, 2013; Reza et al., 2014a).

The stability of the aromatic structures is an essential element in hydrochar formation. This stability is observed in zone 3, between 200-220°C and 210-230°C for CS and CS, respectively, as shown in **Figure 4-28**. The intermediates of unsaturated compounds such as aldehydes,

furfural, and 5-HMF produced from dehydration and decarboxylation reactions are highly reactive. These monomers are followed by condensation, polymerization, and aromatization (Reza et al., 2014b; Sevilla and Fuertes, 2009b). The results of these reactions are called bio-crude. After successive polymerization and aromatization, this liquid bio-crude converts into a solid product (Reza et al., 2014a). This polymerization increases the total solid yield, as shown in zone 4 in (**Figure 4-28**), between 220 and 250ºC for AS and from 230 to 250ºC for CS. Similar behavior was observed by Yang et al. (2014) during the carbonization of cellulose at a temperature above 245°C

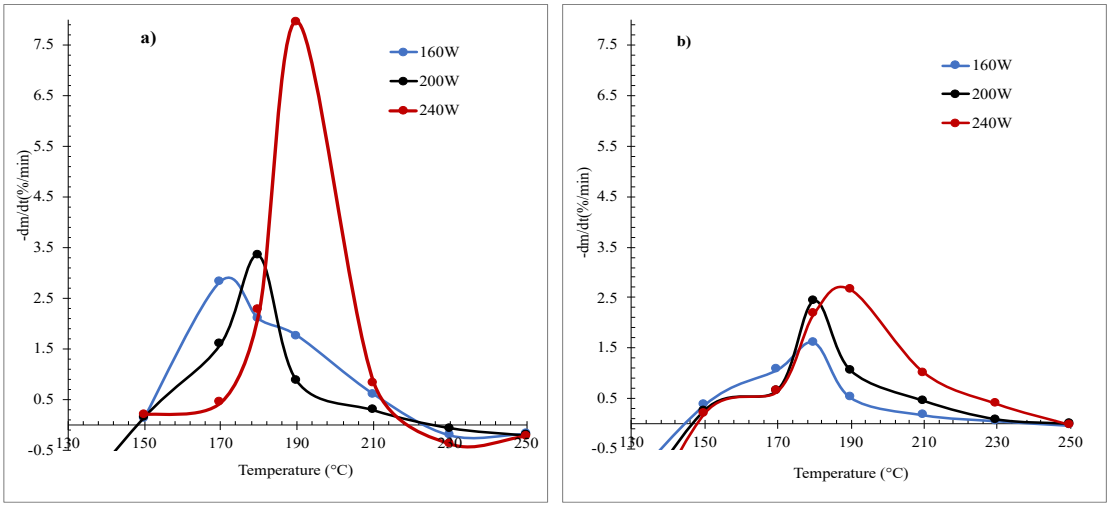

Figure 4-29: Derivative hydrochar yield (DY_{HC}) curves of various powers (heating rates) of 160, 200 and 240W, (**a**) AS and (**b**) CS.

The heating rate is an essential factor during the thermochemical conversion process of biomass since it affects the process through heat transfer and mass transfer through the biomass particles. As shown in **Figure 4-28**, and **Figure 4-29**, the Y_{HC} and DY_{HC} curves shape at various heating rates has a similar trend. However, the DY_{HC} curve (**Figure 4-29)** became sharper as the heating rate increased; higher heating rates significantly enhanced total solid yield loss rates than those by the lower heating rates.

Figure 4-29 shows that the peaks of DY_{HC} curves slightly shifted to the right as the heating rate increased because the gradient temperature of a particle and distribution of temperature was smaller at low heating rates. The DY_{HC} peaks differed in their height and position because the heating rate acted as a significant factor in lignocellulosic thermal decomposition (Wu et al., 2010). For AS, the maximum decomposition peaks were observed of 174, 182, and 189ºC for a power of 160, 200, and 240 W, respectively. Moreover, for CS, the maximum

decomposition peaks were observed of 178, 182, and 187ºC for the powers of 160, 200, and 240 W, respectively.

As can be seen in **Figure 4-28**, an increase in total solids yield is observed from 210 °C for AS and 220 °C for CS. This increase is a product of the polymerization and aromatization reactions of the intermediates. After successive polymerization and aromatization, the intermediates are converted into a solid product known as secondary hydrochar or tar (Reza et al., 2014a)The non-hydrolyzed fraction of the biomass undergoes a solid-to-solid reaction, giving rise to primary hydrochar. Subsequently, the final hydrochar or total solid is a mixture of primary and secondary hydrochar. Although it has been reported that it is not easy to distinguish analytically between the characteristics of primary and secondary hydrochar, both appear as a single solid mass of char (Paksung et al., 2020), the property and amorphous structure of the tar could help us separate these two components.

4.2.4.4. *Tar content and analysis*

It has been reported that, unlike biochar with a highly aromatized carbon structure, hydrochar is mainly composed of aliphatic hydrocarbons due to the formation of secondary hydrochar (Fuertes et al., 2010; Schimmelpfennig and Glaser, 2012; Wiedner et al., 2013). This means that the environmental stability of hydrochar is considerably lower (Abel et al., 2013; Sun et al., 2014) than that of biochar with a higher degree of carbonization and higher aromaticity.

On the other hand, during the HTC process of biomass, cellulose and lignin are degraded and produce phenolic compounds including polyaromatic hydrocarbons (PAHs) and dioxins, thereby causing potential risk to soil biota (Garlapalli et al., 2016). PAHs toxicity in soil amended with hydrochar has recently been reported (Busch et al., 2013; Visioli et al., 2016).Therefore, it is important to determine ecotoxicological compositions of hydrochar before application as a soil amendment, in order to prevent negative effects on soil biota.

During the HTC process, condensation, polymerization, and aromatization reactions form secondary hydrochar (tar) on the surface of the hydrochar. The tar is described as a complex mixture of condensable hydrocarbons (all the hydrocarbons with a molecular weight higher than that of benzene), including single and multiple ring aromatic compounds along with oxygen-containing hydrocarbons and complex PAHs (Zeng et al., 2020). This tar is derived from the decomposition of hemicellulose, cellulose, and amorphous carbonaceous compounds during HTC. The increase in temperature and time of HTC gradually increases the amorphous

carbon, such as aliphatic and aromatic groups, on the surface of the hydrochar (Jaruwat et al., 2018). The condensation of amorphous carbon on the hydrochar surface during HTC results in PAHs retention (Al-Wabel et al., 2019). This tar was separated from the hydrochars produced at 190, 210, 230, and 250 °C (power used 200W) by Soxhlet extraction with toluene (100%). Also, extraction was done with raw biomasses. The amount extracted in the hydrochar structures and the raw biomasses are presented in **Table 4-5**. It was noteworthy that a significant increase of tar removed in hydrochar was observed when the temperature was above 190 ºC for hydrochar derived from AS; this explains the increase in total solid yield as explained in **Section 4.2.4.2.** (**Figure 4-28**). The analyses of tar solutions removed from biomass and hydrochars structures show different aliphatic and PAHs compounds.

The high amount of tar in CS separated from the primary hydrochar structure of CS is because it contains high content of extractive compounds (25.25%). Perhaps this extractive compound does not pass into the liquid phase during hydrothermal carbonization. Therefore, it remains stuck in the hydrochar structure, increasing the concentration of separated tars in the primary hydrochar structure. On the other hand, the tars separated to the AS hydrochar exhibit a linear behavior with increasing HTC temperature.

Table 4-5: The tar removed in the structure of the hydrochars at different HTC temperatures.

	Tar removed (%. wt.)	
HTC-Temperature	AS	CS
HC-250ºC	19.01	46.96
HC-230ºC	13.86	48.13
HC-210ºC	10.05	44.69
HC-190ºC	5.48	47.48
Raw	3.80	25.25

A rotary evaporator was used to concentrate the tar solution for further analysis. The 250 mL of initial toluene mixed with the hydrochar was evaporated to obtain a volume of 25 mL. To find out the compounds within the tar solution, an analysis of aliphatic compounds and PAHs was performed.

4.2.4.4.1. *Aliphatic content analysis*

The long-chain aliphatic hydrocarbons that were found are shown in **Figure 4-30** for AS and **Figure 4-31** for CS. During HTC, a series of reactions of coalification occurred. The oxygenated hydrocarbons are initially converted to aliphatic (alkanes, olefins) and aromatics compounds and then transformed to higher hydrocarbons and larger PAHs with a further increase in temperature (Peng et al., 2017; Shen et al., 2017). The high molecular weight hydrocarbons, which were found in the tar solution, include long-chain alkanes, such as tetradecane (RT ≈8.9min), pentadecane (RT ≈10.1min), hexadecane (RT ≈ 11.3min), heptadecane (RT ≈ 12.4min), octadecane (RT ≈ 13.5min), and eicosane (RT ≈ 14.6min). The signal of these aliphatic compounds increases with increasing temperature, and it was not detected in the tar solution removed from the raw biomass.

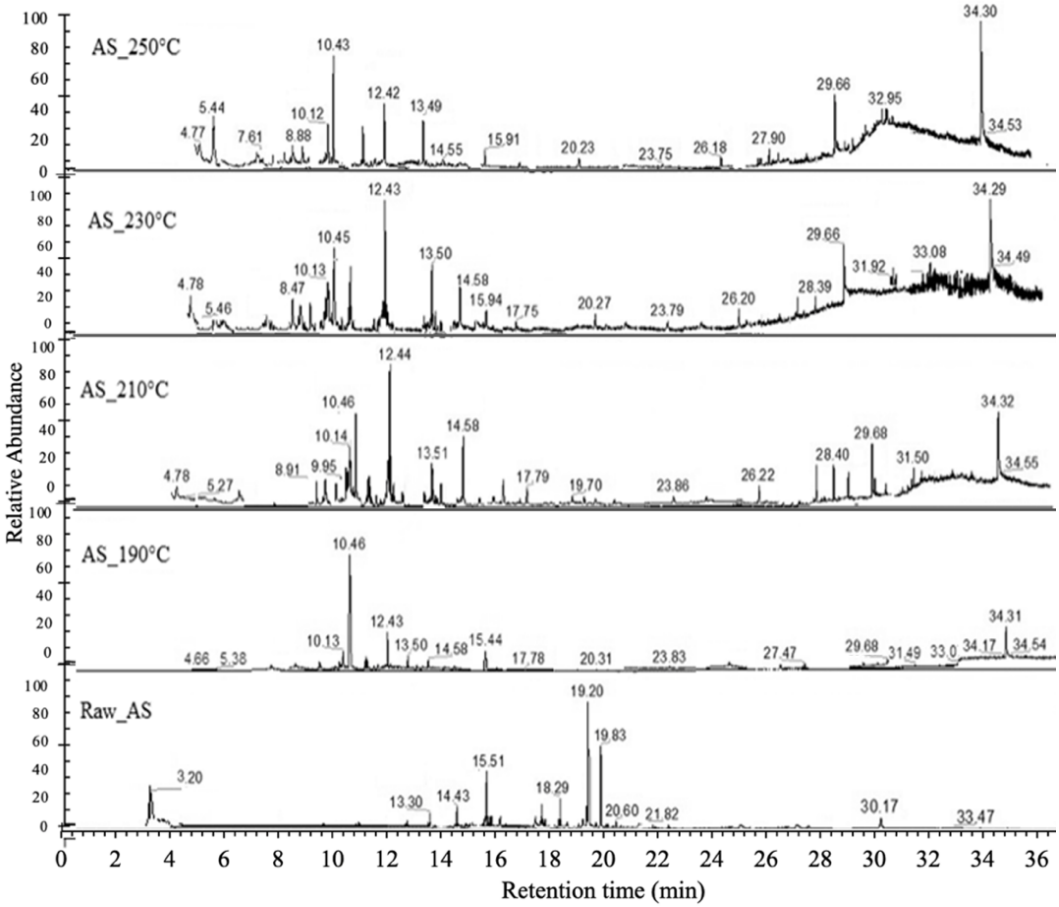

Figure 4-30: The main aliphatic compounds detected in the tar solution removed in the hydrochar structure and raw AS.

The main olefin of high molecular weight detected was 9-octadecenoic acid (oleic acid), an 18-carbon monounsaturated fatty acid (RT ≈ 34.3min). Also, it was detected 9-octadecenamide (RT≈ 29.7min), an amide derived from oleic fatty acid. All these compounds were detected in all the hydrochars produced. Comparing the CS and AS tar solutions, it is observed that CS contains a high proportion of saturated fats and monounsaturated acid, which usually appears in each triglyceride. The predominant triglycerides are palmitic acid in crude CS, oleic acid, stearic acid, and traces of caffeine for hydrochar produced at 230 and 250 ºC.

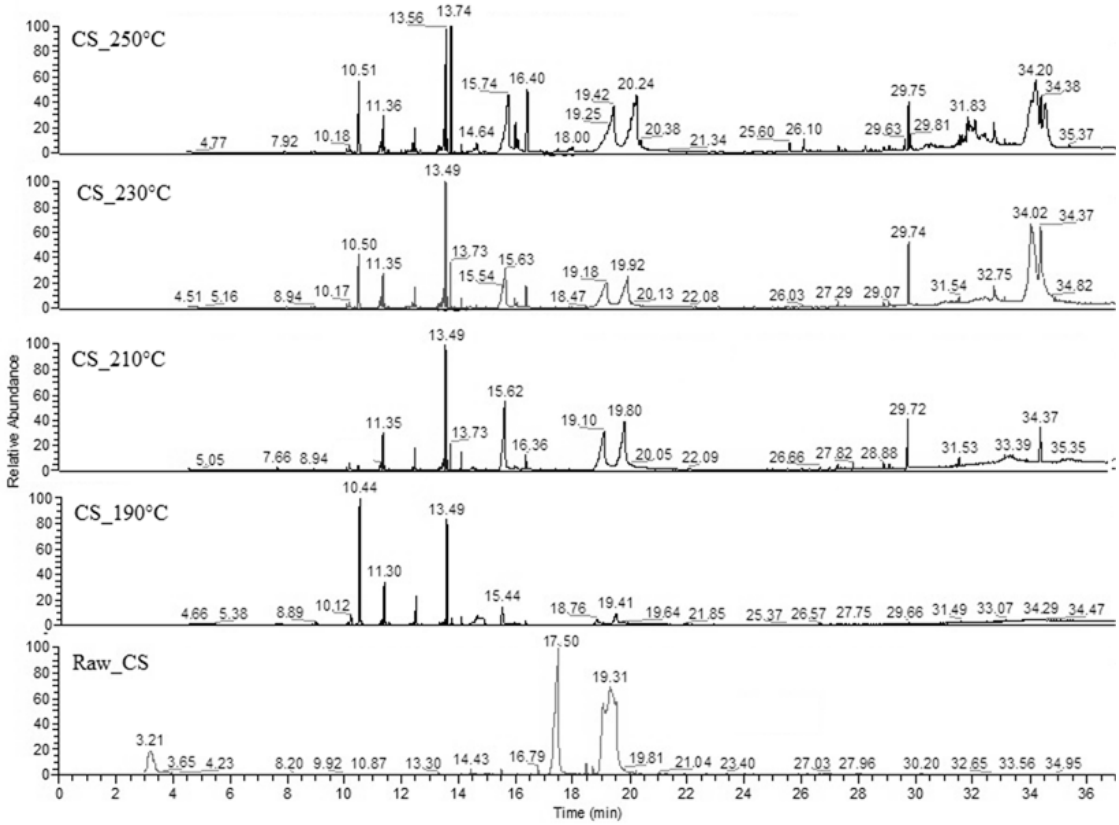

Figure 4-31: The main aliphatic compounds detected in the tar solution removed in the hydrochar structure and raw CS.

The main aliphatic components detected in the tar solution and their relative concentration and retention time are presented in **Table 4-6.**

Table 4-6: main aliphatic components detected in the tar solution.

RT (min)	Components	Relative concentration									
		Raw		HC_190°C		HC_210°C		HC_230°C		HC_250°C	
		AS	CS	AS	CS	AS	CS	AS	CS	AS	CS
8.5	Ethanedione, di-2-furanyl	0	0	0	0	0	0	5.3	0	0	0
8.9	Tetradecane	0	0	0	0	0	0	2.0	0	3.6	0
10.1	Pentadecane	0	0	0	0	5.4	0	29.9	0	3.1	0
10.5	Bibenzyl	0	0	67.6	38.7	25.3	0.2	14.9	4.0	32.9	3.7
11.3	Hexadecane	0	0	4.0	13.2	12.0	1.2	16.9	1.3	3.4	0.7
12.4	Heptadecane	0	0	13.5	10.6	28.1	0.9	8.3	0.7	7.7	1.6
13.5	Octadecane	0	0	0	34.9	5.1	1.4	0	4.1	3.8	4.6
13.7	E-15-heptacenal	0	0	0	0	0	0	0	0	0	0.9
14.1	Caffeine	0	0	0	0	0	0	0	0.41	0	0.5
14.6	Eicosane	0	0	0	0	6.72	1.0	0	1.5	0	4.4
15.5	n-hexadecanoic acid	22.4	0	0	0.85	0	23.4	0	9.0	0	19.4
16.4	Octadecanal	0	0	0	0	0	5.1	0	1.6	0	4.4
17.5	Palmitic acid	0	37.8	0	0	0	0	0	0	0	0
19.2	Stearic acid	43.5	62.2	0	1.23	0	30.8	0	28.9	0	14.9
19.8	(11E)-11-octadecenoic acid	34.1	0	0	0.52	0	28.0	0	31.8	0	17.1
29.7	9-Octadecenamide	0	0	0	0	3.18	3.7	4.4	2.9	9.7	2.0
31.8	Sitosterol acetate	0	0	0	0	0	0.3	0	4.2	0	3.2
34.3	9-Octadecenoic acid	0	0	14.9	0	14.17	4.0	18.3	9.6	35.8	22.6

4.2.4.4.2. *PAHs content analysis*

Polycyclic aromatic hydrocarbons (PAHs) are a group of over 200 different organic compounds with two or more fused aromatic rings (Domingo and Nadal, 2015). The International Agency for Research on Cancer (IARC) of the World Health Organization has determined that benzo[a]anthracene (BaA), chrysene (Chr), benzo[b]fluoranthene (BbF) are in Group 2B, possibly carcinogenic to humans and benzo[a]pyrene (BaP) was included in the Group 1A, carcinogenic to animals and humans (IARC, 1996).

The chromatogram of total PAHs in hydrochar and raw AS are presented in **Figure 4-32**. PAHs were not detected in the CS tars solution. The results showed that total PAHs in the hydrochars were higher than those in raw AS. The PAHs detected in the raw biomass were bibenzyl (RT≈ 30.98min), the simplest PAHs (2 rings). The peak with a retention time of 17 and 23min are benzaldehyde and Benzyl alcohol, respectively. The number of PAHs detected in the hydrochars increases with increasing temperature; this may be explained by polymerization and aromatization reactions during the HTC process. At the lower temperature of HTC (190ºC and 210ºC), the PAHs detected were mainly 2-3 rings. The 2-ring were biphenyl, bibenzyl, and naphthalene with the retention time of 29.91, 31, and 27.78min, respectively.

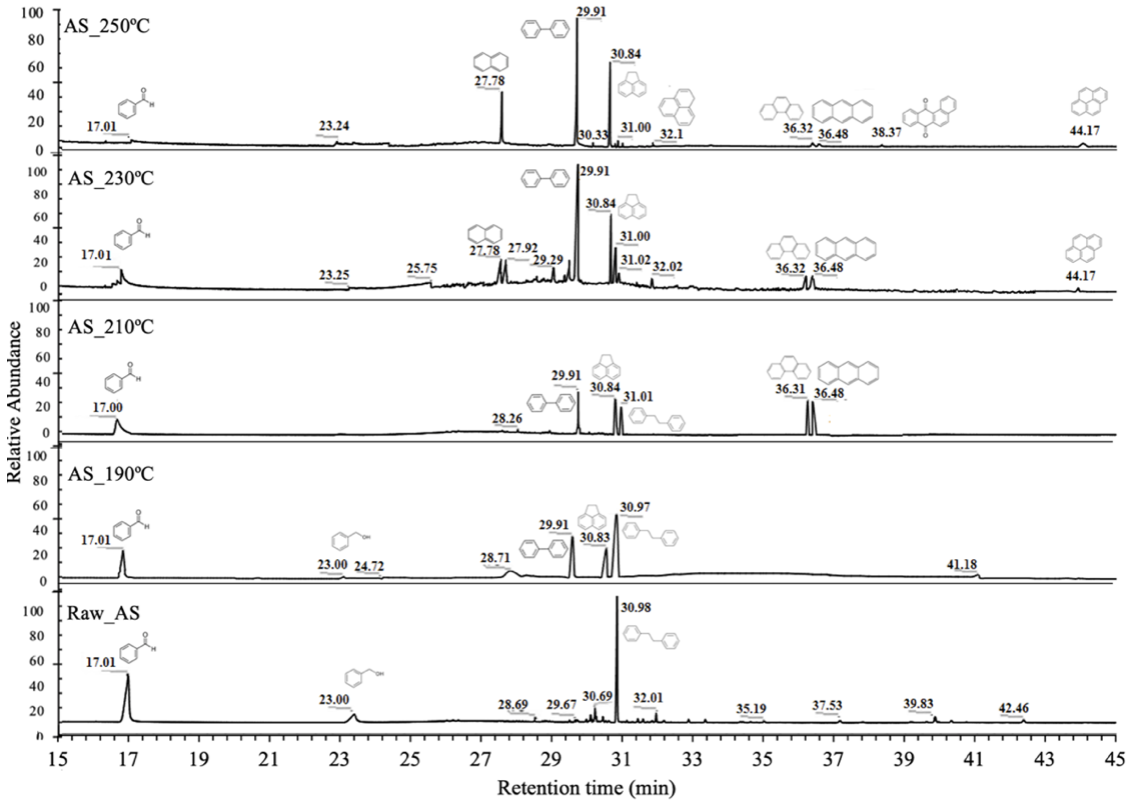

Figure 4-32: The main PAHs compounds detected in the tar solution removed in the hydrochar structure and raw AS.

The PAHs with three rings detected were acenaphthene, phenanthrene, and anthracene with retention times 30.84, 36.32, and 36.48min, respectively. In addition to the fact that all these mentioned PAHs were detected at a high temperature of HTC (230 and 250 °C), other PAHs were detected, such as 4-methyl biphenyl, acenaphthene, cis-stilbene, 1H-phenalene, and pyrene, with the retention time of 30.33, 31.07, 31.22 32.1, and 44.17 min respectively. At a temperature of 250ºC, another 4-ring oxygenated PAHs was detected, such as 7,12-

dihydrobenzo[a]antracene, with a retention time of 38.37min. At low temperatures, the biomass was subjected to initial hydrolysis, dehydration, and depolymerization reaction (Krylova and Zaitchenko, 2018), which led to a decrease in total PAHs because the polymerization and aromatization reaction have not started. The intermediates unsaturated compounds produced from dehydration and decarboxylation promoted PAHs formation with increasing temperature by aromatization and polymerization reactions, so increasing the PAHs rings formed. The hydrochars obtained at temperatures from 190 to 210 °C, biphenyl and bibenzyl (2 rings) were dominant while phenanthrene, Anthracene, and Pyrene were most prevalent at high HTC temperature (230 - 250 °C).

The results obtained are in agreement with other work published in the literature. For example, Peng et al. (2017) reported a significant increase of PAHs in the hydrochar of municipal solid waste, with the increase in temperature of HTC between 160°C and 240°C. On the other hand, Sharma and Hajaligol (2003) explain that the formation of PAHs from biomass is probably a multistep process. As in pyrolysis, the biomass is converted first into primary products, such as tar and char, which then undergo secondary reactions to form PAHs.

4.2.4.5. *Analysis of the kinetic studies of hydrochar formation*

Biomass decomposition by HTC is dominated by chemical reactions similar to pyrolysis; however, the HTC process is initiated by hydrolysis, leading to biomass decomposition temperatures lower than those of pyrolysis (Kambo and Dutta, 2015). The HTC reaction mechanisms complexity has led some authors to develop lumped kinetics models to describe it. For simplification, the authors have used the biomass components model, such as cellulose, hemicellulose, and lignin. For example, Reza et al. (2013) determined the activation energy of cellulose and hemicellulose in the temperature range between 200 and 260°C. They reported that cellulose degradation is described by a first-order rate constant with an activation energy of 73±6 kJ/mol, and hemicellulose degradation has an activation energy of 30±12 kJ/mol. For the same operating conditions (200-260°C), Keiller et al. (2019) reported activation energy values equal to 61 kJ/mol and 127 kJ/mol for hemicellulose and cellulose, respectively. On the other hand, Liu and Balasubramanian (2012) considered the HTC process as a first-order reaction and estimated the activation energy for coconut fibers (67.5 kJ/mol) and eucalyptus leaves (59.2 kJ/mol). Recently Pecchi et al. (2020) reported Ea values of 139.16 and 161.68 kJ/mol and reaction orders of about 2.68 and 2.46, for digestate and sludge, respectively, using Differential Scanning Calorimetry. As can be seen, different approaches have been used to

determine the kinetic parameters during the HTC process of the biomass. However, researchers have used conventional methods in only a few studies to determine kinetic parameters. Methods based on thermal analysis, such as thermogravimetric analysis, have been widely used in the literature to study biomass decomposition kinetics. High-precision methods can be used for the quantitative examination of processes and estimate proper kinetic parameters for various thermal decomposition reactions. Since thermogravimetric analysis is a technique based on mass loss or conversion as a function of temperature and time during thermochemical conversion, a similar analogy can be used for the HTC process.

For this reason, this part of the research is focused on the determination of kinetic parameters that described the hydrothermal carbonization process of the biomasses (AS and CS), using the thermal analysis technique in an open-loop controller system. The biomasses HTC behavior was studied using the total solid mass yield or hydrochar yield produced at different temperatures and times. The kinetic predictions were performed using the Model-Free Method, such as FWO, KAS, and Friedman, and the Model-Fitting Methods were used to determine the most appropriate kinetic model mechanism of HTC reactions. Although model-free methods can reliably estimate the kinetic parameters, the information obtained is limited; it does not allow the definition of the reaction mechanism, unlike model-fitting methods (Ali et al., 2018).

4.2.4.5.1. *Model-free method*

The model-free methods first analyzed the kinetics of the HTC of AS and CS. They were starting from **Eq. (4-5)** and applying above mentioned isoconversional methods. The activation energy (Eα), pre-exponential factor (A), and linear correlation coefficient (R^2) at various conversion rates of 0.1–0.9 were calculated using the FWO, KAS, and Friedman methods. The calculated average values of Eα, A, and R^2 are shown in **Table 4-7**. These parameters were calculated in two temperature zones for AS. The first zone corresponds to the decrease in the Y_{HC} (150 - 210°C); the second zone corresponds to the increase of the Y_{HC} from 210 to 250°C. For CS, the kinetic parameters were calculated in a single zone between 150°C and 230°C, because in the second zone, the Y_{HC} value obtained from 230°C to 250°C was similar. As shown in **Table 4-7**, the Eα values obtained for the integral methods (FWO and KAS) are similar and show the best fit correlation coefficient (R^2) compared to the differential method (Friedman). The Friedman method requires derivative conversion data, which would lead to being numerically unstable and noise-sensitive (Cai et al., 2018). For this reason, in

general, the integral methods show the best-fit correlation coefficient values than the differential method.

As shown in **Table 4-7**, a higher value of Eα was obtained for CS than AS. The higher value of Eα for CS means that a higher temperature is required to initiate CS decomposition to produce hydrochar than that required for AS. In these temperature ranges, the average Eα values of AS were 89.61±12.19 kJ/mol, 86.79±12.82 kJ/mol, and 73.81±35.47 kJ/mol for FWO, KAS, and Friedman methods, respectively. For CS, the average Eα values were 108.58±9.64 kJ/mol, 106.77±9.4 kJ/mol, and 104.78±27.31 kJ/mol for FWO, KAS, and Friedman method. In both cases, a lower R^2 is obtained for the Friedman method.

Table 4-7: Kinetic parameters of AS and CS determined by the model-free kinetics methods.

Temperature	**AS**								
(°C)	**FWO**			**KAS**			**Friedman**		
	Eα (kJ/mol)	A (min^{-1})	R^2	Eα (kJ/mol)	A (min^{-1})	R^2	Eα (kJ/mol)	A (min^{-1})	R^2
150-210	89.61±12.19	$7.55x10^{9}$	0.982	86.79±12.82	$3.39x10^{9}$	0.979	73.81±35.47	$2.24x10^{12}$	0.630
210-250	181.28±20.13	$78x10^{-19}$	0.909	199.12±21.16	$1.38x10^{-19}$	0.916	223.27±31.56	$2.49x10^{-6}$	0.801
	CS								
	FWO			**KAS**			**Friedman**		
	Eα (kJ/mol)	A (min^{-1})	R^2	Eα (kJ/mol)	A (min^{-1})	R^2	Eα (kJ/mol)	A (min^{-1})	R^2
150-230°C	108.58±9.64	$1.22x10^{12}$	0.984	106.77±9.94	$7.21x10^{11}$	0.981	104.78±36.61	$6.33x10^{14}$	0.789

The Friedman method cannot be used to determine the kinetic parameters in this case. The slight differences observed in Eα values obtained using KAS and FWO can be assigned to the different approximations of the temperature integral. In **Figure 4-33**, it can be observed that the values of Eα are not similar for all conversion values, indicating the existence of a complex multi-step mechanism that occurs in the biomasses HTC process. The progressive variation of Eα values could correspond to competitive or consecutive reactions and the multiphasic biomass conversion.

In the case of AS, for α values from 0.1 to 0.6, a decrease in Eα values from 99 to 68 kJ/mol (FWO and KAS) for AS was observed. However, from 0.6, an increase of Eα is observed; this may be due to the change in chemical reactions. For CS, slow growth of Eα values as a

conversion function (α) was observed, as shown in **Figure 4-33**. In the temperature range from 200 to 220ºC, similar values of Eα were reported by Keiller et al. (2019) for cellulose and hemicellulose using the nonlinear least-square minimization method. Also, Danso Boateng et al. (2013) reported the value of activation energy (77.8 kJ/mol, with pre-exponential factor $1.5x10^7$ min^{-1}) for synthetic feces and 70.4 kJ/mol, with a pre-exponential factor of $4.0x10^6$ min^{-1} for primary sewage sludge. In the second zone (210 to 250°C), they correspond to an increase in Y_{HC} for AS. The Eα values are displayed in **Table 4-7** and **Figure 4-34**. The values obtained are a similar trend for integral methods.

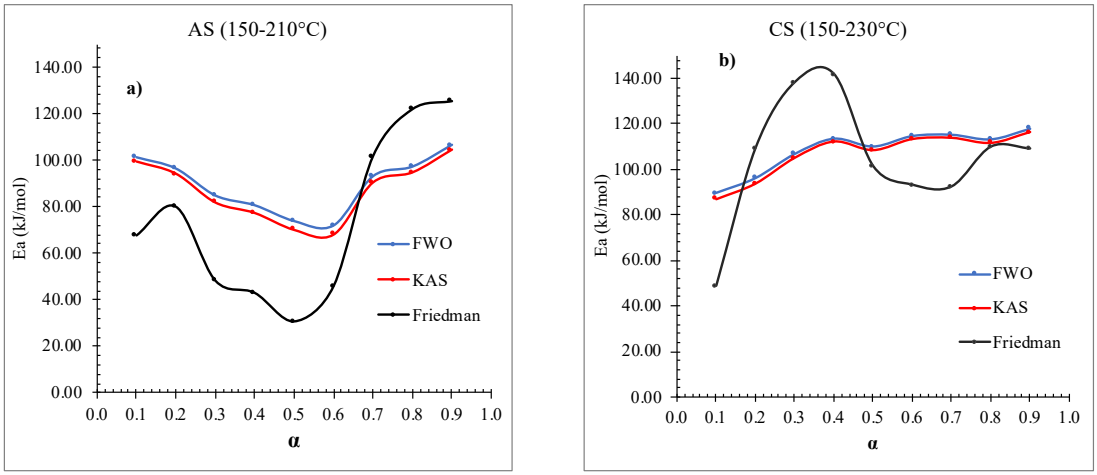

Figure 4-33: The dependence of Eα on the degree of conversion (α) for HTC process of (a) AS and (b) CS according to FWO, KAS, and Friedman model-free kinetics methods

As in the previous one, there is also a change in the trend of Eα showing a complex multi-step mechanism reaction. The values of Eα vary from 145.28 to 210.74 kJ/mol and 245.28 to 229.95 kJ/mol for FWO and KAS, respectively. As a comparison, the FWO and KAS method was more reliably attributed to its higher R^2 values. The high Eα values obtained in this temperature zone are due to the condensation, polymerization, and aromatization reactions. This reaction occurs at higher temperatures and reaction times (Reza et al., 2014a; Sevilla and Fuertes, 2009b; Yu et al., 2008). In the same temperature range (205-245 °C), Yang et al. (2014) reported values of 226.5 kJ/mol of HTC for cellulose.

As explained above, the model-free methods can estimate the kinetic parameters; however, the information obtained is limited. As observed in **Figure 4-33** and **Figure 4-34**, there are different Eα; this shows different reaction mechanisms. Therefore, there can be a different kinetic model to explain these mechanisms. The model-fitting methods can explain the different models for each stage of conversion.

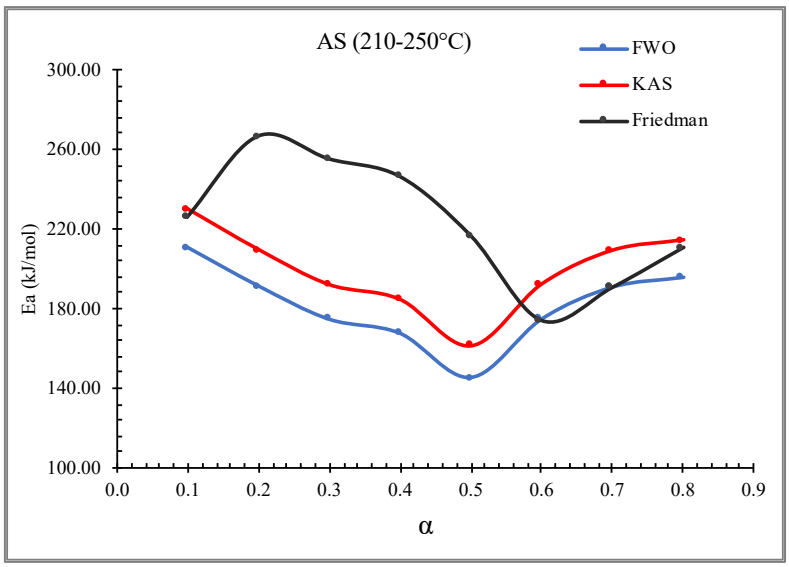

Figure 4-34: Eα values according to the degree of conversion (α) for HTC process of AS from 210 °C to 250 ºC according to the FWO and KAS methods.

4.2.4.5.2. *Model-fitting method*

The model-fitting method applied in this study was the Coats-Redfern method; this method enabled the determination of the kinetic parameters, i.e., activation energy and kinetic model (g(α)). Based on the highest correlation coefficients obtained from these plots. In **Table 4-8**, the average activation energy of different heating rates is displayed to identify the kinetic reaction model of HTC for AS and CS. As shown in the table, the Eα value determined is somewhat mildly variable when changing the reaction model. The model-fitting method is adopted to evaluate the validity of the model-free method and provide the most suitable reaction model for the decomposition of biomass (Dhaundiyal et al., 2018). In **Table 4-8**, it can be observed that the average Ea computed at different models by the model-fitting method has shown an appreciable variation from the model-free method. Two main hypotheses explain the inconsistency between the model-free and model-fitting methods. The first the existence of multi-reaction mechanisms for thermal decomposition of biomass, with different Ea values, as the contribution of these steps to the overall decomposition rate is influenced by temperature and range of conversion (Dhaundiyal et al., 2018; Yao et al., 2020).

The second hypothesis, unlike the model-free method, which is based on the conversion and heating rate, the model-fitting method depends on conversion and temperature. As mentioned earlier, the choice of f(α) depends on the reaction model used. In most biomass thermal

degradation works in literature, the chosen kinetic model is the reaction first order (f(α)=1- α), even if each phase could be described as a different model. In this case, if the mean value of Ea for different heating rates at a specified conversion range based upon one particular model is most close to the value by the model-free methods, in addition to the high correlation coefficients (R^2), then this model may dominate the reactions in this range (Chen et al., 2017; Pan et al., 2018). The calculated Eα for AS and CS at different heating rates is shown in **Figure 4-35** and **Figure 4-36**. It can be seen in **Figure 4-35** that for the reaction order model series, the estimated average value of Eα for the cases of the three heating rates varies from 148.8 kJ/mol to 292.87kJ/mol. None of the estimated average Eα based upon this series reaction model is close to 89.61 kJ/mol. Although higher correlation values are obtained for this model series (R^2>0.968), the Ea values obtained are much greater than the free model values. For the nucleation model series (power-law), the estimated average value of Eα varies from 19.86 kJ/mol to 120.94 kJ/mol). None of the estimated average activation energy calculated by the reaction model in this series is close to 89.61 kJ/mol.

The case is similar to the geometrical contraction models series and diffusion models series. However, the high correlation coefficients in random nucleation (Avrami-Erofeev (1)) and its similarity of Ea values with model-free methods for AS in the temperature between 150 and 210 ºC indicate that the HTC kinetics of AS follows a random nucleation model (g(α) = [-ln (1- α)]2/3) in this temperature range. The kinetic transformations of Avarami-Erofeev models usually follow a characteristic sigmoidal profile (S-shape) where the transformation rates are low at the beginning and the end of the transformation but rapid in between; this explains the shape of the curve in **Figure 4-28a**. A similar observation was reported by Álvarez-Murillo et al. (2016) in the HTC process for the cellulose decomposition curve. However, for CS in the temperature range between 150 and 230°C, the model best describes the reaction order model's kinetics reaction (**Figure 4-36**). The reaction order model series, especially first order (R1) reaction model (g(α)=-ln (1- α)), the estimated average value of Ea (105.67 kJ/mol) close to the best values obtained by the model-free methods (108.58kJ/mol, as shown in **Table 4-7**).

In the second zone (210 to 250°C) corresponding to increase in Y_{HC} for AS (**Figure 4-37**), as in the case of CS, the nucleation model series, diffusional model series, and contracting geometry model series, none of the estimated average activation energies based on these reaction models are close to the best values obtained by the model-free methods (199.12kJ/mol, **Table 4-7**).

However, for the first-order reaction model (R1), the estimated average value of Ea varies from 199.26 kJ/mol to 255.65 kJ/mol, similar to the model-free value methods.

Table 4-8: Kinetic parameters of AS determined by model-fitting method in HTC process for AS and CS

	AS				CS	
	150-210°C		210-250°C		150-230°C	
Model-Symbols	Ea_{mean} (kJ/mol)	R^2_{mean}	Ea_{mean} (kJ/mol)	R^2_{mean}	Ea_{mean} (kJ/mol)	R^2_{mean}
R1	148.84±4.93	0.968	**230.96±28.84**	**0.916**	**105.67±3.46**	**0.964**
R2	212.95±5.53	0.988	330.30±37.72	0.937	153.26±5.72	0.994
R3	292.87±6.57	0.977	453.89±48.76	0.928	212.71±8.60	0.990
R4	178.58±5.19	0.983	277.12±32.98	0.933	127.73±4.50	0.985
D1	223.07±8.94	0.909	329.16±44.61	0.853	152.11±4.04	0.896
D2	249.83±9.26	0.931	367.69±48.32	0.877	170.13±4.81	0.920
D3	263.91±9.55	0.953	417.00±52.85	0.902	193.44±5.86	0.947
D4	245.84±9.35	0.939	383.89±49.81	0.887	177.78±5.15	0.930
P1	120.94±6.70	0.907	244.76±33.45	0.850	112.22±3.01	0.892
P2	41.73±2.22	0.888	75.96±11.14	0.831	32.44±0.94	0.860
P3	26.39±1.48	0.870	47.83±7.42	0.813	19.14±0.60	0.827
P4	19.86±1.10	0.847	33.76±5.56	0.794	12.49±0.42	0.783
A1	**87.84±3.28**	**0.966**	151.16±19.22	0.913	67.96±2.28	0.961
A2	61.79±2.46	0.964	111.26±14.41	0.910	49.11±1.68	0.958
A3	40.18±1.64	0.960	71.36±9.60	0.903	30.25±1.09	0.951
A4	54.31±1.23	0.955	51.41±7.20	0.896	20.83±0.79	0.942
A5	137.79±2.32	0.903	161.50±16.08	0.870	73.48±3.65	0.924
A6	212.11±4.59	0.869	331.44±32.16	0.906	154.41±7.40	0.935
F1	41.73±2.22	0.888	75.96±11.14	0.831	32.44±0.94	0.860
F2	29.59±1.48	0.870	47.83±7.42	0.813	19.14±0.60	0.827

The first-order reaction model may be the most appropriate model to express the HTC process of AS in this temperature range.

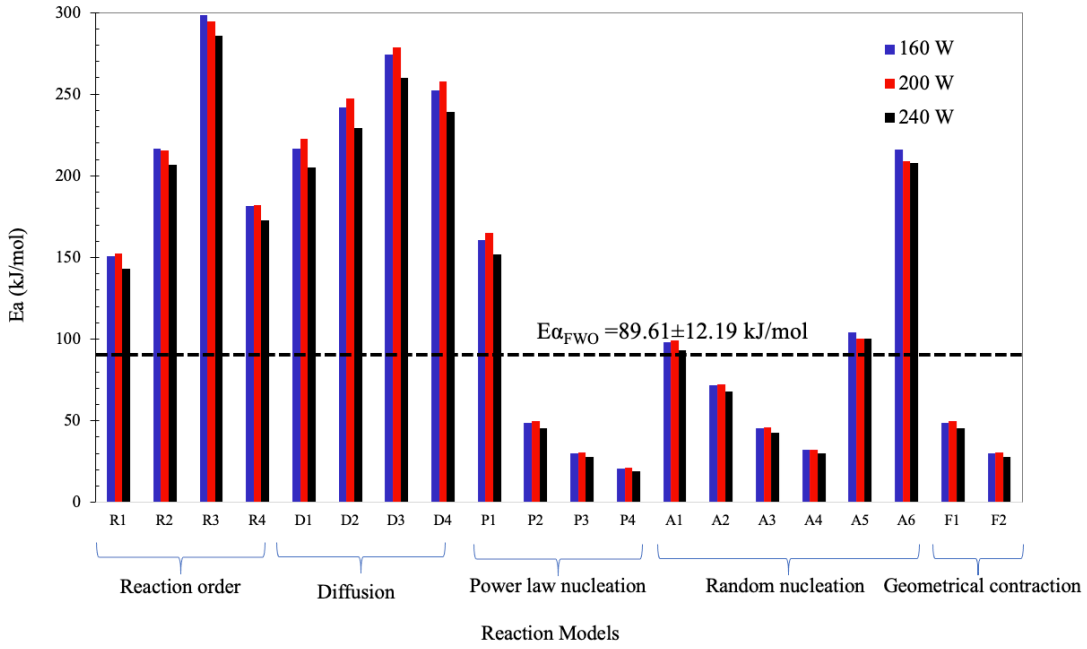

Figure 4-35: Comparison of kinetic parameters from model-fitting methods for AS of temperature between 150 and 210ºC

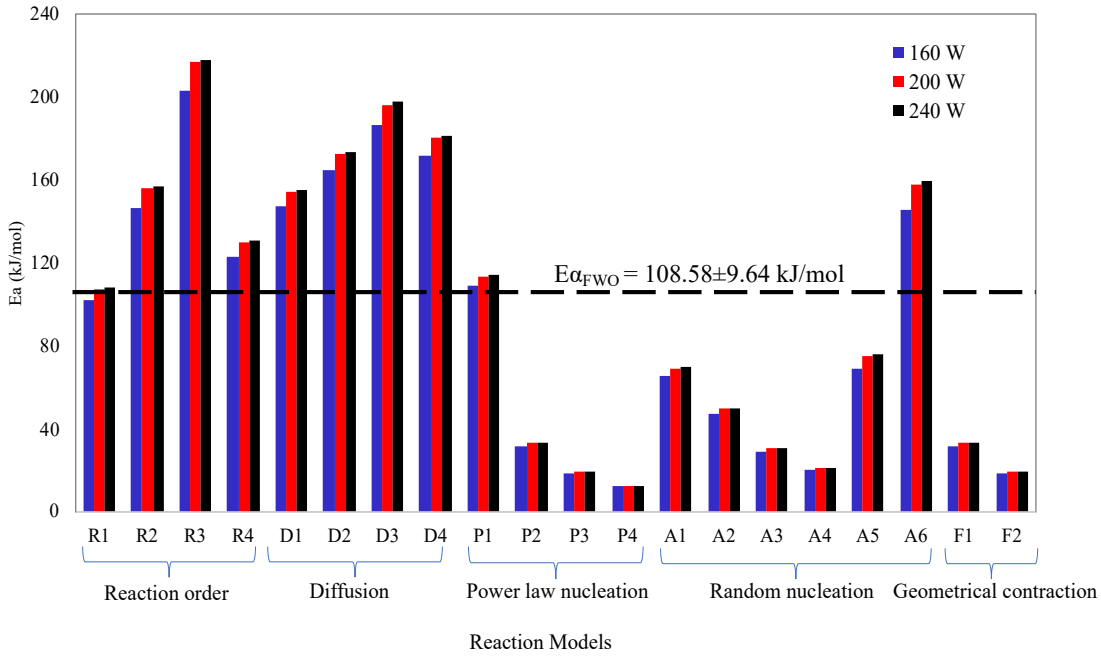

Figure 4-36: Comparison of kinetic parameters from model-fitting methods for CS of temperature between 150 and 230ºC

Although model-free methods were generally regarded as reliable ones, they can calculate both Ea and A values. However, this method is based on supposed first-order reaction models, and the thermal decomposition can follow different reaction models, which are not necessarily first-order model reactions, as demonstrated for AS between 150 and 210 ºC. On the other hand,

model-fitting methods have enabled the determination of the kinetic model (g(α)), also activation energy (Ea), but any list of the model-fitting method is certainly incomplete, and it is entirely possible that the studied process is not described by any of them (Cai et al., 2018). Moreover, this method depends on the temperature and range of conversion. Consequently, it was recommended that model-fitting methods and model-free methods support each other to investigate the HTC mechanism.

Therefore, according to comparing the activation energy obtained by the model-free and model-fitting methods, the random nucleation (Avrami-Erofeev (1)) model may be considered the most suitable model to characterize the HTC of AS in the range from 150 to 210 °C. Simultaneously, for a temperature between 210 and 250 ºC, it follows a first-order reaction model. For CS, the order reaction model is the most appropriate model to express the HTC process.

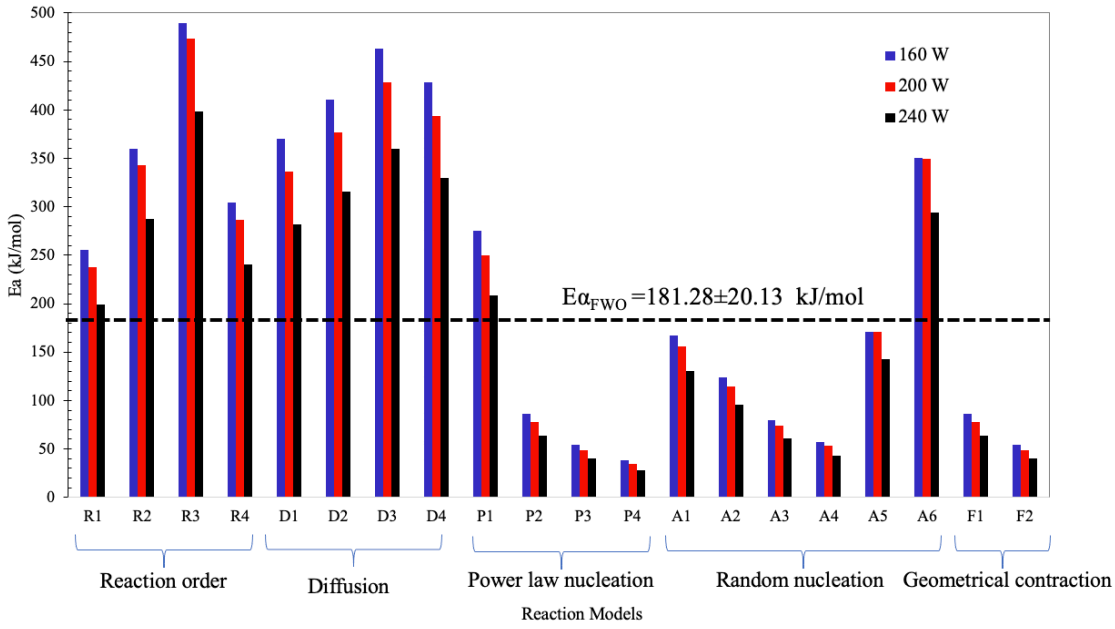

Figure 4-37: Comparison of kinetic parameters from model-fitting methods for AS of temperature between 210 and 250ºC

4.2.5. Higher heating value of biomasses and hydrochars

HTC has been investigated to produce hydrochar, a solid material rich in carbon (55–74% carbon), stable, a lignite-like material that is characterized by a high heating value (21.1–30.6 MJ/kg) (Heidari et al., 2018; Hitzl et al., 2015; Xiao et al., 2012). The high energy content of hydrochar makes it more attractive for use as an energy source.

The HHV of the hydrochar is an important index to evaluate the performance of the hydrothermal carbonization, so the HHV value of the hydrochars produced was determined. **Figure 4-38** shows the HHV of hydrochars of AS, ASB, CS, and CEL obtained in a range of temperatures from 150 to 250 °C. **Figure 4-38** shown the strong effect of temperature on the energy densification of these hydrochars. The hydrochars obtained at the lowest temperatures (150-170 °C) showed a modest increase of HHV in all biomasses. At HTC temperature from 170 to 250 °C, the HHV values of hydrochars increased from 19.3 to 25.81 MJ/kg for AS, 17.24 to 22.54 MJ/kg for ASB, 23.18 to 32.27 MJ/kg for CS, and 16.75 to 24.55 MJ/kg for CEL. These increases correspond to energetic densification of 33.74, 30.72, 39.93 and 46.61% of AS, ASB, CS and CEL, respectively. The increase in energy content demonstrates that the HTC process is an effective way to densify biomass energy

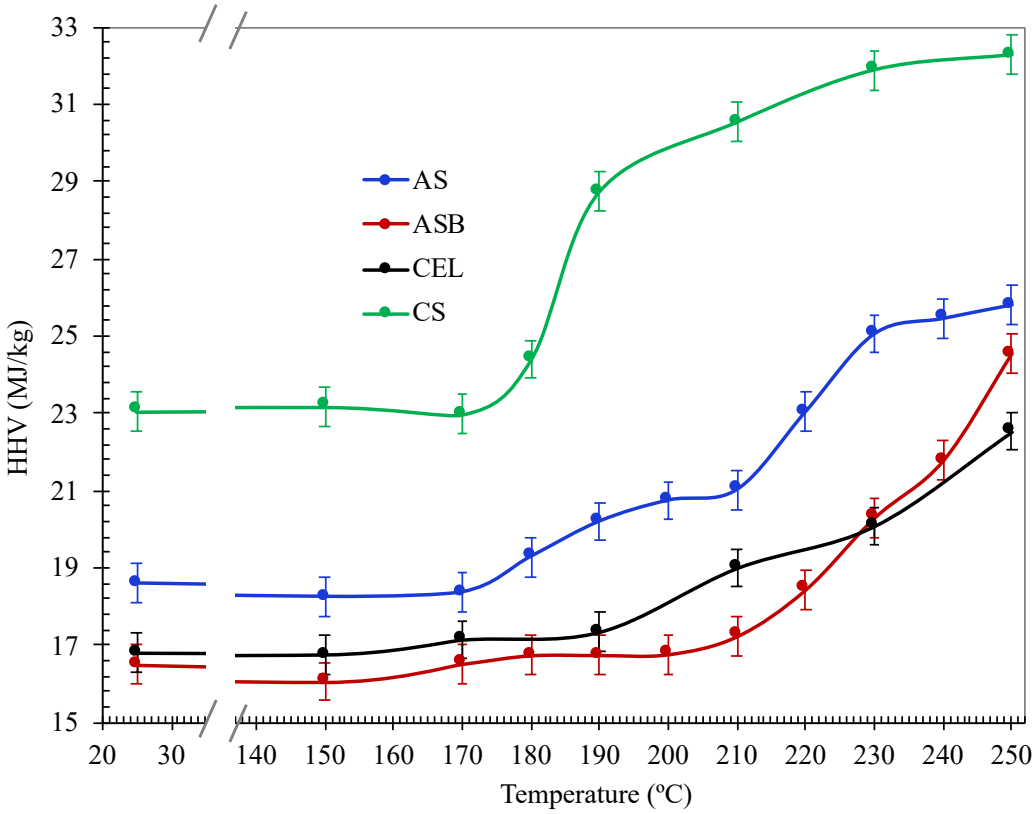

Figure 4-38. Effect of temperature on HHV of hydrochars

The HHV of these hydrochars could be compared with some commercial coals such as Northumberland Anth. Coal (24.7 MJ /kg), German Braunkohole lignite (25.10 MJ/kg), and Jhanjra Bonbahal Seam Coal (24.1 MJ /kg) (Ben and Ragauskas, 2012; Channiwala and Parikh, 2002). Similar results were reported by Yang et al. (2015) for HTC of husks of nuts from Carya Cathayensis, where HHV values increased from 22 to 28.2 MJ/kg at temperatures from 180 to

260 °C. The increase in HHV is due to dehydration and decarboxylation reactions due to a decrease in oxygen content.

4.2.6. Analysis of the main products in the HTC liquid phase.

Generally, the liquid obtained during the biomass HTC process is complex and rich in organic compounds. Due to the difficulty of identifying and quantify all of the compounds in the liquid phase, an HTC liquid sample first analyzed in a GC–MS to identify the main components. The results obtained by GC-MS showed many organic compounds in biocrude; this large number of compounds identified by GC-MS makes it difficult to quantify each of these compounds. In order to quantify the compounds in the liquid phase, the compounds were selected based on their stability and also the studies carried out in the literature on the main compounds in biocrude (Reza et al., 2014b; Reza et al., 2013; Usman et al., 2019). The main compounds followed during the HTC were: total sugars, acids (formic, lactic, and acetic), furfural, 5-HMF, and polyphenols. These compounds were quantified using HPLC and spectrophotometry.

The biomasses used to study this part were AS, ASB and CEL.

4.2.6.1. *Quantification of main compounds in biocrude produced*

The effects of HTC reaction temperature on the concentrations of the main intermediate products in biocrude are illustrated in **Figure 4-39** and **Figure 4-40**.

Figure 4-39a depicts the TOC content as a measure of total organic load in the liquid phase. The HTC liquids of the three biomasses lead to a TOC between 0.4 and 17.31 g/L under the applied HTC conditions. The HTC liquid of AS and ASB exhibit a significant increase of the TOC concentrations in the temperature range between 150 and 210 °C. The increase in TOC in this temperature range is related to the decomposition of hemicellulose. The highest TOC contents obtained are 12.4 g/L and 11.92 g/L for AS and ASB, respectively. These maxima occur at 190 ºC and represent 27.07 % and 31.38 % of the feedstock carbon. The decrease of TOC for AS samples in the temperature range between 210 to 250 ºC is related to the formation of secondary hydrochar. The small decrease for TOC in the ASB sample between 210-230 ºC is related to the initial decomposition of oxygenated compounds in the AB cellulosic structure. From 250 °C, an increase of TOC in ASB is observed due to cellulose decomposition. In the case of CEL, a significant increase in TOC was observed between 210 and 250 ºC corresponding to the cellulose decomposition temperature during the HTC process. The TOC of the runs at 250 °C represents about 41.82% of the feedstock carbon.

In the liquid fractions obtained in all biomasses, there are considerable amounts of individual compounds of sugars, organic acids, and furans. The sugars are mainly composed of pentose and hexose sugars, including xylose, glucose, fructose, mannose, and galactose. These sugars are obtained from the hydrolysis reactions of cellulose and hemicellulose. Also, a significant quantity of organic acids (lactic acid, formic acid, and acetic) is present in the HTC liquids.

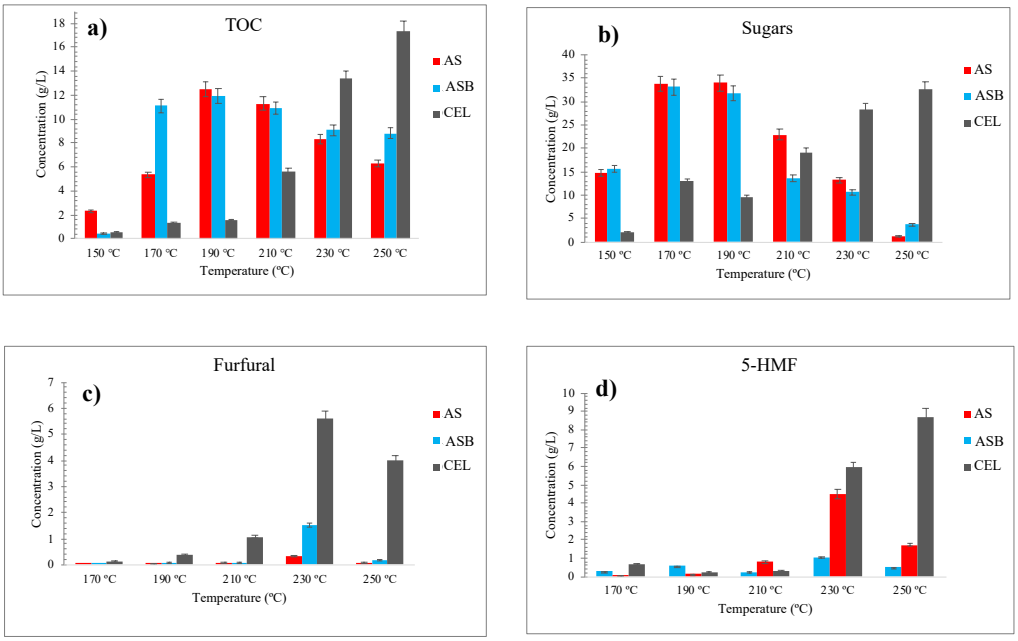

Figure 4-39. Effect of temperature on the main components in the liquid phases during HTC of the 3 biomasses: (a) TOC; (b) Sugars; (c) Furfural; (d) 5-HMF. (means and standard deviations, n = 3).

Lactic acid is produced by the decomposition of glucose from hemicelluloses. Formic acid comes from the oxidation of glucose and xylose. Acetic acid is one of the decomposition products of the monomeric sugars of hemicellulose (Sánchez et al., 2012; Sánchez et al., 2014). Additionally, aldehydes (furans) were detected in the HTC liquids, mainly 5-HMF and furfural produced due to dehydration of the sugars (Funke and Ziegler, 2010; Hoekman et al., 2011). Total sugar concentrations are shown in **Figure 4-39b.** As can be seen, the values of the concentrations change significantly within the range of temperatures studied. However, the maximum concentration of sugar is similar (33.3±0.69 g/L). The concentrations of total sugars are higher for AS and ASB at lower temperatures between 170 and 190 ºC. The increase in sugar concentrations at this temperature is due to the decomposition of hemicellulose.

The highest total sugar concentrations in the CEL sample are obtained at temperatures above 230 ºC. These sugars are subsequently transformed into organic acids and furfural, and 5-HMF

for dehydration reaction as reported by Hoekman et al. (2013). **Figure 4-39c-d** presents the contents of furfural and 5- HMF, known as the main HTC intermediates product (Becker et al., 2014). The variation of the concentration of these compounds with an increase in HTC temperature reflects the rapid formation of furfural and HMF after hydrolysis of cellulose and hemicellulose and dehydration of the resulting sugars (hexoses and pentoses), followed by a decrease due to transformation to biocrude and organic acids and, subsequently, into carbonaceous polymers, as proposed in the literature (Becker et al., 2014; Funke and Ziegler, 2010). The Furfural and HMF reach their maximum concentration at 230 °C for AS and ASB, while for CEL, the maximum concentration of furfural was obtained at 230 ºC and HMF at 250 ºC. The maximum furfural and 5-HMF concentrations were 5.5±0.1 g/L and 8.7±0.23 g/L, respectively, and they were produced for CEL at 230 and 250 ºC as shown in **Figure 4-39c-d**.

AS and ASB present maximum furfural and HMF concentrations significantly lower than CEL. The respective sources of sugars can explain these during HTC. The concentrations of furfural and 5-HMF were reduced at high temperatures, in part by polymerization to form secondary hydrochar, (Reza et al., 2014a) in another part by dehydration to produce organic acid (Funke and Ziegler, 2010; Hoekman et al., 2011). The concentrations of the acids are shown in **Figure 4-40a-c**.

One of the main intermediates formed during the HTC process are mixed organic acids from the degradation of glucose and the dehydration of furfural and 5-HMF. The main acids formed are acetic, lactic, and formic acids. Moreover, levulinic acid can also be produced from the rehydration of 5-HMF (Oh et al., 2015) and fumaric acid can be formed from furfural oxidation (Araji et al., 2017). Formic and acetic acid concentrations increase gradually with an increase in temperature up to 230 ºC, then decrease for AS and ASB at 250 ºC as shown in **Figure 4-40a-b**. In fact, at the 230 ºC, AS and ASB aqueous phase exhibit their highest values of formic and acetic acids. The maximum concentrations of formic acids are 11.93 g/L and 9.24 g/L for AS and ASB, respectively, while for acetic acid, the maximum concentrations were 13.01 g/L and 9.23 g/L for AS and ASB, respectively. For lactic acid, the decreasing trend was observed with an increase in temperature, the maximum concentrations of lactic acid are obtained at 190 °C and they are 6.75 g/L and 9.01 g/L for ASB and CEL, respectively. However, for AS, the maximum lactic acid concentration is 4.49 g/L, and it is obtained at 230 ºC, as shown in **Figure 4-40c**.

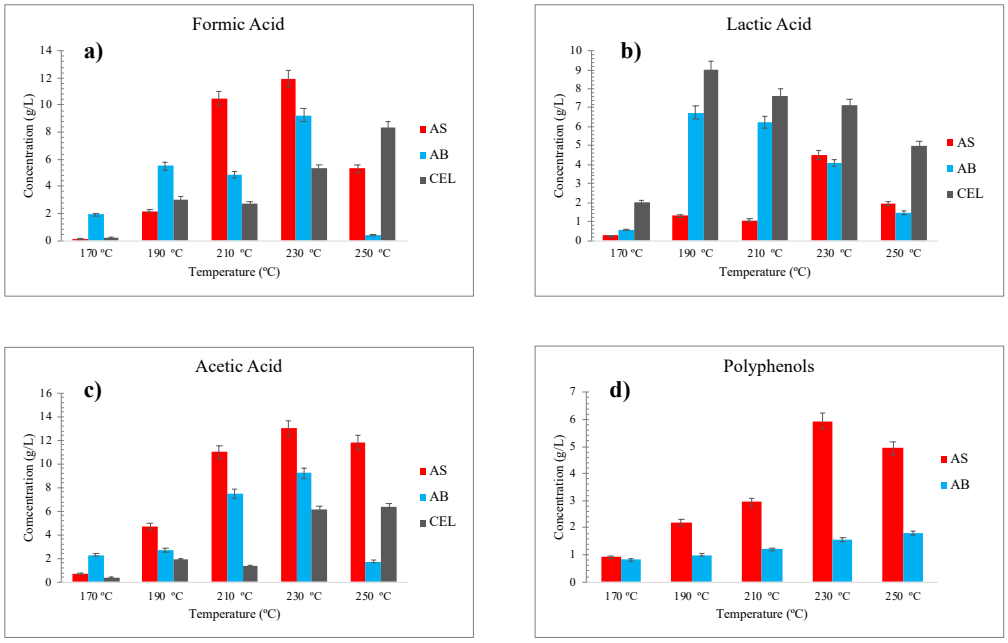

Figure 4-40. Effect of temperature on the main components in biocrude during HTC of the 3 biomasses (means and standard deviations, n = 3): (a) Formic acid; (b) Lactic acid; (c) Acetic acid; (d) Polyphenols.

The organic acids are transformed into gases by decarboxylation reactions. This explains the decrease in organic acids concentrations with an increase in HTC temperature. As it is known, as the temperature increases, the gas mass yield increases.

A low quantity of polyphenolic compounds is formed for ASB by partial lignin depolymerization, such as phenol, gallic acid, p-cresol, catechol, vanillin, guaiacol and so forth (Sasaki and Goto, 2008). **Figure 4-40d** shows the maximum concentration of polyphenols produced for AS and it is 5.9±0.4 g/L due to its high lignin content. Phenols are products of the degradation of unstable ether bonds connecting lignin monomers to hemicellulose under hydrothermal conditions. The influence of holding time on the stability of intermediate compounds during HTC of AS is presented in **Figure 4-41** to **Figure 4-47**.

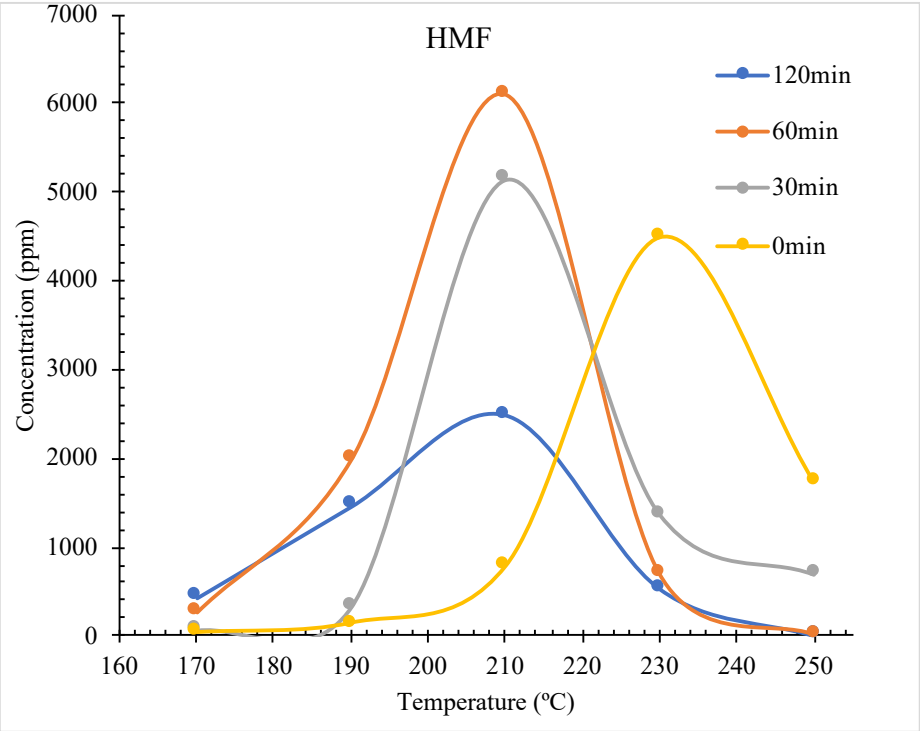

Figure 4-41: The influence of holding time on the stability of 5-HMF in HTC of AS

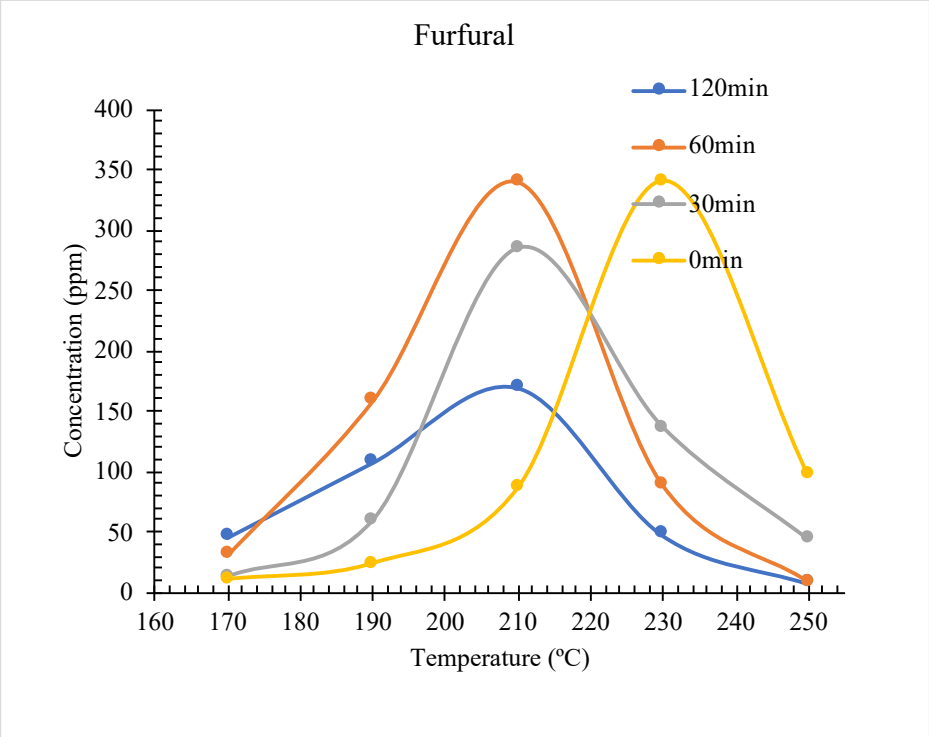

Figure 4-42: The influence of holding time on the stability of furfural in HTC of AS

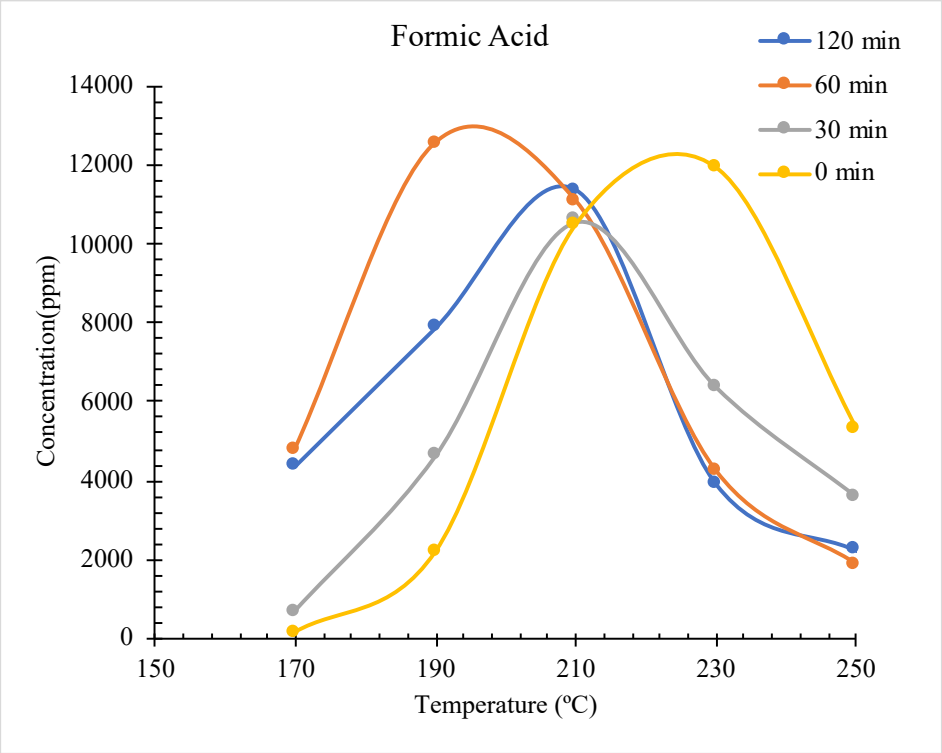

Figure 4-43: The influence of holding time on the stability of formic acid in HTC of AS

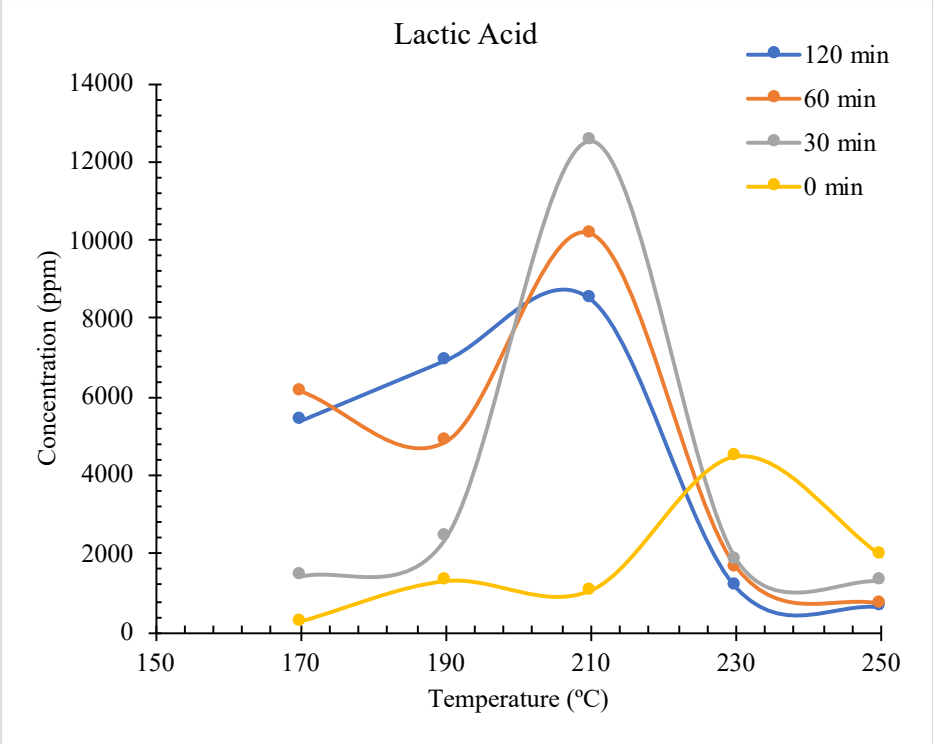

Figure 4-44: The influence of holding time on the stability of lactic acid in HTC of AS

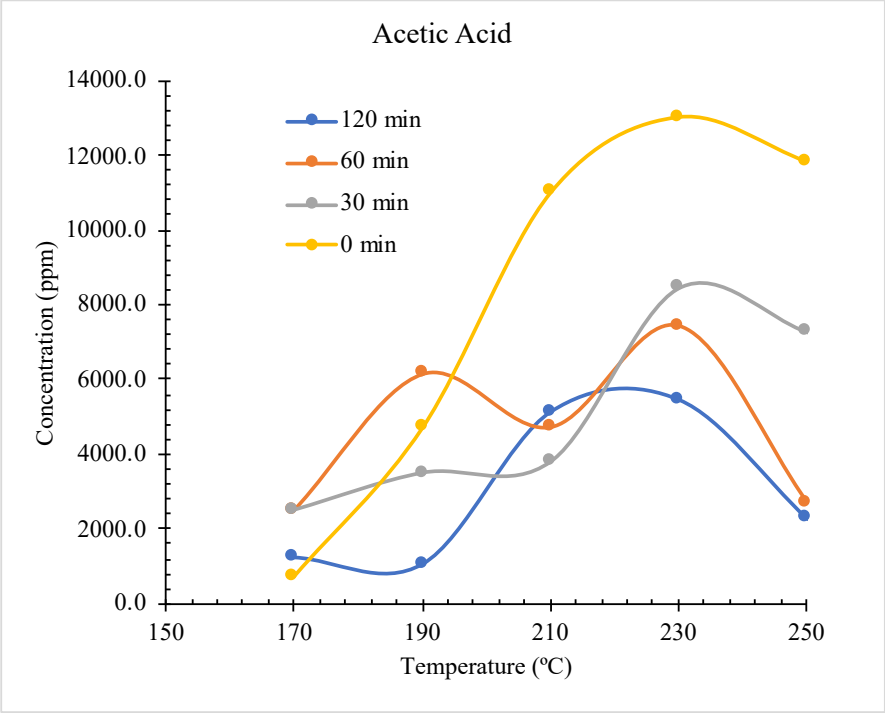

Figure 4-45: The influence of holding time on the stability of formic acid in HTC of AS

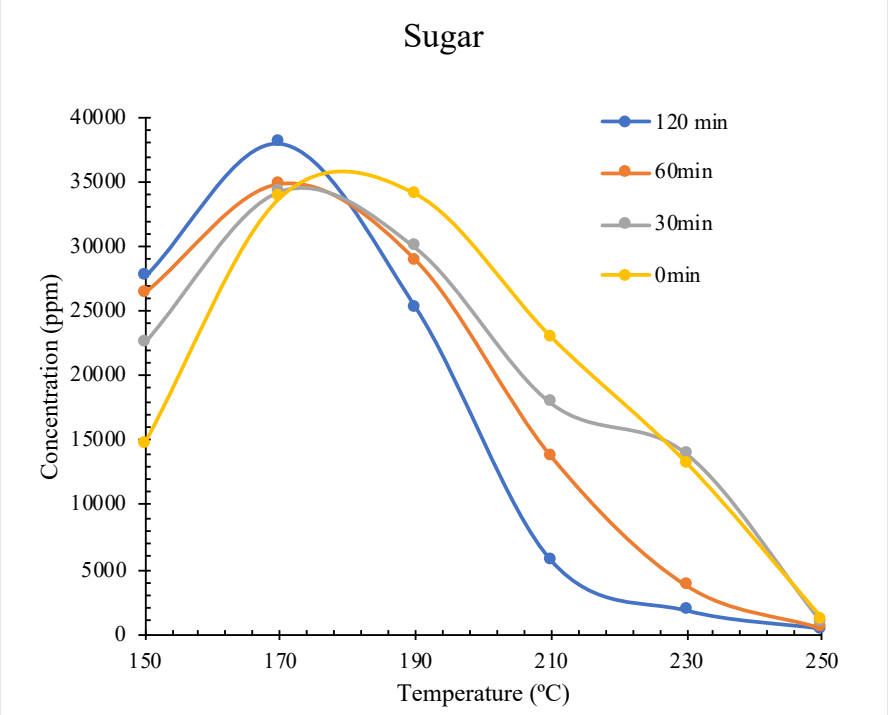

Figure 4-46: The influence of holding time on the stability of sugar in HTC of AS

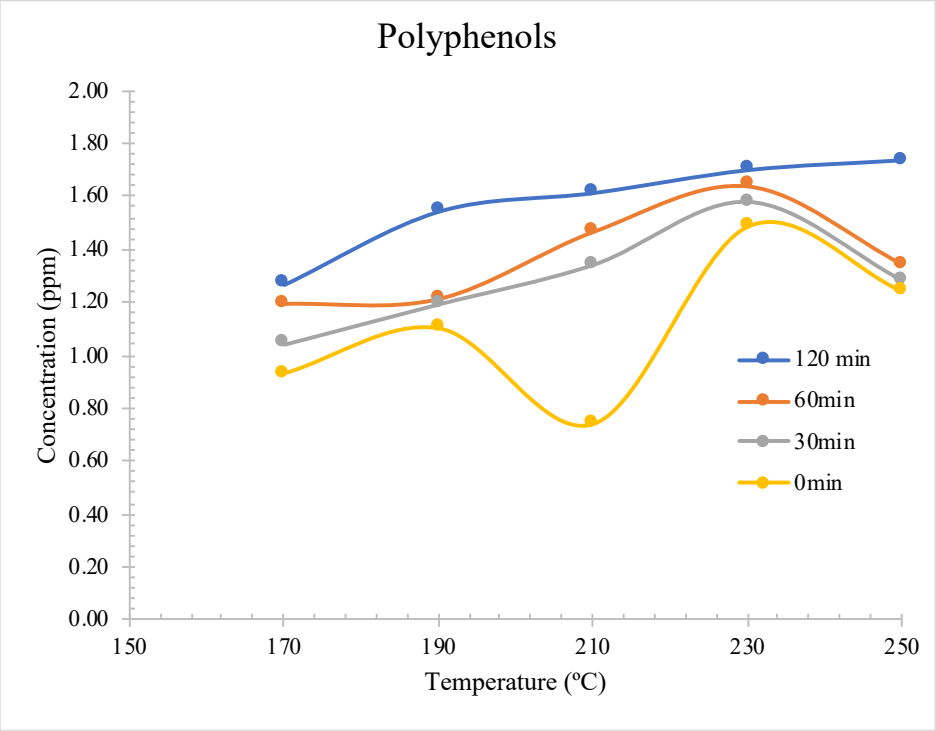

Figure 4-47: The influence of holding time on the stability of polyphenols in HTC of AS

4.2.7. Effect of biomass-to-water ratio and heat of HTC reaction

4.2.7.1. *Temperature profiles inside the HTC reactor*

Temperature or heat transfer is the main factor that controls the reactions in the HTC process and improves biomass conversion efficiency by providing more energy for breaking the intermolecular bonds in the biomass (Heidari et al., 2019a; Nakason et al., 2018b). To study the effect of the biomass-to-water ratio on heat transfer, AS was used as biomass, and HTC experiments were carried out under stirring conditions of 540 rpm to obtain a uniform temperature inside the reactor, power supplied in the reactor of 120W, and particle diameters between 2.5 and 4 mm.

Tests were performed with different biomass-to-water ratios (1/10, 1/8, 1/6, and 1/4) under the same operating conditions (reaction time, power supplied to the reactor, and the volume occupied inside the reactor). The temperature profiles inside the reactor for each of the experiments is shown in **Figure 4-48**. The temperature profiles recorded by two thermocouples inside the batch reactor include the heating times up to the equilibrium temperature and then immediate cooling of the reactor by recirculation of cold water. The two temperatures measured were bottom temperature (T_{bottom}) and top temperature (T_{top}).

Figure 4-48a corresponds to the temperature profile of the gases produced (top) inside the reactor, while **Figure 4-48b** corresponds to the temperature profile of the liquid phase (bottom). As shown in **Figure 4-48a**, there are practically no differences between the gas temperature measured during the HTC of different biomass water ratios; all temperatures reach equilibrium at 180±3 °C. It was expected that the temperature measured in the top of the reactor would be the same since only gases or steam are measured in this part. However, there is a significant variation in temperature profiles between the water and the different biomass water ratios. When the biomass-to-water ratio is increased, the equilibrium temperature of the liquid (bottom) increases, as shown in **Figure 4-48b**.

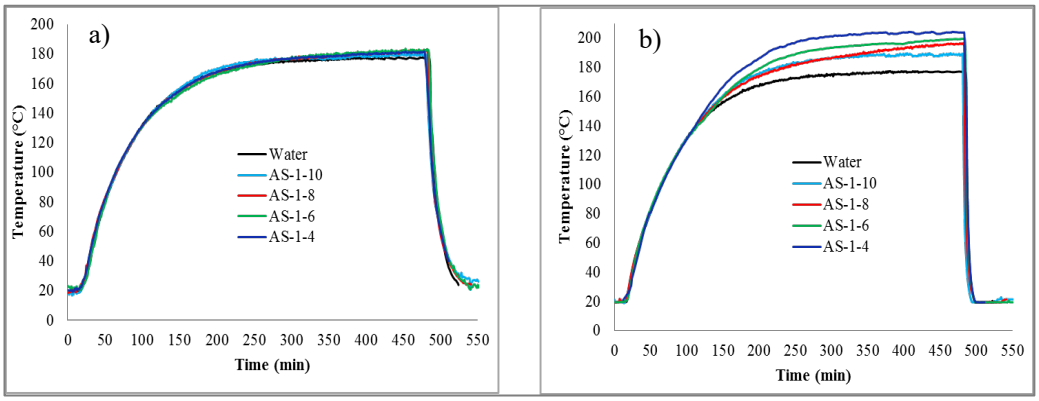

Figure 4-48: Temperature profile inside the reactor: a) T_{Top}, b) T_{Bottom} versus heating time of HTC process (pure water, B/W: 1/10, 1/8, 1/6, and 1/4).

Despite the variation of temperature between pure water and different biomass concentration inside the reactor, at the beginning of heating up to 150°C, the temperature variation is insignificant. As shown in **Figure 4-48b**, from 150°C, the variation between the temperature of pure water and the different ratios begins to be observed until the system reaches equilibrium. All experiments were carried out during the heating period of more than 8 hours to ensure that the system reached equilibrium. The temperatures in equilibrium in each experiment are presented in **Table 4-9.** All experiments reach their equilibrium temperature after 300 minutes of heating. As mentioned above, there are no significant variations in the top of the reactor (gas temperature). The most significant difference in bottom temperature between the water and biomass proportion is 26.81°C. This difference was observed between water and AS-1-4; and decreases to 12.18°C, as the ratio decreases in AS-1-10. The temperature profiles inside the reactor depend on the type and level of insulation for a reactor working in an open-loop; because the power supplied to the reactor is constant, in this case, 120 W. The temperature

profiles presented above were obtained when the reactor was insulated on the sides and bottom with cotton wool insulation (**Figure 4-3**).

Table 4-9: Equilibrium temperature reached at the top and bottom

Samples	T_{Bottom} (°C)	T_{Top} (°C)
Water	177.54	178.58
AS-1-10	189.72	179.99
AS-1-8	196.66	182.95
AS-1-6	200.35	183.52
AS-1-4	204.35	181.75

However, the upper part of the reactor is not insulated. Therefore, it was decided to insulate the upper (reactor cover) with the same type of insulation as the bottom and sides. Temperature profiles revealed that this reactor insulation could avoid an average of 20% of the heat loss. The temperatures in equilibrium after the insulation in each experiment are presented in **Table 4-10**. As in the first case (without insulation), there is no significant variation in the top temperature in the reactor, as shown in **Figure 8b).** In each experiment, the equilibrium temperature at the top of the reactor is 215°C, the same value as the equilibrium temperature at the bottom for pure water.

Table 4-10: Equilibrium temperature reached at the UP and down after insulation

Samples	T_{Bottom} (°C)	T_{Top} (°C)
Water	215.89	215.94
AS-1-10	224.14	215.32
AS-1-8	228.73	212.08
AS-1-6	231.88	215.48
AS-1-4	238.36	215.42

The most significant difference in the down temperature between water and biomass/water ratio is 22.47 °C, and it is observed between water and AS-1-4; this difference is decreasing, as the ratio decreases to 8.25 °C in AS-1-10, as shown in **Figure 4-49b).** This temperature

variation inside the reactor is due to the heat produced by the different reactions during the HTC process.

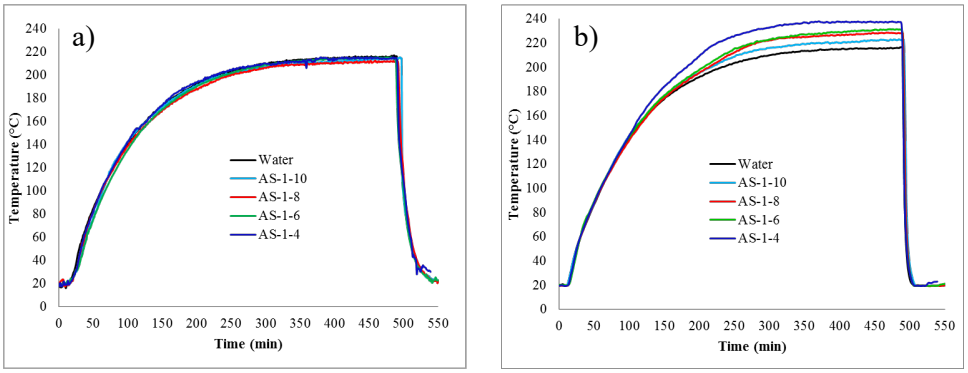

Figure 4-49: Temperature profile inside the reactor: a) T_{Top}, b) T_{Bottom} versus heating time of HTC process (pure water, B/W: 1/10, 1/8, 1/6, and 1/4) after isolation

4.2.7.2. *Heat of reaction*

Results from measured heats of reaction are summarized in **Table 4-11**. It can be observed that when the temperature rises, the heat of the reaction increases. During the first heating times to above 150 °C, the reaction is slightly endothermic; this is due mainly to the hydrolysis reaction, which is an endothermic reaction, and appears in the early stages of the HTC reaction because it has the lowest activation energy (Fang et al., 2018; Gao et al., 2016a). However, the reaction becomes more exothermic above 150 °C, due to the decarboxylation and dehydration reactions.

At 180 °C, the heat released by the chemical reaction was -2.47 MJ/kg of feed after 160 min to start heating. The highest temperature reached was 237 °C for the biomass-to-water ratio AS-1-4; this allowed to obtain a maximum heat of reaction at 215 °C, and it was -7.49 MJ/kg of feed. Similar values were reported by Merzari et al. (2018) , from -1.0 MJ/kg of feed at 180 °C, to -3.9 MJ/kg of feed at 250 °C for agave pulp, and -7.3 MJ/kg feed at 220 °C of organic fraction of municipal solid waste and residence time 3h. As explained above, the temperature inside the reactor increases with the increase of the biomass-to-water ratio; this causes a higher exothermic reaction. For example, for the AS-1-10 ratio, the total heat of reaction released during 8 hours of heating was -140.36 kJ, while at the same time, the AS-1-4 ratio released -321.36 kJ. Therefore, the higher biomass-to-water ratio favors the HTC reaction due to the heat produced. Higher HTC temperature, higher carbonization reactions. It can be concluded that the global HTC reaction is exothermic, although, in the first heating period, it appears as endothermic. The exothermic character of the HTC reaction found here agrees with that

reported by Funke and Ziegler (2011) and Merzari et al. (2018). It is also important to mention that the biomass-to-water ratio affects the heat transfer of HTC.

Table 4-11: Experimental results for the heat of reaction of hydrothermal carbonization of Avocado Stone

Temperature (°C)	Heat of reaction (MJ/kg of feed)
100	-0.06
120	+0.29
140	+0.05
160	-1.41
180	-2.47
200	-5.75
215	-7.49

In addition, the main characteristic of HTC that differentiates it from other thermochemical processes is that it is carried out under an aqueous medium. All biomass particles in HTC must be in contact with water; however, it is evident that the more water is used, the more energy is required for the process. Therefore, the water-to-biomass ratio is one of the critical parameters for designing an HTC reactor. Consequently, it is suggested that the use of water should be minimized after it is ensured that the biomass is fully submerged in the water.

4.2.7.3. *Pressure profiles inside the HTC reactor*

Usually, the reaction pressure is not controlled in the process and is autogenic with the saturation vapor pressure of water corresponding to the reaction temperature (Batidzirai et al., 2016; Kambo and Dutta, 2015). The increase of vapor pressure with temperature is a thermodynamic equilibrium property. The pressure inside the reactor rises isotropically. However, gas formation such as CO_2 and CO during decarboxylation can increase the pressure in the system beyond the water saturation pressure, as shown in **Figure 4-50**. During the first heating times up to about 120 min, the system pressure coincides with the vapor pressure of water at the variable temperature. After 120 min of heating, a pressure variation is observed with the variation of the biomass-to-water ratio. The system temperature reaches equilibrium in each experiment around 300 min of heating, as explained above. However, even though the

temperature reaches equilibrium, the pressure increases, as seen in **Figure 4-50.** The pressure increases due to gas formation: gases are formed throughout the whole duration of the process. This same effect was observed by Basso et al. (2015).

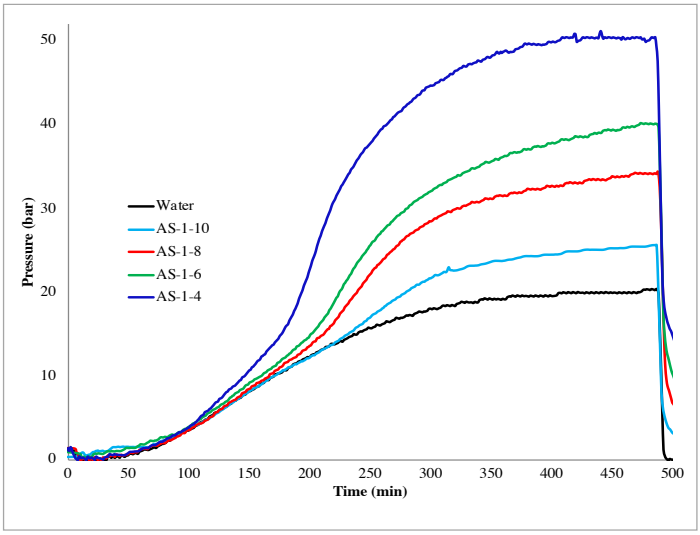

Figure 4-50: Pressure profile inside the reactor and heating time of HTC process (water, biomass-to-water ratio (B/W): 1/10, 1/8, 1/6, and 1/4).

The increase in pressure leads to the conclusion that decarboxylation is one of the primary reactions when the temperature reaches equilibrium. In **Table 4-12**, for B/W =1/4, the equilibrium temperature inside the reactor is 237 °C. At this condition, the theoretical saturation pressure of water is 31.96 bar. However, the system pressure reaches 52.03 bar; this corresponds to a 62.8% increase in the system pressure concerning the water saturation pressure. The system pressure value decreases to 4.78 % for B/W=1/10. **Table 4-12**, shows the maximum values reached for the system pressure at the equilibrium temperature and the corresponding water saturation pressure at the same temperature (P_{water}).

Table 4-12: Pressure behavior at different equilibrium temperature reached

Samples	T_{Bottom} (°C)	P_{max} (bar)	P_{water} (bar)	Pressure variation (%)
Water	215.98	21.81	21.04	-
AS-1-10	222.85	25.64	24.47	4.78
AS-1-8	228.45	35.65	27.17	31.21
AS-1-6	230.95	41.51	28.45	49.42
AS-1-4	237.40	52.03	31.96	62.80

Therefore, it is possible to have an indirect measure of the gas production during HTC by observing the pressure inside the reactor as a function of the reaction time and the volume used

for the gas. It is also possible to determine the amount of non-condensable gas produced after reactor cooling. In this sense, the amount of gas produced is determined from the system pressure after the reactor cooldown. In this regard, the amount of gas produced is determined from the system pressure after the reactor cooldown to perform a mass balance. It should be remembered that the reactor used has a total volume of 300 mL. However, the volume used for each experiment (water + biomass) was 200 mL, and the gas volume is 100 mL.

4.2.8. Gas by-products

Gas composition resulting from carbonization of biomass has not been well-explored or well-reported. The purpose of this analysis was to identify gases being produced during HTC to determine potential environmental impacts and any energy significance. The gas product was then collected using a gasbag and analyzed using micro gas chromatography (μ-GC). The results of the gas analysis of HTC produced are presented in **Table 8**. The gas produced because of carbonization is small (< 6.7%). Analysis of the HTC gas samples showed CO_2 to be the main component for all biomasses, and its concentration varies relatively little depending on the type of biomass.

Table 4-13: HTC gas composition at 250 ºC, B/W=1/10

Biomass	H_2	CH_4	CO	CO_2	Others
AS	0.14	0.20	9.75	87.25	2.66
ASB	0.36	0.00	7.80	91.85	-
CS	0.31	0.00	7.62	89.23	2.84
CEL	1.40	0.19	14.79	83.62	-

The second major gas produced is CO, a product of the decarboxylation reaction. Several traces of others gases were also identified (H_2, H_2, O_2, and CH_4). Results suggest gas composition does not vary significantly with biomass. These values are similar to results in the literature (Berge et al., 2011; Fakkaew et al., 2018; Funke et al., 2013). The gases produced by the HTC process were at most 6.7 % (w/w), i.e., around 67 g-gas/kg biomass; therefore, CO_2 emission from the HTC process could be estimated to be 20-60 g-CO_2 equivalent/kg of dry biomass. The maximum CO_2 emission from the HTC process of 0.3 g-CO_2 equivalent/g-wet biomass is previously reported, and it is lower than those expected from landfill, compost, and incineration

of the same biomass (Lu et al., 2013). Thus, the HTC process could substantially reduce greenhouse gas emissions from current treatment processes.

4.3. Conclusion

The following conclusions can be drawn from the results of the study:

- According to the analysis of total solids yield, the HTC of the AS and CS can be divided into four main zones. Initial induction period in the first zone in which the reaction rate is relatively slow (up to 160 °C), followed by a maximum loss of total solid yield up to 200 ºC for AS and 210 ºC for CS. The third zone corresponds to the stabilization zone, dominated by condensation reactions; this stability is observed from 200 to 220 °C for AS and 210 to 230 °C for CS. The last zone is the increase in the total solid mass yield. The increase of the total solid mass yield is related to the aromatization and polymerization reactions. This increase was confirmed with the Soxhlet extraction and analysis of the secondary hydrochars (tars) formed.
- The results of GC–MS analysis of the tars solution indicate that tar contains aliphatic and PAHs components. The aliphatic compounds detected were mainly characterized by long-chain alkanes and some unsaturated fatty acids. For AS, the number of PAHs increases with the increasing temperature of HTC. The most abundant PAHs were two and three-ring. However, 4-ring PAHs were detected in low numbers in hydrochars produced at 230 and 250 ºC. However, no PAHs were detected for CS.
- Hydrochar formation of AS in temperatures range between 150 and 210°C follows a random nucleation reaction mechanism (Avrami-Erofeev-1) whereas in the temperature between 210 and 250 ºC follows a first-order reaction model. The average activation energy estimated for Avrami-Erofeev-1 is 87.84±3.28 kJ/mol. The values obtained from FWO and KAS are consistent with Avrami-Erofeev-1, where the activation energies are 89.61±12.19 kJ/mol and 86.79±12.82 kJ/mol, respectively. The first-order reaction model, the average activation energy estimated for the first-order reaction model is 230.96±28.84 kJ/mol. The best values obtained for model-free were 192.97±64.64 kJ/mol and 211.42±68.07kJmol for FWO and KAS methods. Moreover, the values of activation energies at different conversions have indicated the multi-reaction scheme's existence during the HTC of AS. On the other hand, the decomposition of CS follows a first order reaction with activation energy of 105.67 kJ/mol.

- The components found in the biocrude were broadly similar in behavior, regardless of the type of biomass used. Total sugars are the first and foremost products found in biocrude at low HTC temperatures. As the temperature increases, the concentrations of sugars decrease, forming the acids, furfural, and 5-HMF.The overall HTC reaction of AS is exothermic at 160 ºC and above; the heat produced is -7.25 ±0.32MJ/kg of feed at 215 ºC. The biomass-to-water ratio has an effect on heat transfer during the HTC process. The reaction starts at 150 °C. Also, it is observed that the mass yield is more significant for the higher biomass-to-water ratio; from an energetic point of view, this acquires specific importance because the more biomass inside the reactor, the more hydrochar is obtained.

Chapter5 THERMOCHEMICAL CONVERSION OF DRY BIOMASS

The increase in fossil fuel prices, the growing energy demand globally, and the increasing emissions of CO_2, NOx, and SOx into the atmosphere are important factors contributing to the use of biomass as an alternative energy source. One of the main biomass-to-energy conversion pathways developed over the years is thermochemical conversion, namely pyrolysis, liquefaction, combustion, gasification, and so forth (Liu et al., 2017; Nsaful et al., 2013). Pyrolysis and gasification make biomass more usable, flexible fuels and high-value chemical compounds suitable for several uses, whereas burning is mostly restricted to the generation of thermal energy from this biomass. In addition, combustion, which includes oxidation into biomass to release its power via carbon dioxide, also generates harmful and unwanted gas products such as CO_2, NOx, and energy less SOx (Okoro et al., 2020).

Biomass gasification is identified as one of the most promising routes for producing renewable energy. The pyrolysis stage is the most essential in a biomass gasification process because it generates the principal products, including permanent gasses (H_2, CO, CO_2, CH_4, C_2), char, and tar (liquids), which define the quality of the finished syngas product. During this early phase, the distribution of tar and char is primarily influenced by the structural composition (cellulose, hemicellulose, and lignin) of the feedstock for biomass which releases volatiles producing tar and cargo residue when digested. Besides, these products depend on the heating rate and pyrolysis temperatures.

Lin et al. (2016b) reported that with increasing heating rate and temperature during the pyrolysis process, the char yield decreases, the gas yield increases, and the tar yield increases until it reaches a maximum value and then decreases due to the decomposition of tar compounds into light gases.

Tar is an inevitable byproduct, exists in the gaseous state in high temperature, uniformly mixed with the gas products. However, at low temperatures (< 200 °C), the tar is easily condensed and binds together water and char, blocking the gas pipeline, resulting in equipment operating difficulties (Devi et al., 2005). The tar is a complex mixture of condensable hydrocarbons (all hydrocarbons with a molecular weight higher than that of benzene), including single and multi-ring aromatic compounds along with oxygen-containing hydrocarbons and complex PAHs (Li and

Suzuki, 2009; Zeng et al., 2020). At high temperatures, cracking of these tars is eventually observed (Yan et al., 2014a).

In the pyro-gasification process, one technique for removing tar from the gasifier is the point of its formation before the start of the char gasification phase. Furthermore, the potential to minimize the tar content in the syngas before its exit from the gasifier helps to improve the quality of the syngas and thus minimize the need for costly syngas cleaning processes (Okoro et al., 2020). In addition to the gasification product distribution being dependent on the heating rate and temperature, another important factor during char gasification is the gasifying agent. Extensive studies had been reported on the gasification of char using several agents such as air gasification (Wang et al., 2008a; Zhang et al., 2015c; Zhang et al., 2017), steam gasification (Elorf et al., 2019; Jayaraman and Gökalp, 2015; Moghadam et al., 2014), oxygen gasification (Niu et al., 2014), carbon dioxide gasification (Gao et al., 2016c), supercritical water gasification (Guo et al., 2015a) and so forth. Generally, oxygen gasification, steam gasification, carbon dioxide gasification, and supercritical water gasification result in higher heating values (HHV) of syngas than air gasification. However, air gasification is the most widely studied and applied because the gasification agent (air) is cheap, the reaction process is easy, the reactor structure is straightforward (Gao et al., 2016b; Okoro et al., 2017).

The air gasification converts biomass into gaseous combustibles under controlled conditions with oxygen. It produces a mixture of gases known as synthesis gases, which can be used in power generation by gas turbines (Hai et al., 2019; Manatura et al., 2017). The producer gas contains H_2, CO, CO_2, CH_4, N_2, water vapors, tar, and other types of impurities (Hai et al., 2019). The yield of each of these gases depends mainly on gasifier type, gasification temperature, biomass feedstock type and the air to biomass ratio (ABR) or equivalent ratio (ER). Karmakar et al. (2013) studied the air gasification of rice husk in an autothermal fluidized bed gasifier to examine the influence of temperature variation from 650 to 725 °C. Their results suggested that with temperature increment, H_2 and CO were increased in the range of 17.22–18.49 % (v/v) and 24.89–26.59% (v/v), while CO_2 and CH_4 were decreased from 14.92 to 12.61% (v/v) and 2.62–1.96% (v/v). Also, the calculated lower heating value (LHV), based on experimentally obtained combustible gas composition, was in the range of 3.86-6.5 MJ/Nm^3 for the temperature between 800 to 725 °C.

Yang et al. (2006b) have investigated the use of palm oil wastes as a feedstock to produce hydrogen-rich gas via pyrolysis process in a fixed bed reactor. The total gas yield improved with increasing reactor temperature, reaching the maximum of 70% (w/w) for raw biomass sample with good portions of H_2 (33.49% (v/v)). On the other hand, Maglinao Jr et al. (2015) analyzed the heating values and gasification efficiencies of three feedstock high tonnage sorghum, beef cattle manure, and cotton gin trash in fluidized bed gasification in the temperature range of 730–790 °C and ER (0.3–0.5). They report that the comparable yields of CH_4 and CO_2 were observed in all three feedstocks. While the production of H_2 and CO were significantly affected by the biomass used during gasification. Gasification efficiency indicated that 48% (w/w) on average of the biomass energy was converted to fuel gas.

5.1. Materials and methods

5.1.1. Experimental setup and procedure.

The pyrolysis and gasification of biomasses was carried out using a Netzsch (STA 449 F3 Jupiter) thermal analyzer combined with a triple channel SRA Instruments Micro GC SOLIA 490 gas chromatograph equipped with thermal conductivity detectors (TCD). The experimental procedure was as follows. A biomass sample was placed in the ceramic crucible. Argon was used as a carrier and protective gas and 20 mL/min was set as gas flow rate. Before starting the heating program, residual air was removed inside TG using a vacuum pump, followed by increasing the protective gas flow to 100 mL/min, whereby atmospheric air was purged from the TG until the O_2, and N_2 concentrations were below 0.10 and 0.25%, respectively. A schematic diagram of the whole experimental set-up is shown in **Figure 5-1** .

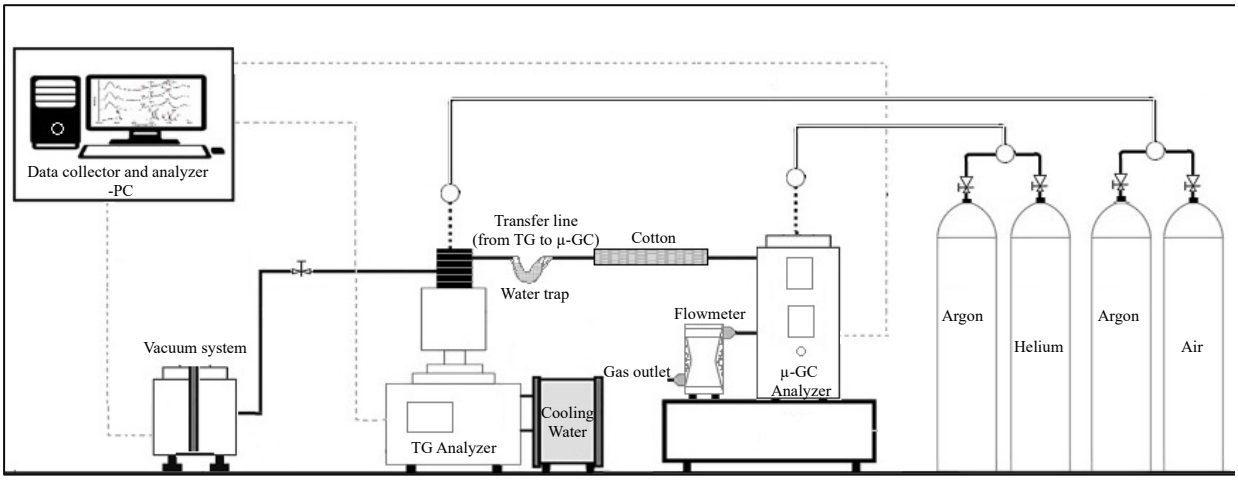

Figure 5-1: Scheme of the TG/µ-GC setup used in this work

The pyrolysis of the biomasses was carried out from ambient temperature up to 1000 ºC. In addition, the gases produced were quantified online as a function of temperature. During the gasification, biomass samples were heated from ambient temperature to 700 °C in an inert argon atmosphere to complete pyrolysis process at different heating rates (10, 20, 40 and 80) °C/min. In the gasification experiments, the air flow rates were set to 2, 3, 4, 6, 8, and 16 mL/min and air was injected from 700 ºC up to 1000 ºC. The TG system outlet is connected to the µ-GC through a line with a separation system for water (water trap), condensable organic vapors (tar), and a gas cleaning system with cotton followed by gas measuring devices (µ-GC). The outlet of µ-GC, is

connected to a flow-meter (Restek ProFLOW 6000) to measure the flow of evolved gases and determine the total volume of gases produced at normal temperature and pressure. Online gas analyses were performed to detect and quantify gaseous products during reaction, and experimental data was stored on a personal computer as a function of time. The gas generated was analyzed at time intervals of ~150s until the reactions were completed. Offline gas analyses were performed using a gasbag. All gases (pyrolysis and gasification) were recovered at the outlet of the μ-GC. They were then injected into the μ-GC for analysis after each experiment.

5.1.2. Analytical methods.

Micro gas chromatography (μ-GC) has been used to analyze qualitatively and quantitatively the gas components from biomass pyro-gasification. In this study, the gas product from cellulose and ASB pyro-gasification were analyzed using a triple channel micro-GC (SOLIA SRA instrument) with thermal conductivity detectors (TCD). Channel A with molecular sieve 5A column (MS-5A) was set at 100°C for determination of H_2, O_2, N_2, CO, and CH_4. Channel B with VAR PPU (PPU) was set at 75 °C for the determination of CO_2. Channel C with VAR Stabilwax was set at 90 °C for checking of Benzene, Toluene, Xylene, Acetone, and Methanol. The column pressure was 28 psi, carrier gas inlets were Argon and Helium. To calibrate the μ-GC, a cylinder of standard gas mixture (containing CO_2: 30 % (v/v), CH_4: 20 % (v/v), CO: 10 % (v/v), H_2: 25 % (v/v), and N_2: 10 % (v/v)) from Air Liquide was used, and the calibration was checked regularly. For O_2, the calibration was conducted using a cylinder of O_2 with 99.99% purity, mixing with argon to obtain different concentrations. Each gas sample was repeated in triplicate giving a maximum standard deviation of 2.3%. For the online analysis, the gas transfer line was flushed with argon, and for offline analysis, the gasbags were cleaned by argon purge and vacuumed before each gas sampling trial.

5.1.3. Pyrolysis and gasification reactions

The biomass gasification process is complicated; this process can be divided into the following steps: drying, devolatilization or pyrolysis, partial oxidation, combustion, and gasification of the devolatilization products (Zeng et al., 2017). **Table 5-1** shows the main reactions that occur during biomass gasification.

Table 5-1: Major gas-phase and gas-solid reactions during biomass pyro-gasification (Acar and Böke, 2019; Hai et al., 2019; Widyawati et al., 2011).

R.	Reaction name	Reactions	ΔH_R^0 (kJ/mol
Major gas-phase and gas-solid reactions during the pyrolysis of biomass			
R- 1	Drying or moisture release	wet biomass ↔ dry biomass + H_2O	>0[a]
R- 2	Devolatilization:	dry biomass → H_2 + CO + CO_2 + CH_4 + $H_2O_{(g)}$ + Tar + Char	>0[b]
R- 3	Steam Reforming: Tar	Tar $(C_nH_mO_P)$ + $(2n-p)H_2O$ ↔ nCO_2 + $\left(\frac{1}{2}m+2n-p\right)H_2$	>0[b]
R- 4	Thermal Cracking	$C_nH_m \leftrightarrow C_{n-x}H_{m-y} + H_2 + CH_4 + C$	>0[b]
R- 5	Steam reforming: CH_4	$CH_4 + H_2O \leftrightarrow CO + 3H_2$	+206.2[b]
R- 6	Water-Gas Shift	$CO + H_2O \leftrightarrow CO_2 + H_2$	-40.9[a]
	Water-Gas		
R- 7		$C + H_2O \leftrightarrow CO + H_2$	+131.3[b]
R- 8		$C + 2H_2O \leftrightarrow CO_2 + 2H_2$	+77.0[b]
R- 9	Boudouard	$C + CO_2 \leftrightarrow 2CO$	+172. 0[b]
R- 10	Methanation	$C + 2H_2 \leftrightarrow CH_4$	-87.0[a]
	Combustion		
R- 11		$C + O_2 \leftrightarrow CO_2$	-393.5[a]
R- 12		$H_2 + 0.5O_2 \leftrightarrow H_2O$	-123.1[a]
Major reactions of gasification			
	Oxidation Reactions		
R- 13		$C + O_2 \leftrightarrow CO_2$	-394. 0[a]
R- 14		$CO + 0.5O_2 \leftrightarrow CO_2$	-284. 0[a]
R- 15		$H_2 + 0.5O_2 \leftrightarrow H_2O$	-123.1[a]
R- 16		$CH_4 + 2O_2 \leftrightarrow CO_2 + H_2O$	-803.1[a]
	Carbon Reactions		
R- 17	Boudouard	$C + CO_2 \leftrightarrow 2CO$	+172. 0[b]
R- 18	Water-gas or steam	$C + H_2O \leftrightarrow CO + H_2$	+131. 0[b]
R- 19	Hydrogasification	$C + 2H_2 \leftrightarrow CH_4$	-74.8[a]
	Methanation reactions		
R- 20		$2CO + 2H_2 \leftrightarrow CH_4 + CO_2$	-247.0[a]
R- 21		$CO + 3H_2 \leftrightarrow CH_4 + H_2O$	-206.0[a]
R- 22		$CO_2 + 4H_2 \leftrightarrow CH_4 + 2H_2O$	-165.0[a]
	Steam-Reforming reactions		
R- 23		$CH_4 + H_2O \leftrightarrow CO + 3H_2$	+206. 0[b]
R- 24		$CH_4 + 0.5O_2 \leftrightarrow CO + 2H_2$	-36.0[a]

[a] Negative sign indicates the exothermic reactions.
[b] Positive sign indicates the endothermic reactions.

Pyrolysis occurs in the total absence of an external oxidizing agent, and only the heat is used to degrade feedstock. The pyrolysis occurs in three stages: (i) devolatilization to produce the main gas products (H_2, CO, CO_2, CH_4, and H_2O), volatile tar formation, and solid char formation; (ii) cracking and reforming of tar and gases; and (iii) char gasification (Ni et al., 2006; Widyawati et al., 2011). Char gasification occurs when a gasifying agent is added inside the reactor. The gasification reactions can be divided into homogeneous reactions (gas-phase reactions) and heterogeneous reactions between the char and the gases produced. Following Le Chaetlier's principle, endothermic products and exothermic reactants are favored at high temperatures. In

general, drying and devolatilization of biomass require heat, and therefore endothermic reactions are promoted.

5.1.4. Estimation of gasification performance

The performance of TGA air Pyro-gasification was investigated by calculating the lower heating value of the gas (LHVg), gas yield (Gy), cold gas efficiency (η) (Gai and Dong, 2012). The system gasifier performance was monitored by comparing the gasification process at different air to biomass ratios (ABR). The ABR is the ratio of the total air addition into the system (kg) to the total biomass feed in the system (kg) (Cao et al., 2006).

$$\mathrm{ABR} = \frac{\text{Total air addition into the system (kg)}}{\text{Total biomass feed in the system (kg)}} \quad (5\text{-}1)$$

The lower heating value of the gas (LHV_g) can be estimated by **Eq. (5-2*)*.**

$$\mathrm{LHV}_g = 0.126 \cdot \mathrm{CO} + 0.108 \cdot \mathrm{H_2} + 0.358 \cdot \mathrm{CH_4} + 0.665 \cdot \mathrm{C_nH_m} \left[\frac{\mathrm{MJ}}{\mathrm{Nm^3}}\right] \quad (5\text{-}2)$$

where CO, H_2, CH_4 and C_nH_m (C_nH_m = C_2H_2 + C_2H_4 + C_2H_6) are percentages of the volume fraction of carbon monoxide, hydrogen, and hydrocarbons in the product gas. The gas yield is calculated as the ratio of gas produced to the dry biomass.

$$\mathrm{G_y} = \frac{\mathrm{V_g}}{\mathrm{M_b}} \left[\frac{\mathrm{Nm^3}}{\mathrm{kg}}\right] \quad (5\text{-}3)$$

where Vg is the volume of gas produced (Nm^3); Mb is the mass of the dry biomass feed (kg). The pyro-gasification efficiency or process efficiency is defined by the ratio of the total amount of lower heating value of the gas to the fuel's lower heating value. It is calculated in **Eq.(5-4).**

$$\eta = \frac{\mathrm{LHV_g}}{\mathrm{LHV_f}} \cdot \mathrm{G_y} \cdot 100\ [\%] \quad (5\text{-}4)$$

The lower heating value (LHV_f) of the fuel is calculated in **Eq.**(5-5**)**

$$\mathrm{LHV_f} = 0.339 \cdot \mathrm{C} + 1.029 \cdot \mathrm{H} + 0.109 \cdot \mathrm{S} - 0.112 \cdot \mathrm{O} - 0.025 \times \mathrm{W} \left[\frac{\mathrm{MJ}}{\mathrm{kg}}\right] \quad (5\text{-}5)$$

where C, H, S, O, and W are percentages of the mass fraction of carbon, hydrogen, sulfur, oxygen, and water in the dry biomass.

5.1.5. Kinetic analysis

5.1.5.1. *Theoretical consideration*

There are several approaches to model pyrolysis and gasification processes. The simplest is the empirical model, which employs global kinetics, where the Arrhenius expression is used to correlate mass loss rates or conversion with temperature. The pyrolysis and gasification process of biomasses can be expressed as follows.

$$\text{bagasse} \xrightarrow{\text{pyrolysis}} \text{volatiles} + \text{Tar} + \text{char} \xrightarrow{\text{gasification}} \text{gases} + \text{ash} \qquad (5\text{-}6)$$

In the thermal decomposition of biomass, pyrolysis uses heat to degrade the biomass; in the absence of an external oxidizing agent (Holladay et al., 2009), the main products are mainly volatile compounds (H_2, CO, CO_2, CH_4, H_2O, so on.), along with char and Tar fractions (Ni et al., 2006). The process occurs in three stages: (i) pyrolysis to produce the main gas products, volatile tar, and solid char; (ii) cracking and reforming of tar and gases; and (iii) char gasification. During each stage, the primary products participate in multiple, interdependent secondary reactions that can alter the nature and distribution of the products (Shafizadeh, 1982). The pyrolysis of biomass produces a significant fraction of volatiles (McKendry, 2002) so secondary gas-phase and gas-solid reactions are especially important for these fuels. The most important secondary reactions are listed along with the primary pyrolysis reaction in **Table 5-1**.

The biomass reaction is a solid-state reaction. Thermal analysis techniques are used to study solid-state phenomena extensively. The mechanics of these activities are either unknown or too complex for a simple kinetic model to be defined. A general kinetic expression for the overall reaction rate of gas-solid reactions is written as follows (Fermoso et al., 2010).

$$\frac{dx}{dt} = K\left(P_g, T\right) \cdot f(x) \qquad (5\text{-}7)$$

where K (Pg, T) is the apparent reaction rate of the solid, which includes the effect of temperature (T) and the effect of the partial pressure of the gasifying agent (Pg) in the case of gasification, and f(x) describes the changes in the physical or chemical properties of the sample as the reaction proceeds. Assuming that the partial pressure of the gassing agent remains constant during the process, the apparent reaction rate of the solid depends on the temperature and can be expressed by the Arrhenius equation, which is written as.

$$K(T) = A\exp\left(\frac{-E_a}{RT}\right) \quad (5\text{-}8)$$

where A is the pre-exponential factor (min^{-1}), Ea is the activation energy (J/mol), R is the universal gas constant (8.314 J/(K.mol)), and T is the absolute temperature (K). The general expression for biomass decomposition can be summarized from the following equation (White et al., 2011):

$$\frac{dx}{dt} = K(T) \cdot f(x) = A\exp\left(\frac{-E_a}{RT}\right) \cdot f(x) \quad (5\text{-}9)$$

where x is the degree of progress of the reaction or conversion defined by

$$x = \frac{m_o - m_t}{m_o - m_f} \quad (5\text{-}10)$$

where m_t is the mass of substrate present at any time t, m_0 is the initial substrate mass, m_f is the final mass of biomass (residue and unreacted substrate) remaining after the reaction.

There are various possibilities to express the conversion function f(x) for the solid-state reactions. Most of the previous authors used the conversion function as follows (Heydari et al., 2015).

$$f(x) = (1 - x)^n \quad (5\text{-}11)$$

where n is reaction order. Combining **Eq (5-9)** and **Eq (5-11)**, the following equation is obtained

$$\frac{dx}{dt} = A\exp\left(\frac{-E_a}{RT}\right)(1 - x)^n \quad (5\text{-}12)$$

$$\frac{dx}{dt} = \beta\frac{dx}{dT} = A\exp\left(\frac{-E_a}{RT}\right)(1 - x)^n \quad (5\text{-}13)$$

where β is the linear heating rate (K/min)

Kinetic modeling has been used for a much longer time in optimization, valuation of the real-time performance of the material, and prediction of a useful lifetime. Chemists tend to develop detailed mechanistic models, while engineers prefer general models (lumped models). Most applications use global models out of necessity because it is impractical or impossible to develop strict mechanical models. Model fitting acquired a poor reputation in the thermal analysis community after it realized, a decade after other disciplines, that deriving the kinetic parameters of an assumed model from a single heating rate produced unreliable and sometimes meaningless results. In its place, advanced isoconversional methods (Vyazovkin, 2001), which have their roots in the Friedman and Ozawa-FlynnWall methods of the 1960s, have become increasingly popular (Burnham and Dinh, 2007). It is possible to obtain valid kinetic parameters by both isoconversion methods and model fits, provided that a thermal data set is used to derive the kinetic parameters (Burnham and Dinh, 2007). Isoconversional methods, sometimes referred to as "model-free" kinetic analyses, are not free of assumptions, and it is essential to understand these assumptions and the limits they impose on predictions outside the calibration range. The essential feature of isoconversional methods is that they are sequential models.

In reality, the conversion factor is defined, which transforms the conversion as a function of temperature or heating rate by providing different activation energies associated with different degrees of conversion. The reaction can be considered first order as long as the conversion step size is sufficiently small (Burnham and Dinh, 2007).

The model-free isoconversion methods provide a practical approach to treat the experimental condensed-phase kinetic data. The acquired kinetic parameters allow the processes to be modeled for temperatures different than those used in the experiments. The major advantage of the model-free analysis is that it is simple and avoids the mistakes related to the selection of a kinetic model. The differential and integral isoconversional methods give the actual values of activation parameters (Simon, 2004).

5.1.5.2. *Kinetic models for non-isothermal decomposition*

Under non-isothermal conditions where samples are heated at constant heating rates, the actual temperature can be expressed as follows.

$$T(t) = T_0 + \beta t \quad (5\text{-}14)$$

Where T0 is the initial temperature and T is the temperature at the time. Non-isothermal methods are usually standard in solid-state kinetics because they require less experimental data than isothermal methods. For non-isothermal experiments, the following expression can be considered (Kim and Eom, 2006):

$$\frac{dx}{dT} = \frac{dx}{dt} \cdot \frac{dt}{dT} \quad (5\text{-}15)$$

where $\frac{dx}{dT}$ is the non-isothermal reaction rate, $\frac{dx}{dt}$ is the isothermal reaction rate, and $\frac{dt}{dT}$ describes the inverse of the heating rate ($1/\beta$).

$$\beta \cdot \frac{dx}{dT} = A \exp\left(\frac{-E_a}{RT}\right) \cdot f(x) \quad (5\text{-}16)$$

Eq. (5-16) represents the differential form of the non-isothermal reaction rate. In this study, the data from the non-isothermal experiments are considered to calculate the kinetic parameters based on model-free methods, such as Kissinger-Akahira-Sunose (KAS), Flynn-Wall-Ozawa (FWO), and Friedman methods, and compared to analyze the thermal behavior of biomass degradation.

5.1.5.2.1. *Kissinger-Akahira-Sunose (KAS) method*

The standard **Eq. (5-16)** can be shown as follows:

$$\frac{dx}{f(x)} = \frac{A}{\beta} \exp\left(\frac{-E_a}{RT}\right) dT \quad (5\text{-}17)$$

which is integrated with the initial condition of x = 0 at T = T_0 to obtain the following expression:

$$g(x) = \int_0^x \frac{dx}{f(x)} = \frac{A}{\beta} \int_{T_0}^{T} \exp\left(-\frac{E_a}{RT}\right) dT \cong \frac{AE_a}{\beta R} \cdot p\left(\frac{E_a}{RT}\right) \quad (5\text{-}18)$$

where p is the integral function. By rearranging **Eq. (5-18)** and integrating, the following equation is obtained.

$$\ln g(x) = \ln\left(\frac{AE_a}{T}\right) - \ln p\left(\frac{E_a}{RT}\right) \quad (5\text{-}19)$$

The KAS method is based on the Coats–Redfern approximation (Coats and Redfern, 1964a) according to which:

$$p\left(\frac{E_a}{RT}\right) \cong \frac{\exp\left(\frac{E_a}{RT}\right)}{\left(\frac{E_a}{RT}\right)^2} \quad (5\text{-}20)$$

Substituting **Eq.(5-20)** to **Eq.(5-19)**, the final equation of KAS is obtained

$$\ln\left(\frac{\beta}{T^2}\right) = \ln\left(\frac{AR}{E_a g(x)}\right) - \frac{E_a}{RT} \quad (5\text{-}21)$$

where g(x) = ln(1-x) is the integral conversion function (reaction model) (Idris et al., 2010). For constant conversion, a plot of the left side of the above equation against 1/*T* at different heating rates is a straight line whose slope and intercept can evaluate the activation energy and pre-exponential factor, respectively.

5.1.5.2.2. *The Flynn-Wall-Ozawa (FWO) method*

This method is derived from the integral isoconversional method. Using Doyle's approximation (Doyle, 1961) .

$$\ln\left(p\left(\frac{E_a}{RT}\right)\right) \cong -5.331 - 1.052\frac{E_a}{RT} \quad (5\text{-}22)$$

Eq. (5-21) now can be simplified as:

$$\ln(\beta) = \ln\left(\frac{AE_a}{Rg(x)}\right) - 5.331 - 1.052\frac{E_a}{RT} \quad (5\text{-}23)$$

For a constant conversion, a plot of the natural logarithm of heating rates, ln(β), versus 1/*T* obtained from thermal curves recorded at different heating rates will be a straight line whose slope (−1.052·(*Ea*/*RT*)) gives the activation energy.

5.1.5.2.3. *Friedman method*

This method is a differential isoconversional method and it directly based on **Eq. (5-16)** whose logarithm is:

$$\ln\left(\beta\frac{dx}{dT}\right) = \ln[Af(x)] - \frac{E_a}{RT} \quad (5\text{-}24)$$

where $f(x) = (1 - x)$ it is considering a first-order reaction (considering that the conversion step size is small).

The activation energy (Ea) is determined from the slope of the plot of $\ln\left(\beta\frac{dx}{dT}\right)$ versus $1/T$ at a constant conversion value.

5.2. Results and discussion

5.2.1. Pyrolysis of biomasses: Overall product distribution

The pyrolysis temperature is important for the production of solid (char), liquid (bio-oil), and gas from biomass pyrolysis. The yields of char, bio-oil, and gas product from biomass pyrolysis are listed in **Table 5-2**. Many researches in the literature have reported that, for most lignocellulosic biomass, higher bio-oil yields are obtained with increasing temperature (Qu et al., 2011). The char content was significantly reduced from 98.5 to 25.39 wt.% for AS, 96.05 to 26.94 wt.% for ASB, 96.05 to 26.67 wt.% for CS, and 96.86 to 19.68 wt.% for CEL as the temperature was increased from 200 to 600 °C. From 600 °C onwards, the char yield decreased slightly, with a mass loss rate of less than 1 wt.%/ºC until reaching a temperature of 1000 °C. The significant mass loss is found between 200 to 600 °C. The gas yields increased with increasing temperature between 200 to 1000 °C; the maximum yields reached were 18.83 wt.% for AS, 22.43 wt.% for ASB, 15.58 wt.% for CS, and 20.32 wt.% for CEL. The major components produced during pyrolysis were the liquids; their yield is higher than the sum of the yields of gases and solids. The yields of the three products at 1000 °C are similar to those found in the literature. For example, Yang et al. (2006b) reported values of 27.1 wt.% for solid yield, 16.32 wt.% for gas yield, and ~57 wt.% for liquid yield during the pyrolysis of palm oil wastes. The temperature had a crucial effect on pyrolysis product yields. However, pyrolysis of cellulose could produce more bio-oil; pyrolysis of lignin could produce more char, while hemicellulose is also helpful for bio-oil production. Therefore, biomass with high cellulose content would produce more bio-oil (such as CEL), biomass with high lignin content will produce more char (case of CS and ASB), while AS (high hemicellulose content also produces more bio-oil). A very significant thing to consider about the distribution of biomass pyrolysis

yields is the ash content. In general, the higher the mineral content in the biomass, the lower the bio-oil yield and the higher the char yield (McKendry, 2002). Therefore, the lowest bio-oil yield is obtained from AS and CS because of their high ash content (1.9 and 6.5 wt.%, respectively). Although the lignin content in AS and CS are the lowest, their final char yields are the highest due to their high ash content

Table 5-2: Overall product distribution of biomasses pyrolysis

Temperature (ºC)	Liquid (bio-oil) (wt.%)				Solid (char) (wt.%)				Gas (wt.%)			
	AS	ASB	CS	CEL	AS	ASB	CS	CEL	AS	ASB	CS	CEL
200	4.7	1.5	3.95	3.14	95.3	98.5	96.05	96.86	0	0	0	0
400	55.42	49.15	43.23	60.92	32.54	36.97	49.1	26.17	12.04	13.88	7.67	12.91
600	58.55	54.98	61.32	65.48	25.39	26.94	26.67	16.84	16.06	18.08	12.01	17.68
1000	57.76	61.97	60.55	64.84	23.41	15.60	23.87	14.84	18.83	22.43	15.58	20.32

5.2.1.1. *Influence of pyrolysis temperature on char product*

The pyrolysis of biomass means that the chemical bonds present in the biomass structure are broken and release gases and volatile compounds as the temperature are increased. Most of these released compounds are oxygenated. Therefore, the carbon content in the char structure increases with increasing temperature. The hydrogen content of char also decreased with increasing temperature during the thermal decomposition of biomass. The main component of char was the element carbon, which had a composition of about twice that of the original. Guizani et al. (2017) reported that the analysis of the chemical composition of char showed that char becomes richer in C and poorer in H and O as the pyrolysis temperature increases. The C content increased from 47.1 mol.% for char at 500 ºC to 84 mol.% for char at 1000 ºC. Many studies in the literature report this increase in C content with increasing temperature. On the other hand, the O and H contents decreased substantially from 15.4 mol.% and 37.5 mol.% to 6.2 mol.% and 9.9 mol.% for char at 500 °C and char at 1000 °C, respectively. The decrease of O and H content in char is mainly due to dehydration and decarbonylation/decarboxylation reactions in the temperature range between 300 to 400 °C. At higher temperatures, the aromatization reaction leads to the evolution of H_2 and light molecular hydrocarbons (CH_4) so that even the H content in the char decreases and almost

no H remains at 1000 °C. However, with the temperature increase from 400 to 1000 °C, the O content remains ~10-12 wt.%, indicating that most of the oxygenated compounds volatilize at a temperature between 300 to 400 °C (Yang et al., 2006a). However, the char yield and its C, H, and O content depend on the type of biomass and its chemical content (hemicellulose, cellulose, and lignin).

The yield of char obtained from the pyrolysis of xylan (hemicellulose) remained nearly constant up to ~200 °C, then decreased with increasing temperature. In the pyrolysis of cellulose, the yield of char was kept constant up to ~300 °C, then decreasing with increasing temperature. On the other hand, the temperature does not affect lignin up to 350 °C; the char obtained from lignin pyrolysis remained high at ~350 °C, then decreases with increasing temperature (Ansari et al., 2019).

5.2.1.2. *Influence of pyrolysis temperature on bio-oil product*

The trend of the bio-oil yield of the four biomasses is similar. The yield increases with increasing temperature, reaching a maximum for AS, CS and CEL, then slightly decreases. While the bio-oil yields of ASB have an increasing trend with increasing temperature.

The increase in bio-oil yield with an increase in temperature and subsequently decrease can be explained as follows: At low pyrolysis temperature, the volatile biomass matter evaporates slowly and dominates the devolatilization or carbonization reaction. The volatile matter is released rapidly with increasing temperature; thus, a large amount of bio-oil is produced up to a specific temperature, then the cracking of the unstable components of the volatile matter results in a decrease of the bio-oil yield. The maximum bio-oil yield of AS, CS, and CEL is 58.55, 61.32, and 65.48 wt.%, respectively, which were obtained temperature at 600 ºC. On the other hand, the non-decrease in the yield of ASB show that the cracking of the unstable components of the volatile matter has not started. Comparing the overall bio-oil yield of the four biomasses indicates that the bio-oil yield of CEL was the highest and that of AS the lowest. Many studies in the literature reported similar results (Ansari et al., 2019; Kojima et al., 1991; Luo et al., 2010); the highest bio-oil yield was obtained for biomass with high cellulose content, while the lowest yield was for biomass with low cellulose and high lignin content.

A typical maximum oil yield of 65% from CEL (cellulose) is comparable with other cellulose pyrolysis studies. Kojima et al. (1991) reported a maximum bio-oil yield from cellulose pyrolysis of 63 wt.% at 400 ºC in a fluidized bed reactor. On the other hand, Luo et al. (2010) obtained a bio-oil yield of 58.6 wt.% at 450 ºC in a fixed bed reactor. At the higher temperature above 550 °C, the bio-oil yield from biomass with high cellulose content decreased faster than the bio-oil yield from biomass with high xylan (hemicellulose) content (Qu et al., 2011).

5.2.1.3. *Influence of pyrolysis temperature on gas product*

The gas yields produced during pyrolysis of the four biomasses are presented in **Table 5-2**. At lower temperatures < 200°C, no gas is produced during pyrolysis. In the temperature range between 200-400°C, gas production is evident for all biomass. The gaseous products contain mainly CO_2, CO, H_2, together with some CH_4. The production of these gases is mainly due to the following factors: In general, CO results mainly from the cracking of carbonyl (COC) and carboxyl (C=O) groups, while CO_2 is mainly released from the cracking and reforming of functional groups of carboxyl (C=O) and COOH and internal dehydration of cellulose char formation (Liu et al., 2011; Qu et al., 2011). The CH_4 formation occurred mainly by fragmentation of the side chains and cracking of the methoxy-O-CH_3 groups, especially above 400 °C. Also, CH_4 formation could be attributed to the breaking of aromatic rings of lignin (Qu et al., 2011; Yan et al., 2018). The H_2 production resulted mainly from the cracking and deformation of C=C and CH groups (Qu et al., 2011; Yang et al., 2007). Furthermore, at higher temperatures, the endothermic tar steam reforming reaction contributes to a higher hydrogen production (Zhu et al., 2018).

5.2.2. Main pathways of lignocellulosic biomass pyrolysis reactions and their products

Lignocellulosic biomass mainly consists of three components (cellulose, hemicellulose, and lignin), which have very different thermal behaviors. The biomass pyrolysis products may be considered the overall pyrolysis performance of three main components, extractives and ash. The three components of biomass are broken down during pyrolysis to produce liquid, solids, and gases. The pyrolysis products depend on the cellulose, hemicellulose and lignin content in biomass.

5.2.2.1. *Main pathways of cellulose pyrolysis reactions and their products*

The reaction pathways of cellulose pyrolysis (under controlled conditions) in a temperature range between 300-1000 ºC are shown in **Figure 5-2**. Cellulose pyrolysis starts at 300 ºC, and the main products formed are anhydrosugars (Ansari et al., 2019) (mainly Levoglucosan (LGA), Levoglucosenone (LGO), dianhydroglucopyranose (DAGP), and 1,6-anhydroglucofuranose (AGF), pyrans (Paulsen et al., 2013) (mainly 2,3-dihydro-3,5-dihydroxy-6-methyl-4H-pyran-4-one (DHMDHP) and 1,5-anhydro-4-deoxy-D-glycerohex-1-en-3-ulose (ADGH), furans (5-HMF and furfural) and char. Cellulose was converted to LGA via a concerted mechanism (225.52 kJ/mol) instead of the ionic (377.82kJ/mol) and free radical (395.39kJ/mol) pathways (Mayes and Broadbelt, 2012). This mechanism involves cleavage of glycosidic bond (preferably through the mechanism of final rupture, for temperature below 467 °C (Zhu et al., 2017), followed by a dehydration reaction (Zhou et al., 2014b). Subsequently, LGO is obtained by dehydration of LGA (287.44kJ/mol) (Assary and Curtiss, 2012). On the other hand, LGO can be formed directly from cellulose without going through an intermediate LGA route. However, Ansari et al. (2019) reported that the experimental yield of LGO does not coincide with the decrease in the yield of LGA; they also claim that the direct formation of LGO from cellulose that requires a marginally lower energy barrier (261.5 kJ/mol) than that of the intermediate LGA route (287.44kJ/mol)(Assary and Curtiss, 2012; Lu et al., 2014). In the same temperature range (300 °C), cellulose (via glucose as a cellulose substitute) can be converted to DAGP and AGF through dehydration reactions by achieving energy of 297.06 and 230.12 kJ/mol, respectively (Arora et al., 2018). The process of pyran formation (i.e., ADGH and DHMDHP) from cellulose (via cellobiose) is carried out through a multi-step mechanism of glycosylation, ring-opening/closing, and dehydration (energy limiting barrier, 246.86 kJ/mol) rather than through a concerted mechanism (267.78 kJ/mol) (Zhang et al., 2015b; Zhu et al., 2017). The cellulose (or cellobiose) can also form furan (HMF) at a temperature of approximately 300°C through the concerted mechanism of glycosidic bond cleavage and dehydration (Arora et al., 2018). The HMF formed can further degrade into other furan compounds (2-furan methanol 5-methyl furfural) by decarboxylation (259,41kJ/mol) (Zhou et al., 2014b) and deoxygenation reactions. On the other hand, HMF can also form furfural a by a deformation reaction (259.41kJ/mol) (Zhou et al., 2014b); however, Ansari et al. (2019) indicated that furfural was formed by anhydrosugars (AGF) and their

derivatives rather than the HMF pathway. As the reaction temperature increases from 300°C to 500°C, LGA can undergo secondary decomposition reactions (retro- Diels-Alder, decarbonylation, and dehydration)(Zhu et al., 2016) to form light oxygen-containing compounds such as methylglyoxal (MG), hydroxyacetone (HAA), formic acid (FA), and glyoxal (GL).

In a similar temperature range (300-500 °C), other anhydrosugars, mainly 1,6-anhydroglucofuranose (AGF) and its derivatives, are converted into (i) formic acid by Grob fragmentation (219.66 kJ/mol) and retro-aldol (152.72 kJ/mol) and (ii) furfural fragmentation reactions through ring-opening reactions (133.89-171.54 kJ/mol), cyclic Grob cracking (219.66 kJ/mol) and dehydration reaction (158.99-240.58kJ/mol) (Zhou et al., 2014b). During the glucose pyrolysis, anhydrosugars can be converted to furan compounds from the monomeric unit of cellulose (glucose) (Ansari et al., 2018). LGO from cellulose can be converted to furans (furfural and 5-methyl furfural) and light oxygen-containing compounds (formaldehyde) above 300-500°C. HMF can be decarbonylated (259.41 kmol/mol) (Zhou et al., 2014b) and deoxygenated by temperature above 300 °C to form 2-furan methanol 5-HMF and CO. Methylfurans (2-methyl furan and 2,5-dimethylfuran) can be produced between 400 and 500 ºC by secondary reactions between pyranes (ADGH and DHMDHP) from cellulose pyrolysis together with CO_2. At a temperature between 400-500 ° C, 2,5(H)-Furanone is produced directly from cellulose and can be formed by ring-opening reaction, dehydration, and enol-ketone tautomerization reactions (Zhou et al., 2014b). At temperatures above 350 °C, light oxygenated compounds are formed by the secondary decomposition reactions (ring-opening and fragmentation) of anhydrosugars, pyrans, and furans during the pyrolysis of cellulose. The compounds formed are MG, HAA, FA, and GL through secondary decomposition reactions of LGA (Zhu et al., 2016). In the same temperature range (300-500 °C), formic acid is produced from AGF and its derivatives. Also, 1,2-cyclopentanedione, 2,3-butanedione, and acetic acid are formed from the side reactions of pyranes up to the temperature of 400 °C. Above 400 °C, glyoxal, acetaldehyde, and CPHM (2-hydroxy-3-methyl-2-cyclopenten-1-one) are formed. Gases such as CO and CO_2 are produced by various pathways during cellulose pyrolysis, while char is formed from cellulose between 300 and 500 °C (Ansari et al., 2019). The charring process of cellulose starts between 380-800 °C. The structure of the cellulose residues changes drastically between 270 to 400 ºC. The conversion of pyran rings is complete for temperatures below 320 ºC (Pastorova et al., 1994). Furans begin to undergo degradation at 350 ºC and above (Pastorova et al., 1994).

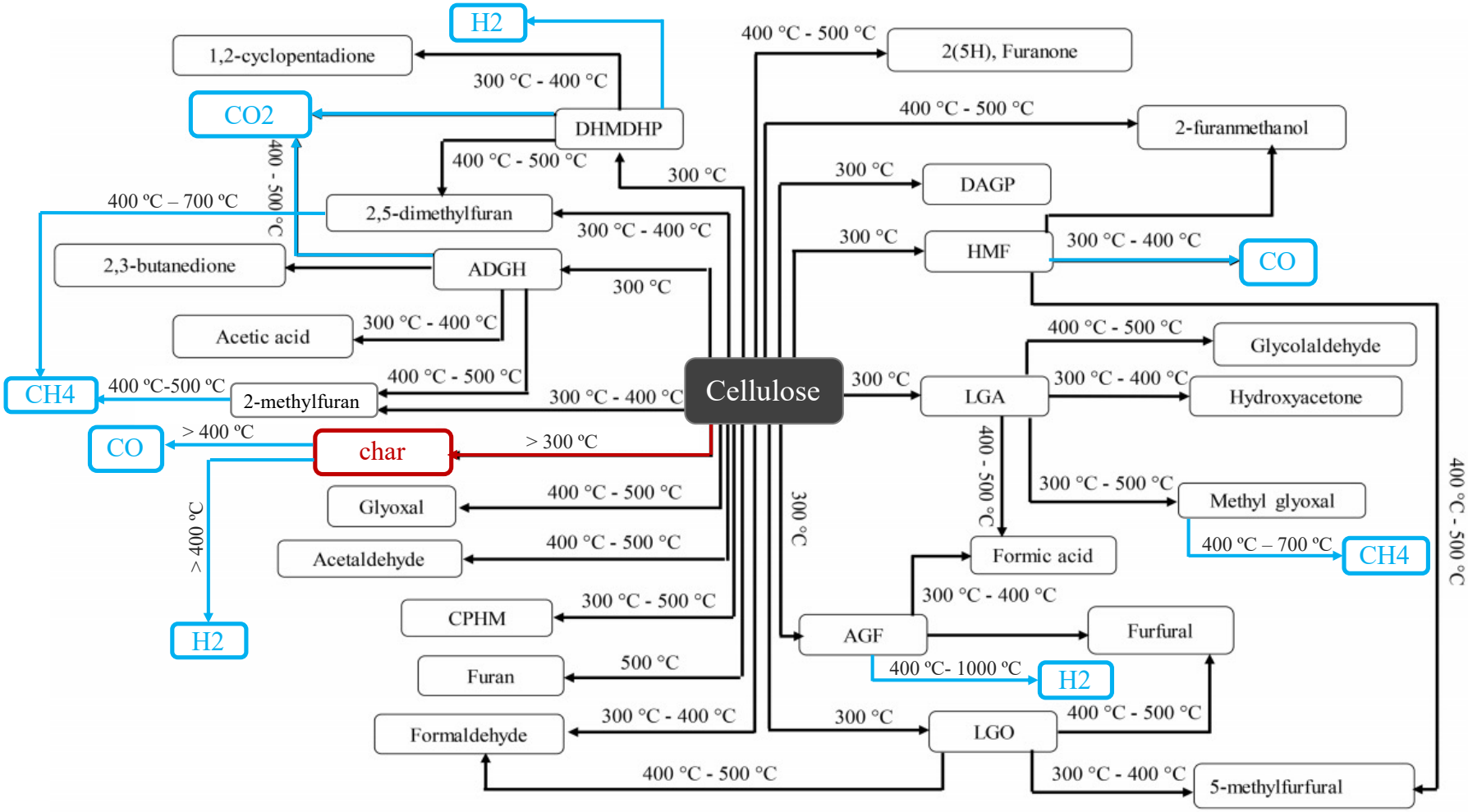

Figure 5-2: The main pathways of cellulose pyrolysis reactions and their products:

The first benzene rings appear at around 300 ºC, and their concentration in carbon becomes predominant at 400 ºC (McGrath et al., 2003; Pastorova et al., 1994). The remaining aliphatic and oxygenated groups (hydroxyl and ether) bind to the benzene rings (McGrath et al., 2003), giving the cellulose char a structure relatively similar to that of the lignin char at 400 ºC. The aliphatic groups disappear in the temperature range between 400 °C and 600 °C (McGrath et al., 2003), thus causing CH_4 production in the temperature range of 500-600 °C (Ansari et al., 2019; Jensen et al., 1998), corresponding to the decrease of methyl groups. These suggest that CH_4 is produced by a demethylation mechanism. CO and H_2 are released from char between 500 and 800 ºC (Yang et al., 2007).

5.2.2.2. *Main pathways of hemicellulose pyrolysis reactions and their products*

Hemicelluloses are heteropolysaccharides whose composition varies according to the type of biomass. Xylan is the major component of hemicellulose, so it is often used to represent hemicellulose as a model structure. Xylans are composed of a linear structure of β-(1-4)-linked β-D-xylopyranose units with branches also containing 4-O-methyl-α-D-glucuronic acid, α-D-glucuronic acid, and α-L-arabinofuranose (Gröndahl et al., 2003). Another compound that hemicellulose has a high content of is glucomannans. Glucomannans are composed of a linear structure of β-Dglucopyranose and β-D-mannopyranose with β-(1-4) linkages and branches containing α-D-galactopyranose (Collard and Blin, 2014). Unlike cellulose, hemicelluloses consist only of an amorphous phase. TG analysis of hemicellulose shows that its conversion occurs mainly in the temperature range between 200 to 350 ºC (Peng and Wu, 2010; Widyawati et al., 2011). As seen above in the case of AS (high hemicellulose content). Temperature above 350 °C, the weight loss is associated with the rearrangement of the char structure during pyrolysis (Peng and Wu, 2010). Xylan will be used as a representative hemicellulose compound for analysis in this study.

The reaction pathways of xylan pyrolysis in a temperature range between 300-1000 ºC are shown in **Figure 5-3**. Dehydration and cleavage of the less stable xylan bonds occur between 150-240 ºC (Collard and Blin, 2014). At temperatures above 200 °C, xylan degrades into anhydrosugar (LGA), furans (HMF and furfural), a phenolic compound (floroglucinol), and char. Xylan depolymerizes and undergoes rearrangement and dehydration reactions to give rise to furfural as the main product, of course, water (dehydration product) (Bodachivskyi et al., 2018; Patwardhan et al., 2011). At

this temperature, methanol is produced from the fragmentation of the methoxy group of 4-O-methyl-α-D-glucuronic acid, and formic acid is produced from the cleavage of the carboxylic acid function of hexuronic acids (Shen et al., 2010a). The intermediate product of xylan degradation is a pentose (C5), for xylan to form hexose (C6) intermediates, an additional carbon atom or a compound is needed to give rise to C6 products such as HMF, levoglucosan, floroglucinol, and 3-methyl cyclopentane-1,2-dione, which were observed experimentally as reported by Ansari et al. (2019). The authors suggest that the necessary additional carbon was provided in situ during the pyrolysis of xylan to finally obtain the products mentioned above. For the temperature range between 200 and 300 °C, LGA and pentose intermediates can be transformed into 3,4-altrosan through a rearrangement reaction, whereas, above 300 °C, LGA is further decomposed into 1-hydroxy-2-butanone and acetic acid through retro-Diels-Alder and fragmentation reactions (Zhu et al., 2016).

The fragments of 3,4-altrosan between 300 and 500 °C form the linear oxygenated compounds such as hydroxyacetone, acetaldehyde, and CO_2. For temperatures between 200 and 300 °C, HMF derived from xylandine by oxidations and hydrodeoxygenation reactions produce furanone compounds and non-condensable gas (CO_2) (Mliki and Trabelsi, 2016). On the other hand, Bodachivskyi et al. (2018) report that in the temperature range between 200 and 400 °C furfural and its by-products through retro-aldol condensation reactions (ring-opening and fragmentation reaction) can form linear oxygenated compounds such as methylglyoxal and hydroxyacetaldehyde. Xylan can also convert to 2-furan methanol and 2-methyl furan between 200-400 °C, due to depolymerization, hydrogenation, and hydrodeoxygenation reactions (Patwardhan et al., 2011). However, 2-Furanmethanol can also be converted to 2-methyl furan 400 to 500 °C (Jenness and Vlachos, 2015). Xylan can also be directly transformed into furanic compounds (acetyl furan and furan) and linear or cyclic oxygenated compounds (2,3-butanedione and cyclopentanone) between 300 to 500 ºC. In a similar temperature range (300-500 °C), 3-methyl cyclopentane-1,2-dione can be hydrodeoxygenated to 2-cyclohexane-1-ol (Ansari et al., 2019). Xylan undergoes a charring process (formation of char between 320-800 ºC) (Shen et al., 2010a). t temperatures above 300 °C, the structure of the residue becomes increasingly aromatic. It has been identified that the benzene rings produced contain methyl or oxygenated substituents (such as methyl phenols in the volatiles obtained between 320 and 350 ºC), which facilitate the aromatization reaction (Peng and Wu, 2010; Wu et al., 2009).

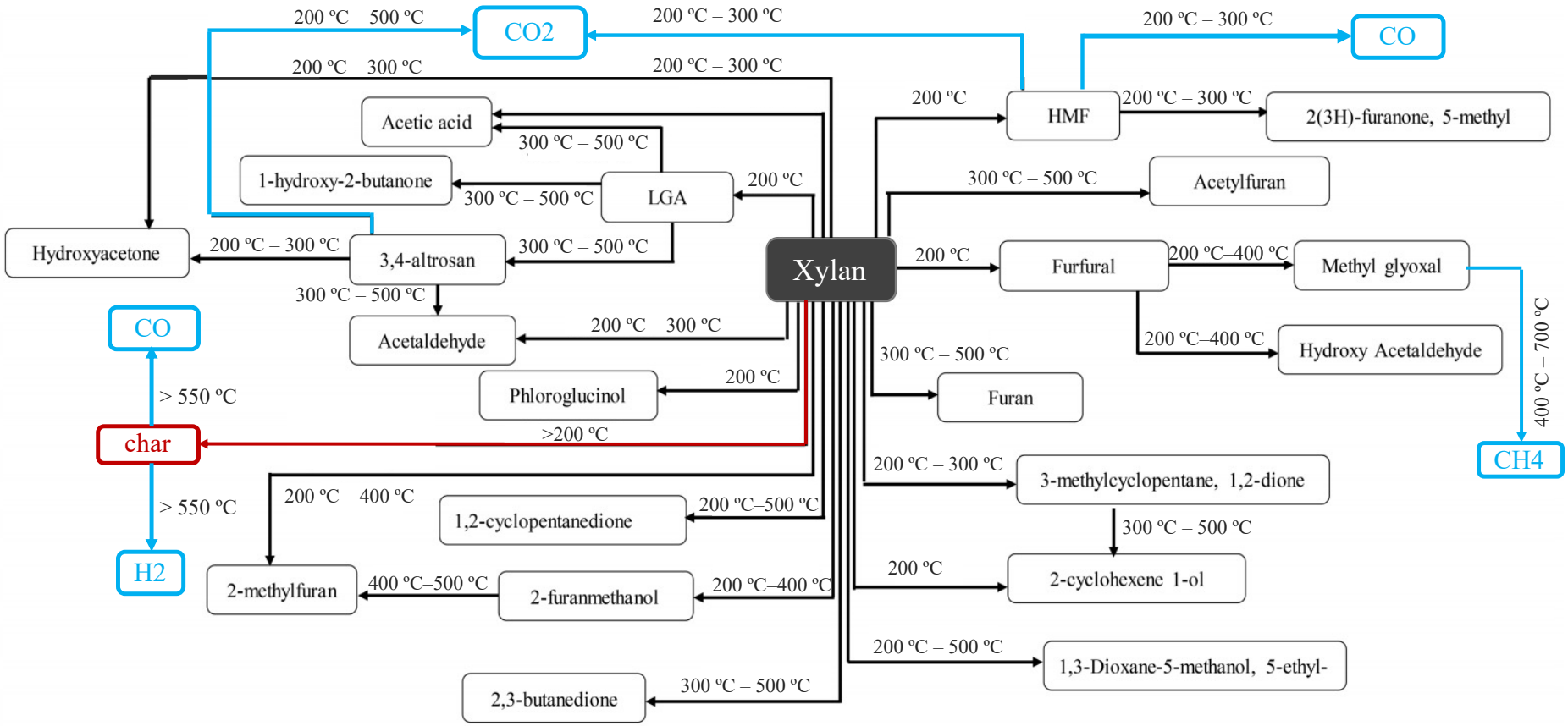

Figure 5-3: The main pathways of Hemicellulose(xylan) pyrolysis reactions and their products

Based on CH_4 production, which is maximal at a temperature of around 550 ºC (Widyawati et al., 2011). The CH_4 formation occurred mainly by fragmentation of the side chains and cracking of the methoxy-O-CH3 groups, especially above 400 °C; methyl substituents are converted by a demethylation mechanism (Qu et al., 2011; Shen et al., 2010a; Yan et al., 2018). Likewise, CO production for temperatures above 500 ºC must be due to the cleavage of oxygenated substituents (Shen et al., 2010a; Yang et al., 2007). Finally, H_2 formation in the temperature range from 480 to 800 ºC is mainly due to dehydrogenation reactions. Furthermore, some vapogasification reactions could also be responsible for the production of H_2 (Widyawati et al., 2011).

5.2.2.3. *Main pathways of lignin pyrolysis reactions and their products*

Lignin is a complex three-dimensional amorphous polymer composed of three phenylpropane units: p-hydroxyphenyl, guaicyl, and syringyl. The proportions of the monomer units are highly variable and mainly depend on the type of lignocellulosic biomass (Collard and Blin, 2014).

The foremost lignin conversion step occurs over a wide temperature range (200 - 450 °C), with the highest decomposition rate generally between 360 and 400 °C (Monteil-Rivera et al., 2013; Shen et al., 2010b; Wang et al., 2009b). The reaction pathways of lignin pyrolysis are shown in **Figure 5-4**. At 350 °C and above, lignin depolymerizes into monolignols (p-curamryl, coniferyl, sinapyl alcohols) (Shen et al., 2010b). These constituents become intermediates for the formation of 2-methyl-4-vinyl phenol, vanillin, apocynin, eugenol, isoeugenol, 4-hydroxy-3-methoxyphenyl acetone, 4-methoxy-3-methyl phenyl creosol, p-cresol, and 2-methoxy phenol. The intermediate coniferyl alcohol is converted to 2-methyl-4-vinyl phenol by a deformylation reaction (Shen et al., 2010b) and vanillin by oxidation and retro-aldol reactions (Wang et al., 2009b). At the same time, this coniferyl alcohol can be converted to eugenol or isoeugenol after cleavage of its hydroxyl group, followed by a hydrogenation reaction (Monteil-Rivera et al., 2013).

On the other hand, the intermediate eugenol-forming can also undergo retro-aldol and alkylation reactions to form creosol (4-methyl guaiacol) (Collard and Blin, 2014). Apocynin and 2-methoxy phenol can be obtained through dehydration, ether bond cleavage inside the lignin compound, and rearrangement reaction (Bridgwater et al., 1999). The 4-methyl guaiacol is obtained at low temperature (~350 °C) directly from lignin. At reaction temperature between 350 and 450 °C, 2-methoxy-4-vinyl phenol can be hydrogenated to form 2-methoxy-4-ethylphenol. At the same time,

apocynin can be converted into 2,3-dimethylphenol and CO_2. Furthermore, vanillin is transformed into cresol and CO_2 by the reactions of hydrodeoxygenation and decarbonylation (Mu et al., 2013). Eugenol, isoeugenol, and their by-products can be transformed to 2-(4-methoxyphenyl)ethanol at 350-450 °C. Vanillin is converted to 2-methyl phenol at 450-550 °C by similar reactions of retro-aldol, hydrodeoxygenation, and decarbonylation (Mu et al., 2013). Lignin is also transformed directly into phenol through several pyrolysis reactions involving the formation of guaiacol by-products followed by its dealkylation and hydrodeoxygenation reactions at a temperature of more than 350–550°C (Lv and Wu, 2012).

Other products are also formed, i.e., 4-hydroxy-3-methoxyphenyl acetone, directly from lignin between 350°C and 550°C, may be generated by depolymerization to yield coniferyl alcohol (intermediate), accompanied by hydrogenation and reduction. At 350-550 °C, 2,3-dihydro benzofuran can be formed directly from lignin via an o-quinonemetic intermediate with an allyl methyl group can undergo a cyclization reaction followed by hydrogen abstraction (Nakamura et al., 2008). Light oxygenates (butyl glycol and methanol) and char are also formed from lignin between 350 and 550 °C.

At 450 °C and above, most of the initial bonds between the lignin monomer units are broken. Only the most stable ones, such as the phenyl bond and the ether bond, remain (Faravelli et al., 2010; Nakamura et al., 2008). The main short substituents of the aromatic rings are -CH3 or -OH. In this condition, the char becomes more aromatic, and most of the compounds produced are incondensable gases. Sharma et al. (2004) reported that the -CH3 substituents disappear between 500 and 600 °C in FTIR analysis. At a temperature between 550 and 580 ºC, many authors (Huang et al., 2012; Liu et al., 2008) state that the main compound evolved is CH_4. At this condition, CH_4 is likely released according to a demethylation mechanism (Asmadi et al., 2011a), leading to a more cross-linked structure. Several authors have found that lignin pyrolysis releases a significant CO between 500 and 800 °C (Huang et al., 2012; Liu et al., 2008). Since very few condensable organic compounds are produced in this temperature range, it is not likely that CO production is due to side reactions of these compounds but to the conversion of some oxygenated groups still present in the residue.

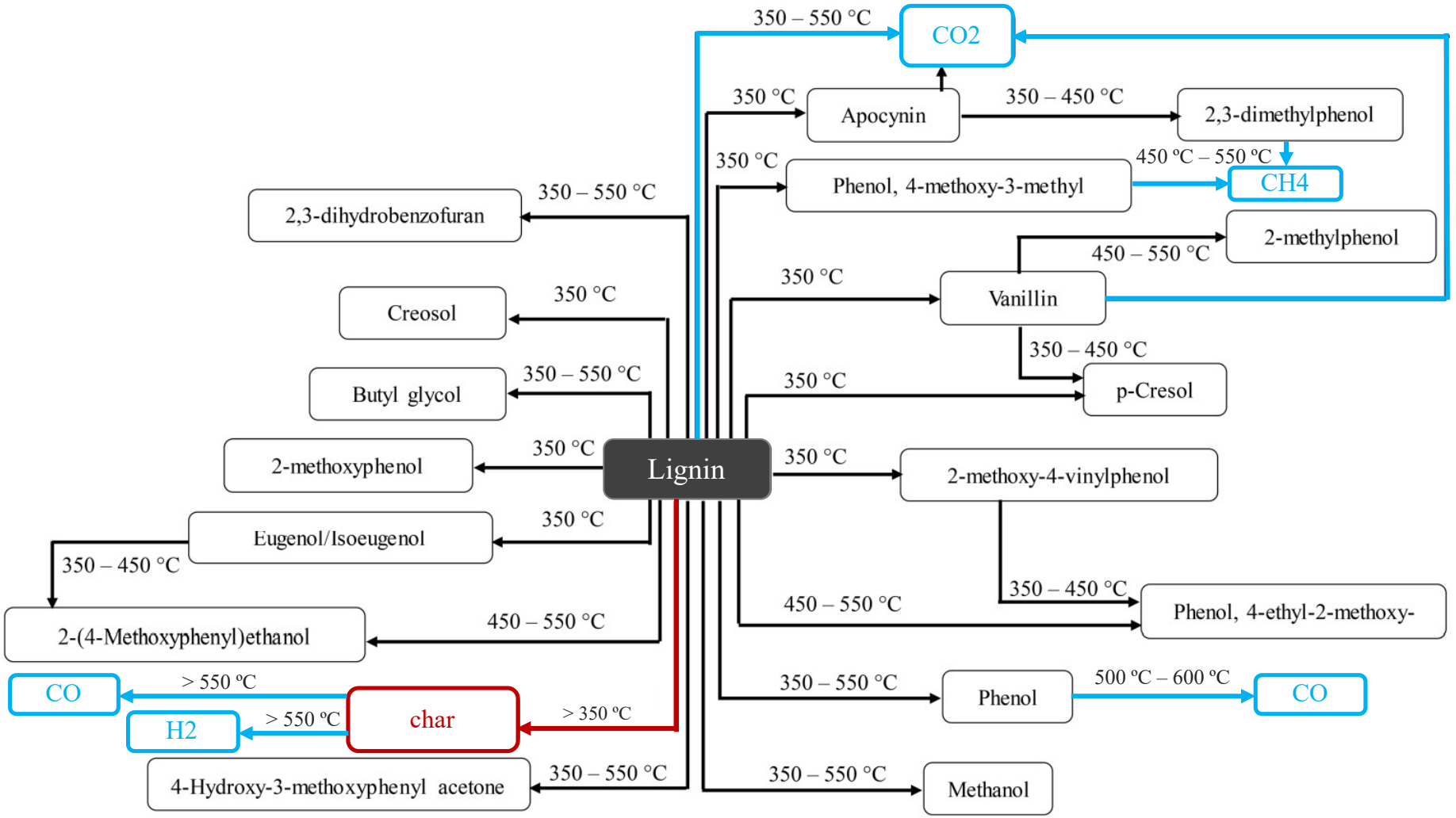

Figure 5-4: The main pathways of lignin pyrolysis reactions and their products

The oxygenated functions remaining in the residue are the ether bond and the hydroxyl substituents. It is assumed that the cleavage of the ether bonds is indeed a source of CO production (Liu et al., 2008; Wang et al., 2008a). The first step of the conversion could be due to hydrogenation of the ether bond, leading to the formation of an additional hydroxyl substituent (Sergeev and Hartwig, 2011), which would then react.

At high temperatures above 600 °C, CO formation is due to the conversion of the phenol rings (containing a single hydroxyl substituent) of the residue, which are known to remain stable at 550 °C (Asmadi et al., 2011c; Sharma et al., 2004). There are few studies on the mechanism of CO formation from the conversion of phenyl rings. However, Asmadi et al. (2011c) suggested a mechanism, but only from one pyrogallol moiety (derived from syringyl unit) Egsgaard and Larsen (2000) detailed a relatively complex mechanism requiring two phenol fractions. These reactions could lead to the formation of H_2O molecules inside the particles, which could immediately react with the char by vaporization to give CO and H_2. Due to the reaction involving the last oxidized organic group, most of the volatile compounds and the aromatic ring of the residue are deoxygenated to perform the conversion at a temperature above 800°C (Sharma et al., 2004). The formation of H_2 is also due to the rearrangement of the aromatic rings in a polycyclic structure (Asmadi et al., 2011b). This reaction is remarkable for the significant amount of H_2 evolved at temperatures above 500 °C (Lou and Wu, 2011; Yang et al., 2007).

5.2.3. Analysis of the gaseous products of biomass pyrolysis

5.2.3.1. *Online analysis of the gaseous products of biomass pyrolysis*

The online analysis was performed by injecting the µ-GC every 150s during the whole heating time up to the set point temperature (1000 ºC), while for offline analysis, all gas product was collected using a gasbag injected into the µ-GC at the end of the experiment. The yields of H_2, CH_4, CO, and CO_2 of pyrolysis of the four biomasses in the temperature range of 100-1000 °C are plotted in **Figure 5-5** to **Figure 5-8**. The influence of pyrolysis temperature on gas composition was significant. The gas yields increased with increasing temperature for all samples, this is probably because pyrolysis became more active as the pyrolysis temperature increases, and more organic compounds were converted into non-condensable gases (Palma, 2013). The pyrolytic gases of the four biomasses are rich in H_2, CO, and CO_2, while the amounts of CH_4 released are generally small. As revealed from the TG analysis, the gas release curves highlight three different stages of decomposition of biomass components that reflect

their intrinsic devolatilization. In the first stage, in the temperature range of 180-450 ºC, the devolatilization of hemicellulose is associated with the release of CO_2 and CO in the gas phase. At the same time, the devolatilization of cellulose is also accompanied by the release of CO_2 and CO into the gas phase. The temperature corresponding to the maximum release rate of these gases are 336, 345, 353, and 365 ºC for CEL, CS, AS, and ASB, respectively.

The second stage, which ranges from 400 to 700 °C, is characterized by a release of CH_4, which is the main gas produced at this stage; lignin degradation is mainly responsible for the CH_4 peak. The temperature corresponding to the maximum rate of CH_4 releases are 511, 355, 560, and 353 ºC for CEL, CS, AS, and ASB, respectively. In addition, at this stage, there is a residual release of CO_2 and CO representative of residual devolatilization of cellulose and lignin. The last stage, temperature above 500 ºC, is characterized by a release of mainly H_2 and residual CO representing residual devolatilization of cellulose and lignin. The CO release is probably associated with steam in the reaction environment that determines the gasification or partial oxidation of char and steam reforming of volatile species.

The differences in the three stages reflect the intrinsic devolatilization behavior of the individual biomass components. A similar point can be observed by comparing the four figures (**Figure 5-5** to **Figure 5-8**), The CO_2 was released at 180-450 °C and obtained the maximum release value at 250-400 °C. CO release showed a pattern similar to that of CO_2 between 180-450 °C. However, its release rate was lower. In general, CO results mainly from the cracking of carbonyl (COC) and carboxyl (C=O) groups, while CO_2 is mainly released from the cracking and reforming of functional groups of carboxyl (C=O) and COOH and internal dehydration of cellulose char formation (Liu et al., 2011; Qu et al., 2011). The CO peaks between 450-540 ºC, which can probably be caused by the breaking of diaryl ether groups and secondary pyrolysis of volatiles. The CO releasing peak at 700 °C was attributed to the break of diaryl ether linkages (Yan et al., 2018). The CO content in the gases remained practically in the whole temperature range. One of the reasons for the formation is the secondary cracking of pyrolytic vapors. Another was due to the incomplete oxidation reaction between high-temperature char and oxygen generated in pyrolysis (Zhao et al., 2017).

H_2 was released at higher temperatures (> 400 °C), and H_2 release increased significantly with increasing temperature; it is because H_2 mainly came from cracking and deformation of C=C and C-H groups, which needed more energy (Qu et al., 2011; Yang et al., 2007). Furthermore, at higher temperatures, the endothermic tar steam reforming reaction **(R- 3)** contributes to a higher H_2 production (Zhu et al., 2018). Therefore, H_2 evolved at a much higher temperature

(> 450 °C), and as the temperature increases, the rate of H_2 evolution increased significantly and reached the maximum value between 680-750 °C for all study biomasses. Then, it gradually decreased to 1000 °C. As can be seen in **Figure 5-5** to **Figure 5-8**, the maximum H_2 production occurs between 650-850 °C. From 750 °C onwards, the trend starts to decrease; therefore, most pyrolysis can be considered practically completed at 750 °C. These results are in agreement with the previous study by Zhao et al. (2017) on the pyrolysis of cellulose. The CH_4 formation occurred mainly by fragmentation of the side chains and cracking of the methoxy-O-CH_3 groups, significantly above 400 °C. Also, CH_4 formation could be attributed to the breaking of aromatic rings of lignin (Qu et al., 2011; Yan et al., 2018). Thus, CH_4 evolution is between 400 and 800 ºC for all biomasses. In **Figure 5-5**, the maximum CO and CO_2 peak values for AS were 10.87 and 10.06 mL/min/ (g of feed), respectively. These correspond to the highest peaks released from these compounds; this may be due to the high hemicellulose content in AS. The CO and CO_2 peaks of ASB are the second-highest, with maximum CO and CO peaks of 8.49 and 9.62 mL/min/ (g of feed).

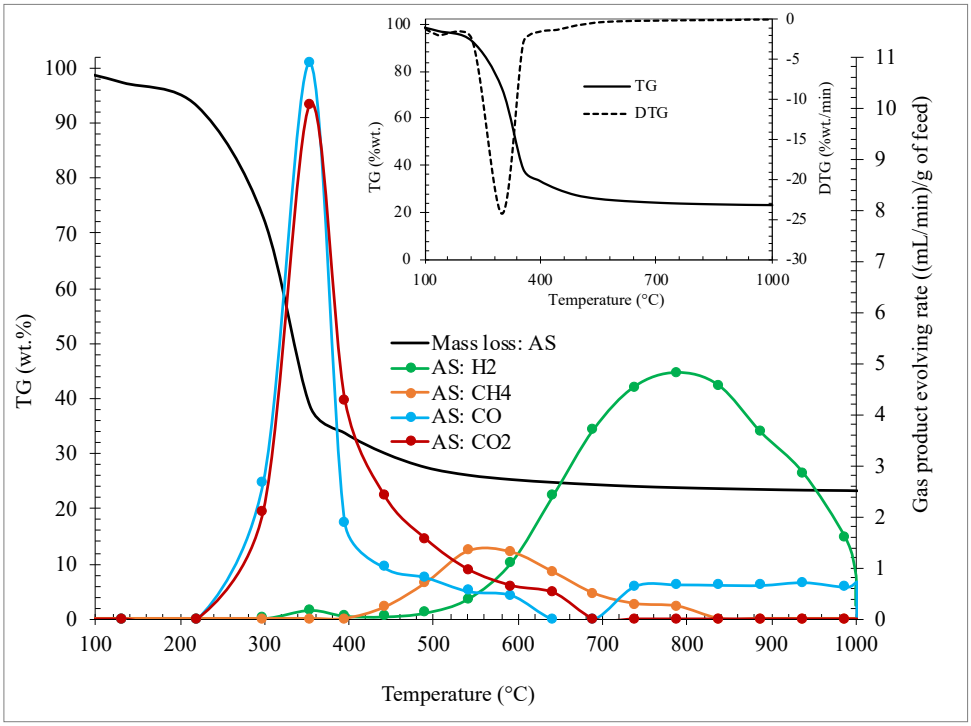

Figure 5-5: TGA and release profile of the gas products during the AS pyrolysis with temperature for 10 ºC/min

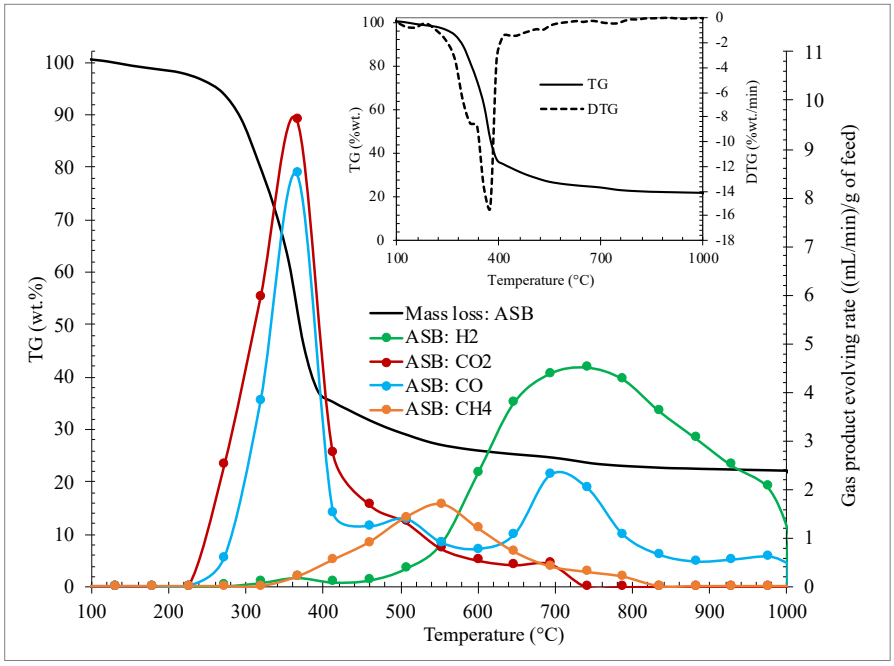

Figure 5-6: TGA and release profile of the gas products during the ASB pyrolysis with temperature for 10 ºC/min

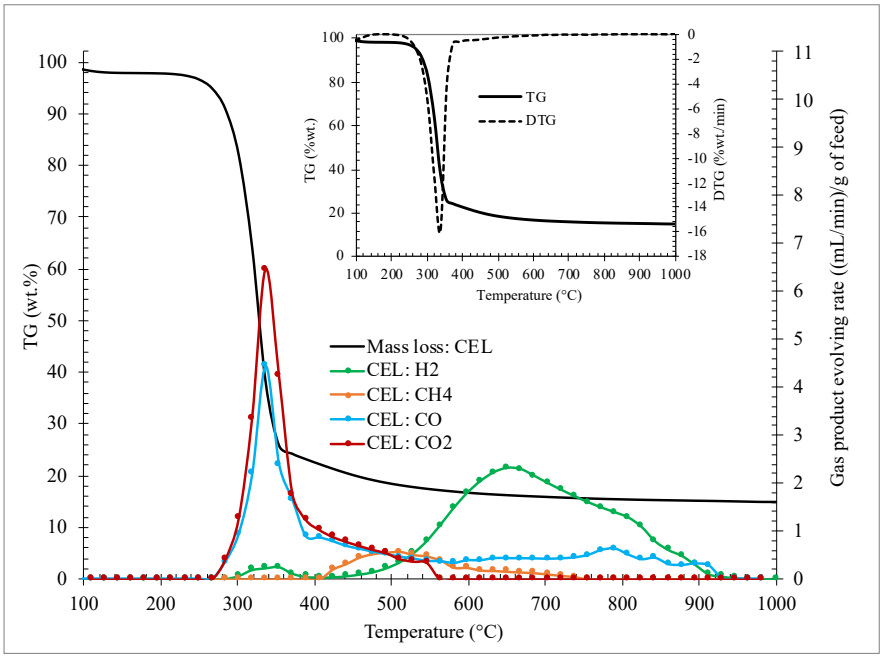

Figure 5-7: TGA and release profile of the gas products during the ASB pyrolysis with temperature for 10 ºC/min

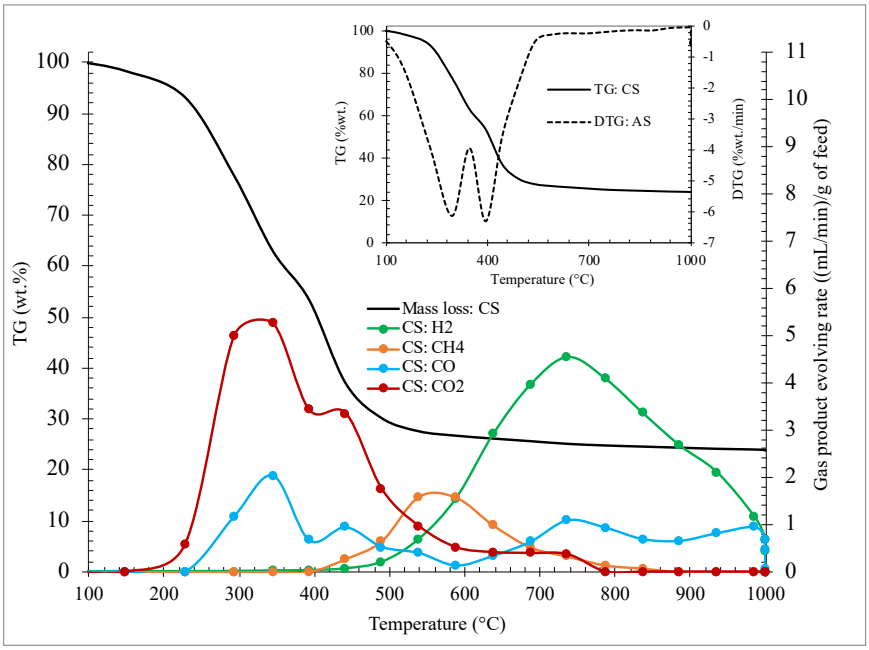

Figure 5-8: TGA and release profile of the gas products during the CS pyrolysis with temperature for 10 ºC/min

The CO production for ASB and CS (**Figure 5-6** and **Figure 5-8**) shows two additional peaks compared to AS and CEL (**Figure 5-5** and **Figure 5-7**). The CO peak between 400- 550 °C for ASB and CS is probably due to the rupture of diaryl ether groups and secondary pyrolysis of volatiles, and the peak around 740 ºC, can be attributed to char oxidation of lignin decomposition. Above 450 °C, CO produced from CEL remained almost constant between 0.38-0.65 mL/min/(g feed) up to 920 °C, and then decreased to almost zero at 920-1000 °C, and CO_2 production became almost zero from 560 °C onwards. Similarly, in AS, CO production remains constant (about 0.67 mL/min/(g feed)) between 700-1000 °C, while above 700 °C CO_2 production is zero. The maximum H_2 peak value for AS was 4.82 mL/min/(g of feed), which corresponds to the highest peaks released from these compounds. However, the highest proportion of H_2 in the gas is obtained from the CS (higher than 41% of all gases produced). This may be due to its high lignin content. CH_4 production for all biomass samples began to evolve at a temperature above 350 ºC; it increased with increasing temperature and reached the maximum evolution rate at 550 ºC, but gradually decreased to zero at 800-1000 ºC. From **Table 5-3**, it can be seen that the biomass with high lignin content possessed the highest H_2 yield since H_2 from pyrolysis of organic products mainly comes from cracking and C=C and C-H deformation.

Table 5-3: Pyrolysis gas product of biomasses

samples	Gas product composition (mol. % N2-free and H_2O-free)			
	H_2	CH_4	CO	CO_2
AS	38.10	6.60	28.34	26.96
ASB	36.27	7.71	29.48	26.54
CS	41.03	8.73	18.85	31.39
CEL	37.06	6.07	29.77	27.10

In addition, the CH_4 release was generally very low for each sample. It can be observed that the biomass with high cellulose content (CEL) obtained the highest CO due to the higher carbonyl content in it. On the other hand, the biomass with high lignin content (CS) possessed the highest CH_4, which could be attributed to the higher content of aromatic rings and O-CH3 functional groups in the source lignin sample. Higher CO was also observed in biomass with high lignin content, perhaps due to its carbonyl content, although a higher CO_2 content was expected for biomass with high hemicellulose content due to the higher carboxyl content (Qu et al., 2011).

5.2.3.2. *Pyrolysis gas yield analysis*

Biomass mainly consists of three components (cellulose, hemicellulose, and lignin), which have very different thermal behaviors. The biomass pyrolysis products may be considered the overall pyrolysis performance of three main components, extractives and ash. The three components of biomass are broken down during pyrolysis to produce liquid, solids, and gases. The main gas components detected by μ-GC were CO, CO_2, CH_4, and H_2. For the qualitative and quantitative analysis of these gases, online and offline methods were used.

In general, lignin produces less gas than cellulose and hemicellulose. Therefore, biomass with more lignin content should produce less gas. As shown in **Figure 5-9**, the CS (175.47 mL/g feed) yield is lower in all biomasses, followed by AS (209.09 mL/g feed). However, the yield of ASB is higher (245.95 mL/g feed) than the yield of CEL (225.67 mL/g feed); the latter may be due to the high hemicellulose and low lignin content in ASB.

The result could be attributed to the weakness of the bonds in the chemical structures of hemicellulose, and hemicellulose is easier to degrade to temperature-influenced

micromolecular volatiles and lignin more difficult to degrade. H_2 yields were the highest for all the biomasses studied, followed by CO and CO_2, while CH_4 yields were the lowest. The highest individual yields were obtained in ASB, while the lowest individual yields were found in CS. Gas production from ASB pyrolysis presented the highest yields in H_2, exceeding 89.22 mL/g feed, followed by CO (72.50 mL/g feed). CO_2 production was 65.27 mL/g feed, whereas CH_4 yield was the lowest (only 18.96 mL/g feed). The total yields of gases produced using online and offline analysis are presented in **Figure 5-10**. As it can be seen, there is practically no difference between the online and offline methods for quantifying the gases produced. A slight difference observed can be attributed to the reactions that may occur when collecting the gases, such as the exothermic reactions of **Table 5-1**. From **Figure 5-10**, it can be observed that ASB showed the highest H_2, CH_4, and CO_2 yield. The high H_2 production might be attributed to the higher content of aromatic ring and O–CH3 functional groups in the ASB sample, as H2 from organic pyrolysis, mainly came from the cracking and deformation of C=C and C–H while the cracking of methoxyl mainly brought CH_4 (Wang and Sarkar, 2018).

The high concentration of CO_2 produced by ASB can be attributed to its higher carboxyl content due to the higher content of hemicellulose. CO yields for both biomasses are similar, attributed to their high carbonyl content (Yang et al., 2007).

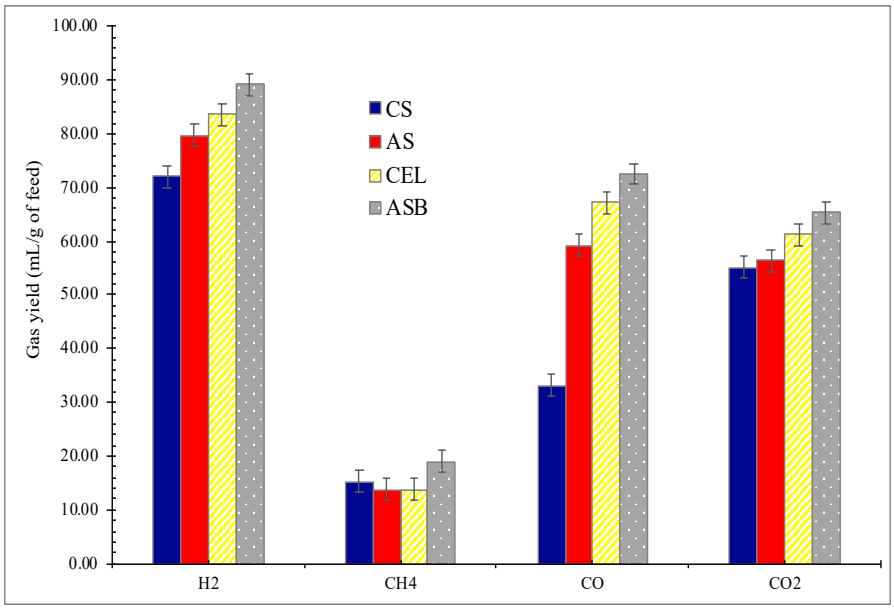

Figure 5-9: The total gas yields produced during the pyrolysis of biomasses.

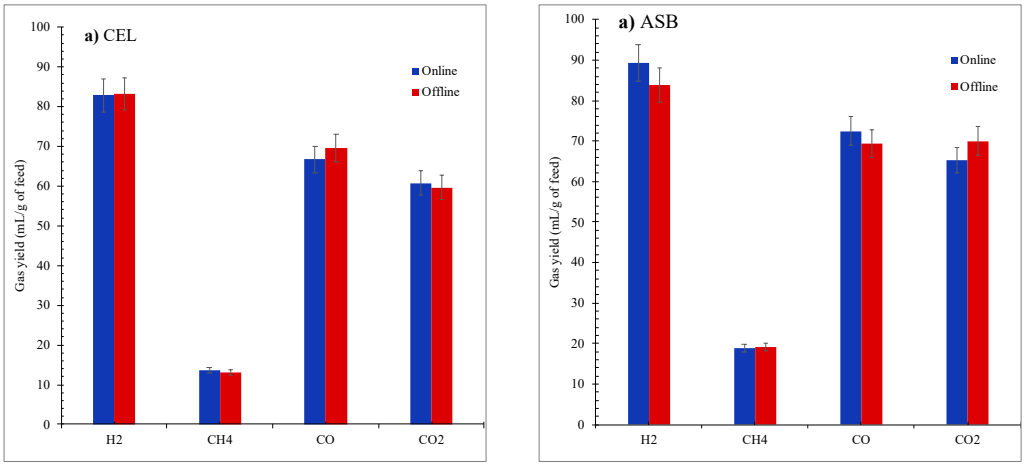

Figure 5-10: Online and offline comparison of gas yield products: a) CEL, b) ASB

5.2.4. Analysis of the gas products during pyro-gasification of ASB

The composition of the syngas includes CO, CO_2, H_2, and CH_4. The exact percentage distribution depends on many parameters such as the type of biomass, air/biomass ratio, heating rate, gasifying agent, temperature, and many others. The gasification agent used was air, using different air to biomass ratios from 0.125 to 1. The heating rates were 10, 20, 40, and 80 ºC/min.

5.2.4.1. *Effect of air to biomass ratio on the gas product evolution*

To show the effect of air to biomass ratio on the gas product evolution during gasification, **Figure 5-11** summarizes the evolution of the experimental results of gases produced during the pyro-gasification of ASB for a fixed heating rate (40 ºC/min). In **Figure 5-11** it can be identified the two pyro-gasification zones. A first zone (50-700 ºC) corresponds to the pyrolysis zone. It is observed that the evolution of each gas is similar for **Figure 5-11a-f**, confirming the repeatability of the results. The second zone (700-1000 ºC) corresponds to the gasification zone, where the air was injected at a different air to biomass ratio (ABR).

In **Figure a-c**, the production of H_2 and CO is more favored than CO_2 due to oxygen deficiency. Partial oxidation reactions are more favored. However, as ABR increases, the evolution of CO_2 increases.

The increases are related to the increase in oxygen supply, thus oxidizing large amounts of H_2 and CO to H_2O and CO_2. This phenomenon may also explain why ABR increases from 0.5 to 1.0, resulting in a higher CO_2 level in **Figure d-f**, as total oxidation reactions were favored. The temperature values influence the decrease of CO and H_2 concentrations since a higher

temperature is favorable for endothermic reactions, promoting reduced reactions, leading to the decrease of these elements as indicated by the water-gas or steam reaction (Jarungthammachote and Dutta, 2012) (**R- 18**).

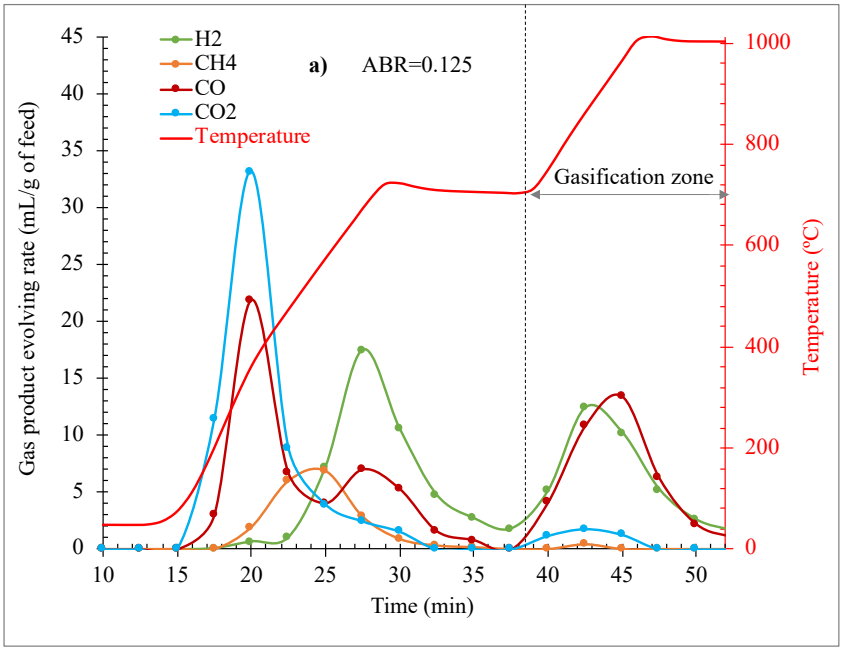

Figure 5-11a: The effect of the air/biomass ratio (ABR) on the evolution of the online gaseous products during pyro-gasification (heating rate 40 ºC/min, ABR=0.125)

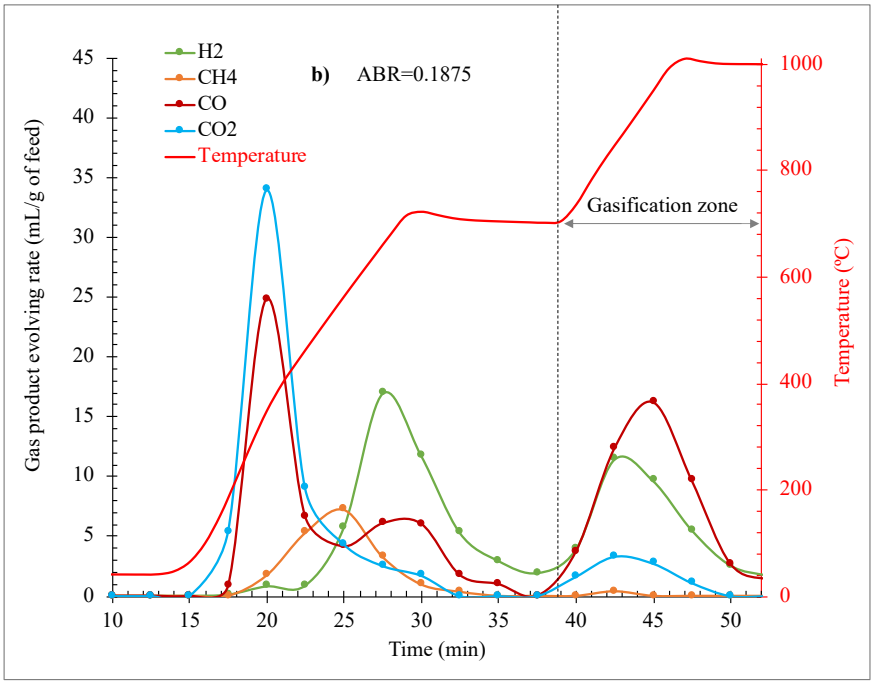

Figure 5-11b: The effect of the air/biomass ratio (ABR) on the evolution of the online gaseous products during pyro-gasification (heating rate 40 ºC/min, ABR=0.187)

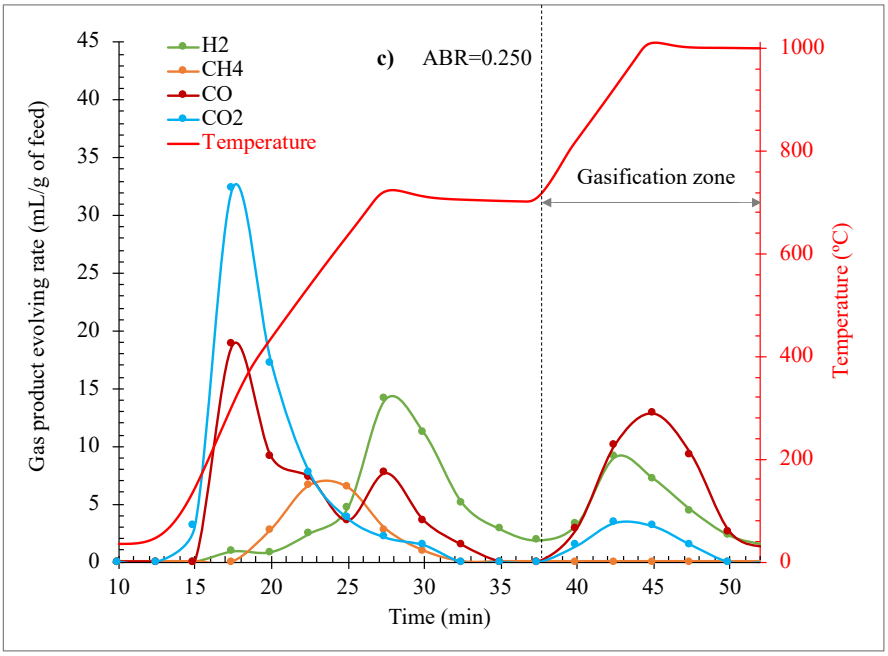

Figure 5-11c: The effect of the air/biomass ratio (ABR) on the evolution of the online gaseous products during pyro-gasification (heating rate 40 °C/min, ABR=0.250)

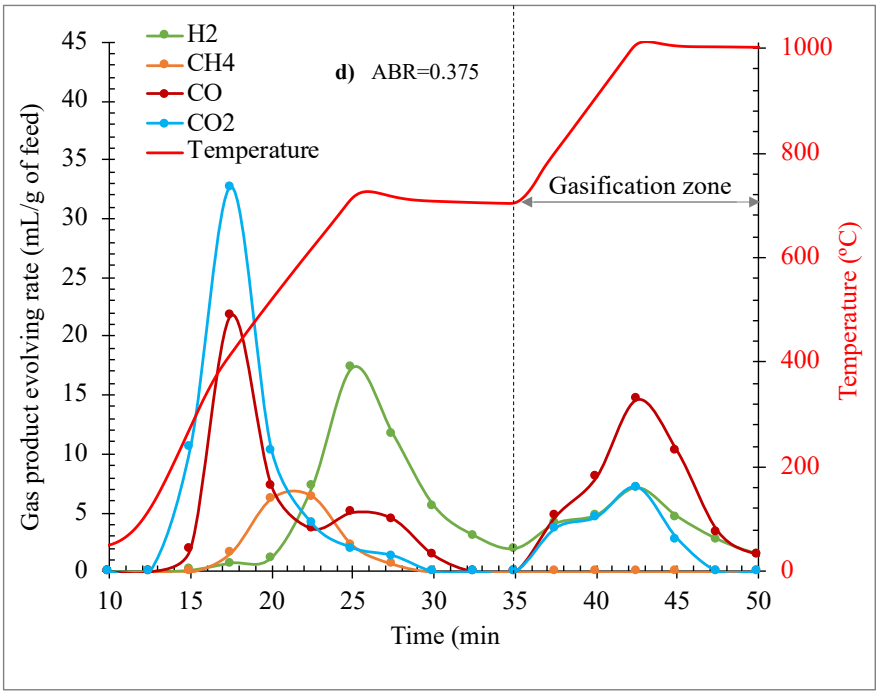

Figure 5-11d: The effect of the air/biomass ratio (ABR) on the evolution of the online gaseous products during pyro-gasification (heating rate 40 °C/min, ABR=0.375)

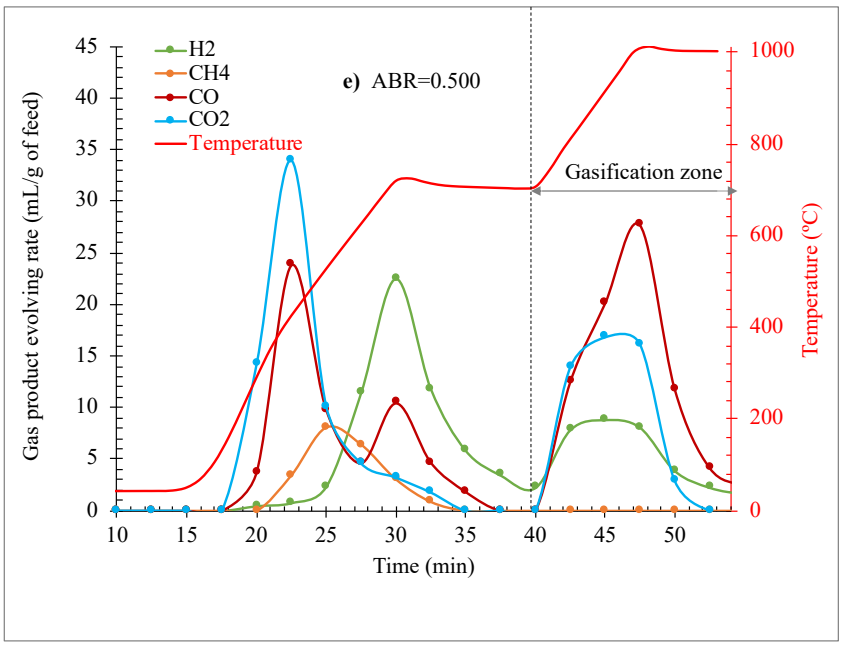

Figure 5-11e: The effect of the air/biomass ratio (ABR) on the evolution of the online gaseous products during pyro-gasification (heating rate 40 °C/min, ABR=0.50)

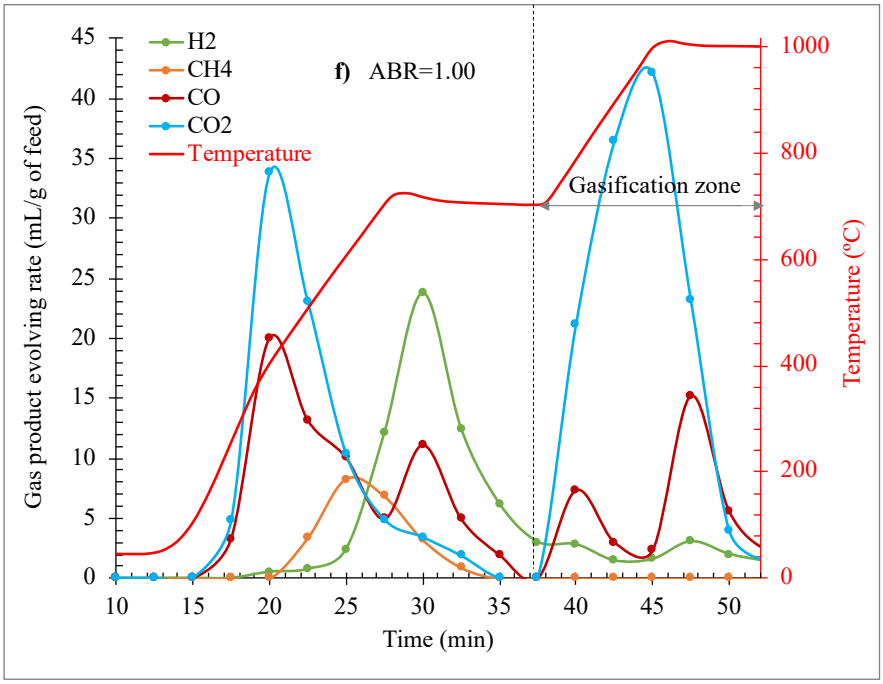

Figure 5-11f: The effect of the air/biomass ratio (ABR) on the evolution of the online gaseous products during pyro-gasification (heating rate 40 °C/min ABR=1.0)

The increase of CO_2 evolution is related to the oxidation reaction that promotes the disappearance of the O_2, which is transformed into CO_2, and part of this element is used in the Boudouard reaction (Favas et al., 2017; Jarungthammachote and Dutta, 2012) **(R- 17)** where it is consumed and subsequently produces novel compounds CO.

5.2.4.2. *Effect of air to biomass ratio on pyro-gasification performance*

The product gas found in the biomass air gasification is composed of combustible gases (CO, H_2, CH_4, CnHm) and non-combustible gases (CO_2 and N_2, where N_2 is derived from the air). The performance of each gas depends mainly on the ABR. In this study, six gasification runs were carried out at different ABR values for a heating rate of 40 ºC/min. **Table 5-4** gives the distribution of product gas composition at various ABR investigated. When ABR varied from 0.125 to 1.0, the composition of combustible gas varied as follows: the fraction of H_2 varied from 26.27 to 7.02 % (v/v). The fraction of CH_4 varied from 5.92 to 2.07 % (v/v). For CO, the composition decreased from 27.38 to 11.39 % (v/v), while non-combustible gases increased from 14.78 to 19.8 % (v/v) and from 24.56 to 59.71 % (v/v) for CO_2 and N_2, respectively. These values show that with increasing ABR value from 0.125 to 1.00, combustible gases' concentration decreased while the non-combustible gases increased.

Table 5-4: Product gas analysis and gasifier performance of ASB at 40 ºC/min.

Feedstock	**ASB**					
ABR	**0.125**	**0.187**	**0.25**	**0.375**	**0.5**	**1,0**
Product gas composition (mol.%)						
H_2	26.27	21.80	20.92	17.88	13.69	7.02
CH_4	5.92	5.03	4.35	3.89	3.12	2.07
CO	27.38	24.46	21.94	14.78	20.11	11.39
Combustibles gases	**59.57**	**51.29**	**47.20**	**36.55**	36.93	**20.48**
N_2	24.56	31.60	36.25	44.37	46.19	59.71
CO_2	15.87	17.11	16.55	14.78	16.89	19.80
Non-combustibles gases	**40.43**	**48.71**	**52.80**	**59.15**	**63.07**	**79.52**
Gy (Nm^3/kg)	0.34	0.39	0.42	0.51	0.69	1.06
LHVg (MJ/Nm^3)	8.72	7.51	6.83	5.38	5.33	3.05
η (%)	38.89	38.08	37.57	35.66	44.57	42.23

The decrease in H_2 concentration was observed because of the water gas shift reaction in which the H_2 consumption rate was greater as compared to the H_2 formation rate. Simultaneously, the decreased concentration of CH_4 with increasing ABR was due to methanation (Liu et al., 2018). By increasing ABR, more air entered into the reactor, CO and CH_4 were reacted with O2 and

formed CO_2 due to excessive air availability. The low concentration of combustible gases was found at a high ABR value and diminished the product gas quality. The low ABR favored endothermic reactions that are char + CO_2 and water gas shift reactions. Therefore, more char and CO_2 are used in these reactions, lowering the CO_2 composition (Hai et al., 2019). Considering the tendencies of gas concentrations with increasing ABR, the maximum decrease is obtained for H_2 concentration, while a slight decrease is found in CH_4 concentration. The decrease in CO concentration is smaller than that of H_2 concentration. Similar results were reported by Hai et al. (2019), which showed increased CO_2 concentration when the ABR value was increased. The increase in non-combustible gas concentration with increasing ABR is directly related to the dilution of gas in N_2. The general effect considering the dilution of a large number of N_2 shows that the gas heating value decreases with increasing ABR. Besides, considering slowly increased gas yield, gasification efficiency declines.

Table 5-4 demonstrates how the gasification results change according to ABR variation from 0.125 to 1.0; the gasification parameters such as gas yield (Gy), LHVg, and process efficiency (η) were investigated to examine the gasifier performance efficiency. As the ABR value is varied from 0.125 to 1.0, all gasification parameters (Gy, LHVg, and η) were also changed. **Table 5-4** shows a decrease in LHV and an increase in product Gy with increasing ABR values. The LHVg was decreased from 8.72 to 3.05 MJ/Nm^3 by increasing ABR from 0.125 to 1.0, while Gy was increased from 0.34 to 1.06 Nm^3/kg. The low production of combustible gases (H_2, CH_4, and CO) with the ABR increase favored the decrease in LHVg. Also, the LHVg was decreased due to exothermic water gas shift reaction and dilution of syngas with air nitrogen (Hai et al., 2019; Manatura et al., 2017). The η is the percentage of LHV of biomass converted into LHV of product gas. At the selected ABR 0.125, 0.187, 0.25, 0.375, 0.5 and 1.0, the η were 38.89, 38.08,37.57,35.66, 44.57 and 42.23 %, respectively. ABR influenced the η. The increase in ABR results in lowering the LHVg of gasification products; this is due to the excessive oxidation of biomass to favoring the biomass combustion reaction, and also more inert nitrogen is introduced with the air, which decreases the quality of gas produced (Shehzad et al., 2018).

5.2.4.3. *Influence of heating rate on pyro-gasification performance*

Heating rate is one of the key parameters that directly influences the gas yield and composition of the products evolved during the pyro-gasification. The effect of heating rate on the composition of gaseous products is shown in **Figure 5-12**. Four heating rates were used (10,

20, 40 and 80 ºC/min), in the presence of inert gases and reagents in the temperature domain between 50 ºC and 1000 ºC. The experiments were carried out in argon atmosphere during pyrolysis from 50 ºC to 700 ºC. From 700 ºC, air was injected for gasification up to 1000 ºC. All gaseous products were collected using a gasbag and analyzed after each experiment. As shown in **Figure 5-12**, the gas composition is correlated with the heating rate. With the increase in heating rate, the concentration of CO_2 slightly decreases, the molar fractions of H_2, CO, and CH_4 exhibited an increasing trend. One of the essential steps in pyro-gasification is pyrolysis. The heating rate has a significant influence during pyrolysis. In general, the performance at the gas release rate increases with increasing heating rate. Yan et al. (2014a) reported that the yield of gases can be enhanced by increasing the heating rate during pyrolysis owing to the tar cracking and reforming reactions (**R- 3** and **R- 4**). Also, Water-Gas Shift (**R- 6)** is favored. The relationship between heating rate and product yield is that higher free radical concentration can be obtained at higher temperatures over a shorter heating time, which benefits the gas and liquid yields (Qiu et al., 2007). Increasing the heating rate can increase the temperature differences in the samples over the same period of time.

The heat energy transferred per unit area and unit time will also increase, leading to rapid decomposition of organic matters into biomass during the same pyrolysis time. After pyrolysis, the influence of heating rate also prevails during char gasification. At high heating rates, the gasification region shifts to high temperature, which favors endothermic reactions. The Boudouard and Water-Gas reactions are favored (**R- 17** and **R- 18**). Furthermore, the endothermic direction of methanation reactions (**R- 20** to **R- 22**) is also favored. The CO_2 yield decreases with increasing heating rate, which contributes to the increased CO formation (Boudouard reaction, **R- 17**). As shown in **Figure 5-12**, at the heating rate of 10 °C/min, CO_2 was the dominant gas product; (118.62 mL/g of feed) and decreased to 82.08 mL/g of feed at 80 °C/min, while CO increased from 99.21 mL/g of feed to 175.06 mL/g of feed. CH_4 yields were relatively similar with increasing heating rate with a small increase at 80 °C/min. All CH_4 is practically produced during pyrolysis process, as shown in **Figure 5-10**. The reactions that form CH_4 are exothermic (methanation reactions (**R- 20** to **R- 22**), which may explain that CH_4 formation is little at high temperature. Similar results were also obtained by Safdari et al. (2019) for live wildland pyrolysis. The largest difference in the CH_4 yield was 15.57mL/g of feed with an increasing heating rate. H_2 yields varied between 70.75 mL/g of feed and 128.89 mL/g of feed with increasing heating rate. Several mechanisms of reactions can explain the increase in H_2 yield. The first is the formation of H_2 from the rupture of the hydrogen bonds attached to

the benzoic rings, which are present in the form of phenolic groups in the lignin structure during high-temperature pyrolysis (Zhou et al., 2014a). The second mechanism is the decomposition of the heavy gaseous hydrocarbons due to secondary pyrolysis reactions, leading to the formation of H_2 (Al Arni, 2018; Ningbo et al., 2015; Safdari et al., 2019). Also, the light gases produced during pyrolysis can react with each other to form H_2, as in the case of methanation reactions (**R- 20** to **R- 22**) and Steam-Reforming reactions (**R- 23** and **R- 24**). Furthermore, a higher heating rate will shorten the residence time of primary volatiles in the reaction zone. Then less time is available for secondary reactions between the volatiles and volatiles with char (Seebauer et al., 1997). As the heating rate increases, the combustible gas production increases; this causes the CO/CO_2 ratio to increase. The average CO/CO_2 ratio increased from 0.84 (at 10 °C/min) to 2.13 (at 80 °C/min), and no significant variation in the H_2/CO ratio is observed by increasing the heating rate as shown in **Table 5-5**. The increase in combustible gases increases the heating value of the gases produced and improves the process's efficiency.

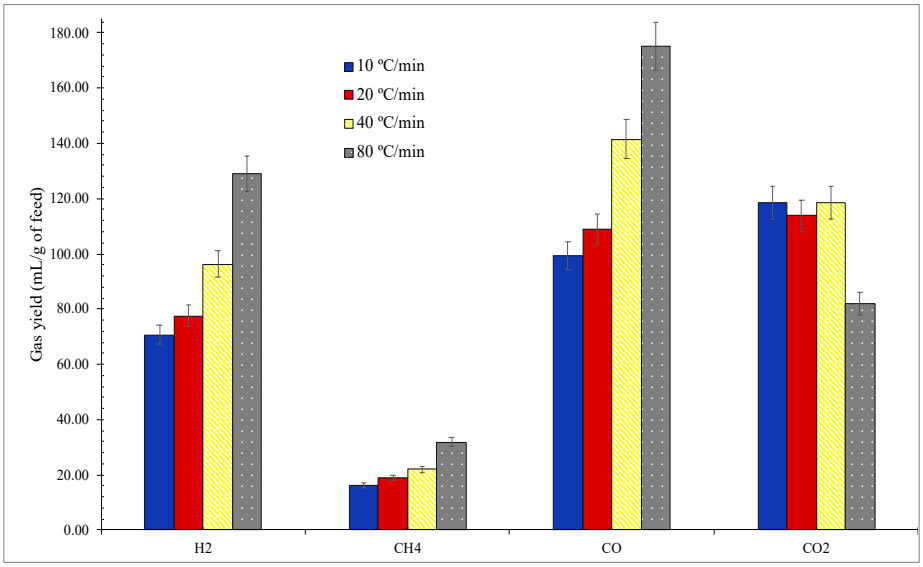

Figure 5-12: Effect of heating rate on gas yield during the pyro-gasification of ASB for ABR=0.50.

The LHVg increased from 4.37 to 6.66 MJ/Nm3, increasing the heating rate between 10 to 80 °C/min. Process efficiency increased from 32.98 to 59.30 % with the increase in heating rate. Despite the increase in process efficiency with heating rate, these values are generally low. The low process efficiency is due to the pyrolysis stage, where many tars are generated.

Table 5-5: The ASB gasification performance at ABR=0.5

Heating rate (ºC/min)	LHV (MJ/ Nm^3)	Gy (Nm^3/kg)	η (%)	CO/CO_2	H_2/CO
10	4.34	0.63	32.98	0.84	0.71
20	4.73	0.64	36.84	0.96	0.71
40	5.33	0.69	44.57	1.19	0.68
80	6.66	0.73	59.30	2.13	0.74

5.2.5. Influence of biomass type on the pyro-gasification products

5.2.5.1. *Effect of biomass type on gas evolution*

In order to show the effect of the type of biomass on the evolution of the gaseous product during gasification, **Figure 5-13** presents the evolution of the experimental results of the gases produced during pyro-gasification of the different types of biomasses studied (CS, AS, ASB, and CEL) for a fixed heating rate (40 ºC/min) and ABR=0.1875. The two pyro-gasification zones can be identified in **Figure 5-13a-d**. A first zone (50-700 ºC) corresponds to the pyrolysis zone, explained in **section 5.2.3.1. .** The second zone (700-1000 ºC) corresponds to the gasification zone, where 3 ml air was injected over the char at an air/biomass ratio (ABR=0.1875). The production of H_2 and CO is more favored than CO_2 due to oxygen deficiency. Partial oxidation reactions are more favored. In **Figure 5-13a-b**, H_2, CO, and CO_2 production behavior are similar, where the maximum peaks are between 7-8, 15-16, and 3-4 mL/ (g of feed) for H_2, CO, and CO, respectively. Perhaps the char of AS and CS are similar; their high lignin content can explain this. In these biomasses, CH_4 was not produced during the gasification of their chars. In **Figure 5-13c-d,** H_2, CH_4, CO, and CO_2 production behavior are similar, where the maximum peaks are between 9.5-11.5, 0.3-0.7, 15-16, and 3.3 -3.4 mL/ (g of feed) for H_2, CO, and CO, respectively. Perhaps the char of ASB and CEL are similar; their high cellulose content can explain this. In these biomasses, CH_4 was not produced during the gasification of their chars. In these biomasses, a small production of CH_4 is observed.

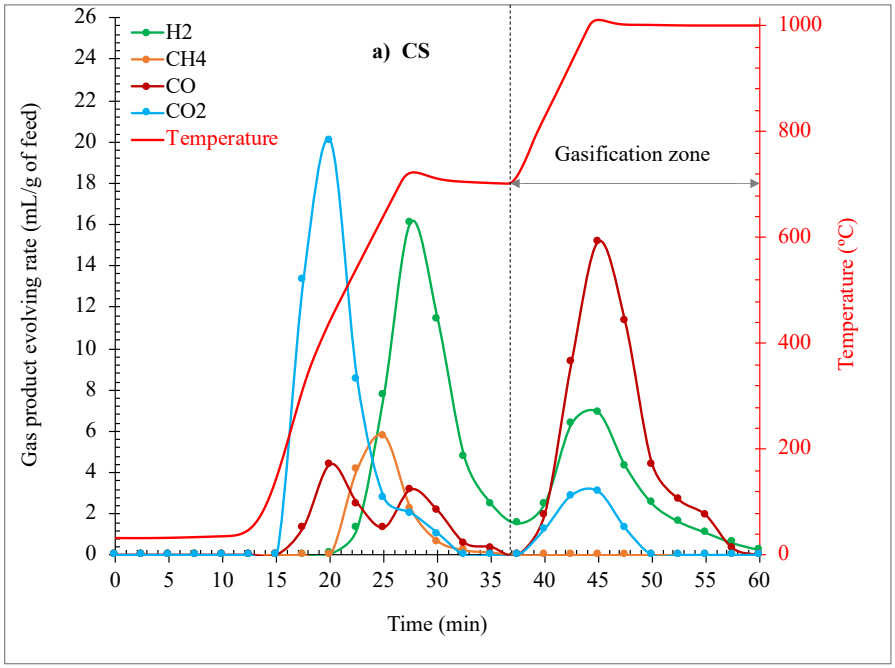

Figure 5-13a: The effect CS evolution of the online gaseous products during pyro-gasification (heating rate 40 ºC/min and ABR=0.1875

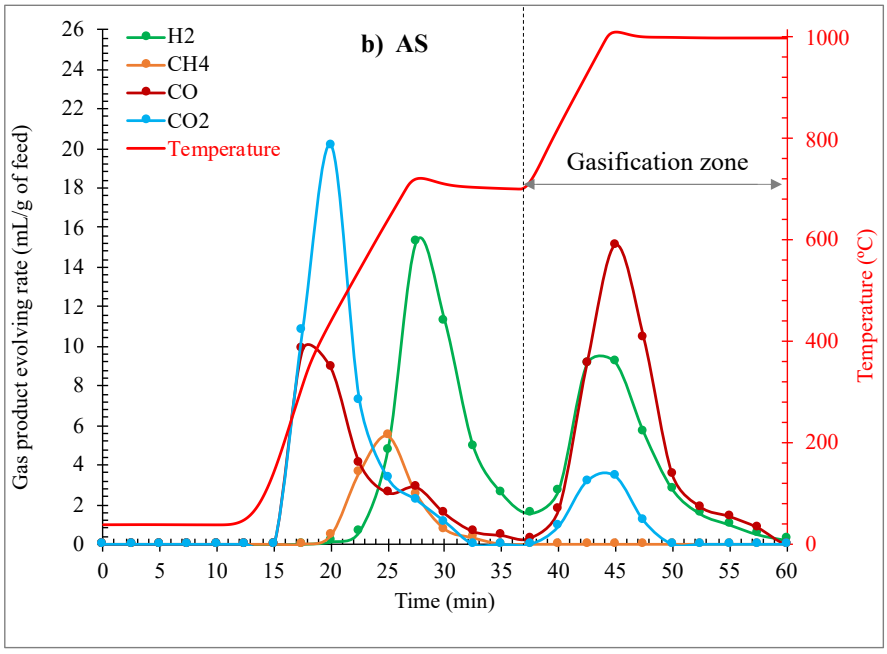

Figure 5-13b: The effect AS evolution of the online gaseous products during pyro-gasification (heating rate 40 ºC/min and ABR=0.1875

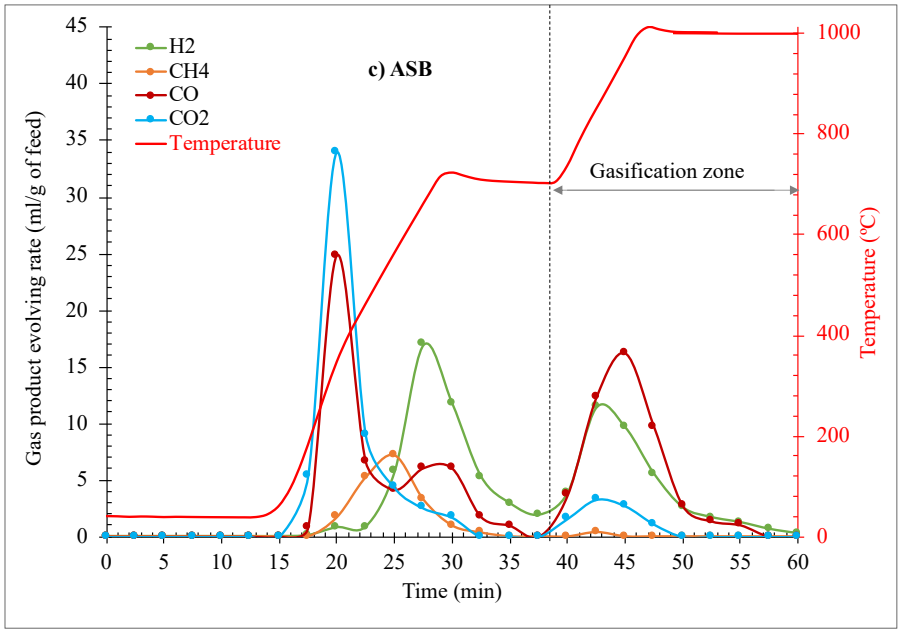

Figure 5-13c: The effect ASB evolution of the online gaseous products during pyro-gasification (heating rate 40 ºC/min and ABR=0.1875

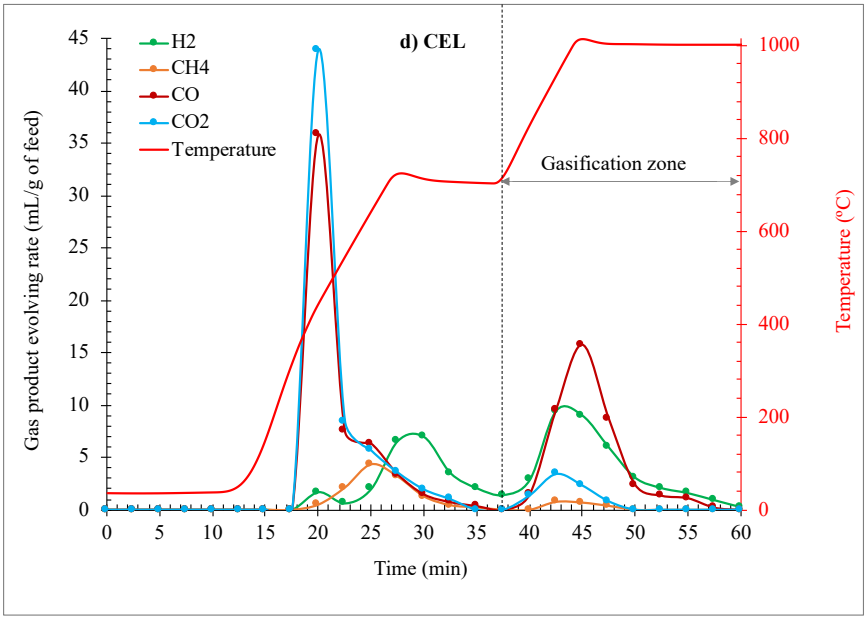

Figure 5-13d: The effect of CEL evolution of the online gaseous products during pyro-gasification (heating rate 40 ºC/min and ABR=0.1875)

5.2.5.2. *Effect of biomass type on pyro-gasification performance*

The biomasses are transformed into gas, bio-oil, and char during thermal conversion. Industrial development of the pyro-gasification processes is slowed down by producing undesirable by-products, which decrease efficiency and occasionally require very costly treatments (De Wild

et al., 2009; Demirbas, 2002). A technology for undesirable solids (ash) recovery is necessary for char since char accumulation obstructs the reactors. Gas-phase recovery must limit by tar condensation, leading to fouling and clogging of process equipment (Kiel et al., 2004). In addition, the gas composition (e.g., H_2/CO and contaminants) needs to be determined with a view to the later application and post-treatment process. Several studies have shown that the type and composition of the biomass feedstock influence the distribution of pyro-gasification products (gas, tar/bio-oil, char) and their characteristics and composition (Aznar et al., 2006; Mastellone et al., 2010). In this pyro-gasification process, all biomasses were subjected to a heating rate of 40 ºC/min, up to 700 ºC as a pyrolysis stage. The air was injected with ABR=0.1875 from 700 to 1000 ºC, as represented in Fig 6a and 6b. The biomass-char gasification reaction starts from 700 °C. This temperature is slightly less when compared to the reported temperature of 800 °C using coal-char steam gasification. Recently, authors (Jayaraman and Gökalp, 2015) also reported that the miscanthus-char and sewage sludge steam gasification process starts around 800 °C and 750 °C, respectively rate of 40 K/min. During the char-gasification process, CO, CO_2, and H_2 gases are released, besides a small amount of CH_4 also. Dong (2016) pyro-gasified (FB, 650 °C, 15 min) 4 potential municipal solid waste components (poplar wood, cardboard, food waste and polyethylene) under 3 reaction atmospheres (N_2, steam and CO_2). In all three atmospheres and for the pure components, H_2 and CH_4 concentrations increased in the following order: poplar wood < cardboard < food waste < polyethylene; for CO and CO_2 the order was reversed. Co-gasification of polyethylene with wood, cardboard or food waste, as binary blends, increased the concentration of H_2 and CH_4 and decreased the concentration of CO and CO_2 more than expected by the linear calculation of the individual components, due to a synergistic effect.

Wilk and Hofbauer (2013) co-gasified (dual fluidized bed (DFB), steam gasification, 850°C) softwood pellets and different types of plastics (up to 100%): polyethylene (PE) from packaging, plastics from MSW, and plastics from end-of-life vehicle treatment (shredder light fraction). It was observed that the H_2 concentration, on average, was almost constant when plastics were added to the wood. In the case of mixtures, nonlinear effects were observed, but there was no particular pattern of H_2 as a function of the proportion of plastics for various plastic materials. As the number of plastics in the mixture increased, the concentration of CO and CO_2 decreased. The decrease was more pronounced for PE plastics than for SLF (end-of-life vehicle light agitation) and MSW, which is attributable to the amount of oxygen in the feedstock, according to Wilk and Hofbauer (2013). CH_4 and CnHm concentrations and tar yield

have increased with the increasing plastic fraction. Pyro Gasification (Fluidized beds with bed olivine content, 725 to 875 °C, air) of wood–PET (polyethylene terephthalate) pellets were reported to be a worse result, by Robinson et al. (2016), than wood pellets alone: the tar levels were much higher, and the energetic content were low; the H_2 gas concentration was lower while the CO_2 and CO concentration of wood pellet were much higher. The authors do not provide an explanation for these observations. However, such results may mean that the co-gasification of plastics and biomass could prevent PET better. As PET recycling practices exist, this should not be a concern. Brachi et al. (2014) (FB, steam + oxygen + nitrogen 745-856 °C) have also found high concentrations of tar in tents recorded by Robinson et al. (2016).

Lee et al. (2014)studied the production of clean gaseous fuels (syngas) using MSW, rubber and plastic, wood (fixed bed, 700 ºC, 1000 ºC steam). The authors implemented a high-temperature gasification process with steam at 1000 °C to produce syngas whose concentration is mainly controlled by H2 and can be used as gaseous fuels due to the gas to water shift reaction. No significant differences were observed between the results obtained for the different feedstocks, which shows that steam gasification can convert any material containing C, H, and O into a gaseous fuel with 50-60% H2, approximately 10% CO and CO_2, and 3% CH_4, despite the different characteristics of the feedstocks (C (43-81%); O (30-40%); moisture (0- 15%)). In the raw materials studied, plastics gave the highest H_2 concentration and the lowest CO, CO_2, and CH_4, while wood gave the lowest H_2 concentration and the highest CO concentration. The highest LHVg value was obtained for rubber (10.8 MJ/m^3) and the lowest for plastics (7.8 MJ/m^3).

Although the gasification products depend on the operating condition, the type of biomass has a great influence on the decomposition of these feedstocks. The influence of the type of biomass was studied by different authors (Cepeliogullar and Putun, 2014; Yang et al., 2016a; Zhou et al., 2015b).

Cepeliogullar and Putun (2014) studied the co-pyrolysis (semi-continuous reactor) of PET and PVC, each blended with four distinct types of biomasses. The authors observed that for PET mixtures, the bio-oil yield increased with the lignin content of the biomass. In the case of PVC and biomass blends, the gas yield increased with the increasing lignin content of the biomass.

Zhou et al. (2015b) used PVC with xylan, cellulose, or lignin (1/1 blends). The authors reported that with increasing xylan and lignin, the gas yield increases while the char yield decreases. On the other hand, cellulose gave the opposite results. Yang et al. (2016a) investigated the presence

of aliphatic and aromatic hydrocarbons in bio-oil obtained by fast co-pyrolysis of polyethylene and different types of biomasses. They observed a positive synergistic effect for aliphatic hydrocarbons; the synergistic effect for aromatic hydrocarbons was either positive or negative, depending on the feedstock type of biomass. As can be seen, the type of biomass has many effects on the gasification products. In order to use biomass during the gasification process, it is not possible to rely on literature studies on other types of biomasses. Therefore, operating conditions, type of biomass, and even the location of the biomass have direct effects on the products. For the four biomasses studied, there is a direct relationship between the chemical composition of the biomass and the gas obtained by gasification. The product gas found in this pyro-air-gasification is composed of combustible gases (CO, H_2, CH_4) and non-combustible gases (CO_2 and N_2, where N_2 is derived from the air). The performance of the products depends mainly on the biomass type. **Table 5-6** shows the experimental values of syngas performances for different types of biomasses.

Table 5-6: Effect of biomass type on pyro-gasification performance for (40 ºC/min and ABR=0.1875)

	Feedstock			
Product gas composition (mol.%)	AS	CS	ASB	CEL
H_2	20.22	20.34	20.49	15.28
CH_4	3.60	3.72	3.72	3.49
CO	20.55	17.74	17.74	24.46
Combustibles gases	**44.36**	**41.80**	**41.94**	**43.23**
N_2	41.01	42.36	42.04	38.34
CO_2	14.63	15.84	16.01	18.43
Non-combustibles gases	**55.64**	**58.20**	**58.06**	**56.77**
Gy (Nm^3/kg)	0.37	0.35	0.42	0.40
LHVg (MJ/Nm^3)	6.06	5.76	5.78	5.98
η (%)	36.88	28.88	56.34	41.36

As shown in **Table 5-6**, the influence of the biomass type is not considered for the H_2 content obtained between AS, CS, and ASB, where its content represents about 20 mol.% of the total gas produced; while for CEL, H_2 represents only 15 mol.% of the total gas. Nevertheless, a high CO content (24.46 mol.%) is obtained in CEL. The CH_4 content is similar for all samples analyzed. The highest heating value (HLVg) of syngas is obtained for AS, and the lowest HLVg

is obtained in CS. The high ash content in CS may explain its low HLVg. All biomasses studied have a lower ash content than CS. Therefore, they are suitable fuels for fixed-bed gasifiers. On the other hand, these biomasses contain a high amount of volatile matter (VM). In an updraft gasification system, they will produce gas containing high concentrations of tar, which must be cleaned before use in the engines. Gas cleaning is a complicated and laborious process. Therefore, these biomasses are not suitable in an updraft gasifier coupled to internal combustion engines. On the other hand, tar-containing gas from an updraft gasifier can be used for direct combustion. Downdraft systems can be designed to deliver virtually tar-free product gas in a specific capacity range when feeding these biomasses with low moisture content. After passing through a relatively simple cleaning train, the gas can be used in internal combustion engines.

5.2.6. Comparison between hydrochar and raw biomass gasification.

In this non-isothermal gasification process, the biomasses (AS, CS, and CEL) and their hydrochars produced at 250 ºC were subjected to a heating rate of 80 ºC/min, up to 1000 °C. Air was injected from 100 °C up to the final temperature. All gases were collected in the gas bag for further analysis.

Figure 5-12 shows the characteristic of gas product between hydrochar and raw biomass gasification. As can be seen, the performances of the combustible gases (H_2, CO, and CH_4) are much higher for the hydrochars than for the raw biomass. In addition, the yield of non-combustible gas (CO_2) is much lower in hydrochars. Generally, the CO_2 produced during biomass gasification comes directly from total oxidation when excess oxygen exists. This excess oxygen can come from the gasifying agent and the oxygen content in the raw biomass. One of the main objectives of hydrothermal carbonization is to produce hydrochar with less oxygen content. This may be one of the reasons why CO_2 production is low for hydrochar. As can be seen in **Figure 5-12b**, among the primary component in the non-condensable gases, the increase in H_2 concentration (based on the amount of total gas) became even more considerable over the other gases after HTC, increasing from 23.09% (AS), 30.44% (CS) and 20.19% (CEL) to 32.19%, 36.61% and 31.70% at 250 °C, respectively. That is an increase of 39.41, 20.29, and 56.96 % for AS, CS, and CEL, respectively. Previous studies showed that the gasification of biomass could take place in two consecutive stages: an initial stage related to the decomposition of volatile compounds (temperature under 600 °C) and a subsequent phase

involving the conversion of char and the reactions of the gases produced in the first stage (above 600 °C) (Álvarez-Murillo et al., 2015a; Duman et al., 2014).

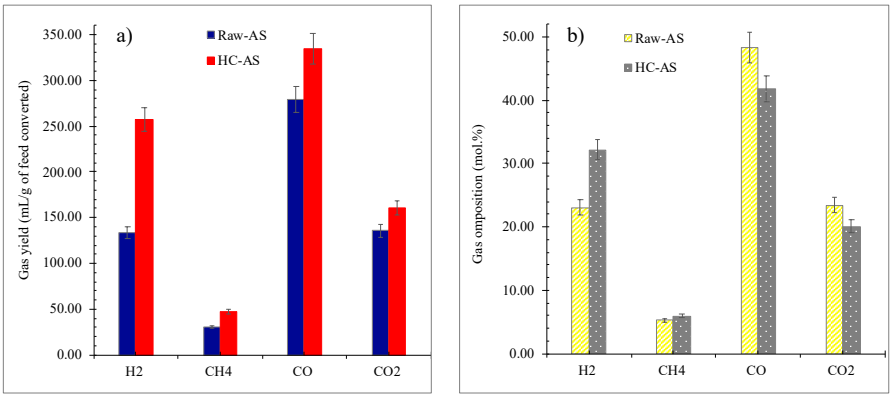

Figure 5-14a: characteristic of gas product of AS gasification between hydrochar and raw biomass

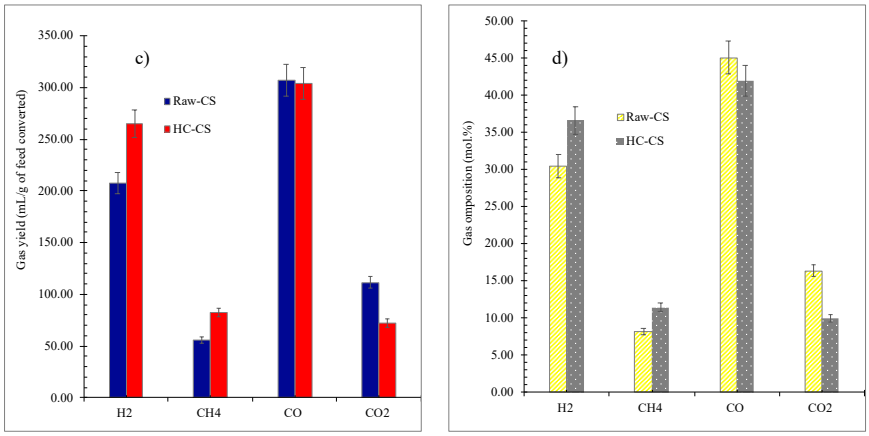

Figure 5-14b: characteristic of gas product of CS gasification between hydrochar and raw biomass

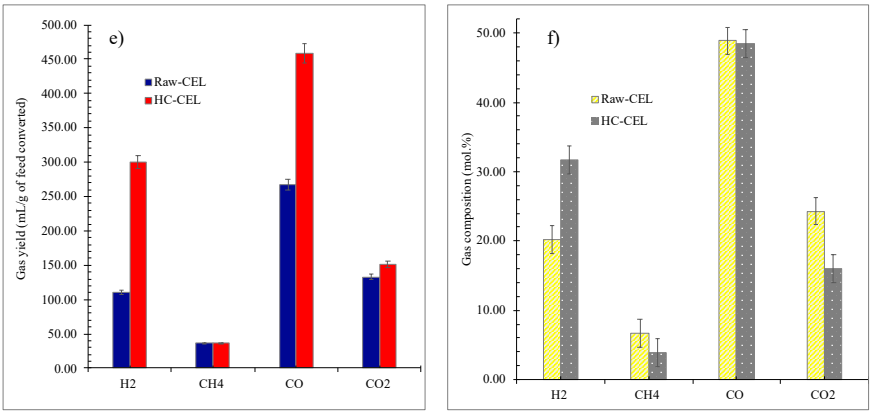

Figure 5-14c: characteristic of gas product of CEL gasification between hydrochar and raw biomass

H_2 formation is therefore grouped in two phases according to the temperature range during the gasification process. In the first stage, a section of H_2 is formed by creaking or reforming (**R-2**), while the rest of H_2 is derived from the secondary steam-tar reforming (**R- 3**), char gasification (**R- 7**), and higher temperatures from water-to-gas (**R- 6**) (Duman et al., 2014; Zhuang et al., 2020). Gai et al. (2016)reported that the secondary reactions provide the most to H_2 production during the gasification process; therefore, it can be said that the higher H_2 content produced by hydrochar is caused by the change in carbonaceous structures that is relevant to the second step of gasification, even though the devolatilization process in HTC somewhat reduces H_2 formation in the first step. Moreover, the structure (surface area and pore volume) of hydrochars were enhanced during hydrothermal carbonization, which can stimulate the diffusion of air and tar into the particle sites and, as a result, promote both the gas-to-water shift reaction and in situ tar reforming (Feng et al., 2018). SEM illustrations by Gai et al. (2016) confirm this explanation since the fragmented structure of hydrochar becomes porous access for steam reforming. Furthermore, the carbonaceous residue in hydrochar constantly grown during HTC, increasing the reagent for char gasification and gas-to-water shift reactions(Álvarez-Murillo et al., 2015a). In addition, alkaline earth metals such as K, Na, Ca, and Mg also enriched in the solid phase after HTC, especially in the case of CS, whose ash content reached the highest value, playing a positive role in catalyzing H_2 production through steam gasification and tar reforming (Feng et al., 2018; Zhuang et al., 2020). Regarding CH_4, whose concentration occupied the smallest part in all gas, the contribution of CH_4 toward gaseous products could be negligible, even though the CH_4 content from samples somewhat increased (**R- 10**) after treated by HTC. Compared to the increasing trend of H_2 and CH_4, the content of CO and CO_2 followed a reverse trend in hydrochars during the gasification process. This downward tendency can be explained by the devolatilization mechanism of the HTC devolatilization mechanism (Moon et al., 2015; Zhang et al., 2016). All of them started from a relatively high value in raw materials and then reduced gradually with the increase of HTC temperatures, CO_2, and CO in particular (follows a reaction pattern of (**R- 17**) and (**R- 23**), respectively). Therefore, it can be inferred that HTC is favorable to remove the oxygen-containing functional groups in biomass structure for the subsequent gasification, thereby avoiding the production of inutile gaseous components(Álvarez-Murillo et al., 2015a; Moon et al., 2015). Furthermore, the elimination of functional groups containing oxygen also suppresses hydrogen consumption (Zhang et al., 2016); thus, the production of CO and CO_2 maintains at a lower fraction in syngas derived from hydrochars, whereas that of H_2 is the opposite. Overall, the total gas yield (as a function of raw feedstock converted) experienced an apparent upward

trend after HTC compared to the raw biomasses. This result is mainly due to the hydrolysis of organic matter in the HTC process; moreover, the syngas derived from the hydrochars improved. As a result, the LHVg in the syngas from hydrochars were better than the raw biomasses. The LHVg of syngas increased from 5.46 to 6.1 MJ/Nm^3 for AS, 6.44 to 7.14 MJ/Nm^3 (CS), and 5.43 to 5.69MJ/Nm^3 for CEL at a hydrothermal temperature of 250 °C. This improvement in LHVg agrees with the gas composition results mentioned above, which is achieved by increasing H_2 and decreasing CO_2 (Feng et al., 2018; Zhuang et al., 2020).

5.2.7. Kinetic analysis of pyrolysis

The isoconversional methods described in **section 5.1.5.2.** were applied in this section to determine the kinetic parameters of the pyrolysis of biomasses. TG/DTG experimental data of biomasses pyrolysis obtained under the nonisothermal condition in argon atmosphere were used for kinetic analysis. Different model-free methods such as Flynn-Wall-Ozawa (FWO), Kissinger-Akahira-Sunose (KAS), and Friedman methods are employed to obtain parameters like the activation energy and preexponential factor. The thermograms recorded for all biomasses at three different heating rates (10, 20, and 40 ºC/min) were used with above mentioned model-free methods to calculate the kinetic parameters. The conversion range up to 90 wt.% was taken as the kinetic analysis range for each heating rate to obtain the isoconversion plot of activation energy Eα with conversion (α). The temperature range for kinetic studies is taken as 150–700 ºC as at temperatures less than 150 ºC, only moisture, and physically absorbed water is removed, and there is almost negligible weight loss after 700 ºC.

5.2.8. Kinetic analysis of AS pyrolysis

The thermal behavior of the AS was studied through TGA in the temperature range of 150-700 ºC. The TG and DTG curves at three different heating rates (10, 20, and 40° C/min) were used to determine the kinetic parameters. These plots were used for the kinetic analysis based on the three kinetic models above described. According to the Friedman differential model, activation energy (Eα), based on **Eq.(5-24)**, can be determined from a plot of ln[da/dt] versus 1/T, and results are presented in **Figure 5-17**. Here, the slopes of the iso-conversational lines give (Ea/R) at progressing conversion degrees a. Activation energy has also been calculated using the integral FWO method using **Eq.(5-23)**, and **Figure 5-15** presents the iso-conversational linear plots of ln(b) versus 1/T where slopes give 0.453 Eα /R at progressing conversion degrees for this method. Finally, **Figure 5-16** shows results for the integral KAS method using **Eq.(5-21)**,

where linear plots of ln (ß/T^2) versus 1/T provide slopes to determine (Ea/R) at progressing conversion degrees (α).

5.2.8.1.1. *Flynn-Wall-Ozawa (FWO) method*

The values obtained for the activation energy are in the range of 54.77-93.83 kJ/mol, with coefficients of determination (R^2) higher than 0.996 for all the conversion range, and the values are represented in **Figure 5-15** and **Table 5-7**. A similar result was reported by Maia and de Morais (2016) during pyrolysis of pepper waste, where the authors obtained activation energy values between 29-147 kJ/mol using the same FWO method.

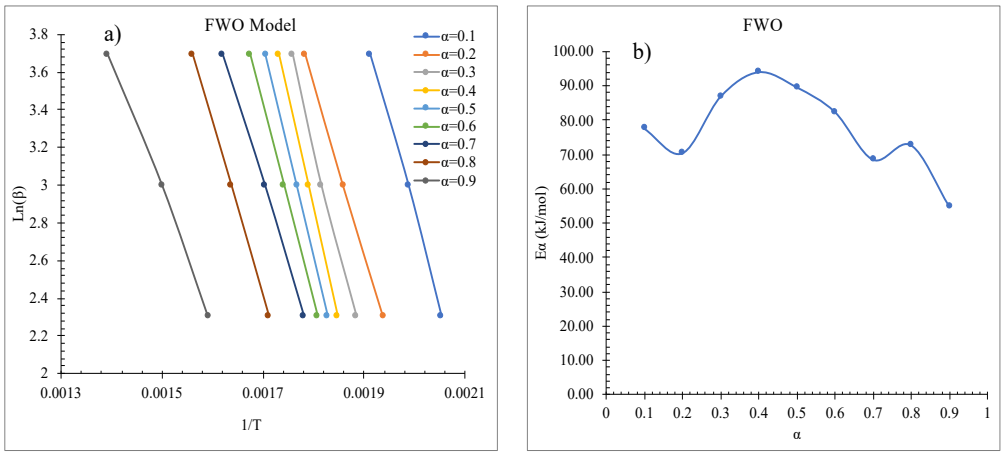

Figure 5-15: FWO-model plots of AS pyrolysis at different values of conversion (**a**) and activation energy vs conversion **(b)**

5.2.8.1.2. *Kissinger-Akahira-Sunose (KAS) method*

The activation energy value obtained using the KAS method is in the range of 71.45-145.91 kJ/mol, with coefficients of determination (R^2) greater than 0.995, and the data are reported in **Figure 5-16** and **Table 5-7**.

These values are similar to those obtained by Zhou et al. (2015a) during the pyrolysis of xylan using the FAS model; the authors reported 26-164 kJ/mol for the activation energy. The activation energy values for KAS and FWO method are similar; it varies with increasing conversions. AS biomass presents three small activation energy values in the range of 20, 70, and 90 %, corresponding to 64.99, 62.15, and 45.46 kJ/mol. The variation of the values of activation energies is not similar to different conversion constant extensions because most solid-state reactions are not simple one-step mechanisms and follow a complex multi-step

reaction. These values may be due to the change of mechanism of the reactions. In general, the activation energy values found for AS are comparatively low. These values indicate that only lower activation energy is needed to decompose biomass with higher hemicellulose content, as is the case for AS. The values obtained for the FWO and KAS models are practically identical. The slight differences observed in Eα values obtained using KAS and FWO can be assigned to the different approximations of the temperature integral.

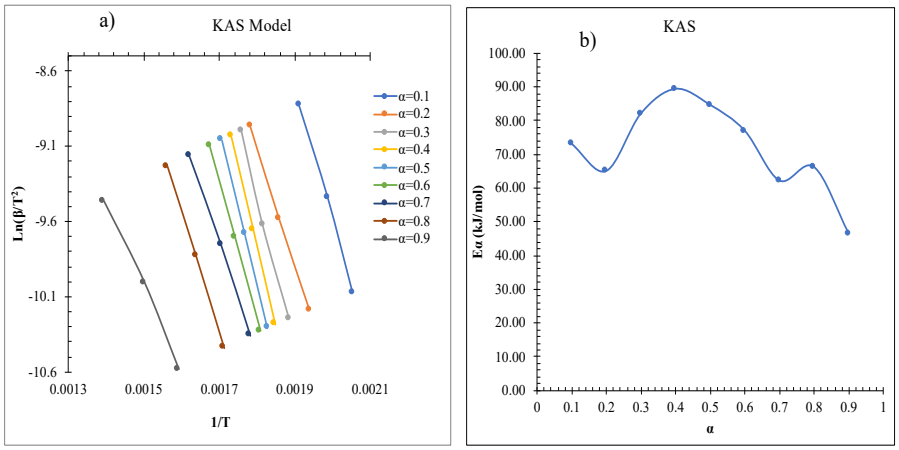

Figure 5-16: KAS-model plots of AS pyrolysis at different values of conversion (**a**) and activation energy vs conversion **(b**)

In **Figure 5-15** and **Figure 5-16** , the values of Eα are not similar for all conversion values, indicating the existence of a complex multi-step mechanism reaction that occurs in the biomass HTC process. The progressive variation of Eα values could correspond to competitive and consecutive reactions and the multiphasic biomass conversion.

5.2.8.1.3. *Friedman method*

The activation energy value obtained using the Friedman method is in the range of 19.03-133.37 kJ/mol, with coefficients of determination (R^2) greater than 0.898, and the data are reported in **Figure 5-17** and **Table 5-7**. Although the Ea values obtained by the Friedman method have a high coefficient of variation, there is a significant fluctuation with these values. The Eα values obtained for the integral methods (FWO and KAS) are similar and show the best fit correlation coefficient (R^2) compared to the differential method (Friedman). The Friedman method requires derivative conversion data, which would lead to being numerically unstable and noise-sensitive (Cai et al., 2018). For this reason, in general, the integral methods show the best-fit correlation coefficient values than the differential method.

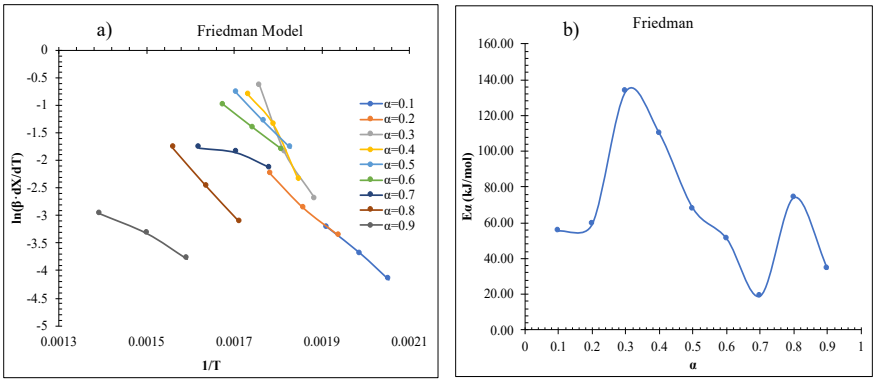

Figure 5-17: Friedman-model plots of AS pyrolysis at different values of conversion (**a**) and activation energy vs conversion **(b**)

5.2.8.2. *Kinetic analysis of ASB pyrolysis*

The TG and DTG results of ASB pyrolysis obtained under conditions at different heating rates of 10, 20, and 40°C/min under argon atmospheres were used for kinetic analysis. In addition, the activation energy and the pre-exponential factor for the pyrolysis process were calculated as a conversion function using the isoconversional methods of KAS, FWO, and Friedman.

5.2.8.3. *Flynn-Wall-Ozawa (FWO) method*

The values obtained for the activation energy are in the range of 76.26-149.15 kJ/mol, with coefficients of determination (R^2) higher than 0.995 for all the conversion range, and the values are represented in **Figure 5-18** and **Table 5-8**. These values are similar to those obtained by Edreis and Yao (2016) during the pyrolysis of sugarcane bagasse using the FWO model; the authors reported 70-174 kJ/mol for the activation energy.

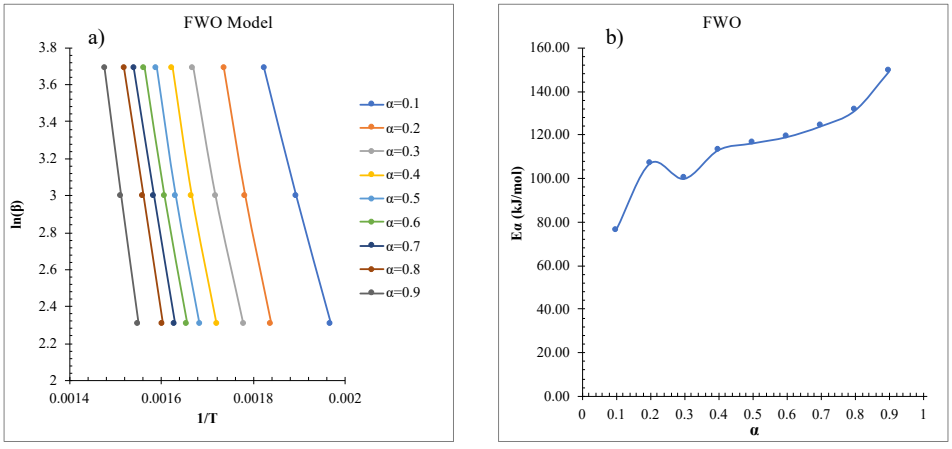

Figure 5-18: FWO-model plots of ASB pyrolysis at different values of conversion (a) and activation energy vs conversion (b)

5.2.8.3.1. *Kissinger-Akahira-Sunose (KAS) method*

The activation energy value obtained using the KAS method is in the range of 71.45-145.91 kJ/mol, with coefficients of determination (R^2) greater than 0.991, and the data are reported in **Figure 5-19** and **Table 5-8**. A similar result was reported by Slopiecka et al. (2012) during pyrolysis of wood, where they obtained activation energy values between 104-209 kJ/mol using the same KAS method. As shown in **Table 5-8**, the change in the activation energy Eα according to the conversion α calculated by the FWO and KAS methods is consistent. The activation energy increases with increasing α-conversion. The average activation energy calculated by the FWO method is slightly higher than that of the KAS methods by about 4.05 kJ/mol. Both models present high correlation coefficient values (R^2>0.99)

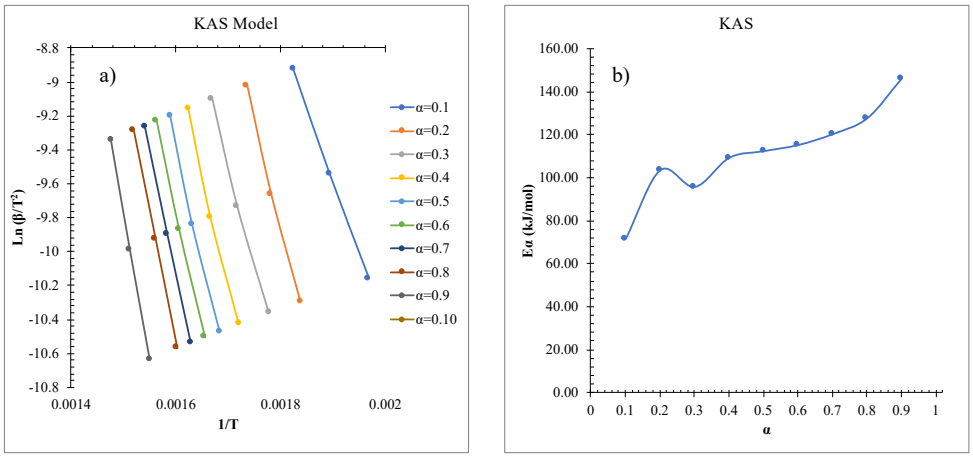

Figure 5-19: KAS-model plots of ASB pyrolysis at different values of conversion (**a**) and activation energy vs conversion **(b)**

5.2.8.4. *Friedman method*

The activation energy value obtained using the Friedman method is in the range of 57.88-169.26 kJ/mol, with coefficients of determination (R^2) greater than 0.984, and the data are reported in **Figure 5-20** and **Table 5-8.** Similar results were reported for other types of biomasses such as miscanthus (131-167kJ/mol) and wood chips (131-214 kJ/mol) using the same Friedman method (Gasparoviv et al., 2010).

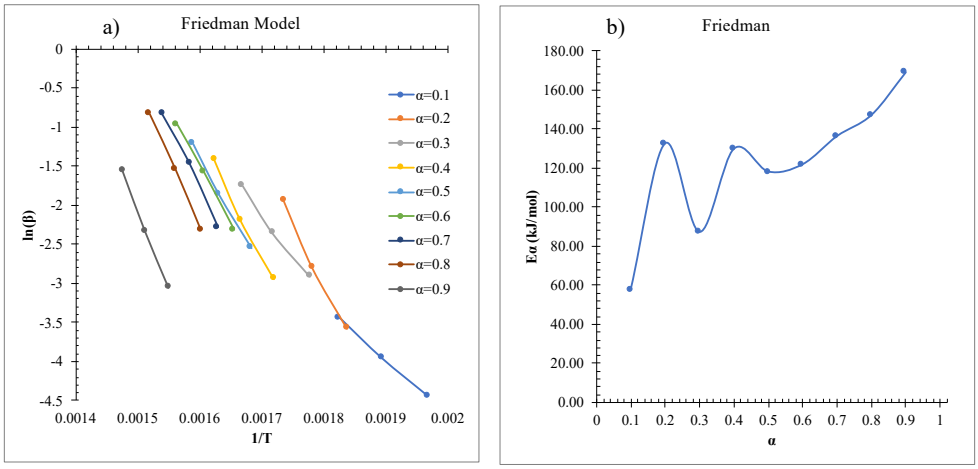

Figure 5-20: Friedman-model plots of ASB pyrolysis at different values of conversion (**a**) and activation energy vs conversion **(b**)

5.2.8.5. *Kinetic analysis of CS pyrolysis*

Similar to AS and ASB, the TG and DTG results of ASB pyrolysis obtained under conditions at different heating rates of 10, 20, and 40°C/min under argon atmospheres were used for kinetic analysis. In addition, the activation energy and the pre-exponential factor for the pyrolysis process were calculated as a conversion function using the isoconversional methods of KAS, FWO, and Friedman.

5.2.8.5.1. *Flynn-Wall-Ozawa (FWO) method*

The values obtained for the activation energy are in the range of 81.38-130.75 kJ/mol, with coefficients of determination (R^2) higher than 0.996 for all the conversion range, and the values are represented in **Figure 5-21** and **Table 5-9**. Mumbach et al. (2020) reported values for cocoa shell activation energy (99 to 271 kJ/mol). The significant difference between the activation energy values obtained in this study and those reported by Mumbach et al. (2020) is due to the chemical structure of each sample. For example, Mumbach et al. (2020) reports high cellulose content in the cocoa shell (30.72 wt.%), while in this work, it is only 7.8 wt.%.

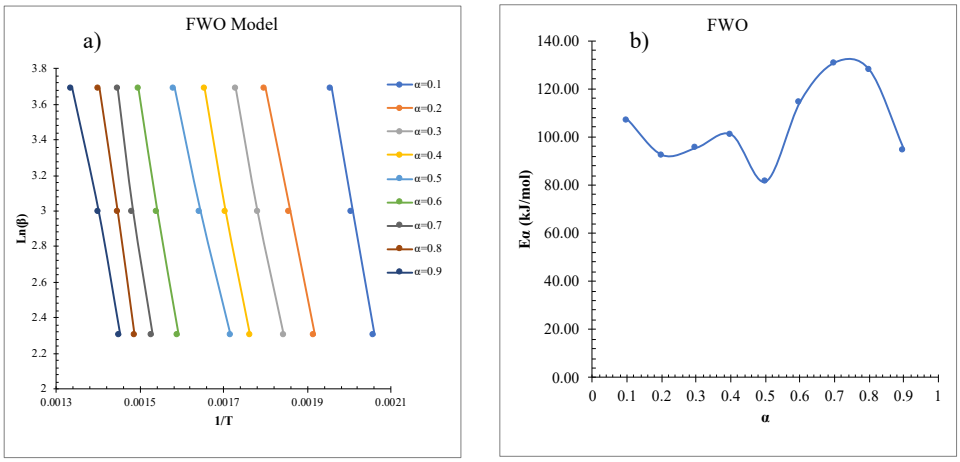

Figure 5-21: FWO-model plots of CS pyrolysis at different values of conversion (a) and activation energy vs conversion (b)

5.2.8.5.2. *Kissinger-Akahira-Sunose (KAS) method*

The values obtained for the activation energy are in the range of 81.38-130.75 kJ/mol.

The coefficients of determination (R^2) are higher than 0.995 for all the conversion range, and the values are represented in **Figure 5-22** and **Table 5-9**. As shown in **Table 5-9** the change in the activation energy Eα according to the conversion α calculated by the FWO and KAS methods is consistent. The average activation energy calculated by the FWO method is slightly higher than that of the KAS methods by only 4.73 kJ/mol. Both models present high correlation coefficient values (R^2>0.995).

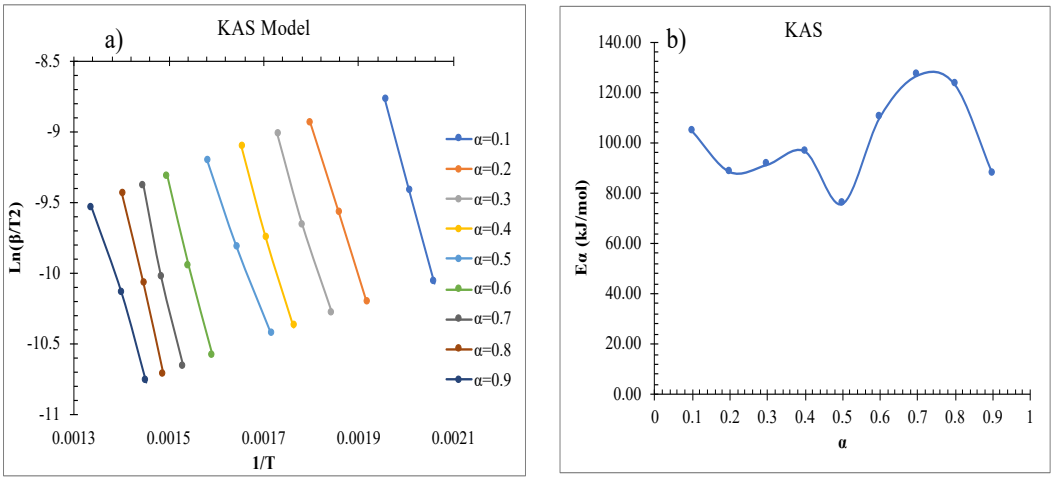

Figure 5-22: KAS-model plots of CS pyrolysis at different values of conversion (a) and activation energy vs conversion (b)

5.2.8.5.3. *Friedman method*

The values obtained for the activation energy are in the range of 81.38-130.75 kJ/mol. The coefficients of determination (R^2) are higher than 0.969 for all the conversion range, and the values are represented in **Figure 5-23** and **Table 5-9**.

The coefficient of variation obtained for the Friedman model is lower than the integral models. In addition, a considerable variation of activation energy is observed compared to FWO and KAS, although all the models present a similar tendency. Although the fluctuation of activation energy with conversion may be due to the mechanism of the reactions, the significant difference in values obtained for the Friedman model may be due to the numerical instability of the model and sensitive noise-sensitive (Cai et al., 2018)

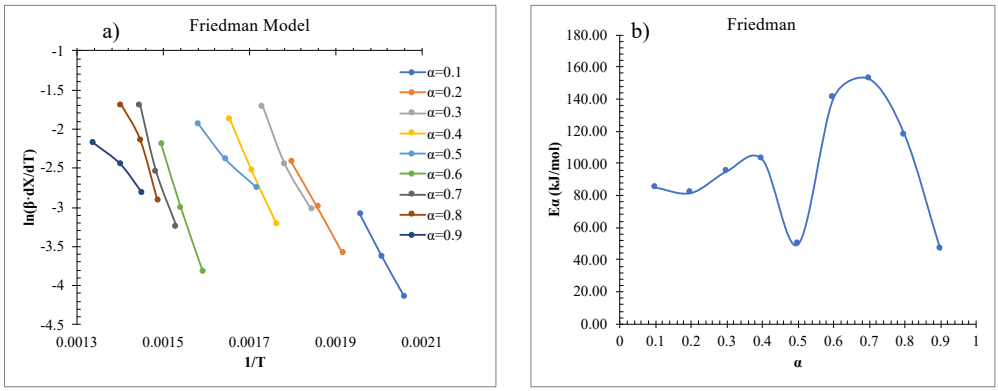

Figure 5-23: Friedman-model plots of CS pyrolysis at different values of conversion (a) and activation energy vs conversion (b)

5.2.8.6. *Kinetic analysis of CEL pyrolysis*

The kinetics of CEL (α-cellulose), a model biomass, has been extensively studied by many authors using different approaches. Different values have been reported, for example,Conesa et al. (1995) (178.9-200.6 kJ/mol), Di Blasi (1998) (152.8-210.4 kJ/mol), Miller and Bellan (1997) (108-242.4 kJ/mol), Ranzi et al. (2008) (192.6 kJ/mol) and Serbanescu (2014) (130-270 kJ/mol). As can be seen, there is a wide range of activation energy values for cellulose pyrolysis. The values range from 108 to 270 kJ/mol. The discrepancy of the values reported in the literature is mainly due to the method used to determine; also, the pyrolysis condition can affect (inert atmosphere used). However, most of these studies use isoconversional models (such as FWO, KAS, Friedeman, or similar) based on TG/DTG analysis. In this study, the TG

and DTG results of CEL pyrolysis obtained under conditions at different heating rates of 10, 20, and 40°C/min in argon atmospheres were used for kinetic analysis. Furthermore, the activation energy and the pre-exponential factor for the pyrolysis process were calculated as a conversion function using the isoconversional methods of KAS, FWO, and Friedman. The values of the kinetic parameters obtained are presented in **Table 5-10**, depending on the model used. The values are between 125.14-262.24 kJ/mol).

5.2.8.6.1. *Flynn-Wall-Ozawa (FWO) method*

The values obtained for the activation energy are in the range of 152.03-214.41 kJ/mol, with coefficients of determination (R^2) higher than 0.998 for all the conversion range, and the values are represented in **Figure 5-24** and **Table 5-10**.These values are similar to those reported by Di Blasi (1998) (152.8-210.4 kJ/mol). also for the values obtained for Conesa et al. (1995) (178.9-200.6 kJ/mol). This shows the accuracy of the FWO model.

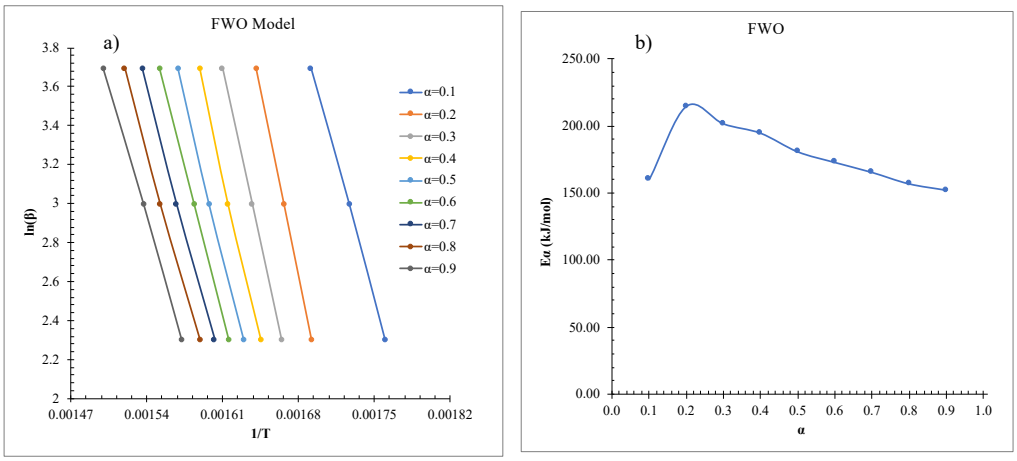

Figure 5-24: FWO-model plots of CEL pyrolysis at different values of conversion (a) and activation energy vs conversion (b)

5.2.8.7. *Kissinger-Akahira-Sunose (KAS) method*

Similar to FWO model, the values obtained for the activation energy are in the range of 149.11-215.58 kJ/mol, with coefficients of determination (R^2) higher than 0.998 for all the conversion range, and the values are represented in **Figure 5-25** and **Table 5-10**. These values are similar to those reported by Di Blasi (1998) (152.8-210.4 kJ/mol). also for the values obtained for Conesa et al. (1995) (178.9-200.6 kJ/mol). This shows the accuracy of the FWO model. As shown in **Table 5-10**, the change in the activation energy Eα according to the conversion α

calculated by the FWO and KAS methods is consistent. The activation energy has an initial peak increase, subsequently decreasing with increasing α-conversion. As a result, the average activation energy calculated by the FWO method is slightly higher than that of the KAS methods with only 1.11 kJ/mol. Therefore, it can be considered that they are equal; moreover, both models present high values of the correlation coefficient (R^2>0.998).

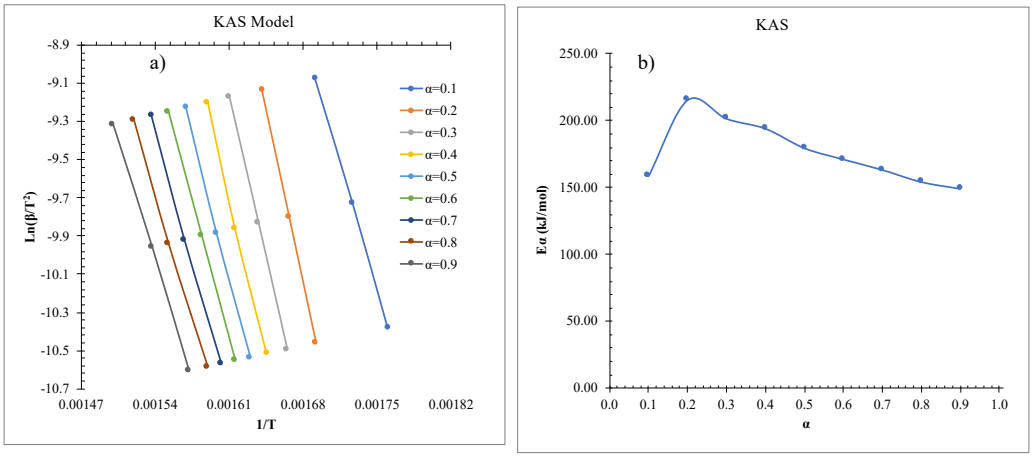

Figure 5-25: KAS-model plots of CEL pyrolysis at different values of conversion (a) and activation energy vs conversion (b)

5.2.8.7.1. *Friedman method*

The values obtained for the activation energy are in the range of 125.41-262.24 kJ/mol. The coefficients of determination (R^2) are higher than 0.976 for all the conversion range, and the values are represented in **Figure 5-26** and **Table 5-10**.

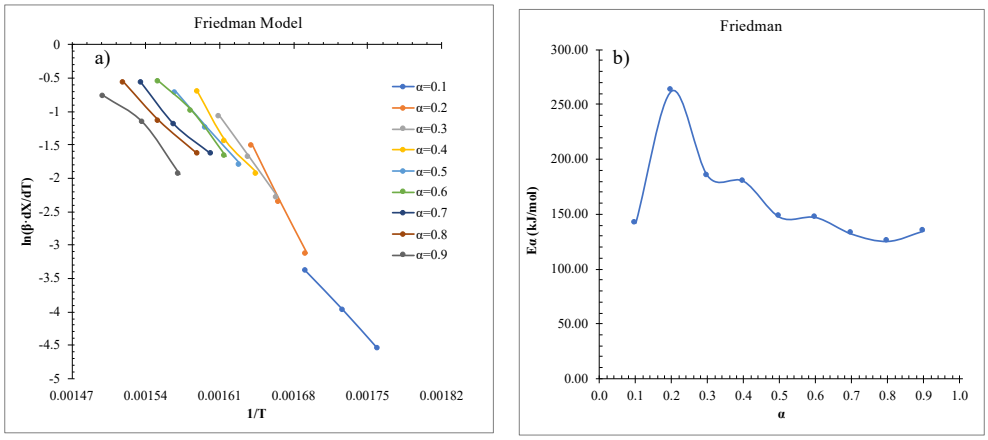

Figure 5-26: Friedman-model plots of CEL pyrolysis at different values of conversion (a) and activation energy vs conversion (b)

Table 5-10 summarizes all the kinetic parameters of the three models and the four biomasses studied. In lignocellulose biomass, the energy activation will vary between 80 kJ and 200 kJ/mol in hemicellulose, between 195 and 286 kJ/mol in cellulose 18 and 65 kJ/mol in lignin (Maia and de Morais, 2016). Therefore, the activation energy values of the biomasses studied in this work vary as follows: The energy activation of AS varied from 29 kJ/mol to 147 kJ/mol. The ASB and CS have energy activation values between 87 and 169 kJ/mol and between 46 and 152 kJ/mol. The CEL has a value of 125–262 kJ/mol. It can be said that the values obtained for this study are in agreement with those obtained in the literature. All the models used were good for determining the kinetic parameters. On the other hand, the Eα values obtained for the integral methods (FWO and KAS) are similar and show the best fit correlation coefficient (R^2) compared to the differential method (Friedman). The Friedman method requires derivative conversion data, which would lead to being numerically unstable and noise-sensitive (Cai et al., 2018).

Table 5-7: Kinetic parameters calculated for AS by three isoconversional methods.

	FWO			KAS			Friedman		
α	Ea(kJ/mol)	A(min^{-1})	R^2	Ea(kJ/mol)	A (min^{-1})	R^2	Ea(kJ/mol)	A(min^{-1})	R^2
0.1	77.41	1.29E+07	0.998	73.04	2.70E+06	0.998	55.22	1.47E+04	0.998
0.2	70.27	1.66E+06	1.000	64.99	2.48E+05	1.000	59.17	4.17E+04	0.993
0.3	86.69	6.58E+07	0.996	82.08	1.47E+07	0.996	133.37	1.19E+12	0.974
0.4	93.83	3.16E+08	1.000	89.41	8.03E+07	1.000	109.59	6.52E+09	0.969
0.5	89.42	1.28E+08	1.000	84.66	2.86E+07	1.000	67.72	9.87E+05	1.000
0.6	82.25	2.84E+07	1.000	76.97	5.16E+06	1.000	50.87	2.60E+04	1.000
0.7	68.39	1.50E+06	0.999	62.15	1.74E+05	0.999	19.03	2.39E+01	0.898
0.8	72.56	2.56E+06	1.000	66.17	3.11E+05	1.000	73.96	9.07E+05	1.000
0.9	54.77	4.57E+04	0.997	46.45	2.43E+03	0.996	33.97	1.57E+02	0.986

Table 5-8: Kinetic parameters calculated for ASB by three isoconversional methods.

	FWO			KAS			Friedman		
α	Ea(kJ/mol)	A(min^{-1})	R^2	Ea(kJ/mol)	A (min^{-1})	R^2	Ea(kJ/mol)	A(min^{-1})	R^2
0.1	76.26	4.15E+06	1.000	71.45	7.70E+05	0.999	57.88	1.15E+04	0.998
0.2	106.96	2.24E+09	0.997	103.22	7.47E+08	0.996	132.77	1.88E+11	0.993
0.3	99.89	3.46E+08	0.996	95.43	9.27E+07	0.995	87.28	9.72E+06	0.992
0.4	113.08	3.71E+09	0.995	109.02	1.21E+09	0.994	130.02	4.14E+10	0.994
0.5	116.18	5.60E+09	0.996	112.06	1.85E+09	0.995	118.28	3.87E+09	0.997
0.6	119.07	8.81E+09	0.998	114.92	2.96E+09	0.998	122.05	8.89E+09	1.000
0.7	124.04	2.10E+10	1.000	119.99	7.43E+09	1.000	136.52	1.44E+11	0.996
0.8	131.23	7.59E+10	1.000	127.40	2.92E+10	1.000	147.33	1.08E+12	0.999
0.9	149.15	1.33E+12	1.000	145.91	6.27E+11	0.991	169.26	2.35E+13	0.984

Table 5-9: Kinetic parameters calculated for CS by three isoconversional methods.

	FWO			KAS			Friedman		
α	Ea(kJ/mol)	A(min^{-1})	R^2	Ea(kJ/mol)	A (min^{-1})	R^2	Ea(kJ/mol)	A(min^{-1})	R^2
0.1	107.05	2.19E+10	1.000	104.33	1.04E+05	1.000	84.90	2.40E+07	1.000
0.2	92.38	2.24E+08	1.000	88.23	8.82E+04	1.000	81.54	5.10E+06	1.000
0.3	95.41	2.94E+08	0.997	91.07	9.11E+04	0.997	94.94	9.30E+07	0.985
0.4	100.87	5.11E+08	0.998	96.39	9.64E+04	0.998	102.40	1.80E+08	0.999
0.5	81.38	6.83E+06	0.998	75.53	7.55E+04	0.998	49.48	3.42E+03	0.989
0.6	114.58	1.43E+09	0.999	109.77	1.10E+05	0.999	140.66	2.70E+10	0.998
0.7	130.75	1.52E+10	0.996	126.38	1.26E+05	0.995	152.50	1.92E+11	0.984
0.8	127.69	6.04E+09	0.999	122.81	1.23E+05	0.999	117.46	3.91E+08	0.969
0.9	94.70	1.54E+07	0.996	87.68	8.77E+04	0.995	46.20	1.97E+03	0.978

Table 5-10: Kinetic parameters calculated for CEL by three isoconversional methods.

	FWO			KAS			Friedman		
x	Ea(kJ/mol)	A(min^{-1})	R^2	Ea(kJ/mol)	A (min^{-1})	R^2	Ea(kJ/mol)	A(min^{-1})	R^2
0.1	159.93	3.36E+13	1.000	158.61	2.40E+13	1.000	141.93	1.32E+11	1.000
0.2	214.41	1.55E+18	1.000	215.58	1.89E+18	1.000	262.24	8.25E+21	1.000
0.3	201.36	8.00E+16	1.000	201.67	8.25E+16	1.000	184.75	1.69E+15	1.000
0.4	194.42	1.70E+16	0.998	194.25	1.59E+16	0.998	179.98	6.81E+14	0.976
0.5	180.61	9.71E+14	0.999	179.60	7.63E+14	0.999	147.27	1.14E+12	1.000
0.6	172.68	1.95E+14	1.000	171.16	1.37E+14	1.000	147.09	1.27E+12	0.988
0.7	165.29	4.44E+13	0.999	163.29	2.79E+13	0.999	131.96	6.99E+10	0.983
0.8	156.76	8.57E+12	0.999	154.22	4.74E+12	0.999	125.41	2.49E+10	0.995
0.9	152.03	3.57E+12	1.000	149.11	1.81E+12	1.000	134.91	1.85E+11	0.960

For this reason, in general, the integral models show the best-fit correlation coefficient values than the differential model. The variations in activation energy are due to the different components of the biomasses and their different decomposition mechanisms. This variation denotes changes in reactivity due to the extent of the reaction and the complex nature of the reactions. In general, the pre-exponential factor values for solid-phase reactions are expected to be in a wide range (six or seven orders of magnitude), and are directly related to the material structure, while the reactivity of samples is determined by the activation energy (Vlaev et al., 2007). In this study, the empirical pre-exponential factor values for an assumed first-order reaction ranged from 10^1 to 10^{21} min^{-1} for CEL, 10^3-10^{11} min^{-1} for CS, 10^1-10^{12} min^{-1} for AS, and 10^4-10^{13} min^{-1} for ASB (**Table 5-8** to **Table 5-10**). Thus, the parameter showed variations in conversion rates. This can be described as the complex composition of biomasses and complex reactions during pyrolysis (Turmanova et al., 2008). For first order reactions, the preexponential factor may vary from 10^5 to 10^{16} min^{-1}(Georgieva et al., 2012). The low factors will often indicate a surface reaction, but if the reactions are not dependent on surface area, the low factor may indicate a "tight" complex. The high factors will usually indicate a "loose" complex (Vlaev et al., 2008). Even higher factors (after correction for surface area) can be obtained for complexes having free translation on the surface. Since the concentrations in solids are not controllable in many cases, it would have been convenient if the magnitude of the preexponential factor indicated for reaction molecularity. However, this appears to be true only

for non-surface-controlled reactions having low ($<10^8$ min^{-1}) pre-exponential factors. Such reactions (if elementary) can only be bimolecular. Lower values of A and Ea represent the faster and easier decomposition of the biomass; in this context, the order of decomposition of these biomasses are as follows AS < CS < ASB < CEL; this means that the decomposition of CEL is more complicated than the other biomasses, while AS is the easiest to decompose. These results are in good agreement with the TG/DTG curves of these biomasses explained in **chapter 2**. Furthermore, it shows that biomass with high hemicellulose content is more straightforward to decompose than biomass with high cellulose content. On the other hand, the degradation of lignin may depend on the part of the hemicellulose because a covalent bond links them. Therefore, as hemicellulose decomposes, lignin begins to decompose partially, so lignin in biomass may lower decomposition temperature than cellulose. However, this is not an exact science because lignin and hemicellulose do not have a defined structure

5.3. Conclusion

- Pyrolysis of biomass produces char, bio-oil, and gases. The overall product distribution and yield of the individual components in these products are primarily temperature-dependent. Cellulosic bio-oil compounds, such as LGA, AGF, LGO, HMF, ADGH, and DHMDHP, underwent further decomposition to form other furans, light oxygenates non-condensable gases with increasing operating temperature. Thermal decomposition of cellulose was apparently initiated by the cleavage of the glycosidic bond, followed by dehydration reactions, to produce anhydrosugars, furans, and pyrans. With increasing operating temperature, ring-opening, fragmentation, retro-Diels-Alder, dehydration, decarbonization, and deoxygenation among cellulose-derived anhydrosugars/furans/pyrans and their intermediates are facilitated. Up to 300 °C, xylan-derived bio-oils, such as LGA and HMF, were transformed into 3,4-altrosan and 5-methyl-2(3H)-furanone, whereas furfural and 3,4-altrosan were converted at even higher temperatures into light oxygenated compounds and non-condensable gases. Initially, xylan underwent depolymerization, rearrangement, and dehydration, while retro-Diels-Alder is facilitated with increasing pyrolysis temperatures by fragmentation of xylan-derived pyrolytic, oxidation, hydrodehydration, and reduction reactions. The lignin pyrolysis bio-oil remained rich in methoxy phenols and phenolic aldehydes/ketones at 350 °C, and with an increase in operating temperature, 2-methyl-

4-vinyl phenol, vanillin, apocynin, and eugenol/isoeugenol were converted to low molecular weight phenols.

- The properties of the volatile pyrolysis products of the four biomasses are highly dependent on the pyrolysis conditions and their chemical structures. In the yield and composition of the volatile products of each pyrolysis sample (or organic oil and gas), the pyrolysis temperature plays an important role. With increasing temperature, the pyrolysis gas yields of the main biomasses had the same pattern, although the gas product compositions of different samples were different. Due to the higher amount of carbonyl, the pyrolysis of CEL produced the highest amount of CO. The pyrolysis of CS provided the highest amount of CO_2 due to its carboxyl content. In addition, due to the higher aromatic rings and methoxyl groups, CS pyrolysis produced the highest amount of CH_4 material, characterized as the highest HHV.
- The thermal behavior and gas evolution profiles (H_2, CH_4, CO, and CO_2) during pyrolysis of both biomasses were analyzed. The results showed that a significant part of CO and CO_2 is released mainly at a temperature below 450 °C and follow almost the same pattern. The evolution rates (CO and CO_2) increased with increasing temperature and reached their maximum peaks at 336 °C for cellulose and 365 ºC for ASB. The H_2 evolved at a much higher temperature (> 450 °C); the maximum H_2 production occurs between 600-700 ºC. The CH_4 started to evolve at a temperature above 300 °C; then it increased as temperature increased and reached the maximum evolution rate at 550 °C, but gradually decreased to almost zero at 820-1000 °C.
- The increase in ABR from 0.125 to 1.0generally decreased the combustible gases composition of H_2, CO, CH_4 decreased in the range of 26.27–7.02 % (v/v), 27.38–11.39 % (v/v), 5.92–2.07 % (v/v) while the fraction of non-combustibles gases was increased from 14.78 to 19.8 % (v/v) and 24.56 to 59.71 % (v/v) for CO_2 and N_2, respectively.
- The increase in heating rate from 10 to 80 °C/min has a positive influence on combustible gas yields for fixed ABR=0.5. At the heating rate of 10 °C/min, CO_2 was the dominant gas product. The CO_2 yield at 10 °C/min was 118.62 mL/kg of feed and decreased to 82.08 mL/kg of feed at 80 °C/min, while the yields of CO, CH_4, and H_2 were increased from 99.21-175.06, 16.14-31.71, and 70.75-128.89 mL/kg of feed, respectively. The LHVg increased from 4.37 to 6.66 MJ/Nm^3 with an increased heating rate between 10 to 80 °C/min. Also, the cold gas efficiency increased from 32.98 to

59.3 %. Despite the increase in cold gas efficiency with heating rate, these values are generally low. The low process efficiency is due to the pyrolysis stage, where many tars are generated.

- The gasification of the hydrochars showed high yields of the fuel gases (H_2, CO and CH_4) compared to the crude biomass. The concentration of H_2 increased considerably in the syngas produced from the hydrochars.
- The activation energy is calculated as a conversion function using isoconversional methods (FWO, KAS, and Friedman). The values obtained in these methods are similar. Among these methods, the FWO and KAS methods were found to be the best for evaluating the kinetic parameters of the pyrolysis reactions of AS, ASB, CS, and CEL. On the other hand, the Friedman method requires derivative conversion data, which would lead to being numerically unstable and noise-sensitive. For this reason, in general, the integral models (FWO and KAS) show the best-fit correlation coefficient values than the Friedman model. The variations in activation energy are due to the different components of the biomasses and their different decomposition mechanisms. The energy activation of AS varied from 29 kJ/mol to 147 kJ/mol. The ASB and CS have energy activation values between 87 and 169 kJ/mol and between 46 and 152 kJ/mol. The CEL has a value of 125–262 kJ/mol

Chapter6 MODELLING AND CFD SIMULATION

Clean and sustainable fuels productions are the main challenges facing the next energy crisis and global warming. These clean and sustainable fuels are called renewable energy and represent the fourth largest energy source globally, behind oil, coal, and natural gas, accounting for about 19% of global primary energy production (Mujtaba et al., 2017). Therefore, renewable energy sources will have to constitute the majority of energy in the future if sustainable development is promoted. There are many forms of renewable energy. Among the forms of renewable energy is bioenergy, i.e., the conversion of biomass into energy. One of the main ways of converting biomass into energy developed over the years is thermochemical conversion, i.e., hydrothermal carbonization, pyrolysis, liquefaction, combustion, and gasification (Liu et al., 2017; Nsaful et al., 2013).

The major challenge for biomass energy utilization is the conversion efficiency and production costs using the existing biomass conversion technologies. The conversion of biomass into energy is complex, involving complex chemical reactions, different transport phenomena, and different reactors. The study of this process in laboratory and pilot plants is very tedious and expensive. Therefore, to obtain high efficiency in converting biomass into energy and reducing the cost of production, many researchers have sought alternatives such as modeling and simulation studies, which are undoubtedly necessary and complementary to experimental studies. Besides, this contributes to the design, operation, optimization, and control of the process.

The performance of thermochemical conversion process, and any transformation process, highly depends on transport phenomena, i.e., the mechanisms by which heat, mass, and momentum are transferred throughout a system, besides chemical reactions. Experimentally it is very difficult to recognize these phenomena during the thermochemical conversion process. For this reason, different simulation approaches were used to understand these phenomena. The different simulation models approach used were: Kinetics models, and Statistical models, Numerical simulation model or Computational Fluid Dynamics (CFD).

6.1.1. Kinetics models

Kinetic models are based on the evaluation of the kinetic constants k (T) of the chemical reactions used to simulate the thermochemical conversion processes. The kinetic models are

known as 0D model, i.e. no influence of spatial variables; the system behaves in the same way at any point of the reactor. The basic kinetic models will be used to determine the kinetic parameters in the liquid phase during biomass carbonization.

6.1.2. Statistical models

To address the study of the effect of process variables on hydrothermal carbonization (HTC), a design of experiments (DoE) was used to plan a series of experiments in the laboratory, and the data were subsequently analyzed using response surface methodology (RSM). Combining the design of experiments with response surface analysis (DoE/RSM) is a practical methodology for revealing interactions between variables. In addition, the distribution of the experimental domain following criteria of optimization of the number of experiments; makes it possible to reduce the resources allocated to experimentation and design the number of total experiments according to the number of independent variables. Thus, on the one hand, a homogeneous distribution is achieved, and, on the other hand, it helps obtain favorable results in the quality indicators of the statistical parameters to be analyzed.

In the present work, the experimental design used was the Doehlert method; this method was applied to model the different factors and their characteristics using the response surface methodology (RSM). In RSM, visualization of the regression model can be obtained using response surface plots and 2D contour plots. These plots are helpful in understanding the nature of the response at different factor levels. In this case, it was used for the process of hydrothermal carbonization. The explanation of the design and calculation methodology will be presented in the experimental materials and methods section.

6.1.3. Numerical simulation model

To understand the transport phenomena inside the HTC reactor, numerical simulation or computational fluid dynamics (CFD) may be necessary and complementary to experimental studies. A better understanding of the transport phenomena inside the HTC reactor at the laboratory level may facilitate its optimization and scale up to a more accurate industrial reactor, which will reduce economic uncertainty.

The HTC reactor simulation was carried out using the COMSOL Multiphysics software, which can be defined as a powerful interface designed in a multidisciplinary way to simulate all phenomena of physical, chemical, mechanics, fluid dynamics, and electrical applications. The calculation generator is based on advanced strategies for solving differential equations using

numerical methods to simulate physical phenomena. The different phenomena can be coupled to be solved simultaneously and allow interaction with geometry conditions, meshing, the physical configuration of the elements, boundary conditions, different studies, equation solving, post-processing, and visualization (de Souza-Santos, 2010). Additionally, the inclusion of equations can be considered manually. There are pre-installed databases of equations in the software describing different phenomena, which can be coupled and customize with different analyses. There are also preset material properties, boundary conditions, and template resources. All of this helps to reduce the working time and provides higher productivity substantially.

The CFD module is used by engineers and scientists to understand, predict and design. These simulations often produce new and better products, device, and process performance compared to pure empirical studies to test and validate computer simulations. For example, simulations give accurate estimates of flow patterns, pressure losses, concentrations, forces on surfaces subjected to flow, and temperature distributions as part of an investigation.

Hence, the main objective of this part of the chapter is to use the CFD technique to produce a 3D simulation of HTC stirred reactor for an open-loop controller system by using COMSOL Multiphysics software: (a) to study the hydrodynamic and determine the distribution of biomass inside the reactor, high mixing intensity, and stagnant zones. (b) to determine the heat of the reaction and the type of chemical reaction. (c) to combine kinetics, temperature, mass, and velocity fields to predict the conversion of the biomass inside the reactor using the kinetic model, considering the thermal properties of the biomass and heat of reaction, and the effect of biomass to water ratio on heat transfer. These results will be compared with the experimental data of the HTC of biomass.

6.2. Computational modeling and simulation methodology

6.2.1. Kinetics models of intermediate product formation by HTC

6.2.1.1. *Reaction pathways and kinetics of intermediate product formation*

In HTC, the reaction network consists of several consecutive and parallel reactions. The three major components of lignocellulosic biomass are cellulose, hemicellulose, and lignin. The main conversions of these polymers during HTC are summarized in **Figure 6-1**, where the blue frames denote the composition in the solid, the green frames show the liquid compounds found

in process and the red frame represents the gas phase. Moreover, the solid lines indicate the reaction pathway, while the dotted lines represent the likely reaction path or secondary reactions. The cellulose breaks down to smaller molecular weight water-soluble compounds (oligomers) and then further to monomers (glucose), which partly isomerizes to fructose, mannose, and galactose during the cellulose hydrolysis (Sevilla and Fuertes, 2009b).

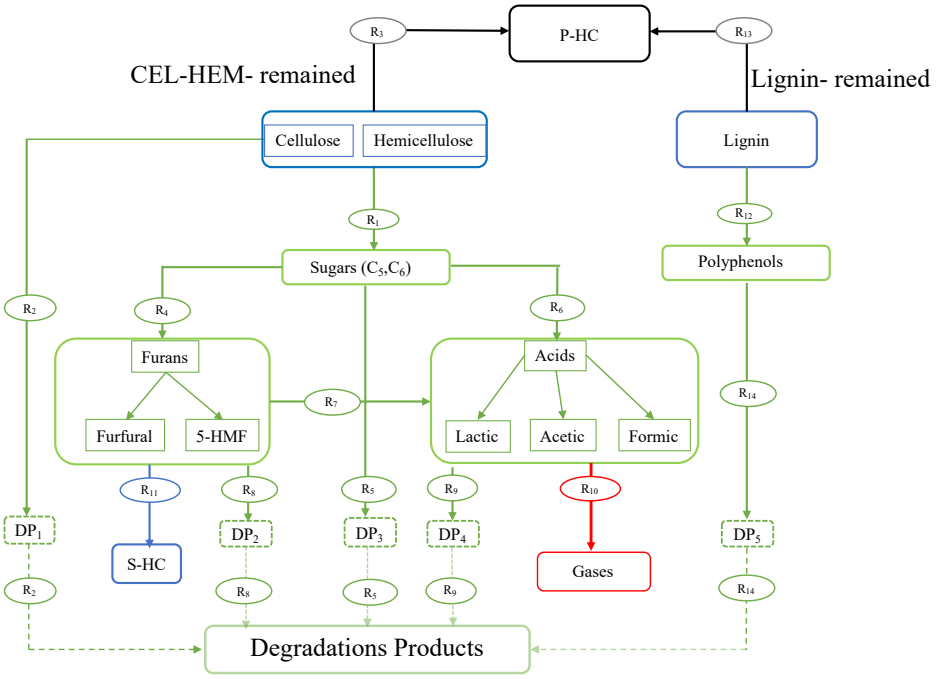

Figure 6-1: Proposed reaction pathway of hydrothermal conversion of biomass

The hydrolysis products subsequently undergo a series of isomerization, dehydration, and fragmentation (ring-opening and C–C bond breaking), producing key intermediates 5-HMF, furfural and their derived products (Funke and Ziegler, 2010; Wang et al., 2018). These intermediates products also produce organic acids, including acetic, lactic, propanoic, levulinic, and formic acids, which lower the pH of the reaction medium. These acidic conditions favor the further degradation of the intermediates; such as the dehydration of glucose into HMF and furfural (Funke and Ziegler, 2010; Hoekman et al., 2011). The organic acids undergo decarboxylation and decarbonylation reactions to form a gas (CO_2 and CO) (Lin et al., 2016a). On the other hand, the 5-HMF and furfural are followed by condensation (Reza et al., 2014b; Sevilla and Fuertes, 2009b);the results of these reactions are called bio-crude. After successive polymerization and aromatization, this liquid bio-crude converts into a solid product known as secondary hydrochar (S-HC) or tar (Reza et al., 2014a). The unhydrolyzed fraction of cellulose undergoes solid-to-solid conversion, yielding so-called primary hydrochar

(P-HC.) Consequently, the final hydrochar is a mixture of primary hydrochar and tar from intermediates polymerization products. Hemicellulose is a complex polymer consisting of various sugars, mainly xylan, which contain short lateral chains, formed by xylose, as well as hexose sugars which have a lower degree of polymerization and more susceptibility to chemical degradation (Kumar, 2013). Like cellulose, hemicellulose is hydrolyzed to form sugars, mainly pentose (xylose) and some hexose (glucose and its isomers). The hexose and pentose derivatives of hemicellulose follow the same cellulose decomposition path but at a lower decomposition temperature. Lignin is an amorphous heteropolymer composed of three methoxy- substituted phenyl propane units (p-coumarin, coniferyl, and sinapyl alcohol) (Wang et al., 2018). Due to its random structure and high molecular weight polymers, the mechanisms of lignin reaction are complex, making it difficult to predict a real mechanism of its decomposition. However, lignin is generally associated with hemicelluloses through covalent bonds. The decomposition of hemicellulose, causing partial depolymerization of lignin to form polyphenols such as phenol, gallic acid, catechol, p-cresol, vanillin, guaiacol (Nakason et al., 2018a). However, relatively low amounts of lignin dissolve in the water (Wang et al., 2018).

6.2.1.2. *Kinetic model for the formation of the main intermediate compounds.*

Based on the initial concentration of 100 g/L biomass, i.e., biomass-to-water ratio (B/W) equal to 1/10 used in each experiment. The initial concentration of both cellulose and hemicellulose is grouped for better evaluation ($C_{C\text{-}H}$) due to the difficulty of separating cellulose and hemicellulose decomposition mechanisms. Their different decomposition mechanism separated the initial lignin concentration (C_L). Experimentally, the concentrations of the dissolved intermediates were comparatively lower than the solid products. Therefore, the products that have similar functional groups are lumped together for better evaluation. That is, glucose, fructose, and xylose are lumped into sugar (C_S), furfural and 5-HMF are lumped into furans (C_F), all the detectable organic acids are lumped into acids (C_A) and all gaseous compound are lumped into a gas (C_G). The lignin is partially depolymerized to give phenol, gallic acid, catechol, p-cresol, vanillin, guaiacol; all these compounds are grouped into polyphenols (C_P). The non-hydrolyzed fraction of cellulose and hemicellulose and the lignin that remained polymerized, undergo a solid-to-solid conversion, yielding so-called primary hydrochar (CP-HC). The successive polymerization and aromatization of the aldehydes, mainly furfural and 5-HMF, becomes the final product known as secondary hydrochar (CS-HC). The unidentified compounds were quantified as degradation products (CDP), which make

up the missing percentages to even the mass balance to 100%. The residuals can be degradation products of cellulose and hemicellulose, sugars, furans, acids, and polyphenols specified as CDP1, CDP2, CDP3, CDP4, and CDP5, respectively. **Eqs. (6-1) - (6-9**) show the set of first-order ordinary differential equations that describe this reaction system in the HTC reactor used experimentally. The hydrochar is formed from the polymerization of HMF and furfural, which is supposed to have a reaction order greater than one, according to several studies (Chuntanapum and Matsumura, 2009; Lucian et al., 2019; Paksung et al., 2020). However, in this study, an order one reaction can be assumed because the hydrochar was produced from low-concentration intermediates and not from the initial substrate of 5-HMF or furfural.

$$\frac{dC_{C-H}}{dt} = -(k_1+k_2+k_3)C_{C-H} \quad (6\text{-}1)$$

$$\frac{dC_S}{dt} = k_1C_{C-H} - (k_4+k_5+k_6)C_S \quad (6\text{-}2)$$

$$\frac{dC_F}{dt} = k_4C_S - (k_7+k_8+k_{11})C_F \quad (6\text{-}3)$$

$$\frac{dC_A}{dt} = k_6C_S + k_7C_F - (k_9+k_{10})C_A \quad (6\text{-}4)$$

$$\frac{dC_G}{dt} = k_{10}C_A \quad (6\text{-}5)$$

$$\frac{dC_{S-HC}}{dt} = k_{11}C_F \quad (6\text{-}6)$$

$$\frac{dC_L}{dt} = -(k_{12}+k_{13})C_L \quad (6\text{-}7)$$

$$\frac{dC_{P-HC}}{dt} = k_3C_{C-H} + k_{13}C_L \quad (6\text{-}8)$$

$$\frac{dC_{DP}}{dt} = k_2C_{C-H} + k_8C_F + k_5C_S + k_9C_A + k_{14}C_P \quad (6\text{-}9)$$

The concentration in component X (C-H, S, F, A, DP, P, G, S-HC, L, P-HC), Cx, is given by:

$$C_X = \frac{m_X}{(V_B+V_w)}Y_i \quad (6\text{-}10)$$

Where m_X is the mass of component X on a dry basis, the term V_B+V_W is the sum of the volumes (expressed in L) of biomass and distilled water feed to the HTC reactor to reach the set B/W ratio, and Y_i is the mass yield of solid, liquid and gas, depending on whether component X is solid, liquid or gas. The concentrations of the different intermediates products at different temperatures and holding times were determined in **Chapter 4** in **section 4.2.6.1**

6.2.1.3. *Parameter determination by optimization techniques*

The proposed kinetic model for the HTC process is nonlinear, implying that finding the best set of values for kinetic parameters requires optimization techniques. In this study, model parameters and reaction constants were determined using the Optimization Module of COMSOL Multiphysics® 5.6. The differential equations system was solved numerically using backward differentiation formula (BDF). The solver estimates the kinetics parameters (k_1-k_{14}) based on experimental data. The fitting accuracy is represented by the sum of the squared estimate of errors (SSE). This objective function was minimized to get ki by using the Levenberg–Marquardt algorithm. Finally, the coefficient of determination (R^2) was calculated to evaluate the model agreement.

$$\mathrm{SSE} = \sum_{\mathrm{i}} \sum_{\mathrm{t}} \left[\mathrm{y_i(t)} - \mathrm{y_{i,m}(t)}\right]^2 \qquad (6\text{-}11)$$

$$\mathrm{R^2} = 1 - \frac{\mathrm{SSE}}{\sum_{\mathrm{i}} \sum_{\mathrm{t}} [\mathrm{y_i(t)} - \ddot{\mathrm{y}}_{\mathrm{i}}(\mathrm{t})]^2} \qquad (6\text{-}12)$$

where y_i (t) and $y_{i,\mathrm{m}}$ (t)are the experimental and predicted value of the concentration of component i at time t; $\ddot{y}_i$ is the average value of all the experimental concentrations.

The reactor heating rate and holding time-temperature profile were included in calculating the rate constants and product concentration at each point in **Eqs. (6-1) - (6-9)**. The data from experiments at 210, 230, and 250 °C were used to determine the model parameters. For holding time of 0, 30, 60 and 120 minutes.

The Arrhenius behavior is considered to determine the activation energy (Ea) and pre-exponential factor (A) of each interest reaction. The use of several rate constants for different temperatures allows graphically to obtain Ea and A. The kinetic rate constant is dependent on T. Thus, Ea and A are specific constants for each reaction, as shown in the following equation:

$$k_i(T) = A_i \exp\left(\frac{-E_{ai}}{RT}\right) \quad (6\text{-}13)$$

6.2.2. Modeling of the HTC conversion using Doehlert experimental design

The Design of Experiments (DoE) methodology is a strategy for planning experiments to obtain satisfactory conclusions efficiently and economically. The DoE is based on the fact that an organized experiment simplifies the analysis and interpretation of results. DoE tries to find a relationship between two quantities:

- The response: physical quantity studied
- The factors: modifiable physical quantities supposed to influence the response.

The first criterion for choosing a design is the number of experiments required. Among the different experimental designs, the Doehlert design was chosen because of its smaller number of experiments.

6.2.2.1. *Design of experiments approach to model and optimize the HTC process*

Doehlert designs for k factors or variables (k > 3) are always generated by allocating the experimental points on the surface of a hypersphere (Araujo and Janagap, 2012). For three and two factors the experimental points are circumscribed into a sphere and a circle of radius 1 respectively (**Figure 6-2**). The combination of the different factors at each experimental point is obtained by projecting the cross-section of the sphere in two dimensions (**Figure 6-2**b), and the total number of experimental combinations (N) as a function of the number of variables (k) understudy is given by the expression:

$$N = k^2 + k + 1 \quad (6\text{-}14)$$

For three and two factors, the total numbers of experiments are 13 and 7, respectively, and their spatial distribution is located at the vertices of a cuboctahedron and a hexagon with a point at their centers, respectively (**Figure 6-2**). A further characteristic of this type of design is the varying experimental levels in the different axes. For example, the three axes in **Figure 6-2** indicate that the factors X_1, X_2 and X_3 must be analyzed at 5, 3, and 7 different experimental levels, respectively. The different levels are essential in cases where the factors studied are subjected to various and inevitable restrictions

The HTC process is reported to have three main factors (temperature, retention time, and biomass water ratio). In this case, k is equal to 3, and the application of the Doehlert design requires 13 experiments. To minimize the number of experiments, we limited the number of parameters to be taken into account to model the responses to two factors: temperature (T) and treatment time (t), because it has been reported that the biomass water ratio (B/W) does not have much effect whenever the biomass is wholly submerged in water. Therefore, a value of B/W=1/9 has been set. The main feature of the Doehlert design is to have a uniform distribution of experimental points. For example, the experimental matrix consists of 7 experiments with a 5-level factor and a 3-level factor for a two-factor design. Thus, it forms a cube-octahedron of the hypersphere (**Figure 6-3**).

The determination of the experimental matrix requires the definition of the boundaries of the study domain and the number of levels. The HTC conversion of biomass is performed in the subcritical range of water between 180°C and 250°C. The upper limit is set at 250°C to avoid entering the hydrothermal liquefaction range. The lower limit is set at 180°C. For the treatment time, the minimum is equal to 0 min corresponds to the flash experiment, which allows the study of the effect of heating and cooling phases in the HTC process. In this study, the maximum holding time was set at 60 min.

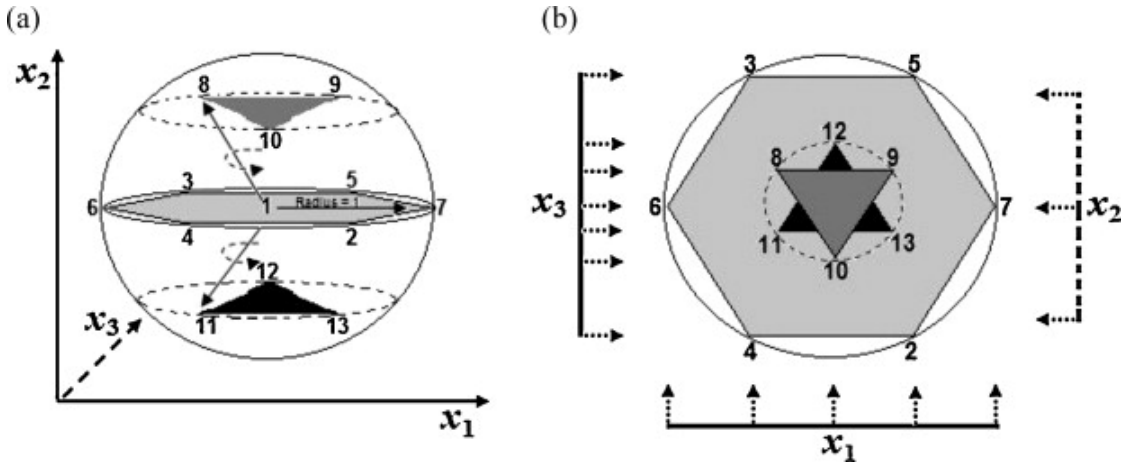

Figure 6-2: Spatial distribution of the experimental points in a Doehlert design (a) for 2 (points 1–7) and 3 (points 1–13) factors; (b) cross section projection of the initial sphere (*Araujo and Janagap, 2012*).

6.2.2.2. *Experimental matrix of the Dohlert design (DoE)*

One of the Doehlert design specifications is the different number of experimental levels (3 and 5 depending on the axis) for the parameters studied (temperature, T, and treatment time, t). The

choice of the number levels for each parameter depends on the ease of control of the variable and its impact on the responses. In this case, the temperature is chosen with five experimental levels and three for retention time. The initial values of the chosen parameters are 215°C for T ($X_1 = 0$) with a step value of 17.5°C, and 30 min for t ($X_2 = 0$) with a step value of 30 min.

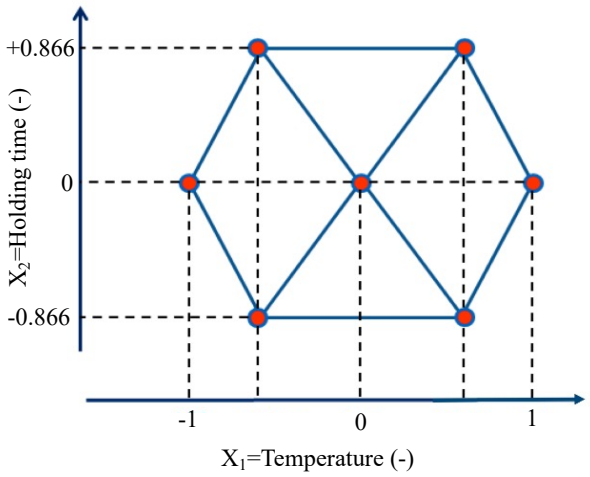

Figure 6-3: Graphical representation of Doehlert design for two-factor optimization

Determining the experimental limits and the distribution of the parameters by several levels leads to the experimental matrix of 7 test presented in **Table 6-1** in actual and reduced coordinates. In addition, test 1was repeated three times to consider the repeatability problems of the results.

Table 6-1 : Experimental matrix of the Doehlert design

Test	X_1	X_2
1-1	215 (0)	30 (0)
2	180 (-1)	30 (0)
3	250 (+1)	30 (0)
4	197 (-0.5)	0 (-0.866)
5	232 (+0.5)	60 (+0.866)
6	197 (-0.5)	60 (+0.866)
7	232 (+0.5)	0 (-0.866)
1-2	215 (0)	30 (0)
1-3	215 (0)	30 (0)

This work focused on the conversion of *Agave salmiana* bagasse (ASB) by the HTC process. To understand the effects of the process parameters (X1 and X2) and the quality of the hydrochar produced, the characteristic factors for the use of hydrochar as an energy source have been studied.

6.2.2.3. *Optimization of the HTC conversion of ASB using a Doehlert experimental design*

Two variables are designated as necessary for HTC conversion of ASB to optimize the HTC process: temperature (X_1) and holding time (X_2). Particle size was not investigated in order to work with the feedstock and avoid further biomass transformation operations. The Doehlert experimental design is selected because it needs fewer points to estimate the second-order terms of **Eq.(6-13)**. The **Eq.(6-13)** is the model used for these two independent factors (Chartier et al., 2013; Ferreira et al., 2002). The minimum number of the experiment is 6 plus 3 replicates in the central domain to estimate the experimental errors. The experimental points are circumscribed in a sphere as explained above, and each factor is analyzed at different numbers of the level depending on its influence on the response. The quadratic model of **Eq.(6-13)** was used to study the relationship between (temperature (X_1) and retention time (X_2)) on 10 responses (oxygen content (O), carbon content (C), mass yield (MY), higher heating value (HHV), volatile matter (VM), fixed carbon (FC), energy yield (EY), ignition temperature (Ti), temperature corresponding to the maximum decomposition (Tm), burnout temperature (Tb)).

$$Y = b_0 + b_1X_1 + b_2X_2 + b_{11}{X_1}^2 + b_{12}X_1X_2 + b_{22}{X_2}^2 \quad (6\text{-}15)$$

where Y is the response, X_1 and X_2 are temperature and holding time, respectively.

The model consists of first-order terms (bi), squared terms (bii), and first-order interactions (bij). The estimation of this polynomial model coefficient (b0, bi, bii, and bij in **Eq.(6-13)** is calculated by the least-squares method using Statgraphics Centurion XV Version software (Sigma-Plus, Paris, France). To evaluate the quality of the models, the following parameters were calculated:

- Regression coefficient (R^2)

$$R^2 = \frac{SS_e}{SS_{tot}} \quad (6\text{-}16)$$

- Adjusted regression coefficient (R^2_{adj})

$${R^2}_{adj} = \frac{SS_{res}/(n-p)}{SS_{tot}/(n-1)} \quad (6\text{-}17)$$

- Predicted variation coefficient (R^2_{pred})

$$R^2_{pred} = 1 - \frac{SS_{pre}}{SS_{tot}} \quad (6\text{-}18)$$

- PRESS means Prediction Error Sum of Square)

$$S_{pre} = PRESS = \sum_{i=1}^{n} e^2_{(i)} = \sum_{i=1}^{n} \left(\frac{e_i}{1 - h_{ii}}\right)^2 \quad (6\text{-}19)$$

- Standard Error of estimate (SEE)

$$SSE = \sqrt{\left(\frac{SS_{res}}{(n - p)}\right)} \quad (6\text{-}20)$$

SSe: sum of squares between calculated values (ŷi) and the mean value; SStot: sum of squares between experimental data and the mean; SSres: sum of the squares of model residuals; p: number of model coeffcients ; n: number of the experimental data; ei = (yi - ŷi) , hii: ith diagonal element of the hat matrix H

6.2.2.4. *Characteristic combustion temperatures*

The ignition and combustion characteristics of crude ASB and hydrochars were determined from thermogravimetric curves. A sample mass of around 10 mg was used to minimize heat and mass transfer limitations. Experiments were carried out in air at a heating rate of 10 °C /min, and samples were heated from 30 °C to 900 °C. Proteus analysis software (Netzsch, Germany) was used for smoothing, calculating derivatives, extrapolation of onset temperatures, and maximum peak values. As in previous studies (Li et al., 2006; Wang et al., 2009a), a common TGA approach was employed to determine ignition, peak reaction rate, and combustion temperature by identifying the relevant points of the curves (TG-DTG). Briefly, the ignition temperature (Ti) is associated with the temperature at which the fuel is likely to self-ignite, which corresponds to the onset temperature of the process. The temperature related to the maximum weight loss rate (dw/dt) max represents the temperature (Tm) at the maximum combustion rate. The last one, the burnout temperature (Tb), is considered the stabilization temperature at which the combustion rate is less than 1wt.%/ min and the sample is completely oxidized (Peng et al., 2016). Repeated measurements for each sample indicated that the standard deviation for the extrapolated temperatures is within 2 °C. In addition, the combustion reactivity (Pala et al., 2014) was estimated to evaluate the fuel combustion performance as follows Rindex = 100·(dw/dt)max/Tm.

The autoignition temperature was determined in the temperature-controlled furnace under an oxygen atmosphere. For this purpose, a TOC was used under a solid configuration. For each experiment, 2 mg of solid was introduced into the furnace at a given temperature. An oxygen flow rate of 170 ml/min was programmed and introduced into the furnace. Temperatures were reduced until no Gaussian peak of CO_2 was observed. The autoignition temperature was obtained from the first temperature at which the CO_2 peak was observed. The characteristic parameters of the present studies are given as mean values of the runs performed in triplicate.

6.2.3. Criteria to determine HTC performances

After each experiment, the hydrochars were dried at 105°C for 24 h to determine the hydrochar mass yield (MY) and energy yield (EY), as follows:

$$\text{Mass yield (\%)} = \frac{\text{Mass}_{\text{Dry hydrochar}}}{\text{Mass}_{\text{Dry ASB}}} \quad (6\text{-}21)$$

$$\text{Energy densification ratio} = \frac{\text{HHV}_{\text{Dry hydrochar}}}{\text{HHV}_{\text{Dry ASB}}} \quad (6\text{-}22)$$

$$\text{Energy yield (\%)} = \text{Mass yield(\%)} \cdot \text{Energy densification ratio} \quad (6\text{-}23)$$

For simplicity, the abbreviation: ASB-T-t will be used hereafter to denote the obtained hydrochars by the studied operating parameters, where T represents the HTC treatment temperature and t the holding time.

6.2.4. Computational Fluid Dynamics (CFD) approach and methodology

Finite element simulations were performed using COMSOL Multiphysics 5.4. This simulator was chosen because of its ability to incorporate several physical phenomena into simulations of complex geometries with relative ease.

The solutions of the transient state simulations were obtained a using MUtifrontal Massively Parallel Sparse direct Solver (MUMPS) with a relative error tolerance of 10^{-3}. The simulations were performed in interactive mode on a Dell Studio XPS 435T/9000 PC intel i7CPU with 16 GB memory. The biomass used in this simulation was avocado stone (AS).

6.2.4.1. *Geometry*

The simulated stirred reactor comprises a reactor vessel and a four-blade impeller. The internal height (H) and the inner diameter (D) of the mixer vessel is 130 mm and 56 mm respectively.

The diameter of the impeller (d) was 35 mm. The pitch of the impeller blades was 45°; the external width (Dex) was 76 mm. The details of the geometry are presented in **Figure 6-4** and the real reactor geometry is shown in **Figure 6-5.** The geometric models were constructed in the COMSOL Multiphysics.

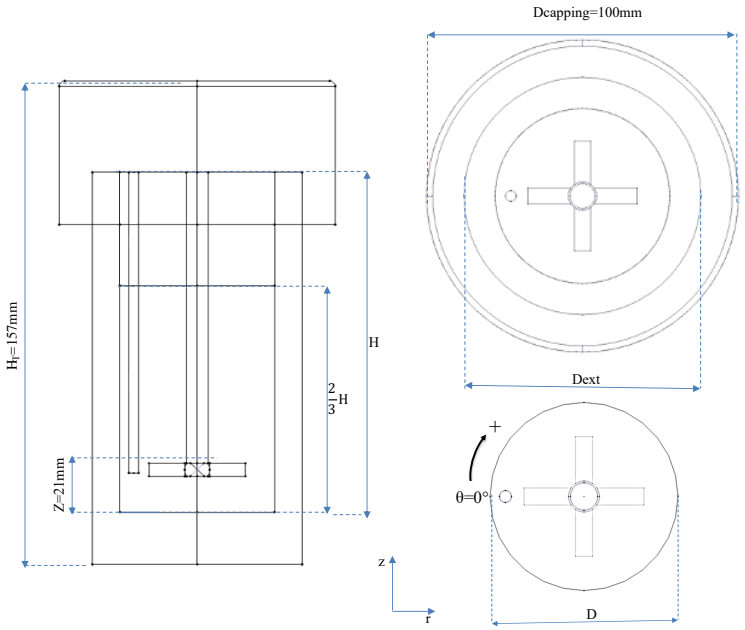

Figure 6-4: Stirred reactor geometry details schematic

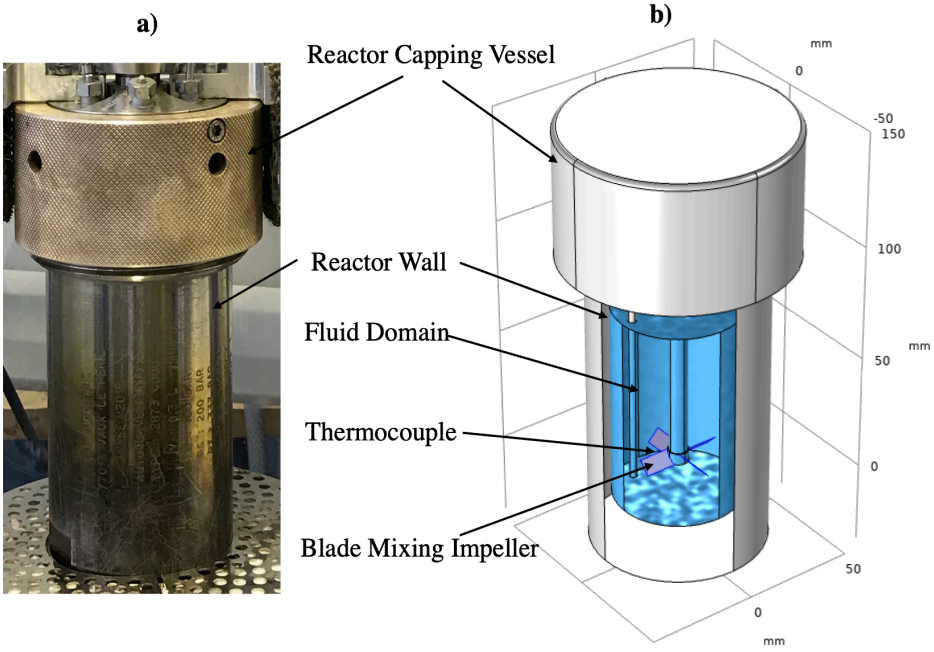

Figure 6-5 : The reactor geometry **a**) experimental **b**) CFD domain

6.2.4.2. *Governing Equations: conservation of momentum, mass, and energy*

The subject of transport phenomena describes the transport of momentum, energy, and mass in the form of mathematical relations (Bird et al., 2007). The basis for these descriptions is found in the laws for conservation of momentum, energy, and mass in combination with the constitutive relations that describe the fluxes of the conserved quantities (Holstein, 1989). Various mathematical models describe the movement of fluids and various engineering correlations that can be used for exceptional cases. However, the most complete and accurate description comes from partial differential equations (PDEs). For instance, a flow field is characterized by the balance in mass, momentum, and total energy described by the continuity equation, the Navier-Stokes equations, and the total energy equation:

$$\frac{\partial \rho}{\partial t} + \nabla \cdot (\rho \boldsymbol{u}) = 0 \qquad (6\text{-}24)$$

$$\frac{\partial \rho \mathrm{u}}{\partial \mathrm{t}} + \nabla \cdot (\rho \mathbf{u}\mathbf{u}) = \nabla \cdot \mathrm{p} + \nabla \cdot \boldsymbol{\tau} + \mathbf{F} \qquad (6\text{-}25)$$

$$\frac{\partial}{\partial \mathrm{t}}\left[\rho\left(\mathrm{e} + \frac{1}{2}\mathbf{u}^2\right)\right] + \nabla \cdot \left[\rho \mathrm{u}\left(\mathrm{e} + \frac{1}{2}\mathbf{u}^2\right)\right] = \nabla \cdot (\mathrm{k}\nabla \mathrm{T}) + \nabla \cdot (\mathrm{p}\mathbf{u} + \boldsymbol{\tau} \cdot \mathbf{u}) + \mathbf{u} \cdot \mathbf{F} + \mathbf{Q} \qquad (6\text{-}26)$$

The solution to the mathematical model equations gives the velocity field (u), pressure (p), and temperature (T); of the fluid in the modeled domain.

6.2.4.2.1. *Navier–Stokes equations: Conservation of momentum and mass*

The Navier–Stokes equations mathematically express conservation of momentum and conservation of mass for Newtonian fluids. The Navier-Stokes equations govern the motion of fluids and can be seen as Newton's second law of motion for fluids. In the case of a compressible Newtonian fluid, these yields

$$\rho\left(\frac{\partial \mathbf{u}}{\partial \mathrm{t}} + \mathbf{u} \cdot \nabla \mathbf{u}\right) = -\nabla \mathrm{p} + \nabla \cdot \left(\mu\left(\nabla \mathbf{u} + (\nabla \mathbf{u})^{\tau} - \frac{2}{3}\mu(\nabla \cdot \mathbf{u})\mathrm{I}\right)\right) + \mathbf{F} \qquad (6\text{-}27)$$

where $\mathbf{u}$ is the fluid velocity, $\boldsymbol{p}$ is the fluid pressure, $\boldsymbol{\rho}$ is the fluid density, and $\boldsymbol{\mu}$ is the fluid dynamic viscosity. The different terms correspond to the inertial forces (red color), pressure forces (blue color), viscous forces (orange color), and the external forces applied to the fluid

(Green color). The **Eq. (6-27)** are always solved together with the continuity **Eq. (6-24)**. The **Eq.(6-27)** is the general Navier-Stokes equation for a homogeneous fluid.

For this specific case study, the system is not homogeneous inside the reactor. Inside the reactor, water and biomass are mixed in function of biomass-to-water ratio. The thermal properties of the reactor and continuous phase (water) inside reactor and its relationship with temperature were taken from the COMSOL Multiphysics database. It was used the thermal properties of the biomass determined in **Chapiter 2**. The fluid was considered weakly incompressible to account for variations in density that arise within the fluid domain for the changing temperature. Since the system is closed, it was considered the pressure point constraint.

The Reynolds-Averaged Navier–Stokes Turbulent Mixture Model k-ε model equations used was expressed as follows:

$$\rho\frac{\partial \mathbf{u}}{\partial t}+\rho(\mathbf{u}.\nabla\mathbf{u})+(\rho_d-\rho_c)(j_{slip}-\nabla)u=\nabla\cdot[-pI+K]-\nabla\cdot K_m+F_m+\rho g+F \quad (6\text{-}28)$$

$$\rho\nabla\mathbf{u}=\mathbf{m_{dc}}\left(\frac{\mathbf{1}}{\boldsymbol{\rho_c}}-\frac{\mathbf{1}}{\boldsymbol{\rho_c}}\right) \quad (6\text{-}29)$$

$$K=(\boldsymbol{\mu}-\boldsymbol{\mu_T})(\nabla\mathbf{u}-(\nabla u)^{\mathbf{T}})-\frac{\mathbf{2}}{\mathbf{3}}(\boldsymbol{\mu}-\boldsymbol{\mu_T})(\nabla\cdot\mathbf{u})\mathbf{I}-\frac{\mathbf{2}}{\mathbf{3}}\boldsymbol{\rho}\mathbf{kI}, \qquad \mathbf{K_m}=(\boldsymbol{\rho_c}+\boldsymbol{\rho_d}-\boldsymbol{\rho})\mathbf{u_{slip}}\mathbf{j^T_{slip}} \quad (6\text{-}30)$$

The transport equation for volume fraction (φ_b) is:

$$\rho\frac{\partial\phi_d}{\partial t}+\mathbf{u}\cdot\nabla\phi_d+\nabla\cdot j_{silp}=\nabla\cdot(D_{md}\nabla\phi_d)-\frac{m_{dc}\rho}{\rho_d\rho_c} \quad (6\text{-}31)$$

$$N_{\phi_d}=\boldsymbol{u}_d-(D_{md}\nabla\phi_d),\ \boldsymbol{u}_d=u+\boldsymbol{u}_{slip}(1-\phi_d) \quad (6\text{-}32)$$

$$\rho=\rho_d\phi_d-\rho_c(1-\phi_d),\ D_{md}=\frac{\mu_T}{\rho\sigma_T},\ \mathbf{u_{slip}}=\mathbf{0} \quad (6\text{-}33)$$

The transport equation for k is:

$$\rho\frac{\partial k}{\partial t}+\rho(\mathbf{u}.\nabla)k=\nabla.\left[\left(\mu+\frac{\mu_T}{\sigma_k}\right)\nabla k\right]+\mu_T\left[\nabla\mathbf{u}:(\nabla\mathbf{u}+(\nabla\mathbf{u})^{\mathbf{T}})-\frac{2}{3}(\nabla.\mathbf{u})^2\ \right]-\frac{2}{3}\rho k\nabla.\mathbf{u}-\rho\varepsilon \quad (6\text{-}34)$$

The transport equation for ε is:

$$\rho\frac{\partial\varepsilon}{\partial t}+\rho(\mathbf{u}.\nabla)\varepsilon=\nabla.\left[\left(\mu+\frac{\mu_T}{\sigma_\varepsilon}\right)\nabla\varepsilon\right]+C_{e1}\frac{\varepsilon}{k}[\mu_T\left[\nabla\mathbf{u}:(\nabla\mathbf{u}+(\nabla\mathbf{u})^{\mathbf{T}})-\frac{2}{3}(\nabla.\mathbf{u})^2\ \right]-\frac{2}{3}\rho k\nabla.\mathbf{u}]-C_{e2}\rho\frac{\varepsilon^2}{k} \quad (6\text{-}35)$$

Turbulent viscosity modeled by

$$\mu_T=\rho C_\mu\frac{k^2}{\varepsilon} \quad (6\text{-}36)$$

where k is the turbulent kinetic energy (m^2/s^2) and ε turbulent dissipation rate (m^2/s^3). The **Eq. (6-34)** also consist of some adjustable constant parameters: $\sigma_k = 1.00, \sigma_\varepsilon = 1.3$, $C_{e1} = 1.44$, $C_{e2} = 1.92$ and $C_\mu = 1.92$ (Versteeg and Malalasekera, 2007).

where D_{mdc} (kg/(m³·s)) is the mass transfer from dispersed to continuous phase. Similar equations of the transport of diluted species were used to incorporate the chemical reactions

$$\frac{\partial x_b}{\partial t} + \nabla.(-D_b \nabla x_b) + u\nabla x_b = R_{bi} \qquad (6\text{-}37)$$

where x_b (kg/m³) is the concentration of the biomass inside the reactor

$$x_b = \rho_d \phi_d \qquad (6\text{-}38)$$

Where R_{bi} is the reaction rate and it will be used in the kinetics of the reaction which will be explained later.

6.2.4.2.2. *Heat transfer: Conservation of energy*

The first law of thermodynamics defines the internal energy by stating that the change in internal energy for a closed system (ΔU), is equal to the heat supplied to the system (Q), minus the work done by the system (W) (Ward-Smith, 1985).

$$\Delta U = Q - W \qquad (6\text{-}39)$$

when the system is moving, **Eq. (6-39)** can be extended to include the kinetic energy (E^k) of the system

$$\Delta(U + E^k) = Q - W \qquad (6\text{-}40)$$

Eq.(6-40) can be written for an infinitely small volume of fluid and the result is known as the equation for conservation of total internal energy (Panton, 2006)

$$\frac{\partial}{\partial t}\left[\rho\left(e + \frac{1}{2}\mathbf{u}^2\right)\right] + \nabla \cdot \left[\rho u\left(e + \frac{1}{2}\mathbf{u}^2\right)\right] = -\nabla \cdot q + \nabla \cdot (\sigma \cdot \mathbf{u}) + \rho \mathbf{u} \cdot \mathbf{F} \qquad (6\text{-}41)$$

where, **ρ** is the density, **e** is the internal energy per unit mass, u is the velocity vector, **q** is the conductive heat flux vector, **σ** is the total stress tensor, and F is the body force per unit mass; i.e., the volume force. The different terms correspond to the rate of increase of energy per unit volume (red color), convection of energy int point by flow (blue color), net heat flux (orange color), work of surface forces (green), and work of body forces (violet). The total stress tensor is written from the following equation

$$\sigma = -\mathrm{pI} + \tau \qquad (6\text{-}42)$$

The work of the surface forces can therefore be described as follows:

$$\nabla \cdot (\sigma \cdot \mathbf{u}) = -\nabla \cdot (\mathrm{pu}) + \nabla \cdot (\tau \cdot \mathrm{u}) \qquad (6\text{-}43)$$

The first term on the right-hand side is the pressure work, whereas the second term is the viscous work. In the **Eq.(6-41)** can be derived by taking the dot product of the velocity (u) with the momentum equation. With some algebraic modification, it can be expressed as follows:

$$\frac{\partial}{\partial \mathrm{t}}[(\rho \mathrm{e})] + \nabla \cdot [(\rho \mathrm{ue})] = -\nabla \cdot \mathrm{q} - \mathrm{p}\nabla \cdot \mathrm{u} + \tau : \nabla \mathrm{u} \qquad (6\text{-}44)$$

For the case where there are internal heat sources caused, for example, by reactions or by interaction with radiation, the additional internal heat source term (Q) is added to the equation, and the internal energy equation can be written as follows:

$$\frac{\partial}{\partial \mathrm{t}}(\rho \mathrm{e}) + \nabla \cdot (\rho \mathrm{ue}) = -\nabla \cdot \mathrm{q} - \mathrm{p}\nabla \cdot \mathrm{u} + \tau : \nabla \mathrm{u} + \mathrm{Q} \qquad (6\text{-}45)$$

The **Eq.(6-45)** is the general equation of energy conservation. However, **Eq.(6-45)** can be written in two different ways, but it does not affect energy conservation. The first way is the enthalpy equation by energy conservation, whereas the second is the temperature equation by energy conservation.

The enthalpy equation for energy conservation

Internal energy is a thermodynamic state variable that is hardly used in real applications. The most commonly used is enthalpy (h), which is related to internal energy from **Eq.(6-46)**:

$$\mathrm{e} = \mathrm{h} - \frac{\mathrm{p}}{\rho} \qquad (6\text{-}46)$$

Substituting **Eq.(6-46)** into **Eq.(6-45)** and rearranging, the energy conservation enthalpy equation is obtained (Bird et al., 2006).

$$\frac{\partial}{\partial \mathrm{t}}(\rho \mathrm{h}) + \nabla \cdot (\rho \mathrm{uh}) = -\nabla \cdot \mathrm{q} + \frac{\partial \mathrm{p}}{\partial \mathrm{t}} + \mathrm{u} \cdot \nabla \mathrm{p} + \tau : \nabla \mathrm{u} + \mathrm{Q} \qquad (6\text{-}47)$$

By a small mathematical modification, taking into account that the continuity equation multiplied by the enthalpy is zero, **Eq.(6-47**) can be written as follows:

$$\rho\frac{\partial h}{\partial t}+\rho u\cdot\nabla h=-\nabla\cdot q+\frac{\partial p}{\partial t}+u\cdot\nabla p+\tau:\nabla u+Q \qquad (6\text{-}48)$$

The **Eq.(6-48)** describes the enthalpy equation of energy conservation.

The enthalpy equation for energy conservation

Many people are familiar with the concept of temperature, so it is convenient to express energy conservation in terms of temperature. Enthalpy is related to temperature (T) and pressure through the following differential relationship:

$$dh=C_p dT+\frac{1}{\rho}\left[1+\frac{T}{\rho}\frac{\partial\rho}{\partial T}\Big|_p\right]dp=C_p dT+\frac{1}{\rho}[1-T\beta]dp \qquad (6\text{-}49)$$

where Cp is the heat capacity at constant pressure and β is the bulk expansion coefficient.

Substituting **Eq.(6-49)** in **Eq.(6-48),** the following relation is obtained.

$$\rho C_P\frac{\partial T}{\partial t}+\rho C_P u\cdot\nabla T=-\nabla\cdot q-T\beta\cdot\left(\frac{\partial p}{\partial t}+u\cdot\nabla p\right)+\tau:\nabla u+Q \qquad (6\text{-}50)$$

where q is the conductive term, can be expressed as follows:

$$q=-k\nabla T \qquad (6\text{-}51)$$

where k is the thermal conductivity.

The temperature equation is the most commonly used form to express energy conservation, which is mathematically equivalent to **Eq.(6-41).** However, the different energy conservation equations do not work identically when implemented by a numerical method. Many commercial codes based on the finite volume method use the total enthalpy equation as the energy conservation equation. However, the total enthalpy equation is prone to numerical oscillations that reduce numerical accuracy. Therefore, it is much more robust and accurate to solve the temperature equation. The finite element method allows solving the temperature equation and still conserving the total energy (Hughes et al., 2000). Therefore, COMSOL Multiphysics was used for the numerical study in this work since most of the study to be

performed deals with heat transfer, specifically the simulation of the hydrothermal carbonization reactor.

6.2.4.2.3. *Kinetics models*

In this kinetic simulation of HTC, the kinetic model proposed by Álvarez-Murillo et al. (2016) was used, with the modification of adding heat of the reaction of the HTC, calculated experimentally. The behavior of each biomass during the HTC process is related to its content in the constituent biopolymers (cellulose, hemicellulose, and lignin). However, the decomposition kinetics of this biopolymer for all types of biomasses may be similar. The overall reaction of biomass in the HTC process is presented in the following reaction:

$$\text{Biomass} + H_2O \rightarrow \text{Hydrochar} + \text{Liquid} + \text{Gas} \qquad \Delta H_r \qquad (6\text{-}52)$$

$$r_{bi} = -\frac{dC_{bi}}{dt} = K_1 . C_{bi} \qquad (6\text{-}53)$$

$$K_1 = \left[\left[\frac{T_{(t,R)}}{T_{ref}}\right]^n e^{\left[\frac{-Ea}{Rg T_{(t,R)}}\right]}\right] . A_0 \qquad T_{ref} = 1K \qquad (6\text{-}54)$$

This is an extension of the Arrhenius equation in which the pre-exponential factor is proportional to T^n where T (t, R) is the temperature (K) as a function of time, biomass concentration, and spatial variables and n is a constant, A_0 (1/s) is temperature-independent constant, Ea (J/mol) is the activation energy, and Rg (8.314 J mol/K) is the constant gas, C_{bi} (kmol/m^3) is the biomass molar concentration inside the reactor and r_{bi} (mol/m^3. s) rate of each reaction.

$$V_r \left[\sum_i C_{bi} C_p \frac{dT}{dt} + \sum_i H_{bi} r_{bi}\right] = Q_{ext} \qquad (6\text{-}55)$$

$$r_{bi} = R_{bi} F_{bi} \qquad (6\text{-}56)$$

The hydrochar formation kinetics is represented by:

$$r_{HC} = R_{bi} . (F_{Hc}) \qquad (6\text{-}57)$$

And liquid formation kinetics as:

$$r_{liq} = R_{bi} . (F_{liq}) \qquad (6\text{-}58)$$

Where Vr (m^3) is the reactor volume, Q_{ext} (W) external heat rate, H_{bi} (J/mol) enthalpy of each reaction, R_{bi} (mol/m^3. s) is the reaction rate for species i of biomass. F_i (-) is the fraction of biomass converted into products, F_{HC}, F_{liq} is the fraction of the biomass converted into

hydrochar and liquid respectively, these values were determined experimentally. The biomass fraction converted in to gas is represented as (1- F_{HC}-F_{liq}).

6.2.4.2.4. *Boundary conditions*

Initial conditions were: T=25°C, p=0 in the pressure point constraint, and u=0 throughout the system. Electrical power of 120 W was applied to the external reactor sidewall. No-slip boundary conditions (u=0) were applied at all solid/fluid interfaces. Natural external convection conditions were applied to the upper and lower sides of the reactor. There was a heat loss due to faulty reactor insulation. The insulator heat transfer coefficient was determined from the following equation:

$$h = \frac{q_0}{T_{ext} - T} \qquad (6\text{-}59)$$

where h is the heat transfer coefficient (W/m^2K), T_{ext} (K) is the external temperature and q_0 (W/m^2) represents heat flux loss.

6.2.4.3. *Spatial discretization (mesh)*

Since finite element simulation (FEM) can represent virtually any type of complex particle geometry, the simulation results generated by this method are especially good at resolving the impact of detailed morphological complexity on transport phenomena processes. Furthermore, the FEM subdivides the simulation geometry into smaller domains or elements, over which the boundary value partial differential equations are solved. A detailed discussion of the mathematical foundations of this approach is beyond the scope of this work; however, a detailed explanation of this topic can be found in "The Finite Element Method in Heat Transfer and Fluid Dynamics (Reddy and Gartling, 2010).

The geometric models and meshes were constructed in the COMSOL Multiphysics software version 5.4. Free tetrahedral meshes were constructed for each of the geometry configurations. The accuracy of the CFD solution is strongly dependent on the mesh quality. When the accuracy is not changing significantly with the increasing number of mesh elements, the calculation can be considered mesh independent (Gyurik et al., 2019). In this context, it was necessary to make a mesh study of all the simulations. The simulation was divided into two main parts: the simulation of the hydrodynamic study and the simulation of the heat transfer and kinetics.

6.2.4.4. *Solver settings*

For solver settings in rotating machinery, the mixture model (turbulent or laminar) interface supports both types of studies' steps (stationary and time-dependent). For time-dependent 3D simulations, it is critical to have an accurate initial value that corresponds to the existing situation. To simplify the simulation, the velocity field was calculated using the frozen rotor assumption, particularly a steady-state study. The results were used as initial values for the time-dependent study.

6.2.4.5. *Stirred reactor hydrodynamic simulations*

In the mixing system analysis, Reynolds number (N_{Re}) is an important design criteria (Jaszczur et al., 2020). For stirred vessels, the flow is laminar for N_{Re} <10 and fully turbulent for N_{Re}>10^4 (Cullen, 2009). The Reynolds number is defined and calculated according to the following equations:

$$N_{Re} = \frac{N d^2 \rho}{\mu} \quad (6\text{-}60)$$

where d (m) is the diameter of the impeller, N (s^{-1}) the represents impeller rotational frequency, μ (Pa. s) is the dynamic viscosity of the mixture, and ρ (kg/m^3) is the density. To study the dispersion or suspension behavior within the fluid, it is considered a diluted system in which the dispersed phase is rigid spheres, and the continuous phase is a Newtonian fluid. The continuous phase viscosity variation of a dispersed phase is described by Einstein's equation (Mardles, 1940):

$$\mu = \mu_0 \left(1 + \frac{\varphi_{bi}}{\varphi_{bi}^{max}}\right)^{2.5\varphi_{bi}^{max}} \quad (6\text{-}61)$$

where μ_0 (Pa. s) is the continuous phase viscosity, φ_{bi} (-) is the volume fraction of biomass particles in the dispersed phase, and φ_{bi}^{max}(-) is considered equal to 0.63 (Laskowski, 2013); this is the maximum packing volume fraction. The mixture density is calculated from the following equation:

$$\rho = \rho_b \varphi_{bi} + \rho_c (1 - \varphi_{bi}) \quad (6\text{-}62)$$

where ρ_b (kg/m^3) is the density of the disperse phase, and ρ_c (kg/m^3) is the continuous phase density. Five rotation frequencies were used: 100, 250, 400, 550, and 700 rpm to find the ideal speed for the system to be homogeneous. The N_{Re} values at different volume fractions corresponding to the different biomass to water ratios are presented in **Table 6-2** at 25°C. All N_{Re} values obtained are higher than 10; therefore, no regime is laminar. The regime is entirely turbulent for N=550 rpm and N=700 rpm, the decision is to use the turbulent regime and also, as the temperature increases, the N_{Re} value increases for constant N.

In all numerical analysis, particularly those using Reynolds-Averaged-Navier–Stokes (RANS) equations, the results accuracy depends on the turbulence flow models used (Khaled et al., 2015). This turbulence flow will be modeled using the k-ε turbulence model. This model can handle various fluid flow conditions, it is the most common model used in CFD to simulate mean flow characteristics for turbulent flow conditions, due to its good convergence rate and relatively low memory requirements **(**Frei, 2013**).**

Table 6-2: N_{Re} values at different rotation frequency and different biomass water ratio

Rotation frequency (N)	Reynolds number				
	Water φ_{bi} =0	AS-1-4 φ_{bi}=0.1375	AS-1-6 φ_{bi} =0.0961	AS-1-8 φ_{bi} =0.0738	AS-1-10 φ_{bi} =0.0600
100 rpm=1.67 s^{-1}	2291.43	1881.88	1983.27	2044.60	2085.26
250 rpm=4.17 s^{-1}	5728.58	4704.71	4958.18	5111.50	5213.16
400 rpm=6.67 s^{-1}	9165.73	7527.54	7933.09	8178.39	8341.06
550 rpm=9.17 s^{-1}	**12602.88**	**10350.36**	**10908.00**	**11245.29**	**11468.95**
700 rpm=11.67 s^{-1}	25043.44	20790.72	21843.53	22480.33	22902.60

It is not feasible to simulate directly the movement of all biomass individual particles in the HTC reactor due to the limitations of current computers and the high computational cost of tracking thousands of particles present in typical reactors. Thus, approximate methods, such as the dispersed multiphase flow models approach or coupling fluid flow and transport of diluted species, are ways to reduce computational overheads. Recently, these approximate methods

were used by many researchers to study the hydrodynamics of the gas-solid during pyrolysis and combustion (Hosseini et al., 2010; Pecha et al., 2018; Xue and Fox, 2015; Xue et al., 2011).

6.3. Results and Discussion

6.3.1. Kinetic model results of intermediate product formation by HTC

Hydrochar formation can be carried out in two reaction pathways. The formation can proceed from the reaction of the solid-solid pathway known as primary hydrochar and the intermediate products called secondary hydrochar. Although hydrochar can be formed from dissolved intermediate components, significant amounts of process liquid are generated as a by-product of the process and require appropriate treatment. The most common uses of this liquid include use in anaerobic reactors for biogas production (Wirth et al., 2012), disposal via wastewater treatment plants (Becker et al., 2014), or reuse this liquid to treat a new biomass load in consecutive runs of the HTC process (Uddin et al., 2014). Under HTC process conditions, the properties of water are similar to an organic solvent due to changes in its polarity and dielectric constant; it acts as a catalyst for biomass conversion. In this condition, the biomass undergoes different chemical reactions such as hydrolysis, decarboxylation, dehydration, condensation, aromatization and polymerization (Kambo and Dutta, 2015; Volpe et al., 2018). The chemistry of the HTC reaction indicates that the biomass feedstock undergoes several chemical reactions that contribute to hydrochar and liquid by-products formation. The liquid by-product contain different compounds of commercial value due to the different chemical reactions that occur during the process (Kambo and Dutta, 2015; Kaushik et al., 2014; Stemann et al., 2013b).

As can be seen above, liquid by-product is rich in several commercially attractive organic compounds, such as total sugars, organic acids (formic, acetic, and lactic), furans (furfural and 5-HMF), and total polyphenols. Recovery of these valuable chemical products can generate additional revenue. It can also be of great benefit to biorefineries and other industries that manufacture biomaterial-based chemicals and polymers (Kambo and Dutta, 2015).

To recover these organic compounds, it is necessary to know their formation and conversion kinetic. Many studies have investigated the HTC process of biomass; however, the main challenge remains how to design and optimize the operating conditions of the process because the mechanism or pathway of the reaction, the kinetics of the reaction are still largely unknown. The analysis of the current kinetic models is focused on different approaches.

Several of these analyses have been carried out following Arrhenius behavior under the assumption of a first-order reaction. Also, most of the current models focus only on the formation of hydrochar. Reza et al. (2013) described the degradation of cellulose and hemicellulose as a first-order reaction with an activation energy of 73±6 kJ/mol 30±12 kJ/mol for cellulose and hemicellulose, respectively. However, the authors did not consider the formation of intermediates. Some authors use the biomass models as cellulose to include the secondary hydrochar formation (Paksung et al., 2020). Conversely, the kinetic parameters obtained from cellulose during the HTC process might also not wholly fit for the HTC of all biomass since a particular dependency on the type of biomass has already been observed. Until now, few studies have focused on understanding the pathway of hydrochar formation from intermediate components, especially the different reaction mechanisms that can occur during the HTC process of different lignocellulosic biomass types. Understanding the mechanism of the biomass-to-hydrochar conversion reaction from intermediates will be possible to quantify these intermediates, recover them and explore the possible uses. For this reason, this part of the study is focused on the HTC reaction when applied to different types of lignocellulosic biomass (AS, ASB, and CEL). The analysis of kinetic parameters of the formation of different intermediates such as sugars, polyphenols, furans (furfural and 5-HMF), organic acids, as well as to examine the formation of primary and secondary hydrochar. These kinetic parameters were determined using the optimization method of the Levenberg-Marquardt algorithm in COMSOL Multiphysics®.

6.3.1.1. *Results of optimized kinetic parameters of HTC*

The reaction pathways of the HTC process are schematically described by a global component model (hemicellulose, cellulose, and lignin), in which the initial raw material is converted into intermediates until the final products in different steps (**Figure 6-1**). All the reactions are assumed as the first order kinetics. The kinetic rate constants k_1- k_{14} were determined using the Levenberg–Marquardt algorithm optimization method in COMSOL Multiphysics 5.6. The differential equations system was solved numerically using backward differentiation formula (BDF). The solver estimates the kinetics parameters based on experimental data. The fitting accuracy is represented by the sum of the squared estimate of errors (SSE). **Table 6-3** shows the results of optimized parameters for the reaction kinetic constants of the three biomasses at temperatures of 210, 230, and 250 °C. In general, the reaction pathway in **Figure 6-1** and the kinetic constants fit the experimental data and their temporal variations, with a coefficient of

determination R^2> 0.98, in all studied case. This value indicates that the model does not explain only the 2% of the variation.

Table 6-3: Optimized parameter results (SSE and R^2) at set temperatures for the three biomasses

	AS		ASB		CEL	
T(ºC)	SSE	R^2	SSE	R^2	SSE	R^2
210	59.84	0.986	18.35	0.997	35.04	0.999
230	44.69	0.994	24.44	0.997	162.2	0.983
250	6.17	0.998	13.42	0.999	7.40	0.999

Table 6-4 shows the optimized values of the kinetic rate constants ki for the proposed reaction pathways at the selected temperatures. As shown in **Table 6-4**, the rate constants ki increase with increasing temperature for all biomasses. The model results showed that biomass conversion to primary hydrochar is the most favored reaction and confirmed that all non-hydrolyzed biomasses constitute primary hydrochar. As suggested by the Arrhenius equation the 1/T vs. ki graphs allow to calculate the Ea and A for each reaction constant. The corresponding kinetic parameters are given in **Table 6-5.** The corresponding Ea for hydrolysis reactions (Ea1) for the three biomasses are 63.08, 85.02 and 136.24 kJ/mol for AS, ASB, and CEL. Furthermore, the activation energy of CEL hydrolysis is higher than AS and ASB ones.

Cellulose structure generally consists of two different parts, the amorphous and the crystalline phases, which have different decomposition reaction rates. The amorphous phase has weaker bonds and participates in the initial phase of the reaction, while the crystalline phase needs to be previously converted into the amorphous phase and then degraded during the HTC process (Yousefifar et al., 2020). Therefore, more energy is required for CEL hydrolysis compared with AS and ASB. This is also noted in the lower solid conversion rate for CEL at low temperatures compared to with AS and ASB. Results agree with previous reports in the literature. Indeed, Paksung et al. (2020) studied the hydrolysis reaction of α-cellulose using a first-order kinetics and they reported activation energy value of 137 kJ/mol. Further, Schwald and Bobleter (1989) reported similar values for the activation energy of α-cellulose (129 kJ/mol). Therefore, reported activation energies and those obtained in the present study are in good agreement. As shown in **Table 6-5**, the Ea for the formation of furfural and 5-HMF are higher than for organic acids and this regardless of biomass. These results agree with the concentrations of

intermediates obtained (**Chapter 3**). Besides, the degradation of sugars to organic acids requires a lower energy than to produce furfural and 5-HMF.

Table 6-4: Reaction rate constants (ki) for the simplified reaction pathway proposed.

Constante ki	ASB			AS			CEL		
T (ºC)	210	230	250	210	230	250	210	230	250
k1	3.28×10^{-4}	8.46×10^{-4}	1.65×10^{-3}	3.60×10^{-4}	5.97×10^{-4}	1.20×10^{-3}	1.50×10^{-4}	5.40×10^{-4}	1.50×10^{-3}
k2	4.57×10^{-4}	8.46×10^{-4}	5.00×10^{-3}	3.62×10^{-4}	5.97×10^{-4}	4.08×10^{-4}	2.75×10^{-4}	5.40×10^{-4}	2.60×10^{-4}
k3	6.98×10^{-4}	9.65×10^{-4}	3.61×10^{-3}	2.93×10^{-4}	4.97×10^{-4}	7.24×10^{-4}	3.09×10^{-3}	1.26×10^{-3}	9.50×10^{-4}
k4	1.39×10^{-6}	1.20×10^{-5}	6.50×10^{-5}	2.92×10^{-5}	1.97×10^{-4}	9.33×10^{-4}	3.02×10^{-6}	4.09×10^{-5}	2.31×10^{-4}
k5	4.67×10^{-5}	1.89×10^{-4}	7.20×10^{-4}	5.00×10^{-6}	5.10×10^{-5}	5.07×10^{-4}	2.58×10^{-6}	8.91×10^{-6}	1.76×10^{-5}
k6	3.47×10^{-4}	3.10×10^{-4}	2.46×10^{-3}	2.31×10^{-4}	4.51×10^{-4}	8.06×10^{-4}	5.20×10^{-6}	6.13×10^{-5}	1.47×10^{-4}
k7	1.01×10^{-4}	1.01×10^{-4}	2.90×10^{-4}	4.55×10^{-6}	4.55×10^{-6}	1.10×10^{-5}	5.48×10^{-5}	8.62×10^{-5}	2.01×10^{-4}
k8	5.98×10^{-6}	9.82×10^{-6}	1.61×10^{-5}	5.00×10^{-6}	5.65×10^{-4}	7.76×10^{-4}	1.10×10^{-4}	3.11×10^{-4}	5.03×10^{-4}
k9	1.49×10^{-5}	9.91×10^{-5}	5.49×10^{-5}	3.88×10^{-5}	9.82×10^{-5}	1.55×10^{-4}	7.05×10^{-5}	1.60×10^{-4}	2.37×10^{-4}
k10	7.55×10^{-5}	1.00×10^{-4}	4.15×10^{-4}	1.02×10^{-5}	3.06×10^{-5}	7.67×10^{-5}	1.03×10^{-6}	2.23×10^{-5}	5.62×10^{-5}
k11	5.23×10^{-5}	1.10×10^{-4}	2.91×10^{-4}	2.03×10^{-5}	1.25×10^{-4}	5.92×10^{-4}	2.31×10^{-7}	2.18×10^{-6}	4.33×10^{-6}
k12	4.33×10^{-5}	1.09×10^{-4}	2.80×10^{-4}	2.50×10^{-5}	7.65×10^{-5}	2.15×10^{-4}	-	-	-
k13	9.67×10^{-4}	2.14×10^{-3}	1.93×10^{-3}	1.26×10^{-3}	1.14×10^{-3}	1.43×10^{-3}	-	-	-
k14	4.57×10^{-6}	9.54×10^{-6}	1.76×10^{-5}	2.51×10^{-5}	4.51×10^{-5}	7.17×10^{-5}	-	-	-

The Arrhenius model parameters for R_{12}-R_{14} were discarded for CEL because to the cellulose used is pure. The Ea_{11} for the conversion of furfural and 5-HMF to secondary hydrochar of AS is 177.32 kJ/mol; this value is relativity high because a high temperature is required to polymerize the intermediates to form the secondary hydrochar. It is important to mention that a first-order reaction was considered; this may be the cause of the high value of Ea_{11} since some studies use higher-order reactions. However, the reason to use a first-order reaction in this case was explained in **Section 6.2.1.2.** .

It is noteworthy that the determination R_2, R_5, R_8, R_9, and R_{14} kinetic parameters are not the object of this study since they correspond to non-identified products. These individual degradation products were not determined experimentally. However, the final degradation

products are calculated by mass balance, and these parameters could be estimated. The activation energies of AS and ASB were relatively small compared to the activation energies of CEL; this is because higher energy is required to decompose CEL, in general. However, it is important to notice that the kinetics parameters values found in this study may be subject to the experimental conditions used in terms of the biomass to water ratio, the biomass type used, the reactor type (a stirrer rector operating in an open-loop control system), and stirring speed (550 rpm).

Table 6-5: Arrhenius model parameters for the reaction pathway at 210 ºC, 230 ºC and 250 ºC.

	ASB			AS			CEL		
	Ea (kJ/mol)	A (1/s)	R^2	Ea (kJ/mol)	A (1/s)	R^2	Ea (kJ/mol)	A(1/s)	R^2
R1	85.02	8.81×10^{3}	0.994	63.08	3.82×10^{1}	0.987	136.24	2.32×10^{9}	0.992
R2	124.96	2.08×10^{8}	0.743	6.24	2.86×10^{-5}	0.987	17.25	1.87×10^{-5}	0.941
R3	85.65	1.81×10^{4}	0.876	47.58	6.94×10^{1}	0.994	40.57	1.17×10^{-9}	0.994
R4	106.58	3.72×10^{4}	0.861	182.13	2.48×10^{13}	0.999	145.43	3.08×10^{8}	0.983
R5	143.68	2.64×10^{9}	1.000	242.59	1.37×10^{19}	1.000	64.04	5.42×10^{-1}	0.997
R6	77.11	1.5×10^{3}	0.470	65.69	4.9×10^{1}	1.000	111.62	6.19×10^{5}	0.993
R7	55.07	1.4×10^{0}	0.933	46.37	7.79×10^{-3}	1.000	44.11	9.09×10^{-2}	0.999
R8	52.01	4.16×10^{-2}	1.000	267.97	1.53×10^{22}	0.815	49.50	7.93×10^{-1}	0.986
R9	70.21	1.43×10^{1}	0.475	72.92	5.3×10^{1}	0.970	40.95	4.41×10^{-2}	0.998
R10	88.94	4.54×10^{3}	0.855	106.08	5.08×10^{4}	0.999	134.51	7.37×10^{7}	0.989
R11	89.96	4.43×10^{3}	0.990	177.32	5.13×10^{12}	1.000	96.44	7.81×10^{2}	0.969
R12	98.00	2.8×10^{4}	0.999	113.15	7.13×10^{5}	1.000	-	-	-
R13	36.88	1.8×10^{-1}	0.663	6.36	5.02×10^{-5}	1.000	-	-	-
R14	70.89	3.55×10^{0}	0.999	55.20	6.59×10^{23}	0.998	-	-	-

6.3.1.2. *Model predictions*

To validate the reaction pathway proposed in **Figure 6-1**, the model was used to predict each of the intermediate concentrations during isothermal HTC of AS, ASB, and CEL at 210 ºC and 250 ºC. **Figure 6-6a** shows the predicted ASB concentration for all components at 210ºC. The total solids concentration decreased from 98.52 g/L to 54.04 g/L during the heating time and was practically constant during the two hours holding time. Only a decrease of 3.1 g/L is

observed during the holding time. However, at 250 ºC **Figure 6-6b** the total solid decreases from 98.52 to 42.56 g/L, a decrease of 12 % of the total solid compared to 210 ºC. As it can be seen, temperature plays a more critical role in the variation of component concentrations than holding time. The total acid content increases sharply over the retention time, reached a maximum and then slowly decreasing. Thus, high acid yields could be achieved at this temperature over a wide range of retention times at 210 °C. The total acid exceeds 16.63 g/L when the reaction time is longer than 60 min. Besides, the ASB hydrolysis is rapid and nearly complete during the heating time, resulting in low sugar concentration at temperatures above 210°C.

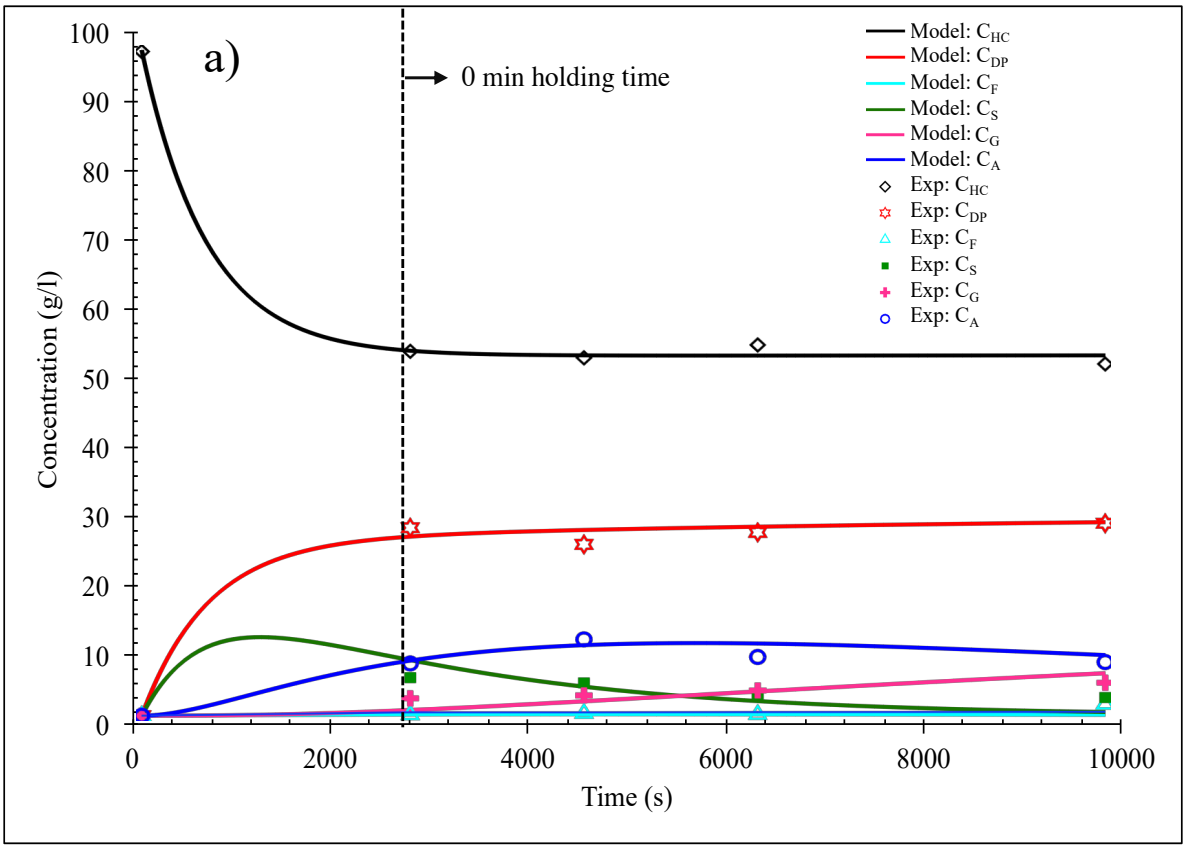

Figure 6-6b. Calculated (continuous curves) and experimental (discrete points) concentration evolution of the HTC intermediates of ASB at 210 ºC

The production of furfural and 5-HMF were also low during the holding time. The predicted gas yield is increased from 2.57 to 4.89 g/L at 210 ºC, while the reaction time increases from 1 min to 120 min. **Figure 6-7a** shows the predicted AS concentrations for all components at 210ºC. As in the case of AB, the total solid concentrations decreased from 96.42g/L to 37.19g/L during the heating time and remained constant during the holding time. The same

decrease of total solid is observed at 250 ºC during the heating time. However, during the holding time an increase of total solid is observed (**Figure 6-7b).**

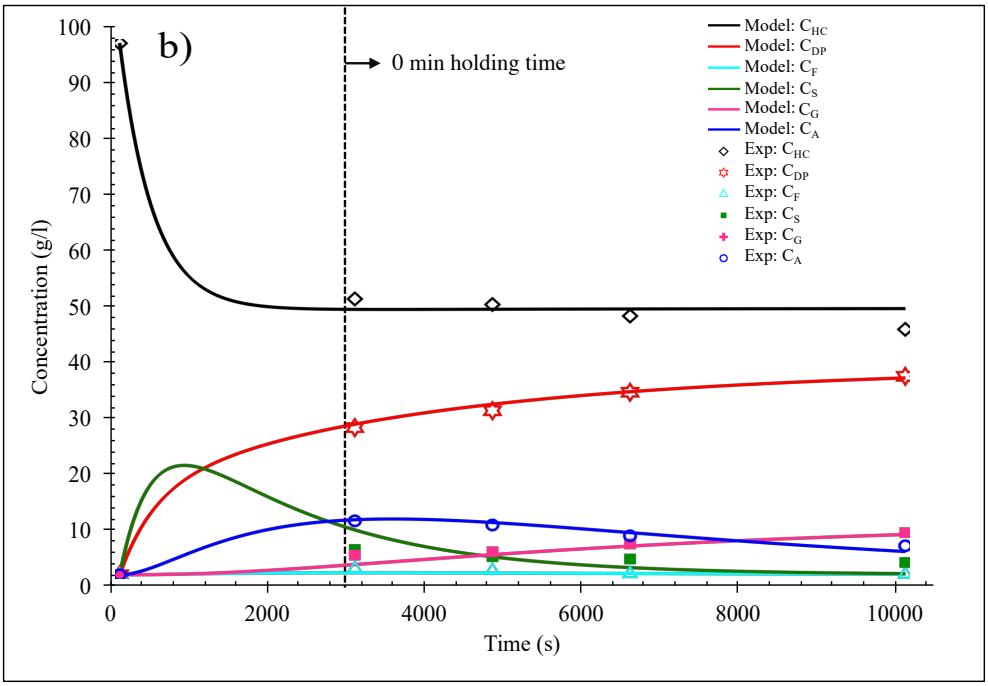

Figure 6-6b. Calculated (continuous curves) and experimental (discrete points) concentration evolution of the HTC intermediates of ASB at 250 ºC.

This increase is due to polymerization reaction as explained in **Chapter 3.** Total acid and sugar products are the most abundant products in the decomposition liquid phase of ASB at 210 °C. The concentrations of unidentified compounds or degradation products, as well as the hydrochar concentrations show that they are the major products. Finally, the gas content practically does not change at 210 ºC, but a small variation is observed at 250 ºC. **Figure 6-8a** shows the predicted CEL concentration for all components at 210ºC. As it can be seen in **Figure 6-8a** no large CEL degradation is observed. Only the total solid concentrations decrease from 100 g/L to 86.17 g/L during the heating time. The concentration of total solids remains practically constant during the holding time. So, most of the intermediary compounds detected were sugars and their maximum concentration is 5.21 g/L. **Figure 6-8b** depicts the predicted biocrude product concentration at 250 ºC. The concentrations of biocrude are higher in this condition. The highest sugar concentration is obtained during the heating time. In addition, a high production of furfural and 5-HMF is observed.

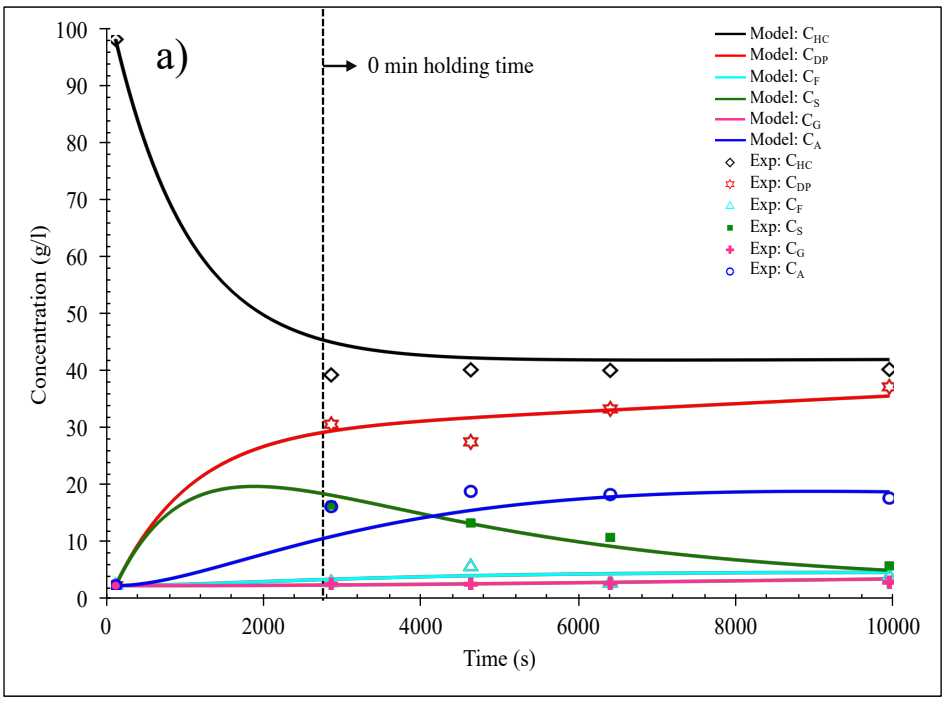

Figure *6-7.* Calculated (continuous curves) and experimental (discrete points) concentration evolution of the HTC intermediates of AS at 210 ºC

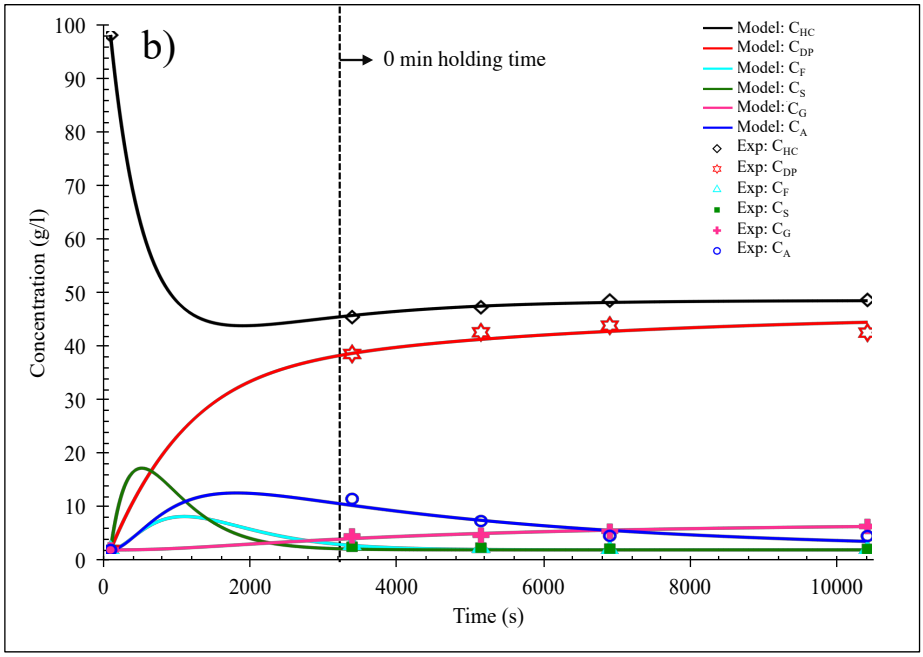

Figure 6 7. Calculated (continuous curves) and experimental (discrete points) concentration evolution of the HTC intermediates of AS at 250 ºC.

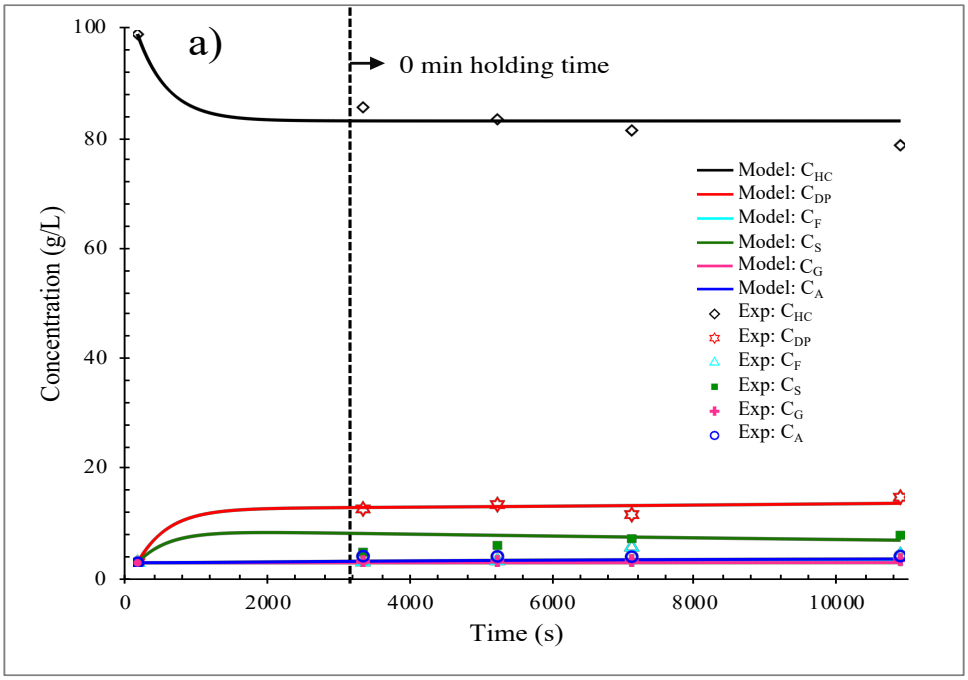

Figure *6-8*. Calculated (continuous curves) and experimental (discrete points) concentration evolution of the HTC intermediates of AS at 210 ºC

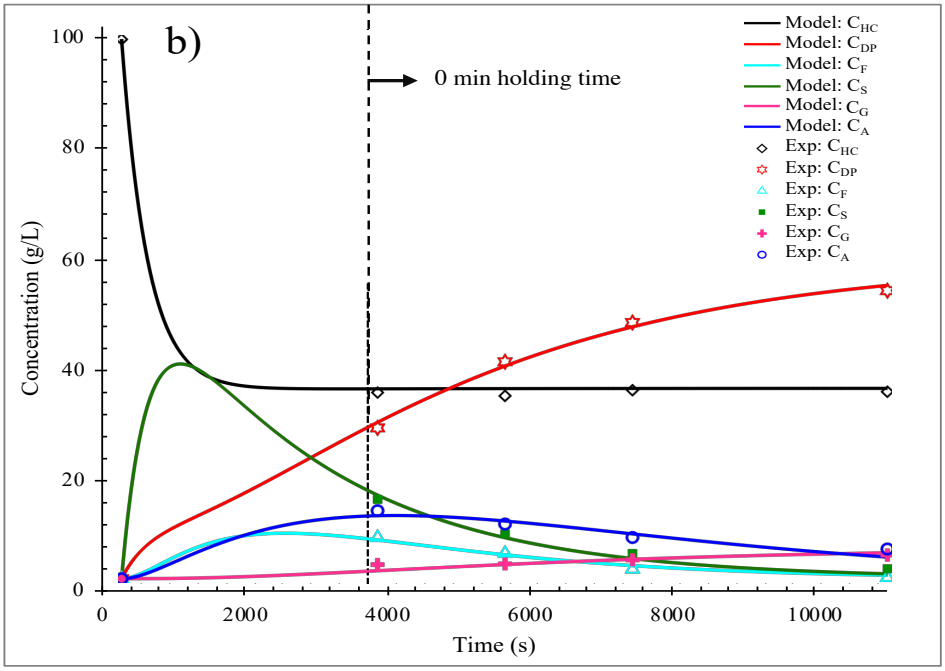

Figure 6-8. Calculated (continuous curves) and experimental (discrete points) concentration evolution of the HTC intermediates of AS at 250 ºC.

6.3.2. Experimental design models result: Doehlert

6.3.2.1. *Raw biomass characterization*

The biomass used in this study was *Agave salmiana* bagasse (ASB). This biomass was used due to its chemical structure (cellulose and hemicellulose are similar proportions). In this study, the particle diameter used were between 0.1 and 1 mm. The results of proximate and ultimate analysis of untreated ASB are shown in **Table 6-6**. The moisture content (MC) of the raw ASB (5.0%) used in this work corresponds to the values found in the literature (Chávez-Guerrero and Hinojosa, 2010; Linan-Montes et al., 2014). VM (77.9%) and FC (13.4%) fractions of raw ASB are also comparable to the values found by Linan-Montes et al. (2014). In addition, the ASB has low ash content (3.8%), which is an advantage for combustion applications.

Table 6-6: Proximate, ultimate, chemical structure analysis, and HHV characteristics of ASB

Proximate analysis (%)	
MC	5.0±1.0
VM	77.9±1.4
FC[a]	13.4±1.6
Ash	3.8±0.4
Ultimate analysis (%)	
C	38.0±0.1
H	4.1±0.1
N	0.6±0.1
S	n.d
O[a]	56.1±0.2
Extractible (%)	1.4±0.0
Hemicellulose (%)	43.8±0.4
Cellulose[a] (%)	40.7±0.5
Lignin (%)	14.2±0.1
HHV (MJ/kg)	16.8±0.2

MC: moisture content, VM: volatile matter, FC: fixed carbon, n.d: not detectable (<0.1%), [a]: by difference.

The ultimate analysis gives the weight percent of the elements C, H, O, N, and S. **Table 6-6** shows the elemental analysis of ASB. A difference of 100 % ASB calculates the quantity of oxygen. Its value is equal to 56.1 %. Similar values were obtained for blue agave bagasse (Linan-Montes et al., 2014). For higher contents of C and H, we observe the higher energy content of the biomass (Guizani et al., 2017). The content of N and S is significant for the use of these materials in combustion. From an environmental viewpoint, The ASB can be an exciting fuel since it has low N and S contents, reduced the risk of producing NOx and SOx emissions.

The results show that raw ASB contains 43.8% of hemicellulose, 40.7% cellulose, 14.2% of lignin, and 1.4% of extractives components. These values are similar to those of the blue agave bagasse fibers (Flores-Sahagun et al., 2013). Ultimate analysis revealed that raw ASB has a lower carbon percent (38.0 %) than the oxygen percent (56.1%). ASB shows a HHV of 16.8 MJ/kg (comparable to the value of 16.3 MJ/kg reported by Linan-Montes et al. (2014).

6.3.2.2. *Thermal behavior (TG/DTG) of raw ASB and hydrochars*

Typical curves of the thermogravimetric (TG) and derivative thermogravimetric (DTG) behavior of raw ASB and produced hydrochars, as a function of the studied parameters (temperature and holding time) are presented in **Figure 6-9** .The TG curves in **Figure 6-9a** show the mass loss percentage of samples over the range of temperature from 100°C to 900 °C in nitrogen and heating rate (10°C/min) conditions. The TG curves below 180°C, related to moisture and volatiles releases, are almost similar for all samples. A significant weight loss was observed at a temperature of 180-380°C. In this range, the cellulose and hemicellulose decomposed, leading to the formation of volatiles, primary char, and gases (Demirbas, 2004). After that, the decomposition rate above 380°C underwent slow progress until 900°C since the rest of the lignin or primary char was discomposed (Wongsiriamnuay and Tippayawong, 2010). The TGA curve of hydrochar (ASB-250°C-30min) suggests that the thermal stability increased with an increase in temperature.

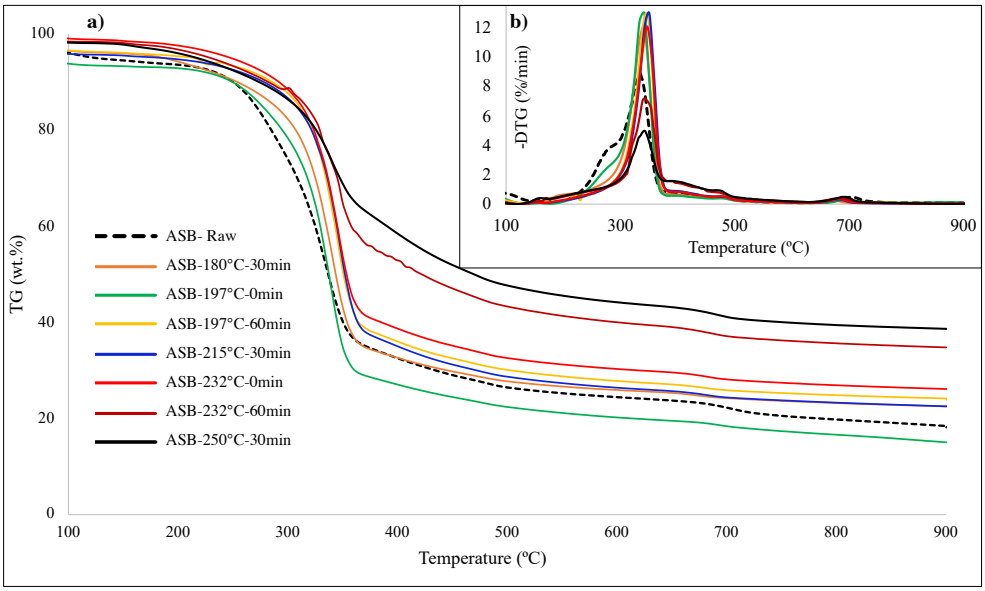

Figure 6-9: a) TG and **b**) DTG curves for raw ASB and hydrochars obtained

The DTG curves presented in **Figure 6-9b** shows that the raw ASB reaches its maximum mass loss at 340°C, which is attributed to cellulose decomposition. Hemicellulose can be attributed to temperatures lower than 300°C (Lee et al., 2013; Wang et al., 2019). The pyrolysis of lignin breaks down gradually over the broad temperature range of 275-500°C. The DTG curve is shifted from 340°C for raw ASB to about 356°C. This shift can be explained by forming carbonaceous materials, such as 5-hydroxy-methyl-furfural, which is a more stable compound than the initial feedstock (Basso et al., 2016; Sevilla and Fuertes, 2009b). For all hydrochars, degradation occurs over a more comprehensive temperature range, with mostly one sharp peak located between 280°C and 380°C. This peak indicates that the most significant mass loss is related to cellulose decomposition.

6.3.2.3. *FTIR of raw ASB and hydrochars produced*

FTIR analysis was performed for all hydrochar samples and ASB to understand the chemical change in biomass during hydrothermal carbonization. The main compounds of lignocellulosic biomass are cellulose, hemicellulose, and lignin, single bonds such as O-H (3000-3700 cm^{-1}), C-H (1378cm^{-1}), C-O (1101 cm^{-1}), and C-O-C (1032cm^{-1}) are characteristic of cellulose and hemicellulose (Missaoui et al., 2017; Rizzi et al., 2017; Xu et al., 2013).

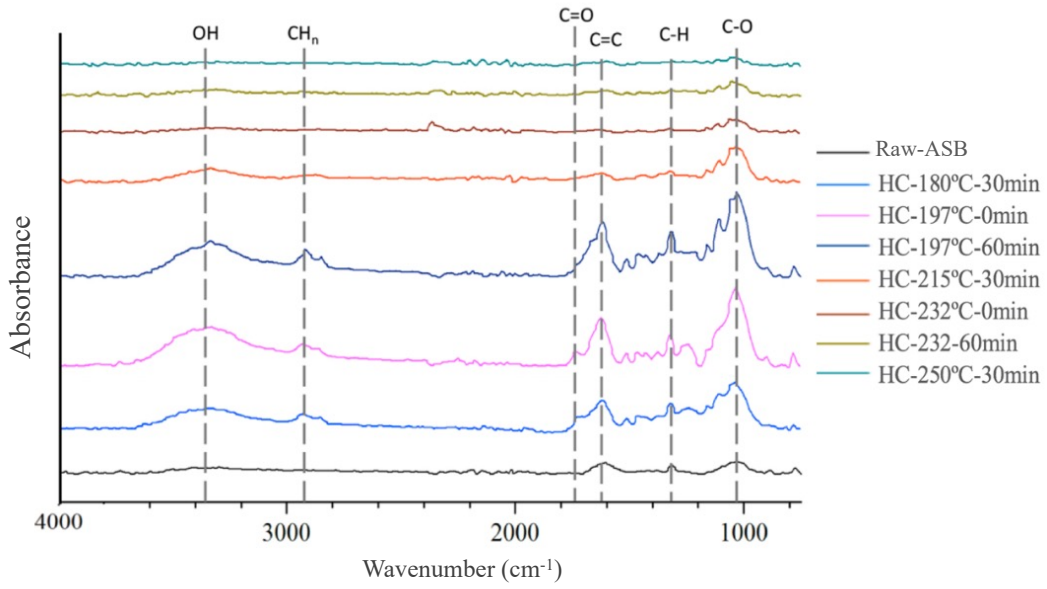

Figure 6-10: FTIR spectra raw ASB and hydrochar obtained

As can be seen in **Figure 6-10**, the raw ASB and hydrochars treated from 180 °C to 215 °C show significant differences. The main differences are found in the increase of oxygen bond

signals, especially in O-H bonds (3000-3700 cm^{-1}) and the C-O-C (1032 cm^{-1}), indicating that a significant chemical transformation may have occurred. The activation of oxygenated groups by the onset of hemicellulose degradation and the reaction of O-H groups in water are the leading causes of this change in structure. In addition, the changes are related to chemical reactions such as hydrolysis, dehydration, decarboxylation, aromatization, and polymerization (Libra et al., 2011; Pala et al., 2014).

The main changes in the structures of the samples during HTC are described below:

- The signal between 1000 - 1700 cm^{-1} is associated with several different groups: The bands between 1200 - 1000 cm^{-1} are attributed to stretching C-O bonds; this is due to the presence of carboxyl, ester, and ether groups; this band reveals the presence of carbohydrate-like structures (saccharides), i.e., hemicellulose and cellulose (Rizzi et al., 2017; Román et al., 2012; Xu et al., 2013).
- The band around 1600 cm^{-1}, the intensity of the peaks is more pronounced for hydrochar prepared at 180 - 215 °C; this can be attributed to C=C bond vibrations in aromatic ring structures. These same phenomena were observed in work done on the effects of temperature on the decomposition of cellulose (Román et al., 2012; Sevilla and Fuertes, 2009b).
- The band around 1700 cm^{-1} can be attributed to the stretching of C=O bonds present in aldehyde, carboxylic acid, and ketone functional groups.
- Peak around 2900 cm-1, which corresponds to the stretching vibrations of the aliphatic and aromatic C-H structures, is associated with the methyl and methylene groups, all of which are present in lignin (Rizzi et al., 2017; Xu et al., 2013).
- The wideband located at 3400 cm^{-1} is associated with O-H bond vibrations in hydroxyl or carboxyl groups; this peak becomes less intense for hydrochar prepared at higher temperatures (232-250 °C)

The decrease of the peak amplitude at 1032 cm^{-1}, 3400 cm^{-1} is due to the elimination of functional groups (C-H, C=C, C-O, and CHn) for hydrochars preparing the highest temperature (232-250 °C); indicate the degradation of hemicellulose and a part of cellulose during HTC, as consequences of deoxygenation by dehydration and decarboxylation of the biomass confirmed by the elemental analysis of hydrochars to be presented below.

6.3.2.4. *Ultimate analyses models*

Results of ultimate analyses are given in **Table 6-7**. The evolution of hydrogen content is relatively stable, around 5.3%. For the oxygen and carbon contents, their evolutions are more important. From the data of **Table 6-7**, the effect of temperature and holding time on oxygen and carbon contents are shown in **Figure 6-11a,1b**. For oxygen, its content decreases with an increase of parameters contrary to carbon content suggesting the carbonization of hydrochar.

The models that describe the evolution of the oxygen and carbon contents are the following:

$$O(\%) = 48.0 - 7.12X_1 - 5.28X_2 - 1.85X_{12} + 1.85X_{22} \quad (6\text{-}63)$$

$$C(\%) = 46.33 + 7.127X_1 + 5.11X_2 + 2.37X_{12} - 1.733X_{22} \quad (6\text{-}64)$$

These models provide the best R^2_{adj} values of 90.6% and 89.9% and SEE equal to 1.73% and 1.79% for oxygen and carbon, respectively. These models permit to trace of the 2D contour plots represented in **Figure 6-11c,d**.

Table 6-7: Fuel characteristics and chemical composition of hydrochars.

Run	X_1 (°C)	X_2 (min)	Proximate analysis (wt.%)				Ultimate analysis (wt.%)				HHV (MJ/kg)
			VM	FC	Moisture	Ash	C	H	O	N	
1	215 (0)	30 (0)	72.0	23.6	3.0	1.4	46±1	5.5±0.1	48±1	0.27±0.01	19.9
2	180 (–1)	30 (0)	73.7	17.3	4.5	4.2	43±1	5.2±0.1	52±2	0.40±0.02	18.1
3	250 (1)	30 (0)	59.4	33.9	2.5	4.2	54.4±0.5	4.94±0.04	40.3±0.1	0.35±0.01	23.2
4	197 (–0.5)	0 (–0.866)	81.3	13.3	4.7	0.7	36.4±0.3	4.7±0.1	58.0±0.5	0.8±0.1	18.5
5	215 (0)	30 (0)	74.7	20.8	3.0	1.4	46±1	5.4±0.1	49±1	0.24±0.05	20.6
6	232 (0.5)	60 (+0.866)	62.1	30.1	3.3	4.5	55.2±0.5	5.3±0.1	39.2±0.4	0.33±0.01	22.4
7	197 (–0.5)	60 (+0.866)	72.9	21.0	4.4	1.8	44.9±0.2	5.4±0.1	49.5±0.2	0.22±0.01	19.1
8	232 (0.5)	0 (–0.866)	71.1	20.8	3.3	4.9	46±1	5.4±0.1	49±1	0.20±0.01	19.1
9	215 (0)	30 (0)	74.2	20.8	3.1	2.0	47±1	5.6±0.1	47±1	0.25±0.02	20.1

The experimental errors are equal to 1%. The oxygen content in hydrochar decreased with increasing temperature while the carbon content in hydrochar increased with temperature. The

carbon content was 36% for weak temperature and holding time and reached its maximum value of 58% for upper temperature and holding time in **Figure 6-11c**. However, the oxygen content had the same variation between 36% and 58% but in the opposite direction in **Figure 6-11d.**

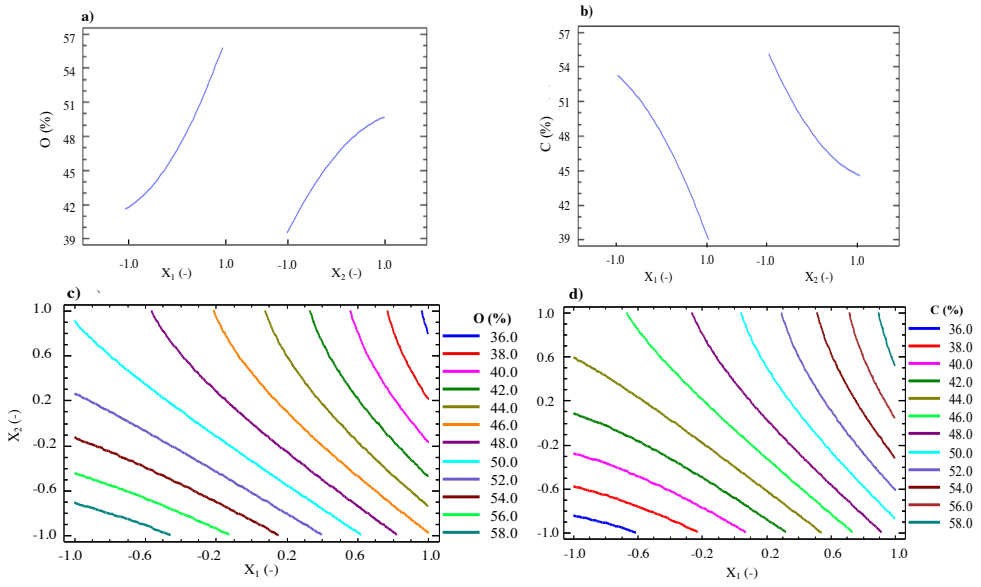

Figure 6-11: The main effect and 2D contour plots of temperature (X_1) and holding time (X_2) on the oxygen (a,c) and carbon (b,d)

6.3.2.5. *Van-Krevelen diagram analysis*

The variation in the elemental composition of the raw ASB and hydrochars was analyzed via a Van-Krevelen diagram as illustrated in **Figure 6-12**.Van-Krevelen diagram provides general information about the quality and the nature of the solid fuel. Lower atomic O/C and H/C ratios reduce the energy loss by fumes and steam released during combustion (Kambo and Dutta, 2015; Liu et al., 2013b). The Van-Krevelen diagram (**Figure 6-12.**) shows that the HTC treatment decreases the O/C and H/C atomic ratios of ASB, resulting in oxygen and hydrogen loss during the HTC process according to elemental analysis results. For example, the ABS-232-60 decreases its H/C and O/C atomic ratios from 1.68 to 1.12 and 1.2 to 0.52 compared to ABS. The evolution of the atomic O/C and H/C ratios allows for the estimation of the degree of deoxygenation of the biomass by decarboxylation or dehydration. The evolution of O/C and H/C shows that ASB decomposition was established by dehydration and decarboxylation

reactions. However, the treatment of ASB at extremes conditions (232°C-60 min and 250°C-30 min) reveals the domination of dehydration reactions.

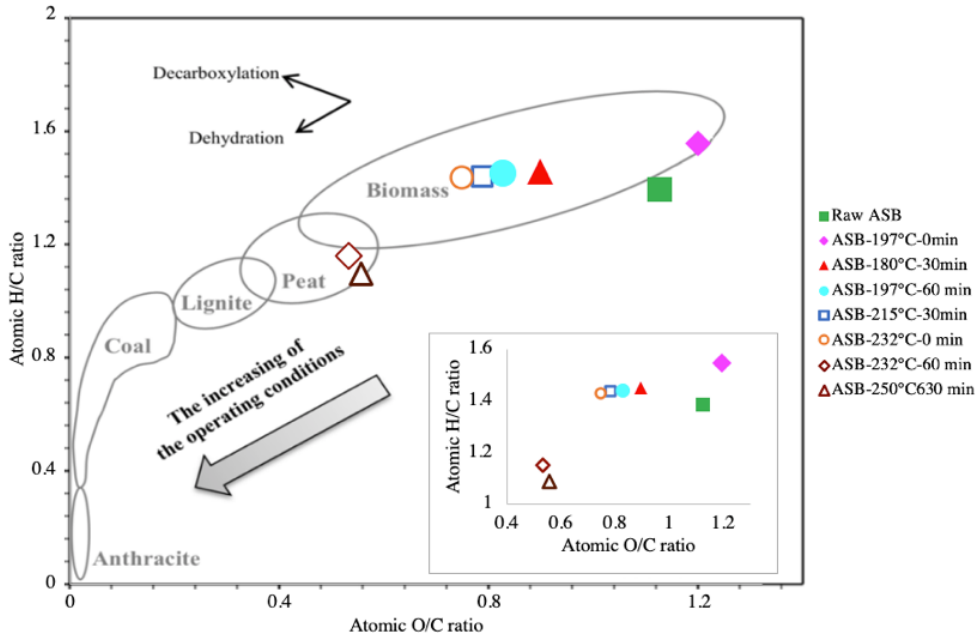

Figure 6-12: Van Krevelen diagram of raw ASB and hydrochars obtained

The positions of the most hydrochars produced in this work are inside the biomass domains, indicating that the applied operating conditions were not sufficient to complete ASB decomposition by HTC reactions. The dehydration and decarboxylation trends became increasingly apparent at higher operating temperatures and longer holding time, indicating that the conversion of ASB during the HTC process may be nearly complete at such a long holding time. The position of hydrochars 232°C-60 min and 250°C-30 min in the peat region is in agreement with these explications. Furthermore, this general tendency is also due to the high oxygen and low carbon contents of raw ASB. A follow-up of the DoE result for the relationship between O/C and H/C values as a temperature and holding time function is of interest. The modeling responses of these ratios are shown in **Figure 6-13**. The values of R^2_{adj} and SEE are: for H/C is (R^2_{adj} = 98.6%; SEE = 0.0174) and for O/C is (R^2_{adj} = 86.5%; SEE = 0.0714). It can be clearly noted that the evolution of O/C and H/C atomic ratios follow the paths of dehydration and decarboxylation reactions, the same trend as in the Van Krevelen diagram (**Figure 6-12**). As shown in the 2D contour plots (**Figure 6-13**), dehydration and decarboxylation are more intense as the HTC temperature (X_1) and holding time (X_2) increase, resulting in low O/C and H/C atomic ratios.

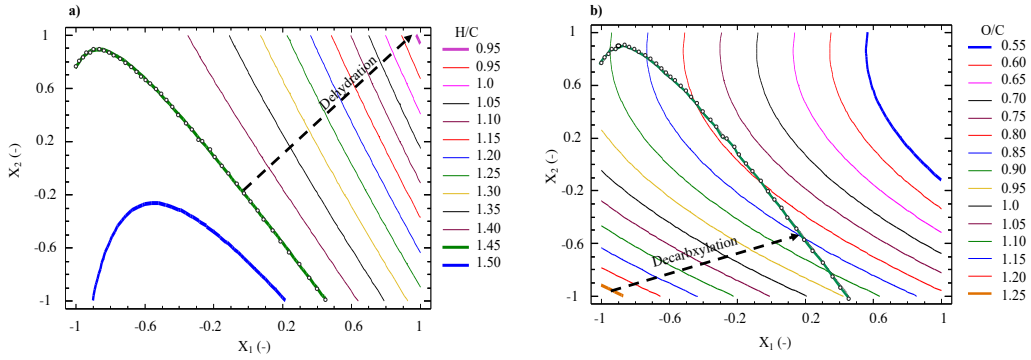

Figure 6-13: 2D contour plots showing the effects of temperature (X_1) and holding time (X_2) on: a) H/C, b) O/C.

The H/C and O/C models are given in the following equations:

$$H/C = 1.4257 - 0.1925X_1 - 0.1048X_2 - 0.1546X_1^2 - 0.0867X_1X_2 \quad (6\text{-}65)$$

$$O/C = 0.7588 - 0.2322X_1 - 0.1832X_2 + 0.1060X_2^2 \quad (6\text{-}66)$$

In addition, the 2D contour plots for the H/C ratio (**Figure 6-13a**) reveal an area in which the parameters (X_1 and X_2) have a weak action on the process. This area is defined to the left of the line representing the H/C value equal to 1.45. This limit was represented in **Figure 6-13b** for the O/C ratio; the same trend was observed towards the right. It is well-known that towards lower values of H/C and O/C ratio, dehydration reactions are favored. Towards lower O/C values, the main reactions are decarboxylation. The model agrees with the Van Krevelen diagram. The most relevant finding is that the mathematical model defines the HTC process zones and the influence of parameters (X_1 and X_2) on the main HTC reactions dehydration and decarboxylation).

6.3.2.6. *Proximate analyses models*

The results of proximate analyses and process characteristics are presented in **Table 6-7** and **Table 6-8**. In all cases, it can be observed that the hydrochar produced is less moisture content than the raw ASB (2.5-4.7% vs. 5%). The same results were observed by other works (Stirling et al., 2018; Yan et al., 2009). HTC removes the hydroxyl and carboxyl groups during the hydrolysis reactions of hemicellulose and cellulose, giving rise to a more hydrophobic residue than the raw material (Funke and Ziegler, 2010; Missaoui et al., 2017; Yan et al., 2009). No significant variation in ash content between hydrochars and raw ASB was observed (0.7-4.5%

vs. 3.8%); similar results were reported by Linan-Montes et al. (2014) for HTC conversion of poplar wood and wheat straw.

Table 6-8: Doehlert matrix design responses for Temperature (X_1) and holding time (X_2) effects.

Run	X_1 (°C)	X_2 (min)	MY (%)	EY (%)	Responses			
					VM_{cal} (%)	FC_{cal} (%)	MY_{cal} (%)	HHVcal (MJ/kg)
1	215 (0)	30 (0)	65	77	73.6	21.7	65.6	20.2
2	180 (–1)	30 (0)	86	91	74.8	17.3	84.1	18.3
3	250 (+1)	30 (0)	45	62	58.2	33.9	47.1	23
4	197 (–0.5)	0 (–0.866)	82	90	80.3	12.9	84	18.3
5	215 (0)	30 (0)	66	81	73.6	21.7	65.6	20.2
6	232 (+0.5)	60 (+0.866)	52	69	63.3	29.7	50	22.6
7	197 (–0.5)	60 (+0.866)	70	80	71.6	21.4	72	18.9
8	232 (+0.5)	0 (–0.866)	71	81	72.1	21.2	69	19.1
9	215 (0)	30 (0)	66	79	73.6	21.7	65.6	20.2

From **Table 6-8** the effects of temperature and holding time on MY, VM, HHV, and FC are shown in **Figure 6-14**. The main effects are similar for MY and VM and HHV and FC. For MY and VM, higher temperatures (X_1) and longer holding times (X_2) are adverse. An increase of parameters (X_1 and X_2) decreases their values. While the HHV and FC values increase (**Figure 6-14a** and **Figure 6-14b**). This same phenomenon was observed in biomass such as corn stover, rice hulls, and switchgrass in HTC (Lynam et al., 2015). It is well known that an increase of this parameter (X_1 and X_2) decreases MY (Wang et al., 2018), but (**Figure 6-14c)** shows that it is mainly due to loss of volatile matter. The HHV increased with HTC reaction temperature and can be related to an increase of fixed carbon (**Figure 6-14a** and **Figure 6-14b**). Hemicellulose and cellulose have a lower HHV and are less stable compared to lignin. When they are removed with increasing operating parameters, a higher proportion of lignin can remain, causing an increased HHV (Demirbas, 2004; Lynam et al., 2015). The increase in HHV may also be related to the proportion of benzene rings obtained by lignin decomposition (Collard and Blin, 2014; Kang et al., 2012).

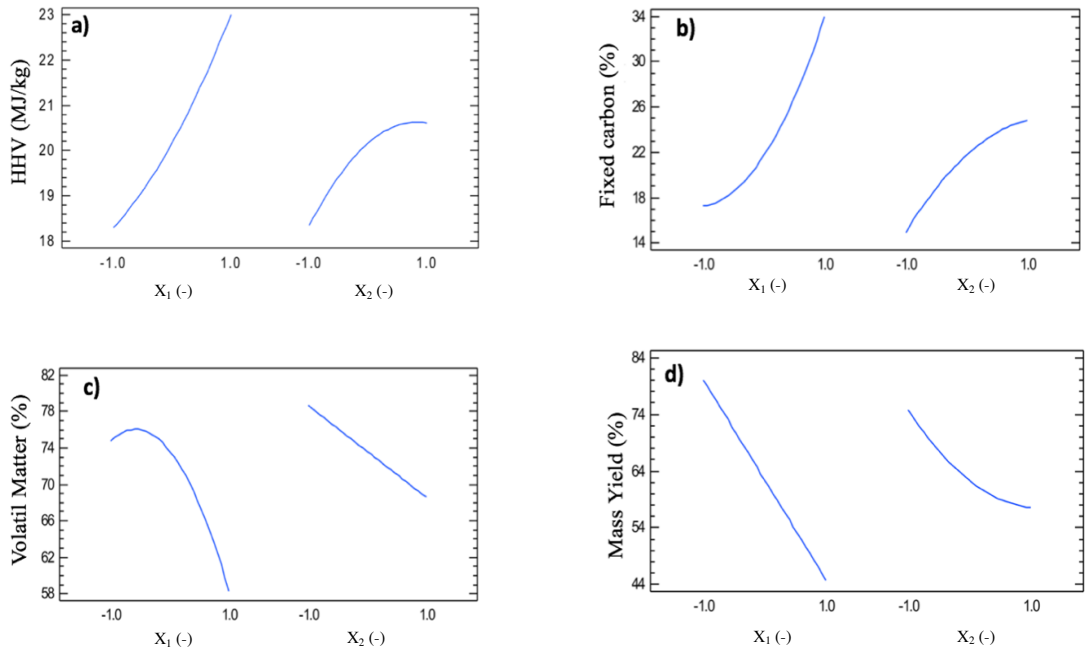

Figure 6-14: Main effects of temperature (X_1) and holding time (X_2) on **a)** HHV, **b)** fixed carbon, **c)** volatile matter, and **d)** mass yield of hydrochar produced

The carbonization of biomass is also demonstrated by the fact that VM decreases when Temperature (X_1) and holding time (X_2) increases (**Figure 6-14c)** and through the evolution of carbon and oxygen percentages showed in **Figure 6-11**. Magdziarz et al. (2020) report that the main types of compounds mainly in VM are aromatic, cyclic, and aliphatic hydrocarbons, phenol and furan derivative, and oxygen compound as acids ketones, aldehydes. The performance of HTC was evaluated through MY, VM, HHV, and FC for various X_1 and X_2 values by applying quadratic **Eq.(6-15)**. The influence of terms is shown on Pareto diagrams in **Figure 6-15**. In fact, from ANOVA, terms have been removed to obtain the maximal value of R^2_{adj} (Chartier et al., 2013). The regression coefficient of the model (R^2) gives the goodness of data fit, and R^2_{adj} considers the number of descriptive terms needed in the model. In **Figure 6-15** , a term is influent if its value is superior to the blue line ($p>0.05$). In all cases, temperature and holding time are influent for each response. The values calculated with the following models (VMcal, FCcal, MYcal, and HHVcal) are reported in **Table 6-8**.

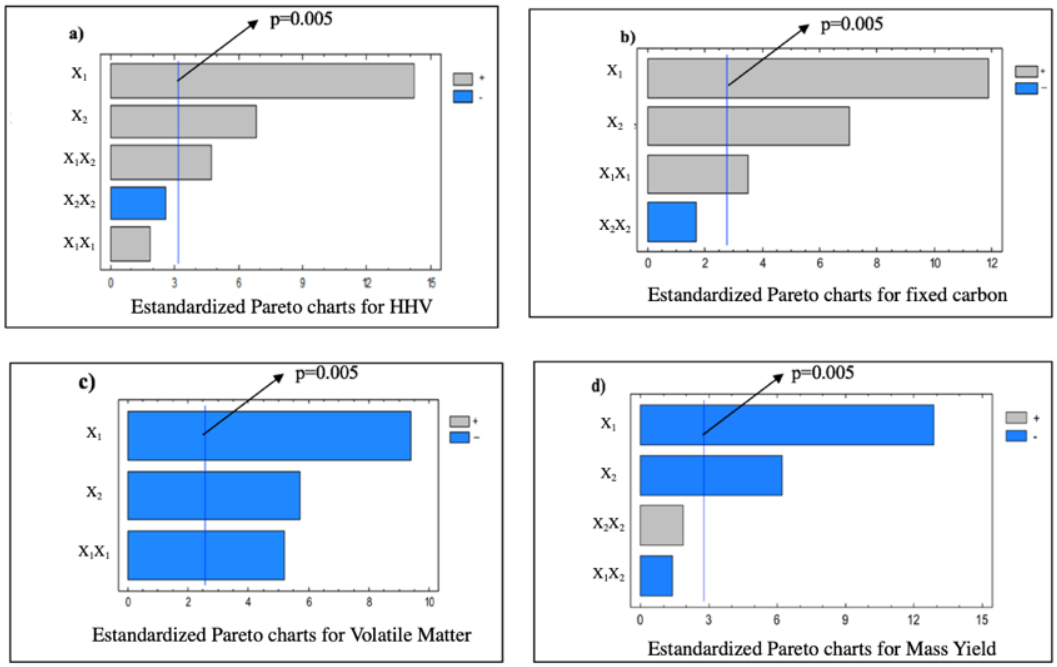

Figure 6-15: Pareto chart of standardized effects of Temperature (X_1) and holding time (X_2) on: a) HHV, b) fixed carbon, c) volatile matter and d) mass yield.

6.3.2.6.1. *HHV model*

For hydrochar HHV, R^2_{adj} reaches a maximum with five coefficients and decreases afterward. Therefore, the ideal combination of having the best fit without excess parameters requires five parameters corresponding to the following equation:

$$HHV(MJ/kg) = 20.2 + 2.35X_1 + 1.13X_2 + 0.45X_1^2 + 1.59X_1X_2 - 0.72\,X_2^2 \quad (6\text{-}67)$$

In this case, the value of the coefficient of determination (R^2) is 98%, and R^2_{adj} is 94%. This value indicates that the model does not explain 6% of the variation. SEE's value is equal to 0.41% and experimental error equal to 0.5%, meaning that the model is well descriptive (R^2_{pred} = 0.61). This model gives a range of HHV between 18 and 24 MJ/kg (**Figure 6-16)**. These values are superior to the HHV of raw ASB. In this case, the energy densification ratio value is superior to 1 and ranges between 1.07 to 1.42. Quadratic models were also reported by Román et al. (2018).

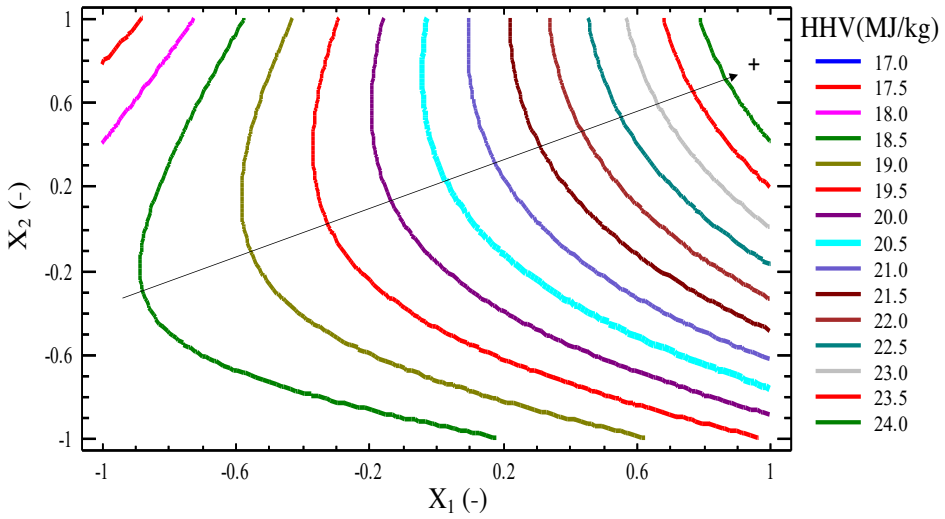

Figure *6-16*: 2D contour plots showing the effects of temperature (X_1) and holding time (X_2) on HHV

6.3.2.6.2. *Fixed carbon model*

For the FC of hydrochar, R^2_{adj} reaches a maximum with four coefficients given following equation:

$$FC\ (\%) = 21.73 + 8.30X_1 + 4.91X_2 + 3.87X_1^2 - 1.87\ X_2^2 \qquad (6\text{-}68)$$

With R^2 = 98%, R^2_{adj}=96%, SSE = 1.21% and R^2_{pred} = 0.95. For FC experimentations, experimental error is equal to 1.61% meanings that FC model is well descriptive but also predictive. FC model range is included between 12% and 36% (**Figure 6-17).**

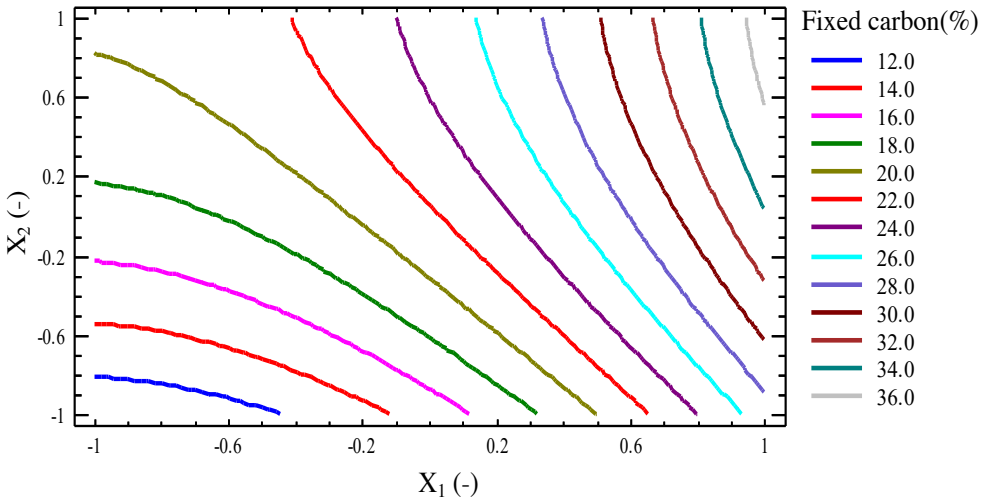

Figure 6-17: 2D contour plots showing the effects of temperature (X_1) and holding time (X_2) on FC

6.3.2.6.3. *Mass yield model*

For MY, the model retained corresponds to the following equation:

$$MY\ (\%) = 65.50 - 18.50X_1 - 8.95X_2 - 4.04X_1X_2 + 4.20\ X_2^2 \quad (6\text{-}69)$$

With $R^2 = 98\%$, $R^2_{adj} = 96\%$, SSE = 2.49% and $R^2_{pred} = 0.54$. The experimental error is 0.58%. The value of R^2_{pred} indicates that this model would be expected to explain 54% of the variability in new data, although R^2_{adj} is 96%. MY model range is comprised between 40% and 90% (**Figure 6-18).**

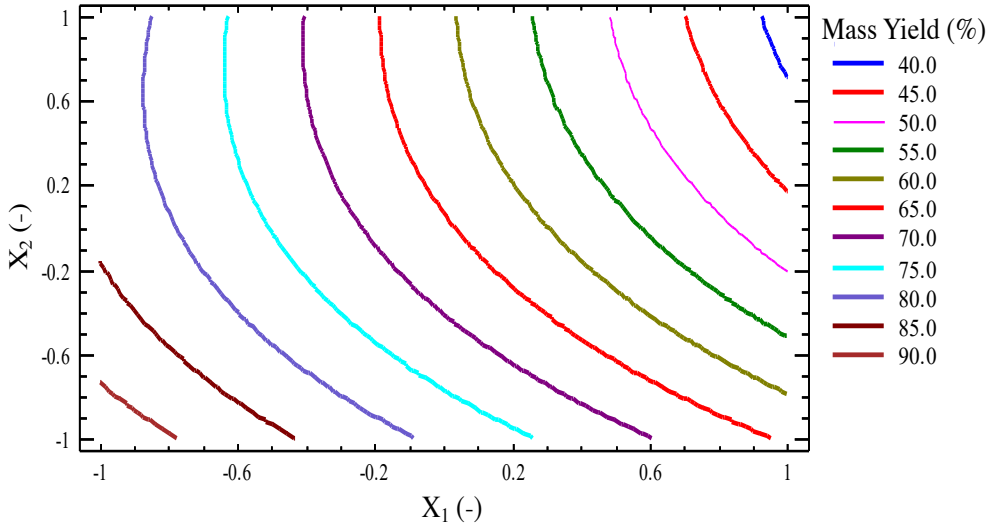

Figure 6-18: 2D contour plots showing the effects of temperature (X_1) and holding time (X_2) on FC

6.3.2.6.4. *Volatile matter model*

For the VM of hydrochar, the adjusted R^2 reaches a maximum with three coefficients and decreases afterward. Therefore, the ideal combination of having the best fit without excess parameters requires three parameters corresponding to the following equation:

$$VM\ (\%) = 73.63 - 8.26X_1 - 5.02X_2 - 7.08\ X_2^2 \quad (6\text{-}70)$$

With $R^2 = 97\%$, $R^2_{adj} = 95\%$, SSE = 1.53%, experimental error is 1.44% and $R^2_{pred} = 0.76$. Model errors are slightly superior to experimental error. VM model range is included between 54% and 80% (**Figure 6-19)**.

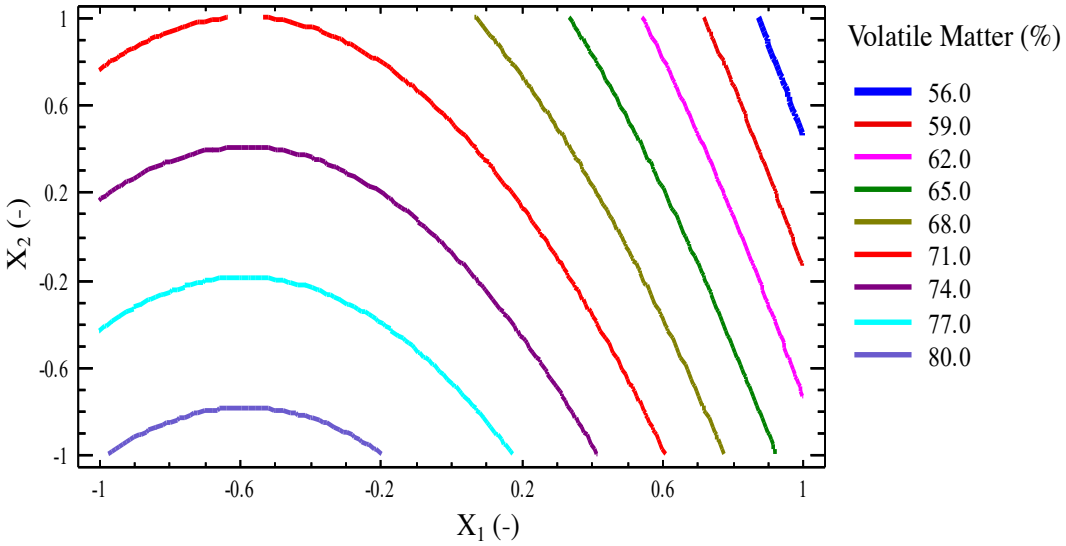

Figure 6-19: 2D contour plots showing the effects of temperature (X_1) and holding time (X_2) on VM

6.3.2.6.5. *HTC performance*

From the results of HHV and MY, we can model the energy yield (EY) due to a compensation effect between the mass yield of the hydrochar and its energy quality (EY = MY × DE). **Figure 6-20** shows the 2D contour graph of EY.

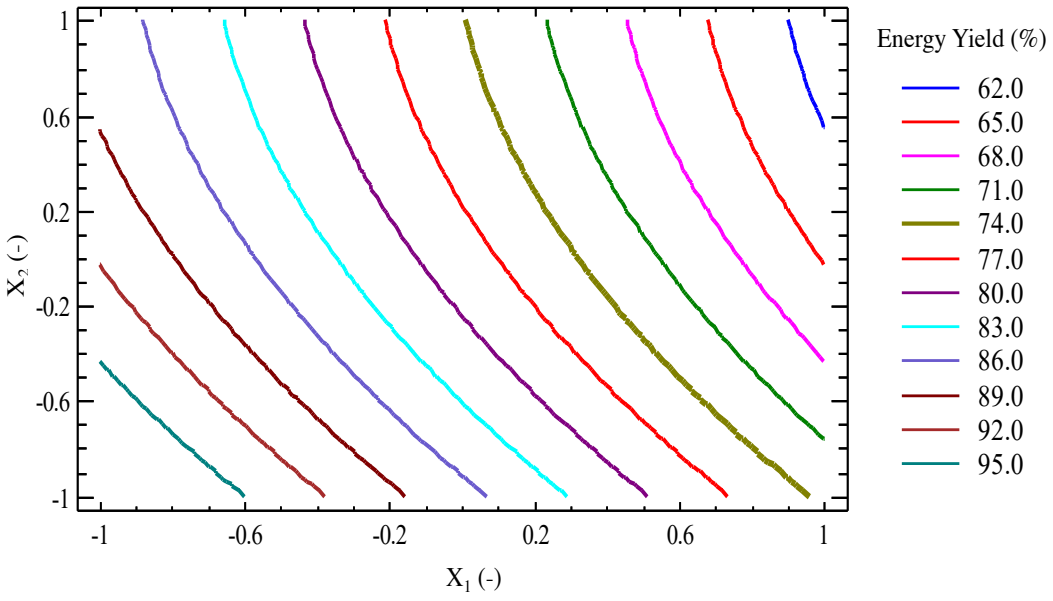

Figure 6-20: 2D contour plots showing the effects of temperature (X_1) and holding time (X_2) on energy yield

The model equation is:

$$EY\ (\%) = 78.33 - 13.48X_1 - 6.38X_2 + 2.20\ X_2^2 \quad (6\text{-}71)$$

With R^2 =96%; R^2_{adj} = 90%; and SEE = 1.79%. The optimal value is obtained for lower X_1 and X_2 following the MY tendency. Therefore, we can conclude that the MY is more influential in comparison to HHV. Furthermore, results show that the HTC treatment at 180°C during 30 min treatment with an ASB/water weight ratio equal to 1/9 maximizes the energy yield (EY = 91%). The performance of energy yield of HTC conversion of ASB is presented in **Table 6-8**. For a generalized energy balance, one liter of mezcal produced generates 15 kg of ASB with 70% moisture equivalent to 4.5 kg of ASB on a dry basis. The energy yield value varies between 62 and 95% as shown in **Figure 6-20**. **Eq.(6-15)** estimated that these hydrochars could produce energy between 46.87 MJ to 71.82MJ, which is equivalent to covering 65.10 % to 99.75% of the energy required in the cooking step mezcal production process. However, a more detailed study of the overall energy balance of the HTC process would have to be carried out before a conclusion could be drawn.

6.3.2.7. *Combustion characteristics*

A series of experiments were conducted to investigate the effect of the HTC operating conditions on the combustion behavior of hydrochars. The characteristic combustion parameters, including Ti, Tm, Tb, (dw/dt) max, and reactivity, are summarized in **Table 6-9**. Above Ti, high decomposition rates occur, which is generally associated with the decomposition of hemicellulose and cellulose. An acceleration of the devolatilization rate $(dw/dt)_{max}$ is noticed for hydrochars produced at 197°C and 60 min ((dw/dt)max ~16.53). On the other hand, hydrochars produced at higher temperatures (232°C and 250°C) with holding times of 30 and 60 minutes presented the lowest mass loss rate and Rindex values compared to the other samples. This thermal behavior could be explained by the higher carbon content in these hydrochars (see **Table 2**) and may be linked to a more ordered carbonaceous structure, as described by Guizani et al. (2017). In addition, the corresponding reactivity increases for hydrochars obtained at 197°C and 60min, which may be due to the abundance of volatile matter and their slow process of combustion in the hydrochar. As assessed essentially by (dw/dt)max, the higher the combustion rate, the more reactive the hydrochar (Pala et al., 2014). By comparing the (dw/dt)max and reactivity values of ASB and hydrochars; the hydrochars

generally showed better fuel characteristics, except for the conditions identified above, e.g., higher temperatures and holding times corresponding to the area the highest FC (**Figure 6-17).**

Table 6-9: Characteristic temperatures and parameters on the combustion of raw ASB and hydrochars, at different HTC X_1 and X_2

Sample	X_1 (°C)	X_2 (min)	Temperature (°C)			$(dw/dt)_{max}$ (%/ min)	R_{index} (%./min·°C)
			T_i	T_m	T_b		
ASB			270	326	479	10.06	3.09
1	215 (0)	30 (0)	301	329	527	15.70	4.78
2	180 (–1)	30 (0)	285	329	474	12.94	3.93
3	250 (+1)	30 (0)	279	323	638	5.21	1.61
4	197 (–0.5)	0 (–0.866)	296	323	490	14.49	4.49
5	215 (0)	30 (0)	300	328	530	12.13	3.68
6	232 (+0.5)	60 (+0.866)	283	315	591	5.04	1.60
7	197 (–0.5)	60 (+0.866)	304	329	495	16.53	5.03
8	232 (+0.5)	0 (–0.866)	301	331	500	14.62	4.42
9	215 (0)	30 (0)	302	328	517	14.68	4.48

T_i: ignition temperature; T_m: temperature at max. weight loss rate; T_b: burn out temperature; $(dw/dt)_{max}$: is the maximum observed reaction rate and R_{index}: is the reactivity index.

6.3.2.7.1. *Ignition temperature model*

The The ignition temperature (Ti) is the temperature that permits the promotion of a flame if the material is exposed to a source of inflammation. The Ti values obtained are superior to ASB, indicating an increased ignition difficulty with the carbonization process. According to He et al. (2013) this can be explained by the lower volatile matter in hydrochars compared to ASB. The range of temperature ignition is between 279 °C and 304 °C for the experiment results. The following equation represents the model that gives the best R^2_{adj} (94.8%):

$$T_i = 300.87 - 4.64X_1 - 2.89X_2 - 18.93\ X_1^2 - 15.01\ X_1X_2 \quad (6\text{-}72)$$

The 2D contour plots (**Figure 6-21**), shows the Ti values between 260°C and 305°C. Thus, it can be observed a large domain where the maximal value is possible and the lower values of Ti are for coordinates (+1; +0.866) or (-1; -0.866).

It is interesting to compare with the VM behavior because the ignition starts when there is enough flammable vapor to allow combustion. Therefore, we can observe where the VM content in **Figure 6-19** is maximal, the Ti is minimal (He et al., 2013). However, the minimal Ti is also observed for high temperature and high treatment where VM content is minimal. That would mean that the onset devolatilization temperatures are equivalent.

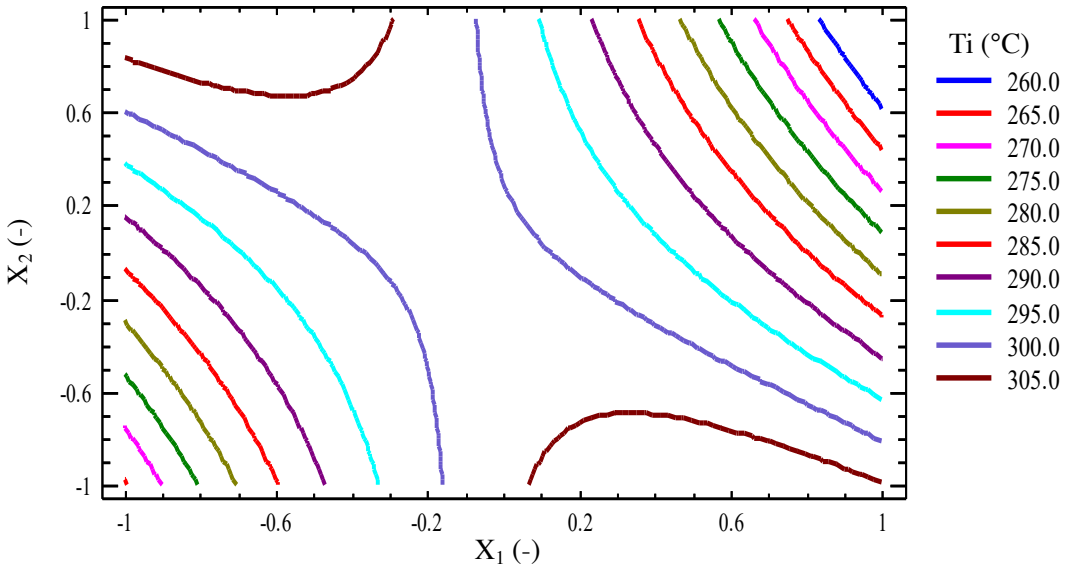

Figure 6-21: 2D contour plots showing the effects of temperature (X_1) and holding time (X_2) on ignition temperature (Ti)

To bring more arguments on this temperature and validate these results, we have determined the autoignition temperature by temperature-controlled oven under oxygen atmosphere. The results of five experiments selected in the studied domain are reported in **Table 6-10**. The results of $T_{autoignition}$ determined (**Table 6-10**) how that the minimum value is for sample ASB-232-60 corresponding to the minimal Ti value; also, it is pretty interesting to see similar values for raw material and ASB-197-0; this can be explained by the fact that the process has not modified ASB-197-0 enough to show a difference in $T_{autoignition}$. Their visual aspect was similar. The ASB-197-0 sample kept the fibrous aspect. Besides, for ASB-232-0 and ASB-197-60 and ASB-197-0, $T_{autoignition}$ values are more significant than Ti; volatile compounds can explain this with a superior $T_{autoignition}$ than Ti. Above Ti, high decomposition rates take place, mainly related to the decomposition of hemicellulose and cellulose.

Table 6-10: Autoignition temperatures of ASB and hydrochars, at different HTC $X_1$and X_2

Sample	$T_{autoignition}$ (°C)	T_i (°C)	$T_{autoignition} - T_i$ (°C)
ASB-232-60 (+0.5;+0.866)	241±4	283	-42
ASB-232-0 (+0.5;-0.866)	325±4	301	+24
ASB-215-30 (0;0)	277±4	301	-24
ASB-197-60 (-0.5 ; +0.866)	330±4	304	+26
ASB-197-0 (-0.5;-0.866)	310±4	296	+14
Raw material	310±4		

6.3.2.7.2. *Temperature at the maximum weight loss rate*

Tm corresponds to the fastest mass loss when the temperature acts. The Tm profile of 2D contour plots **(Figure 6-22)** has a similar shape to the Ti one. To build the 2D contour plots, the model retained has the following equation:

$$Tm = 328.33 - 3.0X_1 - 2.874X_2 - 2.33\ X_1^2 - 4.33\ X_2^2 - 12.7\ X_1X_2 \quad (6\text{-}73)$$

The model gives an R^2_{adj} value of 99.11%. The minimum value equal to 306 °C is for (+1; +0.866) experiment and also corresponds to the experiment that has the maximal FC content. The maximal values are obtained for the (-1; +0.866) and (-1; -0.866) experiments corresponding to the domain with no maximum VM content or FC content.

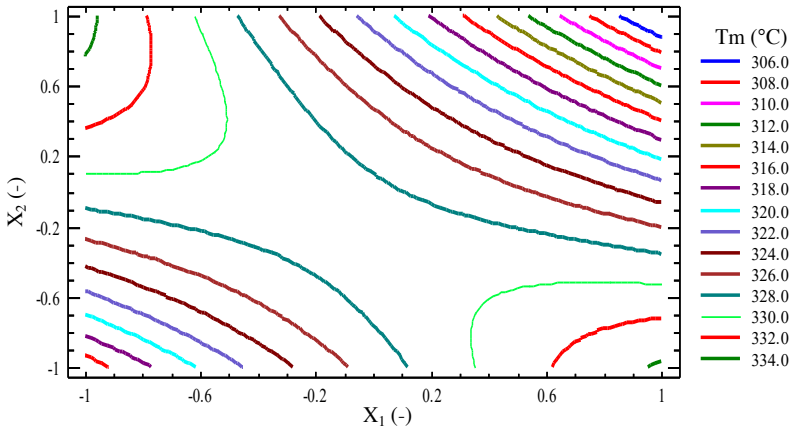

Figure 6-22: 2D contour plots showing the effects of temperature (X_1) and holding time (X_2) on the temperature at the point of the maximum weight loss rate (Tm)

6.3.2.7.3. *Burnout temperature*

The 2D contour plots are shown in **Figure 6-23**. It is obtained with the following equation with R^2_{adj} = 92.2%.

$$Tb = 524.68 + 72.33X_1 + 27.71X_2 + 31.33\ X_1^2 - 18.00\ X_2^2 + 12.7\ X_1X_2 \quad (6\text{-}74)$$

The maximal value equal to 680°C is for (+1; +0.866) experiment. The evolution of Tb follows the FC content evolution. More the content of FC is important more the Tb is also essential due to an increase of thermal stability of hydrochar.

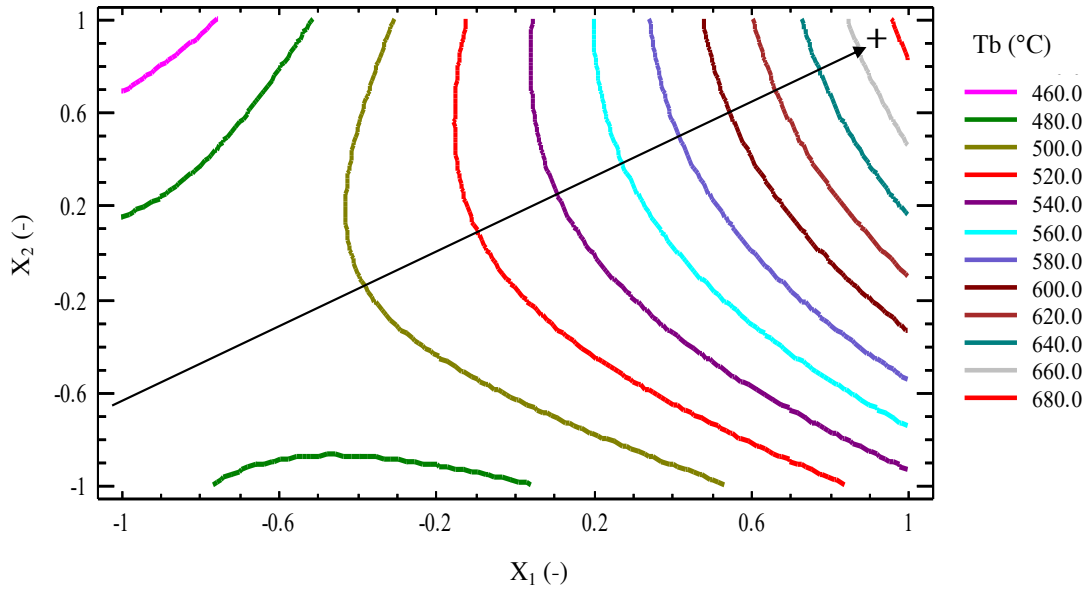

Figure 6-23: 2D contour plots showing the effects of temperature (X_1) and holding time (X_2) on the burnout temperature (Tb)

6.3.3. Computational Fluid Dynamics (CFD) modelling results

In comparison with experimental data, CFD model results can predict qualitative information and, most of the time, accurate quantitative information (Wang and Yan, 2008). In this regard, many researchers have used CFD to simulate and analyze thermochemical conversion equipment performance, such as fluidized beds, fixed beds, firing boilers, combustion furnaces, so on. Papadikis et al. (2009) use CFD modeling in fluid-particle interaction within a fluidized bed reactor in fast pyrolysis; the model predicted the residence time of the vapors and biomass particle inside the reactor, as well as the properties of the pyrolytic particle. On the other hand, Xue et al. (2011) proposed a model able to predict the critical features of fast pyrolysis of any biomass with known compositions of cellulose, hemicellulose, and lignin in a fluidized bed reactor. Similar studies were reported by Thankachan et al. (2014) on biomass gasification

using a fluidized bed reactor. Kumar and Paul (2019) use CFD to investigate the syngas production of various biomass feedstocks. Hooshdaran et al. (2017) studied the heat transfer in a draft tube conical spouted bed reactor under pyrolysis conditions. The CFD prediction results were in close quantitative agreement with measurements in terms of heat-transfer coefficients. Also, CFD has been used in gas-solid fluidized bed hydrodynamics studies (Ahuja and Patwardhan, 2008; Hosseini et al., 2010); their models have been able to predict the hydrodynamic behavior of gas-solid fluidized beds. Xie et al. (2017) showed the importance of CFD to understand the effects of agitation on the velocity, temperature, and concentration distributions of a stirred tank reactor and the importance of the stirring rate in copolymerization. CFD has been used in many thermochemical conversion studies of biomass; however, there are minimal studies on the simulation of an HTC reactor and especially a stirred reactor. Most of the current simulation is based on the 0D kinetic model (without the influence of spatial variables; the system behaves similarly at any point of the reactor) (Baratieri et al., 2015; Gallifuoco, 2019; Lucian et al., 2019).

All these studies assume that the reaction temperature is constant during the whole experiment, but a constant temperature during HTC is difficult to achieve in batch autoclave reactors where there is a heat-up time, a constant temperature period, and finally, a cooling time. Therefore, the validity of these results depends only on their experimental conditions. Some investigators have incorporated the effects of heat-up time as in the case of Álvarez-Murillo et al. (2016). In this case, the authors applied the computational model by using COMSOL Multiphysics to examine the kinetics of cellulose HTC over different reaction times and temperatures. They developed a first order-reaction model based on the Arrhenius equation, which also shows the importance of the heating time. The authors reported activation energy of 90.1 kJ/mol similar value reported by Reza et al. (2013) and Keiller et al. (2019) the latter not considering heat-up time. The CFD simulation carried out by Álvarez-Murillo et al. (2016) considers batching HTC reactor that received heat from hot air and modeled radiation and convection and under the assumption that the reactor contains only water, and does not consider the properties of biomass. However, the thermal properties of biomasses may differ from the thermal properties of water in the reaction medium. The biomass properties, such as density, porosity, permeability, and chemical composition, change for unexplored chemical reactions (Pecha et al., 2019). Also, Funke and Ziegler (2011)report that the global biomass HTC reaction is exothermic; therefore, the biomass-to-water ratio influences the heat transfer. According to Funke and Ziegler, the HTC reaction of biomass can release heat to -5.8 MJ/kg of fed biomass.

For this reason, in this work, we have considered temperature as a function of time (t), spatial variables (x, y, z), and biomass-to-water ratio (R), given the difference between the thermal properties of biomass and water. Also, it is a stirred reactor of constant volume and working in an open-loop controller system. To determine T (t, R, x, y, z) inside the reactor, the model resolves the mass, heat, momentum transfer, and reaction kinetics simultaneously. Besides, most of the HTC reactor studies in the literature are non-agitated reactors and operated with the furnace in a closed-loop system (Álvarez-Murillo et al., 2015b; Álvarez-Murillo et al., 2016; Missaoui et al., 2017; Sabio et al., 2016). In non-agitated reactors, the biomass/water mixture is not uniform inside the reactor due to the different physical properties of biomass and water (e.g., density). Consequently, a gradient of concentration, temperature, and other properties may exist inside the reactor. These affect the mechanisms of reaction of HTC, also makes difficult their hydrodynamics analyses and thermal studies. The inclusion of a stirrer reactor can help avoid these problems, and the use of CFD simulation can contribute to the design, optimization, and scaling up to the industrial level. In addition, CFD can assist in the analysis of hydrodynamic and thermal effects inside the reactor during the HTC process.

The CFD simulation was divided into two main parts: the simulation of the hydrodynamic study and the simulation of the heat transfer and kinetics. For the simulation of the hydrodynamic study, only the interior of the reactor was considered (mixture of water with biomass domain and the rotation domain were considered, it was unnecessary to consider the walls of the reactor. For the heat transfer simulation, the entire reactor was considered.

6.3.3.1. *Mesh independence study*

Mesh independence study is one of the most crucial steps in any CFD problem. The accuracy of the CFD solution is strongly dependent on the mesh quality. When the accuracy does not change significantly with the increasing number of mesh elements, the calculation can be considered mesh independent (Gyurik et al., 2019). It is important to mention that the agreement between simulation results and experimental data does not necessarily mean that the solution is mesh-independent. Achieving a mesh-independent solution is an essential step in analyzing the results obtained using CFD simulation. However, there is no specific method in the literature on achieving a mesh-independent solution (Almohammadi et al., 2013). In this case, the average velocity of the dispersed phase was used in the hydrodynamic study and the average temperature inside the reactor for the mesh independence study. The mesh domain for

the hydrodynamic study is presented in **Figure 6-24**. Different meshing configurations were applied, explicitly using user-defined meshing. The element numbers were varied from 34k to 2 240k elements to study the influence of element numbers on the average velocity inside the reactor. The results of these meshing studies in the hydrodynamic domain are shown in **Figure 6-26**. As shown in **Figure 6-26a**, from 550k elements, the variation of the average velocity of the dispersed phase is negligible. This simulation takes a minimum of 500 k elements to consider the results are mesh-independent. The independent mesh study was conducted using an agitation speed equal to 550rpm and fraction volume φ_b=0.1375.

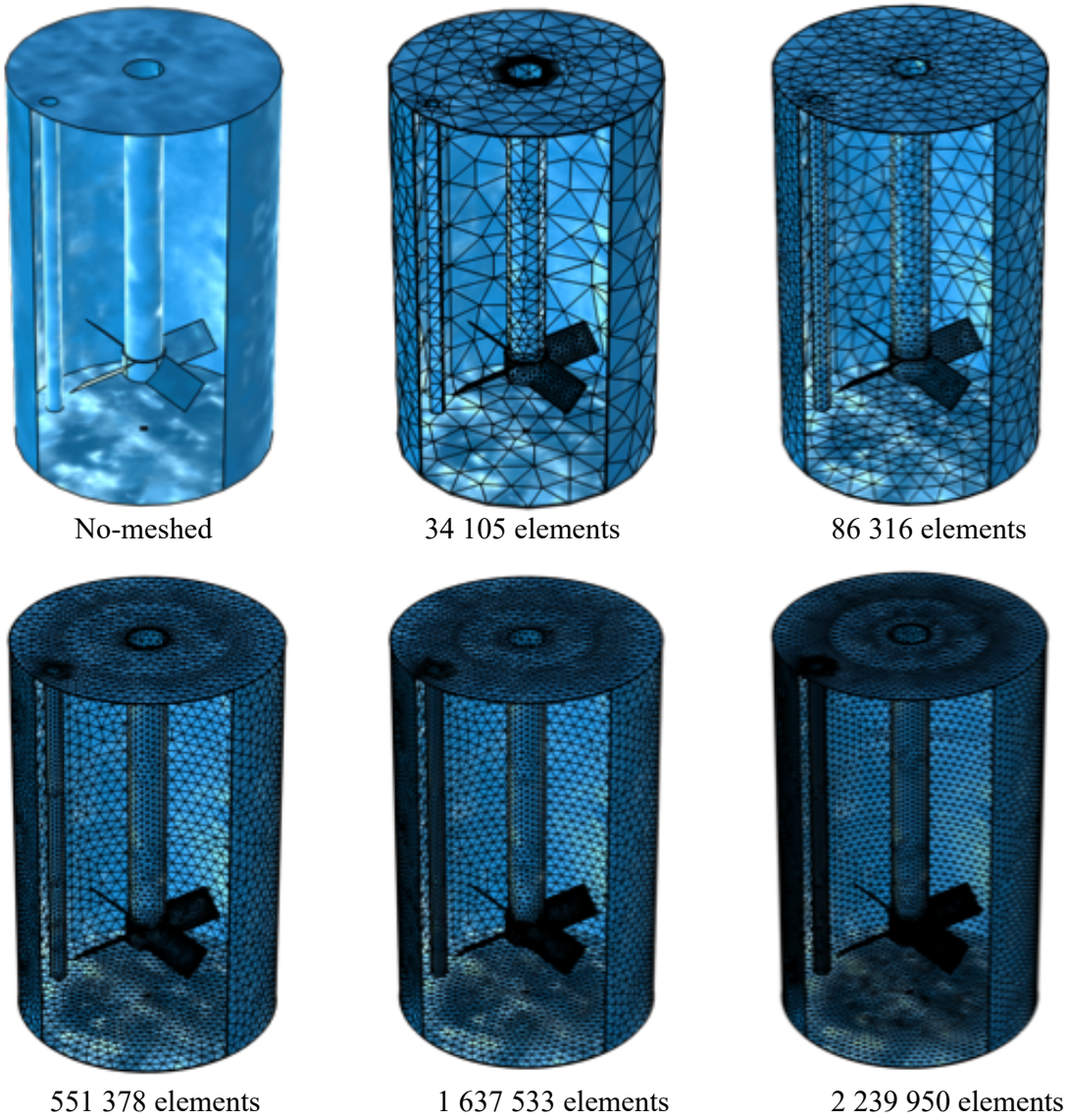

Figure 6-24: Meshed hydrodynamic domain for mesh independence study

The Mixture Model (Turbulent or Laminar) interface supports both types of study steps (stationary and time-dependent). For time-dependent 3D simulations, it is critical to have an accurate initial value that corresponds to the physical situation. Therefore, to simplify the simulation, it computed the velocity field using the frozen rotor assumption, a particular case of a steady-state study, using the solution as the initial values for the time-dependent study.

For the heat transfer study, the same procedure as above was used. The element numbers were varied from 17k to 1093k elements to study the influence of element numbers on the average temperature in the mixture domain. The mesh domain for the hydrodynamic study is presented in **Figure 6-25.**

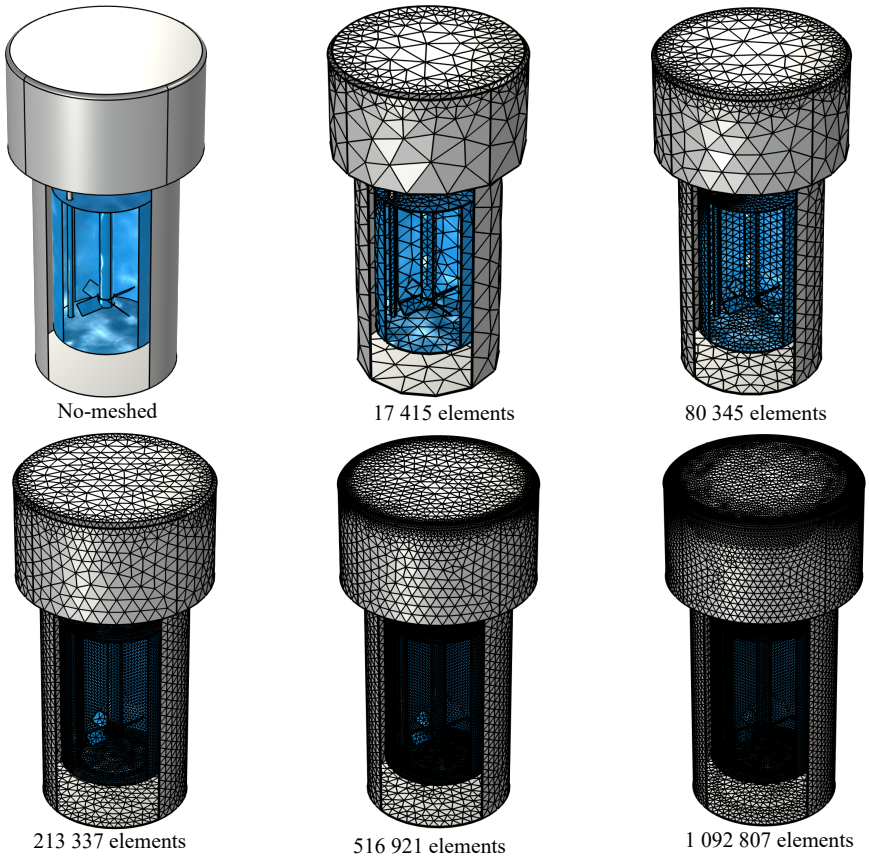

Figure 6-25: Meshed hydrodynamic domain for mesh independence study

As shown in **Figure 6-26b**, in this simulation, at least 200k elements are needed to consider that the mesh is independent of the results. In addition, a user-controlled mesh was used, where the fluid domain a finer element size 0.5 to 3 mm; solid domain (reactor walls) fine element size between 0.8 to 4 mm was used. The finer mesh was used at the interface between fluid-solid and all boundaries, and mesh refinement the impeller zones.

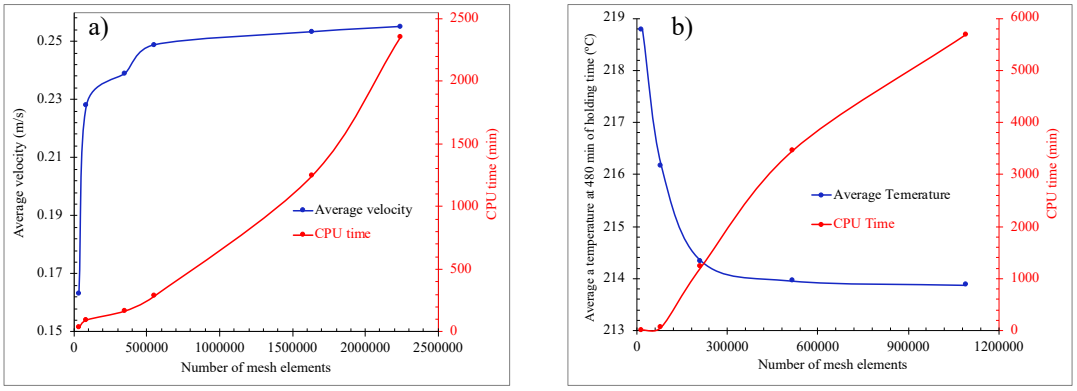

Figure 6-26: Effect of number of mesh elements on: a) average velocity of the dispersed phase, b) average temperature at 480 min of holding time and CPU time

6.3.3.2. *Hydrodynamics*

6.3.3.2.1. *The effect of stirring speed.*

The primary objective in mixing is to achieve a homogenous mixture; generally, this means attaining a nearly uniform distribution of the ingredients, in this case, the uniform distribution of AS particles inside the reactor. To find the ideal speed for the system to be homogeneous. The criterion we set for considering the particles as uniformly distributed was based on the Reynolds number (**Table 6-2)**. If the regime is turbulent, it was considered that the particles are distributed uniformly inside the reactor. **Figure 6-27** shows the velocities contours for different impeller speeds in the same initial volume fraction (φb=0.1375). The impeller speed varies between 100 and 700 rpm. In the mixture between solid and fluid particles, two main forces govern the flow velocities in the agitator, inertial forces resulting from the rotation of the impeller and dispersed-phase buoyancy forces, or hydrostatic force result from density differences between the phases. For N=100 rpm, in **Figure 6-27a** and **Figure 6-27f**, no agitation effect is observed; the flow velocity is practically null inside the entire reactor. The average velocity in the dispersed phase is 0.03m/s. The same tendency is observed for N=250 rpm, and the flow velocity variation is only observed in the impeller zone where the maximum velocity is less than 0.15m/s, and the average velocity is 0.09m/s (**Figure 6-27b** and **Figure 6-27g)**. For N=400 rpm, a high velocity starts to be observed at the bottom of the reactor (**Figure 6-27c** and **Figure 6-27h)**. However, on the top of the reactor, the flow velocity is controlled by gravity or hydrostatic force, and the average velocity is 0.16m/s. **Figure 6-27d** and **Figure 6-27i,** that a uniform distribution of particles is observed inside the reactor.

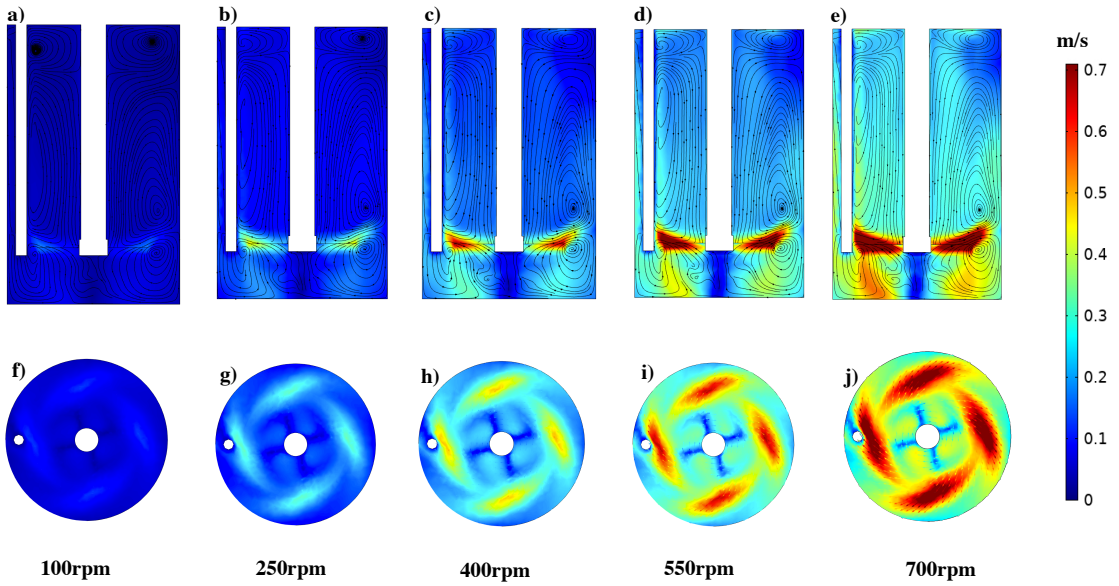

Figure 6-27: The effect of the stirring rate on the volume fraction φb=0.1375: **a-d**) r-z plane defined by the angular coordinate θ = 0° and **e-h**) r-θ plane defined at the top of the impeller for z=21mm

The highest velocities vectors are in an upward direction, except in regions just below the impeller shaft. Therefore, it can be concluded that the predominant forces for the movement of particles inside the reactor are inertial forces. The hydrostatic force has no significant effect on the movements of the particles for N=550 rpm, corresponding to a Reynolds number value superior to 10^4, meaning a turbulent regime. From this speed, the regime is entirely turbulent, as shown in **Table 6-2**. The average velocity in the dispersed phase is 0.24 m/s. This velocity can be considered the ideal velocity to achieve a uniform distribution of the particles inside the reactor. The same phenomenon can be seen in **Figure 6-27e** and **Figure 6-27j** for N=700 rpm.

The higher rotation speed reduces the volume fraction dispersion time from the bottom to a uniform distribution inside the reactor and increases the reaction mechanisms in the HTC process. However, the increased rotation speed is associated with higher energy consumption. Therefore, a compromise is sought between the energy consumption of the agitator and the homogenization of the reactor. For a relatively high speed (550 rpm), the reactor can be considered perfectly homogeneous. The experimental studies used a rotation speed of N=550 rpm, creating a homogeneous system inside the reactor and a turbulent regime ($N_{Re}>10^4$).

6.3.3.2.2. *Validation of the flow velocities*

The results of any simulation are useful when they are validated with experimental data. To ensure that the CFD models are reliable to describe hydrodynamics inside the HTC reactor, a

simulation was performed using only water. The axial and tangential velocities were validated with experimental curves from Özcan-Taskin and Wei (2003). The authors determined the fluid velocities using Laser Doppler Anemometry (LDA) measurements with a pitched-blade turbine agitator. In this CFD simulation, a k-ε turbulent model was used, the same model used by Özcan-Taskin and Wei (2003) for their simulation. In a cylindrical reactor coordinate system, the velocity at any point can be decomposed into its radial, axial and tangential values. The axial and tangential velocities results were compared with experimental data. The velocity results were obtained in a stationary state (frozen rotor). The axial coordinates r-θ is located just on the top of the impeller for z=21 mm and tangential plane r-z for θ=0° rotation angle. The results obtained are presented in **Figure 6-28**.

The CFD results show the same tendency of axial and tangential velocity distribution with the experimental data, which means that the simulations could capture the general characteristics of the flow field inside the reactor during the HTC process. Once the model was validated with experimental data, the simulations were carried out with a different fraction volume according to the experimental data used in this work.

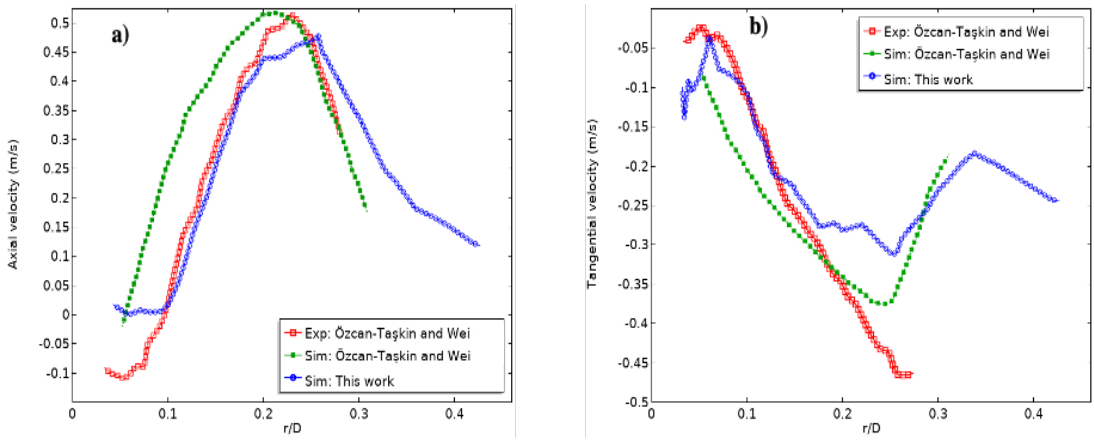

Figure 6-28: Comparisons of a) Axial velocity for z=21mm and b) tangential velocity for θ=0° in this simulation with previous works

6.3.3.2.3. *Comparison of flow velocity for pure water and with biomass -to-water mixture.*

In this simulation, the flow velocity for pure water and water with volume fraction equal to φb=0.1375 was compared at a rotation speed N=550 rpm. **Figure 6-29**, the flow patterns of primary velocity vectors on the impeller top for z=21 mm are shown in **Figure 6-29a-b** in the r-θ plane and the secondary flow in the r-z plane for θ=0° on the **Figure 6-29c-d.**

There is no difference between the velocity vectors in the r-θ plane at z=21 mm. In the secondary flow, the r-z plane recirculation zones are observed; up and down the impeller, the usual double-loop flow structure corresponding to radial impellers can be observed in both r-z planes (**Figure 6-29a-b).** However, in the r-z plane (**Figure 6-29b**), an additional recirculation zone is observed at the top of the reactor. In this area, the flow velocity is higher and varies between 0.25 and 0.3 m/s; this may be due to dispersed-phase buoyancy forces of some particles. On the other hand, in the reactor with water (**Figure 6-29a**), this recirculation zone at the top of the reactor is not observed, the velocity is low, and it varies between 0.1 and 0.15 m/s.

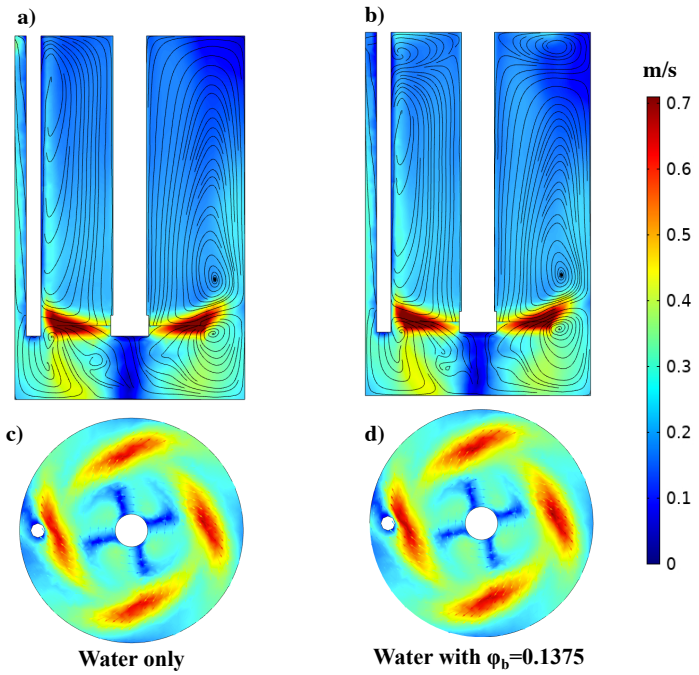

Figure 6-29: Distribution of turbulent flow velocity induced in a, b) r–z plane for θ = 0° and c, d) r–θ plane on the impeller top for z=21mm, and N=550 rpm

The flow velocity is strongly dominated by the rotational component near the impeller, where the flow velocity varies between 0.6 and 0.75 m/s. Also, it can be seen that the thermocouple probe also disturbs the flow velocity in the tangential direction (**Figure 6-29c-d**). Below the impeller, there are stagnant areas inside the reactor, where the flow velocity varies between 0 and 0.05 m/s. This stagnation may be due to the perpendicular flow of the impeller, which could maintain the low velocity in this area.

6.3.3.2.4. *Flow and solid distributions*

The homogeneous distribution of the solid particles inside the reactor is the main objective of agitation. This subsection shows a simplified CFD model implemented to understand the system. It is also necessary to have a more realistic model that accounts for solid and their distribution inside the reactor; by observing region stagnation, it may be possible to improve the reactor design. **Figure 6-30** shows a cross-section of the contours of the volume fraction φb=0.1375 at 550 rpm in the reactor at 0s, 0.1s, 1s, and 5s. Initially, the solids are found at the bottom of the reactor, owing to the density of the particles of AS and gravity.

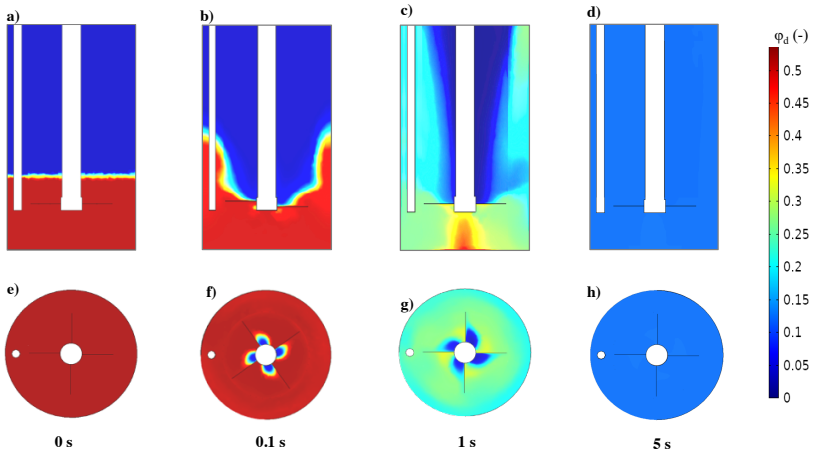

Figure 6-30: Two-phase CFD simulation of volume fraction φ_b=0.1375 on water: the rheological distribution: **a-d**) induced in the r-z plane defined by the angular coordinate θ = 0° and **e-h**) in the r-θ plane defined at the top of the impeller for z=21mm, and N=550 rpm

The red color indicates the dispersed phase or the biomass concentration, while the blue color shows the continuous phase or absence of the solid particles. The AS particles are not entirely spherical; therefore, the maximum volume fraction was determined experimentally and corresponded to φb=0.52. For reference, the maximum packing volume fraction would be 0.63 if the particles were spherical (Laskowski, 2013).

At 0s, the major concentration of biomass is at the bottom and represents a φ_b=0.52, and at the top, the volume fraction φ_b=0, as shown in **Figure 6-30a, e.** Although particles are not entirely spherical, it was observed that they packed up effortlessly at the bottom of the reactor owing to their higher density than water. At 0.1s, the impeller moves most of the solids into the reactor wall, as shown in **Figure 6-30b,f.** This is due to the agitation force, which pushes the particles away from the impeller. However, regions of higher volume fractions of the dispersed phase are also observed at the bottom of the reactor and the sidewalls near the impeller. As shown in

Figure 6-30c,g, at 1s of agitation time, the impeller moves most of the particles to the top and the reactor walls. Therefore, the volume fraction is between 0.2 and 0.3. However, near the impeller shaft, the center of the reactor is the least agitated zone, so there can be found the most concentrated part of the volume fraction. Below the impeller, there are stagnant areas inside the reactor, as explained in **section 6.3.3.2.3. .** At 5s, as shown in **Figure 6-30d, h,** the reactor is wholly mixed, and the volume fraction in the dispersed phase is 0.1375 everywhere inside the reactor. Thus, little time was needed to obtain a homogeneous mixture inside the reactor with a 550 rpm speed. Likewise, the particle tracing module was used to represent the biomass particles inside the reactor and compare them with the experimental visual stirring. To visualize the movement of the biomass particles inside the reactor, a transparent vessel with the same inner diameter as the reactor was used. Stirring was done using different velocity speeds. However, results are only presented for stirring speed equal to 550 rpm. The results of this comparison are presented in **Figure 6-31**.

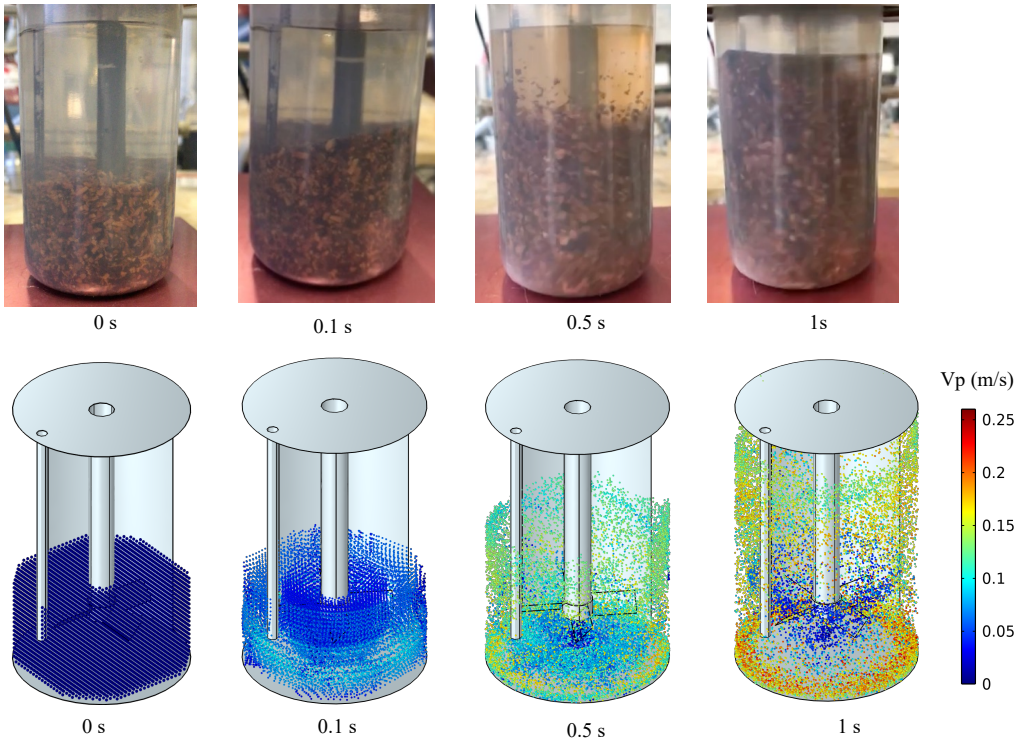

Figure 6-31: Biomass particles distributions inside the reactor: Experimental comparison and CFD simulation using particle tracing, for biomass-water-ratio ¼ and N=550 rpm

As can be seen in **Figure 6-31** the experimental data are visually very similar to the simulation data. In addition, the simulation clearly shows the stagnation zone just below the impeller shaft, as explained above.

6.3.3.3. *Heat transfer study results*

6.3.3.3.1. *Temperature profiles inside the HTC reactor*

As explained in in the previous section, the volume fraction in the dispersed phase is completely homogeneous inside the reactor after 5 seconds of stirring. Thus, agitation was not considered in this part of the simulation to reduce the computation time, and we can consider that the particles are entirely distributed within the reactor. The experimental temperature profile data was also used to validate the CFD simulation.

To validate the simulation with experimental data, the insulator heat transfer coefficient of **Eq. (6-59)** has to be determined. The average heat-transfer coefficient (h) in the insulation to the environment was estimated using experimental data values recorded during the water heating (**Figure 6-32**) under HTC conditions. Different values of heat-transfer coefficient were used in **Eq. (6-59)** in order to match the simulated curve with the experimental one, based on a constant heat flow (120 W) over the external surface of the reactor. The average heat transfer coefficient that best fits the experimental data is 11.66 W/m^2·K.

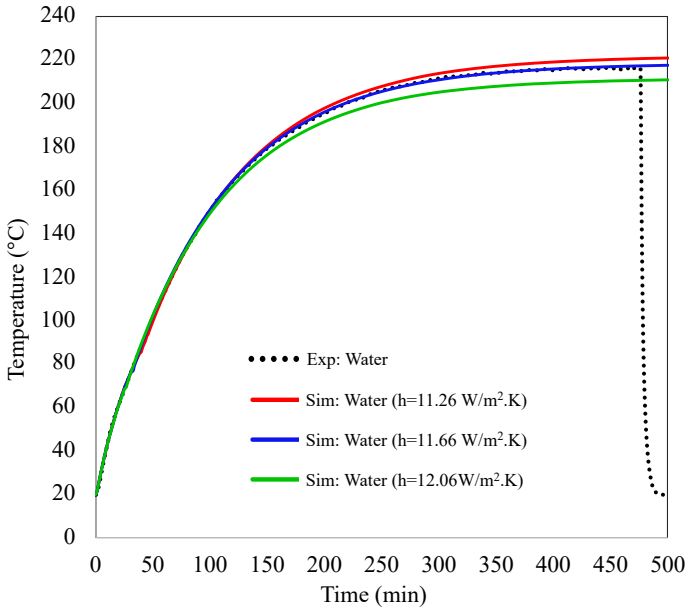

Figure 6-32: Determination of the heat-transfer coefficient between the insulator and the environment

This value was used to set the heat loss during the HTC process of different biomass-to-water ratios in the CFD simulation. In addition, the thermal properties of AS determined in Chapiter 2 were used and the thermal properties of water. These data allowed the simulation of the

temperature profile evolution according to the volume fraction used. The results in **Figure 6-33** show that there is practically no difference between the experimental temperature profile of water and the modeling temperature profiles with different volume fractions of biomass. The maximum temperature difference observed is less than 3°C; this difference can be considered negligible. However, experimentally, there is a significant difference between the water temperature profile with different volume fractions of biomass, as shown in **Figure 6-33.** The most notable difference is 21.42 °C, and it was observed for the higher volume fraction of biomass (φ_b=0.1375), this difference is decreasing to 6.87 °C for φ_b=0.06. These variations are essential, considering that temperature is the main factor that controls the HTC process. Also, this variation begins to be observed from 150 °C, as shown in **Figure 6-33.**

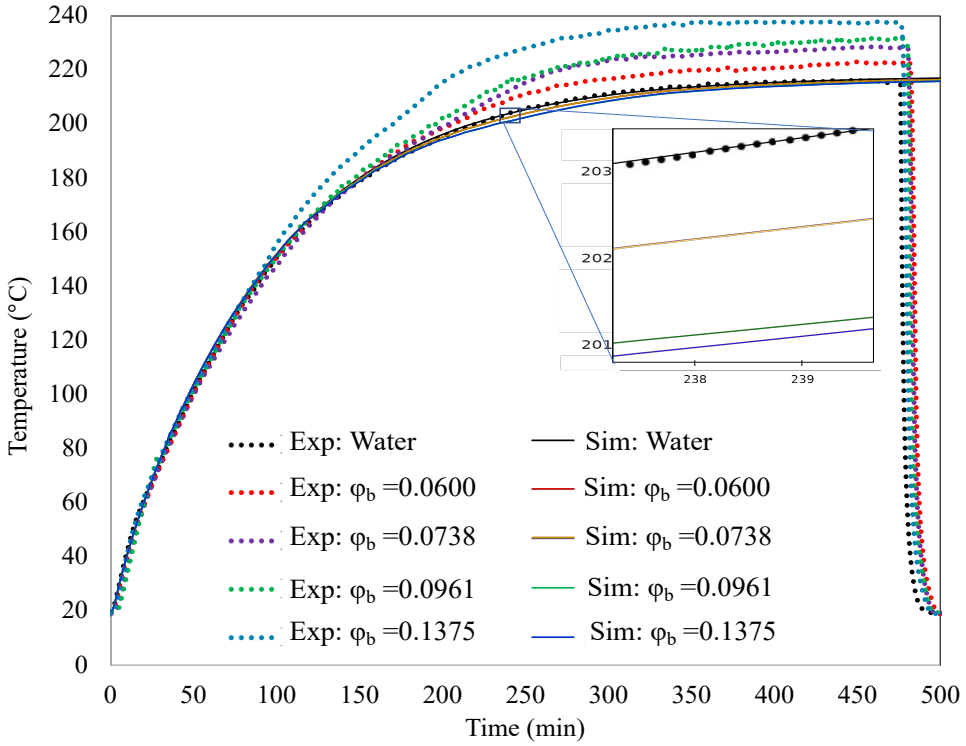

Figure 6-33: Comparison of simulated and experimental data using the thermal properties of biomass

There are indeed differences between the thermal properties of biomass and saturated water in the HTC condition; however, this difference is not significant to observe a variation in temperature up to 21.42 ºC. Using the biomass thermal properties for the different volume fractions with CFD simulation, the difference between profiles temperature calculated was less than 3 ºC. Furthermore, if the temperature variation is the result of the difference between the physical properties of water and biomass, this variation would be noticed from the beginning

of the heating process, and not from 150 ºC, where the main components of biomass start to decompose (Dupont et al., 2014; Gupta et al., 2003; Liu et al., 2013b). Only chemical reactions can cause temperature variation from 150 ºC to the equilibrium temperature. Therefore, it can be stated that the overall reaction of avocado stone HTC is exothermic, and also, the biomass to water ratio influences the heat transfer, therefore the reaction kinetics.

6.3.3.3.2. *Temperature profiles inside the HTC reactor using kinetic parameter and model validation with experimental data*

Most of the kinetic models reported in the literature for the biomass HTC process are dimensionless models, i.e., no influence of spatial variables; the system behaves the same way at any point in the reactor, constant temperature, and no influence of biomass concentration inside the reactor. However, Álvarez-Murillo et al. (2016) proposed a model that incorporates the heat-up time, but his model is independent of the biomass concentration.

Initially, to determine the temperature profiles inside the reactor, the model proposed by Álvarez-Murillo et al. (2016) was used. However, this model could not reproduce the temperature profiles inside the reactor during the HTC of AS because the model is biomass concentration-independent. Furthermore, the model proposed by Álvarez-Murillo et al. (2016) is incomplete because the overall reaction of the HTC is exothermic. In this context, we decided to use the reaction heat (-7.25 MJ/kg, determined in **Chapter 3**), which depends on the biomass concentration. **Figure 6-34a-d** shows the results of the models proposed in this work. The results of the CFD simulation temperature profiles were validated with experimental data in different volume fractions. The initial condition and kinetic parameters used for this simulation are presented in **Table 6-11**.

The CFD simulation reproduces reasonably well, the temperature profiles for volume fraction φ_b=0.06; φ_b=0.0738 and φ_b=0.0961 (**Figure 6-34a-c**). However, for φ_b =0.1375 (**Figure 6-34d**), after 360 minutes of heating, the temperature profile reaches a maximum and starts to decrease. It seems that the exothermic reactions are over; the temperature profile tries to return to the equilibrium temperature, which is 215°C, due to the loss of energy. The temporal evolution of the temperature inside the reactor, different product relative mass yield (total solid or hydrochar, liquid, and gas) are shown in **Figure 6-34a-d.** Three zones can be noted in these CFD simulation figures for the relative mass yield of volume fraction of AS.

In the first zone, there is a horizontal period up to 150 °C, which could be called induction; in this zone, no decomposition of avocado stone is observed. This initial non-reactive period would be explained by the existence of the heating ramp inside the reactor. In this period, the temperature is not high enough to reach an energy level that allows energy activation. Therefore, the reaction starts at a temperature of ~150 °C. This observation is in line with the experimental data, where from 150 °C, the temperature profile variation between the water and the different biomass volume fractions is observed.

Table 6-11: The values used for the kinetic study

Biomass-to water ratio	Initial condition			Product	
	Biomass volume in reactor (mL)	Water volume in reactor (mL)	volume fraction φ_b (-)	F_{HC}	F_{Liq}
AS-1-10	11.99	188.01	0.0600	0.42	0.55
AS-1-8	14.77	185.23	0.0738	0.48	0.47
AS-1-6	19.22	180.78	0.0961	0.50	0.44
AS-1-4	27.50	172.50	0.1375	0.52	0.42
Density of AS	1548 (kg/m^3)	The total volume of each experiment was 200mL			
Heat of reaction of AS	-7.25 (MJ/kg of feed)	Kinetic parameters			
Molar mass of AS	96.59 (kg/kmol)	E_a=90.1 kJ/mol[b]	n=2.2[b]	A_0=0.55 s^{-1}	

[a] Molar mass was determined from elemental analysis of AS

[b] The kinetic parameters taken in the Álvarez-Murillo et al. (2016) model

It is important to note that from 150 °C, the HTC reaction starts; this confirms the importance of considering the heat-up time and not only the temperature fixed period during the experiments for the kinetic models; the same phenomenon was also observed by Álvarez-Murillo et al. (2016). **Figure 6-34a** shows that the maximum amount of total solid or hydrochar inside the reactor is 45% in this simulation; a similar value was obtained experimentally 42%. However, the reaction does not seem to end. The same behavior can be observed in **Figure 6-34b.** In **Figure 6-34c-d**, although the temperature inside the reactor is high, the mass yield is higher than the lower biomass to water ratio (**Figure 6-34a-b**). Finally, it is observed that in **Figure 6-34a-c**, there is still a tiny quantity of the AS (~10 %) that has not yet reacted, this is due to the high value of the activation energy (90.1 kJ/mol), showing that these reactions are not over.

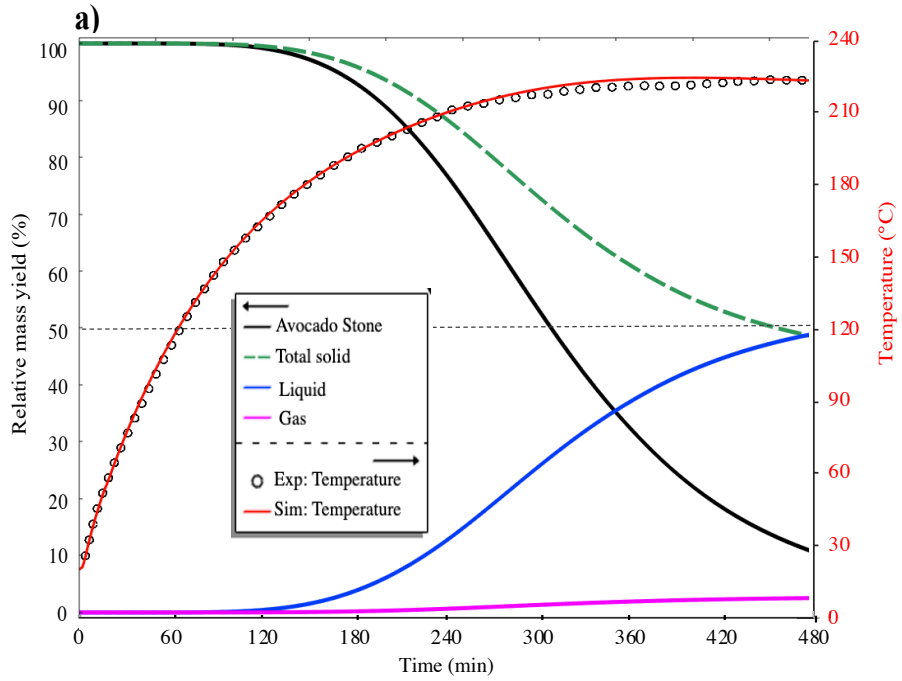

Figure 5-34a: Temperature profiles and relative mass yield on different HTC products, using the reaction heat of reaction for φb=0.06

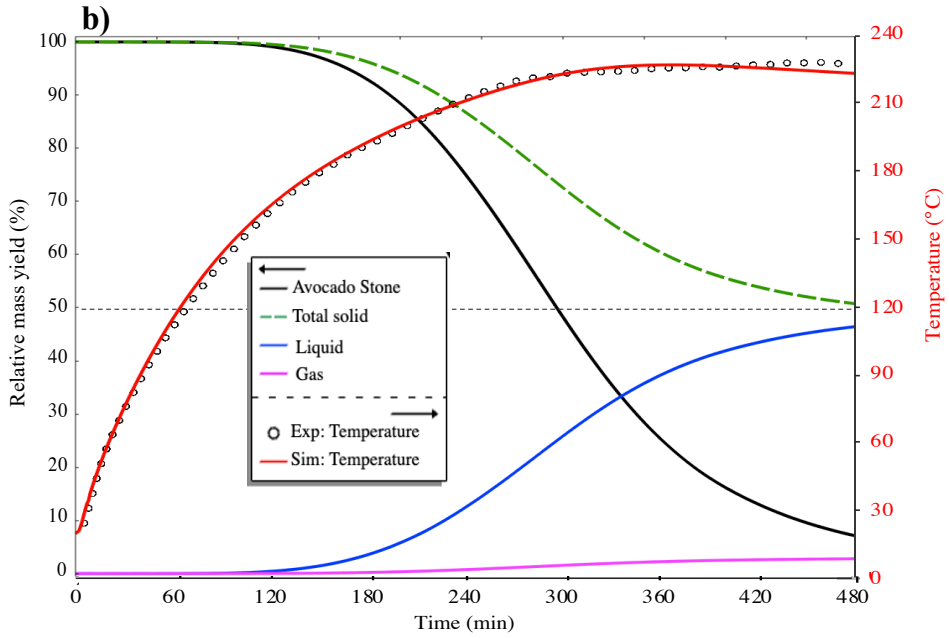

Figure 5-34b: Temperature profiles and relative mass yield on different HTC products, using the reaction heat of reaction for φb=0.0738

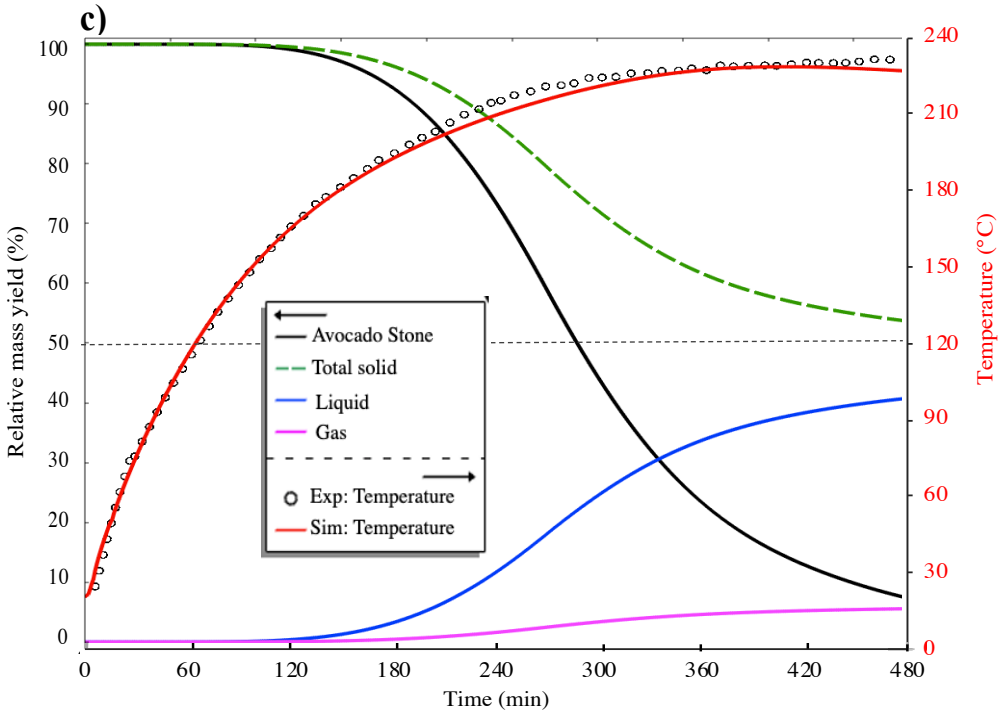

Figure 5-34c: Temperature profiles and relative mass yield on different HTC products, using the reaction heat of reaction for φb=0.0961

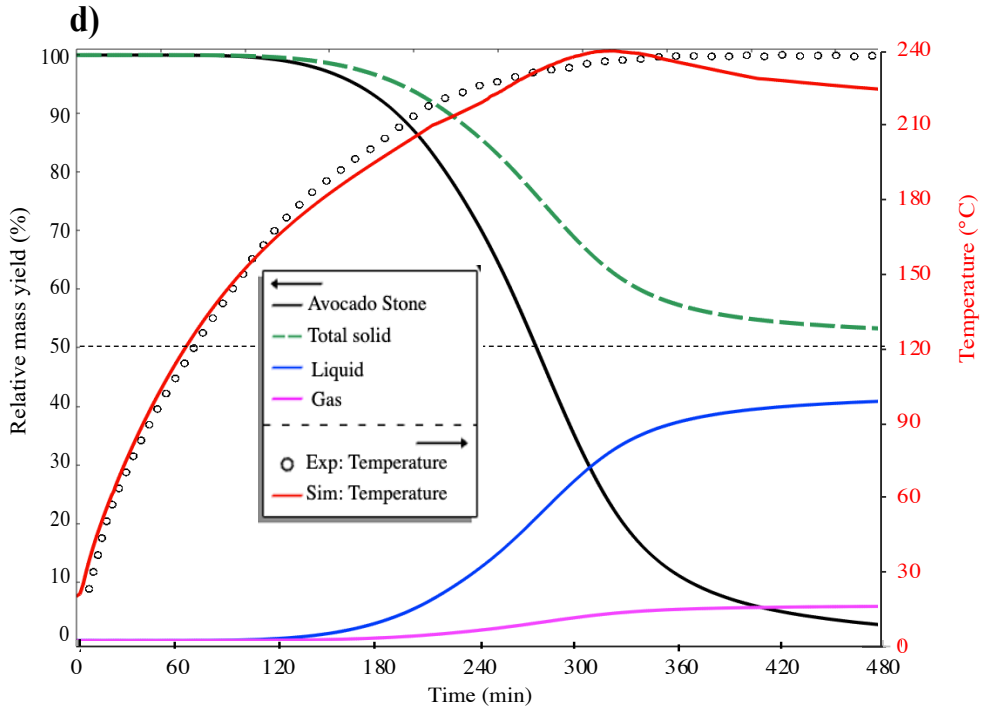

Figure 6-34d: Temperature profiles and relative mass yield on different HTC products, using the reaction heat of reaction for φ_b=0.1375

6.3.3.3.3. *Coupling of hydrodynamics, heat transfer and chemical reactions*

CFD simulations could be performed by coupling the different elements that were studied in this chapter. **Figure 6-35** shows an illustrative example of a simulation, where it can see the hydrodynamic effect (particle velocity inside the reactor), heat transfer, and concentration evolution (volume fraction). This figure is important because it allows validating the experimental data and, therefore, to propose extrapolations of the HTC process.

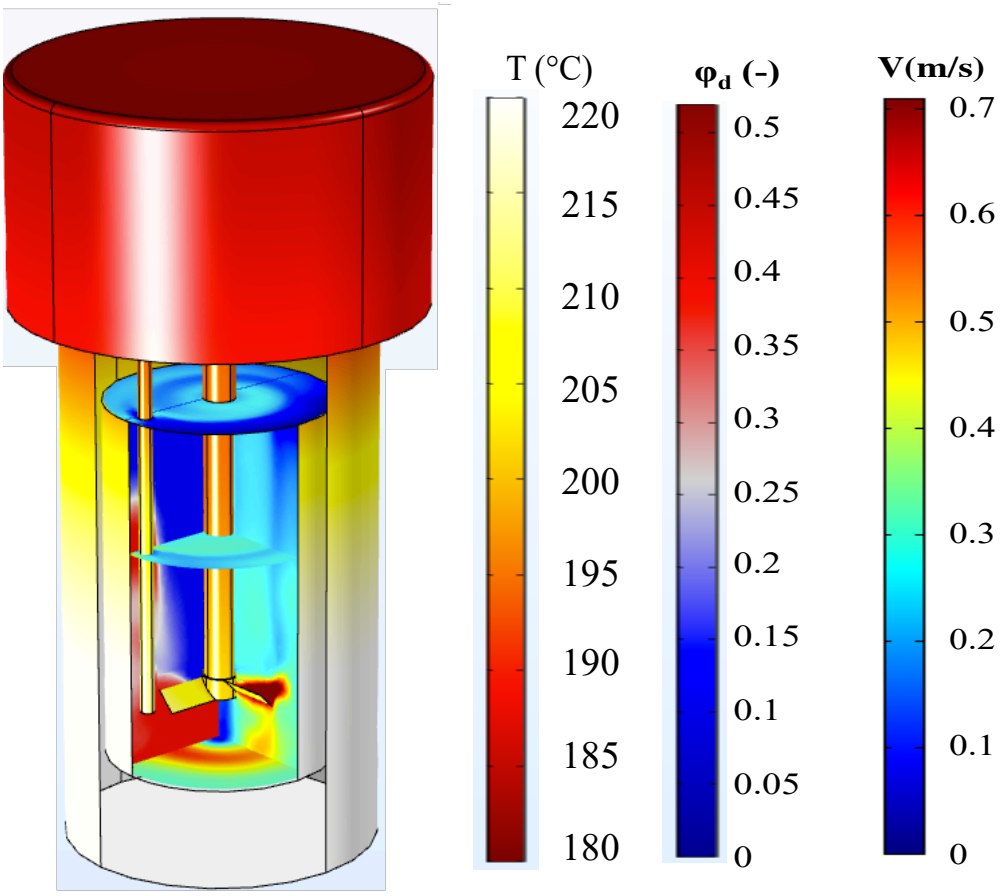

Figure 6-35: The temperature, velocity and volume fraction evolution contour

6.4. Conclusion

The following conclusions can be drawn from the results of the study:

- The kinetic parameters for the formation of this intermediate products were determined using the Levenberg–Marquardt algorithm optimization method in COMSOL Multiphysics®5.6. The kinetic results showed that the activation energy of CEL hydrolysis was 136.24 kJ/mol higher than AS and ASB, 63.08 and 85.02 kJ/mol, respectively. The high activation energy of the CEL is because the cellulose structure consists of two different regions, amorphous and crystalline, which have different reaction rates. The amorphous fraction has weaker bonds and is involved in the early stage of the reaction. In contrast, the crystalline fraction needs to be transformed into the amorphous state first and then undergoes further degradation during the HTC process. Therefore, more energy is required for CEL hydrolysis than AS and ASB; this is also noted in the lower solids conversion rate for CEL at low temperatures than AS and ASB. The activation energy for the formation of furfural and 5-HMF is higher than for forming organic acids for all biomasses; this is in agreement with these intermediates' concentrations. Also, the degradation of sugars to organic acids requires lower energy than for the furfural and 5-HMF.
- Modeling of ASB conversion by HTC at different process conditions using repones surface methodology (RSM) has been investigated. The HHV modeling gives a maximal value equal to 24.0 MJ/kg against 16.8MJ/kg for raw ASB. It is also shown that the energy yield provided by the hydrochar could compensate for the energy required in the cooking step of the mezcal production process. However, a more detailed study of the overall energy balance of the HTC process would have to be carried out before a conclusion can be drawn. Models describing the behavior of HHV, MY, FC, VM, Ti, Tm, and Tb as a function of the process conditions (temperature, holding time) were obtained. These models could be helpful to select the optimal experimental conditions to produce hydrochars with a high energy content for their use as fuel. RSM of H/C and O/C showed that increased HTC conditions favored dehydration reactions, while decarboxylation reactions were favored in mild HTC conditions. The proposed 2D contour plots bring helpful supplementary information to the Van Krevelen diagram. Moreover, the investigation of combustion parameters provided a better understanding of the thermal behavior of biomass and hydrochars. For

example, the lowest autoignition temperature was 241°C for hydrochars against 310°C for raw bagasse. In general, it was observed that the minimum Ti and Tm values occur for a minimal and maximal degree of devolatilization. In addition, lower temperatures and holding times promote a maximum volatile matter release for all hydrochars. Furthermore, an increase in the burnout temperature was related to an increase in the fixed carbon content.

- The hydrodynamic study shows that the ideal stirring speed to obtain a homogeneous mixture inside the reactor is 550 rpm, given a turbulent regime, and the average velocity corresponding to the dispersed phase is 0.24m/s, owing to AS particles high density. At this stirring rate, the predominant forces for the movement of the particles inside the reactor are inertial forces. For a lower stirring speed, the hydrostatic force predominates in the movement of the particles. The application of CFD simulation allowed the model construction that describes the heat transfer inside the reactor during the HTC of the AS. The model considers the reactor heat-up time, inside the reactor biomass concentration, and the water thermal properties evolution, and the thermal properties of biomass during the HTC process. The good fit to the experimental data gives this model the validity to predict the process behavior for specific experimental conditions. This model is general and can be used for any biomass with the known kinetic parameter and ultimate analysis. The CFD simulation results show that the difference between the thermal properties of biomass and water under HTC conditions is negligible. The biomass-to-water ratio has an effect on heat transfer during the HTC process. It is crucial to consider the biomass concentration in the kinetic model of the HTC process and heat-up time. The reaction starts at 150 °C. Also, it is observed that the mass yield is more significant for the higher biomass to water ratio; from an energetic point of view, this acquires particular importance because the more biomass inside the reactor, the more hydrochar is obtained. The present modeling approach thus shows a promising way to simulate biomass HTC processes on an industrial scale.

Chapter7 PROCESS SIMULATION OF BIOMASS CONVERSION

Chemical process simulation aims to represent a chemical or physical transformation process through a mathematical model that calculates mass and energy balances with phase equilibrium and transport and chemical kinetics equations. The objective is to find the establishment (prediction) of the behavior of a known structure, in which some preliminary data of the equipment composing the process are known (Chaves et al., 2016).The mathematical models applied in process simulation are generally known as thermodynamic models. They include linear, nonlinear, and differential-algebraic equations, which represent the equipment or process operations, the physical-chemical properties, the includes linear, nonlinear, and differential-algebraic equations, which represent the equipment or operations of the process, the physical-chemical properties, the connections between the equipment and the operations and their specifications. These connections are resumed in the process flow diagram (Gmehling et al., 2019). Process flow diagrams are considered the language of chemical processes or the route from raw feedstock to the final product. Thus, these diagrams show the state of the art of a real or hypothetical mechanism. Process simulators are used to visualize and analyze the information found in the process flow diagrams to predict errors and measure process results. Finally, the process is analyzed using a mathematical model composed of a series of equations that link process variables such as temperature, pressure, flow rates, and compositions with geometric configurations, valve set points, and so more (Foo and Elyas, 2017). In particular, process simulation and process synthesis are two crucial and interrelated elements used to achieve optimum process design in chemical process design. Process simulation aims to predict how a given process would behave under specific operating conditions. These predictions are performed using process simulators.

In most simulators, the equation scheme is solved linearly, solving each unit separately and advancing the system until the variables possible for the calculation of the next unit are understood. However, when there are flow recycles in the method, the process is useless since some of the variables to be calculated are necessary for the initialization of the process.

There is another alternative to this problem: taking one stream as a tear stream. To begin the calculations, the initial values of that stream are assumed; later, each of the following units is solved based on the assumed facts, yielding new values for the tear stream's parameters. Following that, the new values aid in repeating these equations before the gap between the

original and measured values meets a predetermined tolerance; this point is known as convergence (Amika, 2010).

A process simulator is a software used to model the behavior of a chemical process, generally in a steady-state, by determining pressures, temperatures, flows, and compositions. However, nowadays, the simulation of processes has been extended in its study to work on the dynamic behavior of the processes and the control systems and their response to the perturbations of the operation. In addition, there are interfaces in the simulators to perform the sizing of equipment, the estimation of the costs of each equipment, the analysis of operability, and the optimization of processes (Gmehling et al., 2019; Upreti, 2017).

Process simulators allow:

- Predict the performance of a process
- Analyze simultaneously different cases, adjusting the values of principal operating variables
- Optimize the operating conditions of new or existing plants
- Follow a chemical plant during its whole useful life in order to foresee extensions o process improvements

The commercial and academic process simulators more revealed actually are, among others: ASPEN PLUS®, ASPEN HYSYS®, DESIGN II®, CHEMCAD®, SpeedUp, PRO II®, gPROMS, so forth.

7.1.1. Types of process simulators

Process simulators are categorized based on the simulation strategy used to set the mathematical model representing the process to simulate. The simulation strategy applies to the approach taken to solving the model solution problem. In general, the technique is determined by the model's complexity and measurement mode. The first refers to the various options available, ranging from simple linear models to complex models involving mass, energy, and momentum transfer rates. The second was about the information (input variables) that needed to be defined to solve the model in terms of the remaining data (output variables) diagram (Gmehling et al., 2019).

- Design mode: Following to the required process conditions, a desired performance is used as beginning point to find the process or equipment specifications that allow the accomplishment of those conditions.
- Rating mode: according to some design specifications provided to the simulator, the performance of the process or equipment is evaluated to meet some specific conditions of the process.

The two basic strategies used in simulation problems are the sequential strategy and the simultaneous strategy.

7.1.1.1. *Sequential modular simulators*

These are simulators in which each process unit is represented by a module containing the procedure model and the numeric algorithm for calculating the outgoing streams. The modules are fully self-contained, and the knowledge flow for the simulation's calculations corresponds to the plant's "physical flow." Thus, modules have the advantage of allowing each equation system to be solved using its methods (Montagna and Iribarren, 1989). In this simulator, each equipment class is not just a model but a built-in solution procedure. Then the simulator has to find an order to solve the equipment and pass the first to the second output solution. If there are recycle streams, it needs to break the loop and iterate until convergence is achieved. Examples of this simulator are Aspen Plus® and Aspen HYSYS®.

Summarizing, the principal features of a sequential modular simulator are following:

- Contains calculation libraries and routines
- The iteration variables are in the recycle streams.
- The individual models are solved efficiently.
- It is easily understandable for engineers, not “simulation specialists,” due to the existing correspondence between the mass flow and the calculation sequence.
- It involves complex convergence methods
- The information entered by the user (related to streams and equipment) is easily verifiable.
- The design problems are easier to solve (parameter selection)

7.1.1.2. *Simultaneous simulators*

In this type of simulator, the mathematical model representing the process is set to build an extensive algebraic equations system. Modules representing process units or subsystems may exist here as well, but they do not contain computational methods for calculating output values; instead, they contain the necessary details to generate the equations that describe the mathematical model. The process model comprises the sum of all the units that include the process or plant in the simulation. This type of simulator is known as "Equation oriented" or "Equation based" due to the compilation and clustering theory of all the equations that make up the operation. The definition of modules is retained here to interact with the user more accessible and enable the problem's necessary details. The critical problem with the simultaneous or equation-oriented solution principle is the system's convergence and the solutions' accuracy. As a result, the highly non-ideal structures that conform to the chemical plant models may generate several solutions. Furthermore, the numeric solution of problems consisting of large equations systems requires proper initialization; this is close to a solution surrounding (status). Examples of this simulator are Aspen Dynamics, gPROMS, Speed Up, so forth.

Summarizing, the principal features of the equation-oriented simulators are:

- Each unit is represented by the equations that model it. The model is the integration of all the subsystems
- The distinction between process variable and operative parameters disappears. In consequence the design problems are simplified
- Simultaneous solution of the system of (nonlinear) algebraic equations
- Higher convergence velocity
- They need a better initialization (the higher the complexity of the problem to solve the better the initialization to be provided)
- The higher the complexity, the less the reliability in the results and the more the convergence problems (solutions without physical meaning)
- Easier to use for “no specialists”

7.1.1.3. *Hybrid simulators*

This simulator employs a combination of sequential and simultaneous strategies. Each iteration consists of two steps: a sequential solution of the model and updating the linear

coefficients to find a solution using a simultaneous strategy. First, the simulation starts a sequential step in which the output variables are calculated from input data and parameters in a sweep of the flowchart. Then, in a second sweep of the procedure, a simultaneous phase begins to solve the linearized models. Some simulators of high industrial applications request a hybrid strategy to ensure convergence, even in the worst cases.

7.1.2. Aspen Plus® and Aspen HYSYS®

Aspen Plus® and Aspen HYSYS® are steady-state process simulators used to predict the behavior of a process or a set of unit operations based on their current relationships. The relations and connections standing in the process determine the phase and chemical equilibrium and chemical transformation rates over the mass and energy balances. In this way, it is possible to simulate current or projected plants' behavior, improve the design specifications, or increase the profitability and efficiency of an operation in the process.

- The main functions that can be found in this simulator are:
- Sensitivity analysis and case studies
- Rating and sizing of equipment
- Analysis of pure components and mixtures properties
- Experimental data adjustment
- Process optimization
- Estimation and regression of physicochemical properties
- Dynamic analysis of processes

Aspen Plus®, like other simulators such as PROII® and CHEMCAD®, is one of a community of simulators that use a sequential strategy. Therefore, it is formed of a group of simulation or program units (subroutines or models) described through blocks and icons, to which the appropriate information must be provided to solve the mass and energy balances. However, this simulation has included in its latest versions the possibility of working with the simultaneous strategy.

Aspen HYSYS® is a process simulator generally used in the manufacturing industry, especially in conceptual design and detailed engineering, control, optimization, and process monitoring. Aspen HYSYS® is generally known for its application in oil and gas processing industries, refineries, and air separation industries. This simulator allows the integration of

steady-state and dynamic models in the only unit. In this way, it is possible to produce the stages of process design with the rigorous analysis of the dynamic behavior and the control of the same, to directly evaluate the effects that the decisions in the detailed design step have over the dynamic and controllability of the process.

In this study, the two simulators described above were used to simulate the process of biomass gasification and subsequent Fisher-Tropsch synthesis.

7.2. Process simulation strategy

To better understand the synthetic fuel production process simulation, it was decided to separate this last chapter into two parts. The first part explains the strategy used for the simulation, and the second part presents the results obtained. Thus, the simulation was divided into two parts: the production of syngas from biomass and the production of synthetic fuels using the Fisher-Tropsch reaction. Experimental results were used in the first part of the simulation, while data in the literature were used for the second part.

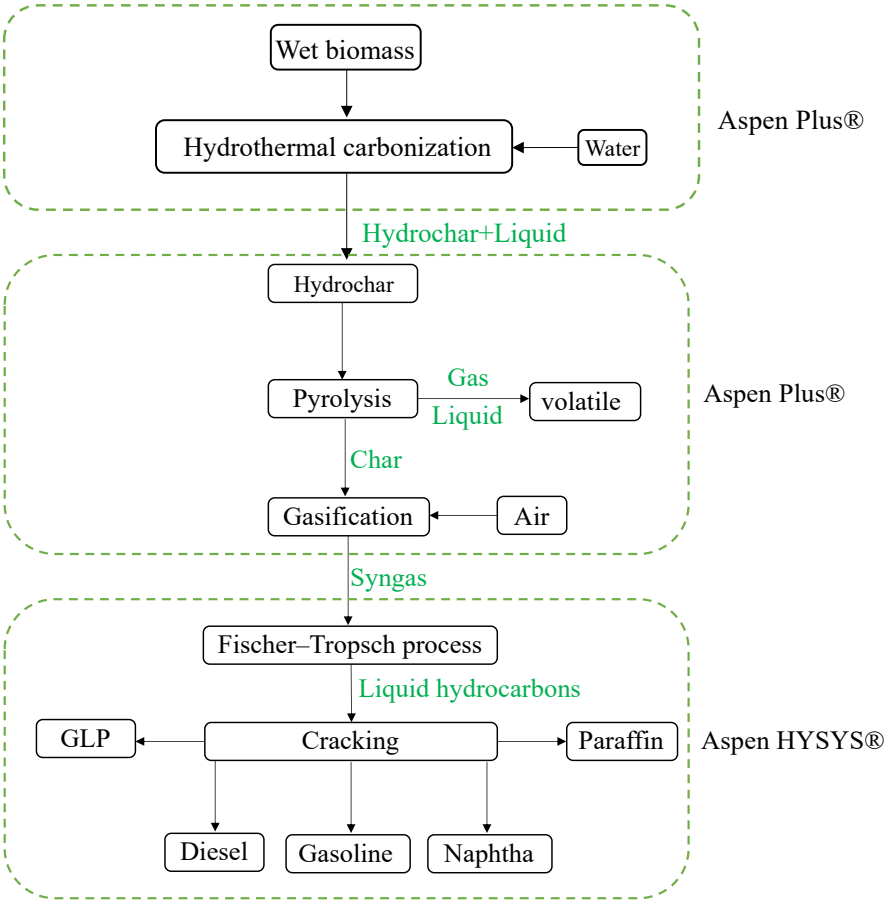

Figure *7-1*: Block diagram of synthetic fuels production process

7.2.1. Description of hydrothermal carbonization simulation process

The development of a validated plant simulation can give an essential vision of the overall process dynamics (Munir et al., 2018). Using a process simulator, operating parameters can be varied to optimize the process taking into account both energy and economic aspects. Commercial simulators such as Aspen plus® and software environments such as Matlab or Fortran allow developing this type of model. Actual process simulators solve the process equations using appropriate databases and solving methods, which require accurate input data on equilibrium and kinetics (Ischia and Fiori, 2020). However, there is currently little data available in the literature on the thermodynamics and kinetics of the HTC process, which limits the reliability of the implemented models. Therefore, the inclusion of these aspects requires first a wide availability and consistency of these data. On the other hand, the experimental data obtained in this study (the main hydrochar products, liquid and gases, and the different products detected in the liquid phase at different temperatures, as well as the kinetics of formation of these products) allows us to implement the necessary data to be able to simulate the hydrothermal carbonization process of biomass. The experimental data from **Chapter 4** was used to create an HTC process model in the Aspen plus® V10 software. Initially, the model was based on experimental data in a batch reactor with a biomass water ratio of 1/10, using the profiles of temperature variation (25 to 250 °C) and time corresponding to this variation within the reactor. The main product of HTC is hydrochar. It is assumed that the formation of hydrochar can be carried out in at least two ways. The first pathway consists of a solid-solid reaction to form a primary hydrochar, while the second pathway is through intermediates in the liquid phase. In the liquid phase, the following components and their reactions were considered. All components in the liquid phases are previously converted to sucrose by biomass hydrolysis; sucrose is converted to sugars (dextrose), dextrose undergoes reactions into furfural, 5-HMF on the one hand, and organic acids (formic, acetic, lactic, levulinic) on the other hand. Furfural and 5-HMF are transformed into organic acids, and the latter are converted into gases (CO_2, CO, CH_4, and H_2). The furfural and 5-HMF, in turn, polymerize to form secondary hydrochar. All these reactions were considered with their respective kinetics, determined in **Chapter 4**.

7.2.2. General description of the biomass gasification process

The gasification process consists mainly of three stages: drying, pyrolysis and gasification. Although these stages are often modeled in series, there is no clear boundary between them,

often overlapping. In a typical process, biomass is heated (dried) and then undergoes thermal degradation or pyrolysis, the products of pyrolysis (gases, solids, and liquids). Subsequently, the char formed during pyrolysis reacts with the gasifying agent to produce gasification gases (syngas). The following is a general description of the process that takes place at each stage:

The biomass is heated up to 150 °C for drying, evaporating part of the moisture contained in it. Most gasification systems use dry biomass with a moisture content between 7 and 20% to produce a fuel gas with an acceptable calorific value.

Above 100 °C, the water on the surface of the biomass is removed. As the temperature increases, the low molecular weight extractives compounds start the volatilization process, which continues until a temperature of approximately 150°C is reached. When the humidity is very high, pre-drying is necessary to remove as much moisture as possible from the biomass before feeding the gasifier. Once drying is complete, the thermal decomposition process begins in an oxidizer-free environment between 150 and 700°C, depending on the operating condition and the type of product required. More volatile combustible gases are released in this phase, although some do not volatilize due to the lack of oxygen and are converted into tar as bio-oil. In addition to the gases, a solid carbonaceous residue known as char is produced. Among the gases produced, the most important are: CO, CO_2, H_2, N_2, O_2, and light hydrocarbons (mainly CH_4).

Once the maximum pyrolysis temperature is reached, the gasifying agent (air) is injected for the gasification reactions. At this stage, the carbonaceous residue (char) is mixed with the gasifying agent, and both react with each other to form the gasification products.

The gasification temperature is commonly considered independent of other operating conditions; consequently, syngas distributions and composition as functions of the oxygen-to-biomass ratio can be found at fixed temperatures (Biagini et al., 2009; Xu et al., 2007).

In the actual reactor, an increase of oxygen in the feed gives a higher temperature in the gasifier. Consequently, these two parameters cannot be assumed independent of each other but should arise from a global heat balance, including reaction heat (devolatilization, combustion, and gasification) as well as feed heating. Furthermore, when steam or hot water is produced, heat recovery should be included. This contribution may be critical to the process's overall efficiency, but it is difficult to derive from equilibrium assumptions (Biagini et al., 2009).

The gasification is carried out in a temperature range between 700 and 1000ºC. Since the oxygen contained in the air (gasifying agent) introduced is lower than that stoichiometrically required for complete combustion, incomplete combustion occurs, forming mainly CO and H_2 (synthesis gas).

7.2.3. Description of the Fischer Tropsch synthesis process

Fischer-Tropsch synthesis is a chemical process for producing liquid hydrocarbons (mainly gasoline, naphtha, diesel, and heavy waxes) from synthesis gas (CO and H_2). In the case of the process proposed in this work, the synthesis gas obtained in the gasification reactor enters a Fischer-Tropsch reactor. The process consists of a series of complex reactions of the synthesis gas with a catalyst, leading to a series of products whose distribution depends on the reaction temperature, H_2/CO ratio, and catalyst. First, the production of liquid paraffinic hydrocarbons (alkanes) is carried out under high-temperature conditions of approximately 210 to 250°C, with a total pressure of 20 to 30 atm and an H_2/CO molar ratio close to 2, using cobalt as a catalyst. Then, the reactions have several stages, including the adsorption of carbon monoxide on the catalyst, followed by the formation of methyl groups, and finally the polymerization to obtain the hydrocarbons. The result is a complex mixture of straight and branched-chain hydrocarbons and oxygenated products such as alcohols, aldehydes, ketones, and esters, although the majority are linear kerosenes depending on the operating condition.

7.2.4. Calculation procedure

Due to the characteristics and limitations of the simulators used, Aspen Plus® was used for biomass hydrothermal carbonization, gasification process simulation and Aspen HYSYS® for Fischer-Tropsch synthesis simulation as well as product fractionation.

7.2.4.1. *Main assumptions for the simulation*

The following assumptions were considered when simulating the process:

- The process is in a steady state.
- HTC process is no isothermal (experimental condition by using batch reactor)
- All gasification stages are considered isothermal., i.e., a constant temperature is considered in the equipment.
- The system is considered a perfect mixture in the gasifier.
- The operation is carried out at atmospheric pressure.
- Pressure drops in the equipment are not considered.
- Drying and devolatilization (pyrolysis) of the biomass takes place instantaneously and occurs at a temperature of 700 °C. The volatile products consist mainly of H_2, CO_2, CO, CH_4, H_2O, O_2, and N_2.

- All nitrogen in the biomass is assumed to be inert, with no nitrogen oxides being produced during the process. The reducing atmosphere conditions in gasification justify this. However, this simplification does not increase inaccuracy significantly due to the low nitrogen content (0.4%) in the biomass.
- It is considered that the tar can be represented as benzene (C_6H_6) during the pyrolysis and gasification simulation).
- The only light hydrocarbon considered in the syngas composition is CH_4.
- Char contains only carbon, hydrogen, nitrogen, oxygen, and ash.
- Methane is the only light hydrocarbon considered in the modeling of the gasification process. Thus, long-chain products formed during devolatilization and gasification of biomass have not been considered to simplify the model
- The model was elaborated considering the experimental operating conditions used at the laboratory scale. Where the raw materials are biomass and air, the latter is used as gasifying agent.
- The operating parameters considered are final pyrolysis temperature 700 °C; gasification temperatures 700, 750, 800, 850, 900, 950, and 1000 °C.
- The gasifier operates at atmospheric pressure and is initially at room temperature.
- Molar ratio H_2/CO at the Fischer-Tropsch reactor inlet was considered to be between 0.8 and 4, based on the experimental results and the analysis of the effects of this ratio.
- The production of alkane hydrocarbons is only considered for the selectivity of the catalyst used towards this type of product.
- Alkanes hydrocarbons are considered C1-C30 (LGP, gasoline, naphtha, diesel, and waxes).

7.2.4.2. *Simulation procedure in Aspen Plus®*

7.2.4.2.1. *Thermodynamic model and physical properties*

The Redlich-Kwong-Soave equation of state was used to calculate the thermodynamic properties. RK-SOAVE is recommended for mixtures formed by hydrocarbons and light gases such as CO_2 and H_2, as well as for estimating some thermodynamic properties of solids (carbon) (François et al., 2013). The property method RK-SOAVE is used to estimate the physical properties of conventional mixed components and solid components.

The enthalpy and density of non-conventional components are determined using HCOALGEN and DCOALIGT models, respectively. For nonconventional components, the HCOALGEN model requires three component attributes: proximate analysis results (denoted as PROXANAL in Aspen Plus®), ultimate analysis results (denoted as ULTANAL in Aspen Plus®), and sulfur analysis results (denoted as SULFANAL in Aspen Plus®). The proximate analysis gives the weight contents of moisture, fixed carbon, volatile matter, and ash. The ultimate analysis gives the weight composition of biomass in ash, carbon, hydrogen, nitrogen, chlorine, sulfur, and oxygen. Finally, the sulfur analysis gives the sulfur divided into pyritic, sulfate, and organic sulfur. For the DCOALIGT model, it requires only two-component attributes: ULTANAL and SULFANAL. **Table 7-1** shows the component attributes of biomass used in this study.

Table 7-1: Ultimate and immediate analysis of biomasses

	Avocado stone (AS)	***Agave salmiana* bagasse (ASB)**	**Cacao shell (CS)**	**Cellulose (CEL)**
		PROXANAL (%)		
MC	3.2	3.4	3.8	2.2
VM	72.5	77.9	71.6	79.1
FC [a]	22.4	14.8	18.0	18.6
Ash	1.9	3.9	6.5	-
		ULTANAL (%)		
Carbon	46.1	38.0	51.4	41.4
Hydrogen	6.4	4.1	6.8	6.5
Nitrogen	0.4	0.6	3.2	0
Sulphur	0	0	0	0
Oxygen [a]	47.1	57.3	34.9	52.1
		SULFANAL		
PYRITIC	0	0	0	0
SULFATE	0	0	0	0
ORGANIC	0	0	0	0
HHV(MJ/kg)	**18.6**	**16.8**	**23.0**	**16.5**

Biomass is defined as a non-conventional solid component specifying its ultimate and immediate composition, as well as its HHV. The **Table 7-1** shows the values used for biomass and char in this work. The conventional components considered are O_2, N_2, H_2, CO, CO_2, CH_4, C_6H_6, H_2O, and C. In addition, to simplify the simulation, benzene (C_6H_6) is selected as a representative compound of all tars; this is because it is present in high proportion. Finally, char was also sectioned as a non-conventional solid component, specifying its ultimate and immediate composition.

The conventional components considered in HTC simulation are sucrose, dextrose, 5-HMF, furfural, formic acid, acetic acid, lactic acid, levulinic acid, guaiacol, methyl-acetoacetate, furan N_2, H_2, CO, CO_2, CH_4, C_6H_6 and H_2O, while the conventional components considered in pyrolysis and gasification are O_2, N_2, H_2, CO, CO_2, CH_4, C_6H_6, H_2O, and C. In addition, to simplify the simulation, benzene (C_6H_6) is selected as a representative compound of all tars; this is because it is present in high proportion. Finally, char was also sectioned as a non-conventional solid component, specifying its ultimate and immediate composition.

7.2.4.2.2. *Biomass HTC reaction*

The HTC reactor is modeled in a batch reactor, with a biomass composition and hydrochar based on experimental laboratory data of the AS, using the profiles of pressure (1-40 bar), temperature (25-250°C), and residence time (0-121 min) corresponding to these profiles. The experimental part was carried out with distilled water, instead of recycled process water, and using high water to biomass ratio of 10:1, neither of which would represent an industrial plant. It was considered that 47.43% of AS is transformed to HTC liquid at a temperature of 250 °C, the pressure of 40 bar, and time of 121 min, according to experimental data. Similar procedures from **Chapter 4** were used to determine the kinetic parameters, in this case considering reaction temperature between 150 to 250 ºC. These reactions were considered according to the mechanism of the reactions proposed in **Chapter 4.** The possible reactions that occur during the HTC process are presented below.

$$\text{wet biomass} + \mathrm{H_2O} \rightarrow \text{Hydrochar} + \mathrm{C_{12}H_{22}O_{11}} \quad (7\text{-}1)$$

$$\mathrm{C_{12}H_{22}O_{11}} + \mathrm{H_2O} \rightarrow 2\mathrm{C_6H_{12}O_6} \quad (7\text{-}2)$$

$$5\mathrm{C_6H_{12}O_6} \rightarrow 6\mathrm{C_5H_4O_2} + 18\mathrm{H_2O} \quad (7\text{-}3)$$

$$\mathrm{C_6H_{12}O_6} \rightarrow \mathrm{C_6H_6O_3} + 3\mathrm{H_2O} \quad (7\text{-}4)$$

$$\mathrm{C_6H_{12}O_6} \rightarrow 2\mathrm{C_3H_6O_3} \quad (7\text{-}5)$$

$$\mathrm{C_6H_{12}O_6} \rightarrow 3\mathrm{C_2H_4O_2} \quad (7\text{-}6)$$

$$\mathrm{C_6H_{12}O_6} \rightarrow \mathrm{CH_2O_2} + \mathrm{C_5H_8O_3}^{*} + \mathrm{H_2O} \quad (7\text{-}7)$$

$$C_6H_6O_3 + 3H_2O \rightarrow 2C_3H_6O_3 \quad (7\text{-}8)$$

$$C_6H_6O_3 + 3H_2O \rightarrow 3C_2H_4O_2 \quad (7\text{-}9)$$

$$C_6H_6O_3 + 2H_2O \rightarrow CH_2O_2 + C_5H_8O_3 \quad (7\text{-}10)$$

$$3C_5H_4O_2 + 9H_2O \rightarrow 5C_3H_6O_3 \quad (7\text{-}11)$$

$$2C_5H_4O_2 + 6H_2O \rightarrow 5C_2H_4O_2 \quad (7\text{-}12)$$

$$CH_2O_2 \rightarrow CO_2 + H_2 \quad (7\text{-}13)$$

$$C_2H_4O_2 \rightarrow 2CO + 2H_2 \quad (7\text{-}14)$$

$$C_2H_4O_2 \rightarrow CH_4 + CO_2 \quad (7\text{-}15)$$

$$2C_3H_6O_3 \rightarrow 3CH_4 + 3CO_2 \quad (7\text{-}16)$$

$$C_5H_8O_3 \rightarrow 2CH_4 + 3CO \quad (7\text{-}17)$$

$$C_6H_{12}O_6 \rightarrow C_4H_4O + H_2 + 2CO \quad (7\text{-}18)$$

$$C_5H_4O_2 \rightarrow C_4H_4O + CO \quad (7\text{-}19)$$

* methyl-acetoacetate

7.2.4.2.3. *Biomass HTC process flow diagram*

Figure 7-2 shows the simulation diagram of the Aspen Plus model. This model shows all the processes occurring in the HTC process, i.e., mixing biomass and water (MIXER), biomass/water reaction in batch reactor (HTC-REAC), reactor cool down (COOLER), valve to recovery HTC gas (VALVE) recovering gases (SEP-GAS), an HTC liquid/hydrochar separator (FILTER) and finally the hydrochar drying in oven (DRYER).

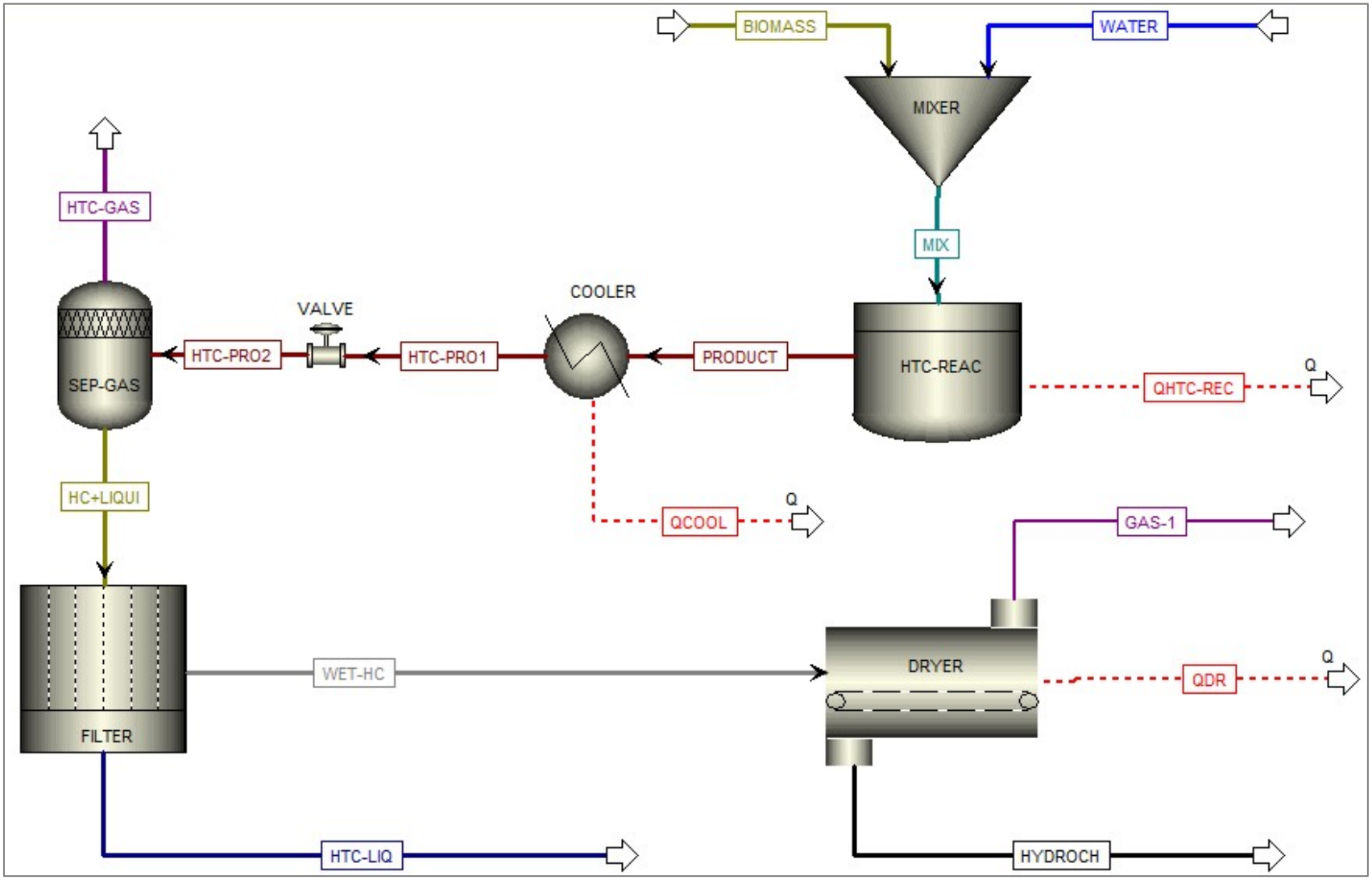

Figure 7-2: Simulation HTC model flowchart with Aspen Plus®

7.2.4.2.4. *Biomass pyrolysis reaction*

Biomass pyrolysis begins with drying. In the biomass drying process, the physical moisture bound to the biomass is released into the gas phase. The resulting dried biomass is represented in the model as DRY-BIOM. A simplified schematic of a moving bed gasifier is shown in **Figure 7-3**.

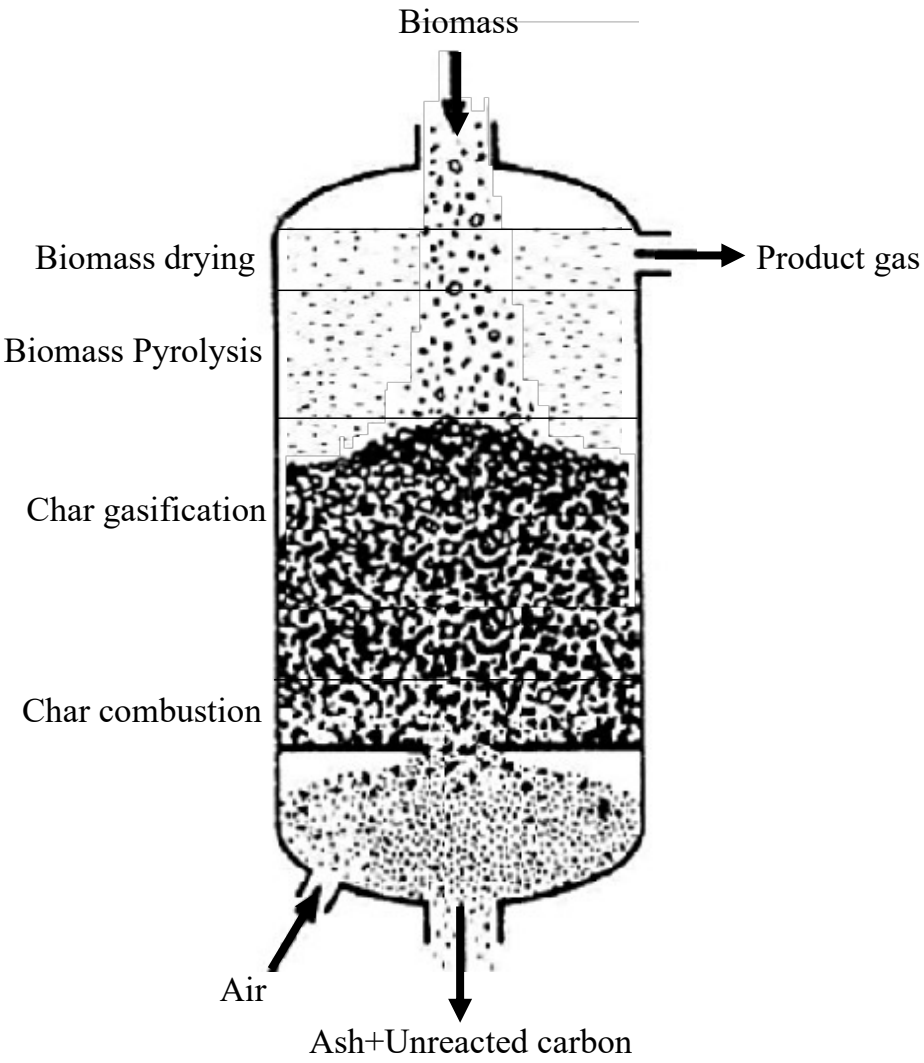

Figure 7-3: Schematic diagram of moving bed biomass gasifier

The amount of vaporized water is determined based on the moisture content in the proximal analysis of biomasses because the temperature in the gasifier is usually high enough to vaporize all the bound water in the biomass. In addition, the drying time of biomass in the gasifier is much shorter than that of other processes (pyrolysis and gasification). Therefore, it was assumed that biomass drying takes place instantaneously in the upper part of the gasifier at a

temperature up to 200 °C. After drying, the biomass undergoes pyrolysis. Biomass undergoes devolatilization during the pyrolysis process, where the final products are volatile matter and char, as shown in **Eq.(7-20)**. In our model, the volatile matter includes CO, H_2, H_2O, CO_2, CH_4, N_2, and C_6H_6. In this case, C_6H_6 is used to represent tar.

$$\text{Dry biomass} \rightarrow \text{Char} + H_2 + CO + CO_2 + CH_4 + H_2O_{(g)} + C_6H_6 + N_2 \quad (7\text{-}20)$$

There are two methods used to obtain the products of biomass pyrolysis. One is based on experiments, and the other uses a theoretical method, like a functional group model (Hobbs et al., 1992). The theoretical method is usually very complicated and challenging to use in practical applications, due to the natural complexity of biomass in its composition. On the other hand, the experiment-based method is more straightforward and more practical. Therefore, the experimental method is used to predict the results of biomass pyrolysis in the model. Moreover, in a biomass gasifier, the pyrolysis stage or pyrolysis length is much less than the gasification stage, so it can be considered that the pyrolysis of biomass is carried out instantaneously at the top of the gasifier, especially in a moving bed reactor (**Figure 7-3**).

7.2.4.3. *Char gasification reaction*

After the biomass pyrolysis process, the char from this pyrolysis is further gasified with air injection by reacting with the gases in the gaseous phase. This process can benefit from the following reactions:

$$C + \frac{1}{\phi}O_2 \rightarrow 2\left(1 - \frac{1}{\phi}\right)CO + \left(\frac{2}{\phi} - 1\right)CO_2 \quad (7\text{-}21)$$

$$C + H_2O \rightarrow CO + H_2 \quad (7\text{-}22)$$

$$C + CO_2 \rightarrow 2CO \quad (7\text{-}23)$$

$$C + 2H_2 \rightarrow CH_4 \quad (7\text{-}24)$$

$$H_2 + 0.5O_2 \leftrightarrow CH_4 \quad (7\text{-}25)$$

$$CO + H_2O \leftrightarrow CO_2 + H_2 \quad (7\text{-}26)$$

$$CO + 0.5O_2 \leftrightarrow CO_2 \quad (7\text{-}27)$$

$$CH_4 + H_2O \leftrightarrow CO + 3H_2 \quad (7\text{-}28)$$

In reaction **Eq. (7-21)**, ϕ is a coefficient that depends on the diameter of the biomass particle (d_p) and can be calculated by the relations in **Table 7-2**. For a given temperature, ϕ is constant at $d_p < 0.005$cm and $d_p > 0.1$cm. At $0.005 \leq d_p > 0.1$cm, ϕ decreases with the increase in d_p. For a given d_p, ϕ shows a slight change with the temperature at $d_p \leq 0.1$cm. At $d_p > 0.1$cm , ϕ is independent of temperature and has the value of 1.0. (Wen and Chaung, 1979).

Table 7-2: Expressions of ϕ for different size of biomass particle

d_p (cm)	ϕ
$d_p < 0.005$	$\frac{2z+2}{z+2}$
$0.005 \leq d_p \leq 0.1$	$\frac{(2z+2)-\frac{z(d_p-0.005)}{0.095}}{z+2}$
$d_p > 0.1$	1
$z = \frac{[CO]}{[CO_2]} = 2500e^{-\frac{6249}{T}}$	
[CO] and $[CO_2]$ are concentrations of CO and CO_2, respectively. T is temperature (K).	

7.2.4.3.1. *Reaction kinetics*

Reactions **Eq. (7-21)** to **(7-24)** are solid-gas reactions caused by the reaction of char with gaseous components. Some of these reactions are volumetric reactions, while others are surface reactions. In volumetric reactions, gas can rapidly diffuse into the particles, and reaction occurs through the particle's inner. In the surface reaction, gas does not penetrate the particle but is confined at the surface of the shrinking core of the unreacted solid. Generally, a volumetric reaction occurs when the chemical reaction is slow compared with diffusion. The surface reaction occurs when the chemical reaction is very fast, and diffusion is the rate-limiting step.

Between these four reactions, the rate reaction **Eq. (7-21)** is generally fast to the diffusion rate of the reactants, hence reaction **Eq. (7-21)** is produced as a surface reaction. However, the rates of the other three reactions are relatively slow due to the low operating temperature in the moving bed biomass gasifier, typically below 1000 ºC. Therefore, reactions (3-5) are volumetric reactions. Based on the above, the unreacted core shrinkage model is used to describe the reaction rate of reaction **Eq. (7-21)** (Taqvi et al., 2015; Wen, 1968). This is attributed to the following two points. The rates of reactions **Eq. (7-22)** to **(7-26)** are expressed in **Table 7-3**.

Table 7-3: Parameters for kinetics of reactions **Eq. (7-25)** and **(7-26)** (Wen and Chaung, 1979)

Reaction	Reaction rate	Comment	Unit
(7-22)	$930e^{-\frac{45000}{1.987T}}[C]\left(P_{H_2O}-P_{H_2O}{}^{*}\right)$	$P_{H_2O}{}^{*}=\frac{P_{H_2}\cdot P_{CO}}{e^{-17.29-\frac{16330}{T}}}$	mol/m^3·s
(7-23)	$930e^{-\frac{45000}{1.987T}}[C]\left(P_{CO_2}-P_{CO_2}{}^{*}\right)$	$P_{CO_2}{}^{*}=\frac{P_{CO}{}^{2}}{e^{-20.92-\frac{20280}{T}}}$	mol/m^3·s
(7-24)	$e^{-7.087-\frac{8078}{T}}[C]\left(P_{H_2}-P_{H_2}{}^{*}\right)$	$P_{H_2}{}^{*}=\left(\frac{P_{CH_4}}{e^{-13.43-\frac{10100}{T}}}\right)^{0.5}$	mol/m^3·s
(7-25)	$F_w\cdot 2.877\cdot 10^5(x_{CO}-x^{*}{}_{CO})e^{-\frac{27760}{1.987T}}\cdot P_T{}^{0.5-\frac{P_T}{250}}\cdot e^{-8.91+\frac{5553}{T}}$	$x_{CO}=\frac{P_{CO}}{P_T}$ $x^{*}{}_{CO}=\frac{1}{P_T}\cdot\frac{P_{CO_2}P_{H_2}}{K_{eq}\cdot P_{H_2O}}$ $K_{eq}=e^{-3.6893+\frac{72.34}{1.87T}}$	mol/[s·(g of ash)]
(7-26)	$8.83\cdot 10^5 e^{-\frac{9.976\cdot 10^4}{8.315T}}[H_2]\cdot[O_2]$		mol/m^3·s
(7-27)	$90.9e^{-\frac{99760}{8.315T}}[CO][O_2]$		mol/m^3·s
(7-28)	$3.552\cdot 10^{11}e^{-\frac{9.976\cdot 10^5}{8.315T}}[CH_4][O_2]$		mol/m^3·s

[C], [CO], [H_2O], [CH_4] and [H_2] are concentrations of C, CO, H_2O, CH_4 and H_2. Fw is adjustable parameter, which represents the relative catalytic reactivity of ash. In the model, Fw= 0.0084. P_{H2O}, P_{CO}, P_{CO2}, P_{H2} and P_{CH4} are partial pressure of components (atm). x_{CO}, x_{CO2}, and x_{H2} are mol fractions of components.

The kinetics of these equations were used in Aspen Plus®, using an external Fortran subroutine.

In the real gasifier, the char-gas reactions can be considered surface reactions due to the high operating temperature. Since the solids loading in the gasifier is usually very small, particle collision is infrequent and, therefore, it can be assumed that the ash layer formed remains on the particle during the reactions. In this model, the effects of ash layer diffusion, gas film diffusion, and chemical reaction are considered. The overall rate is expressed by **Eq.(7-29):**

$$R_{c-O_2}=\frac{1}{\frac{1}{k_{film}}+\frac{1}{k_s Y^2}+\frac{1}{k_{dash}}\left(\frac{1}{Y}-1\right)}\left(P_{O_2}\right) \qquad (7\text{-}29)$$

Where R_{C-O_2} is the reaction rate (mol/ cm^3·s), k_{diff} is the gas film diffusion constant (mol/cm^3·atm·s), k_s chemical reaction constant (mol/cm^3·atm·s), k_{dash} is the ash film diffusion constant (mol/ cm^3·atm·s), P_{O2} is partial pressure of oxygen (atm).

$$k_{dash} = k_{film} \cdot \varepsilon^{n} \quad (7\text{-}30)$$

where ε is void age in the ash layer; n is a constant ranging from 2 to 3. In this model, it was assumed that ε = 0.75 and n = 2.5

$$Y = \frac{r_{core}}{r_{particle}} = \left(\frac{1-x}{1-f}\right)^{\frac{1}{3}} \quad (7\text{-}31)$$

where r_{core} is the radius of the unreacted core; $r_{particle}$ is the radius of the whole particle including the ash layer; x is coal or biomass conversion at any time after pyrolysis is completed, based on raw feedstock; and f is coal conversion when pyrolysis is completed, based on raw biomass. The diffusion coefficient of the gas film is determined from the following equation:

$$k_{film} = 0.292 \cdot 4.26 \cdot \frac{\left(\frac{T}{1800}\right)^{1.75}}{d_p T} \quad (7\text{-}32)$$

where dp is the diameter of biomass particle size (cm).

7.2.4.3.2. *Biomass gasification process flow diagram*

Figure 7-4 shows the simulation diagram of the Aspen Plus model. The function of each block is described in **Table 7-4**. This model shows all the processes appearing in the gasifier, i.e., biomass drying, biomass pyrolysis, and char gasification. An RYield block (DRYING), is used to simulate the drying of biomasses. The feedstock is fed into the block, and the bound water from this feedstock is vaporized in this block. The yield of the gaseous water is determined by the moisture content in the proximate analysis of the biomasses (**Table 7-1**). In this block, all moisture in the feedstock is considered to be removed. Once the drying process is completed, the gaseous water and the dried sample pass through a gas-solids separator (SEP-1). The separated gaseous water is mixed with the gas streams from the pyrolysis and gasification of the biomass to produce the final product gas (GAS-P). The separated dry biomass is passed to the next block for the pyrolysis process. The pyrolysis was considered as instantaneous at 700 °C, due to the limitation of the simulator (steady-state simulator). In addition, the experimental results affirm that the pyrolysis can be considered as finished at 700 ºC.

Table 7-4: Function of Each Block

Block	Model	Function
DRYING	RYield	Simulate biomass drying based on the value of the moisture content in the proximate analysis of biomass
PYROLYS	RYield	Simulate biomass pyrolysis based on the results data of pyrolysis experiment of biomasses
SEP-1...3	SEP	Separate the gas and solid
CHAR-DEC		Decompose char into C, H, O, N, and ash in order to easily deal with solid reaction in the simulation of char gasification
RET-700…1000	RCSTR	Simulate char gasification. Seven reactors were used, each one with a different temperature (between 700 and 1000 ºC); this was done because the gasification was non-isothermal, where the air was injected from 700 up to 1000 ºC. In these reactors, an average residence time of 10 s was considered.
M-GAS	Mixer	Mix the product gas: Mixing of pyrolysis and gasification product gases as well as the water evaporated during drying.

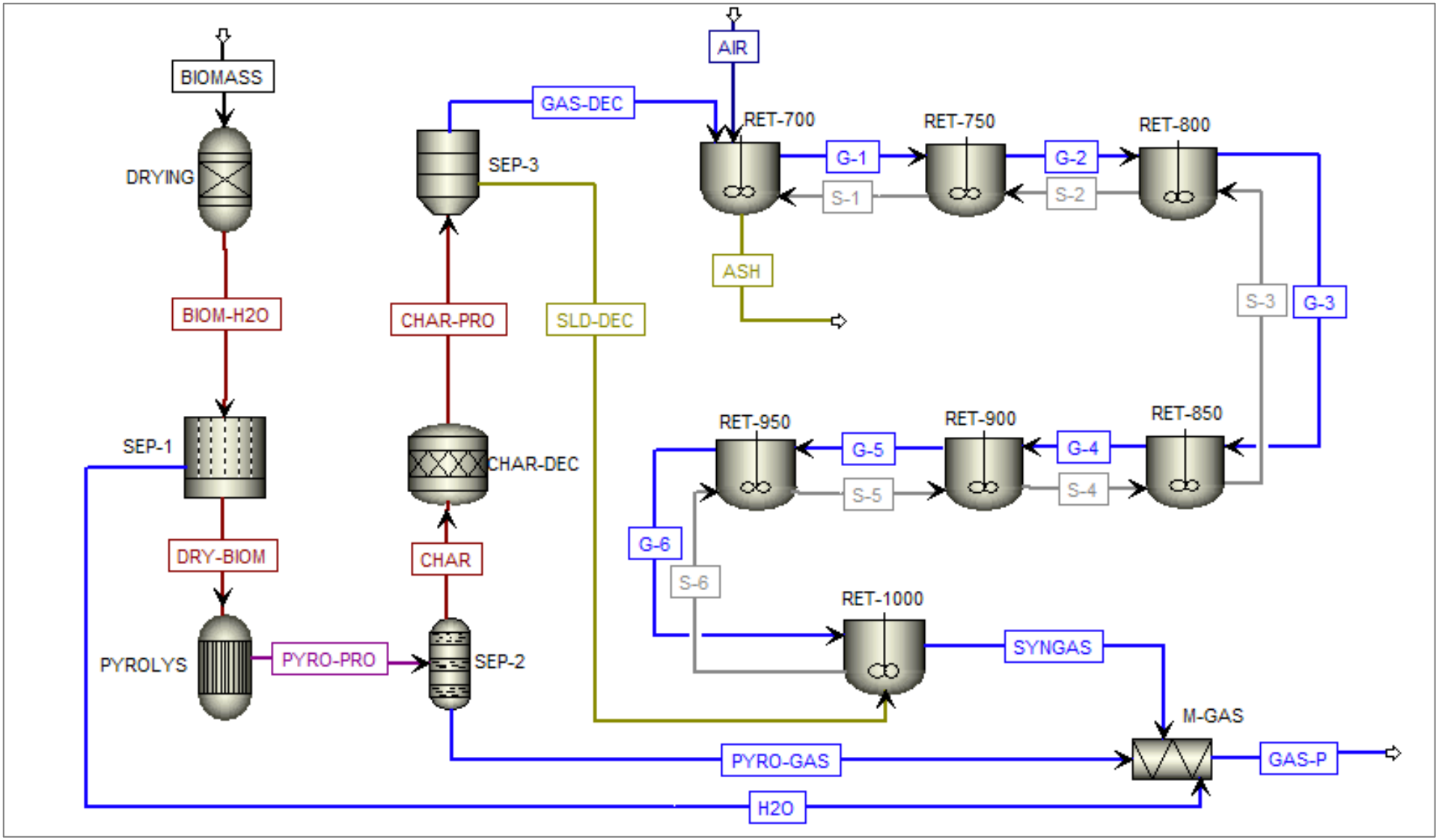

Figure 7-4: Simulation model flowchart with Aspen Plus®

The pyrolysis of biomass is simulated with an RYield block (PYROLYS). In this block, the dry biomass is decomposed into CO, H_2, CO_2, H_2O, N_2, CH_4, C_6H_6, and char. The yield of each component is specified according to the experimental results obtained. In this case, C6H6 is considered to represent all the liquid phases (bio-oil and tars). H_2O production was estimated from the results of the analysis performed by Stefanidis et al. (2014) as a function of cellulose, hemicellulose, and lignin content. These data were used to estimate the H_2O production since it could not be determined experimentally due to the limitations of the liquid product analysis technique.

After pyrolysis, the pyrolysis products flow into the SEP-2 block to separate the gas and solid (char). The gases from SEP-2 pass into gas-mixer (M-GAS). The SEP-2 char enters a RStoic (DEC-CHAR) to decompose to its elemental components, according to the result of the ultimate analysis of the biomass and based on atomic mass balance after pyrolysis. Ultimate analysis biomass char was also considered as a guide at 700 ºC (Fu et al., 2011) . The elemental compound enters the gasifier series from 700 to 1000 ºC. This series of reactors represents a moving bed biomass gasifier is a countercurrent reactor. In this case, a countercurrent reactor model is required to simulate the char gasification processes. Nevertheless, Aspen Plus® does not have a built-in reactor model for dealing with the countercurrent reactor. Benjamin (1985) developed a user solution program for the countercurrent moving bed coal gasifier and then integrated it into Aspen Plus®, but their results revealed that the solution was very time-consuming; this is attributed to the following reason: The form of the mathematical model of the countercurrent moving-bed biomass gasifier is a two-point boundary value problem. Its solution requires fitting several variables, some specified at the top and some at the bottom of the gasifier. This feature makes the solution process usually complicated and time-consuming. Thus, from the point of view of directly utilizing the built-in algorithm in Aspen Plus® and simplifying the problem, a series of continuous stirred-tank reactor (RCSTR) in series is proposed to model the char gasification processes. The RCSTR reactor has the characteristic that all phases have the same temperature, which means that the temperatures of the solid and gas phases in the char gasification processes are equal in the model for each reactor.

As previously mentioned, the simulation of char gasification processes is performed by a series of RCSTRs. However, to quickly deal with the solid-gas reactions in this process, an RStoic block (CHAR-DEC) is set up before the series of RCSTRs. The char is decomposed into the elements H_2, O_2, and N_2, and ash in this block. The stoichiometric coefficients of these elements are determined according to the ultimate analysis of the char. These values

were entered into the Aspen Plus® calculator. The products are leaving the CHAR-DEC enter a solids and gas separator, the SEP-3. The gases (H_2, O_2, and N_2) are fed into the bottom of the gasifier along with the air. The separated solid component (C) and ash pass through a series of RCSTRs to participate in the gasification reactions. The average residence time of the reactors is 10 seconds. The reaction kinetics described in **Section 7.2.4.3.1.** is written in an external Fortran code.

7.2.4.4. *Simulation procedure in Aspen HYSYS®*

7.2.4.4.1. *Process description for Aspen HYSYS® Simulation*

Figure 7-7 shows the different parts of the Fischer-Tropsch synthesis for the production of synthetic fuels, as well as the separation of these fuels.

Syngas sweetening zone

The synthesis gas obtained experimentally has a high concentration of CO_2 (18 mole %), so it is subjected to a process for its elimination. This process is carried out by contacting the synthesis gas (25 ºC and 1 atm) with an aqueous solution of monoethanolamine (MEA) at 20 wt.% (25 ºC and 1 atm), in an absorption column, where the chemical absorption of CO_2 takes place, obtaining a synthesis gas with a molar concentration of CO_2 of less than 1%.

Fischer-Tropsch synthesis zone

The syngas-sweet obtained in the absorption column is compressed in a compressor to increase the pressure up to 20 atm and a further temperature decrease to 323°C before being sent into the Fischer Tropsch reactor.

Stream "2" resulting from compression and cooling enters a Fischer Tropsch synthesis reactor (Plug Flow Reactor) with a different molar ratio of H_2/CO. In this simulation block, kinetics, sizing and operating conditions need to be specified. The kinetics of the reaction is catalytic. A cobalt catalyst is used to recombine hydrogen and carbon monoxide, leading to forming the long-chain paraffinic hydrocarbons. It was assumed that the chemical reaction must occur with a molar ratio of H_2/CO between 2 to 2.5, for the formation of paraffinic compounds according to the following general reaction.

$$nCO + (n+2)H_2 \rightarrow C_nH_{2n+2} + nH_2O \quad (7\text{-}33)$$

This reaction releases a large amount of heat (highly exothermic). For this reason, to control the temperature in the reactor, a cooling fluid was used to keep the temperature constant.

Yates and Satterfield (1991) determined the best fitting reaction rate model for this reaction using the Langmuir-Hinshelwood equation, with the parameters as follows.

$$n - r_{CO} = \frac{KT_1 P_{H_2} P_{CO}}{(1+K_2\, T_2 P_{CO})^{\,2}} \quad (7\text{-}34)$$

$$T_1 = Exp\left[-4492\left(\frac{1}{T} - \frac{1}{473}\right)\right] \quad (7\text{-}35)$$

$$T_2 = Exp\left[-8237\left(\frac{1}{T} - \frac{1}{473}\right)\right] \quad (7\text{-}36)$$

where K = 0.0173 gmol-CO/h-cm^3 cat-atm^2 (apparent density of catalyst is 0.8 g/cm^3), k2 = 4.512 atm^{-1}, P_{H2}, P_{CO} = partial pressure of H_2 and CO (atm), T = operating temperature of the reactor (K).

It was assumed that the products of the Fischer-Tropsch reaction are only alkanes because of the established H_2/CO ratio. In addition, the distribution of the C5+ products are characterized by the Anderson-Schulz-Flory (ASF) probability distribution equation (Tavakoli et al., 2008), as follows

$$\frac{W_n}{n} = \left[\frac{(1-\alpha)^2}{\alpha}\right]\alpha^n, \text{and } M_n = (1-\alpha)\alpha^{n-1} \quad (7\text{-}37)$$

where Wn is mass fraction of the hydrocarbon of n atoms of carbon, n is the number of carbon atoms, α is the Schulz-Flory coefficient (the probability of chain growth or degree of polymerization) and Mn is the mol fraction of the hydrocarbon of n atoms of carbon. The theoretical mole fraction of the chain growth probability is presented in **Figure 7-5**.

The selectivity of light hydrocarbons (C1-C4) can be expressed as follows:

$$S_{CH4} = \frac{r_{CH4}}{-r_{CO}} = 0.03T_3\ \left(\frac{mol}{mol}\right) \quad (7\text{-}38)$$

$$T_3 = Exp\left[-10000\left(\frac{1}{T} - \frac{1}{473}\right)\right]\ ;\ T(K) \quad (7\text{-}39)$$

The parameter α (the probability of chain growth) is temperature dependent according to.

$$\alpha = 0.93T_4 \quad (7\text{-}40)$$

$$T_4 = Exp\left[250\left(\frac{1}{T} - \frac{1}{473}\right)\right] \quad (7\text{-}41)$$

Ethane to butane selectivity is related to methane selectivity by:

$$S_{C_n} = 0.03 S_{CH4} \left(\frac{mol}{mol}\right) \text{ for n} = 2,3 \text{ and } 4 \quad (7\text{-}42)$$

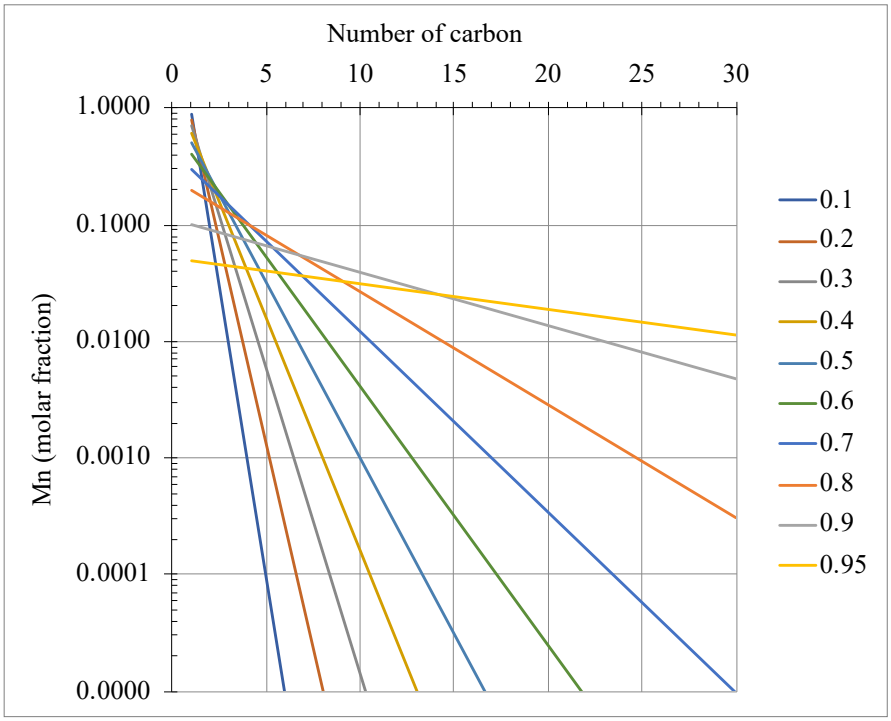

Figure 7-5: The mole fraction of the chain growth probability as a function of the n carbon atoms.

For the Fischer-Tropsch reactor simulation, the products were considered to range from methane to triacontane (C1-C30) through all alkane intermediates.

The preceding kinetic model was used in the Aspen HYSYS® simulator, implementing it in a catalytic kinetic type reaction, the reaction rate of which is presented as follows.

$$-r_{CO} = \frac{A * e^{\left(-\frac{E}{RT}\right)} * f(Basis)}{1 + A\prime(exp^{\left(-\frac{-E\prime}{RT}\right)}) * f1(Basis)} \quad (7\text{-}43)$$

This equation was then fitted with the reaction rate equation that best fits the experimental data as follows:

$$-r_{CO} = \frac{[P_{H_2} K_1 e^{-4492\left(\frac{1}{T} - \frac{1}{473}\right)} * P_{CO}]}{\left[1 + K_2 e^{8237\left(\frac{1}{T} - \frac{1}{473}\right)} * P_{CO}\right]^2} \quad (7\text{-}44)$$

The terms that are assigned explicitly in Aspen HYSYS® were evaluated. The values of A, A', E, and E,' are reported in **Table 7-5** correspond to the parameters for calculating the kinetic constants (K1 and K2) of **Eq.(7-44)** The operating temperature of the reactor was considered to be 232°C.

Table 7-5: Values of the pre-exponential factor and energy of activation for the kinetic constants of the Fischer-Tropsch reaction

Temperature (ºC)	Kinetic parameter			
	Energy activation (kJ/mol)		Pre-exponential factor(mol/h.cm^3.atm)	
232	E	E’	A	A’
	37.348	0	230.43*	1.4967

(*) The pre-exponential factor values depend on each reaction's selectivity, such that ACn=A*SCn, where SCn is the selectivity for the formation of each hydrocarbon.

Figure 7-6 shows the calculated selectivity values for each alkane in the considered range (C1-C30), from **Eqs. (1-2)** to **(7-42).** The Fischer-Tropsch synthesis was performed under temperature and pressure conditions of 232°C and 20 atm, respectively; this was to increase the process's yield. The product obtained at the Fischer-Tropsch reactor outlet consists of a mixture of hydrocarbons with an extensive distribution of molecular weights, ranging from liquefied petroleum gases to waxes through gasoline, naphtha, and diesel (C1-C30). Consequently, the nature and proportion of the products depend on the reactor operating conditions.

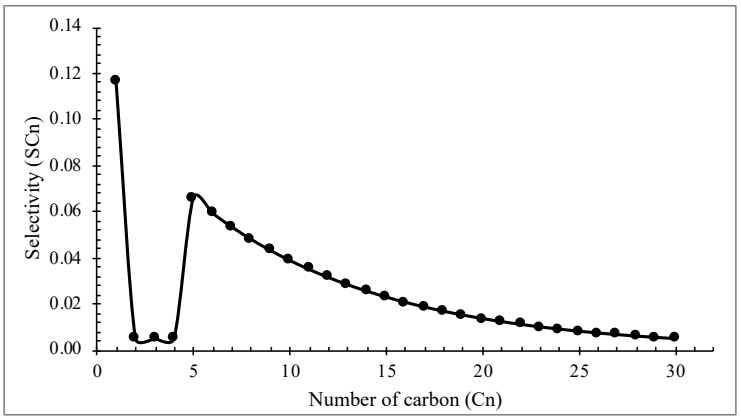

Figure 7-6: The selectivity of the catalytic reaction products of the Fischer Tropsch synthesis.

Product cracking or fractionation zone.

The hydrocarbon mixture obtained in the Fischer-Tropsch reactor is cooled to 50 °C, in order to condense and eliminate water in a three-phase separator. Subsequently, the hydrocarbon mixture is separated by fractional distillation into LGP, gasoline, naphtha, diesel and wax or heavy, based on their different volatilities. The cracking begins with a decrease in pressure to 5 atm and heating of the product to 75 ºC before entering the distillation column. The lower boiling point fraction (<20 ºC), called light gas (LGP), consists mainly of methane, ethane, propane, and butane. The boiling point fraction between 20 ºC and 150 ºC is gasoline composed mainly of a mixture of pentane to undecane (C5-C11). The boiling point fraction between 100 ºC to 200 ºC is naphtha, a mixture of octane to dodecane hydrocarbons (C8-C12). The boiling point fraction between 180 ºC to 380 ºC is diesel (C12-C19). Finally, the heavy ones are composed of a mixture of alkanes with a boiling point above 380 °C.

A pressure drops of 0.2 atm in the distiller was considered, and the reflux rate for fractionation was varied between 0.75 and 1.0. **Table 7-6** summarizes the main operating conditions of the different equipment implemented.

Table 7-6: Main simulation units and their operating conditions

Equipment in Aspen HYSYS®	Operating conditions
Absorber	P=1atm; T=25°C; ΔP=0
Compressor	T=25°C; ΔP=19 atm
Cooler -1	P=20atm; ΔT=-197.6°C; ΔP=0
RFT	P=20atm; T=232,2°C; ΔP=0
Cooler -2	P=20atm; ΔT=-80.1°C; ΔP=0
Separator	P=20atm; T=50°C; ΔP=0
Valve	P=20atm; T=50°C; ΔP=15atm
Heater	P=20atm; ΔT=75°C; ΔP=0
Distiller	P=5atm; ΔP=0.2 atm

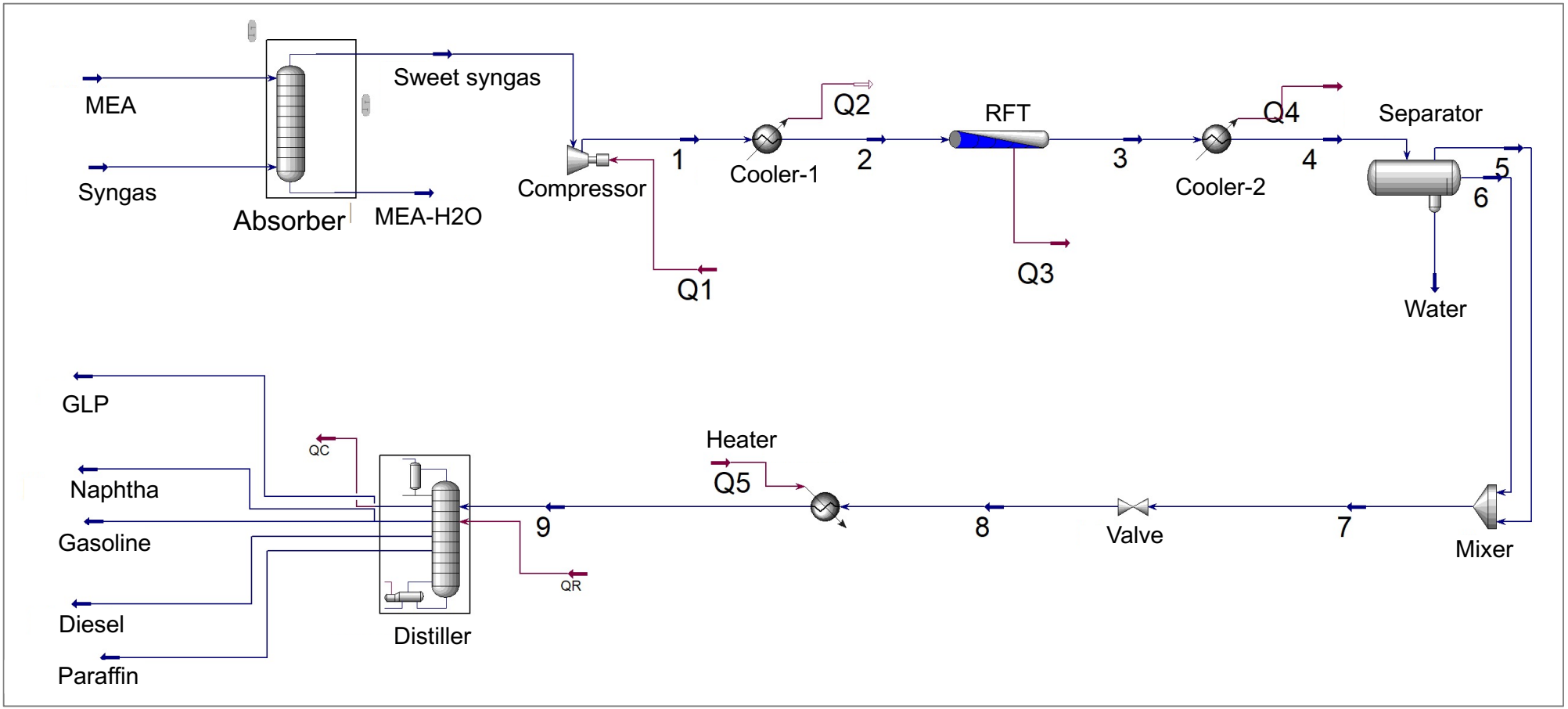

Figure 7-7: Simulation model flowchart with Aspen HYSYS®.

7.3. Discussion of simulation results

7.3.1. Simulation results of HTC process

The compositions and yields of the HTC products of the biomasses (AS, ASB, and CEL) in the reactor developed in the Aspen plus simulator were compared with the experimental data. As mentioned above, parameters such as pressure, temperature evolutions, and residence time were considered when simulating the process in Aspen plus. Intermediates of similar functional groups are grouped to better compare with the experimental data. All hydrolysable cellulose and hemicellulose are considered sucrose, which hydrolyzes completely to form sugars. In this case, dextrose was considered total sugar, furfural, and 5-HMF, grouped as FUR+HMF, organic acids (formic, acetic, and lactic) grouped as ACIDS gaseous compounds are grouped into GAS. Partial depolymerization of lignin is considered below. Therefore, it has not been taken into account in the simulation. The non-hydrolyzed fraction of cellulose, hemicellulose and lignin undergoes a solid-solid reaction, forming the primary hydrochar. The successive polymerization of furfural and 5-HMF becomes the final product known as secondary hydrochar. In this case, it was considered that the intermediate product of the polymerization of furfural and 5-HMF is furan. This consideration was made to facilitate the kinetics of the formation of secondary hydrochar since the secondary hydrochar does not have a well-defined structure. The unidentified fraction in the experimental liquid phase was not considered because products such as methyl-acetoacetate formed by the dehydration of dextrose to formic acid and levulinic acid as a product of the transformation of furfural to formic acid were not used in the validation of the results.

Figure 8 shows the validation of the results with experimental data. The mass yield is represented by the total mass of each component inside the reactor in the mass of biomass feed to the reactor on a dry basis (g of components/kg of biomass feed to the reactor). The simulation data reproduces reasonably well the experimental data. The slight difference between the simulation and experimental results is observed in the total solids yield at 230°C and above; this is because the polymerization reactions under consideration (from furfural and 5-HMF) are insufficient to form all the secondary hydrochar produced during the process. Therefore, one must consider other intermediates that can polymerize to form the secondary hydrochar. This result is not surprising since these compounds in the liquid phase that can polymerize to form this secondary hydrochar were not taken into account. Due to difficulties in identifying and quantifying each intermediate component, it was taken into account only the intermediate's

stable products in the liquid phase. In addition, a slight difference is observed in the formation of total acids; this is perhaps due to the kinetics of the reaction since it was considered that the formation of the three acids (formic, acetic, and lactic) has the same kinetics. However, this model is an approximation to carry out the simulation and optimization of the batch HTC process to an accurate industrial-scale continue system.

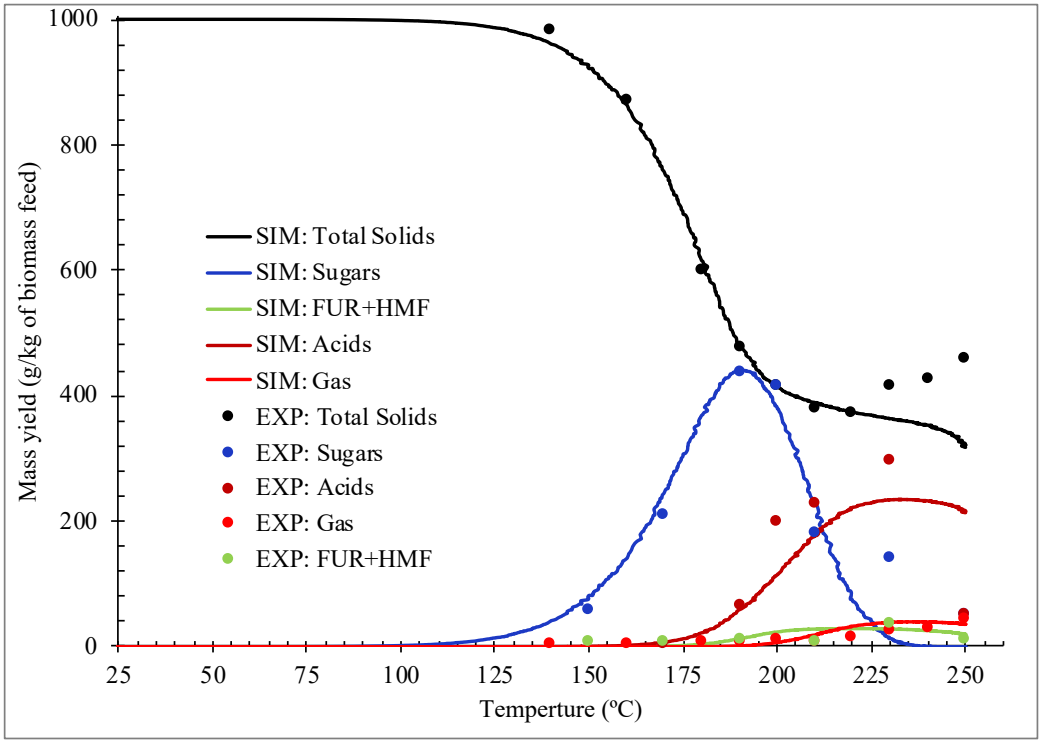

Figure 8. Simulated (continuous curves) and experimental (discrete points) concentration evolutions of biomasses during HTC process of AS.

7.3.2. Simulation results of the gasification process

The results and discussions are presented in this part, and the results are validated for each of the biomass (ASB, CS, and AS) by experimental data. In addition, the effect of the air/biomass ratio on the gas composition is also presented, based on an analyzed sensitivity; the results have been compared to the experimental data for ASB.

7.3.2.1. *Validation of the simulation result*

The input data to the Aspen Plus simulator were the experimental data, such as elemental analysis, immediate analysis, HHV of the raw biomasses, and the experimental results of the pyrolysis of the biomasses. The results obtained for the composition of the syngas (H_2, CO, CO_2, and CH_4) in the gasifier outlet were compared with experimental data obtained in the

laboratory for each biomass. The results are presented in **Figure 7-9** to **Figure 7-11**. These results correspond to the air/biomass mass ratio ABR=0.1875. The evolution of each gas during the pyro-gasification of biomass was detailed in **Chapter 4**.

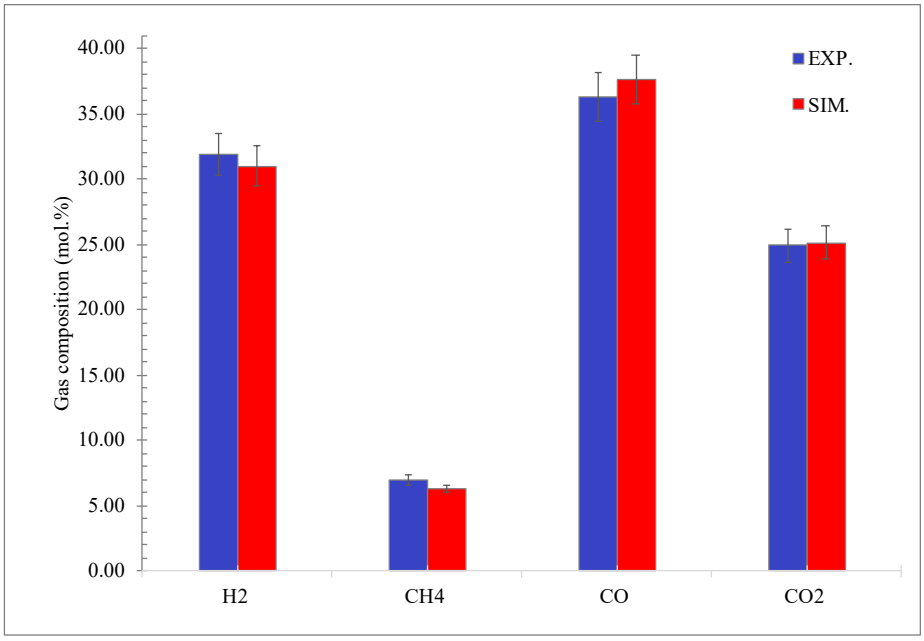

Figure 7-9: Comparison between simulation and experimental results for ASB.

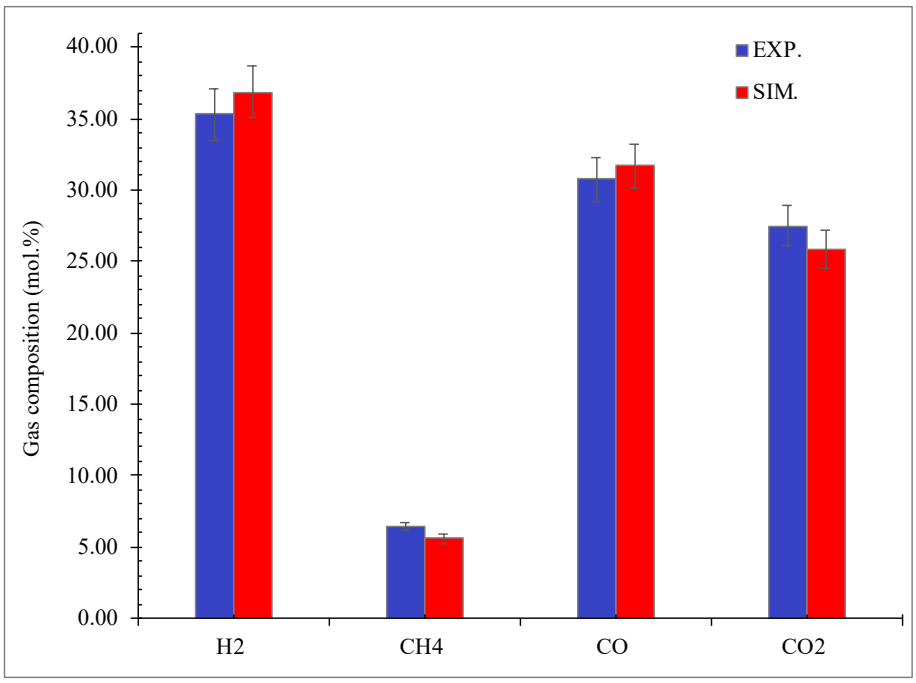

Figure 7-10: Comparison between simulation and experimental results for CS.

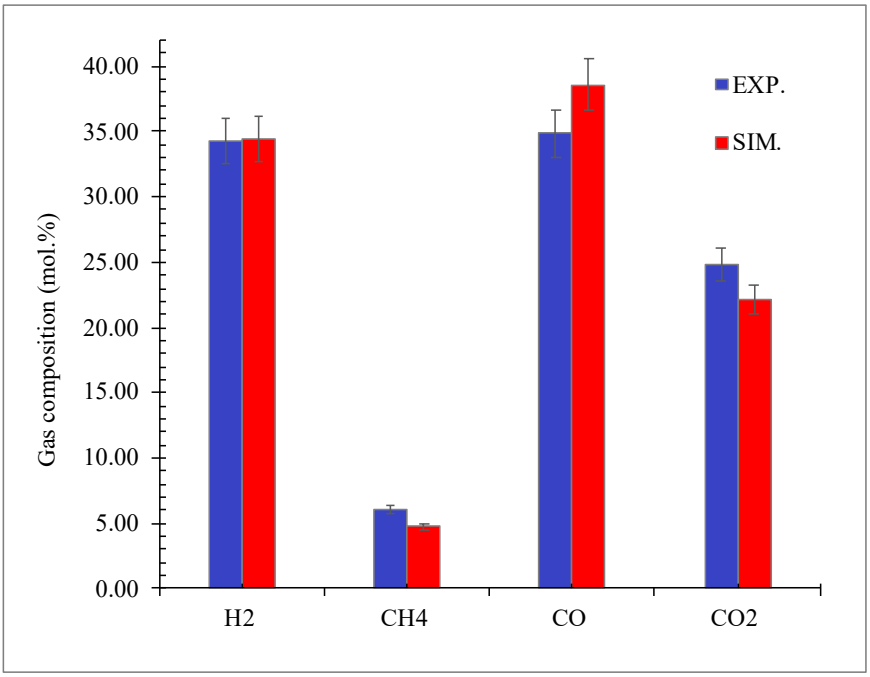

Figure 7-11: Comparison between simulation and experimental results for AS.

In general, the simulation results agree better with the experimental data. However, for all biomass simulations, a slight difference in CO and CO_2 composition is observed compared to the experimental data. That is, the molar concentrations of CO are higher than the experimental data. The CO_2 concentration is lower than the experimental data for CS and AS. The variations observed can be associated with the complexity of the process to be described and the eventual variations in the chemical reactions considered. To simplify the simulations, only the nine most essential reactions of the gasification process were considered. However, there may be other reactions for the formation of CO_2, which were not considered. In addition, the simulation temperature is more controlled than the experimental temperature since any temperature variation can influence the different chemical reactions, thus the compositions of the gas products. For example, increasing the temperature of the gasifier accelerates the reaction rate of the char and gases, i.e., the rate of the reactions **Eqs.(7-21)** to **(7-24)**. The concentration of CO and CO_2 differ depending on the reaction **Eq. (7-26)**; this is an exothermic reaction. Increasing the temperature will cause the reaction to shift in the opposite direction, i.e., increasing CO and decreasing CO_2. As can be observed in **Figure 7-9** to **Figure 7-11**, statically, the values obtained in the Aspen Plus simulator are similar to the experimental data. The most significant difference observed was 3.77 mol.% CO of AS. Once the simulation results have

been validated, sensitivity studies can be carried out to study the influence of different operating variables on the model results. In this work, the effect of the residence time inside the reactor and the air/biomass mass ratio was studied.

7.3.2.2. *Effect of air/biomass ratio during the gasification process.*

The gasifying agent is one of the most influential factors in the biomass gasification process. In order to study its effect, simulations were performed using an air/biomass mass ratio from 0.1 to 2, at a residence time inside the reactor of 15 s.

Figure 7-11 shows the composition of the gasification product as a function of ABR in some cases known with equivalence ratio (equivalence ratio refers to stoichiometric ratio or air/biomass molar ratio). In the gasification process, the results show that the product composition is highly dependent on the amount of oxidant, referred to here as the air/biomass mass ratio. The significant influence of this ratio has to do with the main products of gasification with air (CO and CO_2). The amount of CO_2 and CO is considered an indicator of stoichiometry or reference points for the ABR or equivalence ratio (ER). In the combustion theory, complete combustion occurs at an equivalence ratio equal to 1, so that most of the carbon in the biomass is oxidized to provide the maximum CO_2 with products (Jangsawang et al., 2015). As the amount of oxygen decreases, the fuel-air mixture will become fuel-rich (ER>1) because CO_2 decreases, and at the same time, CO increases. Thus, there is a direct relationship between ABR and ER, but it depends on the type of biomass, in this case, ER=1.096ABR. The simulation result shows that there is a crossover point between CO_2 and CO. This point is the so-called carbon limit point, at which the fuel reacts exactly with enough oxygen for gasification to be complete and no solid carbon formation occurs (Prins, 2005) and is referred to here as the optimal equivalence ratio for the gasification process. As indicated by the results, CO_2 is produced at the equivalence ratio below the crossover point. This implies that there is an excess of gasifying agents present in the gasification process.

In general, increased airflow increases CO_2 production; this is because an increase in oxygen content favors total oxidations reactions **Eq.(7-21)** and **Eq.(7-27).**

As can be seen in **Figure 7-11**, two distinct regions can be observed. A first region of ABR between 0.1 and 0.75, where CO_2 production remains practically constant between 25-29 mol.%; and the second region corresponds to ABR between 0.75 and 2; in this region the effect

of the total oxidation reactions is clearly observed. In the first region 0.1<ABR<0.75 the ratio is dominated by partial oxidation, i.e., the formation of CO.

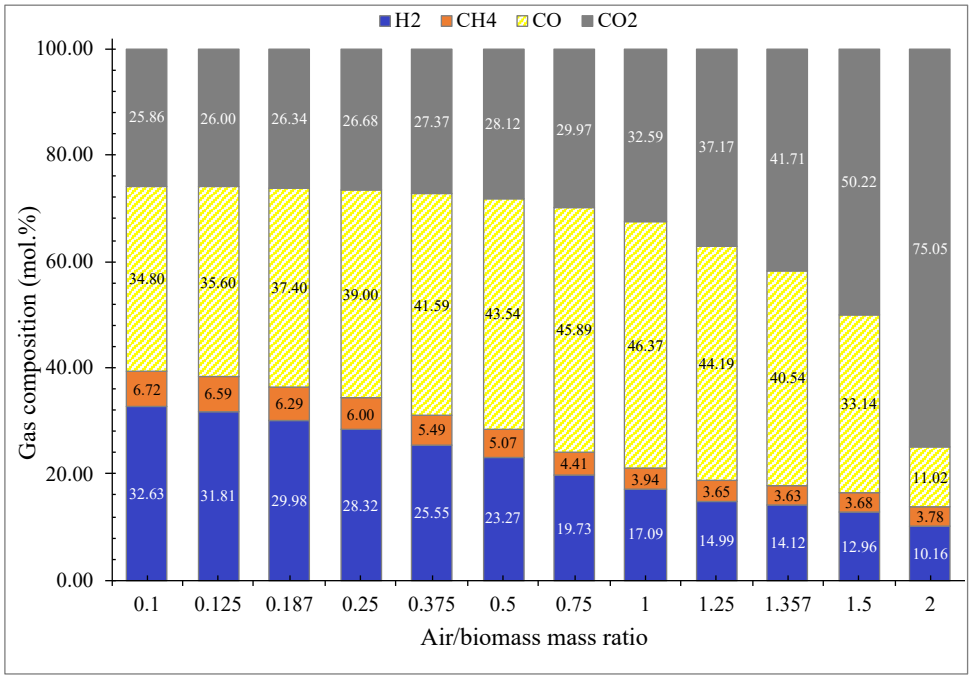

Figure 7-12: Effect of air/biomass ratio during the ASB gasification for residence time 15s.

In this region a large increase in CO concentration is observed from 34 to 46 mol.% of total gases analyzed. However, from ABR=0.1, the CO concentration starts to decrease because the CO produced is being consumed by the reaction **Eq.(7-27).** due to the high concentration of oxygen inside the reactor. Furthermore, it is observed that H_2 production decreases with increasing ABR. This is due to reaction **Eq.(7-24)**, where the hydrogen produced is being consumed for CH_4. For ABR>1, the amount of CO produced is practically due to pyrolysis, since in this condition, CO production is non-existent during gasification. The above simulations allow for establishing the operating conditions that maximize the quality of the syngas and the efficiency of the gasification process.

7.3.2.3. *Effect of residence time in the gasifier*

The residence time or reactor volume influences the composition of the gas produced during biomass gasification. A longer residence time will give the reactions more time to reach equilibrium. Increasing the residence time is necessary to increase the reactor volume or reduce the reactor inlet flow. **Figure 7-13** shows the composition of the gas produced at different residence times inside the gasifier.

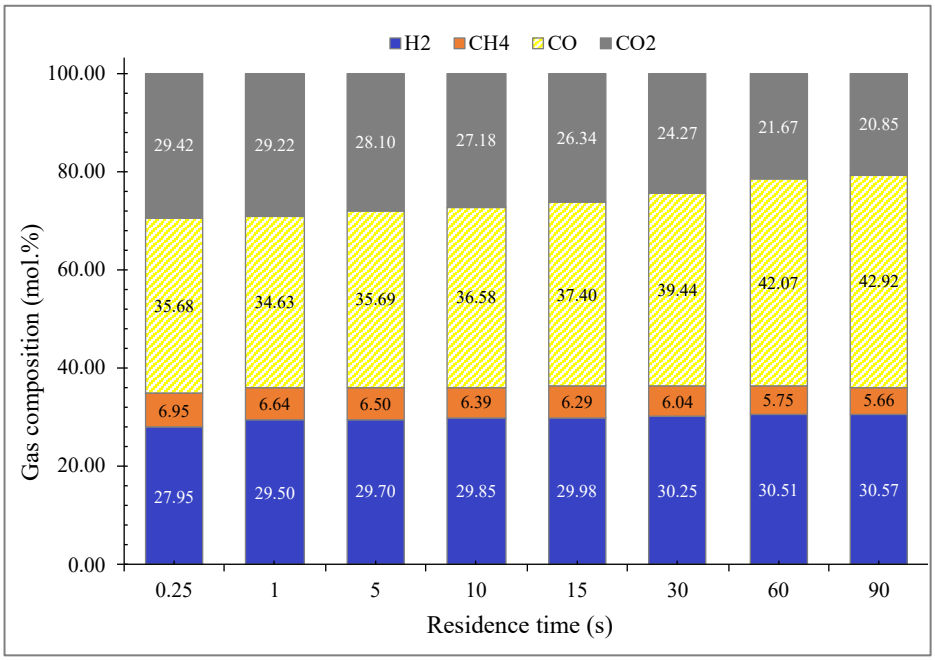

Figure 7-13: Effect of residence time during the ASB gasification for ABR=0.187.

As can be seen, the H_2 concentration increases with increasing residence time. Longer residence time is an essential parameter for H_2 production because it depends on the hydrodynamic characteristics of the reactor, such as length and minimum fluidization rate. Therefore, with increasing reactor length, a longer residence time is required to complete the conversion of char and tar (Ling et al., 2016). Furthermore, the longer the residence time, the endothermic reactions involved, such as water–gas-shift reactions, improves.

7.3.3. Simulation results of Fischer-Tropsch synthesis

The Fischer-Tropsch (FT) reaction products are hydrocarbons of different lengths, more considerable amount of water. FT synthesis has a high selectivity towards liquid, which is necessary to obtain a maximum amount of long-chain (C5+) hydrocarbons. The FT reaction is not selective towards a single reaction product, except for methane or molecules of a narrow range of carbon atoms in some operating conditions (usually based on the iron catalyst and high temperature). Typically, for an FT synthesis reaction, the product range is from low molecular weight gaseous products to heavy waxes (paraffin) with a very high molecular weight. The hydrocarbon mixture formed is mainly composed of linear alkanes depending on the operating condition. The range of products obtained by the Fischer-Tropsch process simulation was divided into five groups: GLP (C1-C4), gasoline (C5-C11), naphtha (C8-C12),

diesel (C12-C19), and paraffin (C19+); to facilitate their analysis. The results at the end of the fractionation of the product are shown in **Figure 7-14**.

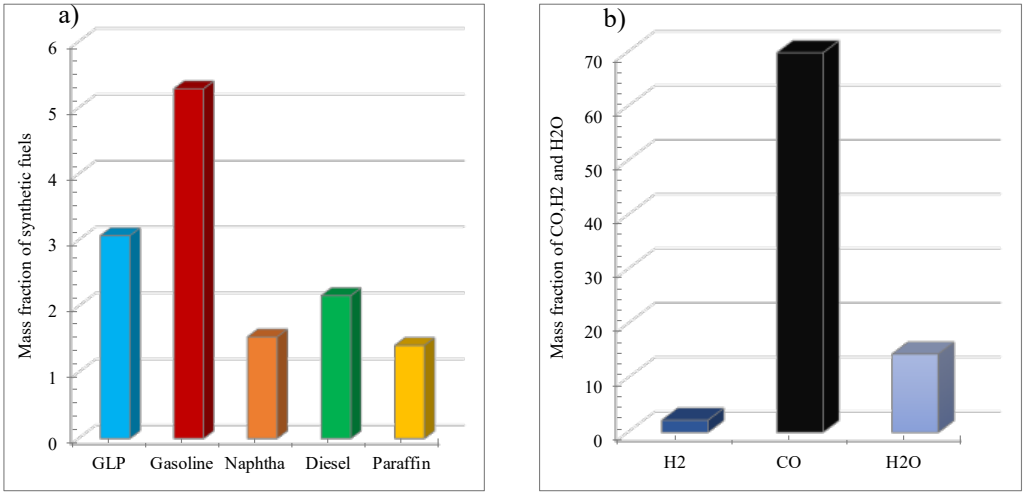

Figure 7-14: Synthetic fuels obtained in the Fischer Tropsch reactor for H_2/CO =0.88: a) main products and b) CO, H_2 unreacted and H_2O product.

The results presented in **Figure 7-14**.are obtained from the experimental results of the ASB gasification with air, where the H_2/CO molar ratio is 0.88. As can be seen in **Figure 7-14b**., almost 65% of CO entering the reactor is unreacted. Therefore, biomass gasification with air is not ideal for Fischer-Tropsch synthesis because the ratio of syngas (H_2/CO) is insufficient to obtain a high yield of the FT process.

In addition, the kinetics proposed for the simulation is based on a high H_2/CO ratio. However, the H_2/CO ratio obtained experimentally may be favorable to the formation of other synthetic hydrocarbons, such as oxygenated hydrocarbons. Therefore, kinetics should be made based on the low H_2/CO. The alternative to increasing the H_2/CO ratio may be vapor gasification, i.e., using steam as the gasifying agent instead of air; although this alternative may increase the process's total cost, a high concentration of H_2 is contained during gasification.

7.3.3.1. *Effect of H_2/CO ratio on product selectivity.*

Relatively high H_2 concentrations in the syngas promote chain termination, while higher CO concentrations increase chain propagation. Consequently, the probability of chain growth and product distribution will depend on the H_2/CO molar ratio. The H_2/CO ratio has a strong influence on the final product of the Fischer-Tropsch synthesis. As can be seen in Figure 5, the

formation of synthetic fuels increases with increasing H_2/CO ratio until an optimum point is reached, then it decreases. The optimum point of production of synthetic fuels is obtained around H_2/CO =2.5.

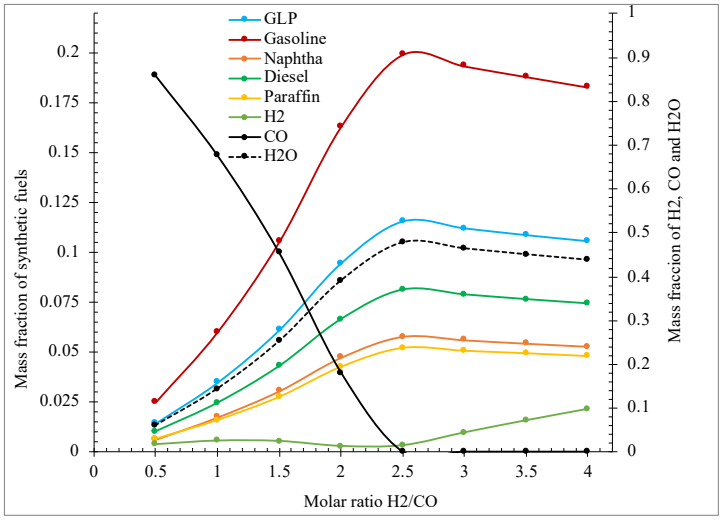

Figure 7-15: Effect of H_2/CO ratio on synthetic fuels product

For a molar ratio of H_2/CO <2.3, not all CO reacts, so fuel production is low. However, for H_2/CO>2.5, the H_2 concentration is in excess. **Figure 7-16** shows the ideal condition for the production of synthetic fuels (H_2/CO ratio). In this case all CO reacts and more than 97 % of H_2 entering the RFT reacts.

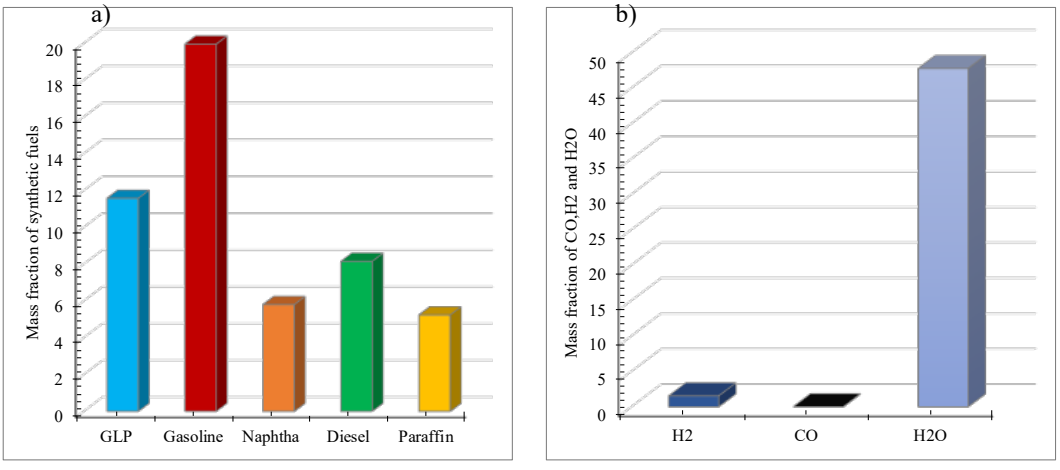

Figure 7-16: Synthetic fuels obtained in the Fischer Tropsch reactor for H_2/CO =2.5: a) main products and b) CO, H_2 unreacted and H_2O product.

The distribution of the products obtained from this simulation is as follows: GLP represents 11.57%; gasoline one 19.96% and represents the most significant fraction of the product

obtained. The yield to gasoline is approximately 39.35% of the synthetic fuels produced. It should be noted that the water content represents 47.76% of the total product, therefore, the fractionation of the products must be eliminated beforehand. As shown in **Figure 7-16**, in addition to gasoline and gases, the most produced product is diesel, representing 8.15 % of total product, followed by naphtha and paraffin, representing 5.80 and 5.23%, respectively.

The general distribution of the products was determined by the chain propagation factor (rp) and the chain termination factor (rt). For the ideal regime of Fischer-Tropsch synthesis, the product distribution can be predicted by a statistical model, with the chain growth probability factor α, where α=rp/(rp+rt). This model is known as Anderson-Schulz-Flory (ASF). A high propagation factor will lead to a distribution of high molecular weight products, whereas a low chain termination factor leads predominantly to light molecules. The ASF model assumes that the chain growth and termination factors are constant for all numbers of carbon atoms (Schulz et al., 1988). However, in the analyses of this result, a large production of LGP is observed; therefore, the product distributions favor the probability of C_1 and C_4 formation. Although LGP account for 22.82% of total hydrocarbons produced, CH_4 alone accounts for more than 73% of total gas. Therefore, the Fischer-Tropsch synthesis reaction can be selective towards CH_4 at elevated temperature conditions because the reactions are highly exothermic.

Also, it should be remembered that the distribution of the products obtained from Fischer-Tropsch synthesis depends on the type of catalyst used. According to many (González Carballo, 2012; Rojas et al., 2011), the most active catalysts in Fischer-Tropsch synthesis are Ru >Ni>Co> Fe. Due to the high price of Ru and Ni, only Fe and Co catalysts are used industrially. Besides being active in the hydrogenation of CO to hydrocarbons, Fe catalysts catalyze the water-gas shift (WGS) reaction, i.e., they are active in the reaction between H_2O and CO to originate H_2 and CO_2. This characteristic makes them mainly used to adjust the H_2/CO ratio in those processes with H_2-poor synthesis gas, i.e., in coal-to-liquid (CTL) and biomass-to-liquid (BTL) processes with high elemental carbon content, which generates a synthesis gas with an H_2/CO ratio close to 1. Fe can be an alternative to increase the H_2 content in the synthesis gas obtained in this work. On the other hand, Co catalysts are used in plants with a synthesis gas having an H_2/CO ratio close to 2.5.

The Fischer-Tropsch synthesis produces a mixture of linear hydrocarbons of high molecular weight and high purity that can have various applications: pharmaceuticals, cosmetics, so on. However, this market is limited and easily saturable. In addition, some of the paraffin obtained

can be used as lubricants. However, the main application of Fischer-Tropsch synthesis products is to obtain synthetic fuels such as gasoline, naphtha, and diesel.

The paraffinic chains of the (C19+) obtained can be transformed into shorter lengths using a hydrocracking process, thus originating a mixture of lighter hydrocarbons whose boiling point is similar to that of petroleum distillates. A distillation process can separate this mixture into different linear fractions, as mentioned above. The linear hydrocarbons obtained in the C13-C18 fraction are excellent for diesel fuel because they have a high cetane number, around 75 (when the minimum requirements are 45-50) (Dry, 2004). Furthermore, these synthetic fuels are of high quality since they are free of aromatic, nitrogenous, and sulfur compounds. For this reason, they can also be blended with other fuels of lower quality to improve the latter's characteristics (Sousa-Aguiar et al., 2005). The diesel fuel obtained from Fischer Tropsch synthesis using synthesis gas produced from biomass (typically lignocellulosic material) is second-generation biodiesel called synthetic biodiesel.

The ideal gasoline consists of a mixture of C5-C12 alkanes with a high level of branching. It must meet several conditions, some for good engine performance and others for environmental reasons, both regulated by law in most countries. The most typical specification is the octane rating. The octane number or, popularly, octane rating indicates the pressure and temperature to which a carbureted fuel mixed with air can be subjected before self-detonating when reaching its ignition temperature due to the ideal gas law.

Naphtha is usually considered the gasoline fraction with a boiling point between 100 to 200°C, mainly C8-C13. It is subdivided into light naphtha (boiling point close to 100°C) and heavy naphtha (the rest). Light naphtha is one of the components of gasoline, with an octane number around 70. However, heavy naphtha is not of sufficient quality to be used for this purpose.

In general, the fuel obtained by the Fischer-Tropsch synthesis process can have superior characteristics to the fuel obtained from petroleum distillate. Among other properties, the fuel produced by Fischer-Tropsch synthesis is clean since it has no aromatic compounds or heteroatoms such as N or S in its formulation, so the emission of NOx and SOx during combustion is low (Dry, 2002).

7.4. Conclusion

- The simulation model developed with Aspen Plus® reproduces reasonably well the experimental results of all biomasses studied. Furthermore, the values obtained in the simulations and the experimental data show good agreement in composition (mole fraction of H_2, CO, CO_2, and CH_4). According to the results obtained in the simulations, the air/biomass ratio and the residence time are variables that significantly influence the biomass gasification process. Thus, the higher the air/biomass ratio, the higher the CO_2 production; however, a lower air/biomass ratio may cause the char not to react. Therefore, a compromise between CO and CO_2 production must be found to produce syngas with high energy quality. The better air/biomass ratio is between 0.18 and 0.5. It was also found that H_2 and CO yield increases with increasing residence time.
- This simulation in Aspen HYSYS® approximates the number of hydrocarbons that can be produced. The hydrocarbons and the water obtained in the Fischer-Tropsch synthesis, once separated, can be used for energy production. According to the results obtained, it is worth highlighting the great usefulness of the simulation process of synthetic fuel production from biomass. Simulation facilitates the understanding of this complex process and reproduces the behavior of the system efficiently. Furthermore, the flexibility of the Aspen Plus® and Aspen HYSYS® simulators allows the system to be adapted to different variables and operating conditions, such as temperature, pressure, flow rates, and feed compositions. In addition, these simulators can estimate the composition of the products obtained and help in the optimization of the operating conditions.

Chapter8 ENERGY BALANCE

The real challenge of any thermochemical biomass-to-energy conversion process is the energy balance; because each stage of the process requires energy consumption, from pretreatment to final energy production. The heterogeneity of the biomass and its intended application determine the treatment required for its use. Pretreatment processes for thermochemical conversion of biomass are generally: drying (natural or forced convection), chipping (shredding or grinding), densification (pellets, briquettes, and baling). For biomass with great moisture content, hydrothermal carbonization (HTC) could be a better option. HTC is a method of thermochemical conversion by which wet biomass is heated in a batch autoclave reactor to temperatures from 180 °C to 250 °C, under autogenous pressure of saturated vapor from 1 to 4 MPa and reaction time or holding time from a few minutes to various hours (Liu and Balasubramanian, 2012; Missaoui et al., 2017). Most of the literature studies evaluate the HTC process's performance based on the energy yield, which includes two criteria: the hydrochar mass yield and the hydrochar energy densification ratio. However, little information is available on the energy balance of the HTC process to show the energy advantage of processing high-moisture biomass by HTC. Since the hydrothermal treatment process does not require drying, the energy required for the process is low (Escala et al., 2013; Xue et al., 2015).

The absence of the drying stage allows the HTC process to consume less energy than dry thermochemical processes to treat wet biomass (Lucian and Fiori, 2017). Recently, HTC has attracted a great deal of research interest. Although a large body of laboratory-level experimental research on the HTC process has been published, there are only a few scientific studies in the literature evaluating the technical potential performance of industrial HTC facilities. Although pilot HTC plants have been constructed in recent years (Burguete et al., 2016; Hitzl et al., 2015), the detailed structure of such plants and their efficiency remains unknown to the vast majority of HTC process researchers. Furthermore, only a few authors have used a modeling approach to analyze the energy efficiency of HTC plants (Lucian and Fiori, 2017; Stemann et al., 2013a; Stemann and Ziegler, 2011). According to Benavente et al. (2015), depending on the operating conditions, the gain in energy consumption of treating wet biomass (70%) by HTC can reach 57% compared to its treatment by torrefaction. On the other hand, Lucian and Fiori (2017) reported that the temperature of 220 °C and the residence time of 1 h is the most suitable conditions for HTC of

residual biomass (grape marc). For that condition, the authors reported that the plant efficiency was 78%, with a specific thermal energy consumption of 1.17 kWh per kilogram of hydrochar and specific electrical consumption of 0.16 kWh per kilogram of hydrochar. However, in the literature, most of the studies are focus on evaluating the energy consumption of the HTC process but without establishing the energy balance of the HTC conversion of biomass. Moreover, the energy consumption of the HTC liquid treatment process for reuse has not been studied comprehensively (Benavente et al., 2015; Yan et al., 2017).Therefore, this chapter aims to estimate the energy balance of the HTC process globally to identify the most influential parameters in this balance. This chapiter consists of two parts: (1) breakdown of the process into unit operations and energy balances, and (2) results of the HTC process energy balance calculations of the four biomasses using in this study.

8.1. Materials and methodology

The solid or hydrochar yield and gas yield was calculated by taking the ratio between the weight of solid and liquid in the final product and the initial weight of the biomass. The liquid yield was calculated by difference.

8.1.1. Design of the current HTC process at laboratory scale.

Figure 8-1 shows the flow diagram of a design of the current HTC process at laboratory scale. First, the biomass (BIOMASS) is mixed with water (WATER) in different proportions; the mixture enters the reactor (HTC-REAC). The reactor is heated by electric power (QHTC-REC) until the set temperature is reached. The temperature is maintained until the desired holding time is obtained. Subsequently, the reactor is cooled with water to room temperature (COOLER), the valve is opened to recover the gas (HTC-GAS). The mixture of hydrochar and liquid is separated in a filter (FILTER), the wet hydrochar (Wet-HC) is dried in an oven at 105 ºC (DRYER) to remove all the moisture from hydrochar with (QDR); this hydrochar, it is further characterized.

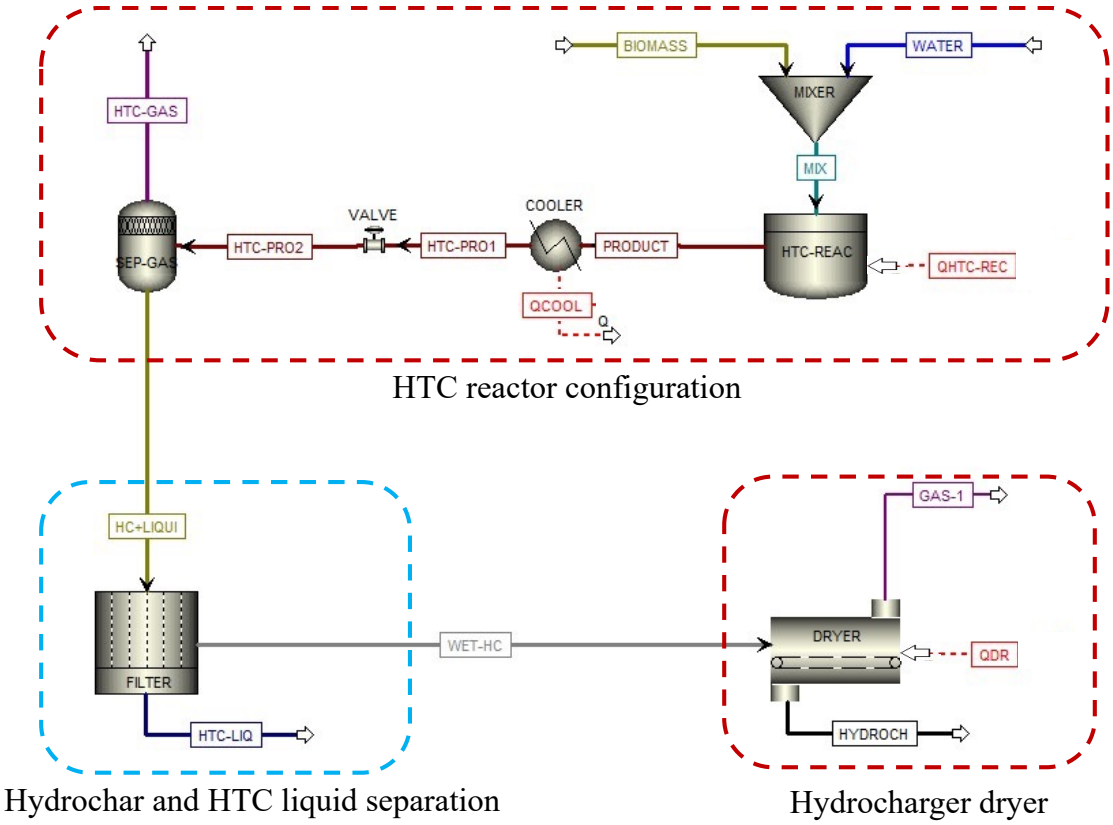

Figure 8-1: Schematic flowsheet of the HTC process at laboratory scale

8.1.1.1. *Energy consumption of the HTC process in laboratory*

Two fundamental parts characterize the higher energy consumption. The electrical energy consumed to heat the reactor and the energy required for drying hydrochar. The electrical power consumption to heat the reactor depends on the operating condition (heating time and holding time). The energy consumption for heating the HTC system includes (1) the energy employed to heat the water and (2) the energy consumed to heat the dry biomass from room temperature to the set point temperature, (3) Energy used to heat the reactor walls, and (4) the energy loss. Based on the experimental data, holding time energy consumption was not considered since once the setpoint temperature was reached, the reactor was immediately cooled down to room temperature. For this study, a completely isolated system is considered, so heat loss was not considered. The energy consumed to heat the reactor wall depends on its nature, which complicates its evaluation and, consequently, the estimation of the energy balance of the HTC process. In addition, the HTC autoclave reactors used in the laboratory require more energy to heat the reactor walls than heating

the biomass-water mixture. This part of the study only demonstrates energy consumption to evaluate the energy balance in the laboratory of the HTC process. For an industrial scale HTC process, the heating of the reactor walls may be negligible. The energy consumed to heat the reactor ($Q_{HTC\text{-}REC}$) can be estimated from **Eq. (8-1)**.

$$Q_{HTC-REC} = m_w \left[\int_{T_0}^{T_1} Cp_{H2O}(T) \cdot dT\right] + m_b \left[\int_{T_0}^{T_1} Cp_b(T) \cdot dT\right] + m_r \left[\int_{T_0}^{T_1} Cp_r(T) \cdot dT\right] \quad (8\text{-}1)$$

where, m_w (kg) is the mass of the water contained in the HTC reactor, m_b (kg) is the mass of dry biomass; m_r (kg) is the mass of reactor; Cp_{H2O} (T) is the heat capacity of water as a function of temperature (kJ/kg.K); Cp_b is the heat capacity of biomass (kJ/kg.K); Cp_r is the heat capacity of reactor (kJ/kg.K); T_0 is the initial temperature equal to 25°C; T_1 is the set point temperature (K).

The energy consumed to dry the hydrochar depends on the moisture content after filtration. At the reactor outlet, the high hydrophobicity of hydrochar facilitates its separation from the liquid phase with simple filtration diminishing energy consumption (Benavente et al., 2015; Parshetti et al., 2013). Therefore, the energy consumption of the drying stage includes (1) the energy consumed to heat the dry hydrochar and the water from the wet hydrochar moisture, and (2) the enthalpy needed to water vaporization **(Eq. (8-2)).**

$$Q_{DR} = m_1 \left[\int_{T_0}^{T2} Cp_{H2O}(T) \cdot dT + \Delta H_{vap}\right] + m_2 \left[\int_{T_0}^{T2} Cp_{hydro}(T) \cdot dT\right] \quad (8\text{-}2)$$

where, m_1 is the mass (kg) of the water contained in the wet hydrochar, m_2 is the mass (kg) of dry hydrochar; Cp_{H2O} (T) is the heat capacity of water as a function of temperature (kJ/kg.K); Cp_{hydro} is the heat capacity of hydrochar (kJ/kg.K); ΔH_{vap} is the enthalpy of water vaporization at 1 atm (2257 kJ/kg); T2 is the boiling temperature of water.

After filtration, the moisture content depends on the type of initial biomass and the conditions of hydrochar production (temperature and holding time). For example, for avocado stone (AS), hydrochar produced between 220 and 250 ºC has a moisture content of 35 to 50% for a filtration time of 5 minutes, while hydrochar produced between 180 and 220 °C has a moisture content of 50-65% after the same filtration period. This is because hydrochar produced at high temperatures increases its hydrophobicity and increases the pore size inside the particle, thus facilitating filtration.

8.1.1.2. *Usable energy from hydrochar*

As a hypothesis, it is considered that usable energy is obtained by the direct combustion of hydrochar, as the main HTC product. In this part, the HTC liquid and gas phases are not considered. The energy obtained from hydrochar (Q_{HC}) is calculated by **Eq.(8-3)**:

$$Q_{HC} = m_{HC} \cdot HHV_{HC} \quad (8\text{-}3)$$

where m_{HC} is the mass of hydrochar (kg) and HHV_{HC} is the heating value (kJ/kg) of the hydrochar.

8.1.1.3. *Carry out of HTC experiments*

The biomass used for these experiments was avocado stone (AS). The reactor described in Chapter 3 (300 ml inner volume reactor) was used. In addition, four biomasses to water ratios (1/4, 1/6, 1/8, and 1/10) were used to evaluate the effects of the biomass to water ratio on energy consumption. The protocol followed to realize the HTC experiments is described in **section 4.2.1.2** of **Chapter 4**. The wet hydrochars were dried at 105°C in the oven, and their HHV was measured. For this study, a power of 200 W was used to heat the reactor to 210, 230, and 250 °C. Once the temperature was reached, the reactor was immediately cooled down to room temperature.

8.1.2. Energy balance of the HTC process at laboratory scale

The energy balance (Q_R) was calculated from the difference between the energy in the hydrochar and the energy used to produce hydrochar.

$$Q_R = Q_{HC} - Q_U \quad (8\text{-}4)$$

$$Q_U = Q_{HTC-REC} + Q_{DR} \quad (8\text{-}5)$$

8.2. Results and discussion

8.2.1. Energy balance results of the HTC process at laboratory scale

The energy balance calculations for the AS HTC process at different HTC temperatures and different biomass to water ratio are presented in **Table 8-1**. For HTC conditions at laboratory scale,

where the biomass water ratio equals 1/10 and 1/8, the results show that the energy balance is negative. This result shows that the usable energy of the HTC products from GAS does not cover the energy consumption of the HTC process. The enormous energy consumption in all HTC conditions is due to the energy used to heat the reactor walls; this energy represents between 72.47 to 83.57% of the total energy consumption to heat the reactor. However, despite the large energy consumption for heating the reactor walls of the HTC reactor, for a biomass water ratio of 1/6 and 1/4, the energy balance is positive from 230 ºC for biomass water ratio equal to 1/6 and from 210 ºC for biomass water ratio equal to 1/4 as shown in

Table 8-1 : Energy balance of the AS HTC process in the laboratory.

	Energy balance (kJ)								
	210 ºC			230 ºC			250 ºC		
	Q_U	Q_{HC}	**Q_R**	Q_U	Q_{HC}	**Q_R**	Q_U	Q_{HC}	**Q_R**
1/10	316.50	150.15	-166.35	362.16	198.98	-163.18	405.73	234.86	-170.87
1/8	323.49	203.24	-120.25	366.79	267.56	-99.23	410.62	302.71	-107.91
1/6	342.04	327.81	-14.22	379.51	427.20	**47.70**	424.11	485.24	**61.14**
1/4	364.03	472.01	**107.98**	394.22	611.51	**217.29**	443.92	751.03	**307.10**

Furthermore, it is important to remember that the autoclave reactors used at laboratory scale are not representative of an industrial scale reactor, as the energy consumption for heating the reactor walls may be negligible. By not considering this large energy consumption, the overall energy balance is positive.

Use of equations detailed above allows us to theoretically estimate the energy consumed (QU) and energy produced for hydrochar (QHC) as a function of the water/biomass ratio. **Figure 8-2** shows their evolution as a function of the AS/water mass ratio. **Chapter 4** showed that the increase of the water/biomass ratio has a positive effect on the mass yield. Moreover, the heating value of hydrochar increases with an increase of the biomass/water ratio. As a consequence, hydrochar produced at high biomass to water ratio has high energy content; this is ideal for an industrial-scale

process since the process liquid would be shallow, hence easy to treat in addition to high yields of hydrochar with high energy content. There are different strategies to increase the energy balance further. One strategy is to recover the energy used to heat the reactor during reactor cooling. This recovered energy can preheat the biomass/water mixture before entering the reactor; it can significantly decrease energy consumption. In addition, the recovered energy can be used to dry the hydrochar after the filtration stage.

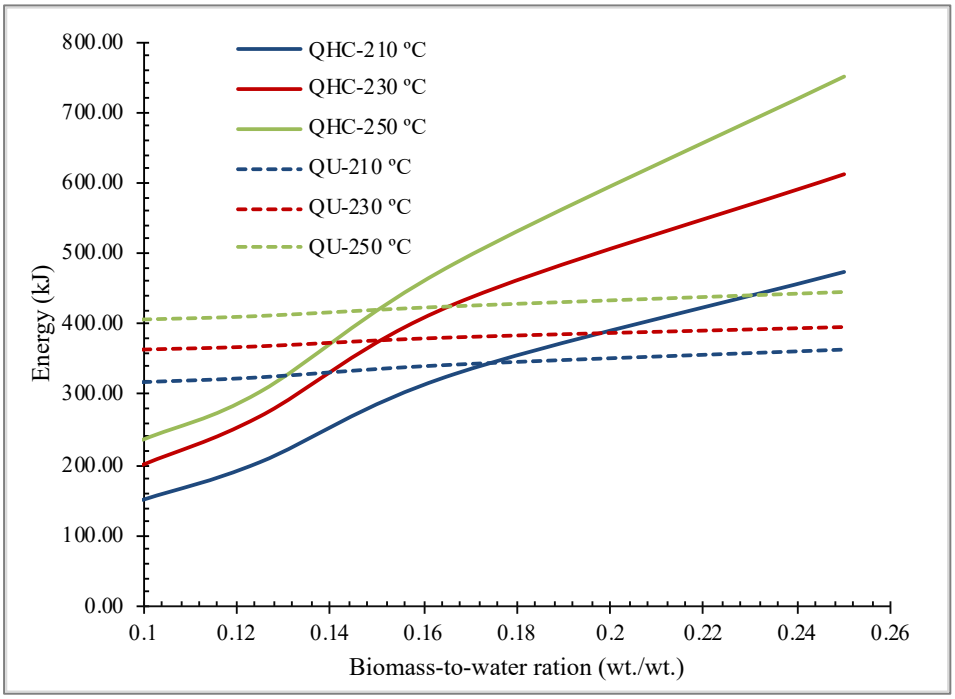

Figure 8-2: Estimated hydrochar energy (QHC) and energy consumed (QU) as a function of biomass/water ratio

8.3. Plant design of the HTC process at industrial scale

8.3.1. Process modelling and simulation

In this part, a conceptual design of the HTC process is proposed, where the energy used to heat the HTC reactor during its cooldown is recovered. Also, it was submitted to valorize the HTC liquid through anaerobic digestion. The HTC plant was considered to have an approximate operating time of 8000 hours/year and capacity of 20,000 tons/year (2500 kg/h) of biomass (AS) with a moisture content of 65%. The plant flow diagram is shown in **Figure 8-3**. The biomass (BIOMASS) is first mixed with recycled HTC liquid (14) and water to form a pumpable slurry (1)

with a solids content around 20%wt. and then reheated with a heat exchanger (P-HEATER) by heat recovered at different temperatures during cooling and depressurization of the HTC hydrochar slurry. The heat recovery scheme is adapted from a pilot plant for hydrothermal peat treatment, the so-called Swedish Peat Process, reported by Stemann et al. (2013b). The pressure levels of the depressurization steps are chosen so that the total amount of heat recovered in each step can be used in the respective mixing preheater and drying hydrochar. The direct heat exchanger at temperatures above 130 °C was considered because, during the condensation of hydrochar, some tar-like substances would likely cause fouling and clogging of the heat exchangers. The preheated mixture (3) is fed in the HTC batch reactor (R-HTC), while all products, the hydrochar, HTC liquid products, and gaseous by-product (5), exit at the bottom of the reactor. An electric furnace (QR-HTC) operating in an open-loop system, according to laboratory-scale experimental studies, was used to raise the temperature of the preheated biomass slurry to the HTC temperature the HTC end temperature 250 °C. The vapors produced by depressurized the mixture of hydrochar, HTC liquid, and gases (FT1 and FT2) are used to preheat the biomass slurry in P-HEATER and dry the hydrochar (DRYER). The produced gas is recovered in SEP-GAS (HTC-GAS), while the hydrochar and HTC liquid are separated in a filter (FILTER). According to the experimental laboratory data, the product (hydrochar) is dehydrated to a moisture content of about 45%; this is a conservative value for a high-performance industrial press. The wet hydrochar (WET-HC) is transported to an air dryer (DRYER), where the main HTC product (dry hydrochar) is obtained. The hydrochar is then dried at a temperature of 105°C and subsequently pelletized (PELLETIZ). The addition of a urea additive can facilitate agglomeration and reduce pelletizing time. The HTC liquid (11) passes to a separator (SEP), where a part is recirculated (13) to prepare biomass slurry, while the remaining water (15) passes to a biogas production plant. Biogas production is carried out at temperatures between 25-35 °C (Chae et al., 2008). Therefore, no additional energy is required. The reactor used is a batch reactor, where the experimental data of the temperature and pressure profile in functions of time inside the reactor were used. According to the experimental data, the temperature and pressure vary between 25 to 250°C and 1 to 52 bar, respectively. Early scale-up experiments indicate that the results of the laboratory batch experiment (**Chapter 7**) can be reproduced at the industrial plant level in a continuous mode of operation.

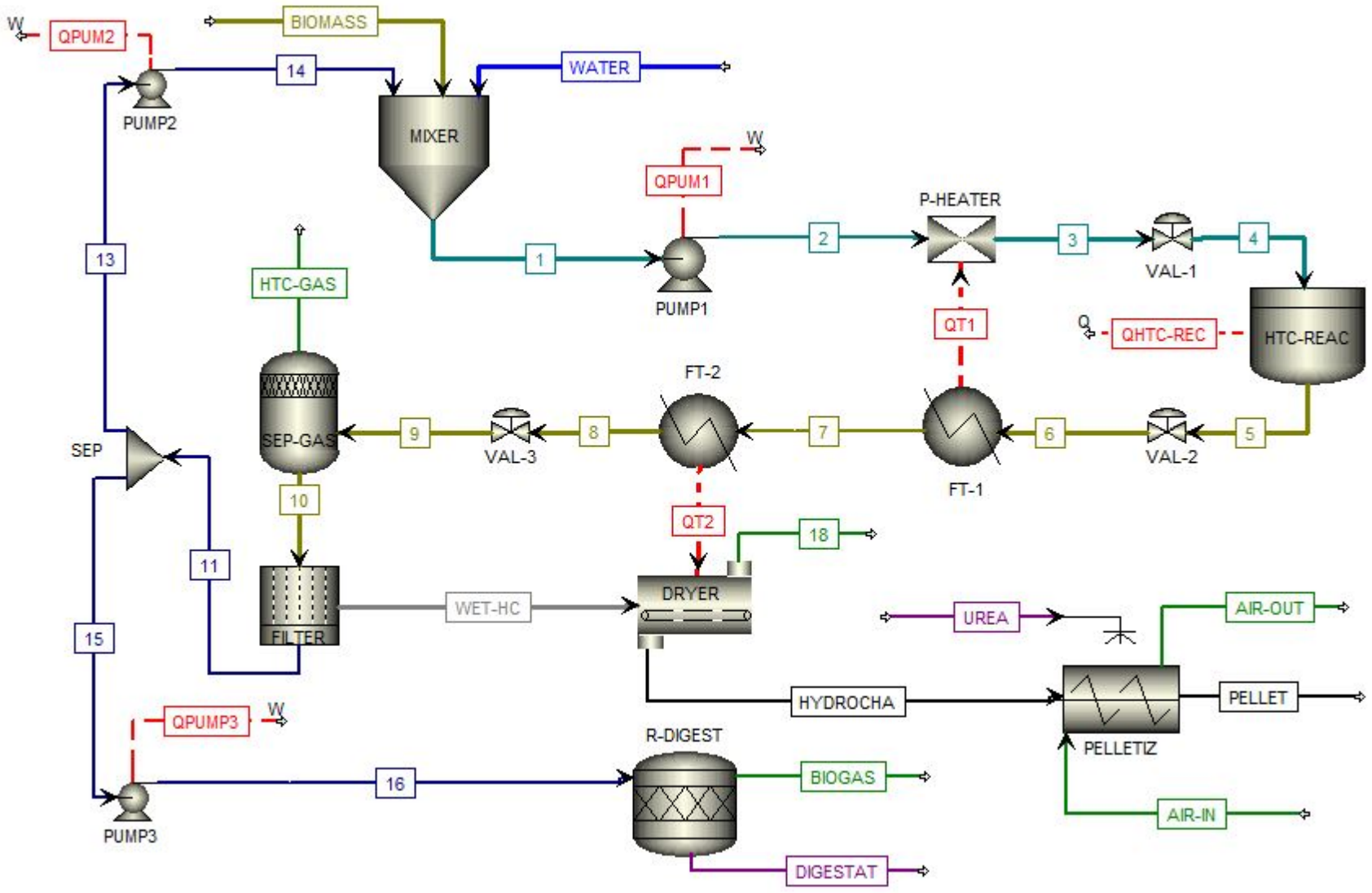

Figure 8-3: Schematic flow sheet of the HTC process an industrial scale

8.3.1.1. *Agitator*

The biomass is mixed with water in the mixer to create a mix that can be easily pumped. An anchor agitator, which is suitable for slurries and moderately viscous liquids, was chosen. The power to drive the impeller (i.e., shaft power) W_M (kW) was estimated from the following equation:

$$W_M = N_P N_M{}^3 D_i{}^5 \rho_s \qquad (8\text{-}6)$$

where N_M is the agitation speed (for mixer is 50 rmp and for R-HTC is 550 rpm), NP, corresponding to a friction factor, was associated with Reynolds number (Re) through **Eq.(8-7)** by the correlation of the extrapolation of Furukawa et al. (2012)

$$N_P = 94.043 \mathrm{Re}^{-0.599} \qquad (8\text{-}7)$$

The impeller diameter Di (m) was estimated via the mixer diameter DM (m) by setting a mixer volume of $3m^3$ and using a Di/DM ratio equal to 0.892 as recommended by Furukawa et al. (2012). The mix biomass density ρ_S was estimated using the mixture law and taking into account a dry biomass density equal to 1548 kg/m^3 (**Chapiter 3**). The apparent viscosity of the slurry of biomass were calculated from the **Eq.(8-8)** (see **Chapiter 6**).

$$\mu = \mu_0 \left(1 + \frac{\varphi_{bi}}{\varphi_{bi}{}^{max}}\right)^{2.5\varphi_{bi}{}^{max}} \qquad (8\text{-}8)$$

To counteract losses in the gearbox, grids and bearings, the motor power was considered higher than that required for the rotor. The power consumption was calculated with a motor efficiency of 75%.

8.3.1.2. *Pumps*

A piston pump was used; this pump is the most suitable for pumping sludge into the reactor: the piston pumps are appropriate for viscous fluids and particulate streams and can be used in many pressure conditions up to 300 bar (White, 1986). For the process to continue, the pump has to guarantee the reactor's pressure (PR) and compensate for the pressure drops in the heat exchanger (P-HEATER). Efficiency of a piston pump was set at 0.5 (Green and Southard, 2019). The pump (PUMP2) is necessary for the recirculation of the HTC liquid. In this case, a

centrifugal pump was used since the pressure rise required is low (3 bar), and the stream to be pumped does not contain solids, and fixing the efficiency of the centrifugal pump at a value of 0.40 (Sinnott and Towler, 2019). The power consumption of all pumps was estimated in Aspen plus.

8.3.1.3. *Heat exchanger (heater)*

The reasonable heat gained by the sludge is provided by the latent heat of condensation of the vapors. The vapor pass in heat exchanger (P-HEATER) in saturated conditions and leave the equipment at condensation temperature exclusive of being cooled. Therefore, the FT-1 pressure was set at 30 bar and its corresponding saturation temperature, which varies depending on the amount of gas produced. The energy used in the P-Heather is the energy recovered during depressurization; therefore, no supplementary energy consumption was considered in this equipment.

8.3.1.4. *Reactor*

The preheated biomass-water mixture enters the HTC reactor (HTC-REAC). A system of valves (VAL-1 and VAL-2) allows maintaining a constant pressure inside the reactor. An electric furnace operating as an open-loop system was used to emulate the experimental results in the laboratory. The energy consumed to bring the mixture biomass/water preheated to setpoint temperature was estimated in Aspen plus. The HTC reaction is exothermic (as explained in **Chapter 3**). The exothermicity of the HTC reaction was not considered in the simulation, so the energy lost due to insulation by the HTC reaction may be equivalent to the heat of the chemical reaction.

8.3.1.5. *Heat exchanger (condensers)*

The direct heat exchanger at temperatures above 120 °C was used during the condensation of hydrochar mixture. The FT-1 and FT-2 were used to reduce the pressure of the mixture hydrochar and HTC liquid in the rector. Saturated water cooling can reduce the pressure. The FT-1 reduces the pressure to 30 bar, and FT-2 to 15 bar. The recovered heats are sufficient to preheat (P-HEATER) up to 150 ºC and FT-2 to dry the hydrochar.

8.3.1.6. *Filter*

The liquid HTC and hydrochar leaving the SEP-GAS are sent to a FILTER, separating the HTC liquid and solid fractions (hydrochar). It was assumed that all hydrochar leaves the FILTER as stream (WET-HC), the solids separation efficiency is 100%. The hydrochar leaves the FILTER with a moisture content of about 45 %. This moisture content is typical for mechanical dewatering systems used to hydrochar.

8.3.1.7. *Dryer*

The hydrochar with 45 % of moisture content is dried in an adiabatic dryer to reduce its humidity to 5%, a value considered adequate for hydrochar storing and its use as fuel (Lucian and Fiori, 2017).

8.3.1.8. *Pelletizer*

The biomass pelletization process consists of multiple steps, including raw material pretreatment, pelletization, and post-treatment. In the case of hydrochar, no pretreatment is required. The energy required to granulate hydrochar was taken from the literature according to the amount of hydrochar produced (Lucian and Fiori, 2017).

8.3.1.9. *HTC liquid composition*

During the HTC process, the main biomass constituents, such as cellulose and hemicellulose, hydrolyze and form sugars (glucose, fructose, and xylose), as explained in **Chapter 4**. These molecules also tend to hydrolyze and form low molecular weight organic acids (lactic, formic, and acetic acids). Sugars can also dehydrate to form hydroxymethylfurfural (HMF), furfurals, anhydroglucose, or degrade, producing water and CO_2 (Reza et al., 2014b). In the results shown in **Chapter 4**, sugars and HMF are only present in mild and intermediate conditions (150 and 220 °C) for biomass in general (ASB and AS) and (210 and 250 °C) for CEL; this confirms the instability of these compounds as a function of biomass type and temperature, also confirmed by other authors (Lucian et al., 2020; Reza et al., 2014b) . In general, the high concentrations of compounds such as sugars and the presence of organic acids (acetic, formic, and lactic acids) make the HTC liquid an ideal feedstock for the anaerobic digestion process.

8.3.1.10. *Biogas production estimation*

Anaerobic digestion is a very complex process containing many biochemical reactions involved in the total absence of oxygen. Anaerobic digestion is a process of reducing biodegradable waste with the help of microorganisms, and the main by-product is CH_4 (50-75%) and CO_2 (25-50%) with a slight trace of H_2S and NH_3 (Ghosh et al., 2019). A theoretical stoichiometric method based on the Buswell equation is an easy way to evaluate the anaerobic digestion process for biogas production from organic waste (Nguyen et al., 2014). The method of the Buswell equation has been widely applied in several studies (Angelidaki and Ahring, 1992; Salanitro and Diaz, 1995; Sialve et al., 2009). Symons and Buswell (1933) represented an equation for the overall anaerobic degradation process.

$$C_cH_hO_oN_nS_s + yH_2O \rightarrow xCH_4 + (c-x)CO_2 + nNH_3 + sH_2S \quad (8\text{-}9)$$

$$\text{where: } x = \frac{1}{8}(4c + h + 2o - 3n - 2s) \text{ and } y = \frac{1}{4}(4c + h - 2o + 3n + 2s) \quad (8\text{-}10)$$

This method was validated in terms of methane yield and other products by Nguyen et al. (2014). This equation was used to estimate all possible chemical reactions of intermediate compound transformations into CH_4 and CO_2. In addition, other reactions were used for the reactions of biogas intermediates.

8.3.2. Criteria to determine HTC performances

The hydrochar mass yield was obtained from the amount of hydrochar (m_{HC}) obtained on dry biomass (m_B) introduced into the reactor. According to experimental data, the hydrochars produced have mass yields of 51.22, 56.20, and 61.03 % at 210, 230, and 250 ºC, respectively. The energy densification ratio of hydrochar is the HHV of hydrochar divided by the HHV of raw biomass. The values of energy densification are 1.16, 1.31, and 1.36 at 210, 230, and 250 ºC, respectively. The energetic yield η_E is calculated according to **Eq. (8-11)** by multiplication of the mass yield by energy densification ratio values.

$$\eta_E = \frac{m_{HC}}{m_B} \cdot \frac{HHV_{HC}}{HHV_B} \quad (8\text{-}11)$$

The plant thermal efficiency (η_T) can be estimated from the ratio between the thermal energy contained in the hydrochar produced (E_{HC}) and the thermal energy used (E_U) to produce it. The following equation describes it:

$$\eta_T = \frac{E_{HC,}\ HHV}{E_U} \quad (8\text{-}12)$$

This thermal efficiency was calculated as the ratio between the HHV of the dry hydrochar produced (kWh/$kg_{hydrochar}$) and the total thermal energy required by the plant (kWh/$kg_{hydrochar}$). The HHV of hydrochar was calculated from the experimental results.

The following equipment requires electrical energy in the proposed scheme: MIXER, PUMP1, PUMP 2, and PUMP3, HTC-REAC, DRYER, and the PALLETIZER. **Table 8-2** shows that the highest consumption is found in this equipment.

Table 8-2 : Electrical energy demand during the AS HTC process.

Equipment	Electric power (kW)		
	210 ºC (81 min)	230 ºC (97 min)	250 ºC (123 min)
MIXER	25.6	25.6	25.6
PUMP1	0.31	0.31	0.30
PUMP2	0.061	0.061	0.058
PUMP3	0.24	0.24	0.23
HTC-REAC	525.40	660.48	824.04
DRYER	0	0	0
PALLETIZER	62.23	48.40	40.10
TOTAL	551.62	686.70	838.31

As seen in **Table 8-2**, the highest energy consumption is the HTC reactor with 85.59, 89.85, and 92.55 % at 210, 230, and 250ºC, respectively. The granulator requires up to 10.14% of the total energy demand. The consumption of the pelletizer depends on the amount of hydrochar produced and its properties. The properties and amount of hydrochar vary with HTC reaction time and temperature. As explained above, a high HTC temperature ensures the highest hydrochar yields (in the case of AS, due to polymerization reactions) with properties that make it easy to pelletize. Hydrochar produced at 250 °C has properties that minimize the energy consumption of the pelletizer. The energy consumption of the pumps is negligible. The energy demand in the mixer is constant, equal to 25.6 kW, and does not depend on process conditions.

The energy released during the depressurization of the HTC product is sufficient to dry the hydrochar, therefore no additional energy is used.

8.3.2.1. *HTC process energy efficiency*

The overall energy efficiency (based on HHV) or energy yield of the process was 59.55% at 210 ºC, 73.60% at 230 ºC, and 83.12% at 250 ºC. The remainder of the energy consumed is lost in organic substances dissolved in water and waste heat. To make a comparison with the use of raw biomass for dry thermochemical conversion. The pretreatment, i.e., drying of biomass to a moisture content of 5% with a thermal energy consumption of 2257 kJ/kg evaporated water, would consume 38.5% of the AS energy for drying. The energy efficiency of HTC at 230 and 250 ºC is therefore superior to that of simple drying and granulation of crude AS.

8.3.2.2. *Thermal efficiency*

The hydrochars produced have mass yields of 51.22, 56.20, and 61.03 % at 210, 230, and 250 ºC, respectively, corresponding to quantities of 3593.60, 3943.51, and 4272.10 kg/year, according to the biomass feed in the reactor (20000 ton/year at 65 % moisture). The HHV of these hydrochars was 22.98 MJ/kg at 210 ºC, 26.13 MJ/kg at 230 ºC, and 26.94 at 250 ºC. The specific thermal energy consumption (the energy of hydrochar between the energy used to produce hydrochar) was 4.74 at 210 ºC, 4.76 at 230 ºC, and 4.12 at 250 ºC. These results show that the HTC process is efficient since the energy contained in the hydrochar is 4.12-4.76 times greater than the energy consumption of the process. It can also be observed that the lowest thermal energy requirement is found at 230 °C HTC temperature. This is due to the fact that no great difference is observed between the HHV of hydrochar at 250 °C and 230 °C, even though the yield at 250 °C is higher. Similar volumes were reported by (Lucian and Fiori, 2017) for HTC of compost. The thermal efficiency values are very important when considering the use of hydrochar as a fuel; The $\eta_T > 1$ for all conditions considered. These data only consider hydrochar, but if the energy that methane from anaerobic digestion can provide is added, the thermal efficiency increases from 4.74 to 6.86 at 210 ºC, 4.76 to 6.06 at 230 ºC, and 4.12 to 4.77 at 250 ºC. The high rise of η_T at 210 °C is due to its high content of organic compounds in the liquid phase that is easily transformed into CH4 during the anaerobic digestion of the HTC liquid. However, no significant increase was observed at 250 °C; this is because there is

a bit organic compound in the liquid phase of HTC that is susceptible to be transformed into CH_4 during the methanation of HTC liquid. Most of the compounds in the liquid phase polymerize at 250 ºC to form secondary hydrochar or transform into HTC gas (mainly CO_2).

Based on the production considered (2000 ton/year) and considering the different treatment conditions. Furthermore, considering the HHV of raw AS (18.6 MJ/kg), hydrochar, and CH4 (35.56MJ/ Nm^3), it is obtained that the overall process efficiencies are 59.47 % at 210 ºC, 79.37% at 230 ºC and 96.32% at 250 ºC. The process efficiency is calculated by taking the ratio between the net energy (hydrochar energy + CH_4 energy - energy required for the hydrothermal process) and the chemical energy of the raw biomass feed in HTC reactor.

8.3.3. Economic feasibility of HTC process

To estimate the economic feasibility, the HTC plant was simulated the operating condition at 250 ºC, the heating time of 2h and 20 % solid inside the HTC reactor. In these operational conditions, the volume of the HTC reactor is equal to 7.54 m^3 (H = 3.73 m; D = 1.61 m), the average density of the biomass mixture (biomass+ water) was equal to 1110 kg/m^3, and the filling degree of the reactor was set at 2/3. The reactor pressure was set at 100 bar, considered the steam pressure of water at 250 °C (40 bar), an overpressure of 15 bar due to gas formation, and a safety factor of 1.5. All equipment considered (including the reactor) is made of stainless steel. The plant configuration takes into account the recirculation of the liquid from the filter to the mixer.

8.3.3.1. *Investment costs*

For the calculation of investment costs, it is not possible to generalize this study since costs vary according to the country where the project is carried out, labor and electrical costs. The costs of each HTC process equipment, including the purchase costs of each unit, its installation, transportation to the plant site, and the associated insurance and tax costs, are shown in **Table 8-3**. All these costs were estimated using Aspen Process Economic Analyzer (APEA) v.10, and the procedure indicated by Turton et al. (2018), considering that the plant location is in North America, which defaults to Aspen. In addition to the equipment costs, capital costs are incurred for site preparation and for the costs allocated to the purchase of the utility plants and cover contingencies and contractor fees. To the above costs were added the costs of land, start-up, and working capital.

Table 8-3 : Estimated capital cost of equipment for the HTC plant

Type of Unit	Cost ($)
HTC-REAC	485,900
FT-1	74,900
P-HEATER	74,500
MIXER	5,110
DRYER	27,300
SEP-GAS	170,100
PUMP1	35,700
FT-2	69,200
PUMP2	32,300
FILTER	1,359
PELLETIZER	30,907
Total cost of equipment (E)	**1,007,276**

8.3.3.2. *Estimated total capital or total investment*

The Fixed Capital Investment (FCI) shown in **Table 8-3** was estimated from the total cost of the leading equipment. The excess liquid HTC can be evaluated at the biogas production plant or water treatment. Costs related to assessing the biogas production plant or water treatment were not considered in this study.

Table 8-4 : Estimated Fixed Capital Investment

Fixed capital estimate	Equation	Value ($)
Total cost of equipment (E)	E=∑ Ei	300,600.00
Main buildings	Mb= 12 % E	36,072.00
Auxiliary buildings	Ab = 10 % E	30,060.00
Installed facilities and services	Fs= 55 % E	165,330.00
Direct plant cost	Dc = Mb + AB + Fs	231,462.00
Earthwork	Ew =13 % E	39,078.00
Freight, insurance and taxes	Fit= 8 % E	24,048.00
Other direct costs	Odt = 6 % Dc	13,887.72
Total direct plant cost	TDC= Dc + Ew + Fit+ Odt	308,475.72
Indirect field personnel	Ifp = 12 % TDC	37,017.09
Other indirect field expenses	Oif= 21 % TDC	64,779.90
Construction cost	Cc = TDC + ifp+ oif	410,272.71
Construction company's head office costs	Cch= 17 % Cc	69,746.36
Project management costs	Pmc= 8 % Cc	32,821.82
Supervisory personnel costs	Spc= 3 % Cc	12,308.18
Depreciable capital excluding contingencies	DCe = Cc+Cch+Pmc+ Spc	525,149.07
Project contingencies	PC = 5 % DCe	26,257.45
Process contingencies	PrC = 8 % DCe	42,011.93
Depreciable capital including contingencies	Dcc= DCe + PC + PrC	593,418.44
Land purchase	Lp = 2 % Dcc	118,68.37
Fixed Capital or Fixed Investment	FC = Dcc + Lp	605,286.81
Operating Capital or Operating Investment	OC = 15 % FC	90,793.02
Fixed Capital Investment	**FCI = FC + OC**	**696,079.84**

8.3.3.2.1. *Estimation of manufacturing cost*

Manufacturing costs can be divided into three categories such as:

Direct Manufacturing Costs: These costs represent overhead costs that vary with the rate of production. For example, when product demand decreases, the production rate is reduced to less than the design capacity. Therefore, minimizing the factors that make up direct manufacturing costs can be expected at this lower rate. These reductions may be directly proportional to the production rate, as in the case of raw materials, or they may be slightly reduced, for example, maintenance costs or labor.

Fixed Manufacturing Costs: These costs are independent of changes in the production rate. They include property taxes, insurance and depreciation, charged at constant rates even when the plant is not operating.

General Expenses: These costs represent an overhead burden that is necessary to carry out business functions. These include administration or management, sales, finance and research. Expenditures rarely fluctuate with levels of productivity. However, if lengthy periods of low production occur, things such as research and development and distribution and sells may drop.

The equation used to evaluate the cost of manufacture using these costs becomes:

Cost of Manufacture (COM) = Direct Manufacturing Costs (DMC) + Fixed Manufacturing Costs (FMC) + General Expenses (GE).

The cost of manufacturing, COM, can be determined when the following costs are known or can be estimated:

- Fixed capital investment (FCI)
- Cost of operating labor (C_{OL})
- Cost of utilities (C_{UT})
- Cost of waste treatment (C_{WT})
- Cost of raw materials (C_{RM})

The FCI was determined in the previous section, the cost of water treatment was not included, as was the cost of raw materials. The cost of water treatment was not included in this study. As explained above, HTC liquid can be used in anaerobic digestion to produce biogas; as a high-

value by-product, raw material cost was also not considered since the raw material is an environmental issue; therefore, it can be obtained low cost or free of charge.

Cost of operating labor

These are the costs attributed to the personnel required to operate the process plant (Turton et al., 2018). The number of operators required per shift (N_{oL}) can be estimated by following equation

$$N_{OL} = (6.29 + 31.7P^2 + 0.23N_{np})^{0.5} \quad (8\text{-}13)$$

where P is the number of processing steps involving the handling of particulate solid for example, transportation and distribution, particulate size control, and particulate removal. N_{np} is the number of other processing steps. For each pf the N_{oL} operators per 8-hour shift, approximately 4.5 operators must be hired for a plant that runs 24 hours per day, to account for the 3 shifts per day and the 3 weeks of leave typically taken by each operator per year (Turton et al., 2008). The salary for a chemical plant operator varies by location, and the estimator should look up the average value for the area.

$$N_{OL} = (6.29 + 31.7(1)^2 + 0.23\ (8))^{0.5} = 6.29 \quad (8\text{-}14)$$

The number of operators required per shift = 6.22. Operating Labor = (4.5) (6.29) = 28.31 (rounding up to the nearest integer yields 29 operators).

Labor Costs (2020) = 29× 6,384.83$ = **185,160.07$ /year**.

With the exception of the cost of raw materials, waste treatment, utilities, and operating labor (all parts of the direct manufacturing costs). The detailed determination of each of these three categories is presented in **Table 8-6**. Escalations of operating, maintenance labor and utilities were considered at 3%/year, and the economic plant life is estimate of 15 years. The interest rate for fixed capital investment is 10%/year.

Table 8-6 presents equations that can be used to estimate each individual item. With each equation, a typical range for the constants (multiplication factors) to estimate an individual cost item is presented. If no other information is available, the midpoint value for each of these ranges is used to estimate the costs involved. The equations for estimating the costs of the three categories mentioned above are as follows:

$$\mathrm{DMC} = C_{UT} + C_{WT} + C_{RM} + 0.0069\mathrm{FCI} + 1.33\mathrm{C}_{OL} + 0.03COM \quad (8\text{-}15)$$

$$\mathrm{FMC} = 0.1068\mathrm{FCI} + 0.708\mathrm{C}_{OL} \quad (8\text{-}16)$$

$$\mathrm{GE} = 0.009\mathrm{FCI} + 0.177 + 0.16COM \quad (8\text{-}17)$$

The total manufacturing cost can be obtained by adding these three cost categories and solving for the total manufacturing cost (COM).

$$\mathrm{COM} = 0.28\mathrm{FCI} + 2.73\mathrm{C}_{OL} + 1.23(C_{UT} + C_{WT} + C_{RM}) \quad (8\text{-}18)$$

The detailed determination of each of these three categories is presented in **Table 8-6**. Escalations of operating, maintenance labor and utilities were considered at 3%/year, and the economic plant life is estimate of 15 years. The interest rate for fixed capital investment is 10%/year.

8.3.3.3. *Estimation of revenue*

Considering the price of wood pellets, usually in the range 150–379 $/ton and depending on the country considered, and the quality (OSI, 2021). In this case, there can be three different scenarios (normal, optimistic, and pessimistic). In the normal scenario, the price of hydrochar pellets is sold at the same current average price of wood pellets. In the optimistic scenario, the pellet produced from hydrochar is sold at the highest price on the market due to its high calorific value. In the pessimistic scenario, it sells for the lowest market price of wood pellets.

Table 8-5: Estimated income for different scenarios

Scenario	Flow (ton/year)	Price ($/ton)	Total revenue ($/year)
Normal	4272.1	250.00	1,068,025.00
Optimist	4272.1	379.00	1,619,125.90
Pessimistic	4272.1	150.00	640,815.00

Table 8-6:Multiplication factors for estimating manufacturing cost

Cost	Typical range of multiplying factors	Value used in this study
Direct Manufacturing Costs		
Raw materials	C_{RM}	
Waste treatment	C_{WT}	
Utilities	C_{UT}	
Operating labor	C_{OL}	C_{OL}
Direct supervisory and clerical labor	$(0.1-0.25) \cdot C_{OL}$	$0.18C_{OL}$
Maintenance and repairs	$(0.02-0.1) \cdot FCI$	0.06FCI
Operating supplies	0.009FCI	
Laboratory charges	$(0.1-0.2) \cdot C_{OL}$	$0.15C_{OL}$
Patents and royalties	$(0-0.06) \cdot COM$	0.03COM
Total Direct Manufacturing Costs	**$C_{RM} + C_{WT} + C_{UT} + 1.33C_{OL} + 0.03COM + 0.069FCI$**	
Fixed Manufacturing Costs		
Depreciation	0.1FC	0.1FCI
Local taxes and insurance	$(0.014-0.05) \cdot FCI$	0.032FCI
Plant overhead costs	$0.708C_{OL} + 0.036FCI$	$0.708C_{OL} + 0.036FCI$
Total Fixed Manufacturing Costs	**$0.708C_{OL} + 0.068FCI$ + depreciation**	
General Manufacturing Expenses		
Administration costs	$0.177C_{OL}+0.009FCI$	$0.177C_{OL}+0.009FCI$
Distribution and selling costs	$(0.02-0.2) \cdot COM$	0.11COM
Research and development	0.05COM	0.05COM
Total General Manufacturing Costs	**$0.177C_{OL} + 0.009FCI + 0.16COM$**	
Total Costs	**$C_{RM} + C_{WT} + C_{UT} + 2.215C_{OL} + 0.190COM + 0.146FCI$ + depreciation**	

8.3.3.4. *Cash flow calculations*

Table 8-7: Cash flow calculations in normal scenario

Years	**0**	**1**	**2**	**3**
Revenue ($)		1068025.00	1068025.00	1068025.00
Total Costs ($)		-680639.76	-697300.12	-714460.29
Depreciation ($)		60528.68	60528.68	60528.68
FCI	**-696079.8**			
Net Cash Flow ($)	**-696079.8**	**326856.56**	**310196.20**	**293036.03**
Years	**4**	**5**	**6**	**7**
Revenue ($)	1068025.00	1068025.00	1068025.00	1068025.00
Total Costs ($)	-732135.27	-750340.50	-769091.88	-788405.80
Depreciation ($)	60528.68	60528.68	60528.68	60528.68
FCI				
Net Cash Flow ($)	**275361.05**	**257155.82**	**238404.44**	**219090.51**
Years	8	9	10	11
Revenue ($)	1068025.00	1068025.00	1068025.00	1068025.00
Total Costs ($)	-808299.15	-828789.29	-849894.14	-871632.13
Depreciation ($)	60528.68	60528.68	60528.68	60528.68
FCI				
Net Cash Flow ($)	**199197.17**	**178707.03**	**157602.18**	**135864.19**
Years	12	13	14	15
Revenue ($)	1068025.00	1068025.00	1068025.00	1068025.00
Total Costs ($)	-894022.26	-917084.10	-940837.79	-965304.10
Depreciation ($)	60528.68	60528.68	60528.68	60528.68
FCI				
Net Cash Flow ($)	**113474.05**	**90412.22**	**66658.53**	**42192.22**

Table 8-8: Cash flow calculations in optimist scenario

Years	**0**	**1**	**2**	**3**
Revenue ($)		1619125.90	1619125.90	1619125.90
Total Costs ($)		-680639.76	-697300.12	-714460.29
Depreciation ($)		60528.68	60528.68	60528.68
FCI	-696079.84			
Net Cash Flow ($)	-696079.84	**877957.46**	**861297.10**	**844136.93**
Years	**4**	**5**	**6**	**7**
Revenue ($)	1619125.90	1619125.90	1619125.90	1619125.90
Total Costs ($)	-732135.27	-750340.50	-769091.88	-788405.80
Depreciation ($)	60528.68	60528.68	60528.68	60528.68
FCI				
Net Cash Flow ($)	**826461.95**	**808256.72**	**789505.34**	**770191.41**
Years	8	9	10	11
Revenue ($)	1619125.90	1619125.90	1619125.90	1619125.90
Total Costs ($)	-808299.15	-828789.29	-849894.14	-871632.13
Depreciation ($)	60528.68	60528.68	60528.68	60528.68
FCI				
Net Cash Flow ($)	**750298.07**	**729807.93**	**708703.08**	**686965.09**
Years	12	13	14	15
Revenue ($)	1619125.90	1619125.90	1619125.90	1619125.90
Total Costs ($)	-894022.26	-917084.10	-940837.79	-965304.10
Depreciation ($)	60528.68	60528.68	60528.68	60528.68
FCI				
Net Cash Flow ($)	**664574.95**	**641513.12**	**617759.43**	**593293.12**

Table 8-9: Cash flow calculations in pessimist scenario

Years	**0**	**1**	**2**	**3**
Revenue ($)		854420.00	854420.00	854420.00
Total Costs ($)		-680639.76	-697300.12	-714460.29
Depreciation ($)		60528.68	60528.68	60528.68
FCI	**-696079.8**			
Net Cash Flow ($)	**-696079.8**	**113251.56**	**96591.20**	**79431.03**
Years	**4**	**5**	**6**	**7**
Revenue ($)	854420.00	854420.00	854420.00	854420.00
Total Costs ($)	-732135.27	-750340.50	-769091.88	-788405.80
Depreciation ($)	60528.68	60528.68	60528.68	60528.68
FCI				
Net Cash Flow ($)	**61756.05**	**43550.82**	**24799.44**	**5485.51**
Years	8	9	10	11
Revenue ($)	854420.00	854420.00	854420.00	854420.00
Total Costs ($)	-808299.15	-828789.29	-849894.14	-871632.13
Depreciation ($)	60528.68	60528.68	60528.68	60528.68
FCI				
Net Cash Flow ($)	**-14407.83**	**-34897.97**	**-56002.82**	**-77740.81**
Years	12	13	14	15
Revenue ($)	854420.00	854420.00	854420.00	854420.00
Total Costs ($)	-894022.26	-917084.10	-940837.79	-965304.10
Depreciation ($)	60528.68	60528.68	60528.68	60528.68
FCI				
Net Cash Flow ($)	**-100130.95**	**-123192.78**	**-146946.47**	**-171412.78**

8.3.3.5. *Economic indicators*

8.3.3.5.1. *Net Present Value (NPV)*

The net present value is important for the valuation of investments in fixed assets, despite its limitations in considering unforeseen or exceptional market circumstances. If its value is greater than zero, the project is profitable, being considered the minimum return value for the investment. A company usually compares different alternatives to check whether a project is worthwhile or not. The alternative with the highest NPV is usually the best for a project, but this does not always have to be the case. Sometimes low NPV values can be accepted for a variety of reasons, such as from an environmental point of view (Zizlavsky, 2014). The NPV value can be estimated from the following equation:

$$NPV = \sum_{t=0}^{N} \left[\frac{NCF_t}{(1+r)^t} \right] - FCI \quad (8\text{-}19)$$

where NPV = net present value; NCFt = net cash flow generated by project in year t; r = discount rate. For constant cash flow (CF), the net present value (NPV) is a finite geometric series and is given by

$$NPV = CF_t \left(\frac{1 - \left(\frac{1}{1+r}\right)^{N+1}}{1 - \left(\frac{1}{1+r}\right)} \right), for\ r \neq 0 \quad (8\text{-}20)$$

Table 8-10: Parameters for NPV estimation

Depreciation	D=0.1FC	$60,528.68
Cash Flow ($)	NFC=R	-
Net Cash Flow ($)	FC=R-D	
Taxes on Gross Profit	T=0.032FC	-
Net Income	NR=NFC-T	-
Inflation Index	f	4-5%
Risk Index	i	10-15%
Minimum Acceptable Discount Rate	r=f+i+i·f	17.56%
Salvage Value	SV=0.1FCI	**$69,607.98**

$$NPV = \left[\frac{NCF_1}{(1+r)^1}\right] + \left[\frac{NCF_2}{(1+r)^2}\right] + \left[\frac{NCF_3}{(1+r)^3}\right] + \cdots + \left[\frac{NCF_n + SV}{(1+r)^n}\right] - FCI \qquad (8\text{-}21)$$

Table 8-11: Values of parameters for NPV estimation in normal scenario

Year	Depreciation ($)	Cash Flow ($)	Gross profit ($)	Net Income ($)	NCF_t ($)
0	-	-	-	-	-
1	60,528.68	387,385.24	326856.56	316397.15	376925.83
2	60,528.68	370,724.88	310196.20	300269.92	360798.60
3	60,528.68	353,564.71	293036.03	283658.87	344187.56
4	60,528.68	335,889.73	275361.05	266549.50	327078.18
5	60,528.68	317,684.50	257155.82	248926.84	309455.52
6	60,528.68	298,933.12	238404.44	230775.50	291304.18
7	60,528.68	279,619.20	219090.51	212079.62	272608.30
8	60,528.68	259,725.85	199197.17	192822.86	253351.54
9	60,528.68	239,235.71	178707.03	172988.40	233517.08
10	60,528.68	218,130.86	157602.18	152558.91	213087.59
11	60,528.68	196,392.87	135864.19	131516.53	192045.21
12	60,528.68	174,002.74	113474.05	109842.88	170371.57
13	60,528.68	150,940.90	90412.22	87519.03	148047.71
14	60,528.68	127,187.21	66658.53	64525.45	125054.13
15	60,528.68	102,720.90	42192.22	40842.07	101370.75
NPV					
Revenue ($/y)				R	1,068,025.00
Fixed Capital Investment				FCI	696,079.84$
Salvage Value				SV=0.1FCI	69,607.98$
Net Present Value				**NPV**	873,880.08$

Table 8-12: Values of parameters for NPV estimation in optimist scenario

Year	Depreciation ($)	Cash Flow ($)	Gross profit ($)	Net Income ($)	NCF_t ($)
0	-	-	-	-	-
1	60,528.68	938,486.14	877,957.46	849,862.82	910,391.50
2	60,528.68	921,825.78	861,297.10	833,735.59	894,264.27
3	60,528.68	904,665.61	844,136.93	817,124.55	877,653.23
4	60,528.68	886,990.63	826,461.95	800,015.17	860,543.85
5	60,528.68	868,785.40	808,256.72	782,392.51	842,921.19
6	60,528.68	850,034.02	789,505.34	764,241.17	824,769.85
7	60,528.68	830,720.10	770,191.41	745,545.29	806,073.97
8	60,528.68	810,826.75	750,298.07	726,288.53	786,817.21
9	60,528.68	790,336.61	729,807.93	706,454.07	766,982.76
10	60,528.68	769,231.76	708,703.08	686,024.58	746,553.26
11	60,528.68	747,493.77	686,965.09	664,982.20	725,510.89
12	60,528.68	725,103.64	664,574.95	643,308.56	703,837.24
13	60,528.68	702,041.80	641,513.12	620,984.70	681,513.38
14	60,528.68	678,288.11	617,759.43	597,991.12	658,519.81
15	60,528.68	653,821.80	593,293.12	574,307.74	634,836.42
NPV					
Revenue ($/y)				R	1,619,125.9
Fixed Capital Investment				FCI	696,079.84$
Salvage Value				SV=0.1FCI	69,607.98$
Net Present Value				**NPV**	3,643,497.70$

Table 8-13: Values of parameters for NPV estimation in pessimist scenario

Year	Depreciation ($)	Cash Flow ($)	Gross rofit ($)	Net Income ($)	NCF_t ($)
0	-	-	-	-	-
1	60,528.68	173,780.24	113,251.56	109,627.51	170,156.19
2	60,528.68	157,119.88	96,591.20	935,00.28	154,028.96
3	60,528.68	139,959.71	79,431.03	76,889.23	137,417.92
4	60,528.68	122,284.73	61,756.05	59,779.86	120,308.54
5	60,528.68	104,079.50	43,550.82	42,157.20	102,685.88
6	60,528.68	85,328.12	24,799.44	24,005.86	84,534.54
7	60,528.68	660,14.20	5,485.51	5,309.98	65,838.66
8	60,528.68	461,20.85	-14,407.83	-13,946.78	46,581.90
9	60,528.68	256,30.71	-34,897.97	-33,781.24	26,747.44
10	60,528.68	4,525.86	-56,002.82	-54,210.73	6,317.95
11	60,528.68	-17,212.13	-77,740.81	-75,253.11	-14,724.43
12	60,528.68	-39,602.26	-100,130.95	-96,926.76	-36,398.07
13	60,528.68	-62,664.10	-123,192.78	-119,250.61	-58,721.93
14	60,528.68	-86,417.79	-146,946.47	-142,244.19	-81,715.51
15	60,528.68	-110,884.10	-171,412.78	-165,927.57	-105,398.89
NPV					
Revenue ($/y)				R	854,420.00
Fixed Capital Investment				FCI	696,079.84$
Salvage Value				SV=0.1FCI	69,607.98$
Net Present Value				**NPV**	**-199,615.12$**

In financial theory, if a choice has to be made between two mutually exclusive alternatives, the one that produces the higher NPV should be selected. A positive net present value indicates that the expected benefits generated by a project or investment exceed the expected costs. This

concept is the basis for the Net Present Value Rule, which dictates that the only investments that should be made are those with positive NPV. As shown in the tables above, only the normal and optimistic scenarios are economically viable NPV >0. The pessimistic scenario is no longer feasible after 7 years of the project. In this sense, only the scenarios where the project is feasible can be used.

8.3.3.5.2. *Internal Rate of Return (IRR).*

The net present value is a function of the rate of return. The internal rate of return is a rate for which this function is zero, i.e., the internal rate of return is a solution to the equation NPV = 0. The IRR is expressed in the following equation.

$$NPV = \sum_{t=0}^{N} \left[\frac{NCF_t}{(1+IRR)^t} \right] - FCI = 0 \qquad (8\text{-}22)$$

IRR calculation

$$\frac{NCF_1}{1+IRR} + \frac{NCF_2}{(1+IRR)^2} + \frac{NCF_3}{(1+IRR)^3} + \cdots + \frac{NCF_n + SV}{(1+IRR)^n} - FCI = 0 \qquad (8\text{-}23)$$

Table 8-14: Values of IRR of the three scenarios

Scenario	IRR
Normal	0.4913
Optimist	1.289
Pessimist	-1.929

In the normal and optimistic scenarios, all values of IRR >r (minimum acceptable rate of return (r=0.1756), therefore in these scenarios, the project is economically reliable, no risk is taken to carry out the project. However, for the pessimistic scenario, IRR<0, this means that there are many risks to carry out the project, this result is following the NPV value.

8.3.3.5.3. *Capital Recovery Period (CRP)*

The capital recovery period (CRP) or payback is the indicator that determines the term of recovery of an investment, also called a payout. This indicator is used to evaluate the attractiveness of the investment (Baio et al., 2017). The CRP is the number of periods necessary for the sum of future net nominal revenues to equal the value of the initial investment. It is easier to decide to rationalize in terms of earnings per period (analogous to the accounting concept of profit per period) than in terms of accumulated gain over several periods.

$$CRP = \frac{FCI}{\overline{NR}} \quad (8\text{-}24)$$

Where $\overline{NR}$ is the average of net income.

Table 8-15: Values of CRP of the three scenarios

Scenario	CRP (year)
Normal	3.71
Optimist	0.96
Pessimist	-35.97

Taking into account that the average interest rate of the loan is 10% per year and assuming a plant amortization period of 15 years, an annual cost of $696,079.84 is obtained for the amortization of the total capital investment plus the cost of operating labor ($185,160.07/year) with a variation of 3% per year. To assess the economic feasibility of the HTC plant, three possible scenarios (optimistic (376$/ton), normal (250$/ton), and pessimistic (200$/ton) prices) for the sale of the hydrochar pellet product were determined. The normal and optimistic scenarios are economically feasible when assuming an annual production of 4272.1 tons of hydrochar (simulation results at T = 250 ºC, biomass water ratio B/W = 1/4, and holding time of 2 hours) and total annual cost (including total manufacturing costs and income taxes). From the energy point of view, the normal scenario value corresponds to 9.64$/$GJ_{HHV}$ ($HHV_{hydrochar}$ = 25.94 GJ/ton). This value is slightly lower than that obtained by Stemann et al. (2013a), who reported a value between 7.9 and 9.7€/GJ (9.13-11.51$/GJ) of empty fruit bunches under similar process conditions (T = 220 ◦C; θ = 4 h; DB/W = 0.2). Taking into consideration the price of wood pellets, which typically ranges from 150 to 379 $/ton and varies depending on the location (OSI, 2021), this value is 293.34$/ton (5800 $MXN/ton, VAT included) in Mexico

(Pellet, 2021), making hydrochar economical with bulk pine wood pellets. The competitive price of hydrochar and its better energy properties in terms of HHV and chemical composition compared to bulk pine wood pellets inspire its use as a fuel in biomass plants and district heating power plants. In contrast, hydrochar cannot compete with coal, which was priced at 134.08$/ton on 04/07/2021 (Economics, 2021). Nevertheless, the costs of environmental co2 emissions, which are mainly eliminated by hydrochar production and use, may promote the creation and supplementation of HTC plants and, as such, the hydrochar market. In addition, in this condition, the initial capital recovery period (CRP) is 3.71 years. This makes the use of avocado stones to produce pellets even more attractive.

8.4. Conclusion

The following conclusion was reached with the energy balance analysis of the HTC process.

- The process temperature and the biomass water ratio (B/W) are important factors in the energy balance. For HTC temperature at 210 ºC, a biomass water ratio higher than 0.19 is needed for the energy consumed to produce hydrochar to be lower than the energy contained in the hydrochar. However, for HTC temperature of 250 °C, this biomass water ratio is lower than 0.15 due to polymerization during HTC of AS at high temperature.
- A complete HTC process was designed and modeled to convert wet avocado pit into dry pelletized hydrochar. The process was simulated at various process conditions (temperature of 210, 230, and 250 °C, with the biomass water ratio of 1/4 (20% solid)). The HTC plant was designed with a capacity to treat 20,000 tons/year of the avocado pit and a moisture content of 65%. The efficiency of the plant was found to be highly dependent on the process temperature. The most favorable condition of the process is at a temperature of 250 ºC and two h of heating time, where the efficiency of the process is higher than 83%, without taking into account the energy that the biogas can provide. The thermal efficiency varies between 4.12 to 4.76, i.e., the energy content in the hydrochars is 4.12 to 4.76 times higher than the energy required for the process.
- The result of the simulation allowed an economic study of the use of hydrochar as an energy source. In general, the HTC process is economically feasible and competitive price of pelletized hydrochar compared to palletized bulk pine wood. This study could encourage the development of HTC plants and, consequently, the hydrochar pellet market.

GENERAL CONCLUSIONS AND PERSPECTIVES

Conclusion

The objective of this work was to establish a suitable methodology for the conversion of wet biomass into synthetic liquid fuels. Different types of biomasses with high moisture content (mc), such as avocado stone AS (65-70 wt.%), *Agave salmiana* bagasse ASB (>70 wt.%), and cocoa shell CS (10 wt.%). Also, cellulose CEL was used in all studies as model biomass for a comparative study.

The compositional analyses showed different chemical structures of the studied biomasses. The results obtained showed a high content of extractives and lignin in the CS, which gives it a higher energy content. The high content of HHV in CS may be necessary for its use as an energy source. However, its high content of extractive compounds may impede its utilization during the thermochemical conversion process. Perhaps the best method to convert CS to energy is the chemical process due to its high oil content. The chemical characteristics of AS, ASB, and CEL made their comparative studies during the thermochemical conversion process interesting. The AS contains 76.4 wt.% hemicelluloses and 3.6 wt.% cellulose; this is interesting because it can be used as model biomass for hemicellulose. ASB has 43.8 wt. % of hemicelluloses and 40.7wt.% of cellulose; this biomass can be used as a mixture of hemicellulose and cellulose. Finally, the cellulose (CEL) was used to complement the comparative studies of the three biomasses, during the hydrothermal carbonization process, where only cellulose and hemicellulose are decomposed.

According to the total solids yield analysis of the HTC study, the AS and CS decompositions can be divided into four main zones. The initial induction period in the first zone where the reaction rate is relatively slow (up to 160 °C), followed by a maximum loss of total solids yield up to 200 °C for AS and 210 °C for CS. The third zone corresponds to the stabilization zone, dominated by condensation reactions; stability was observed from 200 to 220 °C for AS and 210 to 230 °C for CS. The last zone corresponds to the increase in total solid mass yield. The increase in total solid mass yield is related to aromatization and polymerization reactions. The results of the GC-MS study of the tar solution indicate that the tar contains aliphatic compounds and PAHs. Nevertheless, no PAHs were detected in CS. PAHs in hydrochars may be an impediment to use as a fertilizer since hydrochar is a favorable soil amendment, increasing cation extraction capacity and reducing the bulk density of solids.

Kinetic study of the HTC process indicates that the activation energy of the hydrolysis reaction depends on biomass composition. Indeed, the higher the hemicellulose content, the lower the activation energy. The activation energy of CEL hydrolysis (136.24 kJ/mol) is higher than in the case of AS and AB, which is 63.08 and 85.02 kJ/mol, respectively. Therefore, more energy is required for CEL hydrolysis than for AS or AB. This was also confirmed by the low solid conversion rate of CEL at low temperatures compared to AS and AB. Furthermore, for all biomasses, the activation energy for the formation of furfural and 5-HMF is higher than for forming organic acids, which was by the concentration of these intermediate products.

The application of design of experiments and response surface methodology (DoE/RSM) permitted to relate the process operating conditions to the hydrochar properties, including mass yield and thermal combustion behavior. The optimized HTC process allowed us to increase the energy content of AS from 18.6 to 26.98 MJ/kg and CS from 23.0 to 32.3 MJ/kg at 250 °C and 2 hours of reaction time.

The CFD study shows that the ideal stirring speed to obtain a homogeneous mixture inside the reactor is 550 rpm, given a turbulent regime. The average velocity corresponding to the dispersed phase is 0.24m/s, owing to AS particle's high density. The application of CFD simulation allowed the model construction that describes the heat transfer inside the reactor during the HTC of the AS, taking into account the kinetics of the HTC reaction. The model considers the reactor heat-up time, inside the reactor biomass concentration, and the water thermal properties evolution, and the thermal properties of biomass during the HTC process. This model can be extrapolated for use in any biomass with the known kinetic parameter and ultimate analysis. The CFD simulation results show that the difference between the thermal properties of biomass and water under HTC conditions is negligible. The biomass-to-water ratio has an effect on heat transfer during the HTC process. It is crucial to consider the biomass concentration in the kinetic model of the HTC process and heat-up time. The present modeling approach thus shows a promising way to simulate biomass HTC processes on an industrial scale. In addition, with the help of this model, the enthalpy of the HTC reaction can be determined.

The results obtained in the three models were used in the simulation of the HTC process, pyrolysis and gasification, using AspenPlus®. First, the experimental design models determine the optimal HTC conditions, determining the kinetic parameters. Then, use the kinetic results in the CFD simulation to study hydrodynamics and the effect of transport phenomena. These

results would help the scaling up of the biomass conversion process and the design of the plant for the production of clean and sustainable energy.

Additionally, an energy balance was performed for the HTC process, where the results showed that the biomass to water ratio inside the reactor and temperature is a fundamental factor for the process scale up. The overall energy efficiency of the HTC process is as high as 85%, without considering the possible uses of the HTC liquid phase (which contains many valuable compounds), with the energy integration of the HTC process. This efficiency shows that hydrochar can store 85% of initial energy within the biomass after HTC, thus showing that the HTC process is ideal for biomass pretreatment with high moisture content. Also, the study of the economic feasibility of using hydrochar as fuels showed that hydrochar pellets can be competitive with commercial wood pellets, with an initial capital recovery period of less than 4 years in normal condition.

Finally, the experimental results of syngas from the gasification were used to predict the production of synthetic fuels in Aspen HYSYS®. The main products obtained in these studies were gasoline with 19.98%, diesel 8.15%, naphtha 5%, kerosene 5%, liquefied petroleum gases 11.57% and the rest of the product was water.

Perspectives and recommendations

Several scientific perspectives for further research on HTC conversion of biomass into an energy source or other uses emerge from this work:

- To study the behavior of hydrochars in combustion and gasification with different gasifying agents such as steam, pure oxygen, CO_2, son on. Also, to study the isothermal gasification process of hydrochars at temperatures higher than 1000 ºC.
- To study the behavior of hydrochars as fertilizers and base for catalysts to see their efficiency. AS hydrochars are not recommended for use as fertilizer due to their high PAH content.
- It is recommended to use the cocoa shell (CS) for biodiesel production due to its high oil content (>25%).
- Use hydrochars to remove heavy metals and dyes in the water and compare the yield with biochar (char obtained by pyrolysis).

- To exploit the experimental methodology developed in this work to understand the complex steps and reaction mechanism of biomass decomposition in aqueous media by characterizing the solid and analyzing the liquid and gas phases.
- Try to valorize the by-products of HTC and optimize its recovery, as it contains high value-added products (furfurals, 5-HMF, organic acids, and many more). Moreover, the liquid phase of the HTC process represents the main problem related to the application of the HTC process to treat wet organic materials. In this work, two alternatives for treating the liquid generated by the HTC process have been studied (using the liquid to produce biogas or recirculating it into the HTC process).

REFERENCES

Abdel-Hamid, A.M., Solbiati, J.O., Cann, I.K. (2013). Insights into lignin degradation and its potential industrial applications. in: *Advances in Applied Microbiology*, Vol. 82, Elsevier, pp. 1-28.

Abel, S., Peters, A., Trinks, S., Schonsky, H., Facklam, M., Wessolek, G. (2013). Impact of biochar and hydrochar addition on water retention and water repellency of sandy soil. *Geoderma*, **202**, 183-191.

Acar, M.C., Böke, Y.E. (2019). Simulation of biomass gasification in a BFBG using chemical equilibrium model and restricted chemical equilibrium method. *Biomass and Bioenergy*, **125**, 131-138.

Acharjee, T.C., Coronella, C.J., Vasquez, V.R. (2011). Effect of thermal pretreatment on equilibrium moisture content of lignocellulosic biomass. *Bioresource technology*, **102**(7), 4849-4854.

Adamafio, N. (2013). Theobromine toxicity and remediation of cocoa by-products: An overview. *Journal of Biological Sciences*, **13**(7), 570-576.

Adesina, A.A. (1996). Hydrocarbon synthesis via Fischer-Tropsch reaction: travails and triumphs. *Applied Catalysis A: General*, **138**(2), 345-367.

Agency, I.E. (2015). CO2 Emissions From Fuel Combustion Highlights. *OECD/IEA, 2015*.

Ahmed, A., Bakar, M.S.A., Azad, A.K., Sukri, R.S., Phusunti, N. (2018). Intermediate pyrolysis of Acacia cincinnata and Acacia holosericea species for bio-oil and biochar production. *Energy Conversion and Management*, **176**, 393-408.

Ahuja, G., Patwardhan, A. (2008). CFD and experimental studies of solids hold-up distribution and circulation patterns in gas–solid fluidized beds. *Chemical Engineering Journal*, **143**(1-3), 147-160.

Akhator, P., Obanor, A., Ugege, A. (2017). Nigerian Wood Waste: A potential resource for economic development. *Journal of Applied Sciences and Environmental Management*, **21**(2), 246-251.

Akhtar, J., Amin, N.A.S. (2011). A review on process conditions for optimum bio-oil yield in hydrothermal liquefaction of biomass. *Renewable and Sustainable Energy Reviews*, **15**(3), 1615-1624.

Akimoto, H., Narita, H. (1994). Distribution of SO2, NOx and CO2 emissions from fuel combustion and industrial activities in Asia with 1× 1 resolution. *Atmospheric Environment*, **28**(2), 213-225.

Al Arni, S. (2018). Comparison of slow and fast pyrolysis for converting biomass into fuel. *Renewable Energy*, **124**, 197-201.

Al-Wabel, M.I., Rafique, M.I., Ahmad, M., Ahmad, M., Hussain, A., Usman, A.R. (2019). Pyrolytic and hydrothermal carbonization of date palm leaflets: Characteristics and ecotoxicological effects on seed germination of lettuce. *Saudi journal of biological sciences*, **26**(4), 665-672.

Ali, I., Naqvi, S.R., Bahadar, A. (2018). Kinetic analysis of Botryococcus braunii pyrolysis using model-free and model fitting methods. *Fuel*, **214**, 369-380.

Almohammadi, K., Ingham, D., Ma, L., Pourkashan, M. (2013). Computational fluid dynamics (CFD) mesh independency techniques for a straight blade vertical axis wind turbine. *Energy*, **58**, 483-493.

Álvarez-Murillo, A., Ledesma, B., Román, S., Sabio, E., Gañán, J. (2015a). Biomass pyrolysis toward hydrocarbonization. Influence on subsequent steam gasification processes. *Journal of analytical and applied pyrolysis*, **113**, 380-389.

Álvarez-Murillo, A., Román, S., Ledesma, B., Sabio, E. (2015b). Study of variables in energy densification of olive stone by hydrothermal carbonization. *Journal of Analytical and Applied Pyrolysis*, **113**, 307-314.

Álvarez-Murillo, A., Sabio, E., Ledesma, B., Román, S., González-García, C. (2016). Generation of biofuel from hydrothermal carbonization of cellulose. Kinetics modelling. *Energy*, **94**, 600-608.

Amika, J. (2010). Process Simulation and Control Using Aspen. *Eastern Economy, pág. 3, 78-80*.

Amonette, J.E., Joseph, S. (2009). Characteristics of biochar: microchemical properties. *Biochar for environmental management: Science and technology*, **33**.

Anderson, R., Hofer, L., Storch, H. (1958). Der Reaktionsmechanismus der Fischer-Tropsch-Synthese. *Chemie Ingenieur Technik*, **30**(9), 560-566.

Angelidaki, I., Ahring, B. (1992). Effects of free long-chain fatty acids on thermophilic anaerobic digestion. *Applied microbiology and biotechnology*, **37**(6), 808-812.

Annamalai, K., Sweeten, J., Ramalingam, S. (1987). Technical Notes: Estimation of gross heating values of biomass fuels. *Transactions of the ASAE*, **30**(4), 1205-1208.

Ansari, K.B., Arora, J.S., Chew, J.W., Dauenhauer, P.J., Mushrif, S.H. (2018). Effect of temperature and transport on the yield and composition of pyrolysis-derived bio-oil from glucose. *Energy & fuels*, **32**(5), 6008-6021.

Ansari, K.B., Arora, J.S., Chew, J.W., Dauenhauer, P.J., Mushrif, S.H. (2019). Fast pyrolysis of cellulose, hemicellulose, and lignin: effect of operating temperature on bio-oil yield and composition and insights into the intrinsic pyrolysis chemistry. *Industrial & Engineering Chemistry Research*, **58**(35), 15838-15852.

Antal Jr, M.J., Mok, W.S., Richards, G.N. (1990). Mechanism of formation of 5-(hydroxymethyl)-2-furaldehyde from D-fructose and sucrose. *Carbohydrate research*, **199**(1), 91-109.

Araji, N., Madjinza, D.D., Chatel, G., Moores, A., Jérôme, F., Vigier, K.D.O. (2017). Synthesis of maleic and fumaric acids from furfural in the presence of betaine hydrochloride and hydrogen peroxide. *Green Chemistry*, **19**(1), 98-101.

Araujo, P., Janagap, S. (2012). Doehlert uniform shell designs and chromatography. *Journal of Chromatography B*, **910**, 14-21.

Arellanoa, O., Flores, M., Guerra, J., Hidalgo, A., Rojas, D., Strubinger, A. (2016). Hydrothermal Carbonization (HTC) of Corncob and Characterization of the Obtained Hydrochar. *CHEMICAL ENGINEERING*, **50**.

Arora, J.S., Chew, J.W., Mushrif, S.H. (2018). Influence of alkali and alkaline-earth metals on the cleavage of glycosidic bond in biomass pyrolysis: a DFT study using cellobiose as a model compound. *The Journal of Physical Chemistry A*, **122**(38), 7646-7658.

Asmadi, M., Kawamoto, H., Saka, S. (2011a). Gas-and solid/liquid-phase reactions during pyrolysis of softwood and hardwood lignins. *Journal of Analytical and Applied Pyrolysis*, **92**(2), 417-425.

Asmadi, M., Kawamoto, H., Saka, S. (2011b). Thermal reactions of guaiacol and syringol as lignin model aromatic nuclei. *Journal of analytical and applied pyrolysis*, **92**(1), 88-98.

Asmadi, M., Kawamoto, H., Saka, S. (2011c). Thermal reactivities of catechols/pyrogallols and cresols/xylenols as lignin pyrolysis intermediates. *Journal of Analytical and Applied Pyrolysis*, **92**(1), 76-87.

Aspinall, G. (1959). Structural chemistry of the hemicelluloses. in: *Advances in carbohydrate chemistry*, Vol. 14, Elsevier, pp. 429-468.

Assary, R.S., Curtiss, L.A. (2012). Thermochemistry and reaction barriers for the formation of levoglucosenone from cellobiose. *ChemCatChem*, **4**(2), 200-205.

Avrami, M. (1939). Kinetics of phase change. I General theory. *The Journal of chemical physics*, **7**(12), 1103-1112.

Avrami, M. (1940). Kinetics of phase change. II transformation-time relations for random distribution of nuclei. *The Journal of chemical physics*, **8**(2), 212-224.

Aznar, M.P., Caballero, M.A., Sancho, J.A., Francés, E. (2006). Plastic waste elimination by co-gasification with coal and biomass in fluidized bed with air in pilot plant. *Fuel processing technology*, **87**(5), 409-420.

Babu, B. (2008). Biomass pyrolysis: a state-of-the-art review. *Biorefining: Innovation for a sustainable economy*, **2**(5), 393-414.

Baena González, A. (2005). Aprovechamiento del bagazo de maguey verde (agave salmiana) de la agroindustria del mezcal en San Luis Potosí para la producción de hongo ostra (pleurotus ostreatus).

Baio, F.H., Silva, S.P.d., Camolese, H.d.S., Neves, D.C. (2017). Financial analysis of the investment in precision agriculture techniques on cotton crop. *Engenharia Agrícola*, **37**(4), 838-847.

Balat, M., Balat, M., Kırtay, E., Balat, H. (2009). Main routes for the thermo-conversion of biomass into fuels and chemicals. Part 1: Pyrolysis systems. *Energy Conversion and Management*, **50**(12), 3147-3157.

Baratieri, M., Basso, D., Patuzzi, F., Castello, D., Fiori, L. (2015). Kinetic and thermal modeling of hydrothermal carbonization applied to grape marc.

Bargmann, I., Rillig, M., Buss, W., Kruse, A., Kuecke, M., science, c. (2013). Hydrochar and biochar effects on germination of spring barley. *%J Journal of agronomy*

crop science, **199**(5), 360-373.

Basso, D., Patuzzi, F., Castello, D., Baratieri, M., Rada, E.C., Weiss-Hortala, E., Fiori, L. (2016). Agro-industrial waste to solid biofuel through hydrothermal carbonization. *Waste Management*, **47**, 114-121.

Basso, D., Weiss-Hortala, E., Patuzzi, F., Castello, D., Baratieri, M., Fiori, L. (2015). Hydrothermal carbonization of off-specification compost: A byproduct of the organic municipal solid waste treatment. *Bioresource technology*, **182**, 217-224.

Bastola, K.P., Guragain, Y.N., Bhadriraju, V., Vadlani, P.V. (2017). Evaluation of standards and interfering compounds in the determination of phenolics by Folin-Ciocalteu assay method for effective bioprocessing of biomass. *American Journal of Analytical Chemistry*, **8**(06), 416.

Basu, P. (2010). *Biomass gasification and pyrolysis: practical design and theory*. Academic press.

Batidzirai, B., Junginger, M., Klemm, M., Schipfer, F., Thrän, D. (2016). Biomass Supply and Trade Opportunities of Preprocessed Biomass for Power Generation. in: *Developing the Global Bioeconomy*, Elsevier: Technical, Market, and Environmental Lessons from Bioenergy, pp. 91-114.

Baum, R., Wajszczuk, K., Pepliński, B., Wawrzynowicz, J. (2013). Potential for agricultural biomass production for energy purposes in Poland: a review. *Contemporary economics*, **7**(1), 63-74.

Beauchet, R., Pinard, L., Kpogbemabou, D., Laduranty, J., Lemee, L., Lemberton, J., Bataille, F., Magnoux, P., Ambles, A., Barbier, J. (2011). Hydroliquefaction of green wastes to produce fuels. *Bioresource technology*, **102**(10), 6200-6207.

Becker, R., Dorgerloh, U., Paulke, E., Mumme, J., Nehls, I. (2014). Hydrothermal carbonization of biomass: major organic components of the aqueous phase. *Chemical Engineering & Technology*, **37**(3), 511-518.

Behrendt, F., Neubauer, Y., Oevermann, M., Wilmes, B., Zobel, N. (2008). Direct liquefaction of biomass. *Chemical Engineering & Technology: Industrial Chemistry-Plant Equipment-Process Engineering-Biotechnology*, **31**(5), 667-677.

Bejarano, M., Laura, M., Aguilar, D., Paola, A. (2017). Evaluación del biochar e hidrochar como medios para captura de carbono en el suelo.

Bélanger, J.M., Paré, J.J., Sigouin, M. (1997). High performance liquid chromatography (HPLC): principles and applications. in: *Techniques and Instrumentation in Analytical Chemistry*, Vol. 18, Elsevier, pp. 37-59.

Ben, H., Ragauskas, A.J. (2012). Torrefaction of Loblolly pine. *Green Chemistry*, **14**(1), 72-76.

Benavente, V., Calabuig, E., Fullana, A. (2015). Upgrading of moist agro-industrial wastes by hydrothermal carbonization. *Journal of Analytical and Applied Pyrolysis*, **113**, 89-98.

Benjamin, B. (1985). Great Plains ASPEN model development: gasifier model. Final topical report. Scientific Design Co., Inc., New York (USA).

Berge, N.D., Ro, K.S., Mao, J., Flora, J.R., Chappell, M.A., Bae, S. (2011). Hydrothermal carbonization of municipal waste streams. *Environmental science & technology*, **45**(13), 5696-5703.

Bevan, E., Fu, J., Zheng, Y. (2020). Challenges and opportunities of hydrothermal carbonisation in the UK; case study in Chirnside. *RSC Advances*, **10**(52), 31586-31610.

Biagini, E., Bardi, A., Pannocchia, G., Tognotti, L. (2009). Development of an entrained flow gasifier model for process optimization study. *Industrial & engineering chemistry research*, **48**(19), 9028-9033.

Biagini, E., Fantei, A., Tognotti, L. (2008). Effect of the heating rate on the devolatilization of biomass residues. *Thermochimica Acta*, **472**(1-2), 55-63.

Biller, P., Ross, A. (2016). Production of biofuels via hydrothermal conversion. in: *Handbook of biofuels production*, Elsevier, pp. 509-547.

Biloen, P., Sachtler, W. (1981). Mechanism of hydrocarbon synthesis over Fischer-Tropsch catalysts. *Advances in Catalysis*, **30**, 165-216.

Bird, R.B., Stewart, W., Lightfoot, E. (2007). Polymeric liquids. *Transport Phenomena, revised 2nd ed., John Wiley & Sons, New York*, 231-242.

Bird, R.B., Stewart, W.E., Lightfoot, E.N. (2006). *Transport phenomena*. John Wiley & Sons.

Blackman, C.F., Black, J.A. (1977). Measurement of microwave radiation absorbed by biological systems: 2. Analysis by Dewar-flask calorimetry. *Radio Science*, **12**(6S), 9-14.

Blocken, B., Gualtieri, C. (2012). Ten iterative steps for model development and evaluation applied to Computational Fluid Dynamics for Environmental Fluid Mechanics. *Environmental Modelling & Software*, **33**, 1-22.

Bobleter, O. (1994). Hydrothermal degradation of polymers derived from plants. *Progress in polymer science*, **19**(5), 797-841.

Bodachivskyi, I., Kuzhiumparambil, U., Williams, D.B.G. (2018). Acid-catalyzed conversion of carbohydrates into value-added small molecules in aqueous media and ionic liquids. *ChemSusChem*.

Börjesson, P., Hansson, J., Berndes, G. (2017). Future demand for forest-based biomass for energy purposes in Sweden. *Forest Ecology and Management*, **383**, 17-26.

Borrero-López, A., Masson, E., Celzard, A., Fierro, V. (2018). Modelling the reactions of cellulose, hemicellulose and lignin submitted to hydrothermal treatment. *Industrial Crops and Products*, **124**, 919-930.

Boz, N., Degirmenbasi, N., Kalyon, D.M.J.A.C.B.E. (2009). Conversion of biomass to fuel: Transesterification of vegetable oil to biodiesel using KF loaded nano-γ-Al2O3 as catalyst. **89**(3-4), 590-596.

BP, G. (2017). BP Statistical Review ofWorld Energy June 2016. Retrieved from https://www.bp.com/en/global/corporate/energy-economics.html

Brachi, P., Chirone, R., Miccio, F., Miccio, M., Picarelli, A., Ruoppolo, G. (2014). Fluidized bed co-gasification of biomass and polymeric wastes for a flexible end-use of the syngas: focus on bio-methanol. *Fuel*, **128**, 88-98.

Braovac, S., Kutzke, H. (2012). The presence of sulfuric acid in alum-conserved wood–Origin and consequences. *Journal of cultural heritage*, **13**(3), S203-S208.

Braun, J.F. (2020). G20 CO2 Emissions from Fuel Combustion (1970-2019).

Brennan, L., Owende, P. (2010). Biofuels from microalgae—a review of technologies for production, processing, and extractions of biofuels and co-products. *Renewable and sustainable energy reviews*, **14**(2), 557-577.

Bridgwater, A. (1999). Principles and practice of biomass fast pyrolysis processes for liquids. *Journal of analytical applied pyrolysis*

, **51**(1-2), 3-22.

Bridgwater, A.V., Meier, D., Radlein, D. (1999). An overview of fast pyrolysis of biomass. *Organic geochemistry*, **30**(12), 1479-1493.

Brown, M.E., Dollimore, D., Galwey, A.K. (1980). *Reactions in the solid state*. Elsevier.

Bull, S.R. (2001). Renewable energy today and tomorrow. *Proceedings of the IEEE*, **89**(8), 1216-1226.

Burguete, P., Corma, A., Hitzl, M., Modrego, R., Ponce, E., Renz, M. (2016). Fuel and chemicals from wet lignocellulosic biomass waste streams by hydrothermal carbonization. *Green Chemistry*, **18**(4), 1051-1060.

Burnham, A.K., Dinh, L. (2007). A comparison of isoconversional and model-fitting approaches to kinetic parameter estimation and application predictions. *Journal of Thermal Analysis and Calorimetry*, **89**(2), 479-490.

Busch, D., Stark, A., Kammann, C.I., Glaser, B. (2013). Genotoxic and phytotoxic risk assessment of fresh and treated hydrochar from hydrothermal carbonization compared to biochar from pyrolysis. *Ecotoxicology and environmental safety*, **97**, 59-66.

Cai, J., He, Y., Yu, X., Banks, S.W., Yang, Y., Zhang, X., Yu, Y., Liu, R., Bridgwater, A.V. (2017). Review of physicochemical properties and analytical characterization of lignocellulosic biomass. *Renewable and Sustainable Energy Reviews*, **76**, 309-322.

Cai, J., Xu, D., Dong, Z., Yu, X., Yang, Y., Banks, S.W., Bridgwater, A.V. (2018). Processing thermogravimetric analysis data for isoconversional kinetic analysis of lignocellulosic biomass pyrolysis: Case study of corn stalk. *Renewable and Sustainable Energy Reviews*, **82**, 2705-2715.

Cao, Y., Wang, Y., Riley, J.T., Pan, W.-P. (2006). A novel biomass air gasification process for producing tar-free higher heating value fuel gas. *Fuel processing technology*, **87**(4), 343-353.

Cavalaglio, G., Cotana, F., Nicolini, A., Coccia, V., Petrozzi, A., Formica, A., Bertini, A. (2020). Characterization of Various Biomass Feedstock Suitable for Small-Scale Energy Plants as Preliminary Activity of Biocheaper Project. *Sustainability*, **12**(16), 6678.

Ceballos, A.M., Montoya, S. (2013). Evaluación química de la fibra en semilla, pulpa y cáscara de tres variedades de aguacate. *Biotecnología en el sector agropecuario y agroindustrial*, **11**(1), 103-112.

Cepeliogullar, O., Putun, A.E. (2014). Products characterization study of a slow pyrolysis of biomass-plastic mixtures in a fixed-bed reactor. *Journal of Analytical and Applied Pyrolysis*, **110**, 363-374.

Chae, K., Jang, A., Yim, S., Kim, I.S. (2008). The effects of digestion temperature and temperature shock on the biogas yields from the mesophilic anaerobic digestion of swine manure. *Bioresource technology*, **99**(1), 1-6.

Channiwala, S., Parikh, P. (2002). A unified correlation for estimating HHV of solid, liquid and gaseous fuels. *Fuel*, **81**(8), 1051-1063.

Charis, G., Danha, G., Muzenda, E. (2020). Characterizations of Biomasses for Subsequent Thermochemical Conversion: A Comparative Study of Pine Sawdust and Acacia Tortilis. *Processes*, **8**(5), 546.

Chartier, A., Beaumesnil, M., de Oliveira, A.L., Elfakir, C., Bostyn, S. (2013). Optimization of the isolation and quantitation of kahweol and cafestol in green coffee oil. *Talanta*, **117**, 102-111.

Chaves, I.D.G., López, J.R.G., Zapata, J.L.G., Robayo, A.L., Niño, G.R. (2016). *Process analysis and simulation in chemical engineering*. Springer.

Chávez-Guerrero, L., Hinojosa, M. (2010). Bagasse from the mezcal industry as an alternative renewable energy produced in arid lands. *Fuel*, **89**(12), 4049-4052.

Chen, R., Lu, S., Zhang, Y., Lo, S. (2017). Pyrolysis study of waste cable hose with thermogravimetry/Fourier transform infrared/mass spectrometry analysis. *Energy Conversion and Management*, **153**, 83-92.

Chen, W.-H., Ye, S.-C., Sheen, H.-K. (2012). Hydrothermal carbonization of sugarcane bagasse via wet torrefaction in association with microwave heating. *Bioresource technology*, **118**, 195-203.

Cheng, J.J., Timilsina, G.R. (2011). Status and barriers of advanced biofuel technologies: a review. *Renewable Energy*, **36**(12), 3541-3549.

Cheng, X., Tang, Y., Wang, B., Jiang, J. (2018). Improvement of charcoal yield and quality by two-step pyrolysis on rice husks. *Waste and Biomass Valorization*, **9**(1), 123-130.

Chuntanapum, A., Matsumura, Y. (2009). Formation of tarry material from 5-HMF in subcritical and supercritical water. *Industrial & engineering chemistry research*, **48**(22), 9837-9846.

Cibulková, Z., Polovková, J., Lukeš, V., Klein, E. (2006). DSC and FTIR study of the gamma radiation effect on cis-1, 4-polyisoprene. *Journal of thermal analysis and calorimetry*, **84**(3), 709-713.

Ciferno, J.P., Marano, J.J. (2002). Benchmarking biomass gasification technologies for fuels, chemicals and hydrogen production. *US Department of Energy. National Energy Technology Laboratory*.

Ciolacu, D., Ciolacu, F., Popa, V.I. (2011). Amorphous cellulose—structure and characterization. *Cellulose chemistry and technology*, **45**(1), 13.

Clarke, S., Preto, F. (2011). *Biomass burn characteristics*. Ministry of Agriculture, Food and Rural Affairs.

Coats, A., Redfern, J. (1964a). Kinetic parameters from thermogravimetric data. *Nature*, **201**(4914), 68-69.

Coats, A.W., Redfern, J. (1964b). Kinetic parameters from thermogravimetric data. *Nature*, **201**(4914), 68-69.

Collard, F.-X., Blin, J. (2014). A review on pyrolysis of biomass constituents: Mechanisms and composition of the products obtained from the conversion of cellulose, hemicelluloses and lignin. *Renewable and Sustainable Energy Reviews*, **38**, 594-608.

Concin, R., Burtscher, P., Burtscher, E., Bobleter, O. (1983). Separation and identification of monomeric lignin degradation products by glc-mass spectrometry. *International Journal of Mass Spectrometry and Ion Physics*, **48**, 63-66.

Conesa, J.A., Caballero, J., Marcilla, A., Font, R. (1995). Analysis of different kinetic models in the dynamic pyrolysis of cellulose. *Thermochimica Acta*, **254**, 175-192.

Copetti, M.V., Pereira, J.L., Iamanaka, B.T., Pitt, J.I., Taniwaki, M.H. (2010). Ochratoxigenic fungi and ochratoxin A in cocoa during farm processing. *International journal of food microbiology*, **143**(1-2), 67-70.

Cordero, T., Marquez, F., Rodriguez-Mirasol, J., Rodriguez, J. (2001). Predicting heating values of lignocellulosics and carbonaceous materials from proximate analysis. *Fuel*, **80**(11), 1567-1571.

Cosentino, S.L., Copani, V., Patanè, C., Mantineo, M., D'Agosta, G.M. (2008). Agronomic, energetic and environmental aspects of biomass energy crops suitable for Italian environments. *Italian Journal of Agronomy*, 81-96.

Crabtree, A., Siman-Tov, M. (1993). Thermophysical properties of saturated light and heavy water for Advanced Neutron Source applications. Oak Ridge National Lab., TN (United States).

Cullen, P.J. (2009). *Food mixing: Principles and applications*. John Wiley & Sons.

Damartzis, T., Zabaniotou, A. (2011). Thermochemical conversion of biomass to second generation biofuels through integrated process design—A review. *Renewable and Sustainable Energy Reviews*, **15**(1), 366-378.

Danso Boateng, E., Holdich, R., Shama, G., Wheatley, A.D., Sohail, M., Martin, S. (2013). Kinetics of faecal biomass hydrothermal carbonisation for hydrochar production. *Applied energy*, **111**, 351-357.

Danso-Boateng, E., Holdich, R., Shama, G., Wheatley, A.D., Sohail, M., Martin, S. (2013). Kinetics of faecal biomass hydrothermal carbonisation for hydrochar production. *Applied energy*, **111**, 351-357.

David Moore, Geoffrey D. Robson, P. J. Trinci. (2011). *21st Century Guidebook to Fungi with CD-ROM*. University of Manchester.

Dayton, D.C., Foust, T.D. (2019). *Analytical Methods for Biomass Characterization and Conversion*. Elsevier.

de Souza-Santos, M.L. (2010). *Solid fuels combustion and gasification: modeling, simulation*. CRC Press.

De Wild, P., Den Uil, H., Reith, J., Kiel, J., Heeres, H. (2009). Biomass valorisation by staged degasification: A new pyrolysis-based thermochemical conversion option to produce value-added chemicals from lignocellulosic biomass. *Journal of analytical and applied Pyrolysis*, **85**(1-2), 124-133.

Deguchi, S., Mukai, S.-a., Tsudome, M., Horikoshi, K. (2006). Facile generation of fullerene nanoparticles by hand-grinding. *Advanced Materials*, **18**(6), 729-732.

Demirbas, A. (2005). Bioethanol from cellulosic materials: a renewable motor fuel from biomass. *Energy sources*, **27**(4), 327-337.

Demirbas, A. (2001a). Biomass resource facilities and biomass conversion processing for fuels and chemicals. *Energy conversion and Management*, **42**(11), 1357-1378.

Demirbas, A. (1997). Calculation of higher heating values of biomass fuels. *Fuel*, **76**(5), 431-434.

Demirbas, A. (2010). Effect of temperature on pyrolysis products from biomass, Part A. *Energy Sources*, **29**(4), 329-336.

Demirbas, A. (2004). Effects of temperature and particle size on bio-char yield from pyrolysis of agricultural residues. *Journal of analytical and applied pyrolysis*, **72**(2), 243-248.

Demirbas, A. (2002). Gaseous products from biomass by pyrolysis and gasification: effects of catalyst on hydrogen yield. *Energy conversion and management*, **43**(7), 897-909.

Demirbas, A. (2007). Progress and recent trends in biofuels. *Progress in energy combustion science*, **33**(1), 1-18.

Demirbas, A. (2001b). Relationships between lignin contents and heating values of biomass. *Energy conversion and management*, **42**(2), 183-188.

Deng, Q., Alvarado, R., Toledo, E., Caraguay, L. (2020). Greenhouse gas emissions, non-renewable energy consumption, and output in South America: the role of the productive structure. *Environmental Science and Pollution Research*, 1-15.

Devi, L., Ptasinski, K.J., Janssen, F.J., van Paasen, S.V., Bergman, P.C., Kiel, J.H. (2005). Catalytic decomposition of biomass tars: use of dolomite and untreated olivine. *Renewable energy*, **30**(4), 565-587.

Dhaundiyal, A., Singh, S.B., Hanon, M.M., Rawat, R. (2018). Determination of kinetic parameters for the thermal decomposition of parthenium hysterophorus. *Environmental and Climate Technologies*, **22**(1), 5-21.

Di Blasi, C. (1998). Comparison of semi-global mechanisms for primary pyrolysis of lignocellulosic fuels. *Journal of Analytical and Applied Pyrolysis*, **47**(1), 43-64.

Ding, L., Wang, Z., Li, Y., Du, Y., Liu, H., Guo, Y. (2012). A novel hydrochar and nickel composite for the electrochemical supercapacitor electrode material. *Materials Letters*, **74**, 111-114.

Doherty, W., Reynolds, A., Kennedy, D. (2009). The effect of air preheating in a biomass CFB gasifier using ASPEN Plus simulation. *Biomass and bioenergy*, **33**(9), 1158-1167.

Domalski, E.S., Jobe Jr, T.L., Milne, T.A. (1986). Thermodynamic data for biomass conversion and waste incineration. National Bureau of Standards, Washington, DC (US); Solar Energy Research ….

Domingo, J.L., Nadal, M. (2015). Human dietary exposure to polycyclic aromatic hydrocarbons: A review of the scientific literature. *Food and Chemical Toxicology*, **86**, 144-153.

Dong, J. (2016). MSWs gasification with emphasis on energy, environment and life cycle assessment, Ecole des Mines d'Albi-Carmaux; Zhejiang University. Institute for Thermal ….

Doyle, C.D. (1961). Kinetic analysis of thermogravimetric data. *Journal of applied polymer science*, **5**(15), 285-292.

Dry, M.E. (2002). High quality diesel via the Fischer–Tropsch process–a review. *Journal of Chemical Technology and Biotechnology*, **77**(1), 43-50.

Dry, M.E. (1996). Practical and theoretical aspects of the catalytic Fischer-Tropsch process. *Applied Catalysis A: General*, **138**(2), 319-344.

Dry, M.E. (2004). Present and future applications of the Fischer–Tropsch process. *Applied Catalysis A: General*, **276**(1), 1-3.

Duman, G., Uddin, M.A., Yanik, J. (2014). Hydrogen production from algal biomass via steam gasification. *Bioresource technology*, **166**, 24-30.

Dunn, P.D. (1986). Renewable energies: sources, conversion and application, Sources & Power Generation, United States.

Dupont, C., Chiriac, R., Gauthier, G., Toche, F. (2014). Heat capacity measurements of various biomass types and pyrolysis residues. *Fuel*, **115**, 644-651.

Economics, T. (2021). Trading Economics. Retrieved from https://tradingeconomics.com/commodity/coal

Edenhofer, O., Pichs-Madruga, R., Sokona, Y., Seyboth, K., Matschoss, P., Kadner, S., Zwickel, T., Eickemeier, P., Hansen, G., Schlömer, S. (2011). IPCC special report on renewable energy sources and climate change mitigation. *Prepared By Working Group III of the Intergovernmental Panel on Climate Change, Cambridge University Press, Cambridge, UK*.

Edreis, E.M., Yao, H. (2016). Kinetic thermal behaviour and evaluation of physical structure of sugar cane bagasse char during non-isothermal steam gasification. *Journal of Materials Research and Technology*, **5**(4), 317-326.

Egedy, A., Varga, T., Chován, T. (2013). Compartment model structure identification with qualitative methods for a stirred vessel. *Mathematical and Computer Modelling of Dynamical Systems*, **19**(2), 115-132.

Egré, D., Milewski, J.C. (2002). The diversity of hydropower projects. *Energy Policy*, **30**(14), 1225-1230.

Egsgaard, H., Larsen, E. (Year) of Conference. Thermal transformation of light tar-specific routes to aromatic aldehydes and PAH. *1st World Conference and Exhibition on Biomass for Energy and Industry*.

El Bassam, N., Maegaard, P., Schlichting, M. (2013). *Distributed renewable energies for off-grid communities: strategies and technologies toward achieving sustainability in energy generation and supply*. Newnes.

Elliott, D.C., Biller, P., Ross, A.B., Schmidt, A.J., Jones, S.B. (2015). Hydrothermal liquefaction of biomass: developments from batch to continuous process. *Bioresource technology*, **178**, 147-156.

Elmay, Y., Le Brech, Y., Delmotte, L., Dufour, A., Brosse, N., Gadiou, R. (2015). Characterization of Miscanthus pyrolysis by DRIFTs, UV Raman spectroscopy and mass spectrometry. *Journal of analytical and applied pyrolysis*, **113**, 402-411.

Elorf, A., Kandasamy, J., Belandria, V., Bostyn, S., Sarh, B., Gökalp, I. (2019). Heating rate effects on pyrolysis, gasification and combustion of olive waste. *Biofuels*, 1-8.

Escala, M., Zumbuhl, T., Koller, C., Junge, R., Krebs, R. (2013). Hydrothermal carbonization as an energy-efficient alternative to established drying technologies for sewage sludge: a feasibility study on a laboratory scale. *Energy & Fuels*, **27**(1), 454-460.

Eser, S., Andrésen, J.M. (2004). Properties of fuels, petroleum pitch, petroleum coke, and carbon materials. *ASTM MANUAL SERIES MNL*, 757-786.

Fakkaew, K., Koottatep, T., Polprasert, C. (2015). Effects of hydrolysis and carbonization reactions on hydrochar production. *Bioresource technology*, **192**, 328-334.

Fakkaew, K., Koottatep, T., Polprasert, C. (2018). Faecal sludge treatment and utilization by hydrothermal carbonization. *Journal of environmental management*, **216**, 421-426.

Falco, C., Baccile, N., Titirici, M.-M. (2011). Morphological and structural differences between glucose, cellulose and lignocellulosic biomass derived hydrothermal carbons. *Green Chemistry*, **13**(11), 3273-3281.

Fang, J., Gao, B., Chen, J., Zimmerman, A. (2015a). Hydrochars derived from plant biomass under various conditions: characterization and potential applications and impacts. *Chemical Engineering Journal*, **267**, 253-259.

Fang, J., Gao, B., Chen, J., Zimmerman, A.R. (2015b). Hydrochars derived from plant biomass under various conditions: characterization and potential applications and impacts. *Chemical Engineering Journal*, **267**, 253-259.

Fang, J., Zhan, L., Ok, Y.S., Gao, B. (2018). Minireview of potential applications of hydrochar derived from hydrothermal carbonization of biomass. *Journal of Industrial and Engineering Chemistry*, **57**, 15-21.

Fang, J., Zhan, L., Ok, Y.S., Gao, B.J.J.o.I., Chemistry, E. (2017). Minireview of potential applications of hydrochar derived from hydrothermal carbonization of biomass.

FAO. (2017). Crops World regions Production quantity of avocados for 2016. *Food and Agriculture Organization of the United Nations, Statistical Division (FAOSTAT)*.

Faravelli, T., Frassoldati, A., Migliavacca, G., Ranzi, E. (2010). Detailed kinetic modeling of the thermal degradation of lignins. *Biomass and bioenergy*, **34**(3), 290-301.

Favas, J., Monteiro, E., Rouboa, A. (2017). Hydrogen production using plasma gasification with steam injection. *international journal of hydrogen energy*, **42**(16), 10997-11005.

Feng, Y., Yu, T., Ma, K., Xu, G., Hu, Y., Chen, D. (2018). Effect of hydrothermal temperature on the steam gasification performance of sewage sludge: Syngas quality and tar formation. *Energy & Fuels*, **32**(6), 6834-6838.

Fermoso, J., Gil, M., Pevida, C., Pis, J., Rubiera, F. (2010). Kinetic models comparison for non-isothermal steam gasification of coal–biomass blend chars. *Chemical Engineering Journal*, **161**(1), 276-284.

Fernandes, M.B., Brooks, P. (2003). Characterization of carbonaceous combustion residues: II. Nonpolar organic compounds. *Chemosphere*, **53**(5), 447-458.

Ferreira, S.L., Queiroz, A.S., Fernandes, M.S., dos Santos, H.C. (2002). Application of factorial designs and Doehlert matrix in optimization of experimental variables associated with the preconcentration and determination of vanadium and copper in seawater by inductively coupled plasma optical emission spectrometry. *Spectrochimica Acta Part B: Atomic Spectroscopy*, **57**(12), 1939-1950.

Fischer, F., Tropsch, H. (1926). The synthesis of petroleum at atmospheric pressures from gasification products of coal. *Brennstoff-Chemie*, **7**, 97-104.

Fitzgerald, G., Mandel, J., Morris, J., Touati, H. (2015). The Economics of Battery Energy Storage: How multi-use, customer-sited batteries deliver the most services and value to customers and the grid. *Rocky Mountain Institute*, 6.

Flores-Sahagun, T.H., Dos Santos, L.P., Dos Santos, J., Mazzaro, I., Mikowski, A. (2013). Characterization of blue agave bagasse fibers of Mexico. *Composites Part A: Applied Science and Manufacturing*, **45**, 153-161.

Flynn, J.H., Wall, L.A. (1966). A quick, direct method for the determination of activation energy from thermogravimetric data. *Journal of Polymer Science Part B: Polymer Letters*, **4**(5), 323-328.

Foo, D.C., Elyas, R. (2017). Introduction to Process Simulation. *Chemical Engineering Process Simulation*, 3-21.

François, J., Abdelouahed, L., Mauviel, G., Patisson, F., Mirgaux, O., Rogaume, C., Rogaume, Y., Feidt, M., Dufour, A. (2013). Detailed process modeling of a wood gasification combined heat and power plant. *Biomass and bioenergy*, **51**, 68-82.

Fregolente, L.G., de Castro, A.J., Moreira, A.B., Ferreira, O.P., Bisinoti, M.C. (2020). New proposal for sugarcane vinasse treatment by hydrothermal carbonization: an evaluation of solid and liquid products. *Journal of the Brazilian Chemical Society*, **31**(1), 40-50.

Frei, W. (2013). Which turbulence model should I choose for my CFD application. *Consulted on*, **7**(05), 2015.

Friedman, H.L. (Year) of Conference. Kinetics of thermal degradation of char-forming plastics from thermogravimetry. Application to a phenolic plastic. *Journal of polymer science part C: polymer symposia*. Wiley Online Library. pp. 183-195.

Fu, P., Yi, W., Bai, X., Li, Z., Hu, S., Xiang, J. (2011). Effect of temperature on gas composition and char structural features of pyrolyzed agricultural residues. *Bioresource Technology*, **102**(17), 8211-8219.

Fuertes, A., Arbestain, M.C., Sevilla, M., Maciá-Agulló, J.A., Fiol, S., López, R., Smernik, R., Aitkenhead, W., Arce, F., Macìas, F. (2010). Chemical and structural properties of carbonaceous products obtained by pyrolysis and hydrothermal carbonisation of corn stover. *Soil Research*, **48**(7), 618-626.

Funke, A., Reebs, F., Kruse, A. (2013). Experimental comparison of hydrothermal and vapothermal carbonization. *Fuel processing technology*, **115**, 261-269.

Funke, A., Ziegler, F. (2011). Heat of reaction measurements for hydrothermal carbonization of biomass. *Bioresource technology*, **102**(16), 7595-7598.

Funke, A., Ziegler, F. (2010). Hydrothermal carbonization of biomass: a summary and discussion of chemical mechanisms for process engineering. *Biofuels, Bioproducts and Biorefining*, **4**(2), 160-177.

Furukawa, H., Kato, Y., Inoue, Y., Kato, T., Tada, Y., Hashimoto, S. (2012). Correlation of power consumption for several kinds of mixing impellers. *International Journal of Chemical Engineering*, **2012**.

Gagliano, A., Nocera, F., Bruno, M. (2018). Simulation models of biomass thermochemical conversion processes, gasification and pyrolysis, for the prediction of the energetic potential. in: *Advances in Renewable Energies and Power Technologies*, Elsevier, pp. 39-85.

Gai, C., Dong, Y. (2012). Experimental study on non-woody biomass gasification in a downdraft gasifier. *International Journal of hydrogen energy*, **37**(6), 4935-4944.

Gai, C., Guo, Y., Liu, T., Peng, N., Liu, Z. (2016). Hydrogen-rich gas production by steam gasification of hydrochar derived from sewage sludge. *International Journal of Hydrogen Energy*, **41**(5), 3363-3372.

Gallifuoco, A. (2019). A new approach to kinetic modeling of biomass hydrothermal carbonization. *ACS Sustainable Chemistry & Engineering*, **7**(15), 13073-13080.

Galwey, A.K., Brown, M.E. (1999). *Thermal decomposition of ionic solids: chemical properties and reactivities of ionic crystalline phases*. Elsevier.

Gamgoum, R., Dutta, A., Santos, R.M., Chiang, Y.W. (2016). Hydrothermal conversion of neutral sulfite semi-chemical red liquor into hydrochar. *Energies*, **9**(6), 435.

Gani, A., Naruse, I. (2007). Effect of cellulose and lignin content on pyrolysis and combustion characteristics for several types of biomass. *Renewable energy*, **32**(4), 649-661.

Gao, P., Zhou, Y., Meng, F., Zhang, Y., Liu, Z., Zhang, W., Xue, G. (2016a). Preparation and characterization of hydrochar from waste eucalyptus bark by hydrothermal carbonization. *Energy*, **97**, 238-245.

Gao, X., Zhang, Y., Li, B., Yu, X. (2016b). Model development for biomass gasification in an entrained flow gasifier using intrinsic reaction rate submodel. *Energy Conversion and Management*, **108**, 120-131.

Gao, X., Zhang, Y., Li, B., Zhao, Y., Jiang, B. (2016c). Determination of the intrinsic reactivities for carbon dioxide gasification of rice husk chars through using random pore model. *Bioresource technology*, **218**, 1073-1081.

García, R., Pizarro, C., Lavín, A.G., Bueno, J.L. (2012). Characterization of Spanish biomass wastes for energy use. *Bioresource technology*, **103**(1), 249-258.

García-Fajardo, J., Ramos-Godínez, M.d.R., Mora-Galindo, J. (1999). Estructura de la semilla de aguacate y cuantificación de la grasa extraída por diferentes técnicas. *Revista Chapingo serie horticultura*, **5**, 123-128.

Garcia-Maraver, A., Salvachúa, D., Martínez, M., Diaz, L., Zamorano, M. (2013). Analysis of the relation between the cellulose, hemicellulose and lignin content and the thermal behavior of residual biomass from olive trees. *Waste Management*, **33**(11), 2245-2249.

Garlapalli, R.K., Wirth, B., Reza, M.T. (2016). Pyrolysis of hydrochar from digestate: Effect of hydrothermal carbonization and pyrolysis temperatures on pyrochar formation. *Bioresource technology*, **220**, 168-174.

Garrote, G., Dominguez, H., Parajo, J. (2001). Study on the deacetylation of hemicelluloses during the hydrothermal processing of Eucalyptus wood. *Holz als Roh-und Werkstoff*, **59**(1-2), 53-59.

Gasparoviv, L., Korenova, Z., Jelemensky, L. (2010). Kinetic study of wood chips decomposition by TGA. *Chemical papers*, **64**(2), 174-181.

Georgieva, V., Zvezdova, D., Vlaev, L. (2012). Non-isothermal kinetics of thermal degradation of chitosan. *Chemistry Central Journal*, **6**(1), 1-10.

Ghosh, A., Sarkar, J.P., Das, B. (2019). A critical analysis on anaerobic digestion of OFMSW in India. *Waste valorisation and recycling*, 237-245.

Giger-Reverdin, S. (1995). Review of the main methods of cell wall estimation: interest and limits for ruminants. *Animal feed science and technology*, **55**(3-4), 295-334.

Gmehling, J., Kleiber, M., Kolbe, B., Rarey, J. (2019). *Chemical thermodynamics for process simulation*. Wiley Online Library.

Goldemberg, J., Coelho, S.T. (2004). Renewable energy—traditional biomass vs. modern biomass. *Energy Policy*, **32**(6), 711-714.

González Carballo, J.M. (2012). Diseño de catalizadores de rutenio para la síntesis Fischer-Tropsch.

González-Alejo, F.A., Barajas-Fernández, J., Olán-Acosta, M.d.l.Á., Lagunes-Gálvez, L.M., García-Alamilla, P. (2019). Supercritical Fluid Extraction of Fat and Caffeine with Theobromine Retention in the Cocoa Shell. *Processes*, **7**(6), 385.

González-Fernández, J.J., Galea, Z., Álvarez, J.M., Hormaza, J.I., López, R. (2015). Evaluation of composition and performance of composts derived from guacamole production residues. *Journal of environmental management*, **147**, 132-139.

Graboski, M., Bain, R. (1981). Properties of biomass relevant to gasification in Biomass gasification–principles and technology, ed. by Reed TB. *Noyes Data Corporation, New Jersey*, 41-69.

Green, D.W., Southard, M.Z. (2019). *Perry's chemical engineers' handbook*. McGraw-Hill Education.

Grioui, N., Halouani, K., Zoulalian, A., Halouani, F. (2006). Thermogravimetric analysis and kinetics modeling of isothermal carbonization of olive wood in inert atmosphere. *Thermochimica Acta*, **440**(1), 23-30.

Gröndahl, M., Teleman, A., Gatenholm, P. (2003). Effect of acetylation on the material properties of glucuronoxylan from aspen wood. *Carbohydrate Polymers*, **52**(4), 359-366.

Gropelli, E., Giampaoli, O. (2001). Ambiente y tecnología socialmente apropiada. El camino de la biodigestión. Centro de publicaciones, Secretaría de extensión. Universidad Nacional del Litoral. Santa Fe. Argentina. 88.

Guizani, C., Jeguirim, M., Valin, S., Limousy, L., Salvador, S. (2017). Biomass chars: The effects of pyrolysis conditions on their morphology, structure, chemical properties and reactivity. *Energies*, **10**(6), 796.

Guo, L., Jin, H., Lu, Y. (2015a). Supercritical water gasification research and development in China. *The Journal of Supercritical Fluids*, **96**, 144-150.

Guo, S., Dong, X., Wu, T., Shi, F., Zhu, C. (2015b). Characteristic evolution of hydrochar from hydrothermal carbonization of corn stalk. *Journal of Analytical and Applied Pyrolysis*, **116**, 1-9.

Guo, S., Dong, X., Wu, T., Zhu, C. (2016). Influence of reaction conditions and feedstock on hydrochar properties. *Energy Conversion and Management*, **123**, 95-103.

Gupta, H.K., Roy, S. (2006). *Geothermal energy: an alternative resource for the 21st century*. Elsevier.

Gupta, M., Yang, J., Roy, C. (2003). Specific heat and thermal conductivity of softwood bark and softwood char particles☆. *Fuel*, **82**(8), 919-927.

Gyurik, L., Egedy, A., Zou, J., Miskolczi, N., Ulbert, Z., Yang, H. (2019). Hydrodynamic modelling of a two-stage biomass gasification reactor. *Journal of the Energy Institute*, **92**(3), 403-412.

Hai, I.U., Sher, F., Yaqoob, A., Liu, H. (2019). Assessment of biomass energy potential for SRC willow woodchips in a pilot scale bubbling fluidized bed gasifier. *Fuel*, **258**, 116143.

Halliday, D., Resnick, R., Walker, J. (2013). *Fundamentals of physics*. John Wiley & Sons.

Hashaikeh, R., Fang, Z., Butler, I., Hawari, J., Kozinski, J. (2007). Hydrothermal dissolution of willow in hot compressed water as a model for biomass conversion. *Fuel*, **86**(10-11), 1614-1622.

Hatcher, P. (Year) of Conference. Coalification reactions of vitrinite derived from coalified wood. Transformations to rank of bituminous coal. *Fuel and Energy Abstracts*. pp. 242.

He, C., Giannis, A., Wang, J.-Y. (2013). Conversion of sewage sludge to clean solid fuel using hydrothermal carbonization: hydrochar fuel characteristics and combustion behavior. *Applied Energy*, **111**, 257-266.

Heidari, M., Dutta, A., Acharya, B., Mahmud, S. (2019a). A review of the current knowledge and challenges of hydrothermal carbonization for biomass conversion. *Journal of the Energy Institute*, **92**(6), 1779-1799.

Heidari, M., Norouzi, O., Salaudeen, S., Acharya, B., Dutta, A. (2019b). Prediction of hydrothermal carbonization with respect to the biomass components and severity factor. *Energy & Fuels*, **33**(10), 9916-9924.

Heidari, M., Salaudeen, S., Dutta, A., Acharya, B. (2018). Effects of process water recycling and particle sizes on hydrothermal carbonization of biomass. *Energy & Fuels*, **32**(11), 11576-11586.

Heinze, T. (2005). Polysaccharides: Structure, characterization and use. *Advances in polymer science*, **186**.

Heydari, M., Rahman, M., Gupta, R. (2015). Kinetic Study and Thermal Decomposition Behavior of Lignite Coal. *International Journal of Chemical Engineering*, **2015**.

Hilber, I., Blum, F., Leifeld, J., Schmidt, H.-P., Bucheli, T.D. (2012). Quantitative determination of PAHs in biochar: a prerequisite to ensure its quality and safe application. *Journal of agricultural and food chemistry*, **60**(12), 3042-3050.

Hindermann, J., Hutchings, G., Kiennemann, A. (1993). Mechanistic aspects of the formation of hydrocarbons and alcohols from CO hydrogenation. *Catalysis Reviews—Science and Engineering*, **35**(1), 1-127.

Hitzl, M., Corma, A., Pomares, F., Renz, M. (2015). The hydrothermal carbonization (HTC) plant as a decentral biorefinery for wet biomass. *Catalysis Today*, **257**, 154-159.

Hobbs, M.L., Radulovic, P.T., Smoot, L.D. (1992). Modeling fixed-bed coal gasifiers. *AIChE Journal*, **38**(5), 681-702.

Hoek, A., Post, M.F., Minderhoud, J.K., Lednor, P.W. (1985). Process for the preparation of a Fischer-Tropsch catalyst and preparation of hydrocarbons from syngas, Google Patents.

Hoekman, S.K., Broch, A., Robbins, C. (2011). Hydrothermal carbonization (HTC) of lignocellulosic biomass. *Energy & Fuels*, **25**(4), 1802-1810.

Hoekman, S.K., Broch, A., Robbins, C., Zielinska, B., Felix, L. (2013). Hydrothermal carbonization (HTC) of selected woody and herbaceous biomass feedstocks. *Biomass Conversion and Biorefinery*, **3**(2), 113-126.

Holladay, J.D., Hu, J., King, D.L., Wang, Y. (2009). An overview of hydrogen production technologies. *Catalysis Today*, **139**(4), 244-260.

Holstein, B.R. (1989). Effective Lagrangians and quantum mechanics: The index of refraction. *American Journal of Physics*, **57**(2), 142-148.

Hooshdaran, B., Hosseini, S., Haghshenasfard, M., Esfahany, M.N., Olazar, M. (2017). CFD modeling of heat transfer and hydrodynamics in a draft tube conical spouted bed reactor under pyrolysis conditions: Impact of wall boundary condition. *Applied Thermal Engineering*, **127**, 224-232.

Horne, P.A., Williams, P.T. (1996). Influence of temperature on the products from the flash pyrolysis of biomass. *Fuel*, **75**(9), 1051-1059.

Hosseini, S.H., Ahmadi, G., Rahimi, R., Zivdar, M., Esfahany, M.N. (2010). CFD studies of solids hold-up distribution and circulation patterns in gas–solid fluidized beds. *Powder technology*, **200**(3), 202-215.

Howard, R., Abotsi, E., Van Rensburg, E.J., Howard, S. (2004). Lignocellulose biotechnology: issues of bioconversion and enzyme production. *African Journal of Biotechnology*, **2**(12), 602-619.

Huang, H., Yan, Z. (2009). Present situation and future prospect of hydropower in China. *Renewable and Sustainable Energy Reviews*, **13**(6-7), 1652-1656.

Huang, M.R., Li, X.G. (1998). Thermal degradation of cellulose and cellulose esters. *Journal of applied polymer science*, **68**(2), 293-304.

Huang, Y., Wei, Z., Qiu, Z., Yin, X., Wu, C. (2012). Study on structure and pyrolysis behavior of lignin derived from corncob acid hydrolysis residue. *Journal of Analytical and Applied Pyrolysis*, **93**, 153-159.

Huber, G.W., Iborra, S., Corma, A. (2006). Synthesis of transportation fuels from biomass: chemistry, catalysts, and engineering. *Chemical reviews*, **106**(9), 4044-4098.

Huber, T., Müssig, J., Curnow, O., Pang, S., Bickerton, S., Staiger, M.P. (2012). A critical review of all-cellulose composites. *Journal of Materials Science*, **47**(3), 1171-1186.

Hughes, T.J., Engel, G., Mazzei, L., Larson, M.G. (2000). The continuous Galerkin method is locally conservative. *Journal of Computational Physics*, **163**(2), 467-488.

IARC. (1996). Iarc monographs on the identification of carcinogenic hazards to humans. Retrieved from https://monographs.iarc.who.int/

Idarraga, G., Ramos, J., Zuñiga, V., Sahin, T., Young, R.A. (1999). Pulp and paper from blue agave waste from tequila production. *Journal of agricultural and food chemistry*, **47**(10), 4450-4455.

Idris, S.S., Rahman, N.A., Ismail, K., Alias, A.B., Rashid, Z.A., Aris, M.J. (2010). Investigation on thermochemical behaviour of low rank Malaysian coal, oil palm biomass and their blends during pyrolysis via thermogravimetric analysis (TGA). *Bioresource technology*, **101**(12), 4584-4592.

IEA. (2018). International Energy Agency, secure sustainable together. *Energy Access Outlook 2017*.

Iñiguez-Covarrubias, G., Lange, S.E., Rowell, R.M. (2001). Utilization of byproducts from the tequila industry: part 1: agave bagasse as a raw material for animal feeding and fiberboard production. *Bioresource Technology*, **77**(1), 25-32.

Ischia, G., Fiori, L. (2020). Hydrothermal Carbonization of Organic Waste and Biomass: A Review on Process, Reactor, and Plant Modeling. *Waste and Biomass Valorization*, 1-28.

Isikgor, F.H., Becer, C.R.J.P.C. (2015). Lignocellulosic biomass: a sustainable platform for the production of bio-based chemicals and polymers. **6**(25), 4497-4559.

J de Oliveira Silva, J., Rodrigues Filho, G., da Silva Meireles, C., Ribeiro, S.D., Vieira, J.G., da Silva, C.V., Cerqueira, D.A. (2012). Thermal analysis and FTIR studies of sewage sludge produced in treatment plants. The case of sludge in the city of Uberlândia-MG, Brazil. *Thermochimica acta*, **528**, 72-75.

Jacobson, M.Z., Delucchi, M.A. (2011). Providing all global energy with wind, water, and solar power, Part I: Technologies, energy resources, quantities and areas of infrastructure, and materials. *Energy policy*, **39**(3), 1154-1169.

Jahurul, M., Zaidul, I., Norulaini, N., Sahena, F., Jinap, S., Azmir, J., Sharif, K., Omar, A.M. (2013). Cocoa butter fats and possibilities of substitution in food products concerning cocoa varieties, alternative sources, extraction methods, composition, and characteristics. *Journal of Food Engineering*, **117**(4), 467-476.

Jain, A., Balasubramanian, R., Srinivasan, M. (2016). Hydrothermal conversion of biomass waste to activated carbon with high porosity: A review. *Chemical Engineering Journal*, **283**, 789-805.

Jangsawang, W., Laohalidanond, K., Kerdsuwan, S. (2015). Optimum equivalence ratio of biomass gasification process based on thermodynamic equilibrium model. *Energy Procedia*, **79**, 520-527.

Jarungthammachote, S., Dutta, A. (2012). Experimental investigation of a multi-stage air-steam gasification process for hydrogen enriched gas production. *International journal of energy research*, **36**(3), 335-345.

Jaruwat, D., Udomsap, P., Chollacoop, N., Fuji, M., Eiad-ua, A. (Year) of Conference. Effects of hydrothermal temperature and time of hydrochar from Cattail leaves. *AIP Conference Proceedings*. AIP Publishing LLC. pp. 020016.

Jaszczur, M., Młynarczykowska, A., Demurtas, L. (2020). Effect of Impeller Design on Power Characteristics and Newtonian Fluids Mixing Efficiency in a Mechanically Agitated Vessel at Low Reynolds Numbers. *Energies*, **13**(3), 640.

Jayaraman, K., Gökalp, I. (2015). Pyrolysis, combustion and gasification characteristics of miscanthus and sewage sludge. *Energy Conversion and Management*, **89**, 83-91.

Jayaraman, K., Kok, M.V., Gokalp, I. (2017). Thermogravimetric and mass spectrometric (TG-MS) analysis and kinetics of coal-biomass blends. *Renewable Energy*, **101**, 293-300.

Jena, U., Das, K. (2011). Comparative evaluation of thermochemical liquefaction and pyrolysis for bio-oil production from microalgae. *Energy & fuels*, **25**(11), 5472-5482.

Jenkins, B., Baxter, L., Miles Jr, T., Miles, T. (1998). Combustion properties of biomass. *Fuel processing technology*, **54**(1-3), 17-46.

Jenness, G.R., Vlachos, D.G. (2015). DFT study of the conversion of furfuryl alcohol to 2-methylfuran on RuO2 (110). *The Journal of Physical Chemistry C*, **119**(11), 5938-5945.

Jensen, A., Dam-Johansen, K., Wójtowicz, M.A., Serio, M.A. (1998). TG-FTIR study of the influence of potassium chloride on wheat straw pyrolysis. *Energy & Fuels*, **12**(5), 929-938.

Jiménez, L., González, F. (1991). Study of the physical and chemical properties of lignocellulosic residues with a view to the production of fuels. *Fuel*, **70**(8), 947-950.

Jonker, M.T., Koelmans, A.A. (2002). Sorption of polycyclic aromatic hydrocarbons and polychlorinated biphenyls to soot and soot-like materials in the aqueous environment: mechanistic considerations. *Environmental science & technology*, **36**(17), 3725-3734.

Kabyemela, B.M., Adschiri, T., Malaluan, R.M., Arai, K. (1999). Glucose and fructose decomposition in subcritical and supercritical water: detailed reaction pathway, mechanisms, and kinetics. *Industrial & Engineering Chemistry Research*, **38**(8), 2888-2895.

Kalkreuth, W., Holz, M., Kern, M., Machado, G., Mexias, A., Silva, M., Willett, J., Finkelman, R., Burger, H. (2006). Petrology and chemistry of Permian coals from the Paraná Basin: 1. Santa Terezinha, Leão-Butiá and Candiota Coalfields, Rio Grande do Sul, Brazil. *International Journal of Coal Geology*, **68**(1-2), 79-116.

Kallioinen, A., Vaari, A., Rättö, M., Konn, J., Siika-aho, M., Viikari, L. (2003). Effects of bacterial treatments on wood extractives. *Journal of biotechnology*, **103**(1), 67-76.

Kambo, H.S., Dutta, A. (2015). A comparative review of biochar and hydrochar in terms of production, physico-chemical properties and applications. *Renewable and Sustainable Energy Reviews*, **45**, 359-378.

Kang, S., Li, X., Fan, J., Chang, J. (2012). Characterization of hydrochars produced by hydrothermal carbonization of lignin, cellulose, D-xylose, and wood meal. *Industrial & engineering chemistry research*, **51**(26), 9023-9031.

Karmakar, M., Mandal, J., Haldar, S., Chatterjee, P. (2013). Investigation of fuel gas generation in a pilot scale fluidized bed autothermal gasifier using rice husk. *Fuel*, **111**, 584-591.

Kataki, R., Chutia, R.S., Mishra, M., Bordoloi, N., Saikia, R., Bhaskar, T. (2015). Feedstock suitability for thermochemical processes. in: *Recent Advances in Thermo-Chemical Conversion of Biomass*, Elsevier, pp. 31-74.

Kaushik, R., Parshetti, G.K., Liu, Z., Balasubramanian, R. (2014). Enzyme-assisted hydrothermal treatment of food waste for co-production of hydrochar and bio-oil. *Bioresource technology*, **168**, 267-274.

Keiller, B.G., Muhlack, R., Burton, R.A., van Eyk, P.J. (2019). Biochemical Compositional Analysis and Kinetic Modeling of Hydrothermal Carbonization of Australian Saltbush. *Energy & Fuels*.

Khaled, C., Driss, N., Nouredine, S.C. (2015). CFD simulation of turbulent flow and heat transfer over rough surfaces. *Energy Procedia*, **74**, 909-918.

Khalil, H.A., Bhat, A., Yusra, A.I. (2012). Green composites from sustainable cellulose nanofibrils: A review. *Carbohydrate polymers*, **87**(2), 963-979.

Khan, N., Mohan, S., Dinesha, P. (2020). Regimes of hydrochar yield from hydrothermal degradation of various lignocellulosic biomass: A review. *Journal of Cleaner Production*, 125629.

Khatoniar, S. (2020). A Review on Power Electronics in Renewable Energy Systems.

Khawam, A. (2007). Application of solid-state kinetics to desolvation reactions. *The journal of physical chemistry B*, **210**(37), 1520-1545.

Khawam, A., Flanagan, D.R. (2006). Solid-state kinetic models: basics and mathematical fundamentals. *The journal of physical chemistry B*, **110**(35), 17315-17328.

Kiel, J., Van Paasen, S., Neeft, J., Devi, L., Ptasinski, K., Janssen, F., Meijer, R., Berends, R., Temmink, H., Brem, G. (2004). Primary measures to reduce tar formation in fluidised-bed biomass gasifiers. *ECN, ECN-C-04-014*.

Kim, S., Eom, Y. (2006). Estimation of kinetic triplet of cellulose pyrolysis reaction from isothermal kinetic results. *Korean Journal of Chemical Engineering*, **23**(3), 409-414.

Kladisios, P., Sagia, A. (2018). Hydrothermal carbonization: production of energy through the thermochemical treatment of biomass. *SUSTAINABLE ENERGY VOL. 9, NO. 2*.

Knauf, M., Moniruzzaman, M. (2004). Lignocellulosic biomass processing: a perspective. *International sugar journal*, **106**(1263), 147-150.

Kojima, E., Miao, Y., Yoshizaki, S. (1991). Pyrolysis of cellulose particles in a fluidized bed. *Journal of chemical engineering of Japan*, **24**(1), 8-14.

Kominko, H., Gorazda, K., Wzorek, Z., Wojtas, K. (2018). Sustainable management of sewage sludge for the production of organo-mineral fertilizers. *Waste and biomass valorization*, **9**(10), 1817-1826.

Kruse, A., Funke, A., Titirici, M.-M. (2013). Hydrothermal conversion of biomass to fuels and energetic materials. *Current opinion in chemical biology*, **17**(3), 515-521.

Krylova, A.Y., Zaitchenko, V. (2018). Hydrothermal carbonization of biomass: a review. *Solid Fuel Chemistry*, **52**(2), 91-103.

Kumar, R.M.D., Anand, R. (2019). Production of biofuel from biomass downdraft gasification and its applications. in: *Advanced Biofuels*, Elsevier, pp. 129-151.

Kumar, S. (2013). Sub-and supercritical water technology for biofuels. in: *Advanced biofuels and bioproducts*, Springer, pp. 147-183.

Kumar, U., Paul, M.C. (2019). CFD modelling of biomass gasification with a volatile break-up approach. *Chemical Engineering Science*, **195**, 413-422.

Kumari, D., Singh, R. (2018). Pretreatment of lignocellulosic wastes for biofuel production: a critical review. *Renewable and Sustainable Energy Reviews*, **90**, 877-891.

Kummer, J., DeWitt, T., Emmett, P. (1948). Some mechanism studies on the Fischer-Tropsch synthesis using C14. *Journal of the American Chemical Society*, **70**(11), 3632-3643.

Laskowski, J. (2013). Surface chemistry fundamentals in fine coal processing. in: *The Coal Handbook: Towards Cleaner Production*, Elsevier, pp. 347-421.

Laureano-Perez, L., Teymouri, F., Alizadeh, H., Dale, B.E. (2005). Understanding factors that limit enzymatic hydrolysis of biomass. *Applied Biochemistry and Biotechnology*, **124**(1), 1081-1099.

Laurentin, A., Edwards, C.A. (2003). A microtiter modification of the anthrone-sulfuric acid colorimetric assay for glucose-based carbohydrates. *Analytical biochemistry*, **315**(1), 143-145.

Lavoie, J.-M., Beauchet, R., Berberi, V., Chornet, M. (2011). Biorefining lignocellulosic biomass via the feedstock impregnation rapid and sequential steam treatment. in: *Biofuel's Engineering Process Technology*, IntechOpen.

Le, C., Stuckey, D.C. (2016). Colorimetric measurement of carbohydrates in biological wastewater treatment systems: a critical evaluation. *Water research*, **94**, 280-287.

Lede, J. (2013). Biomass fast pyrolysis reactors: a review of a few scientific challenges and of related recommended research topics. *Oil Gas Science Technology–Revue d'IFP Energies nouvelles*, **68**(5), 801-814.

Lee, U., Chung, J., Ingley, H.A. (2014). High-temperature steam gasification of municipal solid waste, rubber, plastic and wood. *Energy & Fuels*, **28**(7), 4573-4587.

Lee, Y., Park, J., Ryu, C., Gang, K.S., Yang, W., Park, Y.-K., Jung, J., Hyun, S. (2013). Comparison of biochar properties from biomass residues produced by slow pyrolysis at 500 C. *Bioresource technology*, **148**, 196-201.

Li, C., Suzuki, K. (2009). Tar property, analysis, reforming mechanism and model for biomass gasification—An overview. *Renewable and Sustainable Energy Reviews*, **13**(3), 594-604.

Li, S., Xu, S., Liu, S., Yang, C., Lu, Q. (2004). Fast pyrolysis of biomass in free-fall reactor for hydrogen-rich gas. *Fuel Processing Technology*, **85**(8-10), 1201-1211.

Li, X.-g., Ma, B.-g., Xu, L., Hu, Z.-w., Wang, X.-g. (2006). Thermogravimetric analysis of the co-combustion of the blends with high ash coal and waste tyres. *Thermochimica Acta*, **441**(1), 79-83.

Libra, J.A., Ro, K.S., Kammann, C., Funke, A., Berge, N.D., Neubauer, Y., Titirici, M.-M., Fühner, C., Bens, O., Kern, J. (2011). Hydrothermal carbonization of biomass residuals: a comparative review of the chemistry, processes and applications of wet and dry pyrolysis. *Biofuels*, **2**(1), 71-106.

Limayem, A., Ricke, S.C. (2012). Lignocellulosic biomass for bioethanol production: current perspectives, potential issues and future prospects. *Progress in energy and combustion science*, **38**(4), 449-467.

Lin, Y., Ma, X., Peng, X., Hu, S., Yu, Z., Fang, S. (2015). Effect of hydrothermal carbonization temperature on combustion behavior of hydrochar fuel from paper sludge. *Applied Thermal Engineering*, **91**, 574-582.

Lin, Y., Ma, X., Peng, X., Yu, Z. (2016a). A mechanism study on hydrothermal carbonization of waste textile. *Energy & Fuels*, **30**(9), 7746-7754.

Lin, Y., Wang, D., Wang, T. (2012). Ethanol production from pulp & paper sludge and monosodium glutamate waste liquor by simultaneous saccharification and fermentation in batch condition. *Chemical engineering journal*, **191**, 31-37.

Lin, Y., Yan, W., Sheng, K. (2016b). Effect of pyrolysis conditions on the characteristics of biochar produced from a tobacco stem. *Waste Management & Research*, **34**(8), 793-801.

Linan-Montes, A., De La Parra-Arciniega, S., Garza-González, M., García-Reyes, R., Soto-Regalado, E., Cerino-Córdova, F. (2014). Characterization and thermal analysis of agave bagasse and malt spent grain. *Journal of Thermal Analysis and Calorimetry*, **115**(1), 751-758.

Ling, M., Esfahani, M.J., Akbari, H., Foroughi, A. (2016). Effects of residence time and heating rate on gasification of petroleum residue. *Petroleum Science and Technology*, **34**(22), 1837-1840.

Liu, C., Huang, J., Huang, X., Li, H., Zhang, Z. (2011). Theoretical studies on formation mechanisms of CO and CO2 in cellulose pyrolysis. *Computational and Theoretical Chemistry*, **964**(1-3), 207-212.

Liu, C., Wang, H., Karim, A.M., Sun, J., Wang, Y. (2014). Catalytic fast pyrolysis of lignocellulosic biomass. *Chemical Society Reviews*, **43**(22), 7594-7623.

Liu, J., Zuo, J., Sun, Z., Zillante, G., Chen, X. (2013a). Sustainability in hydropower development—A case study. *Renewable and Sustainable Energy Reviews*, **19**, 230-237.

Liu, L., Huang, Y., Cao, J., Liu, C., Dong, L., Xu, L., Zha, J. (2018). Experimental study of biomass gasification with oxygen-enriched air in fluidized bed gasifier. *Science of the Total Environment*, **626**, 423-433.

Liu, N., Fan, W., Dobashi, R., Huang, L. (2002). Kinetic modeling of thermal decomposition of natural cellulosic materials in air atmosphere. *Journal of Analytical and Applied Pyrolysis*, **63**(2), 303-325.

Liu, Q., Chmely, S.C., Abdoulmoumine, N. (2017). Biomass treatment strategies for thermochemical conversion. *Energy & Fuels*, **31**(4), 3525-3536.

Liu, Q., Wang, S., Zheng, Y., Luo, Z., Cen, K. (2008). Mechanism study of wood lignin pyrolysis by using TG–FTIR analysis. *Journal of Analytical and Applied Pyrolysis*, **82**(1), 170-177.

Liu, Z., Balasubramanian, R. (2012). Hydrothermal carbonization of waste biomass for energy generation. *Procedia Environmental Sciences*, **16**, 159-166.

Liu, Z., Quek, A., Hoekman, S.K., Balasubramanian, R. (2013b). Production of solid biochar fuel from waste biomass by hydrothermal carbonization. *Fuel*, **103**, 943-949.

Looney, B. (2020). Statistical Review of World Energy 2020 | 69th edition. *bp Statistical Review of World Energy 2020*.

López González, D. (2013). Valorización de Biomasa de origen vegetal mediante procesos térmicos y termoquímicos.

Lou, R., Wu, S.-b. (2011). Products properties from fast pyrolysis of enzymatic/mild acidolysis lignin. *Applied Energy*, **88**(1), 316-322.

Lozano, Y., Mayer, C.D., Bannon, C., Gaydou, E.M. (1993). Unsaponifiable matter, total sterol and tocopherol contents of avocado oil varieties. *Journal of the American Oil Chemists' Society*, **70**(6), 561-565.

Lu, Q., Zhang, Y., Dong, C.-q., Yang, Y.-p., Yu, H.-z. (2014). The mechanism for the formation of levoglucosenone during pyrolysis of β-d-glucopyranose and cellobiose: a density functional theory study. *Journal of analytical and applied pyrolysis*, **110**, 34-43.

Lu, X., Jordan, B., Berge, N.D. (2012). Thermal conversion of municipal solid waste via hydrothermal carbonization: Comparison of carbonization products to products from current waste management techniques. *Waste management*, **32**(7), 1353-1365.

Lu, X., Pellechia, P.J., Flora, J.R., Berge, N.D. (2013). Influence of reaction time and temperature on product formation and characteristics associated with the hydrothermal carbonization of cellulose. *Bioresource technology*, **138**, 180-190.

Lucian, M., Fiori, L. (2017). Hydrothermal carbonization of waste biomass: Process design, modeling, energy efficiency and cost analysis. *Energies*, **10**(2), 211.

Lucian, M., Volpe, M., Fiori, L. (2019). Hydrothermal carbonization kinetics of lignocellulosic agro-wastes: experimental data and modeling. *Energies*, **12**(3), 516.

Lucian, M., Volpe, M., Merzari, F., Wüst, D., Kruse, A., Andreottola, G., Fiori, L. (2020). Hydrothermal carbonization coupled with anaerobic digestion for the valorization of the organic fraction of municipal solid waste. *Bioresource Technology*, **314**, 123734.

Luo, Y., Yu, F., Nie, Y., Ji, J. (2010). Study on the pyrolysis of cellulose. *Kezaisheng Nengyuan/Renewable Energy Resources*, **28**(1), 40-43.

Lv, G., Wu, S. (2012). Analytical pyrolysis studies of corn stalk and its three main components by TG-MS and Py-GC/MS. *Journal of Analytical and Applied Pyrolysis*, **97**, 11-18.

Lynam, J.G., Reza, M.T., Yan, W., Vásquez, V.R., Coronella, C.J. (2015). Hydrothermal carbonization of various lignocellulosic biomass. *Biomass Conversion and Biorefinery*, **5**(2), 173-181.

Mafakheri, F., Nasiri, F. (2014). Modeling of biomass-to-energy supply chain operations: Applications, challenges and research directions. *Energy policy*, **67**, 116-126.

Magdziarz, A., Wilk, M., Wądrzyk, M. (2020). Pyrolysis of hydrochar derived from biomass–Experimental investigation. *Fuel*, **267**, 117246.

Maglinao Jr, A.L., Capareda, S.C., Nam, H. (2015). Fluidized bed gasification of high tonnage sorghum, cotton gin trash and beef cattle manure: Evaluation of synthesis gas production. *Energy conversion and management*, **105**, 578-587.

Maia, A.A.D., de Morais, L.C. (2016). Kinetic parameters of red pepper waste as biomass to solid biofuel. *Bioresource Technology*, **204**, 157-163.

Manatura, K., Lu, J.-H., Wu, K.-T., Hsu, H.-T. (2017). Exergy analysis on torrefied rice husk pellet in fluidized bed gasification. *Applied Thermal Engineering*, **111**, 1016-1024.

Marcilla, A., Gómez-Siurana, A., Gomis, C., Chápuli, E., Catalá, M.C., Valdés, F.J. (2009). Characterization of microalgal species through TGA/FTIR analysis: Application to nannochloropsis sp. *Thermochimica Acta*, **484**(1-2), 41-47.

Mardles, E. (1940). Viscosity of suspensions and the Einstein equation. *Nature*, **145**(3686), 970-970.

Marín, P.C.-G., Saavedra, A.L., Eguiarte, L., Zizumbo-Villareal, D. (2007). En lo ancestral hay futuro: del tequila, los mezcales y otros agaves. *NÚMEROS*, **245**, 246.

Martinez, C.L.M., Sermyagina, E., Saari, J., de Jesus, M.S., Cardoso, M., de Almeida, G.M., Vakkilainen, E. (2021). Hydrothermal carbonization of lignocellulosic agro-forest based biomass residues. *Biomass and Bioenergy*, **147**, 106004.

Martinez Gutierrez, G.A., Iniguez Covarrubias, G., Ortiz-Hernandez, Y.D., Lopez-Cruz, J.Y., Bautista Cruz, M.A. (2013). Stacking times of mezcal bagasse waste and its effects in compost properties used for culture of tomato. *REVISTA INTERNACIONAL DE CONTAMINACION AMBIENTAL*, **29**(3), 209-216.

Martínez, P.E.P. (2014). Biomasa residual vegetal: tecnologías de transformación y estado actual. *Innovaciencia*, **2**(1), 45-52.

Mason, P., Darvell, L., Jones, J., Williams, A. (2016). Comparative study of the thermal conductivity of solid biomass fuels. *Energy & Fuels*, **30**(3), 2158-2163.

Masselter, S., Zemann, A., Bobleter, O. (1995). Analysis of lignin degradation products by capillary electrophoresis. *Chromatographia*, **40**(1-2), 51-57.

Mastellone, M.L., Zaccariello, L., Arena, U. (2010). Co-gasification of coal, plastic waste and wood in a bubbling fluidized bed reactor. *Fuel*, **89**(10), 2991-3000.

Mattiussi, C. (1997). An analysis of finite volume, finite element, and finite difference methods using some concepts from algebraic topology. *Journal of Computational Physics*, **133**(2), 289-309.

Mayes, H.B., Broadbelt, L.J. (2012). Unraveling the reactions that unravel cellulose. *The Journal of Physical Chemistry A*, **116**(26), 7098-7106.

McCollom, T.M., Ritter, G., Simoneit, B.R. (1999). Lipid synthesis under hydrothermal conditions by Fischer-Tropsch-type reactions. *Origins of Life and Evolution of the Biosphere*, **29**(2), 153-166.

McGrath, T.E., Chan, W.G., Hajaligol, M.R. (2003). Low temperature mechanism for the formation of polycyclic aromatic hydrocarbons from the pyrolysis of cellulose. *Journal of Analytical and Applied Pyrolysis*, **66**(1-2), 51-70.

McKendry, P. (2002). Energy production from biomass (part 1): overview of biomass. *Bioresource technology*, **83**(1), 37-46.

Medic, D., Darr, M., Potter, B., Shah, A. (Year) of Conference. Effect of torrefaction process parameters on biomass feedstock upgrading. *2010 Pittsburgh, Pennsylvania, June 20-June 23, 2010*. American Society of Agricultural and Biological Engineers. pp. 1.

Mehrabi, N., McPhee, J. (2019). Model-based control of biomechatronic systems. *Handbook of Biomechatronics*, 95-126.

Melgar, A., Borge, D., Pérez, J.F. (2008). Kynetic study of the biomass devolatilization process in particles sizes between 2-19 mm by means of thermogravimetric analysis. *Dyna*, **75**(155), 123-131.

Menon, V., Rao, M. (2012). Trends in bioconversion of lignocellulose: biofuels, platform chemicals & biorefinery concept. *Progress in energy and combustion science*, **38**(4), 522-550.

Merzari, F., Lucian, M., Volpe, M., Andreottola, G., Fiori, L. (2018). Hydrothermal carbonization of biomass: design of a bench-Scale reactor for evaluating the heat of reaction. *Chemical Engineering Transactions*, **65**, 43-48.

Michelin, M., Ruíz, H.A., Silva, D.P.d., Ruzene, D.S., Teixeira, J., Polizeli, M.d.L. (2015). *Cellulose from lignocellulosic waste*. Springer International Publishing AG.

Migliavacca, G., Parodi, E., Bonfanti, L., Faravelli, T., Pierucci, S., Ranzi, E. (2005). A general mathematical model of solid fuels pyrolysis. *Energy*, **30**(8), 1453-1468.

Mihajlovic, M., Petrovic, J., Maletic, S., Isakovski, M.K., Stojanovic, M., Lopicic, Z., Trifunovic, S. (2018). Hydrothermal carbonization of Miscanthus× giganteus: Structural and fuel properties of hydrochars and organic profile with the ecotoxicological assessment of the liquid phase. *Energy conversion and management*, **159**, 254-263.

Miller, R.S., Bellan, J. (1997). A generalized biomass pyrolysis model based on superimposed cellulose, hemicelluloseand liqnin kinetics. *Combustion science and technology*, **126**(1-6), 97-137.

Milne, T.A., Evans, R.J., Abatzaglou, N. (1998). Biomass gasifier"Tars": their nature, formation, and conversion. National Renewable Energy Laboratory, Golden, CO (US).

Milosavljevic, I., Oja, V., Suuberg, E.M. (1996). Thermal effects in cellulose pyrolysis: relationship to char formation processes. *Industrial & Engineering Chemistry Research*, **35**(3), 653-662.

Mishra, G., Kumar, J., Bhaskar, T. (2015). Kinetic studies on the pyrolysis of pinewood. *Bioresource Technology*, **182**, 282-288.

Missaoui, A., Bostyn, S., Belandria, V., Cagnon, B., Sarh, B., Gökalp, I. (2017). Hydrothermal carbonization of dried olive pomace: Energy potential and process performances. *Journal of Analytical and Applied Pyrolysis*, **128**, 281-290.

Mliki, K., Trabelsi, M. (2016). Efficient mild oxidation of 5-hydroxymethylfurfural to 5-hydroxymethyl-2 (5H)-furanone, a versatile chemical intermediate. *Research on Chemical Intermediates*, **42**(12), 8253-8260.

Mochidzuki, K., Sato, N., Sakoda, A. (2005). Production and characterization of carbonaceous adsorbents from biomass wastes by aqueous phase carbonization. *Adsorption*, **11**(1), 669-673.

Moghadam, R.A., Yusup, S., Azlina, W., Nehzati, S., Tavasoli, A. (2014). Investigation on syngas production via biomass conversion through the integration of pyrolysis and air–steam gasification processes. *Energy conversion and management*, **87**, 670-675.

Mohamed, M.A., Jaafar, J., Ismail, A., Othman, M., Rahman, M. (2017). Fourier transform infrared (FTIR) spectroscopy. in: *Membrane Characterization*, Elsevier, pp. 3-29.

Mohtasham, J. (2015). renewable energies. *Energy Procedia*, **74**, 1289-1297.

Möller, M., Nilges, P., Harnisch, F., Schröder, U. (2011). Subcritical water as reaction environment: fundamentals of hydrothermal biomass transformation. *ChemSusChem*, **4**(5), 566-579.

Montagna, J.M., Iribarren, O.A. (1989). A new strategy for process simulation with the sequential modular approach. *Computers in industry*, **12**(1), 23-29.

Monteil-Rivera, F., Phuong, M., Ye, M., Halasz, A., Hawari, J. (2013). Isolation and characterization of herbaceous lignins for applications in biomaterials. *Industrial Crops and Products*, **41**, 356-364.

Montero, G., Coronado, M.A., Torres, R., Jaramillo, B.E., García, C., Stoytcheva, M., Vázquez, A.M., León, J.A., Lambert, A.A., Valenzuela, E. (2016). Higher heating value determination of wheat straw from Baja California, Mexico. *Energy*, **109**, 612-619.

Moon, J., Mun, T.-Y., Yang, W., Lee, U., Hwang, J., Jang, E., Choi, C. (2015). Effects of hydrothermal treatment of sewage sludge on pyrolysis and steam gasification. *Energy Conversion and Management*, **103**, 401-407.

Moulé, A.J. (2010). Power from plastic. *Current Opinion in Solid State and Materials Science*, **14**(6), 123-130.

Mu, W., Ben, H., Ragauskas, A., Deng, Y. (2013). Lignin pyrolysis components and upgrading—technology review. *Bioenergy research*, **6**(4), 1183-1204.

Mujtaba, I., Srinivasan, R., Elbashir, N. (2017). *The water-food-energy nexus: processes, technologies, and challenges*. CRC Press.

Mumbach, G.D., Alves, J.L.F., da Silva, J.C.G., Di Domenico, M., de Sena, R.F., Marangoni, C., Machado, R.A.F., Bolzan, A. (2020). Pyrolysis of cocoa shell and its bioenergy potential: evaluating the kinetic triplet, thermodynamic parameters, and evolved gas analysis using TGA-FTIR. *Biomass Conversion and Biorefinery*, 1-17.

Munir, M.T., Mansouri, S.S., Udugama, I.A., Baroutian, S., Gernaey, K.V., Young, B.R. (2018). Resource recovery from organic solid waste using hydrothermal processing: Opportunities and challenges. *Renewable and Sustainable Energy Reviews*, **96**, 64-75.

Murray, J.a., Evans, D. (1972). The brown-coal/water system: Part 3. Thermal dewatering of brown coal. *Fuel*, **51**(4), 290-296.

Murthy, P.S., Naidu, M.M. (2012). Recovery of phenolic antioxidants and functional compounds from coffee industry by-products. *Food and Bioprocess Technology*, **5**(3), 897-903.

Mussatto, S.I. (2015). Generating biomedical polyphenolic compounds from spent coffee or silverskin. in: *Coffee in health and disease prevention*, Elsevier, pp. 93-106.

Nakamura, T., Kawamoto, H., Saka, S. (2008). Pyrolysis behavior of Japanese cedar wood lignin studied with various model dimers. *Journal of Analytical and Applied Pyrolysis*, **81**(2), 173-182.

Nakason, K., Panyapinyopol, B., Kanokkantapong, V., Viriya-empikul, N., Kraithong, W., Pavasant, P. (2018a). Characteristics of hydrochar and hydrothermal liquid products from hydrothermal carbonization of corncob. *Biomass Conversion and Biorefinery*, **8**(1), 199-210.

Nakason, K., Panyapinyopol, B., Kanokkantapong, V., Viriya-empikul, N., Kraithong, W., Pavasant, P. (2018b). Characteristics of hydrochar and liquid fraction from hydrothermal carbonization of cassava rhizome. *Journal of the Energy Institute*, **91**(2), 184-193.

Nelson, D.A., Molton, P.M., Russell, J.A., Hallen, R.T. (1984). Application of direct thermal liquefaction for the conversion of cellulosic biomass. *Industrial & engineering chemistry product research and development*, **23**(3), 471-475.

Nguyen, H.H., Heaven, S., Banks, C. (2014). Energy potential from the anaerobic digestion of food waste in municipal solid waste stream of urban areas in Vietnam. *International Journal of Energy and Environmental Engineering*, **5**(4), 365-374.

Ni, M., Leung, D.Y., Leung, M.K., Sumathy, K. (2006). An overview of hydrogen production from biomass. *Fuel processing technology*, **87**(5), 461-472.

Ningbo, G., Baoling, L., Aimin, L., Juanjuan, L. (2015). Continuous pyrolysis of pine sawdust at different pyrolysis temperatures and solid residence times. *Journal of analytical and applied pyrolysis*, **114**, 155-162.

Niu, M., Huang, Y., Jin, B., Wang, X. (2014). Oxygen gasification of municipal solid waste in a fixed-bed gasifier. *Chinese Journal of Chemical Engineering*, **22**(9), 1021-1026.

Nsaful, F., Görgens, J., Knoetze, J. (2013). Comparison of combustion and pyrolysis for energy generation in a sugarcane mill. *Energy Conversion and Management*, **74**, 524-534.

Odetoye, T., Ibarhiam, S., Titiloye, J. (2020). Thermochemical Characterization of Biomass Residues and Wastes for Bioenergy. in: *Valorization of Biomass to Value-Added Commodities*, Springer, pp. 93-100.

Oh, S.J., Park, J., Na, J.G., Oh, Y.K., Chang, Y.K. (2015). Production of 5-hydroxymethylfurfural from agarose by using a solid acid catalyst in dimethyl sulfoxide. *RSC Advances*, **5**(59), 47983-47989.

Okiyama, D.C., Navarro, S.L., Rodrigues, C.E. (2017). Cocoa shell and its compounds: Applications in the food industry. *Trends in Food Science & Technology*, **63**, 103-112.

Okoro, N., Harding, K., Daramola, M. (2020). Pyro-gasification of Invasive Plants to Syngas. in: *Valorization of Biomass to Value-Added Commodities*, Springer, pp. 317-340.

Okoro, O.V., Sun, Z., Birch, J. (2017). Meat processing waste as a potential feedstock for biochemicals and biofuels–A review of possible conversion technologies. *Journal of cleaner production*, **142**, 1583-1608.

Onay, O., Kockar, O.M. (2003). Slow, fast and flash pyrolysis of rapeseed. *Renewable energy*, **28**(15), 2417-2433.

Ortega, C. (2014). Biomass as a sustainable energy source for the future: fundamentals of conversion processes. *Green Processing and Synthesis*.

OSI. (2021). Wood Pellet Prices. Retrieved from https://www.nh.gov/osi/energy/energy-nh/fuel-prices/wood-pellet-prices.htm

Oviedo, P.M., López, L.L. Variedades de aguacate y su produccion en mexico avocado varieties and its production in mexico.

Özcan-Taskin, G., Wei, H. (2003). The effect of impeller-to-tank diameter ratio on draw down of solids. *Chemical engineering science*, **58**(10), 2011-2022.

Paksung, N., Pfersich, J., Arauzo, P.J., Jung, D., Kruse, A. (2020). Structural effects of cellulose on hydrolysis and carbonization behavior during hydrothermal treatment. *ACS omega*, **5**(21), 12210-12223.

Pala, M., Kantarli, I.C., Buyukisik, H.B., Yanik, J. (2014). Hydrothermal carbonization and torrefaction of grape pomace: A comparative evaluation. *Bioresource technology*, **161**, 255-262.

Palma, C.F. (2013). Modelling of tar formation and evolution for biomass gasification: A review. *Applied energy*, **111**, 129-141.

Pan, L., Jiang, Y., Wang, L., Xu, W. (2018). Kinetic study on the pyrolysis of medium density fiberboard: Effects of secondary charring reactions. *Energies*, **11**(9), 2481.

Pandey, A., Bhaskar, T., Stöcker, M., Sukumaran, R. (2015). Recent advances in thermochemical conversion of biomass.

Pandey, A., Larroche, C., Gnansounou, E., Khanal, S.K., Dussap, C.-G., Ricke, S. (2019). *Biomass, Biofuels, Biochemicals: Biofuels: Alternative Feedstocks and Conversion Processes for the Production of Liquid and Gaseous Biofuels*. Academic Press.

Pandey, K., Pitman, A. (2003). FTIR studies of the changes in wood chemistry following decay by brown-rot and white-rot fungi. *International biodeterioration & biodegradation*, **52**(3), 151-160.

Panton, R.L. (2006). *Incompressible flow*. John Wiley & Sons.

Panwar, N., Kothari, R., Tyagi, V. (2012). Thermo chemical conversion of biomass–Eco friendly energy routes. *Renewable and Sustainable Energy Reviews*, **16**(4), 1801-1816.

Papadikis, K., Gu, S., Bridgwater, A. (2009). CFD modelling of the fast pyrolysis of biomass in fluidised bed reactors. Part B: Heat, momentum and mass transport in bubbling fluidised beds. *Chemical Engineering Science*, **64**(5), 1036-1045.

Papari, S., Hawboldt, K. (2015). A review on the pyrolysis of woody biomass to bio-oil: Focus on kinetic models. *Renewable and Sustainable Energy Reviews*, **52**, 1580-1595.

Parikh, J., Channiwala, S., Ghosal, G. (2005). A correlation for calculating HHV from proximate analysis of solid fuels. *Fuel*, **84**(5), 487-494.

Parshetti, G.K., Chowdhury, S., Balasubramanian, R.J.B.t. (2014). Hydrothermal conversion of urban food waste to chars for removal of textile dyes from contaminated waters. **161**, 310-319.

Parshetti, G.K., Hoekman, S.K., Balasubramanian, R. (2013). Chemical, structural and combustion characteristics of carbonaceous products obtained by hydrothermal carbonization of palm empty fruit bunches. *Bioresource technology*, **135**, 683-689.

Partridge, A., Sermyagina, E., Vakkilainen, E. (2020). Impact of Pretreatment on Hydrothermally Carbonized Spruce. *Energies*, **13**(11), 2984.

Pastorova, I., Botto, R.E., Arisz, P.W., Boon, J.J. (1994). Cellulose char structure: a combined analytical Py-GC-MS, FTIR, and NMR study. *Carbohydrate research*, **262**(1), 27-47.

Patel, S.U., Kumar, B.J., Badhe, Y.P., Sharma, B., Saha, S., Biswas, S., Chaudhury, A., Tambe, S.S., Kulkarni, B.D. (2007). Estimation of gross calorific value of coals using artificial neural networks. *Fuel*, **86**(3), 334-344.

Patwardhan, P.R., Brown, R.C., Shanks, B.H. (2011). Product distribution from the fast pyrolysis of hemicellulose. *ChemSusChem*, **4**(5), 636-643.

Paulsen, A.D., Mettler, M.S., Dauenhauer, P.J. (2013). The role of sample dimension and temperature in cellulose pyrolysis. *Energy & Fuels*, **27**(4), 2126-2134.

Pavlovic, I., Knez, Z.e., Skerget, M. (2013). Hydrothermal reactions of agricultural and food processing wastes in sub-and supercritical water: a review of fundamentals, mechanisms, and state of research. *Journal of agricultural and food chemistry*, **61**(34), 8003-8025.

Pecchi, M., Patuzzi, F., Benedetti, V., Di Maggio, R., Baratieri, M. (2020). Kinetic analysis of hydrothermal carbonization using high-pressure differential scanning calorimetry applied to biomass. *Applied Energy*, **265**, 114810.

Pecha, M.B., Arbelaez, J.I.M., Garcia-Perez, M., Chejne, F., Ciesielski, P.N. (2019). Progress in understanding the four dominant intra-particle phenomena of lignocellulose pyrolysis: chemical reactions, heat transfer, mass transfer, and phase change. *Green chemistry*, **21**(11), 2868-2898.

Pecha, M.B., Ramirez, E., Wiggins, G.M., Carpenter, D., Kappes, B., Daw, S., Ciesielski, P.N. (2018). Integrated Particle-and Reactor-Scale Simulation of Pine Pyrolysis in a Fluidized Bed. *Energy & fuels*, **32**(10), 10683-10694.

Pellet. (2021). Pellet Valle de Bravo. Retrieved from https://pellet.mx/

Peng, C., Zhai, Y., Zhu, Y., Xu, B., Wang, T., Li, C., Zeng, G. (2016). Production of char from sewage sludge employing hydrothermal carbonization: char properties, combustion behavior and thermal characteristics. *Fuel*, **176**, 110-118.

Peng, N., Li, Y., Liu, T., Lang, Q., Gai, C., Liu, Z. (2017). Polycyclic aromatic hydrocarbons and toxic heavy metals in municipal solid waste and corresponding hydrochars. *Energy & Fuels*, **31**(2), 1665-1671.

Peng, Y., Wu, S. (2010). The structural and thermal characteristics of wheat straw hemicellulose. *Journal of Analytical and Applied Pyrolysis*, **88**(2), 134-139.

Pentassuglia, S., Agostino, V., Tommasi, T. (2018). EAB—electroactive biofilm: a biotechnological resource.

Perea-Moreno, A.-J., Aguilera-Ureña, M.-J., Manzano-Agugliaro, F. (2016). Fuel properties of avocado stone. *Fuel*, **186**, 358-364.

Peterson, A.A., Vogel, F., Lachance, R.P., Fröling, M., Antal Jr, M.J., Tester, J.W. (2008). Thermochemical biofuel production in hydrothermal media: a review of sub-and supercritical water technologies. *Energy & Environmental Science*, **1**(1), 32-65.

PetroviL, J., PerisiL, N., MaksimoviL, J.D., MaksimoviL, V., KragoviL, M., StojanoviL, M., LauseviL, M., MihajloviL, M. (2016). Hydrothermal conversion of grape pomace: Detailed characterization of obtained hydrochar and liquid phase. *Journal of Analytical and Applied Pyrolysis*, **118**, 267-277.

Pichler, v.H., Schulz, H. (1970). Neuere Erkenntnisse auf dem Gebiet der Synthese von Kohlenwasserstoffen aus CO und H2. *Chemie Ingenieur Technik*, **42**(18), 1162-1174.

Pimentel, D., Harvey, C., Resosudarmo, P., Sinclair, K., Kurz, D., McNair, M., Crist, S., Shpritz, L., Fitton, L., Saffouri, R. (1995). Environmental and economic costs of soil erosion and conservation benefits. *Science*, **267**(5201), 1117-1123.

Pogson, M., Hastings, A., Smith, P. (2013). How does bioenergy compare with other land-based renewable energy sources globally? *Gcb Bioenergy*, **5**(5), 513-524.

Poletto, M., Ornaghi, H.L., Zattera, A.J. (2014). Native cellulose: structure, characterization and thermal properties. *Materials*, **7**(9), 6105-6119.

Poletto, M., Zattera, A.J., Santana, R.M. (2012). Structural differences between wood species: evidence from chemical composition, FTIR spectroscopy, and thermogravimetric analysis. *Journal of Applied Polymer Science*, **126**(S1), E337-E344.

Popescu, C.-M., Singurel, G., Popescu, M.-C., Vasile, C., Argyropoulos, D.S., Willför, S. (2009). Vibrational spectroscopy and X-ray diffraction methods to establish the differences between hardwood and softwood. *Carbohydrate Polymers*, **77**(4), 851-857.

Prins, M.J. (2005). Thermodynamic analysis of biomass gasification and torrefaction.

Ptasinski, K.J. (2008). Thermodynamic efficiency of biomass gasification and biofuels conversion. *Biofuels, Bioproducts and Biorefining*, **2**(3), 239-253.

Qiu, N., Li, H., Jin, Z., Zhu, Y. (2007). Temperature and time effect on the concentrations of free radicals in coal: Evidence from laboratory pyrolysis experiments. *International journal of coal geology*, **69**(3), 220-228.

Qiu, Y., Chen, Y., Zhang, G.G., Yu, L., Mantri, R.V. (2016). *Developing solid oral dosage forms: pharmaceutical theory and practice*. Academic press.

Qu, T., Guo, W., Shen, L., Xiao, J., Zhao, K. (2011). Experimental study of biomass pyrolysis based on three major components: hemicellulose, cellulose, and lignin. *Industrial & engineering chemistry research*, **50**(18), 10424-10433.

Ragland, K., Aerts, D., Baker, A. (1991). Properties of wood for combustion analysis. *Bioresource technology*, **37**(2), 161-168.

Ramtahal, G.A., Akingbala, J.O., Baccus-Taylor, G.S. (2007). Laboratory preparation and evaluation of Pollock variety avocado (Persea americana Mill) guacamole. *Journal of the Science of Food and Agriculture*, **87**(11), 2068-2074.

Ranzi, E., Cuoci, A., Faravelli, T., Frassoldati, A., Migliavacca, G., Pierucci, S., Sommariva, S. (2008). Chemical kinetics of biomass pyrolysis. *Energy & Fuels*, **22**(6), 4292-4300.

Ratna, D. (2012). Thermal properties of thermosets. in: *Thermosets*, Elsevier, pp. 62-91.

Raznjevic, K. (1976). Handbook of thermodynamic tables and charts.

Reddy, J.N., Gartling, D.K. (2010). *The finite element method in heat transfer and fluid dynamics*. CRC press.

Reed, T.B., Das, A. (1988). *Handbook of biomass downdraft gasifier engine systems*. Biomass Energy Foundation.

REN21, R. (2017). Global Status Report, REN21 Secretariat, Paris, France. in: *Tech. Rep.*

Reza, M.S., Ahmed, A., Caesarendra, W., Abu Bakar, M.S., Shams, S., Saidur, R., Aslfattahi, N., Azad, A.K. (2019). Acacia holosericea: an invasive species for bio-char, bio-oil, and biogas production. *Bioengineering*, **6**(2), 33.

Reza, M.T. (2013). Upgrading biomass by hydrothermal and chemical conditioning, University of Nevada, Reno.

Reza, M.T., Andert, J., Wirth, B., Busch, D., Pielert, J., Lynam, J.G., Mumme, J. (2014a). Hydrothermal carbonization of biomass for energy and crop production. *Applied Bioenergy*, **1**(1), 11-29.

Reza, M.T., Rottler, E., Herklotz, L., Wirth, B. (2015). Hydrothermal carbonization (HTC) of wheat straw: Influence of feedwater pH prepared by acetic acid and potassium hydroxide. *Bioresource technology*, **182**, 336-344.

Reza, M.T., Uddin, M.H., Lynam, J.G., Hoekman, S.K., Coronella, C.J. (2014b). Hydrothermal carbonization of loblolly pine: reaction chemistry and water balance. *Biomass Conversion and Biorefinery*, **4**(4), 311-321.

Reza, M.T., Yan, W., Uddin, M.H., Lynam, J.G., Hoekman, S.K., Coronella, C.J., Vásquez, V.R. (2013). Reaction kinetics of hydrothermal carbonization of loblolly pine. *Bioresource technology*, **139**, 161-169.

Ríos Saucedo, J.C., Rubilar Pons, R., Cancino Cancino, J., Acuña Carmona, E., Corral Rivas, J.J., Rosales Serna, R. (2018). Basic density of wood and heating value of shoots of three dendro-energy crops. *Revista mexicana de ciencias forestales*, **9**(47), 253-272.

Rizzi, V., D'Agostino, F., Fini, P., Semeraro, P., Cosma, P. (2017). An interesting environmental friendly cleanup: The excellent potential of olive pomace for disperse blue adsorption/desorption from wastewater. *Dyes and Pigments*, **140**, 480-490.

Robinson, T., Bronson, B., Gogolek, P., Mehrani, P. (2016). Comparison of the air-blown bubbling fluidized bed gasification of wood and wood–PET pellets. *Fuel*, **178**, 263-271.

Rodríguez-Sánchez, D.G., Pacheco, A., García-Cruz, M.I., Gutiérrez-Uribe, J.A., Benavides-Lozano, J.A., Hernández-Brenes, C. (2013). Isolation and structure elucidation of avocado seed (Persea americana) lipid derivatives that inhibit Clostridium sporogenes endospore germination. *Journal of agricultural and food chemistry*, **61**(30), 7403-7411.

Rojas, S., Ojeda, M., Herranz, T., Alonso, F.J.P., González, J.M., Ladera, R.M., Fierro, J.L. (Year) of Conference. Producción de combustibles líquidos sintéticos. *Anales de Química*.

Román, S., Libra, J., Berge, N., Sabio, E., Ro, K., Li, L., Ledesma, B., Álvarez, A., Bae, S. (2018). Hydrothermal carbonization: modeling, final properties design and applications: a review. *Energies*, **11**(1), 216.

Román, S., Nabais, J., Laginhas, C., Ledesma, B., González, J. (2012). Hydrothermal carbonization as an effective way of densifying the energy content of biomass. *Fuel Processing Technology*, **103**, 78-83.

Rowell, R.M. (2012). *Handbook of wood chemistry and wood composites*. CRC press.

Roy, C., Pakdel, H., Brouillard, D. (1990). The role of extractives during vacuum pyrolysis of wood. *Journal of Applied Polymer Science*, **41**(1-2), 337-348.

Rubin, E.M. (2008). Genomics of cellulosic biofuels. *Nature*, **454**(7206), 841-845.

Sabio, E., Álvarez-Murillo, A., Román, S., Ledesma, B. (2016). Conversion of tomato-peel waste into solid fuel by hydrothermal carbonization: Influence of the processing variables. *Waste management*, **47**, 122-132.

Safdari, M.-S., Amini, E., Weise, D.R., Fletcher, T.H. (2019). Heating rate and temperature effects on pyrolysis products from live wildland fuels. *Fuel*, **242**, 295-304.

SAGARPA. (2018). Secretaría de Agricultura, Ganadería, Desarrollo Rural, Pesca y Alimentación (México).

Salame, C., Aillerie, M., Papageorgas, P. (2015). The International Conference on Technologies and Materials for Renewable Energy, Environment and Sustainability, Elsevier.

Salanitro, J.P., Diaz, L.A. (1995). Anaerobic biodegradability testing of surfactants. *Chemosphere*, **30**(5), 813-830.

Salgado, J.M., Danieli, F., Regitano-D'Arce, M.A.B., Frias, A., Mansi, D.N. (2008). The Avocado Oil (persea Americana Mill) As A Raw Material For The Food Industry [o óleo De Abacate (persea Americana Mill) Como Matéria-prima Para A Indústria Alimentícia]. *Ciencia e Tecnologia de Alimentos*.

Sánchez, C., Egüés, I., García, A., Llano-Ponte, R., Labidi, J. (2012). Lactic acid production by alkaline hydrothermal treatment of corn cobs. *Chemical Engineering Journal*, **181**, 655-660.

Sánchez, C., Egüés, I., Labidi, J. (2014). Study of different post-hydrolysis methods to improve hemicellulosic monomers extraction. *Biomass Conversion and Biorefinery*, **4**(3), 249-258.

Sasaki, M., Goto, M. (2008). Recovery of phenolic compounds through the decomposition of lignin in near and supercritical water. *Chemical Engineering and Processing: Process Intensification*, **47**(9-10), 1609-1619.

Schaffer, B.A., Wolstenholme, B.N., Whiley, A.W. (2013). *The avocado: botany, production and uses*. CABI.

Scheller, H.V., Ulvskov, P. (2010a). Hemicelluloses. *Annual review of plant biology*, **61**(1), 263-289.

Scheller, H.V., Ulvskov, P. (2010b). Hemicelluloses. *Annual review of plant biology*, **61**(1), 263-289.

Schimmelpfennig, S., Glaser, B. (2012). One step forward toward characterization: some important material properties to distinguish biochars. *Journal of environmental quality*, **41**(4), 1001-1013.

Schulz, H., Beck, K., Erich, E. (1988). Mechanism of the Fischer Tropsch process. in: *Studies in Surface Science and Catalysis*, Vol. 36, Elsevier, pp. 457-471.

Schwald, W., Bobleter, O. (1989). Hydrothermolysis of cellulose under static and dynamic conditions at high temperatures. *Journal of Carbohydrate Chemistry*, **8**(4), 565-578.

Seebauer, V., Petek, J., Staudinger, G. (1997). Effects of particle size, heating rate and pressure on measurement of pyrolysis kinetics by thermogravimetric analysis. *Fuel*, **76**(13), 1277-1282.

Segovia Gómez, F.J., Corral, J.J., Almajano Pablos, M.P. (Year) of Conference. Estudio cinético de la extracción sólido-líquido de los compuestos polifenólicos del residuo del aguacate. *Jornades de recerca EUETIB*. EUETIB. pp. 131-138.

Selvaraju, G., Bakar, N.K.A. (2017). Production of a new industrially viable green-activated carbon from Artocarpus integer fruit processing waste and evaluation of its chemical, morphological and adsorption properties. *Journal of cleaner production*, **141**, 989-999.

Sensöz, S., Can, M. (2002). Pyrolysis of pine (Pinus brutia Ten.) chips: 1. Effect of pyrolysis temperature and heating rate on the product yields. *Energy Sources*, **24**(4), 347-355.

Serbanescu, C. (2014). Kinetic analysis of cellulose pyrolysis: a short review. *Chemical Papers*, **68**(7), 847-860.

Sergeev, A.G., Hartwig, J.F. (2011). Selective, nickel-catalyzed hydrogenolysis of aryl ethers. *Science*, **332**(6028), 439-443.

Sermyagina, E., Saari, J., Kaikko, J., Vakkilainen, E. (2015). Hydrothermal carbonization of coniferous biomass: Effect of process parameters on mass and energy yields. *Journal of Analytical and Applied Pyrolysis*, **113**, 551-556.

Sevilla, M., Fuertes, A.B. (2009a). Chemical and structural properties of carbonaceous products obtained by hydrothermal carbonization of saccharides. *Chemistry–A European Journal*, **15**(16), 4195-4203.

Sevilla, M., Fuertes, A.B. (2009b). The production of carbon materials by hydrothermal carbonization of cellulose. *Carbon*, **47**(9), 2281-2289.

Shafizadeh, F. (1984). The chemistry of pyrolysis and combustion, ACS Publications.

Shafizadeh, F. (1982). Introduction to pyrolysis of biomass. *Journal of Analytical and Applied Pyrolysis*, **3**(4), 283-305.

Shahbandeh, M. (2021). Cocoa bean production worldwide 2018/19 & 2020/21, by country. Retrieved from https://www.statista.com/statistics/263855/cocoa-bean-production-worldwide-by-region/

Sharma, R.K., Hajaligol, M.R. (2003). Effect of pyrolysis conditions on the formation of polycyclic aromatic hydrocarbons (PAHs) from polyphenolic compounds. *Journal of Analytical and Applied Pyrolysis*, **66**(1-2), 123-144.

Sharma, R.K., Wooten, J.B., Baliga, V.L., Lin, X., Chan, W.G., Hajaligol, M.R. (2004). Characterization of chars from pyrolysis of lignin. *Fuel*, **83**(11-12), 1469-1482.

Shehzad, A., Bashir, M.J., Horttanainen, M., Manttari, M., Havukainen, J., Abbas, G. (2018). Modeling and comparative assessment of bubbling fluidized bed gasification system for syngas production–a gateway for a cleaner future in Pakistan. *Environmental technology*, **39**(14), 1841-1850.

Shen, D., Gu, S., Bridgwater, A.V. (2010a). Study on the pyrolytic behaviour of xylan-based hemicellulose using TG–FTIR and Py–GC–FTIR. *Journal of analytical and applied pyrolysis*, **87**(2), 199-206.

Shen, D., Gu, S., Luo, K., Wang, S., Fang, M. (2010b). The pyrolytic degradation of wood-derived lignin from pulping process. *Bioresource technology*, **101**(15), 6136-6146.

Shen, Y., Ma, D., Ge, X. (2017). CO 2-looping in biomass pyrolysis or gasification. *Sustainable Energy & Fuels*, **1**(8), 1700-1729.

Sheng, C., Azevedo, J. (2005). Estimating the higher heating value of biomass fuels from basic analysis data. *Biomass and bioenergy*, **28**(5), 499-507.

Shoji, D., Sugimoto, K., Uchida, H., Itatani, K., Fujie, M., Koda, S. (2005). Visualized kinetic aspects of decomposition of a wood block in sub-and supercritical water. *Industrial & engineering chemistry research*, **44**(9), 2975-2981.

Sialve, B., Bernet, N., Bernard, O. (2009). Anaerobic digestion of microalgae as a necessary step to make microalgal biodiesel sustainable. *Biotechnology advances*, **27**(4), 409-416.

Sik, Y., Chang, S.X., Gao, B., Chung, H.-J. (2015). SMART biochar technology—a shifting paradigm towards advanced materials and healthcare research. *Environmental Technology Innovation*, **4**, 206-209.

Simon, P. (2004). Isoconversional methods. *Journal of Thermal Analysis and Calorimetry*, **76**(1), 123-132.

Sinnott, R., Towler, G. (2019). *Chemical engineering design: SI Edition*. Butterworth-Heinemann.

Slominska, M., Zygler, A., Namiesnik, J. (2012). Soxhlet Extraction and New Developments Such as Soxtec in: Comprehansive Sampling and Sample Preparation.

Slopiecka, K., Bartocci, P., Fantozzi, F. (2012). Thermogravimetric analysis and kinetic study of poplar wood pyrolysis. *Applied Energy*, **97**, 491-497.

Solomon, P.R., Hamblen, D.G., Serio, M.A., Yu, Z.-Z., Charpenay, S. (1993). A characterization method and model for predicting coal conversion behaviour. *Fuel*, **72**(4), 469-488.

Solomon, P.R., Serio, M.A., Suuberg, E.M. (1992). Coal pyrolysis: experiments, kinetic rates and mechanisms. *Progress in energy and combustion science*, **18**(2), 133-220.

Somerville, C., Youngs, H., Taylor, C., Davis, S.C., Long, S.P.J.s. (2010). Feedstocks for lignocellulosic biofuels. **329**(5993), 790-792.

Sousa-Aguiar, E.F., Appel, L.G., Mota, C. (2005). Natural gas chemical transformations: The path to refining in the future. *Catalysis Today*, **101**(1), 3-7.

Spath, P.L., Mann, M.K. (2004). *Life Cycle Assessment of Renewable Hydrogen Production Via Wind/electrolysis*. National Renewable Energy Laboratory Golden.

Stefanidis, S.D., Kalogiannis, K.G., Iliopoulou, E.F., Michailof, C.M., Pilavachi, P.A., Lappas, A.A. (2014). A study of lignocellulosic biomass pyrolysis via the pyrolysis of cellulose, hemicellulose and lignin. *Journal of analytical and applied pyrolysis*, **105**, 143-150.

Stemann, J., Erlach, B., Ziegler, F. (2013a). Hydrothermal carbonisation of empty palm oil fruit bunches: laboratory trials, plant simulation, carbon avoidance, and economic feasibility. *Waste and Biomass Valorization*, **4**(3), 441-454.

Stemann, J., Putschew, A., Ziegler, F. (2013b). Hydrothermal carbonization: process water characterization and effects of water recirculation. *Bioresource technology*, **143**, 139-146.

Stemann, J., Ziegler, F. (Year) of Conference. Assessment of the energetic efficiency of a continuously operating plant for hydrothermal carbonisation of biomass. *World Renewable Energy Congress-Sweden; 8-13 May; 2011; Linköping; Sweden*. Linköping University Electronic Press. pp. 125-132.

Stirling, R.J., Snape, C.E., Meredith, W. (2018). The impact of hydrothermal carbonisation on the char reactivity of biomass. *Fuel processing technology*, **177**, 152-158.

Sun, J., He, F., Pan, Y., Zhang, Z. (2017). Effects of pyrolysis temperature and residence time on physicochemical properties of different biochar types. *Acta Agriculturae Scandinavica, Section B—Soil & Plant Science*, **67**(1), 12-22.

Sun, R., Tomkinson, J., Wang, Y., Xiao, B. (2000). Physico-chemical and structural characterization of hemicelluloses from wheat straw by alkaline peroxide extraction. *Polymer*, **41**(7), 2647-2656.

Sun, Y., Gao, B., Yao, Y., Fang, J., Zhang, M., Zhou, Y., Chen, H., Yang, L. (2014). Effects of feedstock type, production method, and pyrolysis temperature on biochar and hydrochar properties. *Chemical Engineering Journal*, **240**, 574-578.

Symons, G., Buswell, A. (1933). The methane fermentation of carbohydrates1, 2. *Journal of the american chemical society*, **55**(5), 2028-2036.

Tanger, P., Field, J.L., Jahn, C.E., DeFoort, M.W., Leach, J.E.J.F.i.p.s. (2013). Biomass for thermochemical conversion: targets and challenges. **4**, 218.

Taqvi, S.A., Uddin, F., Tufa, L., Memon, I., Hussain, M. (2015). Aspen Plus® simulation of a coal gasification process (geometric analysis). *J Chem Eng Process Technol*, **6**, 264.

Tavakoli, A., Sohrabi, M., Kargari, A. (2008). Application of Anderson–Schulz–Flory (ASF) equation in the product distribution of slurry phase FT synthesis with nanosized iron catalysts. *Chemical Engineering Journal*, **136**(2-3), 358-363.

Thankachan, I., Rupesh, S., Muraleedharan, C. (Year) of Conference. CFD Modelling of Biomass Gasification in Fluidized-Bed Reactor Using the Eulerian-Eulerian Approach. *Applied Mechanics and Materials*. Trans Tech Publ. pp. 1903-1908.

Thrän, D. (2015). Smart Bioenergy: Technologies and concepts for a more flexible bioenergy provision in future energy systems.

Tillman, D., Duong, D., Harding, N.S. (2012). *Solid fuel blending: principles, practices, and problems*. Elsevier.

Tillman, D.A. (2012). *Wood as an energy resource*. Elsevier.

Titirici, M.-M., Antonietti, M. (2010). Chemistry and materials options of sustainable carbon materials made by hydrothermal carbonization. *Chemical Society Reviews*, **39**(1), 103-116.

Titirici, M.-M., Thomas, A., Antonietti, M. (2007). Back in the black: hydrothermal carbonization of plant material as an efficient chemical process to treat the CO 2 problem? *New Journal of Chemistry*, **31**(6), 787-789.

ToolBox, E. (2004). Water - Specific Heat .https://www.engineeringtoolbox.com/specific-heat-capacity-water-d_660.html

Toor, S.S., Rosendahl, L., Rudolf, A. (2011). Hydrothermal liquefaction of biomass: a review of subcritical water technologies. *Energy*, **36**(5), 2328-2342.

Trubetskaya, A. (2016). Fast pyrolysis of biomass at high temperatures, Danmarks Tekniske Universitet, DTU.

Turmanova, S.C., Genieva, S., Dimitrova, A., Vlaev, L. (2008). Non-isothermal degradation kinetics of filled with rise husk ash polypropene composites. *Express Polymer Letters*, **2**(2), 133-146.

Turton, R., Bailie, R.C., Whiting, W.B., Shaeiwitz, J.A. (2008). *Analysis, synthesis and design of chemical processes*. Pearson Education.

Turton, R., Shaeiwitz, J.A., Bailie, R.C., Whiting, W.B. (2018). *Analysis, synthesis and design of chemical processes*. Pearson Education.

Uddin, M.H., Reza, M.T., Lynam, J.G., Coronella, C.J. (2014). Effects of water recycling in hydrothermal carbonization of loblolly pine. *Environmental Progress & Sustainable Energy*, **33**(4), 1309-1315.

Upreti, S.R. (2017). *Process Modeling and Simulation for Chemical Engineers: Theory and Practice*. John Wiley & Sons.

Usman, M., Chen, H., Chen, K., Ren, S., Clark, J.H., Fan, J., Luo, G., Zhang, S. (2019). Characterization and utilization of aqueous products from hydrothermal conversion of biomass for bio-oil and hydro-char production: a review. *Green chemistry*, **21**(7), 1553-1572.

Van Dyk, J., Pletschke, B. (2012). A review of lignocellulose bioconversion using enzymatic hydrolysis and synergistic cooperation between enzymes—factors affecting enzymes, conversion and synergy. *Biotechnology advances*, **30**(6), 1458-1480.

Vasquez, V., Coronella, C. (2009). A simple model for vapor-moisture equilibrium in biomass subtrates. *AIChE journal*, **55**(6), 1595-1603.

Vassilev, S.V., Baxter, D., Andersen, L.K., Vassileva, C.G.J.F. (2010). An overview of the chemical composition of biomass. **89**(5), 913-933.

Veiga, T.R.L.A., Lima, J.T., Dessimoni, A.L.d.A., Pego, M.F.F., Soares, J.R., Trugilho, P.F. (2017). Different plant biomass characterizations for biochar production. *Cerne*, **23**(4), 529-536.

Velazquez-Jimenez, L.H., Pavlick, A., Rangel-Mendez, J.R. (2013). Chemical characterization of raw and treated agave bagasse and its potential as adsorbent of metal cations from water. *Industrial Crops and Products*, **43**, 200-206.

Versteeg, H.K., Malalasekera, W. (2007). *An introduction to computational fluid dynamics: the finite volume method*. Pearson education.

Vickers, N.J. (2017). Animal communication: when i'm calling you, will you answer too? *Current biology*, **27**(14), R713-R715.

Visioli, G., Conti, F.D., Menta, C., Bandiera, M., Malcevschi, A., Jones, D.L., Vamerali, T. (2016). Assessing biochar ecotoxicology for soil amendment by root phytotoxicity bioassays. *Environmental monitoring and assessment*, **188**(3), 166.

Vlaev, L., Georgieva, V., Genieva, S. (2007). Products and kinetics of non-isothermal decomposition of vanadium (IV) oxide compounds. *Journal of Thermal Analysis and Calorimetry*, **88**(3), 805-812.

Vlaev, L., Nedelchev, N., Gyurova, K., Zagorcheva, M. (2008). A comparative study of non-isothermal kinetics of decomposition of calcium oxalate monohydrate. *Journal of Analytical and applied Pyrolysis*, **81**(2), 253-262.

Volpe, M., Fiori, L. (2017). From olive waste to solid biofuel through hydrothermal carbonisation: The role of temperature and solid load on secondary char formation and hydrochar energy properties. *Journal of Analytical and Applied Pyrolysis*, **124**, 63-72.

Volpe, M., Goldfarb, J.L., Fiori, L. (2018). Hydrothermal carbonization of Opuntia ficus-indica cladodes: Role of process parameters on hydrochar properties. *Bioresource technology*, **247**, 310-318.

Volpe, M., Messineo, A., Mäkelä, M., Barr, M.R., Volpe, R., Corrado, C., Fiori, L. (2020). Reactivity of cellulose during hydrothermal carbonization of lignocellulosic biomass. *Fuel Processing Technology*, **206**, 106456.

Vyazovkin, S. (2001). Modification of the integral isoconversional method to account for variation in the activation energy. *Journal of Computational Chemistry*, **22**(2), 178-183.

Wang, C., Wang, F., Yang, Q., Liang, R. (2009a). Thermogravimetric studies of the behavior of wheat straw with added coal during combustion. *Biomass and Bioenergy*, **33**(1), 50-56.

Wang, H., Chu, P.K. (2013). Surface characterization of biomaterials. in: *Characterization of biomaterials*, Elsevier, pp. 105-174.

Wang, J., Shen, B., Kang, D., Yuan, P., Wu, C. (2019). Investigate the interactions between biomass components during pyrolysis using in-situ DRIFTS and TGA. *Chemical Engineering Science*, **195**, 767-776.

Wang, L., Weller, C.L., Jones, D.D., Hanna, M.A. (2008a). Contemporary issues in thermal gasification of biomass and its application to electricity and fuel production. *Biomass and bioenergy*, **32**(7), 573-581.

Wang, L., Weller, C.L., Jones, D.D., Hanna, M.A. (2008b). Contemporary issues in thermal gasification of biomass and its application to electricity and fuel production. *Biomass bioenergy*

, **32**(7), 573-581.

Wang, Q., Sarkar, J. (2018). Pyrolysis behaviors of waste coconut shell and husk biomasses. *Towards Energy Sustainability*, 111.

Wang, S., Wang, K., Liu, Q., Gu, Y., Luo, Z., Cen, K., Fransson, T. (2009b). Comparison of the pyrolysis behavior of lignins from different tree species. *Biotechnology Advances*, **27**(5), 562-567.

Wang, T., Zhai, Y., Zhu, Y., Li, C., Zeng, G. (2018). A review of the hydrothermal carbonization of biomass waste for hydrochar formation: Process conditions, fundamentals, and physicochemical properties. *Renewable and Sustainable Energy Reviews*, **90**, 223-247.

Wang, X., Hu, M., Hu, W., Chen, Z., Liu, S., Hu, Z., Xiao, B. (2016). Thermogravimetric kinetic study of agricultural residue biomass pyrolysis based on combined kinetics. *Bioresource technology*, **219**, 510-520.

Wang, Y., Yan, L. (2008). CFD studies on biomass thermochemical conversion. *International journal of molecular sciences*, **9**(6), 1108-1130.

Ward-Smith, A. (1985). A mathematical theory of running, based on the first law of thermodynamics, and its application to the performance of world-class athletes. *Journal of biomechanics*, **18**(5), 337-349.

Weggler, B.A., Gruber, B., Teehan, P., Jaramillo, R., Dorman, F.L. (2020). Inlets and sampling. in: *Separation Science and Technology*, Vol. 12, Elsevier, pp. 141-203.

Welfle, A.J. (2015). Biomass Resource Analyses & Future Bioenergy Scenarios.

Wen, C. (1968). Noncatalytic heterogeneous solid-fluid reaction models. *Industrial & Engineering Chemistry*, **60**(9), 34-54.

Wen, C.Y., Chaung, T. (1979). Entrainment coal gasification modeling. *Industrial & Engineering Chemistry Process Design and Development*, **18**(4), 684-695.

Werman, M., Neeman, I. (1987). Avocado oil production and chemical characteristics. *Journal of the American Oil Chemists' Society*, **64**(2), 229-232.

Werner, K., Pommer, L., Broström, M. (2014). Thermal decomposition of hemicelluloses. *Journal of Analytical and Applied Pyrolysis*, **110**, 130-137.

White, F.M. (1986). Compressible flow. *Fluid mechanics*.

White, J.E., Catallo, W.J., Legendre, B.L. (2011). Biomass pyrolysis kinetics: a comparative critical review with relevant agricultural residue case studies. *Journal of analytical and applied pyrolysis*, **91**(1), 1-33.

Widyawati, M., Church, T.L., Florin, N.H., Harris, A.T. (2011). Hydrogen synthesis from biomass pyrolysis with in situ carbon dioxide capture using calcium oxide. *International journal of hydrogen energy*, **36**(8), 4800-4813.

Wiedner, K., Rumpel, C., Steiner, C., Pozzi, A., Maas, R., Glaser, B. (2013). Chemical evaluation of chars produced by thermochemical conversion (gasification, pyrolysis and hydrothermal

carbonization) of agro-industrial biomass on a commercial scale. *Biomass and Bioenergy*, **59**, 264-278.

Wiley, V. (2017). *Ullmann's Energy: Resources, Processes, Products*, pp. 341.

Wilk, V., Hofbauer, H. (2013). Co-gasification of plastics and biomass in a dual fluidized-bed steam gasifier: possible interactions of fuels. *Energy & Fuels*, **27**(6), 3261-3273.

Wirth, B., Mumme, J., Erlach, B. (Year) of Conference. Anaerobic treatment of waste water derived from hydrothermal carbonization. *20th European Biomass Conference and Exhibition*. pp. 18-22.

Wongsiriamnuay, T., Tippayawong, N. (2010). Non-isothermal pyrolysis characteristics of giant sensitive plants using thermogravimetric analysis. *Bioresource Technology*, **101**(14), 5638-5644.

Wood, E. (2008). The Science of Chocolate, Taylor & Francis.

Wu, S., Lou, R., Lv, G. (2010). Analysis of wheat straw lignin by thermogravimetry and pyrolysis–gas chromatography/mass spectrometry. *Journal of Analytical and Applied Pyrolysis*, **87**(1), 65-69.

Wu, Y.-m., Zhao, Z.-l., Li, H.-b., Fang, H. (2009). Low temperature pyrolysis characteristics of major components of biomass. *Journal of Fuel Chemistry and Technology*, **37**(4), 427-432.

Wüst, D., Correa, C.R., Jung, D., Zimmermann, M., Kruse, A., Fiori, L. (2019). Understanding the influence of biomass particle size and reaction medium on the formation pathways of hydrochar. *Biomass Conversion and Biorefinery*, 1-24.

Xiao, L.-P., Shi, Z.-J., Xu, F., Sun, R.-C. (2012). Hydrothermal carbonization of lignocellulosic biomass. *Bioresource technology*, **118**, 619-623.

Xie, L., Zhu, L.T., Luo, Z.H., Jiang, C.W. (2017). Multiscale modeling of mixing behavior in a 3D atom transfer radical copolymerization stirred-tank reactor. *Macromolecular Reaction Engineering*, **11**(2), 1600022.

Xin, S., Yang, H., Chen, Y., Yang, M., Chen, L., Wang, X., Chen, H. (2015). Chemical structure evolution of char during the pyrolysis of cellulose. *Journal of analytical and applied pyrolysis*, **116**, 263-271.

Xiu, S., Shahbazi, A., Shirley, V., Cheng, D. (2010). Hydrothermal pyrolysis of swine manure to bio-oil: effects of operating parameters on products yield and characterization of bio-oil. *Journal of analytical and applied pyrolysis*, **88**(1), 73-79.

Xu, F., Yu, J., Tesso, T., Dowell, F., Wang, D. (2013). Qualitative and quantitative analysis of lignocellulosic biomass using infrared techniques: a mini-review. *Applied Energy*, **104**, 801-809.

Xu, X., Xiao, Y., Qiao, C. (2007). System design and analysis of a direct hydrogen from coal system with CO2 capture. *Energy & fuels*, **21**(3), 1688-1694.

Xue, Q., Fox, R.O. (2015). Computational modeling of biomass thermochemical conversion in fluidized beds: particle density variation and size distribution. *Industrial & Engineering Chemistry Research*, **54**(16), 4084-4094.

Xue, Q., Heindel, T., Fox, R. (2011). A CFD model for biomass fast pyrolysis in fluidized-bed reactors. *Chemical Engineering Science*, **66**(11), 2440-2452.

Xue, X., Chen, D., Song, X., Dai, X. (2015). Hydrothermal and pyrolysis treatment for sewage sludge: choice from product and from energy benefit. *Energy Procedia*, **66**, 301-304.

Yan, B.-H., Cao, C.-X., Cheng, Y., Jin, Y., Cheng, Y. (2014a). Experimental investigation on coal devolatilization at high temperatures with different heating rates. *Fuel*, **117**, 1215-1222.

Yan, Q., Li, J., Zhang, X., Wang, C., Zhang, J., Cai, Z. (2018). Catalytic graphitization of kraft lignin to graphene-based structures with four different transitional metals. *Journal of Nanoparticle Research*, **20**(9), 1-20.

Yan, W., Acharjee, T.C., Coronella, C.J., Vasquez, V.R. (2009). Thermal pretreatment of lignocellulosic biomass. *Environmental Progress & Sustainable Energy: An Official Publication of the American Institute of Chemical Engineers*, **28**(3), 435-440.

Yan, W., Hastings, J.T., Acharjee, T.C., Coronella, C.J., Vásquez, V.R. (2010). Mass and energy balances of wet torrefaction of lignocellulosic biomass. *Energy & Fuels*, **24**(9), 4738-4742.

Yan, W., Hoekman, S.K., Broch, A., Coronella, C.J. (2014b). Effect of hydrothermal carbonization reaction parameters on the properties of hydrochar and pellets. *Environmental Progress & Sustainable Energy*, **33**(3), 676-680.

Yan, W., Perez, S., Sheng, K. (2017). Upgrading fuel quality of moso bamboo via low temperature thermochemical treatments: dry torrefaction and hydrothermal carbonization. *Fuel*, **196**, 473-480.

Yaneva, Z., Georgieva, N. (2018). Physicochemical and morphological characterization of pharmaceutical nanocarriers and mathematical modeling of drug encapsulation/release mass transfer processes. in: *Nanoscale Fabrication, Optimization, Scale-Up and Biological Aspects of Pharmaceutical Nanotechnology*, Elsevier, pp. 173-218.

Yang, H., Yan, R., Chen, H., Lee, D.H., Liang, D.T., Zheng, C. (2006a). Mechanism of palm oil waste pyrolysis in a packed bed. *Energy & Fuels*, **20**(3), 1321-1328.

Yang, H., Yan, R., Chen, H., Lee, D.H., Liang, D.T., Zheng, C. (2006b). Pyrolysis of palm oil wastes for enhanced production of hydrogen rich gases. *Fuel processing technology*, **87**(10), 935-942.

Yang, H., Yan, R., Chen, H., Lee, D.H., Zheng, C. (2007). Characteristics of hemicellulose, cellulose and lignin pyrolysis. *Fuel*, **86**(12-13), 1781-1788.

Yang, H., Yan, R., Chen, H., Zheng, C., Lee, D.H., Liang, D.T. (2006c). In-depth investigation of biomass pyrolysis based on three major components: hemicellulose, cellulose and lignin. *Energy & Fuels*, **20**(1), 388-393.

Yang, J., Rizkiana, J., Widayatno, W.B., Karnjanakom, S., Kaewpanha, M., Hao, X., Abudula, A., Guan, G. (2016a). Fast co-pyrolysis of low density polyethylene and biomass residue for oil production. *Energy conversion and management*, **120**, 422-429.

Yang, W., Shimanouchi, T., Kimura, Y. (2015). Characterization of the residue and liquid products produced from husks of nuts from Carya cathayensis sarg by hydrothermal carbonization. *ACS Sustainable Chemistry & Engineering*, **3**(4), 591-598.

Yang, W., Shimanouchi, T., Wu, S., Kimura, Y. (2014). Investigation of the degradation kinetic parameters and structure changes of microcrystalline cellulose in subcritical water. *Energy & fuels*, **28**(11), 6974-6980.

Yang, W., Wang, H. (2016). Fuel properties and combustion kinetics of hydrochar prepared by hydrothermal carbonization of bamboo. *Bioresource technology*, **205**, 199-204.

Yang, W., Wang, H., Zhang, M., Zhu, J., Zhou, J. (2016b). Fuel properties and combustion kinetics of hydrochar prepared by hydrothermal carbonization of bamboo. *Bioresource technology*, **205**, 199-204.

Yao, Z., Yu, S., Su, W., Wu, W., Tang, J., Qi, W. (2020). Kinetic studies on the pyrolysis of plastic waste using a combination of model-fitting and model-free methods. *Waste Management & Research*, **38**(1_suppl), 77-85.

Yates, I.C., Satterfield, C.N. (1991). Intrinsic kinetics of the Fischer-Tropsch synthesis on a cobalt catalyst. *Energy & fuels*, **5**(1), 168-173.

Yin, C.-Y. (2011). Prediction of higher heating values of biomass from proximate and ultimate analyses. *Fuel*, **90**(3), 1128-1132.

Yousefifar, A., Farid, M.M., Gapes, D.J., Young, B.R. (2020). An improved model for the kinetics of non-oxidative hydrothermal process. *Journal of environmental management*, **253**, 109704.

Yu, Y., Lou, X., Wu, H. (2008). Some recent advances in hydrolysis of biomass in hot-compressed water and its comparisons with other hydrolysis methods. *Energy & fuels*, **22**(1), 46-60.

Yuan, T., Tahmasebi, A., Yu, J. (2015). Comparative study on pyrolysis of lignocellulosic and algal biomass using a thermogravimetric and a fixed-bed reactor. *Bioresource Technology*, **175**, 333-341.

Yusof, F., Khanahmadi, S., Amid, A., Mahmod, S.S. (2016). Cocoa pod husk, a new source of hydrolase enzymes for preparation of cross-linked enzyme aggregate. *Springerplus*, **5**(1), 1-18.

Zeng, J., Xiao, R., Zhang, H., Chen, X., Zeng, D., Ma, Z. (2017). Syngas production via biomass self-moisture chemical looping gasification. *Biomass and Bioenergy*, **104**, 1-7.

Zeng, X., Ueki, Y., Yoshiie, R., Naruse, I., Wang, F., Han, Z., Xu, G. (2020). Recent progress in tar removal by char and the applications: A comprehensive analysis. *Carbon Resources Conversion*, **3**, 1-18.

Zhang, B., Heidari, M., Regmi, B., Salaudeen, S., Arku, P., Thimmannagari, M., Dutta, A. (2018). Hydrothermal carbonization of fruit wastes: A promising technique for generating hydrochar. *Energies*, **11**(8), 2022.

Zhang, D., Liu, P., Lu, X., Wang, L., Pan, T. (2016). Upgrading of low rank coal by hydrothermal treatment: Coal tar yield during pyrolysis. *Fuel Processing Technology*, **141**, 117-122.

Zhang, L., Liu, S., Wang, B., Wang, Q., Yang, G., Chen, J. (2015a). Effect of residence time on hydrothermal carbonization of corn cob residual. *BioResources*, **10**(3), 3979-3986.

Zhang, X., Li, Y., Wang, M., Han, L., Liu, X. (2019). Effects of Hydrothermal Carbonization Conditions on the Combustion and Kinetics of Wheat Straw Hydrochar Pellets and Efficiency Improvement Analyses. *Energy & Fuels*, **34**(1), 587-598.

Zhang, Y. (2010). Hydrothermal liquefaction to convert biomass into crude oil. *Biofuels from agricultural wastes and byproducts*, **42**(37), 201-232.

Zhang, Y., Liu, C., Chen, X. (2015b). Unveiling the initial pyrolytic mechanisms of cellulose by DFT study. *Journal of analytical and applied pyrolysis*, **113**, 621-629.

Zhang, Y., Zhao, Y., Gao, X., Li, B., Huang, J. (2015c). Energy and exergy analyses of syngas produced from rice husk gasification in an entrained flow reactor. *Journal of Cleaner Production*, **95**, 273-280.

Zhang, Y., Zhao, Y., Li, B., Gao, X., Jiang, B. (2017). Energy and exergy characteristics of syngas produced from air gasification of walnut sawdust in an entrained flow reactor. *International Journal of Exergy*, **23**(3), 244-262.

Zhao, C., Jiang, E., Chen, A. (2017). Volatile production from pyrolysis of cellulose, hemicellulose and lignin. *Journal of the Energy Institute*, **90**(6), 902-913.

Zhou, C.-H., Xia, X., Lin, C.-X., Tong, D.-S., Beltramini, J.J.C.S.R. (2011). Catalytic conversion of lignocellulosic biomass to fine chemicals and fuels. **40**(11), 5588-5617.

Zhou, H., Long, Y., Meng, A., Chen, S., Li, Q., Zhang, Y. (2015a). A novel method for kinetics analysis of pyrolysis of hemicellulose, cellulose, and lignin in TGA and macro-TGA. *Rsc Advances*, **5**(34), 26509-26516.

Zhou, H., Wu, C., Onwudili, J.A., Meng, A., Zhang, Y., Williams, P.T. (2015b). Effect of interactions of PVC and biomass components on the formation of polycyclic aromatic hydrocarbons (PAH) during fast co-pyrolysis. *RSC advances*, **5**(15), 11371-11377.

Zhou, S., Pecha, B., van Kuppevelt, M., McDonald, A.G., Garcia-Perez, M. (2014a). Slow and fast pyrolysis of Douglas-fir lignin: Importance of liquid-intermediate formation on the distribution of products. *Biomass and Bioenergy*, **66**, 398-409.

Zhou, X., Nolte, M.W., Mayes, H.B., Shanks, B.H., Broadbelt, L.J. (2014b). Experimental and mechanistic modeling of fast pyrolysis of neat glucose-based carbohydrates. 1. Experiments and development of a detailed mechanistic model. *Industrial & Engineering Chemistry Research*, **53**(34), 13274-13289.

Zhu, C., Krumm, C., Facas, G.G., Neurock, M., Dauenhauer, P.J. (2017). Energetics of cellulose and cyclodextrin glycosidic bond cleavage. *Reaction Chemistry & Engineering*, **2**(2), 201-214.

Zhu, C., Maduskar, S., Paulsen, A.D., Dauenhauer, P.J. (2016). Alkaline-Earth-Metal-Catalyzed Thin-Film Pyrolysis of Cellulose. *ChemCatChem*, **8**(4), 818-829.

Zhu, L., Zhang, Y., Lei, H., Zhang, X., Wang, L., Bu, Q., Wei, Y. (2018). Production of hydrocarbons from biomass-derived biochar assisted microwave catalytic pyrolysis. *Sustainable Energy & Fuels*, **2**(8), 1781-1790.

Zhuang, X., Song, Y., Zhan, H., Yin, X., Wu, C. (2020). Gasification performance of biowaste-derived hydrochar: The properties of products and the conversion processes. *Fuel*, **260**, 116320.

Zinoviev, S., Müller-Langer, F., Das, P., Bertero, N.s., Fornasiero, P., Kaltschmitt, M., Centi, G., Miertus, S. (2010). Next-generation biofuels: survey of emerging technologies and sustainability issues. *ChemSusChem*, **3**(10), 1106-1133.

Zizlavsky, O. (2014). Net present value approach: method for economic assessment of innovation projects. *Procedia-Social and Behavioral Sciences*, **156**, 506-512.

Publication of scientific papers

Bioresource Technology Reports xx (2021) 100xxx

Contents lists available at ScienceDirect

Bioresource Technology Reports

journal homepage: www.sciencedirect.com/journal/bioresource-technology-reports

Quantification and Kinetic Study of the Main Compounds in Biocrude Produced by Hydrothermal Carbonization of Lignocellulosic Biomass

Diakaridia Sangare[a,b], Stéphane Bostyn[a,c], Mario Moscosa-Santillan[b,*], Verónica Belandria[a,c], Iskender Gökalp[a]

[a] Institut de Combustion, Aérothermique, Réactivité et Environnement (ICARE)-CNRS UPR3021, 1C avenue de la Recherche Scientifique, 45071 Orléans Cedex 2, France
[b] Facultad de Ciencias Químicas Universidad Autónoma de San Luis Potosí Av. Dr. Nava # 6, Zona Universitaria, San Luis Potosí, C.P. 78210, México
[c] Université d'Orléans, Institut Universitaire de Technologie, 16 rue d'Issoudun, BP16724, 45067 Orléans Cedex 2, France

ARTICLEINFO

Keywords:
Agave bagasse
Avocado stone
Biocrude
Hydrothermal carbonization
Kinetic model

ABSTRACT

The biomass hydrothermal carbonization (HTC) reaction pathway to the formation of primary and secondary hydrochar is proposed in this study. Total sugars were the main product in biocrude at low temperature; their concentration decreased as the temperature increased, producing organic acids and furans. Kinetic study reveals that the hydrolysis activation energy increased as hemicellulose content decreased. Indeed, a value of 63.08 kJ/mol was found for biomass rich in hemicellulose (avocado stone) while for biomass composed of a hemicellulose-cellulose mixture (agave bagasse) the value was -85.02 kJ/mol, and for α-cellulose it was -136.24 kJ/mol. Contrastively, the activation energy for furans formation was higher than that for organic acids in any case. A proposed14-reactions mechanism adequately describes the HTC process considering intermediate to final products (R^2>0.98). The higher heating value (HHV) of hydrochars was between 22 and 26 MJ/kg, with an energy densification of 34 to 49 % compared to the corresponding feedstock.

1. Introduction

Hydrothermal carbonization is a method of thermochemical conversion by which wet biomass is heated in a batch autoclave reactor to temperatures from 180 °C to 250 °C, under autogenous pressure of saturated vapor from 1 to 4 MPa and reaction time or holding time from a few minutes to several hours (Liu and Balasubramanian, 2012; Missaoui et al., 2017; Tradler et al., 2018). The main HTC product is hydrochar; however, a large amount of by-product is generated as liquid (biocrude mixed with water) and small gas fractions (Becker et al., 2014). Recently, different biomasses have been investigated to produce hydrochar. Nevertheless, the quality of hydrochar obtained depends principally on the types of biomasses and operating conditions of the process. The hydrochar obtained is a solid material rich in carbon (55–74% carbon), stable, a lignite-like material that is characterized by a high heating value (21.1–30.6 MJ/kg) (Sangare et al., 2020b); its physical, chemical and mechanical properties make it susceptible to different uses. Hydrochar has wide applications; in agriculture, for soil amendment purposes (Kambo and Dutta, 2015), supercapacitor and CO2 capture (Demir et al., 2018), or as a fuel source (Libra et al., 2011). During the HTC process, hydrochar formation can be carried out in two reaction pathways. The formation can proceed from the reaction of the solid-solid pathway known as primary hydrochar (P-HC) and the intermediate products called secondary hydrochar (S-HC). In the HTC process of cellulose, it has been reported that the solid-solid reaction pathway was the dominant reaction due to the large aromatic groups in the hydrochar structure (Falco et al., 2011). However, secondary hydrochar formation may be favored by a high content of 5-hydroxymethylfurfural (5-HMF) in HTC liquid (Chuntanapum and Matsumura, 2009). Furthermore, Paksung et al. (2020) reported that it is not easy to distinguish analytically between P-HC and S-HC; because both appear as a single solid mass of char.

Under HTC process conditions, water behaves like an organic solvent. Indeed, it acts as a catalyst for biomass reactions, such as hydrolysis, decarboxylation, dehydration, condensation, aromatization, and polymerization (Kambo and Dutta, 2015; Volpe et al., 2018). The main products of the HTC process are solid hydrochar and a liquid by-product containing several valuable organic compounds, such as sugars (pentoses and hexoses), furans (furfural and 5-HMF), organic acid mixtures (formic, acetic, lactic), as well asphenolic products and their derivatives (phenol, gallic acid, catechol, and p-cresol) (Fujimoto et al., 2018; Kambo et al., 2018; Kang et al., 2012). The concentration of these compounds depends on the type of biomass and the operating conditions. However, their valorization in biorefineries requires their identification and recovery process, as well as knowing the chemical mechanism of formation and reaction kinetics (Kambo and Dutta, 2015).

The biomass conversion process by HTC has been largely investigated. However, the main challenge remains the process design and the operating conditions optimization. This is because reaction pathway and kinetics are still largely unknown. Even though different approaches are currently used to

* Corresponding author.
E-mail address: mario.moscosa@uaslp.mx (M. Moscosa-Santillan).

Energy 219 (2021) 119635

Contents lists available at ScienceDirect

Energy

journal homepage: www.elsevier.com/locate/energy

Hydrodynamics, heat transfer and kinetics reaction of CFD modeling of a batch stirred reactor under hydrothermal carbonization conditions

Diakaridia Sangare [a, b], Stéphane Bostyn [b, c, *], Mario Moscosa-Santillan [a], Iskender Gökalp [b]

[a] Facultad de Ciencias Químicas Universidad Autónoma de San Luis Potosí Av. Dr. Nava # 6, Zona Universitaria San Luis Potosí, S.L.P., CP: 78210, Mexico
[b] Institut de Combustion, Aérothermique, Réactivité, et Environnement (ICARE)-CNRS UPR3021, 1C Avenue de La Recherche Scientifique, Orléans Cedex 2, 45071, France
[c] Université D'Orléans, Institut Universitaire de Technologie, 16 Rue D'Issoudun BP16724 45067 Orléans Cedex 2, France

ARTICLE INFO

Article history:
Received 3 September 2020
Received in revised form
9 November 2020
Accepted 15 December 2020
Available online 22 December 2020

Keywords:
Avocado stone
Hydrothermal carbonization
CFD Modeling
Stirred reactor
Open-loop controller system
Hydrodynamics
Heat transfer
Kinetic model

ABSTRACT

Computational Fluid Dynamics simulation was used to study hydrothermal carbonization of avocado stone (AS) in a batch stirred reactor, using an open-loop controller system. The corresponding simulations were carried out in COMSOL Multiphysics 5.2. The different biomass-to-water ratio was investigated. The hydrodynamic study shows that the ideal stirring speed to obtain a homogeneous mixture inside the reactor is 550 rpm, due to the high density of AS particles (1547.64 ± 27.33 kg/m^3). However, a stagnant zone was observed just below the impeller. To validate the CFD simulations temperature profiles with experimental data, the heat transfer coefficient of the insulator was determined (11.66 W/m^2.K), this value was used to set the heat loss in the CFD simulation. According to the model, the difference between the thermal properties of biomass and water under hydrothermal carbonization conditions is negligible. However, experimentally, an increase in temperature was observed with increasing biomass to-water-ratio; this is due to the global hydrothermal carbonization of AS is exothermic reaction. The heat released during 8 h, including heat-up time, was −7.25 ± 0.32 MJ/kg of feedstock. Finally, a kinetic model was proposed taking into account the influence of temperature, heat-up time, reactor volume, and biomass concentration.

© 2020 Elsevier Ltd. All rights reserved.

1. Introduction

The production of clean and sustainable fuels is the main challenge of the upcoming energy crisis and climate change. The potential of lignocellulosic biomass as an abundant source of renewable energy. Although there are different processes to convert biomass into energy, its direct use as fuel, faces several challenges (inefficiency of conversion facility, low-energy, biological instability, high moisture content, and so forth [1]. Pretreatment processes are necessary to improve the organic feedstock characteristics for most biomass to energy conversion processes.

Hydrothermal carbonization (HTC), also known as a wet thermochemical process, emulates the natural process of coalification, virtually no pretreatment is required [2]. HTC is a thermochemical conversion process by which biomass is converted into carbonized material (hydrochar), liquid (bio-oil mixed with water) and small fractions of gases; this process is performed in the temperature range of 180–250 °C under autogenous saturated vapor pressure between 10 and 40 bars, and a residence time range from a few minutes up to several hours [3–5]. The performance and composition of the final products are directly related to biomass type, and process conditions such as reaction temperature, residence time, and water-to-biomass ratio. HTC process has investigated distinct types of biomass; sugarcane bagasse [6], corn cob [7], tomato waste [8], olive pomace [4], olive stones [9], and so forth. Most of these biomasses are agro-industrial wastes, in Mexico, one of the most significant agro-industrial wastes generated is avocado stones (AS). The products of HTC can be used directly as a solid fuel, soil amendment, and so on [10–12].

* Corresponding author. Institut de Combustion, Aérothermique, Réactivité, et Environnement (ICARE)-CNRS UPR3021, 1C avenue de la recherche scientifique, 45071, Orléans Cedex 2, France.
E-mail address: stephane.bostyn@univ-orleans.fr (S. Bostyn).

https://doi.org/10.1016/j.energy.2020.119635
0360-5442/© 2020 Elsevier Ltd. All rights reserved.

AIMS Energy, 8(4): 538–562.
DOI: 10.3934/energy.2020.4.538
Received: 22 April 2020
Accepted: 18 June 2020
Published: 28 June 2020

http://www.aimspress.com/journal/energy

Research article

Modeling of *Agave Salmiana* bagasse conversion by hydrothermal carbonization (HTC) for solid fuel combustion using surface response methodology

Diakaridia Sangare[1,2], Ayoub Missaoui[2], Stéphane Bostyn[2,3,*], Verónica Belandria[2,3], Mario Moscosa-Santillan[1] and Iskender Gökalp[2]

[1] Facultad de Ciencias Químicas Universidad Autónoma de San Luis Potosí Av. Dr. Nava # 6, Zona Universitaria San Luis Potosí, S.L.P., México 78210
[2] Institut de Combustion, Aérothermique, Réactivité, et Environnement (ICARE)-CNRS UPR3021, 1C avenue de la recherche scientifique 45071 Orléans Cedex 2, France
[3] Université d'Orléans, Institut Universitaire de Technologie, 16 rue d'Issoudun BP16724 45067 Orléans Cedex 2, France

* **Correspondence:** Email: stephane.bostyn@univ-orleans.fr; Tel: +33238255476; Fax: +33238696004.

Abstract: Hydrothermal carbonization (HTC) of *Agave Salmiana* bagasse was investigated to assess the potential of hydrochar as an energy resource. The effect of operating conditions on the mass yield and the energy quality of hydrochar was examined by varying the temperature and the holding time over the ranges of 180–250 °C (T) and 0–60 min (t), respectively. These parameters were screened using the response surface methodology through a Doehlert design. Performances of HTC were assessed on the basis of the hydrochar mass yield higher heating value ultimate and proximate analyses. In the studied domain, the modeling results indicated that the hydrochar mass yield varies between 45% and 86% and higher heating valuesfrom18 to 23 $MJ.kg^{-1}$, which is similar to that of peat. In addition, the volatile matter and fixed carbon fractions of hydrochars ranged from 54 to 80% and between 12 and 36%, respectively. Energy yield modeling indicated that the mass yield is the most influent parameter. The maximal energy yield value was obtained at 180 °C with time equal to 0 min. Globally, the evolution of H/C ratio is amplified for temperatures greater than 215 °C by increasing the holding time from 30 to 60 min. For O/C ratio the maximal variation is below these conditions. It is concluded that increased hydrothermal carbonization conditions favor dehydration reactions, while decarboxylation reactions are favored in mild HTC conditions. The combustion characteristics such as ignition peak and burnout temperatures were significantly modified for hydrochars. The model results

In the process of publication

Kinetic Studies of Hydrothermal Carbonization of Avocado Stone and Analysis of the Polycyclic Aromatic Hydrocarbon Contents in the Hydrochars Produced.

Diakaridia Sangare [a,b], Agnes Chartier [c], Mario Moscosa-Santillan [a], Iskender Gökalp [b], Stéphane Bostyn [b,d,*]

[a] Facultad de Ciencias Químicas Universidad Autónoma de San Luis Potosí Av. Dr. Nava # 6, Zona Universitaria San Luis Potosí, S.L.P., CP: 78210, México

[b] Institut de Combustion, Aérothermique, Réactivité, et Environnement (ICARE)-CNRS UPR3021, 1C avenue de la recherche scientifique 45071 Orléans Cedex 2, France

[c] Institut de Chimie Organique et Analytique (ICOA), Université d'Orléans-CNRS, 8 Rue de Chartres BP 6759, 45067 Orléans cedex 2, France

[d] Université d'Orléans, Institut Universitaire de Technologie, 16 rue d'Issoudun BP16724 45067 Orléans Cedex 2, France

* Correspondence: Email: stephane.bostyn@univ-orleans.fr; Tel: +33238255476; Fax: +33238696004.

Abstract:

Model-free and model-fitting kinetic approaches were used to investigate the hydrothermal carbonization of avocado stone. The kinetic parameters and reaction mechanism were determined in two temperature zones, from 150 to 210 ºC and 210 to 250 ºC. In the first zone, the decomposition of avocado stone during the hydrothermal carbonization process followed a random nucleation reaction mechanism (Avrami-Erofeev-1) with the activation energy of 87.84 ± 3.28 kJ/mol. In contrast, in the second zone, it followed a first-order reaction model, and the activation energy was 230.96 ± 28.84 kJ/mol. Analysis of PAHs with gas chromatography-mass spectrometry showed that the number of PAHs in the hydrochar increases with an increase in temperature from 190 to 250 ºC. The 3-4 rings PAHs were dominant in the hydrochars prepared at a temperature between 230 and 250 ºC, while two rings were largely prevalent in the hydrochar obtained at low temperatures.

Keywords: Avocado stone; Hydrothermal carbonization; Kinetic model; PAHs

Pyro-gasification of Biomass: Use of TGA Coupled to µ-GC for Analysis and Quantification of Gas Evolution.

Diakaridia Sangare[1,2], Stéphane Bostyn[2,3*], Mario Moscosa-Santillan[1,*], Verónica Belandria[2,3] Iskender Gökalp[2]

[1] Facultad de Ciencias Químicas Universidad Autónoma de San Luis Potosí Av. Dr. Nava # 6, Zona Universitaria San Luis Potosí, S.L.P., CP: 78210, México

[2] Institut de Combustion, Aérothermique, Réactivité, et Environnement (ICARE)-CNRS UPR3021, 1C avenue de la recherche scientifique 45071 Orléans Cedex 2, France

[3] Université d'Orléans, Institut Universitaire de Technologie, 16 rue d'Issoudun BP16724 45067 Orléans Cedex 2, France

* Correspondence: Email: stephane.bostyn@univ-orleans.fr; Tel: +33238255476; Fax: +33238696004.

ABSTRACT:

This study is focused on the pyro-gasification of agave salmiana bagasse (AB) and cellulose by employing a combined thermogravimetry and gas chromatography experimental setup. The thermogravimetric analysis (TGA), and derivative thermogravimetry (DTG) were performed to examine the thermal degradation of both biomasses. The product gas composition (CO, CO_2, CH_4 and H_2) produced during pyro-gasification was analyzed systematically by using an online and offline TCD-micro gas chromatograph (µ-GC) analyzer. The influence of different air to biomass ratio (ABR) and heating rate on product gas composition was investigated during AB pyro-gasification. The thermal behavior and the evolution of the gases produced during the pyrolysis of both biomasses showed that significant part of CO and CO_2 were mainly released at a temperature below 450 °C and followed almost the same pattern. The CH_4 started to evolve at a temperature above 300 °C, while the maximum H_2 production was obtained between 600-700 ºC. The experimental results showed that with an increment in ABR from 0.125 to 1.0, the combustible gases composition of H_2, CO, CH_4 decreased in the range of 26.27–7.02 mol.%, 27.38–11.39 mol.%, 5.92–2.07 mol.% while the fraction of non-combustibles gases was increased from 14.78 to 19.8 mol.% and 24.56 to 59.71 mol.% for CO_2 and N_2, respectively.

Hydrothermal Carbonization of biomass: Laboratory Trials, Energy balance, Process Simulation, Design and Cost Analysis*

Diakaridia Sangare[1,2], Stéphane Bostyn[2,3], Mario Moscosa-Santillan[1,*], ….

[1] Facultad de Ciencias Químicas Universidad Autónoma de San Luis Potosí Av. Dr. Nava # 6, Zona Universitaria San Luis Potosí, S.L.P., CP: 78210, México

[2] Institut de Combustion, Aérothermique, Réactivité, et Environnement (ICARE)-CNRS UPR3021, 1C avenue de la recherche scientifique 45071 Orléans Cedex 2, France

[3] Université d'Orléans, Institut Universitaire de Technologie, 16 rue d'Issoudun BP16724 45067 Orléans Cedex 2, France

* Correspondence: Email: mario.moscosa@uaslp.mx ; Tel: +33238255476; Fax: +33238696004.

ABSTRACT:

The energy balance of the hydrothermal carbonization (HTC) process is fundamental to determining the application of hydrochar as an energy source. In this work, an HTC process is designed and modeled from experimental data obtained for two representative agro-industrial wastes: avocado stone (AS) and cocoa shell (CS). The process was simulated, including all the steps and equipment necessary to convert these biomasses into dry hydrochar and pellets. The energy balance study of the process showed that the energy efficiency of the process can reach 83.12% for AS and 71.36% for CS, while the thermal efficiencies were 4.12 for AS and 4.49 for CS. The result of the simulation allowed that the HTC process is economically feasible and competitive price of pelletized hydrochar compared to palletized bulk pine wood. Moreover, under the conditions studied, the initial capital recovery period (CRP) is lower at 3.8 years for each of the biomasses. This study could encourage the development of HTC plants and, therefore, the market for hydrochar pellets.